Lecture Notes in Physics

The Lecture Notes in Physics

The series Lecture Notes in Physics (LNP), founded in 1969, reports new developments in physics research and teaching – quickly and informally, but with a high quality and the explicit aim to summarize and communicate current knowledge in an accessible way. Books published in this series are conceived as bridging material between advanced graduate textbooks and the forefront of research and to serve three purposes:

- to be a compact and modern up-to-date source of reference on a well-defined topic
- to serve as an accessible introduction to the field to postgraduate students and nonspecialist researchers from related areas
- to be a source of advanced teaching material for specialized seminars, courses and schools

Both monographs and multi-author volumes will be considered for publication. Edited volumes should, however, consist of a very limited number of contributions only. Proceedings will not be considered for LNP.

Volumes published in LNP are disseminated both in print and in electronic formats, the electronic archive being available at springerlink.com. The series content is indexed, abstracted and referenced by many abstracting and information services, bibliographic networks, subscription agencies, library networks, and consortia.

Proposals should be sent to a member of the Editorial Board, or directly to the managing editor at Springer:

Christian Caron
Springer Heidelberg
Physics Editorial Department I
Tiergartenstrasse 17
69121 Heidelberg / Germany
christian.caron@springer.com

N. Akhmediev
A. Ankiewicz (Eds.)

Dissipative Solitons: From Optics to Biology and Medicine

Springer

Nail Akhmediev
Australian National University
Optical Sciences Center
Canberra ACT 0200
Australia
nna124@rsphy1.anu.edu.au

Adrian Ankiewicz
Australian National University
Optical Sciences Center
Canberra ACT 0200
Australia
ana124@rsphy1.anu.edu.au

Akhmediev, N., Ankiewicz, A.(Eds.), *Dissipative Solitons: From Optics to Biology and Medicine*, Lect. Notes Phys. 751 (Springer, Berlin Heidelberg 2008), DOI 10.1007/978-3-540-78217-9

ISBN: 978-3-540-78216-2 e-ISBN: 978-3-540-78217-9

DOI 10.1007/978-3-540-78217-9

Lecture Notes in Physics ISSN: 0075-8450

Library of Congress Control Number: 2008922888

Cover design: eStudio Calamar S.L., F. Steinen-Broo, Pau/Girona, Spain

Printed on acid-free paper

9 8 7 6 5 4 3 2 1

springer.com

Preface

The aim of publishing this book is the further development of the concept of dissipative solitons, which has been in the air for at least the last decade and a half. Since the development of classical soliton theory in the 1960s, the theory of these "nonlinear modes" of integrable systems outgrew its initial ideas. The purely mathematical concept, as it appeared in the work of Zabusky and Kruskal in 1965, required experimental verification, and this was successfully carried out in liquids, optical fibers, and some other exotic media. Scientists came to the conclusion that "solitons are everywhere". Indeed, the notion of solitons gave a powerful boost to the multibillion industry of telecommunications. The idea of solitons underlies our understanding of tidal bores, cyclones and massive ocean waves like tsunamis. There is no doubt that the magnificent phenomenon known as "Morning Glory" – a cloud wave hundreds of kilometers long – is also a dissipative soliton.

During almost four decades of blossoming, soliton science produced brilliant results based on the "inverse scattering technique", which allowed for construction of soliton solutions for a variety of integrable systems describing physics of water waves, light propagation, etc. At the same time, experimental scientists realized that the framework of a few particular "integrable systems" does not fully allow us to describe real applications which do not exactly belong to the class of "integrable equations". Life is actually more complicated than the exceptional image of ideal solitons in an "integrable world".

The dissipative soliton concept is a fundamental extension of that for solitons in conservative and integrable systems. It includes ideas from three major sources, viz. standard soliton theory developed since the 1960s, ideas from nonlinear dynamics theory developed by Poincaré and his followers and Prigogine's ideas of systems far from equilibrium. These are basically the three sources and three component parts of this novel paradigm. Physically speaking, the major part of standard soliton theory is the notion of the balance between dispersion/diffraction and nonlinearity that allows stationary localized solutions to exist. For dissipative systems, we have to allow for the fact that the major balance is between gain and loss – this is necessary for the solitons to be stationary objects. Nonlinear dynamics inspires us with the idea of soliton bifurcations and the chaotic evolution of solitons. Finally,

the theory of systems far from equilibrium tells us that solitons are self-organized formations requiring a continuous supply of matter and/or energy. As soon as that supply finishes, a dissipative soliton ceases to exist. These are basic cornerstones of the powerful concept of the dissipative soliton. A dissipative soliton can be a pulse of light, a distribution of temperature or pressure, an electric or magnetic field, a nerve impulse, a pattern of a sand dune, a formation of plants, a star like the sun or a biological entity like a cell, organ or entire animal. All of these owe their existence and specific shapes to the input and output of matter or energy across their boundaries.

A common misconception regarding dissipative systems is that they can only have losses and hence only decaying solutions. The name "dissipative system" was coined by Prigogine for systems considered in non-equilibrium thermodynamics. These systems are not isolated but are kept in contact with an external source that provides energy for the smaller sub-system. Thus, dissipation is essential for the transfer of pumped energy to a "cooler" part. Hence, the notion "dissipative system" is more complicated. It assumes that there is also an energy supply part, rather than just losses. A localized structure in such a system, i.e., a "dissipative soliton" truly deserves to be an established scientific keyword.

More than 2 years have passed since the publication of the first book on "Dissipative Solitons" by Springer [Lecture Notes in Physics **661** (2005)]. Many new ideas have been developed during this time and the concept has been widely accepted as a new scientific paradigm, in the sense that it brings about a change in our view of the world, as explained in Kuhn's famous book. The workshop "Dissipative Solitons", held in Dresden, Germany, in January 2006 in the Max Planck Institute for Complex Systems, facilitated the consolidation of all the new ideas in this area and the crystallization of the concept. This workshop made it clear that the publication of a second book would be both timely and necessary for the encouragement of further progress in this exciting area of research. Now, this new book is in front of you.

As the title of the book suggests, the ordering of the chapters starts from conventional optical dissipative solitons and finishes with examples of solitons in biology and medicine. The optical soliton topic traditionally occupies the major part of the book. We feel that research on localized structures in biology and medicine covers an enormous area by itself. However, only a limited number of ideas can be presented in the frame of this book. These examples are to show that this is the way in which this science can advance in the future.

The book commences with Chap. 1 discussing the general concept of a dissipative soliton and some common features of dissipative solitons in various nonlinear dynamical systems. A discussion of a rich panoply of mathematical model equations, whose solutions are dissipative solitons, is given in Chap. 2 by Velarde and Nepomnyashchy.

Wide-aperture lasers are systems where spatial dissipative solitons can be observed quite naturally. This topic is covered by Chaps. 3, 4 and 5. Chapter 3 is a review by Lugiato et al. which illuminates the physics of cavity solitons in semiconductor devices. The authors discuss experiments which have demonstrated cavity solitons in vertical-cavity surface-emitting lasers and all the theory which

accompanies such experiments. The stress is on the features of the experimental results which can lead to prospective applications. Rosanov et al., in Chap. 4, consider dissipative optical solitons in wide-aperture lasers with saturable absorption in the case where non-locality and relaxation of nonlinearity are important. They find stable stationary dissipative solitons which are similar to those in class A lasers, as well as slowly moving dissipative solitons, and a new type of flying soliton which is characterized by a high velocity of motion and a high peak intensity. Colet et al., in Chap. 5, discuss the instabilities that can affect cavity solitons appearing in Kerr cavities. They show that cavity solitons may exhibit a Hopf bifurcation leading to self-pulsating behavior, which is then followed by the destruction of the oscillation in a saddle-loop bifurcation. Using the notion of excitability, they show that cavity solitons can be used for fast and compact optical information storage.

Dissipative solitons in the temporal domain are covered in Chaps. 6 and 7. In Chap. 6, Grelu and Soto-Crespo discuss a large variety of multi-soliton complexes that reveal interesting new behaviors in passively mode-locked lasers. In particular, they concentrate on collisions, pulsations and vibrations of dissipative solitons inside fiber laser cavities. Several ways of creating soliton compounds or soliton ensembles in optical fiber links are discussed by Mitschke in Chap. 7. In addition, he discusses the idea of soliton molecules, as well as recently discovered chains of dark solitons. He shows that concepts beyond individual soliton pulses might be helpful in pushing beyond the fundamental limit of the data-carrying capacity of optical fibers.

Turitsyn and Boscolo, in Chap. 8, discuss the theory and applications of dissipative solitons in the next generation of advanced optical communication systems. In particular, they discuss the design of all-optical high-speed signal processing devices, based on nonlinear dissipative structures.

Dissipative solitons which are created by the interaction of waves with several frequencies, i.e., parametric dissipative solitons, are presented in Chaps. 9 and 10. Theoretical and experimental studies of stimulated Brillouin back-scattering of a c.w. pump, resulting in backward-traveling solitary pulses in long fiber-ring cavities, are presented in Chap. 9 by Montes. A stable continuous family of super-luminous and sub-luminous backward-traveling dissipative solitary pulses is obtained as a result of a Hopf bifurcation when changing a single control parameter. Nonlinear optical cavities with three-wave interaction in a nonlinear crystal, where spatial dissipative solitons can form spontaneously, are considered by Coulibaly et al. in Chap. 10. These studies reveal a self-frequency shift, a slowing down and a nonlinear symmetry-breaking effect in the envelope of dissipative solitons emitted by an optical parametric oscillator.

Dissipative solitons in discrete systems are discussed, from various points of view, in Chaps. 11 and 12. Flach and Gorbach consider the interplay between discreteness and nonlinearity which leads to the emergence of a new class of nonlinear excitations, viz. discrete breathers. A special focus is placed on a sub-class of dissipative discrete breathers. They discuss applications of the discrete breather concept in systems where dissipation is not only unavoidable but actually essential. Velarde et al., in Chap. 12, consider an electro-mechanical Toda lattice that is able

to maintain a non-Ohmic soliton-driven supersonic electric current and discuss its striking characteristics. They demonstrate that the lattice seems very much like a versatile neural transmission line. A somewhat related subject is the propagation of solitary waves in Bragg gratings. This topic is covered in Chap. 13 by Gabitov et al. They find exact solitary solutions for a system of equations, of Maxwell–Duffing type, which describe forward and backward propagating waves in a grating. New phenomena of collective self-focusing of light and atoms, and stable dissipative atom-optical solitons, are presented in the chapter by Saffman and Wang.

From the biological arena, the chapter by Tlidi et al. presents clustering behavior of arid vegetation ecosystems. This is a rather unusual example of dissipative solitons occurring in nature. The propagation of traveling solitary pulses in one-dimensional cortical networks is presented in the chapter by Golomb. This work shows that simple models of spiking neurons exhibit a large variety of propagating pulses with various spatio-temporal properties. The chapter by Troy presents mathematical models of traveling wave solutions which describe the activity of large-scale networks of excitatory neurons on spatially extended domains. Various regimes of excitation and functional behavior of the central nervous system are modeled by localized solutions of a system of integro-differential equations. The book concludes with the chapter of Zykov discussing spiral waves and propagating wave segments. These are further examples of dissipative solitons in assorted excitable media, including heart muscle, the retina of the eye, social amoeba colonies and the chemical Belousov–Zhabotinsky reaction.

The editors acknowledge support from the Australian Research Council.

Canberra, Australia *Nail Akhmediev*
August, 2007 *Adrian Ankiewicz*

Contents

Three Sources and Three Component Parts of the Concept of Dissipative Solitons

N. Akhmediev and A. Ankiewicz

Abstract We explain the notion of dissipative solitons within a historical perspective. We show that the ideas of the theory of dissipative solitons emerge from several fields, including classical soliton theory, nonlinear dynamics, with its theory of bifurcations, and Prigogine's concept of self-organization. A new notion, emerging from this three-part foundation, allows us to build the novel concept of the dissipative soliton. We also show that reductions to lower dimensional systems have to be done carefully and should always include a comparison of the results with numerical simulations of the original equations.

1 Introduction

This book is a collection of works in various fields that have the common concept of the "dissipative soliton" behind each specific topic. Before turning to the chapters, written by experts in their fields, it is instructive to start with general "definitions" and a little history of the terms. Our introductory chapter summarizes the main ideas and explains what a "dissipative soliton" entails, in simple terms. The ideas have been developed over a number of years and have appeared in various publications [1, 2, 3], but a compact presentation of all these ideas in a single volume is important.

The term "soliton" was first introduced in 1965 by Zabusky and Kruskal [4] when studying the numerical solutions of the Korteveg-de Vries equation. General solutions of this equation behaved "strangely" as a superposition of solitary waves or "solitons" and radiation waves, despite the fact that the governing equation was

N. Akhmediev
Optical Sciences Group, Research School of Physical Sciences and Engineering, Australian National University, Acton, ACT 0200, Australia, nna124@rsphysse.anu.edu.au

A. Ankiewicz
Optical Sciences Group, Research School of Physical Sciences and Engineering, Australian National University, Acton, ACT 0200, Australia

Akhmediev, N., Ankiewicz, A.: *Three Sources and Three Component Parts of the Concept of Dissipative Solitons.* Lect. Notes Phys. **751**, 1–28 (2008)
DOI 10.1007/978-3-540-78217-9_1

nonlinear. Clearly, the solitons were modes of a nonlinear system. At that point, it was understood that "waves of translation", first observed by John Scott Russell in 1834 [5], are also solitons. Later, a rigorous mathematical theory was developed [6], and this allowed us to construct a general solution of a certain class of equations in terms of solitons and radiation waves. Since this pioneering work of Gardner, Greene, Kruskal and Miura in 1967, scientists tend to use the term "soliton" to describe the modes of nonlinear partial differential equations that happen to be integrable by means of the "inverse scattering technique" [7, 8]. These "integrable" solitons do not change their shape and velocity after colliding with each other, and they remain intact when interacting with radiation waves. Occasionally, other types of localized solutions in physics were named "solitons" as well. However, this custom met serious resistance from the mathematicians who were studying "true" solitons of "integrable models".

A dramatic turning point occurred at the beginning of the 1990s, which was a time when many physicists understood the limitations of the theory. They observed the fact that "solitary waves" do exist in a variety of systems, though they do not behave exactly as the classical theory predicts for "true" solitons. In particular, "soliton-like" pulse propagation in a real optical fiber satisfies equations which are more complicated than the integrable nonlinear Schrödinger equation [9]. These equations still have solutions in the form of solitons, but they usually include additional terms that destroy integrability. The additional terms could describe physical effects, of both conservative and non-conservative nature, which modify the properties of solitons, but leave them as distinctively localized solutions of the system under consideration. Thus, the theory had to be extended, firstly, to cover localized solutions in conservative and Hamiltonian systems and later to construct a theory of solitons in systems with loss and gain. On the one hand, new solitons could not be used as superpositions in order to construct a general solution of the system, but on the other hand they appeared in physical systems as localized solutions describing certain classes of phenomena. Thus, new terms had to be used, such as "solitary pulse" for conservative systems or "dissipative soliton" in cases of systems with gain and loss. In this respect, it is worthwhile mentioning early works [10, 11] where the term "dissipative solitons" was used to describe solitons in such systems. We also have to mention that there is a very wide variety of systems with gain and loss, so that even the rather specific term "dissipative soliton" may need a finer definition in more complicated systems.

The first book "Dissipative Solitons" was published by Springer in 2005 [12]. This was the time when major principles had to be unified and presented in a single volume. This first attempt turned out to be highly successful. It generated a multiplicity of ideas and brought the scientific community to the idea of organizing a workshop with the same name. The workshop took place in January 2006 in Dresden, Germany, within the Max Planck Institute for Physics of Complex Systems. This meeting solidified the ideas behind the concept of "dissipative solitons". It also became clearer than ever that the notion of "dissipative solitons" could be applied to biology and even medicine, and hence not only to physical systems. Hence, in publishing this book, the editors attempt to spread these ideas broadly and attract

more scientists to consider localized solutions from the new point of view. This may open new facets in the perception of known phenomena, as well as assisting in the understanding of novel phenomena.

The dissipative soliton concept is a fundamental extension of that for solitons in conservative and integrable systems. It includes ideas from three major sources, viz. standard soliton theory developed since the 1960s, ideas from nonlinear dynamics theory and Prigogine's ideas of systems far from equilibrium and self-organization (see Fig. 1). These are basically the three sources and three component parts of this novel paradigm. Physically speaking, the major part of standard soliton theory is the notion of the balance between dispersion and nonlinearity that allows stationary localized solutions to exist. For dissipative systems, we need to observe that the important balance is between gain and loss – this condition is necessary for solitons to be stationary objects. Even the slightest imbalance will result in the solution either growing indefinitely, if gain prevails, or disappearing completely because of the dissipation. Thus, instead of a single balance, we have to consider a composite balance between several physical phenomena.

The second part of our foundation – nonlinear dynamics – inspires us with the idea of a soliton as a fixed point of an infinite-dimensional dynamical system. Stability properties of fixed points determine the stability of the soliton itself. Fixed points can be transformed into limit cycles at certain values of the system parameters, and then the soliton becomes a pulsating object. Further transformations may include irregular behavior of the trajectory, thus creating chaotic solitons. Therefore, nonlinear dynamics supplies us with the ideas of soliton bifurcations and the chaotic

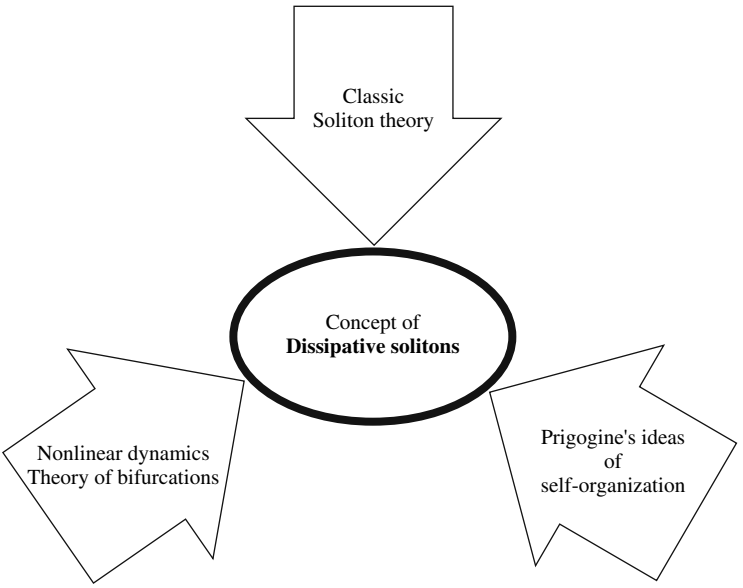

Fig. 1 Three sources and three component parts of the concept of dissipative solitons

evolution of solitons. Since we consider infinite-dimensional dynamical systems, there is a huge variety of types of solitons and their bifurcations.

Finally, the third part of the basis – the theory of systems far from equilibrium – tells us that solitons are self-organized formations requiring a continuous supply of matter or energy. As soon as that supply finishes, a dissipative soliton ceases to exist. In simple terms, self-organization is a convergence of certain initial conditions to a localized solution of the system that is stable for a given set of external parameters. Thus, the final state is determined by the physical laws and not by the initial condition. For infinite-dimensional dynamical systems, this stable solution can be very complicated. It is not necessarily a smooth function with a single maximum and exponentially decaying tails. Moreover, there can be several stable solutions existing for the same set of parameters. This can even happen in the case of a relatively simple equation like the complex cubic-quintic Ginzburg–Landau equation. The majority of processes in nature are governed by far more complicated dynamical factors. Thus, stationary solutions of these systems can be considerably more involved.

From this point of view, the idea of self-organization allows us to extend the concept of dissipative solitons to highly complicated objects such as animal species and the formation of life itself. How far we can go in extending our principles in this direction only depends upon our imagination. Adding to this complexity, when a system converges to a solution, is not necessarily a stationary solution but can be a limit cycle or a strange attractor in an infinite-dimensional phase space. Many biological processes such as heart beats and nerve pulse propagation have been described using simple mathematical modeling. Scientific progress in this direction continues and the reader can find some examples in other chapters of this book.

There is the older term "autosoliton" which comes from the book by Kerner and Osipov [13]. As the title of the book suggests, the authors consider localized solutions from Prigogine's point of view as self-organized structures. As we can see from Fig. 1, this is one of the foundation stones of the new concept. More specifically, the name "autosoliton" came naturally from the theory of reaction-diffusion systems [14]. Usually, it had to be supplemented with the notions of "activator" and "inhibitor" to be understood in its full complexity. The root of the word itself originates from the term "auto-oscillations" in the theory of "flutter and shimmy" which can be understood as "self-propelled" solitons. In a few cases, this term has even been used in optics. Throughout this book, the term "dissipative soliton" is used as the one that covers the majority of relevant phenomena in optics, biology and medicine. As a fuller explanation, it means "soliton in a dissipative system", where "dissipative system" is to be understood in Prigogine's sense as a sub-system with an external pump of energy, rather than a system with losses only. An optical laser is one of the examples of such subsystem in optics [15].

There is a significant difference between solitons in Hamiltonian systems and in dissipative ones. In Hamiltonian systems, soliton solutions appear as a result of a balance between diffraction (or dispersion) and nonlinearity. Diffraction spreads the beam, while nonlinearity focuses it and makes it narrower. The balance between the two results in stationary solutions. These usually form a one-parameter family. In

systems with gain and loss, in order to have stationary solutions, gain and loss must be balanced in the first place. The two balances result in solutions which are fixed. The shape, amplitude and the width are all fixed and depend on the parameters of the equation. This situation is represented qualitatively in Fig. 2. For telecommunication applications, the rigidity of the soliton may provide efficient suppression of noise and stop any drift in the soliton parameters.

Clearly, stationary dissipative solitons can be considered as fixed points of an infinite-dimensional dynamical system. Thus, their parameters are fixed. These formations are stable on propagation, provided the system parameters are chosen in appropriate regions. In general, dissipative solitons are not necessarily stationary. In other words, fixed points are not the only objects that may exist in such systems. For example, a limit cycle is another, more complicated, object that can exist in the phase space of the dynamical system. It corresponds to a pulsating soliton where the parameters oscillate periodically [25]. These solitons usually exist in regions of the parameter space which are adjacent to those of stationary solitons. However, even in this case, the soliton characteristics are fixed, i.e., the period of the pulsations and the shapes at particular points of the period are all fixed, since they are functions

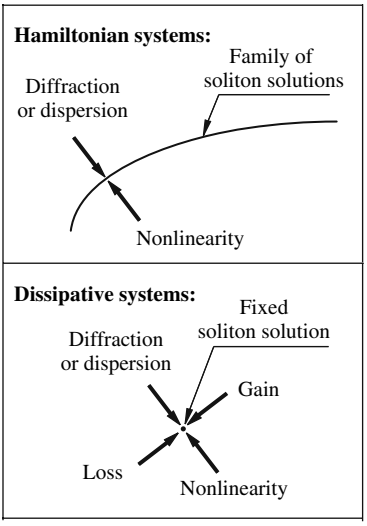

Fig. 2 Qualitative difference between soliton solutions in Hamiltonian and dissipative systems [1]. In Hamiltonian systems, soliton solutions are the result of a single balance, and comprise one- or few-parameter families, whereas, in dissipative systems, the soliton solutions are the result of a double balance and, in general, are isolated. There can be exceptions to this rule [16, 17, 18], but, usually, the solutions are fixed (i.e., isolated from each other). On the other hand, it is quite possible for several isolated soliton solutions to exist for the same equation parameters. This is valid for (1+1), (2+1) dimensional as well as for (3+1) dimensional cases. In the latter case, the terms "localized structures" [19] and "bullets" [20, 21, 22, 23] are also used, along with the term "solitons" [24]

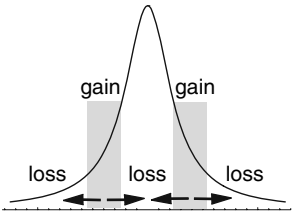

Fig. 3 Qualitative description of solitons in dissipative systems [1]. The soliton has areas of consumption as well as expenditure of energy, and these can be both frequency (spatial or temporal) and intensity dependent. *Arrows* show the energy flow across the soliton. The soliton is the result of complicated dynamical processes of energy exchange with the environment and between its own parts

of the system parameters. One more possibility is that the dissipative soliton can be chaotic [25]. If the soliton is chaotic, the characteristics of this chaotic behavior are also given by the parameters of the system.

Another simple qualitative picture is presented in Fig. 3. In order to be stationary, solitons in dissipative systems need to have regions where they extract energy from an external source, as well as regions where energy is dissipated to the environment. A stationary soliton is the result of a dynamical process of continuous energy exchange with the environment and its redistribution between various parts of the soliton. As soon as this energy redistribution ends, the soliton disappears. In more complicated cases, a matter exchange is involved as well. In this sense, the dissipative soliton is more like a living thing than an object of the inanimate world. It is like a species in biology which is fixed (or isolated) in its properties.

So we have just described, albeit briefly, the basic cornerstones of the powerful concept of the dissipative soliton, and we present them schematically in Figs. 1, 2 and 3. Our observations are mostly related to dynamical systems whose evolution can be described by differential equations with partial derivatives. Such dynamical systems have an infinite number of degrees of freedom and, surely, they may have a countless number of soliton solutions with a countless number of bifurcations between them. As a rule, these systems are non-integrable, which means that exact solutions in their full complexity can be studied only numerically. To describe fine features of soliton bifurcations analytically, we need approximations and some techniques to reduce the dimensionality of the dynamical system. These methods may help, to some extent, in describing stationary or pulsating solitons and their bifurcations over a limited range of the system parameters. However, they cannot be used as a total substitute for rigorous studies of the solutions. Only the most prominent features of the solitons, along with selected bifurcations, can be determined in this way. For a full picture, we still need numerical simulations. In the rest of this chapter, we give a few examples of studies that involve reductions to finite-dimensional approximations. We also show that direct comparisons with the results of numerical simulations are essential in these studies.

2 Cubic-Quintic Complex Ginzburg–Landau Equation

Throughout this chapter, we are dealing with an infinite-dimensional dynamical system governed by the cubic-quintic complex Ginzburg–Landau equation (CGLE) which in optics has been widely used to describe the pulsed operation of passively mode-locked lasers and all-optical long-haul soliton transmission lines. Generally, the CGLE has a wide range of applications in various branches of physics, chemistry and biology. An extensive list of applications can be found in the review paper by Aranson and Kramer [26]. This enormous sphere of knowledge has been dubbed "The world of the Ginzburg–Landau equation" [26]. The cubic-quintic complex equation has so many different types of solutions that this area of expertise is a whole world by itself. Even if we restrict ourselves to localized solutions, i.e., dissipative solitons of CGLE, the variety of these objects is still not known in its full complexity although the regions of soliton existence have been studied quite extensively [27, 28, 29].

One of the difficulties is that analytic solutions are known only for a special class of CGLE solitons [30] when parameters of the equation are related by a specific algebraic equation. All other soliton solutions can only be found numerically. One of the features of these solutions is that they have rich structure of bifurcations [31, 32]. Having this structure leaves little hope for exact analytical description. Nevertheless, approximate methods are always a possibility. Such approximations are the main subject in the rest of this chapter. We give an example of the application of the so-called method of moments, which allows us to approximate, for example, periodicity in the motion of the soliton and the bifurcation from stationary to pulsating solitons. We stress that only simple properties of the dissipative solitons can be approximated by employing reductions. Using this technique, we consider three examples where simple approximations can give qualitative descriptions of the soliton behavior and even predict the existence of unknown branches of solitons.

In our notation, the CGLE is

$$\mathrm{i}\psi_t + \frac{D}{2}\,\psi_{xx} + |\psi|^2\psi + \nu|\psi|^4\psi = \mathrm{i}\delta\psi + \mathrm{i}\varepsilon|\psi|^2\psi + \mathrm{i}\beta\psi_{xx} + \mathrm{i}\mu|\psi|^4\psi. \qquad (1)$$

When used to describe passively mode-locked lasers, the CGLE represents a distributed propagation model, in which t is the distance traveled inside the cavity, x is the retarded time, ψ is the normalized envelope of the field, D is the group velocity dispersion coefficient, with $D = \pm 1$, depending on whether the group velocity dispersion (GVD) is anomalous or normal, respectively, δ is the linear gain–loss coefficient, $\mathrm{i}\beta\psi_{xx}$ accounts for spectral filtering or linear parabolic gain ($\beta > 0$), $\varepsilon|\psi|^2\psi$ represents the nonlinear gain (which arises, for example, from saturable absorption), the term with μ represents, if negative, the saturation of the nonlinear gain, while the one with ν corresponds, also if negative, to the saturation of the nonlinear refractive index.

During numerical computations with the propagation equation, the magnitude that we most often monitor is the energy, Q, carried by a certain solution after a propagation distance of t. It is defined by

$$Q = \int_{-\infty}^{\infty} |\psi(x,t)|^2 \mathrm{d}x.$$

For a dissipative system, Q is a function of t rather than a conserved quantity. The convenience of monitoring the energy Q is clear from the following considerations. For localized solutions, Q is finite. Decaying solutions result in Q converging to zero. When the localized solution is stationary, Q takes a constant value. Stable localized solutions show convergence of Q to a constant when starting from an initial condition that is not a solution of the CGLE. Thus, stability of a soliton obtained this way follows directly from numerical simulations. When the soliton solution is pulsating in t, the quantity Q also oscillates on propagation. In this instance, we denote its maxima and minima of Q by Q_{M} and Q_{m}, respectively. Chaotic solitons generally produce chaotic evolution of Q. Of course, a more detailed study of solitons should involve more of these integral parameters. However, there will always be a limitation because of the gap between the finite number of the parameters that we are able to use and the fact that our dynamical system has an infinite number of degrees of freedom.

3 The Method of Moments

In this section, we briefly outline the approach that we use to derive the dynamical model. The method of moments [33] is a reduction of the complete evolution problem with an infinite number degrees of freedom to the evolution of a finite set of pulse characteristics. For a localized solution with a single maximum, these characteristics include the peak amplitude, pulse width, center-of-mass position and phase parameters. For an arbitrary localized field, one can introduce two integrals, namely the energy Q and momentum M,

$$Q = \int_{-\infty}^{\infty} |\psi|^2 \mathrm{d}x, \quad M = \frac{1}{2} \int_{-\infty}^{\infty} (\psi \psi_x^* - \psi^* \psi_x) \mathrm{d}x, \tag{2}$$

and higher-order generalized moments [33],

$$I_1 = \int_{-\infty}^{\infty} x|\psi|^2 \mathrm{d}x, \quad I_2 = \int_{-\infty}^{\infty} (x-x_0)^2 |\psi|^2 \mathrm{d}x,$$

$$I_3 = \int_{-\infty}^{\infty} (x-x_0)(\psi^* \psi_x - \psi \psi_x^*) \mathrm{d}x. \tag{3}$$

The number of higher-order generalized moments is infinite. Depending on the complexity of the reduced model, we can restrict ourselves to a finite number of them. Using the original equation (1), we can derive the evolution equations for the generalized moments [33],

$$
\begin{aligned}
\frac{\mathrm{d}Q}{\mathrm{d}t} &= \mathrm{i}\int_{-\infty}^{\infty}(\psi R^* - \psi^* R)\mathrm{d}x,\\
\frac{\mathrm{d}M}{\mathrm{d}t} &= -\mathrm{i}\int_{-\infty}^{\infty}(\psi_x R^* + \psi_x^* R)\mathrm{d}x,\\
\frac{\mathrm{d}I_1}{\mathrm{d}t} &= \mathrm{i}DP + \mathrm{i}\int_{-\infty}^{\infty} x(\psi R^* - \psi^* R)\mathrm{d}x,\\
\frac{\mathrm{d}I_2}{\mathrm{d}t} &= -\mathrm{i}DI_3 + \mathrm{i}\int_{-\infty}^{\infty}(x-x_0)^2(\psi R^* - \psi^* R)\mathrm{d}x,\\
\frac{\mathrm{d}I_3}{\mathrm{d}t} &= 2P\frac{\mathrm{d}x_0}{\mathrm{d}t} + \mathrm{i}\int_{-\infty}^{\infty}(2D|\psi_x|^2 - |\psi|^4)\mathrm{d}x\\
&\quad + 2\mathrm{i}\int_{-\infty}^{\infty}(x-x_0)(\psi_x R^* + \psi_x^* R)\mathrm{d}x\\
&\quad + \mathrm{i}\int_{-\infty}^{\infty}(\psi R^* + \psi^* R)\mathrm{d}x.
\end{aligned}
\tag{4}
$$

Equations (4) are quite general, i.e., they are valid for a large class of NLSE-type evolution equations, including (1) with arbitrary coefficients. Up to this point, the equations are exact if we use an exact solution of (1) for ψ.

In practice, one uses a trial function with a few parameters which depend on t. Equations for the evolution of these parameters are found from a system similar to (4). A suitable choice of trial function can be deduced from the general symmetries of the problem, and from results of experiments and numerical simulations. The minimum number of parameters needed to describe localized solutions is usually five (see Sect. 4). More parameters may improve the accuracy, but the complexity of the analysis then increases dramatically. Since the number of the moments should correspond to the number of the parameters, we consider only five moments.

The method of moments has been applied to various problems described by the perturbed NLSE [33, 34, 35]. The method was also used for the CGLE in [36, 37, 38], where simplified trial functions were considered. For special problems, even the first two equations (4) may be sufficient when we deal with specific two-dimensional reductions of the CGLE [39]. In more complicated cases, we need more equations. It turns out that the complete set of equations (4) is the minimum required for modeling the pulsating solitons.

4 Pulsating Solitons and Their Approximations [37, 38]

A pulsating soliton is a localized solution of the CGLE that changes its width, amplitude and other parameters periodically in t. A pulsating soliton is a limit cycle of the infinite-dimensional dynamical system and can be described by a closed loop in the phase space of the system. Exact analytical solutions for pulsating solitons are not known. Thus, we have to use finite-dimensional approximations. One of them is an approximation using a trial function with a finite number of variable parameters. The choice of trial function is usually motivated by numerical simulations of the CGLE (1). It was found [25, 31, 40] that for various sets of the system parameters, a dissipative soliton is a single-humped pulse with phase modulation. We consider two forms of the trial function in order to demonstrate that the results may vary, but qualitative features of the solution can be picked up, provided a reasonable choice of the function has been made.

4.1 Trial Function: Sech-Pulse

The first type of trial function that we use has the form of a *sech*-function:

$$\psi(x,t) = A\ \mathrm{sech}\left(\frac{x-x_0}{w}\right)\exp\left[\mathrm{i}\left[\phi + b(x-x_0) + c(x-x_0)^2\right]\right], \tag{5}$$

where $A(t)$, $w(t)$ and $x_0(t)$ are the amplitude, width and position of the pulse maximum, respectively, $\phi(t)$ is the phase shift, $b(t)$ is the linear phase coefficient, and $c(t)$ is the chirp parameter. The phase in (5) is expanded up to the second order. This form differs from the trial function used in [36], where only linear terms in the phase were considered. We emphasize that the chirp is highly important for solutions of the CGLE. As numerical simulations show, even stationary solitons have appreciable phase modulation, not to mention more complicated localized waves, such as pulsating and exploding solitons.

Now, the generalized moments can be expressed in terms of the soliton parameters in the trial function. Evaluation of integrals (2) and (3), with the help of (5), gives the following expressions:

$$\begin{aligned} &Q = 2A^2 w, \quad M = -2\mathrm{i}A^2 wb, \quad I_1 = 2A^2 wx_0, \\ &I_2 = (\pi^2/6)A^2 w^3, \quad I_3 = \mathrm{i}(2\pi^2/3)A^2 w^3 c. \end{aligned} \tag{6}$$

Then, using (4), one can obtain a set of ordinary differential equations for the soliton parameters in (5):

$$Q_t = F_1 \equiv 2Q\left[\delta - \beta\left(b^2 + \frac{1}{3w^2} + \frac{\pi^2}{3}c^2w^2\right) + \frac{\varepsilon}{3}\frac{Q}{w} + \frac{2\mu}{15}\frac{Q^2}{w^2}\right],$$

$$w_t = F_2 \equiv 2Dcw + \beta\left(\frac{8}{\pi^2 w} - \frac{16\pi^2}{15}c^2 w^3\right) - \frac{2\varepsilon}{\pi^2}Q - \frac{\mu}{\pi^2}\frac{Q^2}{w},$$

$$c_t = F_3 \equiv 2D\left(\frac{1}{\pi^2 w^4} - c^2\right) - \frac{1}{\pi^2}\frac{Q}{w^3} - 4\left(\frac{1}{3} + \frac{1}{\pi^2}\right)\beta\frac{c}{w^2} - \frac{8\nu}{15\pi^2}\frac{Q^2}{w^4}. \quad (7)$$

We have made additional reductions in (7), namely two equations

$$x_{0,t} = F_4 \equiv b\,(D - \frac{2\pi^2}{3}\beta c w^2),$$

$$b_t = F_5 \equiv -\frac{4}{3}\beta\,(\frac{1}{w^2} + \pi^2 c^2 w^2)\,b, \quad (8)$$

can be removed. For $\beta > 0$, the value of the linear phase b tends to zero for $t \to \infty$. Then, the soliton center $x_0(t)$ tends to a *constant* value for $t \to \infty$. This allows us to consider a system with only three variables, viz. Q, w and c. In other words, the three-dimensional subset describes the asymptotic dynamics of the five-dimensional model (7) for $t \to \infty$.

4.2 Trial Function: Generalized Gaussian Pulse

As numerical simulations show [25, 31], pulsating solitons change their shape during one period from a bell-shaped pulse to a flat-top pulse. Therefore, we consider a second trial function which is a combination of Gaussian and super-Gaussian types of functions:

$$\psi(x,t) = A\exp\left(-\frac{x^2}{w^2} - \frac{x^4}{4m w^4} + \mathrm{i}\,c x^2\right), \quad (9)$$

where $A(t), w(t)$ and $c(t)$ have the same meaning as in (5). The constant m can be chosen arbitrarily, but it is independent of t. Note that, following the discussion in Sect. 4.1, $x_0(t)$ and the linear phase b are taken to be zero implicitly in the ansatz. This leaves three parameters, A, w and c, to be found from the three-dimensional model.

The trial function (9), with $m > 0$, gives better results than the *sech* function or the Gaussian function alone or the super-Gaussian function with a quartic term alone. Also, the case $4m = 1$ agrees well with the numerical simulations of the CGLE. However, this value is not critical and other values of m can be used.

Since the function (9) is symmetric in x, the integrals M and I_1 are identically zero. Other moments in (2) and (3), for $4m = 1$, are given by

$$Q = 1.051A^2 w, \quad I_2 = 0.1448Qw^2, \quad I_3 = \frac{\mathrm{i}}{4}\,c I_2. \quad (10)$$

Then (4) results in the following dynamical model ($4m = 1$):

$$Q_t = F_1 \equiv \frac{Q}{w^2}\left[2\delta w^2 - 3.737\beta - 1.158\beta c^2 w^4 + 1.433\varepsilon w Q + 1.143\mu Q^2\right],$$

$$w_t = F_2 \equiv \frac{1}{w}\left[2.142\beta + 2cw^2 - 0.8738\beta c^2 w^4 - 0.2896\varepsilon w Q - 0.3254\mu Q^2\right],$$

$$c_t = F_3 \equiv \frac{1}{w^4}\left[6.453 - 2c^2 w^4 - 1.237 w Q - 1.319\nu Q^2 - 19.62\beta w^2 c\right]. \quad (11)$$

As expected, the equations for Q_t, w_t and c_t in (7) and (11) are similar. The only difference lies in the numerical values of the coefficients of the terms.

4.3 Fixed Points and Their Stability [38]

Fixed points (FPs) of (7) with $x_0 = b = 0$, or of (11), are found from the set of algebraic equations $F_j = 0,\ j = 1,2,3$. The stability of the FPs is determined from the analysis of the eigenvalues λ_j, $j = 1,2,3$, of the Jacobian matrix $M_{ij} = \partial F_i/\partial p_j$, where $\{p_1, p_2, p_3\} \equiv \{Q, w, c\}$, and $i = 1,2,3$. When the real part of any eigenvalue becomes positive, the corresponding fixed point becomes unstable. Since the characteristic equation for the eigenvalues is cubic, either $\lambda_1 = \lambda_2^*$ and λ_3 is real or all three λ_j are real.

We analyze the models (7) with $x_0 = b = 0$ and (11) for different signs of D and values of the parameters ν, ε, μ and β. We set $\delta = -0.1$. Firstly, we compare the results of numerical simulations of the CGLE (1) with those of the models (7) and (11). The results of numerical simulations of the CGLE (1) for $\beta = 0.08$ and $\mu = -0.1$ are shown in Fig. 4a. The figure shows the bifurcation boundaries between various types of localized waves that exist at particular values of the system parameters. The region with vertical shading corresponds to stationary solitons. Solutions describing two fronts moving in opposite directions exist in the region with horizontal shading. Pulsating solitons with periodic or chaotic variations of their parameters occupy the area between these two regions.

There are four types of fixed points for the three-dimensional model:

$$\begin{aligned} S_1 &= \{(-,+),\ \lambda_1^\star,\ (-,0)\},\\ S_2 &= \{(-,0),\ (-,0),\ (-,0)\},\\ U_1 &= \{(+,+),\ \lambda_1^\star,\ (-,0)\},\\ U_2 &= \{(-,+),\ \lambda_1^\star,\ (+,0)\}, \end{aligned} \quad (12)$$

where the variables in curled brackets are complex eigenvalues $\{\lambda_1, \lambda_2, \lambda_3\}$ of the fixed point. The symbols in parentheses show that the corresponding parts of $\lambda_j = (\mathrm{Re}\lambda_j, \mathrm{Im}\lambda_j)$ are either positive $(+)$, negative $(-)$ or zero. The types S_1 and S_2 (U_1 and U_2) correspond to stable (unstable) FPs.

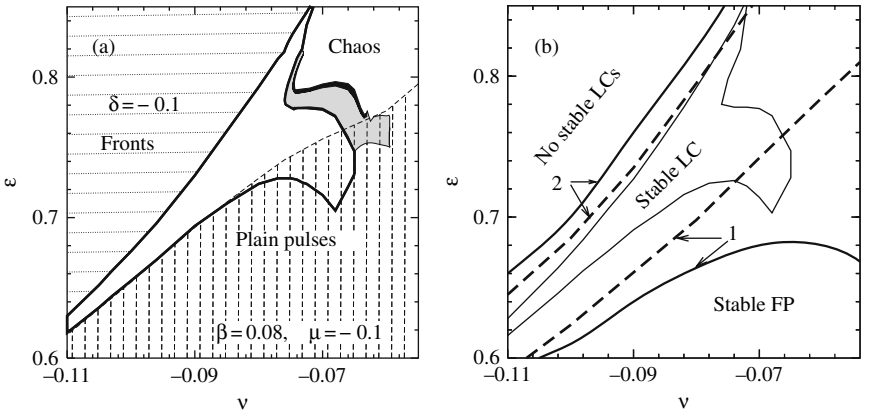

Fig. 4 (**a**) Regions of existence of various solutions obtained from numerical simulations [31] of the CGLE (1). (**b**) Regions of existence and stability of FPs and limit cycles of the reduced systems in (ν, ε)-plane. The region between the two *solid* [*dashed*] *lines*, 1 and 2, corresponds to the region of existence of stable LCs in the models Eqs. (7) [Eqs. (11)]. The region for pulsating solitons is copied from (**a**) to (**b**) for comparison. The system parameters are shown in (**a**)

The bifurcation diagram for the models (7) and (11) is shown in Fig. 4b. When the value of gain, ε, is small, there are no FPs in the system. The threshold for FP existence, ε_{ex}, can be estimated roughly as $\varepsilon_{ex} \approx 2\sqrt{\delta\mu}$. For the parameters in Fig. 4, $\varepsilon_{ex} \approx 0.2$. If $\varepsilon > \varepsilon_{ex}$, then there are two FPs. In the region below the solid [dashed] curve 1 for model (7) [for model (11)], one FP is of the type S_1, while the other FP is of the type U_2. The second point, U_2, does not change its type and is unstable in the whole square region shown in Fig. 4b. Therefore, the bifurcation line 1 in Fig. 4b is related to the transformation of the first FP.

Curve 1 is the bifurcation boundary (threshold) where the stable FP of type S_1 becomes an unstable one of type U_1. The following condition is satisfied at the threshold:

$$\mathrm{Re}[\lambda_1] = \mathrm{Re}[\lambda_2] = 0. \tag{13}$$

The loss of stability of an FP can either be a result of merging with another unstable FP or be due to the creation of (annihilation with) a *limit cycle* [41]. The latter transition corresponds to a super-critical (sub-critical) Hopf bifurcation [41]. Since the number of the FPs does not change in the whole area in Fig. 4b, the curve 1 is related to the threshold of the Hopf bifurcation in the models (7) and (11).

If the Hopf bifurcation is super-critical, a stable LC would appear exactly at the same value of ε where the FP loses stability. When the Hopf bifurcation is sub-critical, the stable LC should appear before the FP becomes unstable [41]. In the latter case, the stable FP and stable LC co-exist for a certain interval of the system parameters. Numerical simulations of (7) and (11) show that for the set of parameters in Fig. 4b, the bifurcation is super-critical. The loss of stability of the FP S_1 is accompanied by the creation of a *stable* limit cycle (LC).

Close to curve 2 in Fig. 4b, the period of the LC tends to infinity. There is no stable LC above curve 2. The soliton energy Q and width w in this region increase monotonically with t, while the ratio Q/w, which is related to the square of the soliton amplitude A^2 [see (6) and (10)], remains roughly constant.

The region in Fig. 4b surrounded by the thin solid curve corresponds to the area of existence of pulsating solitons of CGLE, as found from direct numerical simulations. It is copied from Fig. 4a. A comparison of Fig. 4a and b shows a clear correspondence between the attractors (FPs and LCs) of the two models (7) or (11) and stable localized solutions of the CGLE. Specifically, an FP of the model (7) or (11) corresponds to a stationary soliton, and an LC obtained in the reduced model corresponds to a pulsating soliton. The solution with almost constant A and increasing w (the area above the curve 2 in Fig. 4b) approximates two fronts moving in opposite directions. Such a solution was observed in numerical simulations of the CGLE [31]. The boundaries obtained in each of the reduced models are fairly close to the exact ones. Thus, each of the models (7) and (11) provides a reasonably good qualitative description of soliton bifurcations inside the squared area of Fig. 4.

In contrast to the stationary state, LCs or pulsating solitons appear due to the *dynamic* balance between dissipation and energy supply. Pulsations involve periodic variations of the soliton-shape parameters A and w and the phase parameter c. This behavior is similar to transient dynamics in the integrable NLSE [42], when a non-soliton pulse adjusts its form to the fundamental soliton via quasi-periodic changes of its amplitude and phase. In the case of the NLSE, such oscillations are damped because the pulse loses energy, radiating linear waves during the transient stage. In the case of pulsating solitons of the CGLE, such oscillations are undamped due to the continuous energy supply.

The parameters of the LC change between curves 1 and 2. The oscillation period of the LC is finite on curve 1 but it varies along this curve. It is inversely proportional to $\mathrm{Im}[\lambda_1]$ of the first FP. The period increases monotonically with ε at any fixed ν. As mentioned above, the oscillation period of the LC becomes infinite on curve 2, and the LC disappears above it. Examples of limit cycles in three-dimensional phase space for two different sets of parameters are presented in Fig. 5.

The dependence of the oscillation period of the LCs on ε, when other parameters are fixed, is shown in Fig. 6 for each of the reduced models. The curve (solid line), obtained from direct numerical simulations of the CGLE (1), is also shown for comparison. There is an apparent difference in the numerical values of the period due to the drastic reduction in the number of degrees of freedom in the models. However, all three curves have the same qualitative behavior. In particular, each curve starts with a finite value of the period T at the lower boundary of the region where pulsating solitons exist. The period T increases to infinity when ε reaches the upper boundary. It is clear that the function given by (9) gives more accurate results.

A comparison of the actual field evolution in z with the one reconstructed from the reduced model is presented in Fig. 7. The results of numerical simulations of the CGLE (1) are shown in Fig. 7a. The field reconstructed from the ansatz (5) and the dynamical systems (7) is plotted in 7b. The qualitative features of the dynamics are

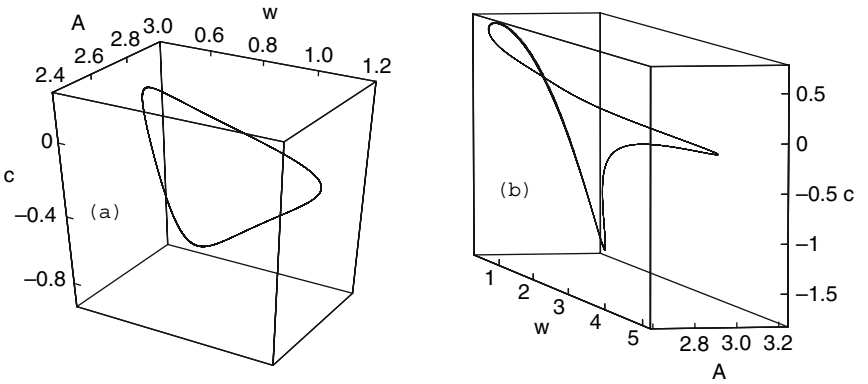

Fig. 5 Examples of limit cycles in (A, w, c)-space for the model (7), $\beta = 0.08$, $\mu = -0.1$ and $\nu = -0.09$. (**a**) $\varepsilon = 0.66$. (**b**) $\varepsilon = 0.72$

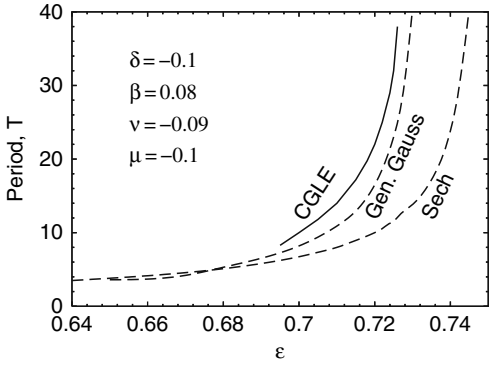

Fig. 6 Period of pulsations, T, as function of ε. The *solid line* is the result of numerical simulations of the CGLE (1). The *dashed lines* correspond to the models (7) and (11)

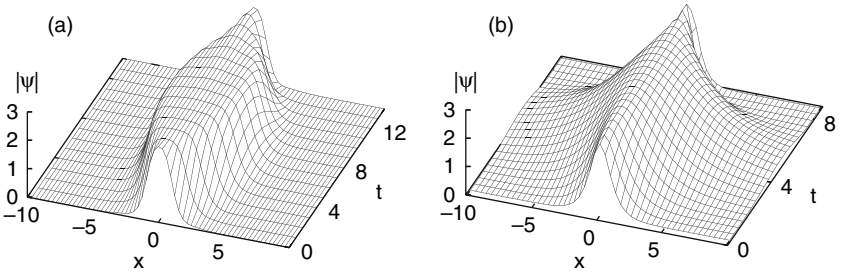

Fig. 7 (**a**) Pulsating soliton found from numerical simulations [31] of (1). (**b**) Soliton reconstructed from the trial function (5) and solution of (7). The system parameters are $\beta = 0.08$, $\varepsilon = 0.66$, $\mu = -0.1$ and $\nu = -0.1$

similar. In particular, the soliton width varies periodically, while the soliton amplitude is close to a constant in each case.

The limited range of parameters in Fig. 1b is chosen in order to establish a correspondence with the known numerical results for CGLE. A comparison of the results obtained from (7) and (11) with the numerical simulations of the full CGLE justifies the validity of the models. Therefore, one can expect that the dynamical systems (7) and (11) will be useful for predicting the bifurcation thresholds in a wider range of the system parameters [38].

5 Creeping Solitons [32, 43]

A creeping soliton is a special type of pulsating localized solution that changes its shape periodically and shifts a finite distance in the transverse direction after each period of oscillation. The value of the shift is constant for each period so that the soliton has a finite average velocity, although the motion occurs as a step-by-step translation in one direction. In most cases, solitons that move in this way have long flat-top profiles that consist of two fronts at the sides of the soliton. The two fronts move asymmetrically in time, thus creating creeping movements of the whole "worm-like" formation. An example is given in Fig. 8.

Creeping solitons were first observed in numerical simulations in [44]. Their existence for various dissipative systems has been confirmed in later publications [31, 45]. There is no technique that would allow us to describe pulsating solutions using exact solutions of the governing equation. Consequently, we have little hope of finding analytical solutions for creeping solitons. The method of moments allows us to approximate roughly the creeping motion. As a particular result, it allows us not only to estimate the period of the pulsations but to include in the model the possibility of translational motion of localized solutions. This requires an additional variable for the velocity of the soliton, and this increases the dimensionality of the finite-dimensional dynamical system. The velocity is also a periodic function of time, and it thus describes the creeping feature of the soliton. The technique also

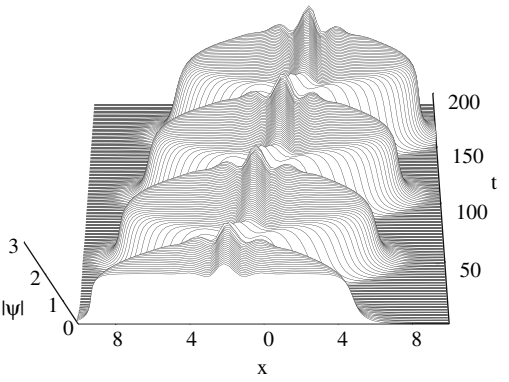

Fig. 8 An example of a creeping soliton of the CGLE. This numerical example was first found in [31]. The present simulation shows more detailed structure of creeping behavior. The asymmetric motion of the two sides of the soliton is clearly visible. The parameters of the equation are $D = 1$, $\delta = -0.1$, $\beta = 0.101$, $\varepsilon = 1.3$, $\mu = -0.3$ and $\nu = -0.101$

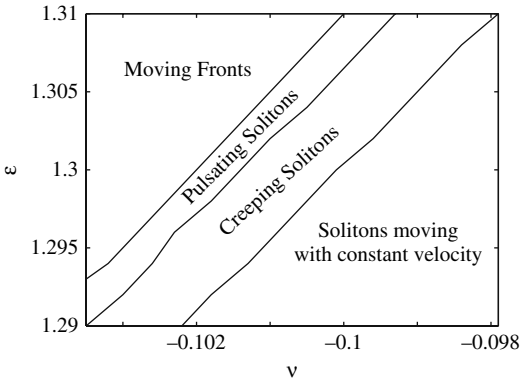

Fig. 9 Region of existence of creeping solitons found by solving the CGLE with δ, β and μ fixed at -0.1, 0.101 and -0.3, respectively. Creeping solitons exist in the central diagonal strip of this plot. Above it, there is a strip that corresponds to pulsating solitons with zero velocity. Above the upper line, solitons increase their width indefinitely, thus transforming into a pair of fronts. Below the central diagonal strip, solitons have stationary profiles and move with constant velocities

allows us to estimate the region of existence of creeping solitons in the space of equation parameters.

Creeping solitons exist in a certain range of the equation parameters. Previously, only isolated examples had been found [31]. Finding the complete region requires extensive numerical simulations. The results of simulations are summarized in Fig. 9. Creeping solitons exist in the central diagonal strip of the (ε, ν) plane. Below this strip, pulsations disappear and pulses are transformed into fixed shape solitons moving with constant velocity. These constant profile pulses are moving along the x-axis. Above the diagonal strip, the pulses are still pulsating but their average velocity is zero. Thus, the creeping feature disappears at the middle solid curve in Fig. 9. Inside the strip, the soliton energy oscillates due to the oscillations of the soliton width. These oscillations are shown in Fig. 10a. The period of the oscillations varies in the range 50–60 across the strip. In each oscillation, the center of mass of the soliton moves by a finite increment. This step wise motion of the center of mass is shown in Fig. 10b. Due to the symmetry of the CGLE with respect to the inversion of the x-axis, a soliton can equally well move to the left or to the right, depending on the initial condition.

5.1 The Choice of Trial Function for Creeping Solitons

As numerical simulations show, a creeping soliton changes its shape during one period from a bell-shaped pulse to a flat-top pulse. Its velocity is generally a constant with an irregular ripple superimposed on it. Therefore, we consider a trial function which is a generalization of a "super-Gaussian" function:

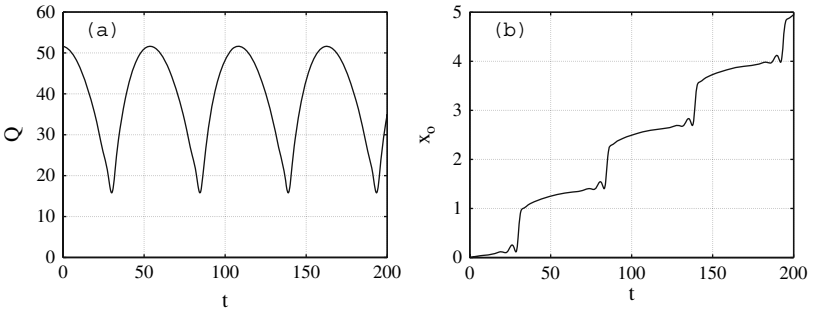

Fig. 10 (**a**) Soliton energy Q vs t for a creeping soliton at the point $\varepsilon = 1.3$, $\nu = -0.101$. The energy oscillates in a wide range showing that the width of the soliton changes appreciably. (**b**) Center of mass of the same soliton vs t. The soliton moves step by step in the direction of increasing x. Due to the symmetry in x, the soliton could also move in the opposite direction if the initial condition was changed

$$\psi(x,t) = a(m)\sqrt{\frac{Q(t)}{w(t)}}\exp\left[-\frac{\sqrt{m}\,y}{w(t)} - \frac{y^4}{32\,w^4(t)} + \mathrm{i}\left(b(t)\,y + c(t)\,y^2\right)\right], \qquad (14)$$

where $y = x - x_0(t)$, $w(t)$ is the width, $b(t)$ and $c(t)$ are the linear part and the quadratic part of the chirp, respectively. The constant m can be chosen arbitrarily, but it is independent of t, while a is a constant that depends on m. It is chosen in such a way that the total energy, $\int_{-\infty}^{\infty} |\psi|^2\,\mathrm{d}x$, equals $Q(t)$. For example, if $m = 0.008$, we have $a = 0.519548$. The trial function given in (14) is deliberately chosen to be non-symmetric in y, otherwise the velocity and linear chirp will approach zero after a short transient. This would mean that we would then effectively have only three ODEs, and the creeping effect could be lost. Using the above trial function, we are still able to obtain analytic results for the integrals required.

The generalized moments in (2) and (3), for any m, are given by

$$\begin{aligned}
M &= -\mathrm{i}\,Q(t)\left(b(t) + 4\sqrt{m}\,\frac{k_t}{k_a}\,c(t)\,w(t)\right),\\
I_1 &= Q(t)\left(2\sqrt{m}\,\frac{k_t}{k_a}\,w(t) + x_0(t)\right),\\
I_2 &= 4\,\frac{k_b}{k_a}\,Q(t)\,w^2(t), \qquad (15)\\
I_3 &= \frac{16\,\mathrm{i}}{3\,k_a}\,w(t)\,Q(t)\left(3\,k_b c(t)\,w(t) - \sqrt{m}\,k_c\,b(t)\right),
\end{aligned}$$

where the constants k_i are given by the following expressions:

$$
\begin{aligned}
k_a &= \Gamma\left(\frac{1}{4}\right) H\left(\frac{1}{2},\frac{3}{4};m\right) + 8m\Gamma\left(\frac{3}{4}\right) H\left(\frac{5}{4},\frac{3}{2};m\right),\\
k_t &= \Gamma\left(-\frac{1}{4}\right) H\left(\frac{1}{2},\frac{5}{4};m\right) + 2m\Gamma\left(-\frac{3}{4}\right) H\left(\frac{3}{2},\frac{7}{4};m\right),\\
k_b &= \Gamma\left(\frac{3}{4}\right) H\left(\frac{1}{4},\frac{1}{2};m\right) + 8m\Gamma\left(\frac{5}{4}\right) H\left(\frac{3}{4},\frac{3}{2};m\right),\\
k_c &= 3\Gamma\left(\frac{3}{4}\right) H\left(\frac{1}{2},\frac{5}{4};m\right) + 8m\Gamma\left(\frac{5}{4}\right) H\left(\frac{3}{2},\frac{7}{4};m\right). \qquad (16)
\end{aligned}
$$

In these terms, we have used the function $H(r,s;m)$ to represent the generalized hypergeometric function ${}_0F_2\left(\{\};r,s;m^2\right)$.

For $m \to 0$, we thus get the expected results for a symmetric function. Now, we are in a position to take the derivatives of (15) with respect to t and equate them with the right hand sides of (4). After rearrangement, we obtain five coupled ODEs for the t-dependent parameters. By solving the ODEs, we obtain equations for evolution of soliton parameters. In particular, we find that solitons can have a non-zero velocity in a certain range of the original equation parameters. All soliton parameters in this region are oscillating. This solution is a limit cycle in the five-dimensional phase space. Two projections of this limit cycle into a two-dimensional plane of parameters are shown in Fig. 11. For lower values of ε, the parametric plot tends to a round shape, and hence the velocity of the center of mass and the energy Q are approximately sinusoidal functions of t. Indeed, with $\varepsilon = 1.29$, the velocity appears to be almost sinusoidal. For larger values of ε, the parametric plot becomes more elongated. This kind of irregularity is more evident as ε reaches the upper boundary of the creeping range. The closed curve parametric plots become larger in area since both x_0' and Q have a larger range of oscillations as ε increases.

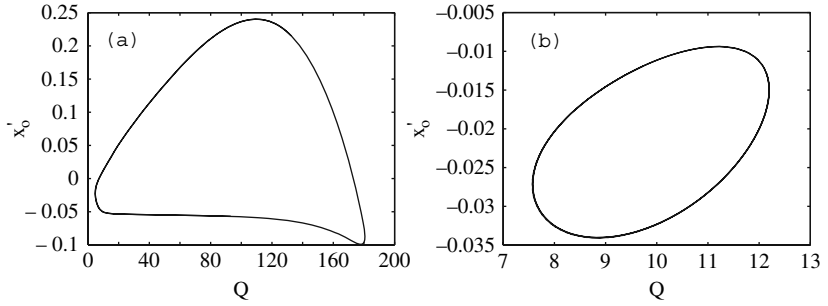

Fig. 11 Parametric plots of the soliton velocity x_0' vs energy Q for (**a**) $\varepsilon = 1.45$ and (**b**) $\varepsilon = 1.29$. Other parameters for this calculation are chosen as $D = 1$, $\delta = -0.1$, $\beta = 0.101$, $\mu = -0.3$, $\nu = -0.101$, while $m = 0.0025$. This value of m gives reasonably good agreement with the numerical solutions of the CGLE

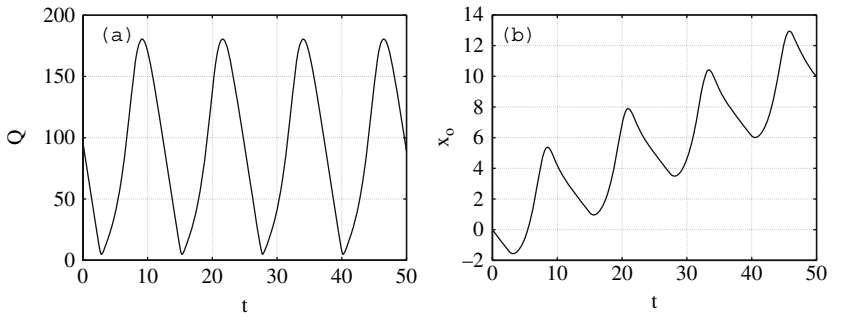

Fig. 12 (**a**) Soliton energy Q and (**b**) center of mass x_0 along the propagation t for a creeping soliton in the reduced model with $\varepsilon = 1.45$. Other parameters for this calculation are chosen as $D = 1$, $\delta = -0.1$, $\beta = 0.101$, $\mu = -0.3$, $\nu = -0.101$, while $m = 0.0025$

Periodic evolution of the energy Q and zig-zag type motion of the center of mass of the soliton x_0 along t are shown in Fig. 12. Qualitatively, these curves are similar to those shown in Fig. 10. Clearly, we cannot expect a better fit because of the dramatic reduction of the number of degrees of freedom when using the trial function. However, the possibility of modeling of the creeping solitons using a simple trial function is remarkable in itself.

The results for the region of existence of creeping solitons in a low-dimensional approximation are shown in Fig. 13. Similar to the numerical results, the creeping solitons occur in a central diagonal strip in Fig. 13. For lower values of ε, the limit cycle contracts to a fixed point with all parameters including the velocity being constant. This transition is a Hopf bifurcation. Thus, below the diagonal strip, we have solitons with constant shape and constant velocity the same way as in numerical simulations.

As ε increases, the period of all five parameters increases. At the upper limit of existence of creeping solitons, the soliton becomes wider while retaining a constant

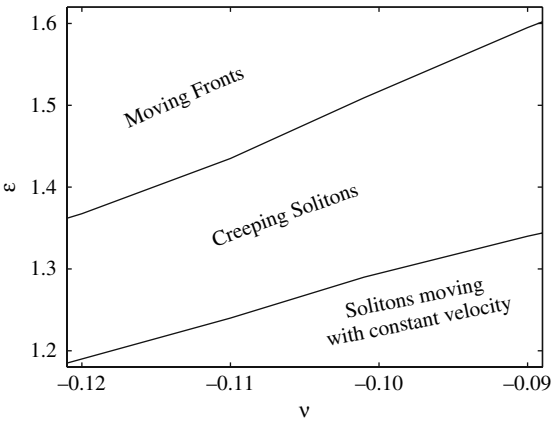

Fig. 13 Region of existence of creeping solitons in $(\varepsilon - \nu)$ plane. Here, $D = 1$, $\delta = -0.1$, $\beta = 0.101$, $\mu = -0.3$, while we set $m = 0.0025$. For $\nu = -0.101$, the transition from fixed point to creeping soliton occurs at $\varepsilon \approx 1.29$, while the bifurcation from creeping to moving fronts occurs at $\varepsilon = \varepsilon_0 \approx 1.5092$

amplitude, so the energy Q becomes approximately proportional to the width. At the top of the "creeping" range, the period becomes infinite, and there is a bifurcation to solitons with constantly increasing width. This behavior corresponds to the splitting of a soliton into a pair of fronts moving away from each other in numerical simulations. However, the velocity of the center of mass for this soliton is not zero, as was the case in the numerical simulations. Thus, in our reduced model we have only a single boundary separating creeping solitons from moving fronts (see Fig. 13). Again, this is hardly surprising if we take into account the drastic reduction in the number of degrees of freedom in our simplified model. Despite these discrepancies, the qualitative location of the region of existence of the creeping solitons and the boundary slopes are remarkably similar to those obtained in the numerical simulations.

6 Solitons and Antisolitons [28]

To conclude our chapter, we give one more example where soliton modeling using a simple trial function can be useful. In particular, this approach allows us to predict the existence of one more branch of stationary solitons that could be important for applications. Due to the many parameters which appear in the CGLE, finding all the branches using numerical simulations of it is indeed a difficult task.

To find the stationary solitons, we shall use again the trial function (9) and the corresponding dynamical system (11). Stationary solutions of (11) are given by the soliton parameters which are t independent, i.e., $Q(t) = Q_0$, $w(t) = w_0$ and $c(t) = c_0$. The latter case corresponds to a fixed point (FP) of the dynamical system (11). Fixed points of this three-variable dynamical system, together with the trial function (9), approximate the stationary solitons of the CGLE. Standard linearization techniques can be used to find the stability of these FPs. Unstable FPs usually correspond to unstable solitons. Stable FPs may correspond to stable solitons, but this has to be confirmed by direct numerical simulations of the CGLE. This is related to the fact that an infinite-dimensional dynamical system has more degrees of freedom to develop a soliton instability.

Solving the dynamical system (11) for various ε, μ and ν, regions of stable and unstable fixed points can be constructed in the space of these three parameters of the CGLE. Two plots representing the regions of stable and unstable FPs for fixed values of D, δ and β are shown in Fig. 14a and b. Each plot is a two-dimensional slice of the six-dimensional space of the equation parameters. Each of these plots clearly shows the existence of two separate regions of stable fixed points. A point from one region cannot be transformed into a point from the other region with a continuous change of parameters. Thus, it appears that these two regions correspond to two different types of solitons of the CGLE. One of the branches has high energy, Q_0, while the other one has low energy. Within the low-dimensional approximation (11), these FPs are stable in both regions. However, the results for the stability of exact CGLE solitons may differ, as we explained above.

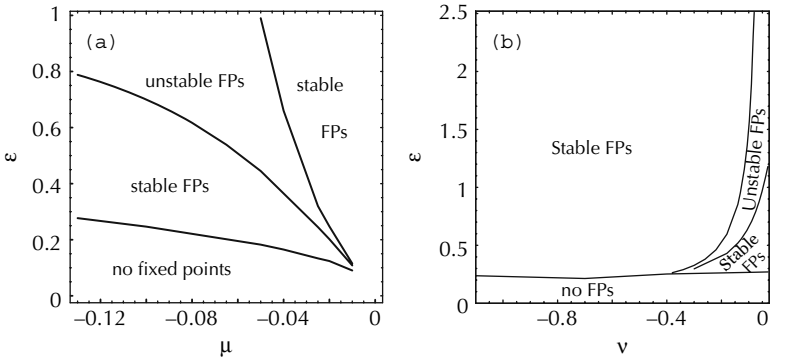

Fig. 14 Soliton bifurcation diagram (**a**) on the $\varepsilon - \mu$ plane and (**b**) on the $\varepsilon - \nu$ plane. There are two regions of stable fixed points that correspond to two quite different branches of solitons. In (**a**), $\delta = -0.1$, $\nu = -0.08$ and $\beta = 0.08$. In (**b**), $\mu - 0.1$, $\delta = -0.1$ and $\beta = 0.125$

Direct simulations of the CGLE (1) confirm the predictions made using the low-dimensional approximation. Figure 15a, numerically obtained, shows regions in the (μ, ε) plane where stationary localized solutions can be found. As predicted by the simple model, there are two separate regions in the parameter space where dissipative solitons exist. The gray regions correspond to stable stationary solitons while the hatched region corresponds to exploding solitons [31, 44, 46]. A comparison between Fig. 14a and Fig. 15a shows that there is not only a qualitative agreement between them, but that they also coincide reasonably well quantitatively. Our simple model, of course, cannot describe the explosive instability that is related to many

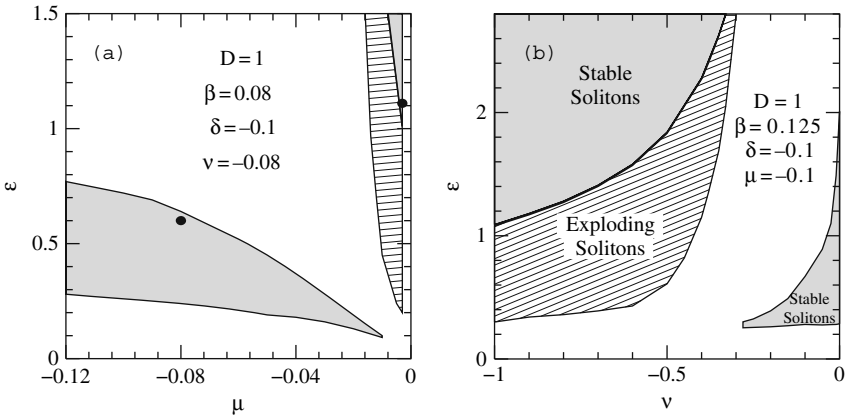

Fig. 15 Regions of existence of the two types of solitons (gray) in (**a**) (ε, μ) and (**b**) (ε, ν) plane. In each case, the two separate regions are quite distinct. Parameters are shown in the plot. The hatched region corresponds to exploding solitons

degrees of freedom of the CGLE solitons [46]. Thus, explosive solitons in a simple model will be in the area of stable fixed points. If we take this into account, the correspondence between the exact numerical results and the predictions of the low-dimensional approximation is remarkably close.

Figure 15b compiles the results of numerical simulations of the CGLE for the plane of parameters (ν, ε). Again, gray regions are for stable solitons while the hatched region is for exploding solitons. Comparing these results with those in Fig. 14b again shows a good qualitative agreement.

The results for the exact field amplitude and phase profiles of the solutions for each region of existence of stable solitons are presented in Fig. 16. The solid lines represent the field amplitude of the solitons, while the dashed lines are their phase profiles. The upper curves (a) in Fig. 16 correspond to the upper-right thick black point in Fig. 15a and vice versa: the lower curves (b) in Fig. 16 correspond to the lower-left thick black point. There are some obvious differences in the energies, widths and amplitudes of the two solitons. However, the most visible qualitative difference is in the soliton chirp. The phase profiles clearly show that the chirps in the two cases are of opposite signs. Due to this difference, the energy flows from the inside to the outside of the soliton in the first case while it flows inwards in the second case.

The results obtained from the finite dimensional model (11) show that, for Fig. 14a, the upper right corner region has $c_0 > 0$ and it is large in magnitude, i.e., there is a strong chirp across the soliton. On the other hand, the stable FP on the lower left region has $c_0 < 0$ and it is small in magnitude, so the soliton is weakly chirped. As regards Fig. 14b, we have $c_0 < 0$ in the lower right hand corner region (low energy Q_0), while we find $c_0 > 0$ in the upper left corner region (high energy Q_0). The same patterns for the chirp signs are obtained in the two distinct regions in Fig. 15a and b when directly solving the CGLE.

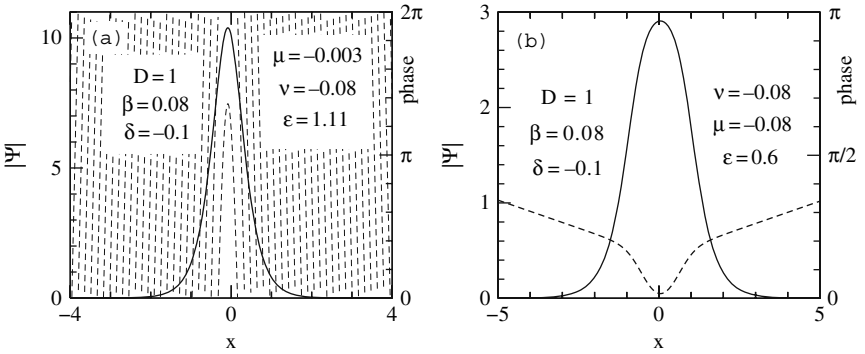

Fig. 16 Exact soliton profiles (*solid lines*) of two examples in the (**a**) upper and (**b**) lower regions in Fig. 15b. They are marked by thick black dots in Fig. 15b. *Dashed lines* show their corresponding phase profiles

The finite-dimensional model can be used to directly relate the chirp to the energy generation $P(x)$ and flux $j(x)$ (see Sect. 6 of [25]). Using the trial function (9) for arbitrary m, with $A = \sqrt{\frac{Q_0}{w_0}}$, for stationary solutions we find

$$j(x) = \frac{\mathrm{i}}{2}(\psi\,\psi_x^* - \psi_x\,\psi^*) = c_0\,GX\,\exp\left[-2X^2\left(1+\frac{X^2}{4m}\right)\right], \tag{17}$$

and

$$P(x) = \frac{\mathrm{d}j}{\mathrm{d}x} = c_0\,\frac{G}{w_0}\left(1-4X^2-\frac{2}{m}X^4\right)\exp\left[-2X^2\left(1+\frac{X^2}{4m}\right)\right], \tag{18}$$

where $G = 2a^2(m)\,Q_0$ and the normalized transverse variable $X = x/w_0$. We have the condition that the total energy generation is zero:

$$\int_{-\infty}^{\infty} P(x)\,\mathrm{d}x = 0. \tag{19}$$

This condition has to be satisfied for stationary solutions and is clearly valid for these trial functions.

The curves for P divided by c_0G/w_0 and j divided by c_0G are shown in Fig. 17. It is clear that both the flux, j, and energy generation, P, change signs with c_0, since they are directly proportional to c_0 ($M > 0$, and $w_0 > 0$). Thus, the sign of the chirp has an important physical implication. If $c_0 < 0$, then $P > 0$ in the wings and $P < 0$ around the pulse center. This means that energy is generated in the wings and flows toward the middle, where it is dissipated. Conversely, if $c_0 > 0$, then $P < 0$ in the wings and $P > 0$ around the pulse center, so energy is generated in the middle and flows toward the wings, where it is lost. This process, involving an internal flux of energy, produces the dynamic equilibrium which we call a dissipative soliton.

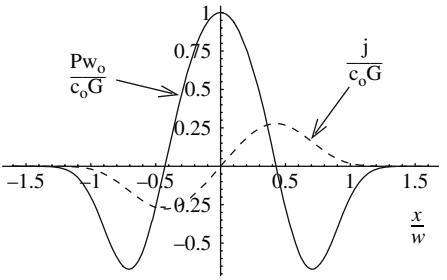

Fig. 17 Density of energy generation P across the soliton divided by c_0G/w_0 (*solid line*) and energy flux j divided by c_0G (*dashed line*) for low-dimensional model with $m = 1/4$. If $c_0 > 0$, then the curve shapes for P and j are as shown here so that energy is generated in the center. However, the curves for P and j are plainly inverted if $c_0 < 0$, and then the energy is dissipated in the center

The different signs of chirp appearing for each region (high Q and low Q) mean that the phase profile across the soliton is concave up in one case and concave down in the other. Hence, we can designate them "solitons" and "antisolitons" for convenience. The phase profile for the CGLE solitons is not exactly parabolic, of course, but it is clear from Fig. 16a and b that the effective chirp coefficients are opposite in sign and that the chirp magnitude in Fig. 16a is much greater than that in Fig. 16b.

For comparison, we plot the distribution of energy generated and dissipated inside of the two types of the CGLE solitons in Fig. 18a and b. We can see clearly that in the first case (a), the energy generation is positive in the middle of the soliton and negative in the wings, while in the second case (b), the energy is generated in the tails of the soliton and dissipated in the middle. Thus, there is a fundamental qualitative difference between the two types of solitons. One type cannot be transformed into the other with a continuous change of parameters. To be specific, we call the solitons with lower energy and $c_0 < 0$ (ordinary) dissipative solitons and the localized solutions of the upper branch (with $c_0 > 0$) "dissipative antisolitons". The fact that antisolitons have much higher energy than solitons may have important consequence for the development of high-power pulse-generating passively mode-locked lasers. It is very likely that antisolitons have been already observed experimentally in the recent paper [47].

Above, we have presented three examples of approximate analysis of dissipative solitons and bifurcations between them. These give some flavor of what can be done analytically in the study of soliton transformations of the CGLE. In these examples, we were able to describe bifurcations between stationary and pulsating solitons as well as bifurcations between pulsating and creeping solitons. The approach also allowed us to predict the existence of a new branch of stationary solitons, and this was then confirmed by direct numerical simulations. Taking into account the fact that several system parameters control bifurcations of CGLE solitons, it is hard to imagine that any other technique would give similar results.

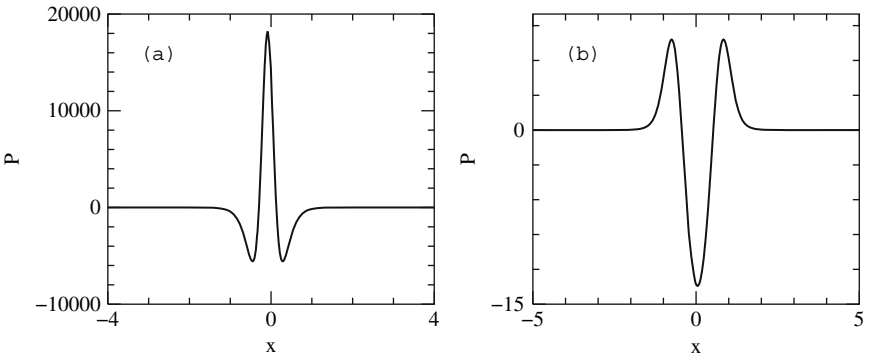

Fig. 18 Energy generation, P, inside the two types of solitons shown in Fig. 16. In (**a**), the energy is generated in the middle of the soliton and is dissipated in the tails, while in (**b**), it is generated in the tails and dissipated in the center

7 Conclusions

The notion of the dissipative soliton has emerged from a three-part foundation. To be specific, these parts are classical soliton theory, nonlinear dynamics (with its theory of bifurcations) and Prigogine's concept of self-organization. These underlying ideas set us up for a comprehensive understanding of the new notion and allow us to explain the basic properties of solitons in dissipative systems. Complications which arise from the fact the dynamical systems usually have an infinite number of degrees of freedom can be overcome by using reductions to low-dimensional systems. However, these reductions always need to be done carefully by comparing the conclusions with the results of particular numerical simulations of the original equation.

Acknowledgements The authors acknowledge support from the Australian Research Council (Discovery Project DP0663216).

References

1. N. Akhmediev and A. Ankiewicz, Solitons around us: Integrable, Hamiltonian and dissipative systems, in *Optical Solitons: Theoretical and Experimental Challenges*, Edited by K. Porsezian and V.C. Kurakose, (Springer, Berlin-Heidelberg, 2003), pp. 105–126. 1, 5, 6
2. N. Akhmediev and A. Ankiewicz, Solitons of the complex Ginzburg–Landau equation, in *Spatial Solitons* 1, Edited by S. Trillo and W.E. Toruellas, (Springer, Berlin-Heidelberg, 2001), pp. 311–342. 1
3. N. Akhmediev, General theory of solitons, in *Soliton-Driven Photonics*, edited by A.D. Boardman and A.P. Sukhorukov, (Kluver Academic Publishers, Netherlands, 2001), pp. 371–395. 1
4. N.J. Zabusky and M.D. Kruskal, Interaction of 'solitons' in a collisionless plasma and the recurrence of initial states, Phys. Rev. Lett. **15**, 240–243 (1965). 1
5. J.S. Russell, Report of the fourteenth meeting of the British Association for the Advancement of Science, York, 1844 (London 1845), pp. 311–390, Plates XLVII-LVII. 2
6. C.S. Gardner, J.M. Greene, M.D. Kruskal, and K.M. Miura, Method for solving the Korteweg–de Vries equation, Phys. Rev. Lett. **19**, 1095–1097 (1967). 2
7. V.E. Zakharov and A.B. Shabat, Exact theory of two dimensional self focusing and one dimensional self modulation of nonlinear waves in nonlinear media, *Sov. Phys. JETP*, **34**, 62–69 (1971)]. Original (in Russian): Zh. Eksp. Teor. Fiz. **61**, 118. 2
8. M.J. Ablowitz and P.A. Clarkson, *Solitons, Nonlinear Evolution Equations and Inverse Scattering*, London Mathematical Society Lecture Notes Series **149**, (Cambridge University Press, Cambridge, (1991). 2
9. G.P. Agrawal, *Nonlinear Fiber Optics*, 2nd edn, (Academic Press Inc., San Diego, CA, 1995). 2
10. E. Picholle, C. Montes, C. Leycuras, O. Legrand, and J. Botineau, Observation of dissipative superluminous solitons in a Brillouin fiber ring laser, Phys. Rev. Lett. **66**, 1454 (1991). 2
11. C.I. Christov and M.G. Velarde, Dissipative solitons, Physica D, **86**, 323–347 (1995). 2
12. Akhmediev, N., Ankiewicz, A. (eds.): *Dissipative Solitons*. Lect. Notes Phys. **V. 661**. Springer, Heidelberg (2005). 2, 27
13. B.S. Kerner and V.V. Osipov, *Autosolitons: A New Approach to Problems of Self-Organization and Turbulence, Fundamental Theories of Physics*, **61**, (Kluwer Academic Publishers, Dordrecht, 1996). 4

14. H.-G. Purwins, H.U. Bödeker and A.W. Liehr, Dissipative Solitons in Reaction-Diffusion Systems, Chapter 10 in the book [12]. 4
15. H. Haken, *Synergetics*, (Springer-Verlag, Berlin, 1983). 4
16. N. Bekki and K. Nozaki, Formations of spatial patterns and holes in the generalized Ginzburg–Landau equation, Phys. Lett. A, **110**, 133–135 (1985). 5
17. W. Van Saarloos and P.C. Hohenberg, Fronts, pulses, sources and sinks in generalized complex Ginzburg–Landau equations, Physica D **56**, 303–367 (1992). 5
18. N. Akhmediev and V. Afanasjev, Novel arbitrary-amplitude soliton solutions of the cubic–quintic complex Ginzburg–Landau equation, Phys. Rev. Lett. **75**, 2320–2323 (1995). 5
19. V.B. Taranenko, K. Staliunas, and C.O. Weiss, Spatial soliton laser: Localized structures in a laser with a saturable absorber in a self-imaging resonator, Phys. Rev. A **56**, 1582–1591 (1997). 5
20. W.J. Firth and A.J. Scroggie, Optical bullet holes: Robust controllable localized states of a nonlinear cavity, Phys. Rev. Lett. **76**, 1623–1626 (1996). 5
21. N.A. Kaliteevstii, N.N. Rozanov, and S. Fedorov, V. Formation of laser bullets, Opt. Spectrosc. **85**, 533–534 (1998). 5
22. D. Mihalache, D. Mazilu, F. Lederer, H. Leblond, and B.A. Malomed, Stability of dissipative optical solitons in the three–dimensional cubic–quintic Ginzburg-Landau equation, Phys. Rev. A **75**, 033811 (2007). 5
23. J.M. Soto-Crespo, N. Akhmediev, and Ph. Grelu, Optical bullets and double bullet complexes in dissipative systems, Phys. Rev. E **74**, 046612 (2006). 5
24. D. Michaelis, U. Peschel, and F. Lederer, Oscillating dark cavity solitons, Opt. Lett. **23**, 1814–1816 (1998). 5
25. N. Akhmediev and A. Ankiewicz, Dissipative Solitons in the Complex Ginzburg–Landau and Swift-Hohenberg Equations, Chapter 1 in [12]. 5, 6, 10, 11, 24
26. I.S. Aranson and L. Kramer, The world of the complex Ginzburg–Landau equation, Rev. Mod. Phys. **74**, 100 (2002). 7
27. J.M. Soto-Crespo, N. Akhmediev, and V.V. Afanasjev, Stability of the pulselike solutions of the quintic complex Ginzburg–Landau equation, JOSA B **13**, No 7, 1439–1449, (1996). 7
28. A. Ankiewicz, N. Devine, N. Akhmediev, and J.M. Soto-Crespo, Dissipative solitons and antisolitons, Phys. Lett. A **368**, September (2007). ix, 7, 21
29. N. Akhmediev, J.M. Soto-Crespo, and Ph. Grelu, Vibrating and shaking soliton pairs in dissipative systems, Phys. Lett. A **364**, 413–416 (2007). 7
30. N. Akhmediev and A. Ankiewicz, *Solitons, Nonlinear Pulses and beams*, (Chapman and Hall, London, 1997). 7
31. N. Akhmediev, J.M. Soto-Crespo, and G. Town, Pulsating solitons, chaotic solitons, period doubling, and pulse coexistence in mode-locked lasers: CGLE approach, Phys. Rev. E **63**, 056602 (2001). 7, 10, 11, 13, 14, 15, 16, 17, 22
32. W. Chang, A. Ankiewicz, N. Akhmediev, and J.M. Soto-Crespo, Creeping solitons in dissipative systems and their bifurctaions, Phys. Rev. E **76**, 016607 (2007). ix, 7, 16
33. A.I. Maimistov, Evolution of solitary waves which are approximately solitons of a nonlinear Schrödinger equation, J. Exp. Theor. Phys. **77**, 727 (1993) [Zh. Eksp. Teor. Fiz. **104**, 3620 (1993), in Russian]. 8, 9
34. E.N. Tsoy and C.M. de Sterke, Propagation of nonlinear pulses in chirped fiber gratings, Phys. Rev. E **62**, 2882 (2000). 9
35. F.Kh. Abdullaev, D.V. Navotny, and B.B. Baizakov, Optical pulse propagation in fibers with random dispersion, Physica D **192**, 83 (2004). 9
36. M.N. Zhuravlev and N.V. Ostrovskaya, Dynamics of NLS solitons described by the cubic–quintic Ginzburg–Landau equation, J. Exper. Theor. Phys. **99**, 427 (2004) [Zh. Eksp. Teor. Fiz. **126**, 483 (2004), in Russian]. 9, 10
37. E. Tsoy and N. Akhmediev, Bifurcations from stationary to pulsating solitons in the cubic–quintic complex Ginzburg–Landau equation, Phys. Lett. A **343**, 417–422 (2005). ix, 9, 10
38. E. Tsoy, A. Ankiewicz, and N. Akhmediev, Dynamical models for dissipative localized waves of the complex Ginzburg–Landau equation, Phys. Rev. E **73**, 036621 (2006). ix, 9, 10, 12, 16

39. N. Akhmediev, A. Ankiewicz and J.M. Soto-Crespo, Stable soliton pairs in optical transmission lines and fiber lasers, J. Opt. Soc. Am. B **15**, 515 (1998). 9
40. J.M. Soto-Crespo, M. Grapinet, Ph. Grelu, and N. Akhmediev, Bifurcations and multiple period soliton pulsations in a passively mode-locked fiber laser, Phys. Rev. E **70**, 066612 (2004). 10
41. J. Guckenheimer and P. Holmes, *Nonlinear Oscillations, Dynamical Systems and Bifurcations of Vector Fields*, (Springer-Verlag, New York, 1983). 13
42. J. Satsuma and N. Yajima, Initial value-problems of one-dimensional self-modulation of nonlinear waves in dispersive media, Progr. Theor. Phys. Suppl. **55**, 284 (1974). 14
43. W. Chang, A. Ankiewicz, N. Akhmediev, and J.M. Soto-Crespo, Creeping solitons of the complex Ginzburg–Landau equation with a low-dimensional dynamical system model, Phys. Lett. A**362**, 31–36 (2007). ix, 16
44. J.M. Soto-Crespo, N. Akhmediev and A. Ankiewicz, Pulsating, creeping, and erupting solitons in dissipative systems, Phys. Rev. Lett. **85**, 2937–2940, (2000). 16, 22
45. H.P. Tian, Z.H. Li, J.P. Tian, G.S. Zhou and J. Zi, Effect of nonlinear gradient terms on pulsating, erupting and creeping solitons, Appl. Phys. B **78**, 199–204 (2004). 16
46. N. Akhmediev and J.M. Soto–Crespo, Exploding solitons and Shil'nikov's theorem, Phys. Lett. A **317**, 287–292 (2003). 22, 23
47. A. Fernandez, T. Fuji, A. Poppe, A. Frbach, F. Krausz, and A. Apolonski, Chirped-pulse oscillators: A route to high-power femtosecond pulses without external amplification, Opt. Lett. **29**, 1366–1368 (2004). 25

Solitons in Viscous Flows

M.G. Velarde and A.A. Nepomnyashchy

Abstract Building upon nonlinearity, dispersion and dissipation (in most cases including an appropriate input–output energy balance), we offer a discussion of a rich panoply of mathematical model equations whose solutions are dissipative solitons. The presentation is made by first introducing heuristic arguments and subsequently developing appropriate long-wave expansions to account for the phenomena involved in the most significant way.

1 Introduction

A deep understanding of a wide variety of nonlinear phenomena in different branches of physics and beyond has been achieved by means of exactly integrable model equations. Such models, which are usually obtained from small-amplitude and long-wavelength asymptotic expansions, describe nature approximately. Additional physical effects (e.g., dissipation, various levels of dispersion and nonlinearity, some external perturbations) spoil integrability. However, for "nearly" integrable systems, the evolution can be described by means of perturbation theory, building upon the dynamics of solitary waves or solitons.

For instance, observations demonstrate "nearly" integrable dynamics of solitary waves produced by the Marangoni instability of a liquid surface in the presence of a transverse concentration or thermal gradient [1] and in some active lattice problems [2]. These observations are quite remarkable, because Marangoni convection

M.G. Velarde
Instituto Pluridisciplinar, Universidad Complutense de Madrid, Paseo Juan XXIII, 1, Madrid E-28040, Spain, mgvelarde@pluri.ucm.es

A.A. Nepomnyashchy
Technion-Israel Institute of Technology, Technion City, Haifa 32000, Israel, nepom@math.technion.ac.il

Velarde, M.G., Nepomnyashchy, A.A.: *Solitons in Viscous Flows.* Lect. Notes Phys. **751**, 29–49 (2008)
DOI 10.1007/978-3-540-78217-9_2

is a typical example of a strongly dissipative system. Nevertheless, it was shown [3, 4, 5] that the problem can be described, in a certain approximation, by means of weakly perturbed Boussinesq–Korteweg–de Vries (BKdV) [6, 7] and Kadomtsev–Petviashvili [5] equations. The paradigmatic BKdV soliton-bearing equation is

$$h_t + \omega_1 h_x - \omega_3 h_{xxx} + \kappa_1 (h^2)_x = 0. \tag{1}$$

This equation governs the weakly nonlinear dynamics of dispersive waves with the dispersion relation between the frequency, ω, and wave-number, k, being

$$\omega(k) = \omega_1 k + \omega_3 k^3. \tag{2}$$

This corresponds to the long-wave limit of the dispersion relation of gravity-capillary waves in a inviscid liquid. Soliton solutions of this equation exist due to the balance of dispersion and nonlinear effects.

In this chapter, we consider solitary waves in viscous flows as dissipative solitons. The existence of such solitons is based on both the balance between the dispersion and nonlinearity and, more importantly, on the balance between viscous dissipation and energy gain caused by an instability. In each case, we start with the construction of a heuristic model which accounts for the basic physical phenomena (dispersion, nonlinearity, energy gain and loss) and justify it with a direct derivation by means of long-wave expansions. It is shown that the complex Ginzburg–Landau equation is not applicable to the description of instabilities in systems with a conservation law, due to the appearance of a Goldstone mode. Also, we discuss the stability of solitary and periodic waves.

2 Basic Models

2.1 Heuristic Arguments

Let us now discuss the conditions for the existence of long-wave solitary waves in a dissipative medium or flow. In the absence of the energy conservation, the quantity $\omega(k)$, corresponding to the evolution of linear waves,

$$h(x,t) = \int_{-\infty}^{\infty} \frac{\mathrm{d}k}{2\pi} \hat{h}(k) \mathrm{e}^{\mathrm{i}(kx - \omega(k)t)}, \tag{3}$$

is not real: $\omega(k) = \omega_r(k) + \mathrm{i}\omega_i(k)$. Because $h(x,t)$ is real, we have

$$\omega(-k) = -\omega^*(k). \tag{4}$$

If $\omega(k)$ is analytic at $k = 0$, then, in the long-wave region,

$$\omega_r(k) = \omega_1 k + \omega_3 k^3 + \cdots, \ \omega_i(k) = \omega_0 + \omega_2 k^2 + \omega_4 k^4 + \cdots. \tag{5}$$

In the case of interfacial waves in an incompressible liquid, $\omega_0 = 0$ because the temporal change of the volume,

$$\int_{-\infty}^{\infty} h(x,t)\mathrm{d}x = \hat{h}(0)\mathrm{e}^{\mathrm{i}\omega_0 t},$$

is not compatible with the liquid's incompressibility.

One can expect that a long-scale soliton may persist if the energy gain and loss are somehow balanced, i.e., if $\omega_i(k)$ is positive in the long-wave region and negative in the short-wave region, so that $\omega_2 > 0$ and $\omega_4 < 0$. Thus, for the construction of the simplest model which includes a long-wave energy gain and a short-wave energy loss, we can add two linear terms to the BKdV equation, in addition to the dispersion and nonlinearity:

$$h_t + \omega_1 h_x - \omega_3 h_{xxx} + \kappa_1 (h^2)_x + \omega_2 h_{xx} + |\omega_4| h_{xxxx} = 0. \tag{6}$$

Equation (6), which is known as the *Kawahara equation*, is a minimum long-wave dissipative model which indeed has solitary-wave solutions, as well as spatially periodic and spatially irregular solutions [8, 9, 10, 11, 12]. Some exact solutions of this equation are known [13]. The stability of periodic solutions of this equation was investigated in [14, 15].

However, the Kawahara equation is not a *generic* equation describing weakly nonlinear dispersive wave generated by a long-wave instability. It contains only *linear* non-conservative terms. Real physical problems also contain some non-conservative nonlinearities which can contribute to the dynamics of long-scale solitons. This question is considered in the next subsection.

2.2 Amplitude Equation for a Long-Wave Instability

Let us now describe the weakly nonlinear development of a long-wave instability characterized by the dispersion relation (5) in a quantitative way. Consider a physical system described by a set of variables $U(\mathbf{r},t)$ and governed by a set of nonlinear partial differential equations. Assume that the system is bounded in the y- and z-directions but is infinite in the x-direction. Also, we assume that the external conditions are homogeneous in x and t, and depend on just one parameter, M. Finally, we suppose that, for each M, there exists a solution $U = U_0(y,z,M)$, called *base flow*, which does not depend on x and t.

An infinitesimal disturbance, $\tilde{U}(\mathbf{r},t)$, governed by a linearized system of equations can be represented as a superposition of normal modes

$$\tilde{u}_n(y,z;k,M)\mathrm{e}^{\lambda_n(k,M)t+\mathrm{i}kx},\ n = 1,2,\dots, \tag{7}$$

where the functions $\tilde{u}_n$ are eigenfunctions of a certain eigenvalue boundary problem, and the $\lambda_n(k,M)$ are the corresponding eigenvalues.

Let us assume that $\mathrm{Re}\lambda_n(k,M) \le 0$ for any k and n, if $M \le M_c$, but that, for $M > M_c$, there exists a single eigenmode

$$\{\tilde{u}_m(k,M),\ \lambda_m(k,M)\},\ \lambda_m(k,M) \equiv \lambda_\mathrm{r}(k,M) + \mathrm{i}\lambda_\mathrm{i}(k,M),$$

such that $\lambda_\mathrm{r}(k,M) > 0$ for some k. Because the original equations are real,

$$\tilde{u}_m(k,M) = \tilde{u}_m^*(-k,M),\ \lambda_m(k,M) = \lambda_m^*(-k,M). \tag{8}$$

Specifically, for $k = 0$ we obtain

$$\tilde{u}_m(0,M) = \tilde{u}_m^*(0,M),\ \lambda_m(0,M) = \lambda_m^*(0,M), \tag{9}$$

therefore

$$\frac{\partial \lambda_\mathrm{r}(0,M)}{\partial k}(0,M) = 0, \tag{10}$$

for any M.

There is a wide class of problems where the growth of a spatially homogeneous disturbance is ruled out by a *conservation law*. For instance, as we discussed in the previous subsection, in the case of a wavy instability of a layer of an incompressible fluid with a free surface, a spatially uniform change of the layer thickness is impossible because of the conservation of the fluid volume. In this case, there exists the *Goldstone mode* with

$$\lambda_m(0,M) = 0, \tag{11}$$

for any M, and it can produce a *long-wavelength instability* for any non-zero k, no matter how small. Now, $\partial^2\lambda_\mathrm{r}(0,M)/\partial k^2(0,M)$ changes its sign at the threshold of instability $M = M_c$, but $\lambda_\mathrm{r}(0,M)$ does not:

$$\lambda_\mathrm{r} = \frac{1}{2}\left(\frac{\partial^3\lambda_\mathrm{r}}{\partial k^2 \partial M}\right)_c k^2(M - M_c) + \frac{1}{24}\left(\frac{\partial^4\lambda_\mathrm{r}}{\partial k^4}\right)_c k^4 + \cdots, \tag{12}$$

$$\lambda_\mathrm{i} = \left(\frac{\partial\lambda_\mathrm{i}}{\partial k}\right)_c k + \left(\frac{\partial^2\lambda_\mathrm{i}}{\partial k \partial M}\right)_c k(M - M_c) + \frac{1}{6}\left(\frac{\partial^3\lambda_\mathrm{i}}{\partial k^3}\right)_c k^3 + \cdots \tag{13}$$

(subscript c means $k = 0,\ M = M_c$).

Let us briefly describe the general scheme for the derivation of long-wavelength amplitude equations [16]. We introduce a new spatial variable $x_1 = \varepsilon x$ and an infinite number sequence of time variables $t_n = \varepsilon^n t$, $n = 1, 2, \ldots$. The deviation of the solution, U, from the base flow, U_0, is expanded into an asymptotic series in powers of ε. Putting $M = M_c + M_2\varepsilon^2$, we collect terms of the same order in ε. For the lowest order, one can find

$$U - U_0 = \varepsilon^p a_1(x_1, t_1, t_2, \ldots)\tilde{u}_m(y, z; 0, M_c) + o(\varepsilon^p), \tag{14}$$

where p is a certain number, and a_1 is a real function appearing as an amplitude equation. Considering solvability conditions at each power of ε, one gets an infinite

system of equations for the amplitudes a_n, $n = 1, 2, \ldots$. This system can be formally written as a single equation

$$\frac{\partial a}{\partial t} = \sum_{n=1}^{\infty} \varepsilon^n L_n(a), \tag{15}$$

where

$$\frac{\partial}{\partial t} = \varepsilon \frac{\partial}{\partial t_1} + \varepsilon^2 \frac{\partial}{\partial t_2} + \cdots, \; a = a_1 + \varepsilon a_2 + \cdots,$$

$L_n(a)$ is a certain function of a and its spatial derivatives.

Then, for the leading order,

$$L_1(a) = \lambda_1 \frac{\partial a}{\partial x_1}, \tag{16}$$

where

$$\lambda_1 = \left(\frac{\partial \lambda_{\mathrm{i}}}{\partial k} \right)_c. \tag{17}$$

The term $L_1(a)$, describing the propagation of waves with their group velocity, can be eliminated by means of a Galilean boost:

$$\xi = x_1 - \lambda_1 t_1. \tag{18}$$

Because of the conservation law, each term in the amplitude equation (15) has the form

$$L_n(\xi) = \frac{\partial}{\partial \xi} Q_n(a).$$

We obtain the following sequence of terms:

$$L_2(a) = 0,$$

$$L_3(a) = \frac{\partial}{\partial \xi} \left(\lambda_1' a + \lambda_3 \frac{\partial^2 a}{\partial \xi^2} + \gamma_1 a^2 \right), \tag{19}$$

$$L_4(a) = \frac{\partial}{\partial \xi} \left[\lambda_2' \frac{\partial a}{\partial \xi} + \lambda_4 \frac{\partial^3 a}{\partial \xi^3} + \gamma_2 \frac{\partial}{\partial \xi}(a^2) \right], \tag{20}$$

etc., where the coefficients in the linear terms are determined by derivatives of $\lambda(k, M)$ taken at the point $(0, M_c)$:

$$\lambda_1' = \left(\frac{\partial^2 \lambda_{\mathrm{i}}}{\partial k \partial M} \right)_c M_2, \quad \lambda_2' = -\frac{1}{2} \left(\frac{\partial^3 \lambda_{\mathrm{r}}}{\partial k^2 \partial M} \right)_c M_2,$$

$$\lambda_3 = -\frac{1}{6} \left(\frac{\partial^3 \lambda_{\mathrm{i}}}{\partial k^3} \right)_c, \quad \lambda_4 = \frac{1}{24} \left(\frac{\partial^4 \lambda_{\mathrm{r}}}{\partial k^4} \right)_c, \tag{21}$$

and γ_1 and γ_2 are real constants. In the expansion (14), $p = 2$. Note that a long-wavelength instability takes place if $\lambda_2' < 0$, $\lambda_4 < 0$. The mean value of a does not change with time, so the class of solutions satisfying the condition

$$\lim_{L\to\infty} \frac{1}{2L} \int_{-L}^{L} a(\xi) \mathrm{d}\xi = 0 \tag{22}$$

should be chosen.

Carrying out an additional change of the reference frame,

$$\bar{\xi} = \xi - \varepsilon^2 \lambda_1' t,$$

and introducing the new variables,

$$T = \varepsilon^2 C_1 t,\ X = C_2 \bar{\xi},\ A = C_3 a,$$

where

$$C_1 = |\lambda_3| \left(\frac{\lambda_2'}{\lambda_4}\right)^{3/2},\ C_2 = -\left(\frac{\lambda_2'}{\lambda_4}\right)^{1/2} \operatorname{sign} \lambda_3,\ C_3 = \frac{\gamma_1 \lambda_4}{3\lambda_3 \lambda_2},$$

we can rewrite the amplitude equation (15) in the following form:

$$\frac{\partial A}{\partial T} + \frac{\partial^3 A}{\partial X^3} + 6A\frac{\partial A}{\partial X} + \delta\left[\frac{\partial^2 A}{\partial X^2} + \frac{\partial^4 A}{\partial X^4} + D\frac{\partial^2}{\partial X^2}(A^2)\right] + O(\varepsilon^2) = 0, \tag{23}$$

where

$$\delta = \varepsilon \frac{(\lambda_2' \lambda_4)^{1/2}}{|\lambda_3|} > 0, \quad D = \frac{3\gamma_2 \lambda_3}{\gamma_1 \lambda_4}. \tag{24}$$

Thus, we obtain the *dissipation-modified Boussinesq–Korteweg–de Vries* (DM-BKdV) equation [4, 5, 17, 18]. This is a generic equation which governs one-dimensional waves produced by a long-wave instability in the presence of a conservation law. In the particular case $D = 0$, the Kawahara equation is recovered.

3 Marangoni Waves

3.1 Marangoni Waves on a Stress-Free Bottom

Equation (23) has been derived in the problem of transverse (gravity-capillary) wave generation in a layer with a stress-free lower boundary where the liquid is heated from above in the presence of the Marangoni effect [4, 5]. Assume that the thickness of the layer is a, the values of dynamic (shear) viscosity, kinematic viscosity and heat diffusivity are η, ν and κ, respectively, and that the dependence of the surface tension σ on the temperature is linear, $\sigma = \sigma_0 - \alpha T$, as for standard liquids. It has been shown that near the instability threshold, $M_c = 12$, the complex growth rate,

$\lambda(k,M) = \lambda_r + i\lambda_i$, is determined by formulae (12), (13) with the following values of coefficients defined by (17), (21):

$$\lambda_1 = \sqrt{G+12}\,, \quad \lambda_1' = \frac{\sqrt{P}}{2\sqrt{G+12}},$$

$$\lambda_2' = -\frac{P}{6}\,, \quad \lambda_3 = \frac{(96P/5+56/5)+G(8P/5+1/3)-C}{2\sqrt{G+12}},$$

$$\lambda_4 = -\frac{2}{105}(17GP^2+204P^2+134P+22).$$

Here $M = \alpha a^2 A/\eta\kappa$ is the Marangoni number, the control parameter of the problem, $P = \nu/\kappa$ is the Prandtl number, $G = ga^3/\nu\kappa$ is the (modified) Galileo number and $C = \sigma_0 a/\eta\kappa$ is the (inverse) capillary number. The nonlinear asymptotic expansions showed that

$$\gamma_1 = -\frac{3(G+8)\sqrt{P}}{4\sqrt{G+12}},\ \gamma_2 = -2P.$$

3.2 Solutions of the Dissipation-Modified Boussinesq–Korteweg–de Vries Equation

At present, the description of solutions of (23) is still far from complete. Let us mention the results [19, 20, 21, 22] concerning traveling wave solutions,

$$A = A(X_1),\ X_1 = X - cT - X_0,\ X_0 = \text{constant}, \tag{25}$$

satisfying conditions

$$A(X_1 + 2\pi/q) = A(X_1), \tag{26}$$

$$\int_0^{2\pi/q} A(X_1)\mathrm{d}X_1 = 0. \tag{27}$$

By means of the asymptotic expansions

$$A = A_0 + \varepsilon A_1 + \varepsilon^2 A_2 + \cdots,\ c = c_0 + \varepsilon c_1 + \varepsilon^2 c_2 + \cdots, \tag{28}$$

one obtains spatially periodic solutions which are cnoidal waves of the BKdV equation in the lowest order of ε:

$$A_0(X_1;q,k) = \frac{2q^2K^2}{\pi^2}\left[\mathrm{dn}^2\left(\frac{qKX_1}{\pi}\right) - \frac{E}{K}\right], \tag{29}$$

$$c_0 = \frac{4q^2K^2}{\pi^2}\left(2 - k^2 - \frac{3E}{K}\right), \tag{30}$$

where dn is Jacobi's delta amplitude function with modulus k, and $E = E(k)$ and $K = K(k)$ are complete elliptic integrals. In contrast to the case of the ideal and original BKdV equation, the parameter k is not arbitrary but is connected to the spatial period, $2\pi/q$. Indeed, when $\varepsilon \neq 0$, the governing equation (23) contains three dissipative terms. The first two terms, which are linear, account for long-wave instability ("negative viscosity" or "active friction", i.e., an energy input) and short-wave dissipation (energy output), respectively. The last term, which is nonlinear, describes the energy distribution between Fourier modes and nonlinear dissipation. The various conservation laws which characterize the ideal BKdV equation, apart from the conservation of the fluid volume, are no longer fulfilled. For instance, in the case where $A(X,T)$ is spatially periodic with period $L = 2\pi/q$, the time evolution of the squared deflection of the interface ("momentum") is governed by the equation

$$\frac{\mathrm{d}}{\mathrm{d}T}\int_0^L H^2 \mathrm{d}X = \delta\left(\int_0^L H_X^2 \mathrm{d}X - \int_0^L H_{XX}^2 \mathrm{d}X + 2D\int_0^L H H_X^2 \mathrm{d}X\right). \tag{31}$$

The right-hand side of (31) only vanishes for some particular values of the wave amplitude, and this means that there is a definite relationship between k and q. The relation is as follows [10, 19, 20]:

$$q^2 = \frac{\pi^2}{12K^2}\left\{\frac{5}{7}(3-D)\frac{(2-4k^2+k^4+k^6)+(-2+3k^2+3k^4-2k^6)E/K}{(-2+3k^2-k^4)+2(1-k^2+k^4)E/K}\right.$$
$$\left.-D[2-k^2-3E/K]\right\}. \tag{32}$$

There are three different types of behavior of the wave amplitude

$$A_m(q) = \max A - \min A = \frac{2q^2k^2K^2}{\pi^2}, \tag{33}$$

depending on D. If $D \leq 5/4$, the function $A_m(q)$ is uniquely defined in the overall region $0 < q < 1$. The limit $q \to 0$ ($k \to 1$) corresponds to a solitary-wave solution

$$A_0 = 2q_1^2 \cosh^{-2} q_1 X_1,\ q_1 = \left[\frac{7}{4(5-4D)}\right]^{1/2}, \tag{34}$$

which is identical (in the lowest order) to the BKdV soliton; however, it has a fixed amplitude. If the initial soliton-like disturbance has an amplitude different from that prescribed by (34), one observes an "aging" of the solitary wave, and this terminates with the amplitude (34) imposed by the steady input–output momentum balance [17]. Analysis of stability of the periodic solutions (25), (26) with respect to quasi-periodic disturbances,

$$\tilde{A}(X_1)\exp(\mathrm{i}\tilde{q}X_1 + \tilde{\lambda}T),\ \tilde{A}(X_1 + 2\pi/q) = \tilde{A}(X_1),$$

shows that the periodic solution is only stable inside a sub-interval $q_-(D) < q < q_+(D)$, which is shifted into the long-wave region as D grows, and which disappears at $D = 5/4$ (for details, see [20]). In the case $D = 0$, this sub-interval was found in [14]. Those solitary waves with an asymptote $A \to 0$ as $X \to \pm\infty$ are unstable because of the instability of their tails. Indeed, chains of waves, rather than solitary waves, and periodic wavetrains, are observed in experiments [1].

If $5/4 < D < 2$, there are two solutions for $A_m(q)$ in a particular region $q_m(D) < q < 1$ (a lower branch and an upper branch), one solution for $q > 1$ and no solutions for $0 < q < q_m(D)$. Only the solutions on the lower branch in the interval $q_m(D) < q < 1$ are stable with respect to strictly periodic disturbances with the same spatial period $2\pi/q$. However, even these solutions are unstable with respect to some quasi-periodic disturbances which violate the periodicity of the solutions.

If $D \geq 2$, there is a unique solution for $q > 1$, and it is unstable.

For finite values of δ, the traveling wave solutions of (23) were studied analytically in [18] and [23]. Numerical simulations of (31) were described in [17], [24] and [25].

3.3 Two-Dimensional Waves

3.3.1 Dissipation-Modified Kadomtsev–Petviashvili Equation

In the nearly one-dimensional case, when slow transverse modulations of one-dimensional waves are taken into account [$a = a(\varepsilon x, \varepsilon^2 y, \varepsilon t, \varepsilon^2 t, \ldots)$], the problem is governed by the *dissipation-modified Kadomtsev–Petviashvili* (DMKP) *equation* [26]. By means of a scaling transformation, this equation is reduced to the following form [22]:

$$\frac{\partial}{\partial X}\left\{\frac{\partial A}{\partial T} + \frac{\partial^3 A}{\partial X^3} + 6A\frac{\partial A}{\partial X} + \delta\left[\frac{\partial^2 A}{\partial X^2} + \frac{\partial^4 A}{\partial X^4} + D\frac{\partial^2}{\partial X^2}(A^2)\right]\right\} - 3s\frac{\partial^2 A}{\partial Y^2} = 0, \quad (35)$$

where δ and D are determined by formulae (24),

$$s = -\mathrm{sign}\left(\frac{\lambda_3}{\lambda_1}\right). \quad (36)$$

Within the framework of (36), it can be shown that all one-dimensional waves are unstable with respect to transverse modulations [22]. Indeed, let us consider disturbances

$$\tilde{a}(X_1, Y, T) = \Phi(X_1)\exp(\Omega T + \mathrm{i}\tilde{q}_y Y),\ |\Phi| < \infty \text{ as } |X_1| \to \infty, \quad (37)$$

propagating on the background of the periodic traveling wave (25). Such disturbances are governed by the following linear eigenvalue problem:

$$\Omega\Phi' - c\Phi'' + 6(A\Phi)'' + \Phi'''' + 3s\tilde{q}_y^2\Phi + \delta\left[\Phi''' + \Phi''''' + 2D(A\Phi)'''\right] = 0. \quad (38)$$

The eigenfunctions $\Phi(X_1)$ have the form of Floquet functions:

$$\Phi(X_1) = F(X_1)\mathrm{e}^{\mathrm{i}\tilde{q}_x X_1},\ F(X_1 + 2\pi/q) = F(X_1). \tag{39}$$

The eigenvalues $\Omega(\tilde{q}_x, \tilde{q}_y)$ can be calculated by means of expansions in δ.

Actually, we do not need $\Omega(\tilde{q}_x, \tilde{q}_y)$ for every $\tilde{q}_y$. To demonstrate the instability of solution (25), it is sufficient to consider the limit $\tilde{q}_y \gg 1$.

In this limit, we find the asymptotic expansions for Ω and Φ in powers of $\tilde{q}_y^{-2}$:

$$\Omega = \tilde{q}_y^2\Omega_{-2} + \Omega_0 + \mathrm{O}(\tilde{q}_y^{-2}),\ \Phi = \Phi_0 + \tilde{q}_y^{-2} + \mathrm{O}(\tilde{q}_y^{-4}). \tag{40}$$

To leading order, we obtain

$$\Omega_{-2}\Phi_0' + 3s\Phi_0. \tag{41}$$

For bounded solutions, we find

$$\Phi_0 = e^{\mathrm{i}\tilde{q}_x X_1},\ \Omega_{-2} = 3\mathrm{i}s/\tilde{q}_x. \tag{42}$$

For the next order, we get the following equation:

$$\Omega_{-2}\Phi_2' + 3s\Phi_2 + \Omega_0\Phi_0' - c\Phi_0'' + \Phi_0'''' + 6(A_0\Phi_0)'' + \delta[\Phi_0''' + \Phi_0''''' + 2D(A_0\Phi_0)'''] = 0. \tag{43}$$

From the solvability condition for (43), and taking into account (27), we find the growth rate, correct to the zeroth order in $\tilde{q}_y^{-2}$:

$$\Omega_0 = \mathrm{i}(\tilde{q}_x c + \tilde{q}_x^3) + \varepsilon(\tilde{q}_x^2 - \tilde{q}_x^4). \tag{44}$$

Thus we find an instability for $0 < |\tilde{q}_x| < 1$.

Actually, the instability appears at finite values of $\tilde{q}_y$, and is thus inside the region of validity of the problem (38). Physically, if the angle between the propagation direction of the traveling wave and that of the disturbance is large enough, the influence of the traveling wave is not sufficient to suppress the growth of the disturbance. Unlike the case of the ideal KP equation, the instability of one-dimensional solutions of DMKP equation does not depend on the sign, s, of the dispersion.

The formula (44) uses no properties of the solution A except (27). Hence, A can actually be an arbitrary solution of (35) satisfying that condition. In particular, the result is valid for doubly periodic solutions of the KP equation [27], if they are gauged in such a way that their mean values are equal to zero. Thus, the assumption $\partial/\partial x = \mathrm{O}(\varepsilon)$, $\partial/\partial y = \mathrm{O}(\varepsilon^2)$, used in the derivation of the DMKP equation, is not sufficient to reveal any stable form of motion.

3.3.2 Oblique Collision of Solitary Waves

In the general case, the waves generated by the instability can propagate in arbitrary directions simultaneously. The full system of long-wave equations which describes

such waves is rather complicated (see [5]). This system was used for an investigation of collisions of one-dimensional solitary waves, i.e., dissipative solitons at arbitrary incident angles.

In the case of two dissipative solitons that move obliquely (where the angle between their directions is 2ψ), it was found that, to the lowest order in ε, their interaction only leads to a *shift* in their positions (i.e., a phase shift) whose value is proportional to

$$\Psi = \frac{\sin^2 \psi_*}{\sin^2 \psi} - 1, \tag{45}$$

$$\sin^2 \psi_* = \frac{1}{4}\left(3 - \frac{M_c}{G + M_c}\right). \tag{46}$$

For a given experiment, the change of sign of the phase shift takes place at the "critical" angle $\psi = \psi_*$. Wider angles than the critical value yield a Mach–Russell third wave or stem. In the limit $G \gg M_c = 12$, the result of Miles [28] for interacting solitons in ideal, viscous-free shallow liquid layers, $\psi_* \to \pi/3$, is recovered. In the opposite limit, $\psi_* \to \pi/4$. Thus the critical angle $2\psi_*$ between normal vectors is between $2\pi/3$ and $\pi/2$, and the corresponding critical angle between wave fronts, $\pi - 2\psi_*$, is between $\pi/3$ and $\pi/2$, in agreement with experiments [29].

In [30], the theory has been extended to the case of cylindrical solitary waves $H(\varepsilon(r - ct), \varepsilon^3 r, \varepsilon\phi)$. A *dissipation-modified cylindrical Kadomtsev–Petviashvili equation* has been derived, and, after rescaling, it can be written in the form (cf. (35))

$$\frac{\partial}{\partial X}\left\{\frac{\partial A}{\partial T} + \frac{1}{2T}A + \frac{\partial^3 A}{\partial X^3} + 6A\frac{\partial A}{\partial X} + \delta\left[\frac{\partial^2 A}{\partial X^2} + \frac{\partial^4 A}{\partial X^4} + D\frac{\partial^2}{\partial X^2}(A^2)\right]\right\} + \frac{1}{2T^2}\frac{\partial^2 A}{\partial \Phi^2} = 0. \tag{47}$$

Results were provided about the time evolution of cylindrical solitons and head-on collisions between concentric cylindrical solitons.

3.4 The Influence of Bottom Friction and the Gas Phase

The model problem considered above has two shortcomings. First, the friction of the fluid at the bottom was completely neglected. Such a drastic simplification has permitted a theoretical study that provides predictions for nonlinear dissipative waves due to an instability triggered by the Marangoni effect. However, the friction at the solid support, and hence the no-slip boundary condition plays quite a significant role. As was shown in [31], the friction at the solid lower boundary suppresses the instability in the limit $k \to 0$, so that the critical wave-number, k_c, is non-zero. Note that the formation of transverse Marangoni waves in a layer with finite thickness by heating from the gas side was justified in [32]. Second, phenomena in the gas phase adjacent to the liquid are ignored.

One can phenomenologically, i.e., in an ad hoc manner, incorporate the friction at the solid bottom boundary and study the influence of the non-zero critical wave-number by adding to (23) a term $\delta\alpha A$ with $\alpha > 0$,

$$\frac{\partial A}{\partial T} + \frac{\partial^3 A}{\partial X^3} + 6A\frac{\partial A}{\partial X} + \delta\left[\frac{\partial^2 A}{\partial X^2} + \frac{\partial^4 A}{\partial X^4} + D\frac{\partial^2}{\partial X^2}(A^2) + \alpha A\right] = 0. \qquad (48)$$

In the framework of (48), the equilibrium solution $A = 0$ is unstable in the interval of wave-numbers $k_-(\alpha) < k < k_+(\alpha)$, $k_\pm^2 = (1 \pm \sqrt{1-4\alpha})/2$, if $\alpha < 1/4$, and is linearly stable if $\alpha > 1/4$. The additional term, with a constant coefficient α, may approximate the influence of the bottom friction reasonably well for wave-numbers in the instability interval, but it is not satisfactory in the long-wave limit, because it violates the basic condition (11). The cnoidal wave solutions of the problem (48) are described by the same formulae (29), (30), but the amplitude A now satisfies a certain quadratic equation [21].

The development of the nonlinear theory in the general case is a formidable task. However, the problem can be essentially simplified in the quite realistic limit $G \gg 1$, because, in this case, the critical wave-number, k_c, is small, and the long-wave approach can be applied. Also, one can take into account the fact that the kinematic viscosity and thermal diffusivity of a gas are typically much larger than the corresponding parameters of a liquid, i.e., $\nu \gg 1$, $\chi \gg 1$ for a two-layer gas–liquid system.

An attempt to use the above-mentioned circumstances for the construction of a nonlinear theory of long transverse Marangoni waves was made in [33]. The authors considered the limit where the characteristic wave-number $k \sim \varepsilon \ll 1$, but $\nu \sim \chi \sim G^{1/2}\varepsilon \gg 1$. (Actually, the relation $\varepsilon \sim G^{-1/10}$ was selected). In this limit, the authors obtained a dissipation-modified BKdV equation incorporating non-locality induced by the coupling of boundary layers at the top and at the bottom of the liquid layer. The approach has been recently improved and completed by S. Kalliadasis and the senior author of this chapter (ms in preparation). It has been shown that dissipation can be viewed as effectively dominating in full just in the boundary layers, whereas viscosity can be disregarded, to a first approximation, in the bulk of the liquid layer. This is somewhat an opposite view to the bottom stress-free boundary condition approach, but it has a bulk viscous flow. However, it clearly shows that dissipation is significant whenever it appears, and hence only a steady input–output energy balance with the Marangoni effect permits us to maintain the dissipative solitons.

Zimmerman [31] performed a direct simulation of the nonlinear system of equations which describe the finite-amplitude Marangoni convection in a layer with a deformable free surface and a solid bottom surface. The flow was assumed to be two-dimensional. The Galerkin finite element method with a grid adaptation procedure, developed previously in [34], was used. In the first series of simulations, the free surface is initially flat up to numerical noise. The latter turned out to be sufficient to produce some Marangoni flow near the surface. In the sub-critical region, it was found that the decay of this flow is essentially related to its deep penetration

into the layer and friction losses in the vicinity of the bottom. Thus, the prediction of the linear stability theory [31, 32, 35] of an increase in the critical Marangoni number due to bottom friction has been justified. In the second series of simulations, the fields of velocity and temperature generated by the surface elevation have been studied. In this case, some growth of disturbances was observed, even below the threshold predicted by the linear stability theory.

4 Waves in Flowing Films

Another example of a dissipative system where nonlinear waves are generated by a long-wave instability is a viscous film flowing down an inclined rigid surface. (The angle between the surface and the horizontal direction is labeled β). The linear waves are described by the same dispersion relation, (12), (13), as the Marangoni wave, with the Marangoni number, M, replaced by the Galileo number $G = ga^3/\nu^2$. (Recall that g is the acceleration due to gravity, a is the mean thickness of the film and ν is the coefficient of kinematic viscosity). For one-dimensional nonlinear waves, (15) is recovered, with the following values for the coefficients [19, 36]:

$$\lambda_1 = -G_0 \sin\beta,\ \lambda_1' = -\sin\beta,$$

$$\lambda_2' = -\frac{1}{3}\cot\beta,\ \lambda_3 = -G_0 \sin\beta,$$

$$\lambda_4 = -\frac{1}{3} G_0 H_0 \cot\beta,$$

$$\gamma_1 = -G_0 \sin\beta,\ \gamma_2 = -\frac{1}{2} G_0 \cos\beta,$$

where

$$G_0 = \frac{5\cos\beta}{2\sin^2\beta} \tag{49}$$

is here the critical Galileo number,

$$H_0 = \gamma \left(\frac{2}{5}\right)^{2/3} \frac{\sin^{4/3}\beta}{\cos^{5/3}\beta} + \frac{7743}{2240} - \cot^2\beta \frac{1}{36036},\ \gamma = \frac{\sigma}{\rho}(\nu^4 g)^{-1/3}. \tag{50}$$

Recall that ρ is the density of the fluid and that σ is the surface-tension coefficient. The long-wavelength instability occurs when $H(\gamma,\beta) > 0$, i.e., when β is larger than a certain angle $\beta_0(\gamma)$. Note that the angle β_0 is very small ($\beta_0 \approx 9'45''$ in the limit $\gamma \approx 9'7''$ for water, $\gamma = 2850$). Thus, the one-dimensional theory described for Marangoni waves is also valid for waves in a viscous film flowing down an inclined plane.

4.1 Waves on an Inclined Plane

A significant difference between waves excited by the Marangoni effect, which develop in a horizontal layer, and waves in an inclined film appears in the case of two-dimensional waves. Indeed, in the former case, the problem is *isotropic*, i.e., the growth rate $\lambda(k_x, k_y)$ depends only on the modulus of the wavevector $k = \sqrt{k_x^2 + k_y^2}$. That leads to a dissipation-modified Kadomtsev–Petviashvili equation in the case $|k_y| \ll k_x$ [26] and to more complicated equations in the general case [5].

In the latter case, the basic flow breaks the isotropy of the problem. The asymptotic expansions lead to (15), with

$$L_n(\xi, y_2) = \frac{\partial}{\partial \xi} Q_n(a) + \frac{\partial}{\partial y_2} P_n(a),$$

where $y_2 = \varepsilon^2 y$. The expressions for L_2 and L_3 are unchanged, while L_4 has an additional term:

$$L_4(a) = \frac{\partial}{\partial \xi}\left[\lambda_2' \frac{\partial a}{\partial \xi} + \lambda_4 \frac{\partial^3 a}{\partial \xi^3} + \gamma_2 \frac{\partial}{\partial \xi}(a^2)\right] + \hat{\lambda}_2 \frac{\partial^2 a}{\partial y_2^2}, \tag{51}$$

where

$$\hat{\lambda}_2 = -\frac{1}{2}\frac{\partial^2 \lambda(k_x, k_y)}{\partial k_y^2} = \frac{1}{3} G_0 \cos\beta.$$

In the case $\beta \neq \pi/2$, one obtains the following *anisotropic dissipation-modified Bousinessq–Korteweg–de Vries equation* by using a scale transformation and an additional change of the reference frame:

$$\frac{\partial A}{\partial T} + \frac{\partial^3 A}{\partial X^3} + 6A\frac{\partial A}{\partial X} + \delta\left[\frac{\partial^2 A}{\partial X^2} + \frac{\partial^4 A}{\partial X^4} + D\frac{\partial^2}{\partial X^2}(A^2) - \frac{\partial^2 A}{\partial Y^2}\right] + \mathrm{O}(\varepsilon^2) = 0. \tag{52}$$

A general investigation of the (2+1)-dimensional problem (52) is beyond the scope of the present chapter. Here, we only discuss the stability of traveling waves with respect to two-dimensional disturbances.

First, let us note that the stability criterion for one-dimensional traveling waves (25) is the same as that for the one-dimensional equation. Indeed, normal disturbances have the form

$$\tilde{a}(X_1, Y, T) = \Phi(X_1)\exp(\Omega T + \mathrm{i}\tilde{q}_y Y),\ |\Phi| < \infty \text{ as } |X_1| \to \infty, \tag{53}$$

and are governed by the following equation:

$$\Omega\Phi - c\Phi' + 6(A\Phi)' + \Phi''' + \delta[\Phi'' + \Phi'''' + 2D(A\Phi)'' + \tilde{q}_y^2\Phi] = 0, \tag{54}$$

where the prime corresponds to differentiation with respect to X_1. Obviously, for any eigenvalue $\Omega(\tilde{q}_y) = \Omega(0) - \delta\tilde{q}_y^2$, so that two-dimensional disturbances are less disruptive than one-dimensional ones.

We now consider a wider class of stationary wavy solutions (oblique waves):

$$A = A(\eta),\ \eta = X + \alpha Y - cT,\ |\alpha| < 1. \tag{55}$$

Let us perform the following transformation of variables:

$$A(X,Y,T) = \gamma^2 B(\xi, y, t),\ t = \gamma^3 T,\ \xi = \gamma\eta,\ y = \gamma Y, \tag{56}$$

where $\gamma^2 = 1 - \alpha^2$. We obtain

$$\frac{\partial B}{\partial t} - \hat{c}\frac{\partial B}{\partial \xi} + 6B\frac{\partial B}{\partial \xi}$$
$$+\hat{\delta}\left[\frac{\partial^2 B}{\partial \xi^2} + \frac{\partial^4 B}{\partial \xi^4} + D\frac{\partial^2 (B^2)}{\partial \xi^2} - \frac{1}{\gamma^2}\left(\frac{\partial^2 B}{\partial y^2} + 2\alpha\frac{\partial^2 B}{\partial y \partial \xi}\right)\right] + \mathrm{O}(\hat{\delta}^2) = 0, \tag{57}$$

where $\gamma^2\hat{c} = c$ and $\hat{\delta} = \gamma\delta$.

The stationary solution satisfying the conditions

$$B = B(\xi) = B\left(\xi + \frac{2\pi}{q}\right),\ \langle B\rangle = \int_0^{2\pi/q} B(\xi)\mathrm{d}\xi = 0 \tag{58}$$

is constructed by means of asymptotic expansions:

$$A = A_0 + \hat{\delta}A_1 + \cdots,\ \hat{c} = \hat{c}_0 + \hat{\delta}c_1 + \cdots. \tag{59}$$

Although the solutions describing the oblique waves are rather similar to those describing one-dimensional waves, the stability properties of these two kinds of waves turn out to be completely different. It has been shown that oblique waves are unstable with respect to two-dimensional disturbances for any $\alpha \neq 0$ and any q [22].

4.2 Waves on a Vertical Plane

In the case of a vertical plane ($\beta = \pi/2$), the expansions leading to the amplitude equation should be changed because the coefficient $\hat{\lambda}_2 = 0$ and $G_0 = 0$. Let us take $G \ll 1$, $\gamma \sim 1$. (The latter condition corresponds to moderate surface tension). In this case, the following *dissipation-modified Zakharov–Kuznetsov (ZK) equation* is obtained [36]:

$$\frac{\partial A}{\partial T} + A\frac{\partial A}{\partial X} + \frac{\partial \Delta A}{\partial X} + \delta\left(\frac{\partial^2 A}{\partial X^2} + \Delta^2 A\right) + \mathrm{o}(\delta) = 0, \tag{60}$$

where $\delta \sim G^{1/6}$ and $\Delta = \partial^2/\partial X^2 + \partial^2/\partial Y^2$.

The one-dimensional solitary and spatially periodic traveling waves governed by the unperturbed ZK equation are unstable with respect to transverse disturbances

[37, 38, 39]. In the case of a primary one-dimensional soliton, the instability leads to the formation of a chain of two-dimensional solitons [37, 40].

Let us discuss the nonlinear evolution of long-wavelength disturbances in the case of the unperturbed ZK equation,

$$\frac{\partial A}{\partial T} + A\frac{\partial A}{\partial X} + \frac{\partial \Delta A}{\partial X} = 0. \tag{61}$$

Consider a class of solutions that can be written in the form

$$A = A[X - \phi(Y,T), \varepsilon Y, \varepsilon T],\ \varepsilon \ll 1, \tag{62}$$

where ε is a small parameter characterizing the spatial scale of disturbances. Assume that ϕ_Y and ϕ_T are slow functions of the transverse coordinate, Y, and time, T:

$$\phi_Y = k(\varepsilon Y, \varepsilon T),\ \phi_T = \omega(\varepsilon Y, \varepsilon T). \tag{63}$$

Define

$$Z = X - \phi(Y,T),\ \eta = \varepsilon Y,\ \tau = \varepsilon T. \tag{64}$$

Hence,

$$k_\tau - \omega_\eta = 0. \tag{65}$$

Let us represent the solution in the form

$$A = A_0 + \varepsilon A_1 + \cdots,\ k = k_0 + \varepsilon k_1 + \cdots,\ \omega = \omega_0 + \varepsilon \omega_1 + \cdots \tag{66}$$

and collect the terms for each order in ε.

To the zeroth order, we obtain the following equation:

$$-\omega_0 A_{0Z} + A_0 A_{0Z} + (1 + k_0^2) A_{0ZZZ} = 0. \tag{67}$$

Recall that ω_0 and k_0 are functions of the slow variables η and τ. We are interested in modulations of the solitary-wave solution

$$A_0 = 3\omega_0 \operatorname{sech}^2\left(\frac{\omega_0^{1/2}}{2\sqrt{1+k_0^2}} Z\right). \tag{68}$$

However, in order to avoid mathematical complications connected with formation of the shelf and radiation [41], we prefer to consider a cnoidal wave with a very large period, so $L \gg 1$. Such a solution is exponentially close to (68) in the region $-L/2 \le Z \le L/2$, but satisfies conditions

$$A_0(Z+L) = A_0(Z) \int_{-L/2}^{L/2} A_0(Z)\mathrm{d}Z = 0. \tag{69}$$

Let us note that, according to (65),

$$k_{0\tau} - \omega_{0\eta} = 0. \tag{70}$$

To the first order in ε, the solvability condition gives the equation

$$\frac{1}{2}\frac{\partial}{\partial\tau}\langle A_0^2\rangle + \frac{\partial}{\partial\eta}\left(\langle A_{0Z}^2\rangle k_0\right) = 0, \tag{71}$$

where

$$\langle f\rangle \equiv \int_{-L/2}^{L/2} f(Z)\mathrm{d}Z.$$

Calculating the integrals in the limit $L \to \infty$, we obtain the following equation:

$$\frac{\partial}{\partial\tau}\left(\omega_0^{3/2}\sqrt{1+k_0^2}\right) + \frac{2}{5}\left(\omega_0^{5/2}\frac{k_0}{\sqrt{1+k_0^2}}\right). \tag{72}$$

Let us consider some particular solutions of the system of equations (70) and (72).

There is a family of solutions with constant values of ω_0 and k_0 that describe solitons with an oblique front. We linearize (70) and (72) near such a solution, and find that the long-wave instability disappears as $k_0^2 > k_*^2 = 3/5$. In other words, the oblique soliton is unstable if the inclination angle, α, is smaller than $\alpha_* = \tan^{-1}\sqrt{3/5} \approx 0.659$. This coincides with the result of [39]. Let us emphasize, however, that for $\alpha > \alpha_*$, there is a short-wave instability of solitons, so that the long-wave analysis is incomplete.

Now let us consider the simple-wave solutions characterized by the uni-valued relation between ω_0 and k_0:

$$\omega_0 = \omega_0(k_0). \tag{73}$$

Substituting (73) into (72), and taking (70) into account, we find that

$$\frac{\mathrm{d}\omega_0}{\mathrm{d}k_0} = -\frac{2}{3}\cdot\frac{k_0 \pm \sqrt{k_0^2 - 3/5}}{1+k_0^2}. \tag{74}$$

Equation (74) has real solutions if $k_0^2 > 3/5$ (i.e., in the stable case). For any solution (73) of (74), (70) has the form

$$\frac{\partial k_0}{\partial\tau} - \frac{\mathrm{d}\omega_0}{\mathrm{d}k_0}\frac{\partial k_0}{\partial\eta} = 0.$$

For any initial conditions of the type $k_0 = k_0(\eta)$, we obtain a simple-wave solution

$$k_0 = k_0[\eta + \omega_0(k_0)\tau].$$

Needless to say, the appearance of a shock wave is unavoidable if the condition $d\omega_0/dX < 0$ applies anywhere at $t = 0$. Analysis of a finite-amplitude shock wave cannot be carried out under the assumption (63). However, one can expect that waves with a piecewise smooth front will develop, and that they will contain fragments of oblique solitons with different inclination angles.

The theory of waves governed by the dissipation-modified ZK equation is still far from completion. Numerical simulations [42, 43, 44] reveal the development of oblique V-shaped chains of two-dimensional solitons on the background of weak chaotic waves.

4.3 Strong Surface Tension

Another kind of expansion is used in the problem of film-flow instability of a liquid with strong surface tension [45], viz., one in the limit $\gamma \gg 1$, $G = O(1)$. Taking into account that the instability interval is $0 < |k| < k_m = O(\gamma^{-1/2})$, we obtain a *perturbed anisotropic Kuramoto–Sivashinsky equation* [36, 46] (after a suitable rescaling):

$$\frac{\partial A}{\partial T} + \frac{\partial (A^2)}{\partial X} + \frac{\partial^2 A}{\partial X^2} - n\frac{\partial^2 A}{\partial Y^2} + \Delta^2 A + \varepsilon \left[\alpha_1 \frac{\partial^3 A}{\partial X^3} + \alpha_2 \frac{\partial^3 A}{\partial X \partial^2 Y} + \alpha_3 \frac{\partial^2 (A^2)}{\partial X^2} + \alpha_4 \frac{\partial^2 (A^2)}{\partial Y^2} + \beta_1 \Delta^2 \frac{\partial A}{\partial X} + \beta_2 \nabla \cdot (A \nabla \Delta A) \right] + o(\varepsilon) = 0, \tag{75}$$

where

$$\nabla = \mathbf{e}_X \frac{\partial}{\partial X} + \mathbf{e}_Y \frac{\partial}{\partial Y};\ \Delta = \nabla^2;\ n = G_0/(G - G_0).$$

The term $\Delta^2 A$ and the terms with coefficients β_1 and β_2 are related to the surface tension.

The stability of one-dimensional spatially periodic waves with the plane front,

$$A = A_0(X);\ A_0(X + 2\pi/q) = A_0(X), \tag{76}$$

governed by the unperturbed anisotropic Kuramoto–Sivashinsky equation, was investigated in [47, 48]. The growth rate Ω of the disturbance

$$\tilde{A}(X, Y, T) = F(X) \exp(i\tilde{q}_x X + i\tilde{q}_y Y) \exp(\Omega T), \tag{77}$$

where $F(X)$ is a $2\pi/q$-periodic function, is obtained from the following boundary value problem:

$$\mu F + \left(\frac{d}{dX} + i\tilde{q}_x \right)^4 F + (1 - 2\tilde{q}_y^2) \left(\frac{d}{dX} + i\tilde{q}_x \right)^2 F + 2 \left(\frac{d}{dX} + i\tilde{q}_x \right) (A_0 F) = 0, \tag{78}$$

where $\mu = \Omega + n\tilde{q}_y^2 + \tilde{q}_y^4$.

For long-wave disturbances, the expansions

$$F = \sum_{n=0}^{\infty} F_n \delta^n,\ \mu = \sum_{n=0}^{\infty} \mu_n \delta^n, \tag{79}$$

where

$$\delta = (\tilde{q}_x^2 + \tilde{q}_y^4)^{1/2},\ \tilde{q}_x = \delta \cos\phi,\ \tilde{q}_y^2 = \delta \sin\phi$$

may be used.

If only one-dimensional disturbances are taken into account ($\phi = 0$), solutions (76) are stable within the interval of wave-numbers $q_2 < q < q_1$, where $q_1 \approx 0.837$ and $q_2 \approx 0.77$ [45, 49, 50]. Both stability boundaries are related to long-wave disturbances. If $q > q_1$, then $\mu_1^2 > 0$; in this case, there are two real roots with opposite signs, and one of them is always positive. If $q < q_1$, then $\mu_1^2 < 0$ (two imaginary roots), while the coefficient μ_2 is negative if $q > q_2$, and positive otherwise.

For two-dimensional disturbances ($\phi \neq 0$), the oscillatory instability boundary, $q = q_2$, does not change (and does not depend on n). The monotonic instability with respect to two-dimensional disturbances is particularly significant in the case of a vertical film ($n = 0$). In the latter case, the boundary between monotonically growing and decaying disturbances, for q close to q_1, is described by the formula

$$\tilde{q}_x^2 \approx \frac{\tilde{q}_y^6}{\tilde{q}_y^2 + c\mu_1^2}, \tag{80}$$

where c is a positive constant. In the region $q < q_1$ ($\mu_1^2 < 0$), where the periodic wave is stable with respect to one-dimensional disturbances, there are monotonically growing two-dimensional modes. The region of growing disturbances is separated from the axis $\tilde{q}_y = 0$ by a gap. Inside the gap, $\tilde{q}_y^2 < -c\mu_1^2$, all the disturbances decay.

The numerical calculations performed for finite values of $\tilde{q}_x$ and $\tilde{q}_y$ show that the two-dimensional disturbances with the maximum growth rate are characterized by the quasi-wave-number $\tilde{q}_x = q/2$. When q decreases, this growth rate also decreases. When $q < q_3 \approx 0.74$, the region of the monotonic two-dimensional instability disappears.

When n grows, the instability region shrinks. For each value of q in the interval $q_3 < q < q_1$, there is a certain value $n = n_*(q)$ such that the wave is stable when $n > n_*(q)$. We find that all the one-dimensional periodic wavy motions are unstable because $q_3 < q_2$. The stability interval for one-dimensional periodic waves shrinks, and then disappears completely, for $G > 9.3G_0$ because the quantity $n = 1/(G/G_0 - 1)$ decreases as G grows. All one-dimensional waves on a vertical plane ($n = 0$) are unstable.

The two-dimensional spatially periodic nonlinear waves generated by the instability described here were studied numerically in [46]. Attracting heteroclinic loops connecting unstable one-dimensional solutions appear because of the symmetry of the system with respect to the transformation $x \to -x$. Petviashvili and Tsvelodub [51] have discovered horseshoe-shaped dissipative solitons governed by the unperturbed anisotropic Kuramoto–Sivashinsky equation.

The influence of the disturbance $O(\varepsilon)$ in (75) on the wave dynamics is not fully clear. In the case of one-dimensional waves, the linear dispersion term suppresses the spatial chaos characteristic for the one-dimensional Kuramoto–Sivashinsky equation [52]. In the two-dimensional case, one can expect that, because the dispersion terms violate the reflection symmetry, the heteroclinic loops will be destroyed, and some limit cycles will appear [48, 53, 54].

Before closing Sect. 4, let us mention that a wealth of analytical and numerical results and experimental data on falling liquid film problems (including heat transfer and the Marangoni effect) has recently been gathered for a forthcoming monograph by Kalliadasis and colleagues, and it includes reference to their earlier joint publications [55].

5 Conclusions

The variety of physical systems exhibiting propagation of dissipative solitons offers a rich panoply of mathematical model equations. All the cases discussed here are characterized by the same basic ingredients: dispersion, nonlinearity, instability and dissipation. In the present chapter, we have considered only waves described by *weakly nonlinear* dissipative wave equations. The next stage in the investigation of dissipative wave systems will be the construction of *strongly nonlinear* equations. One can expect that dissipative solitons will play a crucial role in the development of the theory of interfacial turbulence. For example, if the Marangoni effect operates, this would be turbulence in strongly dissipative flows (i.e., space–time chaos at the opposite extreme of Reynolds–Kolmogorov turbulence which is mostly inertial).

References

1. A.A. Nepomnyashchy, M.G. Velarde, and P. Colinet, *Interfacial Phenomena and Convection*, (Chapman & Hall/CRC, London, 2002), Chapter 5. 29, 37
2. V.I. Nekorkin and M.G. Velarde, *Synergetic Phenomena in Active Lattices. Patterns, Waves, Solitons, Chaos*, (Springer, Berlin, 2002). 29
3. X.-L. Chu and M.G. Velarde, Phys. Rev. A **43**, 1094 (1991). 30
4. A.N. Garazo and M.G. Velarde, Phys. Fluids A **3**, 2295 (1991). 30, 34
5. A.A. Nepomnyashchy and M.G. Velarde, Phys. Fluids **6**, 187 (1994). 30, 34, 39, 42
6. J.V. Boussinesq, Mem. Presentes par Divers Savants a l'Acad. Sci. Inst. France (Paris) **23**, 1 (1877). 30
7. D.J. Korteweg and G. de Vries, Phil. Mag. **39**, 422 (1895). 30
8. J. Topper and T. Kawahara, J. Phys. Soc. Jpn **44**, 663 (1978). 31
9. T. Kawahara, Phys. Rev. Lett. **51**, 381 (1983). 31
10. T. Kawahara and S. Toh, Phys. Fluids **28**, 1636 (1985). 31, 36
11. T. Kawahara and S. Toh, Phys. Fluids **31**, 2103 (1988). 31
12. C. Elphick, G.R. Ierley, O. Regev, et al., Phys. Rev. A **44**, 1110 (1991). 31
13. N.A. Kudryashov, Phys. Lett. A **147**, 287 (1990). 31
14. H.-C. Chang, E.A. Demekhin, and D.I. Kopelevich, Physica D **63**, 299 (1993). 31, 37

15. N.M. Ercolani, D.W. McLaughlin, and H.J. Roitner, J. Nonlinear Sci. **3**, 477 (1993). 31
16. A.A. Nepomnyashchy, Physica D **86**, 90 (1995). 32
17. C.I. Christov and M.G. Velarde, Physica D **86**, 323 (1995). 34, 36, 37
18. V.I. Nekorkin and M.G. Velarde, Int. J. Bifurc. Chaos **4**, 1135 (1994). 34, 37
19. A.A. Nepomnyashchy, Trans. Perm State Univ. **369**, 114 (1976) (in Russian). 35, 36, 41
20. D.E. Bar and A.A. Nepomnyashchy, Physica D **86**, 586 (1995). 35, 36, 37
21. A.Ye. Rednikov, M.G. Velarde, Yu.S. Ryazantsev, A.A. Nepomnyashchy, and V.N. Kurdyumov, Acta Appl. Math. **39**, 457 (1995). 35, 40
22. D.E. Bar and A.A. Nepomnyashchy, Physica D **132**, 411 (1999). 35, 37, 43
23. M.G. Velarde, V.I. Nekorkin, and A.G. Maksimov, Int. J. Bifurc. Chaos **5**, 831 (1995). 37
24. A. Oron and Ph. Rosenau, Phys. Rev. E **55**, R1267 (1997). 37
25. I.L. Kliakhandler, A.V. Porubov, and M.G. Velarde: Phys. Rev. E **62**, 4959 (2000). 37
26. A.N. Garazo and M.G. Velarde, Marangoni-driven solitary waves, In *Proceedings of the VIII European Symposium on Materials and Fluid Sciences in Microgravity*, ESA SP-333 (European Space Agency, Paris, 1992), pp. 2295–2300. 37, 42
27. M. Tajiri and Y. Murakami, J. Math. Phys. **34**, 2400 (1993). 38
28. J.W. Miles, J. Fluid Mech. **79**, 157 (1977). 39
29. H. Linde, X.-L. Chu, and M.G. Velarde, Phys. Fluids A **5**, 1068 (1993); see also H. Linde, M.G. Velarde, W. Waldhelm, and A. Wierschem, J. Colloid Interface Sci. **236**, 214 (2001). 39
30. G.-X. Huang, M.G. Velarde, and V.N. Kurdyumov, Phys. Rev. E **57**, 5473 (1998). 39
31. W.B. Zimmerman, Excitation of surface waves due to thermocapillary effects on a stable stratified fluid layer, unpublished. 39, 40, 41
32. M. Takashima, J. Phys. Soc. Jpn. **50**, 2751 (1981). 39, 41
33. M.G. Velarde, A.Ye. Rednikov, and H. Linde, Waves generated by surface-tension gradients and instability. In: *Fluid Dynamics at Interfaces* (Cambridge University Press, Cambridge 1999) pp. 43–56. 40
34. R.T. Goodwin and W.R. Schowalter, Phys. Fluids **7**, 954 (1995). 40
35. M. Takashima, J. Phys. Soc. Jpn. **50**, 2745 (1981). 41
36. A.A. Nepomnyashchy, Three-dimensional waves in thin liquid films. In: *Fluid Dynamics at Interfaces*, edited by W. Shyy, R. Narayanan, (Cambridge University Press, Cambridge, 1999) pp. 85–98. 41, 43, 46
37. V.E. Zakharov and E.A. Kuznetsov, Sov. Phys. JETP **39**, 285 (1974). 44
38. M.D. Spektor, Sov. Phys. JETP **61**, 104 (1988). 44
39. M.A. Allen and G. Rowlands, J. Plasma Phys. **53**, 63 (1995). 44, 45
40. P. Frycz and E. Infeld, Phys. Rev. Lett. **63**, 384 (1989). 44
41. Y. Kodama and M.J. Ablowitz, Stud. Appl. Math. **64**, 225 (1981). 44
42. S. Toh, H. Iwasaki, and T. Kawahara, Phys. Rev. A **40**, 5472 (1989). 46
43. A.L. Frenkel and I. Indireshkumar, Derivation and simulations of evolution equations of wavy film flows. In: *Mathematical Modeling and Simulation in Hydrodynamic Stability*, edited by D.N. Riahi, (World Scientific, Singapore, 1996) pp. 35–81. 46
44. T. Ogawa and C.-F. Liu, Physica D **108**, 277 (1997). 46
45. A.A. Nepomnyashchy, Fluid Dyn. **9**, 354 (1974). 46, 47
46. A.A. Nepomnyashchy, Three-dimensional spatially periodic motions in a liquid film flowing down a vertical plane. *Hydrodynamics*, pt 7, 43–52 (Perm, 1974). 46, 47
47. A.A. Nepomnyashchy, Trans. Perm State Univ. **316**, 91 (1974) (in Russian). 46
48. H.-C. Chang, M. Cheng, E.A. Demekhin, and D.I. Kopelevich, J. Fluid Mech. **270**, 251 (1994). 46, 48
49. B.I. Cohen, J.A. Krommes, W.M. Tang, and M.N. Rosenbluth, Nucl. Fusion **16**, 971 (1976). 47
50. U. Frisch, Z.S. She, and O. Thual, J. Fluid Mech. **168**, 221 (1986). 47
51. V.I. Petviashvili and O.Yu. Tsvelodub, Sov. Phys. Dokl. **23**, 117 (1978). 47
52. H.-C. Chang, Ann. Rev. Fluid Mech. **26**, 103 (1994). 48
53. E.A. Demekhin and V.Ya. Shkadov, Fluid Dyn. **19**, 689 (1984). 48
54. Yu.Ya. Trifonov, Izv. Akad. Nauk SSSR, Mekh. Zhidk. Gaza **5**, 109 (1990) (in Russian). 48
55. S. Kalliadasis, C. Ruyer-Quil, B. Scheid, and M.G. Velarde, Film Flows, Wave Instabilities and Heat Transfer (Springer-Verlag, London) (to be published). 48

Cavity Solitons in Semiconductor Devices

L.A. Lugiato, F. Prati, G. Tissoni, M. Brambilla, S. Barland, M. Giudici, and J.R. Tredicce

Abstract Cavity solitons represent a class of dissipative solitons which are generated inside an optical resonator. They have attracted considerable interest in the recent years due to their possible application to optical information processing. First of all, this review chapter illustrates the physics of cavity solitons in semiconductor devices. We discuss the experiments which demonstrated cavity solitons in vertical-cavity surface-emitting lasers, both below and above threshold, and all the theory which accompanied such experiments. Those features of the experimental results, which relate to prospective applications, are highlighted. The final part of the chapter deals with the theory of the cavity soliton laser.

L.A. Lugiato
CNISM and INFM–CNR, Dipartimento di Fisica e Matematica, Università dell'Insubria, Via Valleggio, 11, 22100 Como, Italy

F. Prati
CNISM and INFM–CNR, Dipartimento di Fisica e Matematica, Università dell'Insubria, Via Valleggio, 11, 22100 Como, Italy

G. Tissoni
CNISM and INFM–CNR, Dipartimento di Fisica e Matematica, Università dell'Insubria, Via Valleggio, 11, 22100 Como, Italy

M. Brambilla
CNISM and INFM–CNR, Dipartimento di Fisica Interateneo, Politecnico di Bari, Via Amendola 173, 70126 Bari, Italy

S. Barland
Institut Non-linéaire de Nice, CNRS–Université de Nice Sophia Antipolis, UMR 6618 CNRS – 1361 route des Lucioles, 06560 Valbonne, France

M. Giudici
Institut Non-linéaire de Nice, CNRS–Université de Nice Sophia Antipolis, UMR 6618 CNRS – 1361 route des Lucioles, 06560 Valbonne, France

J.R. Tredicce
Institut Non-linéaire de Nice, CNRS–Université de Nice Sophia Antipolis, UMR 6618 CNRS – 1361 route des Lucioles, 06560 Valbonne, France

Lugiato, L.A. et al.: *Cavity Solitons in Semiconductor Devices.* Lect. Notes Phys. **751**, 51–92 (2008)
DOI 10.1007/978-3-540-78217-9_3

1 Introduction

The topic of cavity solitons (CS) is rooted in that of optical pattern formation (OPF), which studies the spontaneous formation of spatial structures in the section of broad-area radiation beams, when they interact with a nonlinear medium [1, 2, 3]. Pattern formation is a most fascinating interdisciplinary subject in science (see e.g. [4, 5]).

Disciplines which are traditionally in the field of pattern formation, such as hydrodynamics or nonlinear chemical reactions, typically study this phenomenon in a 2D configuration. From a theoretical standpoint, optical systems present the additional difficulty of the presence of a third spatial dimension, viz. the longitudinal dimension, along which the radiation beam propagates. Models for OPF that are really 2D, e.g., paradigmatic models for nonlinear chemical reactions [5], have been obtained by considering the case of a "short"nonlinear medium included in a cavity. In the so-called "mean field" limit [6], the electric field becomes practically uniform along the medium, and the longitudinal direction becomes irrelevant. The first mean field model for OPF was formulated for a Kerr medium in a cavity driven by an external coherent field [7]. Others were derived for a saturable absorber [8, 9], for a laser [10], for a degenerate optical parametric oscillator (OPO) [11], and so on. The presence of a cavity makes the system dissipative because photons escape from the cavity.

The mechanism which gives rise to the spontaneous formation of an optical pattern is usually the onset of modulational instability (MI), i.e., a random initial spatial modulation, on top of a homogeneous background, grows and gives rise to the formation of a pattern. In the case of OPF, the instability arises from the combination of the nonlinearity of the dynamics and of diffraction of radiation, instead of the diffusion which occurs in nonlinear chemical reactions and fluid dynamics. In the paraxial approximation, diffraction is described by the transverse Laplacian, i.e., the sum of the second derivatives with respect to the transverse variables, multiplied by an imaginary coefficient.

From a practical viewpoint, the situation defined by the mean field limit is ideally realized in broad-area vertical-cavity surface-emitting lasers (VCSELs), such as those considered in the experiments described in this chapter. On the other hand, a configuration for an OPF which can be realized in a straightforward manner is that of a single feedback mirror, theoretically proposed in [12, 13] and experimentally confirmed later in many laboratories.

Optical systems are fast and have a large bandwidth. Hence, an attractive feature of OPF is that it offers, in principle, the possibility of applications to parallel information processing. A naïve idea is to use the intensity peaks of an optical pattern as a set of binary units, which can be set on and off individually. The basic difficulty with this concept is that a pattern is typically a strongly correlated entity in which the single units cannot be manipulated independently because by operating on an element, one affects, in general, many other elements or even the entire pattern. However, by varying the system parameters, one may meet cases in which the pattern becomes "loose", i.e., it can indeed be considered as an ensemble of independent pieces. This situation is typically met when there is bistability between a pattern

and a homogeneous state. In this case, one may realize "localized structures", i.e., configurations in which a small portion of a pattern is embedded in a homogeneous state. The concept of a localized structure is general in the field of pattern formation; it has been described in the framework of Ginzburg–Landau models [14] and Swift–Hohenberg models [15]; it has been observed in fluids [16], in nonlinear chemical reactions [17], in vibrated granular layers [18, 19], etc.

Actually, there is a sort of continuous transition, in parameter space, between the configuration of a rigid pattern and that of a loose pattern [20]; this is concisely described in a chapter of a previous volume on dissipative solitons [21], written by Ackemann and Firth [22]. For 1D systems, a theory of localized structures has been formulated in [23]. Related localization phenomena (called diffractive autosolitons), linked to the presence of bistability between two homogeneous states and the role of switching waves, have been predicted in [24].

In the case of optical systems, the possibility of localized structures was first predicted in [25]. The elementary optical localized structure, consisting of a single isolated intensity peak sitting on a homogeneous background, is now customarily called a cavity soliton (CS). Papers in the nineties showed the potential usefulness of CSs as binary elements which can be set on and off in a controlled manner, can be arranged in appropriate arrays or put in controlled motion by introducing phase and/or intensity gradients in the external driving field, also called a "holding beam" (HB). These results focused attention on this topic. Overviews on the subject of CSs can be found in [22] and [26].

The name "soliton" immediately reminds of spatial solitons which emerge during the propagation of light in nonlinear media (see e.g. [27, 28]). A paradigmatic model which predicts them is the nonlinear Schrödinger equation (NSE). The model of [7] amounts to an NSE with some additional terms that describe the escape of photons from the cavity, the cavity mistuning, and the external driving coherent field injected into the cavity. While the standard NSE describes purely Hamiltonian dynamics, the model [7] corresponds to a dissipative situation.

A significant feature of CSs is that they are "rigid", in the sense that their characteristics, such as height, width, or shape, are fixed, and they cannot be changed by varying the initial conditions, once the parameters of the system have been set. Another major difference is that a dissipative soliton displays "attractors" – for example, a CS persists after the writing pulse which created it dies away, until another pulse switches it off. From the viewpoint of prospective applications, semiconductors represent the most interesting materials because they allow for the realization of miniaturized and fast devices. In this chapter, we describe the experimental realization of CSs in broad-area VCSELs slightly below threshold (but above transparency, i.e., in the amplifying regime) or above threshold, and the associated theory. The existence of CSs has been clearly proved for the first time for semiconductor devices in exactly this type of system [29].

The models which describe the pattern or CS formation in semiconductors consist of a field equation coupled with some material equations (in the rate equation approximation one equation which governs the carrier dynamics and includes the carrier diffusion). In the framework of such models, it becomes evident that CSs

have both a light component and a material component, i.e., they are localized structures not only with respect to the intensity profile but also with respect to the carrier density profile. Presumably, these two components are linked by quantum correlations, in a state of quantum entanglement. The vision and the bibliography contained in this chapter can be completed by reading [22] and [26] and also two other chapters of [21], one chapter of [30] describing the experiments on localized structures in semiconductor devices, and the other [31] discussing CSs in lasers with saturable absorbers.

In Sect. 2, we recall the basic properties and applicative features of CSs, including a discussion about addressing and motion under the action of gradients. Section 3, which represents the bulk of this chapter, discusses cavity solitons in driven VCSELs. Section 3.1 illustrates the theoretical scenario for CSs below threshold, including the action of noise, whereas Sect. 3.2 illustrates the experimental results, including a description of the experimental set-up, the behavior of the VCSEL upon injection of an HB, the creation and control of CSs, the scenario of CSs in the parameter space, a comparison with adaptive numerical simulations, a discussion of the switch-on time and a comparison with numerical predictions, and the positioning of CSs in the presence of phase modulation in the HB field. Section 3.3 deals with theory and experiment for CSs in driven VCSELs above threshold. Section 4 discusses the generation of CSs in VCSELs with a saturable absorber. This is a configuration that does not require an HB, and it allows for the realization of a novel device, viz. the cavity soliton laser. The final part, Sect. 5, includes some conclusions and perspectives.

2 Cavity Solitons: Properties and Applicative Features

2.1 Basics

The properties of self-confinement of a CS endow it with especially appealing properties which are highly valuable for applications. First of all, the intrinsic independence of the localized structure makes the CS an ideal light pixel [29] that can act as an individual light source in a semiconductor device, in close similarity to the etched VCSEL arrays as they have been conceived and realized. However, in contrast to the latter, the pixel associated with the CS is not rigidly inscribed within the device cross-section – it is physically and geometrically defined by the self-confinement of radiation, and it is not determined by the material inhomogeneities linked to the array etching.

While the density of a VCSEL array is essentially determined by the cleaving/etching limits, along with the requirements for the lasing action of each micropillar, the density of a CS-based array of pixels is determined by the minimum distance below which CSs begin experiencing mutual interaction. From the theoretical point of view, this distance is conceptually related to the critical wave-vector

of the MI responsible for the pattern formation in the transverse profile of the optical system. Since the MI at threshold is associated with a bifurcated lattice [32], the CSs interact when brought to distances comparable with the global structure of which they represent localized elements. In any case, they are comparable with the CS dimensions themselves. When two CSs are brought to interaction, below the limit distance, they will merge into a single structure which is identical to either of the former ones. A more accurate analysis has shown that CSs may exhibit ringing tails, whose number and spread around the central peak depend on the character of the nonlinearity, as well as on device parameters such as medium diffusive processes and cavity detuning. When two CSs are close to one another, the ring-like modulations of the first one perturb the second one, and vice versa, so that it may happen that the two structures lock one to another, pinning reciprocally in their respective tails, at the minima or maxima of intensity [33]. This effect may lead to "clusters of CSs", as observed in Na vapors [34], where CSs are not, strictly speaking, still independent. As it turns out, though, such locking of the localization regions (if one wishes to regard the CS tails as the domain borders of the localized solutions) does not impede the possibility of addressing each CS for information encoding. This is done by turning it on and off, according to the description which will be provided below.

Of course, the possibility of actually creating a CS at any desired location of the cross-section of a real semiconductor micro-cavity strongly depends on the degree of homogeneity that the device exhibits – a vertical micro-cavity is subject to a number of phenomena that can modify, in a stochastic or deterministic way, the transversal homogeneity of the optical response in its broad sense.

Simply as an example, and first of all, one has to face the problem of epitaxial growth processes, which are always liable to induce lattice defects, strains, etc. When they grow above the micron size, they are likely to perturb the homogeneity as far as the CS (whose size is around 10–15 μm, see Fig. 1d) is concerned. While GaAs-based growth is very well mastered now, the growth of other materials, such as In or Sb compounds, may suffer from higher strains and defects. Up till now, this makes the extension of CS demonstration more critical in classes of devices closer to photonic wavelengths. Then, the turntable spinning of samples leads to the formation of a wedge-like structure in the wafer. Such a thickness gradient is irrelevant in the active region, generally limited to few quantum wells, but it becomes relevant in several tens of layers which are deposited for the realization of high-reflectivity Bragg mirrors. Moreover, the requirement of having broad-area devices implies that the gradients lead to a significant center-to-border deviance of certain parameters, mainly the cavity resonance frequency. Finally, the device processing stages are responsible for further sources of inhomogeneities. The deposition of ring contacts, typical of narrow-area VCSELs, causes a large inhomogeneity in the current flux, and it must be overcome by using bottom emitters [29] or more sophisticated optical pumping techniques [35].

Apart from the medium architecture and growth, another source of inhomogeneity is the transverse profile of the injected coherent field which is driving the resonator. It is relatively easy to employ broad beams, thus maintaining a satisfactory

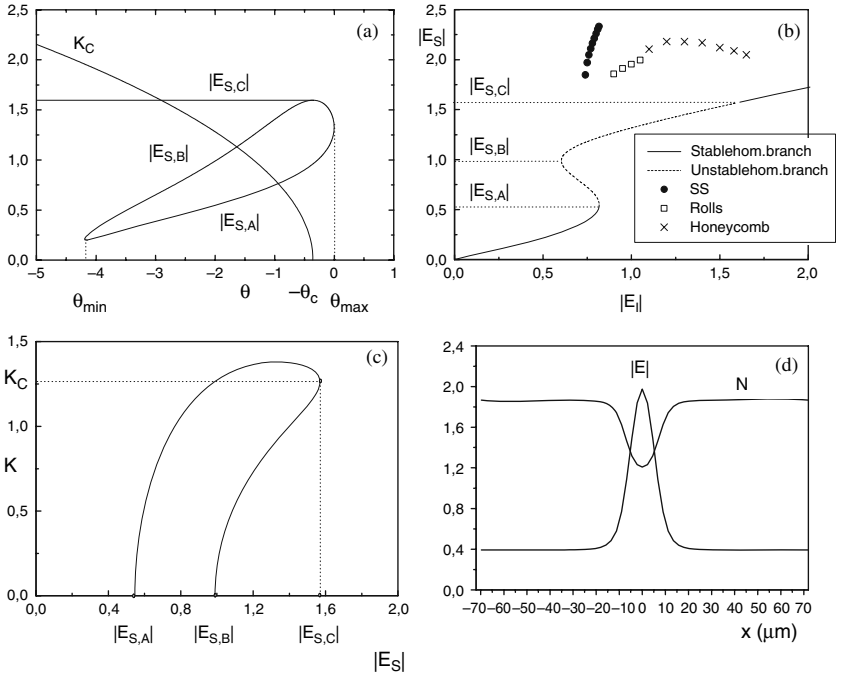

Fig. 1 (**a**) The turning points $|E_{S,A}|$ and $|E_{S,B}|$ of the stationary curve and the coordinates $|E_{S,C}|$ and K_C of the critical point of the MI domain are shown as functions of the cavity detuning parameter θ for $\mu = 0.9$ and $\alpha = 5$. (**b**) Stationary curve and (**c**) MI domain for $\theta = -2$ and $d = 0.052$. (**d**) Profile of the field amplitude and of the carrier density for the CS obtained with $E_I = 0.75$

gaussian profile and allowing us to consider the central area, impinging onto the micro-cavity, as being approximately plane. However, it must be noted that the collimation and the power loss represent an additional requirement in the set-up. For this reason, the next step, which is a current research issue in this field, is the realization of a micro-cavity above lasing threshold which may emit CSs spontaneously right at threshold, with no need to drive the system by means of external coherent injection. This so-called "cavity-soliton-laser" concept will be presented in Sect. 3.2.

Additional inhomogeneities are also induced by the local heating caused by the holding and addressing beams, which cause a refractive index drift in the semiconductor bulk. This effect causes a loss of independence of the structure and brings about thermal switching [36, 37, 38]. The use of devices with a highly homogenous current pumping in the amplifying regime allowed for the reduction of the coherent optical energy inflow and made it possible to overcome the thermal effects. The effect of medium and external gradients is not limited to a discussion concerning CS stability and the possibility of encoding them at arbitrary locations, but is also quite important for the motion of CSs, as will be discussed in the following paragraphs.

An additional bonus when realizing patterns in semiconductor devices is the possibility of accessing timescales for the CS response which are generally well below the microsecond scale, and have been demonstrated to reach the sub-nanosecond domain in non-optimized conditions [39]. While the present figures can certainly be improved, it should be noted that, insofar as the demonstration of CS has been achieved in devices with a marked absorptive response, one should expect an intrinsic limit of these scales on the band-to-band transition rate providing the coherent emission. Faster devices will have to rely on different mechanisms or on a strongly dispersive regime [40], although the latter approach leads back to strong field injection. Photonic band-gap materials might prove quite interesting in achieving new perspectives here.

2.2 Addressing

Provided that the absolute stability of the localized solution throughout the whole cross-section of the device is guaranteed, the next issue for CS control is the addressing of the CS "pixel", i.e., how the local conditions of the system can be deterministically altered in such a way as to cause the local transition from the homogeneous profile to the self-confined intensity peak. The addressing of a CS pixel has to cover both the CS switch-on and its switch-off, and it should rely on reasonably simple techniques. Further, it must work at any transverse location of the device and it must act on the single location addressed, leaving the rest of the emission profile unchanged, i.e., the process must not cause the disappearance or appearance of other CSs outside of the addressed location. Of course, the most intuitive way of addressing an all-optical device also proves to be the most efficient working principle – the switch-on of a CS is readily obtained by shining a narrow pulse of coherent radiation superimposed on the driving homogeneous beam and in phase with it. As has been shown, the intensity and duration of the switching pulse must be above certain lower limits, dependent on the system parameters and on the medium characteristics. Beyond such limits, when the pulse is stronger, then its injection can be shorter. Early analysis suggested that an area-preserving law may hold for the pulse amplitude and duration [32], while in the case of a multi-quantum-well device, more systematic numerical investigations showed that typical switch-on power and duration range in the microwatt and nanosecond scale, respectively, for a current-pumped device [41].

The switch-off procedure to erase an existing CS consists of shining a pulse of the same form, but setting it in phase opposition with respect to the input field phase. Experimentally, such a procedure has been easily implemented by using wave plates of suitable optical thickness. The switch-off process acts on a somewhat shorter timescale and usually involves reduced powers. While the optimal conditions for CS switch-on and off are achieved for perfect phase match or opposition, it has been predicted [41] and demonstrated (see Sect. 3.2) that a remarkable tolerance is allowed in the determination of the pulse phase. This constitutes an excellent

loosening of the constraint, since the wave-front distortions in play when a coherent field enters a semiconductor micro-cavity through facets, thermal lensing, etc. may well introduce slight deviations from the desired conditions.

The above-mentioned technique proved to be effective for all driven devices, both theoretically and experimentally (with good quantitative agreement in the case of a VCSEL amplifier, see Sect. 3.2). The initiation of researches on undriven devices, though, posed the question of how to switch a CS on or off when no determined phase relation can be set with a background or with the existing structure. The incoherent addressing of a soliton, relying just on the power and localization of the pulse, will be addressed in some detail in Sect. 4, for the case of a VCSEL with a saturable absorber.

Experimental results on incoherent switch-on and -off in an optically pumped VCSEL below threshold were presented in [35, 42].

2.3 Motion in Gradients

Possibly, the most appealing property of CSs is their plasticity, i.e., their capability of drifting freely across the device cross-section (provided no defects or inhomogeneities alter the local properties of the device). This capability, initially predicted in prototype systems [43], is based on the sensitivity of a CS to spatial gradients of the external field, both in intensity and phase. The existence of a neutral eigenvector (associated with the translational invariance of the CS solution) makes it possible for the CS to follow the gradient without losing stability, i.e., remaining self-confined and stable. In a constant gradient, a CS moves with constant speed, proportional to the field gradient. The specific properties of CS drift in semiconductor microresonators were studied in [41] in configurations where the phase gradient profile realized a matrix of stable locations where CSs could be pinned against Brownian motion induced by stochastic processes. The effect of slope-like gradients was reported in [44, 45] – which predicted drift speeds on the order of 1 μs/ns, which were later substantially confirmed by experiments [29, 46]; under different gradient shapes, speeds of up to 10 μm/ns have been measured [47].

In general, CSs in semiconductors will move spontaneously, following the gradient, and will thus rest on the maxima of the field phase or intensity profile. In considering the CS motion, one must remember that the structure of the coherent intra-cavity field is intimately linked, in the case of a semiconductor, to the spatial distribution of the carriers in the medium. A CS in the field is associated with a minimum (maximum) of the local carrier density profile in a current-pumped (an unbiased) device. The carrier dynamics evolves on timescales much longer than those of the field, typically a few nanoseconds versus a few picoseconds for the photon lifetime in a high-Q micro-cavity. This sort of carrier "inertia" in dragging the CS poses a limit on the CS speed upon increasing the gradient strength. In fact, as one would expect, the CS speed eventually saturates due to the carrier drag [48]. It may be noted, in addition, that gradients, which act as an Aristotelian force imposing a

motion on the CS, may be used to overcome pinning of a CS due to layer imperfections (as studied in [46] and achieve CS guiding, or to force CS locking in clusters or pairs, and lead them to a strong interaction).

In the absence of a driving field, as happens in the case of a laser with a saturable absorber, it is possible, in principle, to study the CS motion under the effects of gradients in the material or in the current profile.

While the motion of a CS in externally imposed gradients is the most appealing for applications, it must be mentioned, for the sake of completeness, that the local gradients induced by heating, possibly in conjunction with external ones, may cause CS drift, as studied in [38, 48, 49].

2.4 Applicative Potentials

The combined properties of spatial multi-stability, addressing and drifting that were progressively observed for CSs, are the basis for several appealing applications which are being progressively validated within the frame of the European STREP Project "FunFACS" (Fundamentals, Functionalities and Applications of Cavity Solitons; visit the website www.funfacs.org). One particularly stimulating scheme is grounded on the consideration that CSs, by drifting throughout the resonator's section, will transfer the information content among physically distinct locations, i.e., channels. On one hand, this property leads to the immediate concept of reconfigurable arrays. In contrast to rigidly etched VCSEL (micropillar) arrays, one can conceive of modifying the phase profile of the HB, and reshuffling at will, and in real time, the array structure (e.g., from square to rectangular) and geometry (e.g., from square to hexagonal). This concept has been proposed in the past from theoretical investigations, and experimental activities are presently validating it by realizing simple demonstrators where the phase landscape is obtained by using a liquid crystal light valve as an optical modulator for the beam driving the cavity. The first evidences are presented in Sect. 3.2.8.

A second aspect is that the information carrier CS, by moving from location A to B, will switch the "optical carrier"between two conveniently located pickup positions. It has been predicted [50] that such a concept can actually serve as a combined all-optical transistor and commutator, insofar as the switching signal (the gradient causing the CS drift between A and B) travels the same optical line as the one leading the "carrier" signal (the two CSs sustained by the modulated HB). Furthermore, in addition, as a third point, there is an intriguing concept, both fundamental and applicative, which depends upon the totally different speeds with which the CS-carried signal propagates inside the resonator when one discriminates the speed of light in the medium and the speed of the CS when it drifts across the device. This peculiar way of "slowing the light down", by making use of dissipative structures which are propagating freely in dimensions other than the propagation one, is quite readily applicable to realizing all-optical delay lines where the signal is delivered at one side of the device cross-section and picked up at the opposite side, where it arrives when the

CS has traveled the whole distance under the action of an externally imposed gradient [51]. The delay is obviously proportional to the combination of (a) the device section and (b) the gradient strength, thus making the lapse widely tunable. While the most advanced solid-state all-optical delay lines based on classical "slow light" operate somewhere in the 0.1–10 ps range [52, 53], timescales in our case span up to tens of nanoseconds, with the upper limit given by the weakness of the gradient which may fail to drive the CS over defect-induced pinning locations, thus stopping the motion. The lower limit is fixed mainly by the saturated CS speed, as discussed above. One limitation of this approach is the achievable bandwidth, defined here as the number of CSs per second that can be generated without disturbance by pulses impinging on the delay line input. Of course, here one needs the time necessary to switch a CS on – a process which at present occurs in the 250–1000 ps range – plus the time to have the written CS drift to a physically displaced location where the switch-on of the second one will not harm either one. This time seems to exceed 10 ns at present, thus putting the device well outside the typical 1–50 GHz requirement for photonic applications. It must be noted, though, that all processes are being studied from the basic proof-of-concept viewpoint, and optimization of the above-mentioned figures has not been attempted yet, either in terms of device architecture or in terms of operating regimes. The same layout described above also leads itself to a different application: when one has "strafed" the sequence of pulses writing the train of CSs on the write-in side of the delay line, and before all of them have traveled the distance to the read-out side, one has a stripe of CSs which encode the pulse sequence in parallel. This is the basis of an all-optical serial-to-parallel converter and a buffer register at the same time, depending on the length of the path the CS stripe might travel with no deformation across the device section.

3 Cavity Solitons in Driven VCSELs

In this section, we describe the case of a driven VCSEL. CSs are studied first in a VCSEL below threshold (amplifier case), where they were demonstrated for the first time for semiconductor devices [29]. The model and experimental results are reported here, and particular attention is devoted to a comparison between the two. Then, the VCSEL above threshold is analyzed (laser case). A new model, containing the semiconductor polarization dynamics, is introduced for this, and numerical and experimental results are reported.

3.1 Cavity Solitons in Driven VCSELs Below Threshold: Theory

CSs in a driven VCSEL below threshold are described theoretically by the rate equations [41]

$$\dot{E} = E + (1 - \mathrm{i}\alpha)DE - (1 + \mathrm{i}\theta)E + \mathrm{i}\nabla_{\perp}^2 E\,, \tag{1}$$

$$\dot{D} = \gamma\left[\mu - D(1 + |E|^2) + \mathrm{d}\nabla_{\perp}^2 D\right]\,, \tag{2}$$

where E is the dimensionless slowly varying envelope of the electric field and D is a population variable related to the carrier density, N, through the equation

$$D = 2C\,(N/N_0 - 1)\,. \tag{3}$$

Here $2C$ is a dimensionless factor defined as the ratio of single-pass gain to cavity losses, and N_0 is the transparency density. Similarly, the pump parameter μ is defined as

$$\mu = 2C\,(I/I_0 - 1)\,, \tag{4}$$

where I is the intensity of the pump, and I_0 is its transparency value. The meaning of $2C$ can be understood if one considers that the value of D at threshold is $D_{\rm thr} = 1$. Hence, if we call $N_{\rm thr}$ the threshold density, we have $N_{\rm thr}/N_0 = 1 + 1/2C$, so, when the value of $2C$ is larger, then the threshold and transparency densities (and pump intensities) are closer to one another. In (1) and (2), time is normalized to $\tau_{\rm p}$ and $\gamma = \tau_{\rm p}/\tau_{\rm c}$, where $\tau_{\rm p} \approx 10\,{\rm ps}$ and $\tau_{\rm c} \approx 1\,{\rm ns}$ are the photon and carrier lifetimes, respectively. The transverse spatial coordinates are scaled to the diffraction length, which has been estimated to be about $4.5\,\mu{\rm m}$, and $\sqrt{d}$ is the diffusion length in that unit. The driving field is described by its amplitude, E_I, and the scaled mismatch between its frequency, ω_0, and the cavity frequency, $\omega_{\rm c}$.

$$\theta = \tau_{\rm p}(\omega_{\rm c} - \omega_0)\,. \tag{5}$$

We remark that (1) and (2) are isomorphous to the equations which describe a two-level class-B laser with injected field. The only difference is in the parameter α, which must be interpreted as the linewidth enhancement factor in semiconductor lasers, and as an atomic detuning parameter in two-level lasers. Equations (1) and (2) can also describe a passive device, provided the term $1 - {\rm i}\alpha$ is replaced by $(1 + {\rm i}\Delta)^{-1}$, where Δ is the detuning with respect to the center of the excitonic line, which is assumed to be Lorentzian [41]. Since the pump is absent ($I = 0$) in a passive device, we have $\mu = -2C$, and $2C$ has the role of a bistability parameter, proportional to absorption.

The dynamical equations admit the plane wave stationary solution $E = E_{\rm S}$, $D = D_{\rm S}$ with

$$E_I = [1 - D_{\rm S} + {\rm i}(\theta + \alpha D_{\rm S})]\,E_{\rm S}\,, \qquad D_{\rm S} = \left(1 + |E_{\rm S}|^2\right)^{-1}\,. \tag{6}$$

With a proper choice of the parameters μ, α, and θ, the curve of the output amplitude $|E_{\rm S}|$ versus the input amplitude E_I may display the S-shape typical of bistable optical devices. This may happen both for a laser below ($\mu < 1$) and above ($\mu > 1$) threshold. For fixed values of μ and α, bistability occurs for $\theta_{\rm min} < \theta < \theta_{\rm max}$, and for a VCSEL close to threshold ($\mu \approx 1$), the following approximate expressions can be found if $\alpha > \sqrt{3}$

$$\theta_{\rm min} \approx -\alpha - \frac{\alpha^2 + 1}{\alpha \pm \sqrt{3}}(\mu - 1), \tag{7}$$

$$\theta_{\max} \approx \frac{(\alpha^2-9)^2-108}{8\alpha^3} + \frac{(\alpha^2+9)^2(\alpha^2+1)}{8\alpha^3(\alpha^2-3)}(\mu-1)\,. \tag{8}$$

In (7), the upper (lower) sign holds for $\mu > 1$ ($\mu < 1$). In practice, we roughly need $\theta < 0$, and $\theta + \alpha > 0$ in order to have bistability. In our model, $\theta + \alpha$ is the frequency of plane wave emission when the laser is above threshold, and the reference frequency is the frequency of the injected field. Hence, the model predicts the existence of bistability when the injected field is red detuned with respect to the solitary laser.

In Fig. 1a, where we have fixed $\mu = 0.9$ and $\alpha = 5$, the closed domain represents the boundaries of the negative slope branch of the stationary curve, i.e., the turning points $|E_{\mathrm{S,A}}|$ and $|E_{\mathrm{S,B}}|$ of the stationary curve.

In the figure, we have also represented the critical values $|E_{\mathrm{S,C}}|$ and K_{C} associated with the MI of the plane wave solution. This instability can be analyzed by adding a modulated perturbation of the form $\exp[\lambda t + K\cdot x]$, $\mathbf{x} = (\mathbf{x},\mathbf{y})$ to the plane wave solution. This yields a third-order characteristic equation $\lambda^3 + c_2\lambda^2 + c_1\lambda + c_0 = 0$, where the coefficients c_i, with $i = 1,2,3$, are real and depend on the system's parameters and on K^2. Since we are looking for instabilities leading to stationary patterns, we are interested in the condition $c_0 = 0$, which implies that a real eigenvalue changes its sign. The instability domain is a closed region in the plane $(|E_{\mathrm{S}}|, K)$ (the inner part being the unstable region), characterized by a critical amplitude $|E_{\mathrm{S,C}}|$ and a critical wave-vector K_{C}. If carrier diffusion is neglected ($d = 0$), then simple analytic expressions for $|E_{\mathrm{S,C}}|$ and K_{C} can be found:

$$\begin{aligned} |E_{\mathrm{S,C}}|^2 &= \sqrt{\mu\alpha/\theta_{\mathrm{c}}(\mu,\alpha)} - 1\,, \qquad K_{\mathrm{C}}^2 = -\theta - \theta_{\mathrm{c}}(\mu,\alpha)\,, \\ \theta_{\mathrm{c}}(\mu,\alpha) &= 4\mu\alpha\left[\sqrt{\mu[\mu(1+\alpha^2) - 4\sqrt{1+\alpha^2}+4]} + \mu\sqrt{1+\alpha^2}\right]^{-2}\,. \end{aligned} \tag{9}$$

Note that, in order for $\theta_{\mathrm{c}}(\mu,\alpha)$ to be real, we must have $\mu > 4(\sqrt{1+\alpha^2}-1)/(1+\alpha^2)$, which means that the VCSEL cannot be pumped too much below threshold. (For $\alpha = 5$, we must have $\mu > 0.63$.) As shown in Fig. 1a, the part of the upper branch between the upper turning point, $|E_{\mathrm{S,B}}|$, and the critical amplitude, $|E_{\mathrm{S,C}}|$, is unstable if $\theta_{\min} < \theta < -\theta_{\mathrm{c}}(\mu,\alpha)$.

In Fig. 1b, c, and d, we have considered the particular value of cavity detuning $\theta = -2$. Figure 1b shows the stationary curve and the results of the numerical simulations performed to study the patterns that emerge from the MI, as described below (in the following subsection). The branches of the patterns are indicated by various symbols, and the ordinate of the symbol corresponds to the maximum amplitude of the pattern. The instability domain in the plane $(|E_{\mathrm{S}}|, K)$ is shown in Fig. 1c. The coordinates of the critical point $|E_{\mathrm{S,C}}| = 1.569$, and $K_{\mathrm{C}} = 1.262$ differ slightly from those given by (9) because carrier diffusion is taken into account here ($d = 0.052$). Finally, in Fig. 1d, the transverse section of a CS and also the transverse profile of the carriers are shown.

The plane wave solution could be also destabilized through a Hopf instability. The condition $c_1 c_2 - c_3 < 0$ for a Hopf instability can easily be analyzed in the limit $\gamma \to 0$, always valid in a semiconductor device, where it reads simply

$$1 + |E_S|^2 - \mu < 0\,. \tag{10}$$

Clearly, the inequality is never satisfied if the laser is below threshold, and it is satisfied for a laser above threshold up to $|E_S|^2 < \mu - 1$, i.e., up to the intensity that would be emitted by the laser in the absence of an injected field (free running laser).

In the plane wave limit, this instability is associated with the phenomenon of injection locking, and $|E_S|^2 = \mu - 1$ is the injection locking point. Below that point, the system develops more or less complex dynamical behavior. Above that point, the output becomes stationary.

Outside the plane wave limit, injection locking is not described correctly by the rate equations because the instability condition (10) does not depend on K, and this means that the plane wave solution below the injection locking point is unstable against every tilted wave with any transverse wave-vector K. Clearly, this is a non-physical effect due to the fact that the spectral dependence of gain is neglected in the rate equations. This was the motivation that forced us to abandon the rate equations and adopt a set of effective Maxwell–Bloch equations when we analyzed CSs in a driven VCSEL above threshold, as shown in Sect. 3.3. However, as long as we limit ourselves to an absorber or an amplifier below threshold, the rate equations are perfectly adequate.

3.1.1 Numerical Methods

The method used to numerically integrate (1) and (2), as well as the other dynamical equations that will be introduced later in this chapter, is a split-step method with periodic boundary conditions. It involves separating the algebraic and the Laplacian terms in the right-hand part of the equations; the algebraic term is integrated using a Runge–Kutta algorithm, while a 2-D FFT is adopted for the Laplacian operator.

By varying the injected field amplitude, we obtained different branches of patterns and spontaneous formation of CSs, as shown in Fig.1b. The CS size (HWHM), as can be seen from Fig. 1d, turns out to be of the order of 10 μm.

As mentioned in Sect. 2, it is also possible to excite a CS at any desired position in the transverse plane. The technique used to switch on a CS requires superimposing a gaussian pulse, centered at the point (x_0, y_0), where we wish to create the soliton, on the homogeneous background of the input field $E_I^{(h)}$ (which we assume to be real and positive, without loss of generality) [32]. The injected field is then

$$E_I(x,y;t) = \begin{cases} E_I^{(h)} + h\mathrm{e}^{\mathrm{i}\phi} \exp\left(-\left[(x-x_0)^2 + (y-y_0)^2\right]/2\sigma^2\right) & 0 \le t \le \bar{t} \\ E_I^{(h)} & t > \bar{t} \end{cases}, \tag{11}$$

where h and ϕ are the amplitude and phase of the gaussian beam, σ is its width and $\bar{t}$ is the pulse duration. We set $\phi = 0$, which means that the gaussian beam is in phase with the background. A similar procedure is used to erase a CS. To this end, we create a dark hole in the homogeneous intensity of the injected field by setting the phase of the gaussian pulse to $\phi = \pi$ (obviously, in this case, the gaussian amplitude h in (11) must not exceed $E_I^{(h)}$).

3.1.2 Modulated Input Field

In order to investigate effects on CSs which arise from using more realistic configurations of the input field, we also performed numerical simulations by considering a background input field with a broad gaussian profile, rather than simply a homogeneous one. In this case, we assume

$$E_I(x,y) = E_I^{(h)} \exp^{(-(x^2+y^2)/2\Sigma^2)}, \tag{12}$$

in the absence of a switching pulse.

This kind of input profile, with an intensity maximum at its center, could be detrimental for CS applications such as the realization of optical memories formed by arrays of CS pixels. As we discussed in Sect. 2, CSs tend to climb the phase/amplitude gradients and to reach the nearest local maximum. Hence, the CSs would move toward the maximum of the field profile and merge into one CS, sitting on that maximum. In order to overcome this effect, and to allow for the creation of regular arrays of CSs, we also introduced an input field with a regular array of phase maxima. (For an experimental realization of this, see Sect. 3.2.)

The pinning effect exerted on solitons by a phase modulation of the input field [43] is simulated by considering, in the transverse plane, two orthogonal standing waves of amplitude ζ, superimposed on the homogeneous background and out of phase, with respect to the latter, by $\pi/2$. Hence the input field takes the form

$$E_I(x,y) = E_I^{(h)} \left[1 + \mathrm{i}\varepsilon(\cos kx + \cos ky)\right], \tag{13}$$

where $\varepsilon = 2\zeta/E_I^{(h)}$. Provided ε is sufficiently small, E_I essentially acquires only a phase modulation – in fact, to first order in ε:

$$E_I(x,y) \approx E_I^{(h)} \exp\left[\mathrm{i}\varepsilon(\cos kx + \cos ky)\right], \tag{14}$$

while the correction to the intensity is only of order ε^2.

The pinning effect has also been analyzed in connection with the simultaneous presence of a gaussian modulation in the amplitude of the injected field. From expressions (12) and (13), the natural choice for the input field in this case is

$$E_I(x,y) = E_I^{(h)} \left[\exp^{(-(x^2+y^2)/2\Sigma^2)} + \mathrm{i}\varepsilon(\cos kx + \cos ky)\right]. \tag{15}$$

We devoted particular attention to verifying the possibility that the pinning action, due to the phase modulation, could be strong enough to overcome the converging effect of the gaussian profile. We observed that it is possible, with a modulation amplitude $\varepsilon = 0.05$, to eliminate the converging motion caused by the gaussian input profile. In Fig. 2a, we present the new profile of $|E_I|$, with both gaussian and phase modulation, while in Fig. 2b and c, we show the phase of E_I, both in 3-D and 2-D plots. Finally, in Fig. 2d, four frames are given; these show that the motion of the CSs is toward the maxima of the phase modulation, even if gaussian curvature of the input field is present. It is evident, from Fig. 2a, that our choice of the phase modulation also produces a modulation in the intensity of E_I. However, the maxima of intensity are completely ignored by the CSs in their motion.

3.1.3 Action of Noise

To simulate the behavior of a realistic device, it is important to analyze the behavior of CSs in the presence of noise. We know that CSs can be excited at any position of the transverse plane, which means that every point turns out to be marginally stable with respect to the presence of a CS. Due to this fact, one expects that the presence of noise could cause a random walk of the CS in the transverse plane. Moreover, if the amount of noise becomes too large, one could also expect that a CS would not persist stably as an individual entity, but would be destroyed by random fluctuations.

To test these possibilities, we added white-noise terms to the equations for the field E and the carrier density D. These terms have the form $g_1 \xi_1(x,y;t)$ and $g_2 \xi_2(x,y;t)$, respectively, where ξ_1 and ξ_2 are gaussian variables with zero mean and δ-correlated, both in space and time, and g_1 and g_2 measure the noise strength.

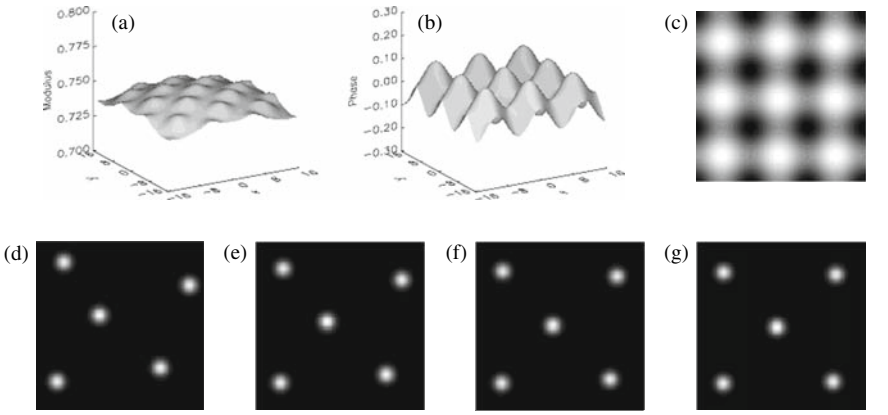

Fig. 2 (**a**) 3-D plot of the modulus of the driving field, E_I, with gaussian profile and phase modulation as given by (15): $E_I^{(h)} = 0.75$, $\Sigma = 100$, $\varepsilon = 0.05$; (**b**) 3-D plot of the phase of the driving field E_I; (**c**) as in (**b**), but in a 2-D gray-scale plot; (**d**) sequence of four frames showing the pinning effect due to the input field given above – the CSs move toward the maxima of the phase of E_I shown in (**c**). Other parameters are as in Fig. 1b. Figure taken from [41]

We observed that under the action of noise, CSs wander around until the distance between two of them becomes less than their interaction range, so that, eventually, they merge into a single CS. Anyway, the CSs are stable, apart from their interaction.

The random walk which CSs undergo can destroy any information encoded in the transverse plane by means of the CSs, in the same way that the presence of a gaussian profile in the driving field E_I does. As in the previous subsection, we exploited the pinning effect exerted by the presence of a small phase modulation in the driving field in order to guide the CSs toward the desired locations of the array.

Figure 3 shows four frames taken at different times during the time evolution of the system in a simulation performed with the same amount of noise as in the previous one, but with a slight phase modulation ($\varepsilon = 0.05$ in (13)) added to the driving field. The added phase modulation is strong enough to overcome the random walk due to the noise and to pin down the CSs at the phase maxima, arranging them at the positions of a 3×3 array. The only remaining effect of noise on CSs is a small random deformation of the peaks and very short random displacements around their equilibrium positions.

3.2 Cavity Solitons in Driven VCSELs Below Threshold: Experimental Results and Comparison with Theory

In order to create several CSs in the transverse plane of semiconductor lasers, we need to use devices with large Fresnel number such that the correlation length is at least one order of magnitude smaller than the transverse size of the resonator. In order to meet this requirement, we used VCSELs having transverse size larger than 150 μm. The effective length of the VCSEL resonator is of the order of few wavelengths, so these devices are the best choice for achieving large Fresnel number. The production of such broad devices is a challenging task in term of thermal management, room temperature lasing and homogeneity of the resonator parameters through the wide section. The VCSELs we use are provided by ULM-photonics. They are oxidized bottom-emitter VCSELs with Bragg mirrors consisting of 20 pairs on the bottom side, 33 pairs on the top side, and 3 quantum wells emitting around 970 nm at threshold [54]. Their diameter ranges between 150 and 250 μm.

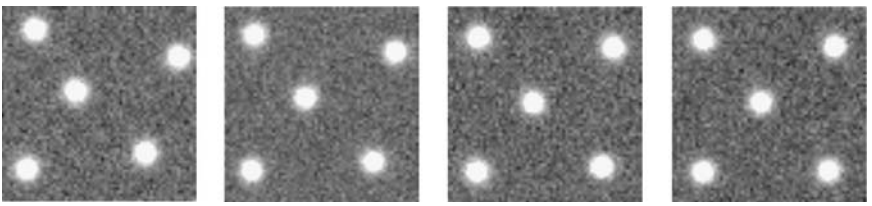

Fig. 3 Sequence of four frames showing the pinning effect due to a driving field with a phase modulation in presence of noise, with $\varepsilon = 0.05$. Other parameters are as in Fig. 1b. Figure taken from [41]

The bottom-emitting geometry significantly increases the homogeneity of the current injection profile in the active region, though residual current crowding is still present on the borders of the device.

The VCSEL is injected by a coherent gaussian HB, with a waist approximately double the VCSEL diameter. The most important control parameters are the HB intensity (P_{HB}), the HB frequency detuning with respect to the longitudinal cavity resonance of the VCSEL (θ), and the VCSEL pumping current level, I. VCSEL pumping current variation also implies a variation of the VCSEL substrate temperature (Joule effect), thus changing the cavity resonance and θ. A narrow beam (writing beam, WB) superimposed on the HB allows for local shining of the VCSEL, and it is used for optically switching the CSs on and off.

In this section, we report on experimental studies of CSs in VCSELs operated as amplifiers (electrically biased below threshold). We briefly describe the experimental set-up used, and we give evidence for the creation of CSs and of their control by using the WB. We characterize the domain of existence of CSs in the parameter space, and we optimize the properties of the CSs in terms of switching time when applying the WB. We show that it is possible to move the CSs in the transverse plane of the VCSELs by introducing a phase or intensity gradient in the HB. As a consequence, we can achieve imposed CS positioning, starting from random CS configurations. We describe the effect of the inhomogeneities of the VCSEL device and we show how these affect the plasticity and the control of CSs. The results obtained give solid indications that CSs are promising objects for building all-optical buffer memories and shift registers. However, the device engineering needs to be improved, in terms of spatial homogeneity, in order to enable full exploitation of CS plasticity.

In this section, there is also a comparison with adaptive numerical simulations.

3.2.1 Experimental Set-Up

The experimental set-up is shown in Fig. 4. Conceptually, this set-up is composed of three parts. In the first, we generate the injection beams (HB and WB), so we call it the "injection part". The second is mainly the slave laser, i.e., the VCSEL, with its own driving apparatus, where we intend to generate CSs, and finally the third part is for the detection of the VCSEL output. A detailed description of the experimental set-up can be found in [46].

The injection beams are generated by a tunable laser, providing an output of up to 100 mW with a linewidth of less than 1 MHz on long (more than 1 min) time acquisitions. This beam is optically amplified, spatially filtered and collimated, with a waist ranging from about 300 to 500 µm, depending on the injected device. The intensity of the HB reaching the VCSEL can be adjusted up to 25 mW. The HB power is controlled by an acousto-optic modulator, together with a polarizer. A spatial modulator can be placed on the HB path in order to change its phase and/or intensity profile. A second low-power beam, emitted from the tunable laser, is used as a WB. This beam is tailored in order to obtain a waist of 10–15 µm while its

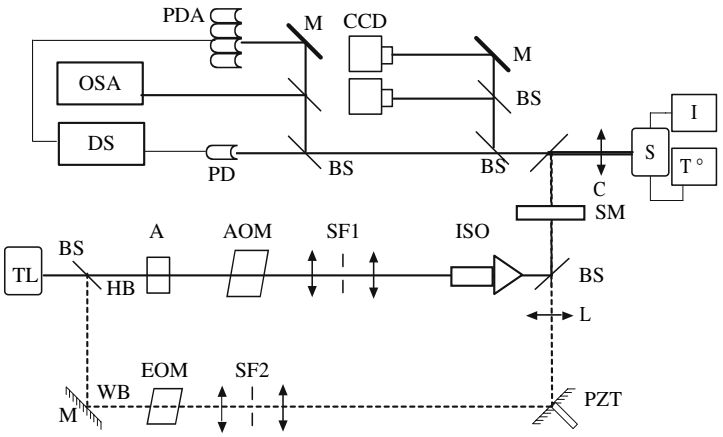

Fig. 4 Experimental set-up. TL: high-power tunable laser. HB: holding beam. WB: writing beam. I: current driver stabilized up to 0.01 mA, T^O: temperature controller, ISO: optical diode, OSA: Fabry–Perot interferometer and optical spectrum analyzer. DS: digital scope. A: optical amplifier. SM: spatial beam modulator. AOM: acousto-optic modulators. EOM: electro-optic modulators. SF1: beam expander-configurator with spatial filtering, SF2: beam reducer-configurator with spatial filtering. S: broad-area vertical-cavity surface-emitting laser. C: collimator. CCD: CCD cameras. PDA: photodetector array. PD: photodetector. PZT: piezo-electric ceramic. M: mirror. BS: beam-splitters

maximum power reaching the VCSEL is 1 mW. The WB power is controlled by an electro-optic modulator. The relative phase of the WB, with respect to the HB, is controlled by piezo-positioning of a mirror on the WB path.

The broad-area VCSEL is biased below threshold using a stabilized current supply and is temperature stabilized by a Peltier cell, up to 1 mK. A large numerical aperture collimator is placed in front of the VCSEL in order to reduce the spreading of the output beam and to enable uniform injection.

The near-field and far-field output profiles of the VCSEL are monitored on CCD cameras, while a photodetector, Thorlabs D400 (rise-time up to 100 ps), monitors a small portion of the VCSEL transverse plane, in order to detect the local dynamics of a CS. This detector may be replaced with a linear array of avalanche photodetectors (350 MHz bandwidth) for fast detection at different positions along the transverse plane of the device. The detectors are connected to a digital oscilloscope (LeCroy Wavemaster 8600 A, 6 GHz analogue bandwidth, 20 GHz digital bandwidth). The optical spectrum of the injection beams is monitored by a scanning Fabry–Perot interferometer (resolution 300 MHz, FSR 30 GHz) and by an optical spectrum analyzer with a resolution of 0.5 Å.

3.2.2 The VCSELs Under Injection

The HB is injected along the VCSEL optical axis, i.e., orthogonal to the VCSEL section. In order to maximize the VCSEL's gain, we adjust its temperature in order

to match the cavity resonance frequency with the gain curve peak. The VCSEL amplification of an external field is maximum when the injected frequency is close to the cavity resonance of the VCSEL cavity. In this situation, the output profile depends strongly on the mismatch between the injection frequency and the VCSEL cavity resonance (θ). In Fig. 5, we plot the near-field output profile of the VCSEL when it is injected by the HB. The HB frequency decreases from Fig. 5a to h. Different kinds of irregular structures are present in these profiles, and we note that the pitch of these structures is significantly affected by the injection frequency, and that, for the same injection frequency, it changes along the horizontal axis of the section of the device. We also note that there is a vertical line in the transverse section (Fig. 5c) that separates a homogeneous emission region from a patterned emission region. The position of this vertical line in the transverse plane depends on the injection frequency. These emission profiles can be understood by noting that broad-area VCSELs exhibit a gradient of the cavity length along the transverse section due to the nonparallel layers forming the cavity. The vertical line separating the pattern and the homogeneous field regions can be interpreted as the locus of the spatial positions where the values of the cavity resonance and field intensity match the condition for the onset of a (pattern-inducing) MI. In a homogeneous system, with all other parameters fixed, this boundary is defined by a critical detuning between the injected field frequency and the longitudinal cavity resonance. Instead, in our system, due to the gradient of the cavity resonance, the MI occurs in the transverse plane of the VCSEL, and the instability border appears as a separation between a patterned spatial region and a uniform one.

When the injected field frequency is varied, we observe a shift of the whole pattern in the transverse plane (Fig. 5). This is due to the shift of the MI boundary to the new locus of points where the critical detuning condition is satisfied. This

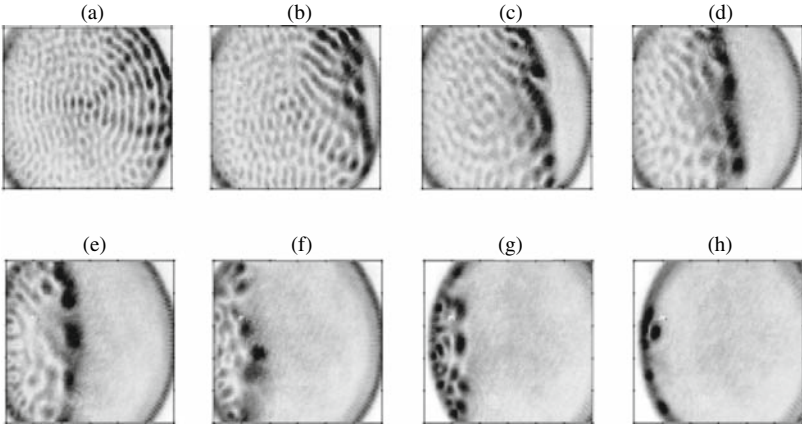

Fig. 5 Average intensity profiles of the VCSEL under various injection frequencies around 970 nm. From (**a**) to (**h**), the frequency is decreased in steps of 50 GHz; $I = 180\,\text{mA}$, $P_{\text{HB}} = 8\,\text{mW}$. Figure taken from [46]

observation can be used in order to estimate the gradient of the cavity resonance in the VCSEL [55]. In the device shown in Fig. 5, a cavity resonance gradient of 2.34 GHz/μm is measured along the horizontal dimension.

3.2.3 Creation and Control of Cavity Solitons

According to theoretical predictions (see Sect. 3.1), CSs in the parameter space are stable solutions in the neighborhood of the MI. So, we will try to switch them on by targeting the homogeneous region of the VCSEL output profile with the WB. The presence of the cavity resonance gradient limits the existence of the CSs to a small region around the vertical line separating the patterned region from the homogeneous region. In order to overcome this problem, we used more homogeneous devices (with cavity resonance gradient around 0.4 GHz/μm). We fix all the parameter values in order to have the homogeneous region cover 75% of the near-field profile, and we inject the WB into the homogeneous region. Starting with no spot, the WB is capable of generating a high-intensity spot with a diameter of the order of 10 μm when it is in phase with the HB. The spot size is in good agreement with the theoretical prediction for the CS size in these devices (see Sect. 3.1). If we remove the WB, the bright spot remains on indefinitely. We then apply this beam in a different location, without changing any parameter value, and a second spot is generated without perturbing the first one we have created. This one also persists after removal of the WB, and two bright spots are now present in the VCSEL profile. By changing the phase of the WB by π with respect to the HB, and reinjecting it successively at each location where the spots have been created, we erase each of them independently. The full series is displayed in Fig. 6. We claim that these two spots, that we have generated and erased independently, are CSs [29]. The minimum power requirement for switching on and off a CS depends on the system parameters, and we give a detailed description in [46]. Typical values for WB are around a few microwatts for HB power of 20 mW.

3.2.4 Cavity Solitons in Parameter Space

CSs can be created by using a WB, but they can also appear spontaneously under the action of the noise present in the system. This can happen when the HB power is close to the critical value for which the homogeneous solution looses its stability. They also appear when the HB power is decreased from values where only pattern solutions are stable to values where only CSs and the homogeneous solution are stable. In Fig. 7, we show, as a function of the VCSEL bias, the values of the HB power at which, for increasing power, the homogeneous solution (Fig. 7, inset 1) looses its stability and the pattern (Fig. 7, inset 3) develops (Fig. 7, upward arrow). For decreasing HB power, patterns evolve to CSs (Fig. 7, inset 2). On continuing to decrease the HB power, the CS solution looses its stability at a critical value, and the system switches to the homogeneous solution (Fig. 7, downward arrow). These

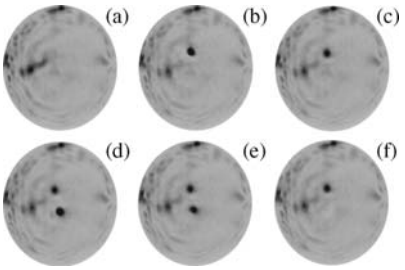

Fig. 6 Intensity distribution of the output field. The HB is always on, and all parameters are kept constant: $P_{HB} = 10\,mW$, $I = 262\,mA$. (**a**) The WB is blocked; (**b**) a 15 μm focused WB ($P_{WB} = 8\,\mu W$) targets a point in the homogeneous region; it induces the appearance of a single CS; (**c**) the WB is blocked again – the CS remains; (**d**) the WB is displaced in position and switched-on again, and it generates a second CS; (**e**) the WB is blocked again and the two bright spots coexist; (**f**) the WB again targets the second CS, but the relative phase of WB, with respect to HB, has been changed by π and the CS is erased. Then the WB again targets the first CS, but the relative phase of WB, with respect to HB, has been changed by π and even the first CS is erased. Once the WB is blocked, the intensity distribution is identical to (**a**)

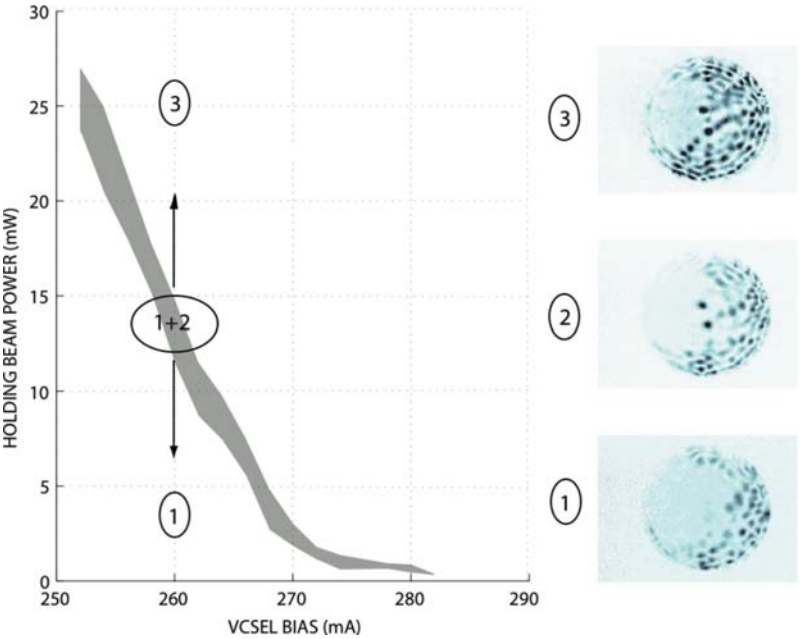

Fig. 7 Existence domain of CSs as a function of the parameters. *Upward arrow* indicates the border in the parameter space where the homogeneous solution switches off for increasing HB intensity. *Downward arrow* indicates the border in the parameter space where the CS switches off for decreasing HB intensity. Region (1) is characterized by the output profile of inset (1), region (3) is characterized by the output profile of inset (3), and, in the gray region (1+2) CSs (inset 2) and a homogeneous solution coexist. Figure taken from [46]

transitions, as in any real system close to a bifurcation, are inevitably blurred by noise. For example, close to the parameter values where the homogeneous solution or CS solution becomes unstable, the noise may induce spontaneous jumps of the system between the two solutions. This results in a relative uncertainty of parameter values of about 20% for the borders of the bistability region (gray part in Fig. 7) where CSs coexist with the homogeneous solution.

3.2.5 Adaptive Numerical Simulations

The particularity of the experimental observations resides mainly in the specific shape of the sample, the variation of the micro-cavity resonance across the VCSEL's diameter, the current crowding on its outer border, and – as our simulations evidenced – the fluctuations in the resonance transverse profile. This forced us to introduce phenomenological modifications, thus increasing the complexity of our simulations and making it impossible to obtain an analytic explanation of the emerging pattern zoology. In summary, we introduced

(1) a broad gaussian profile for the HB, as described in Sect. 3.1, to reproduce its experimental shape. The width of the gaussian is usually twice the spatial size of the integration grid, which means that $E_I(x,y)$ is almost a plane wave;
(2) a constant gradient in the cavity length, which amounts to replacing the parameter θ in (1) with a spatially dependent detuning

$$\theta(x) = \theta_1 - \eta x\,, \tag{16}$$

where x is the horizontal coordinate. This accounts for the measured varying cavity resonance (see the previous subsection); the chosen values for η were deduced from the experimental indications about the DBR reflectivity and the cavity frequency variations along the sample diameter;
(3) irregularities in the layers of the Bragg reflectors. These are modeled by setting

$$\theta_1 = \theta_0 + \delta\theta(x,y)\,, \tag{17}$$

where $\delta\theta(x,y)$ is a gaussian stochastic process with zero average and transverse correlation length of a few microns. The magnitude of the fluctuations depends on the reflectivity and on the distribution of layer jumps associated with the epitaxial deposition. The correlation length is related to the typical transverse dimensions of the layer defects. Values for this stochastic process were deduced from previous works [56];
(4) a spatial profile of the electric current $I(x,y)$ which is capable of simulating the circular symmetry of the sample. This is related to the physical etching of the VCSEL and to the annular electrode deposition. A top-hat profile turns out to be adequate to describe the pattern and the CS scenario in the operative regimes.

We introduced the cavity resonance gradient and tried to reproduce the pattern zoology under broken azimuthal symmetry. Our experimental investigations showed

up the onset of two separated regions for patterns and the homogeneous profile. According to our numerical results, for an appropriate range of values of the HB intensity, on the left the reflected field features a dynamical pattern, whose intensity peaks irregularly oscillate in time, while it features a homogeneous region on the right (see Fig. 8b). The location of the boundary between the two is determined by the threshold of the MI causing the formation of patterns. As is well known, this threshold depends on the cavity detuning (amongst other parameters, such as the input field intensity – see below), hence, when it changes across the sample, one finds the boundary in terms of the locus of the local MI thresholds. Note that it produces an almost straight line when the input field is near to a plane wave. Our interpretation is supported by an analytical evaluation of the MI threshold for an unbounded system, with plane wave injection (see Fig. 8a), where the predicted threshold matches the numerical evidence, and we also provide an indication of the sample region where CSs are expected to be stable. As for the CS positioning across the sample, we refer the reader to the following subsections.

In the experiment, a shift of the boundary was observed by changing either the input field frequency or its intensity, so we validated this evidence in terms of the drift of the MI threshold with those two quantities. Simulations fully confirm this behavior, as seen in Fig. 9. The slight boundary curvature sometimes observed in the experiment is due to the gaussian shape of the input field, whose iso-intensity lines are circles – for weaker local intensities, the threshold is pushed toward lower cavity detunings. As it turns out, a beam waist around the size of the sample diameter makes the HB departures from a plane wave irrelevant for all practical purposes.

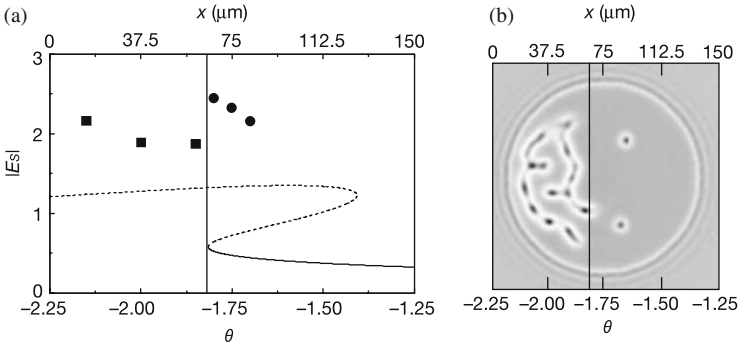

Fig. 8 Numerical simulation and theoretical interpretation of the spatial field profile. Panel (**a**) shows the stable (*solid*) and unstable (*broken*) portions of the curve of the intra-cavity field versus the cavity detuning parameter, θ, in the homogeneous stationary solution. The stable part of the plane wave stationary curve terminates at $\theta = -1.81$, which corresponds to the instability boundary; it is indicated by the vertical line. To the *left* of this line, one finds patterns whose maximum intensity is marked by squares. To the *right*, where the homogeneous background is still stable, one can excite CSs (maximum intensity marked by circles). Panel (**b**) shows the numerical transverse field intensity profile at regime. The lower and upper scales indicate the value of θ that corresponds to each coordinate x. The vertical line in panel (**b**) corresponds to that in panel (**a**). This simulation includes time-averaging comparable (1 ms) to that of the CCD used in the experiments. Figure taken from [29]

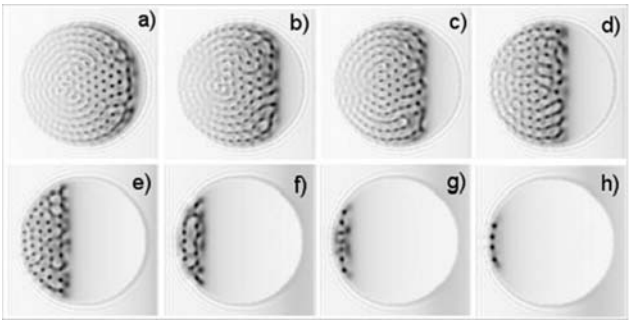

Fig. 9 Field intensity profile (gray scale) for decreasing values (from **a** to **h**) of the cavity detuning θ. This matches the experimentally observed shift of the boundary upon decreasing the injected wavelength (see Fig. 5). Figure taken from [46]

Another agreement between experiment and theory here is the reduction of the structure size when the cavity detuning becomes smaller, as a consequence of the increase of the MI critical wave-vector, K_c, for decreasing cavity detunings, as predicted by (9). The patterns (filaments, occasionally breaking up into spots) are dynamic, and they continuously evolve in time.

3.2.6 Cavity Soliton Switch-On Time: Experiment

In order to assess CSs as competitive objects for applications to all-optical information processing, we need to measure their switch-on time after the application of the WB. To analyze this process, we drive the electro-optical modulator (EOM) on the path of the WB in order to generate WB pulses of 100 ns width, rise-time (10%–90%) $\tau = 575 \pm 50$ ps, with a repetition rate of 1 kHz. To switch off a CS, once ignited by the WB pulse, we reset the system by gating off the HB through an acousto-optical modulator (AOM) on the HB path. This is necessary because CSs are bistable, and so, once they are switched-on, they persist even when the WB is gated off by the EOM. The switching process is characterized by a high-intensity peak followed by damped oscillations and relaxation to a stationary value. The switch-on time has two contributions: a lethargic stage following the application of the switching pulse, during which the intensity does not grow significantly, and a characteristic steep front of the CS intensity which rises in 520 ± 50 ps. The former is significantly affected by the system parameters and WB phase, ϕ, and power, P_{WB}, in contrast to the latter.

The existence of a lethargic delay may be understood by considering that, in order to switch a CS on, the WB energy (E_{WB}) must reach a critical value, E^C_{WB}. This is the minimal energy required to induce the system to jump (locally) from the homogeneous solution to the CS solution. Then, the lethargic delay corresponds to the time necessary for the system to accumulate this critical energy. The value of E^C_{WB} depends on the system parameters, namely the HB power P_{HB}, the VCSEL current

I and the detuning, θ, between VCSEL cavity resonance and the HB frequency. We have optimized these parameters in order to minimize the lethargic delay. Of course, the range of variation of these parameters is limited by the parameter region where CSs exist. Moreover, it is limited by the following criterion: the corresponding E^C_{WB} must be large enough to prevent the CS from switching on spontaneously (noise-induced switching) and low enough to be attainable by our experimental set-up (the largest value for P_{WB} is about 160 μW).

The experimental conditions that minimize the switch-on time are the following: P_{WB} is set to the maximum value available in our experimental set-up, while the system parameters are set in order to minimize E^C_{WB}, compatibly with the requirement of avoiding noise-induced CS switching. The duration of the global CS switch (10–90%) that we obtain in these conditions is 800 ± 50 ps.

If the phase difference, ϕ, between HB and WB is varied, then the efficiency of the energy injection through the WB is decreased, since the interference with the intra-cavity field, whose phase is fixed by the HB phase, is not fully constructive. In Fig. 10, we plot the switching process for different values of ϕ. We observe that the lethargic stage increases up to 45 ns, shifting the CS rising front, which remains unchanged to about 0.5 ns. Of course, the same thing happens if WB power is decreased.

For the same reasons, the lethargic delay increases when decreasing the WB power and fixing the phase $\phi = 0$ rad; since the critical duration of injection necessary to reach the energy increases, so does the lethargic time. For $I = 270$ mA

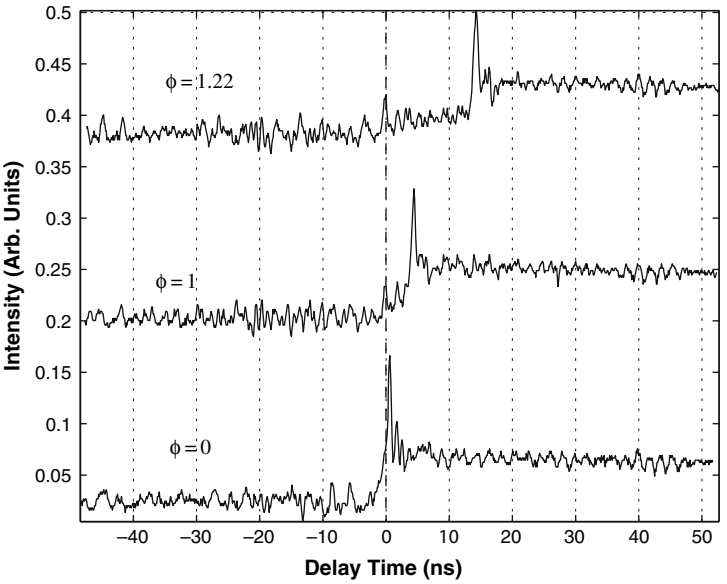

Fig. 10 Rising fronts of CSs for different values of ϕ. The other parameters are $I = 271$ mA, $P_{\mathrm{HB}} = 7.8$ mW, $P_{\mathrm{WB}} = 145$ μW. The curves for $\phi = 1$ rad and $\phi = 1.22$ rad have been displaced vertically by 0.18 units and 0.36 units, respectively. Figure taken from [39]

and $P_{HB} = 7.8\,\text{mW}$, it varies from around 1 ns when $P^s_{WB} = 160\,\mu\text{W}$, to 30 ns when $P^s_{WB} = 10\,\mu\text{W}$. Fixing $\phi = 0$ and $P^s_{WB} = 160\,\mu\text{W}$, the lethargic time is affected by the pumping current of the VCSEL, and it increases as I decreases. Again, the rising front of the CS remains unchanged relative to variations in I.

The same applies for increasing HB power: the lethargic time becomes shorter as this parameter becomes higher and gets close to the maximum values acceptable for avoiding spontaneous CS switching [39]. For $I = 271\,\text{mA}$ and $P^s_{WB} = 10\,\mu\text{W}$, the delay time ranges from a negligible value when $P_{HB} = 27\,\text{mW}$, to 25 ns when $P_{HB} = 15\,\text{mW}$.

3.2.7 Cavity Soliton Switch-on Time: Numerical Simulations

Simulations of the switch-on dynamics of the CS were performed by adopting (1) and (2). We start from the plane wave (PW) stationary curve with the coexisting stable CS branch, as predicted by the stability analysis, in Fig. 1b. By injecting a narrow WB pulse, we can access the CS branch and create a soliton. We model a gaussian HB with waist $\sigma_{HB} = 200\ \mu\text{m}$, as in the experiment, and a maximum amplitude $E_I = 0.75$ in our scaled units. Then we add a narrow gaussian WB at an arbitrary position with a waist $\sigma_{WB} = 10\,\mu\text{m}$. The duration and temporal shape of the WB pulse is the same as in the experiment – the stationary value (P^s_{WB}) is reached after a linear growth and with a rise-time of 560 ps (10–90%), and then the WB remains stationary for 100 ns. All simulations are performed after adding white-noise terms to the field and carrier density equations to simulate noise in the injected field and current, respectively, as in Sect. 3.1. It is worth noting that, as in the experiment, the amount of noise included in the equations is not enough to cause a spontaneous switch-on of the CSs.

Typically, if we calculate the intensity of the intra-cavity field at CS center during the injection, we find that a delay time of about 1 ns, followed by a steep front of about 400 ps, characterizes the switch-on process, and this is in excellent agreement with the experiment. One difference from the experimental result is that the overshoot peak is much less pronounced, and the subsequent relaxation oscillations are absent.

The second step is to evaluate the effect of parametric changes on the build-up time and on the delay time. The steep front duration mainly depends on the intrinsic parameters of the system, such as the carrier recombination rate and cavity loss rate, and these cannot be varied in the experiment. On the other hand, the delay time is strongly affected by the control parameters. First of all, we vary the relative WB/HB phase, ϕ. As in the experiment, the optimal phase is zero, and the delay time increases with ϕ. In Fig. 11a, we show the switch-on process for increasing values of ϕ. When $\phi = 1.5$ rad, more injected power is needed to create a CS and the delay time reaches 36 ns. As for the variation of the pump parameter μ, related to variations of the injected current, it must be said that simulations in our simple model yield an *increasing* delay time upon increasing μ, in contrast to the experimental evidence. The reason is that our model does not include thermal effects

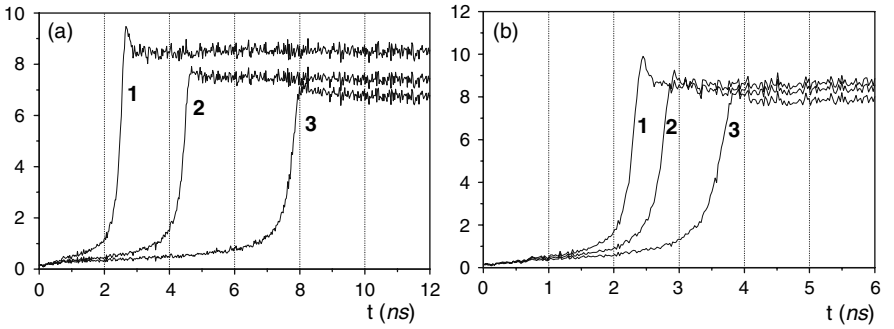

Fig. 11 CS switch-on process, numerical simulation. Panel (**a**): The intensity at the CS peak is displayed as a function of time, for different values of ϕ: $\phi = 0$ rad (curve 1), $\phi = 1$ rad (curve 2), and $\phi = 1.22$ rad (curve 3). Other parameters are $\theta = -2$, $\mu = 0.9$, $E_{\mathrm{WB}} = 0.4$. Panel (**b**): The intensity at the CS peak is displayed as a function of time, for different values of the pump parameter: $\mu = 0.909$ and $\theta = -2.05$ (curve 1); $\mu = 0.891$ and $\theta = -1.95$ (curve 2); $\mu = 0.864$ and $\theta = -1.8$ (curve 3). The cavity detuning parameter, θ, has been decreased slightly as μ is increased, in order to simulate the thermal red-shift of the cavity resonance. Other parameters are ϕ = 0 rad $E_{\mathrm{WB}} = 0.4$. Figure taken from [39]

which account for the experimentally observed red-shift of the cavity resonance with injected current. In our device, it is estimated to be $-0.7\,\mathrm{GHz/mA}$, which, in our scaled variables, is equivalent to a variation in θ of -0.05 for an increase of μ equal to 0.09. If we include this phenomenological dependence of θ on μ [38], our model correctly predicts a delay time decrease with increasing current, as shown in Fig. 11b.

Finally, we were able to confirm that decreasing the WB and HB intensities causes the delay time to increase, while leaving the build-up time practically unchanged, as in the experiment. In particular we could confirm that the delay time varies considerably, from a negligible value to more than 20 ns (for $E_{\mathrm{WB}} = 0.75$ and $E_{\mathrm{WB}} = 0.15$, respectively).

3.2.8 Cavity Soliton Positioning: Experiment

One of the most interesting properties of a CS is its plasticity, i.e., the possibility of moving it in the transverse plane through a parameter gradient [41, 43]. This motion, if demonstrated experimentally in sufficiently fast media, such as semiconductor devices, could be used to implement an all-optical shift register. Another application of parameters gradients is the positioning of CSs following an imposed pattern [41, 43, 57]. This feature allows us to consider an ensemble of CSs as a *reconfigurable* array of independent bistable optical bits.

Plasticity relies on the transverse invariance of our system and hence translation is a neutral mode. In real devices, this property may be detrimentally affected by the presence of spurious gradients and by the presence of defects in the transverse plane of the resonator. The effect of spurious gradients, like the cavity length gradient

described above, is to limit the existence region in space for CSs, but they also induce unwanted motions of CSs which are blown outside their stability region. On the other hand, the presence of roughness in the semiconductor layers, together with randomly distributed impurities across the transverse plane, may trap the CSs at fixed positions. In Fig. 12, we use the WB to target a point in a slightly different location from the one targeted in Fig. 6b. We can generate a CS, but, after removal of the WB, it migrates toward the position of Fig. 6b, suggesting that this location is an attracting locus for a CS. As a result, CSs are only stationary at fixed positions. Indeed, it is worth noting that, in devices with spurious gradients, the observation of stationary CSs is made possible by the presence of surface defects, since otherwise the CSs would be blown away. In order to get rid of these problems, ULM-photonics provided a device with negligible cavity length gradient. In this device, the main limitation comes from the surface defects, but, in principle, all of the transverse surface is available for generating CSs, and space invariance in the device is only broken by local defects.

We demonstrate experimentally the effects of parameter gradients by using the optically addressable spatial beam modulator shown in the experimental set-up of Fig. 4. This liquid crystal-based device allows us (via an optical intensity profile applied upon it) to locally control the phase of the HB injected into the VCSEL. For the spatial modulation to be efficient, the phase profile of the HB is first adjusted to be as homogeneous as possible at the VCSEL input mirror. Then we set the spatial light modulator in order to generate a phase landscape having a homogeneous background with a regular pattern of circular areas which are phase-shifted by $0.8\ \pi$ radians with respect to the background. The diameter of each circular area is about $20\,\mu$m and their centers are separated by about $40\,\mu$m. The phase slope at the boundaries of these areas is $0.1\pi\,\mathrm{rad}/\mu$m. The scheme described above allows us to

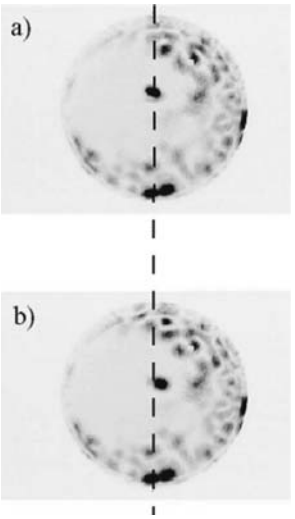

Fig. 12 CS drift – we target an arbitrary point with the WB and, as we remove it, the CS migrates to a point nearby. The vertical line helps as reference for the CS position. Figure taken from [46]

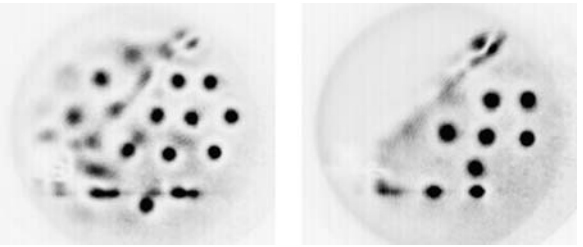

Fig. 13 Illustration of the plasticity of CSs – their positions can be set thanks to a controlled phase landscape. Taken from [47]

overcome the device imperfections to some extent, as shown in Fig. 13. In the same device, depending on the geometry of the pattern of the phase profile we apply, a CS can be pinned on a hexagonal grid (left) or on a square grid (right). In both pictures, we note the presence of two defect lines (horizontal and approximately 45°), related to device ageing, whose effect is too strong to be compensated for. However, in the right part of the device, which is sufficiently homogeneous, CSs can be organized into a matrix, which can be reconfigured simply by modifying the HB phase profile, and this is an optical operation. We note that, even if the modulation is intended to be applied only on the phase of the HB, some small intensity effects are unavoidable with our spatial light modulator when using such large phase slopes. This results in a small spatial intensity modulation of the HB at the VCSEL input. However, the effect of this modulation appears to be small when compared with the effects of the phase gradients, since CSs actually turn out to be located close to the injected intensity minima.

The gradient-induced CS motion is currently under investigation. Preliminary results have been obtained using HB profiles composed of intensity fringes [47] with a phase gradient parallel to the fringes. The intensity fringe forces the trajectory of the CS along a straight line, while the phase gradient provides the force inducing the motion. A linear array of detectors placed along the fringe shows a light pulse that travels while maintaining its shape and has a velocity comparable with the speed values found for CSs in numerical simulations. This observation indicates the possibility of using the motion properties of CSs in order to build an all-optical shift register. Experimental work is currently in progress in order to control the motion in terms of triggering and speed [51].

3.2.9 Cavity Soliton Positioning: Numerical Simulations

The last part of our investigation was devoted to a characterization of the positioning properties of CSs, as determined by the experiments. In particular, we tried to reproduce the positioning of CSs in preferred locations of the sample section.

A general theoretical treatment of the CS dynamical response in the presence of external perturbations, in particular of those amounting to a parameter gradient

in the spatial domain (whether it is phase, intensity or detuning), was reported in [33, 44, 58]. Although the detuning gradient in the investigated sample cannot be treated perturbatively, we could nevertheless expect the detuning gradient to act as a sort of Aristotelian force, where the velocity is vectorially proportional to the force itself.

We assumed a linear cavity detuning gradient with the form of (16), with a total variation in the parameter θ of 0.5 scaled units across the sample. The CSs were excited by adding the WB in the usual way, and, in the absence of irregularities in the layers of the Bragg reflectors, they immediately behaved as expected, sliding leftward and following the gradient lines. As it turns out, a CS slides directly into the patterned domain, melting into the structures and ceasing to exist as an individual entity.

Then, we added irregularities to the transverse profile of the cavity detuning θ, in order to simulate inhomogeneities in the layers of the Bragg reflectors, as in (17), and the CSs were observed sliding toward a certain location where they could remain still.

Based on our previous experience of the role of the roughness in the detuning profile (due to the layer jumps intrinsic to the DBR epitaxial deposition [56]), we interpreted the existence of equilibrium positions as the result of sizeable local variations in the detuning so that, if we may introduce a pictorial image, the CS can be imagined as a rock, rolling downhill, that can be stopped by a hump (or a dip) in the terrain, provided it is sufficiently elevated (or hollow). When the slope is more shallow, it is easier to find a "land scar" capable of accomplishing the trapping.

Indeed, as shown in Fig. 14, the CS moves to the left with a velocity of about 550 m/s, reaches a location where it gets trapped and then stays still forever. It must be noted that, in principle, the roughness-induced equilibrium locations limit the continuum of positions where a CS can be encoded to a countable set, but, on the other hand, in our simulations, they appear to be interspersed densely enough throughout the sample's cross-section, so as to ensure a satisfactory density of equilibrium positions. It must be kept in mind that there exist interaction distances between CSs [32, 41, 33, 58], and the spatial encoding density of CSs seems to be more severely limited by this factor. Also, in absence of the "roughness trapping", CSs would slide undisturbed, and one would need to greatly reduce the diameter resonance gradient in the sample, with a consequent increase in sample costs and growth times.

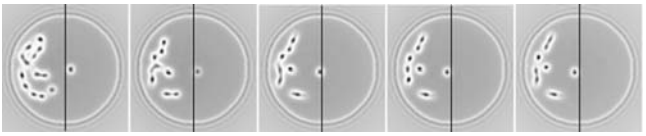

Fig. 14 The CS slides leftward and is trapped in a roughness-determined location. As commented in the text, the patterns in the left domain are not stationary, but continuously evolving in time. A vertical diameter has been added to make the movement more evident. The last frame represents a stationary configuration. Figure taken from [46]

As for the simulations with a phase landscape, in order to create regular arrays of CSs, we refer the reader to Sect. 3.1. Simulations are also in progress for the case of a linear gradient, and the HB is engineered into the form of interference fringes, in order to better adapt to the experimental situation. The CS velocity turns out to be of the order of a few kilometers per second, depending on the gradient strength and on the system parameters, such as cavity detuning and current [51].

3.3 Cavity Solitons in Driven VCSELs Above Threshold

3.3.1 The model

In Sect. 3.1, we pointed out that the rate equations (1) and (2) are not suitable for describing the formation of patterns and CSs in a driven VCSEL above threshold because they predict unphysical small wavelength instabilities below the injection locking point. The reason for this wrong result stems from the fact that the dependence of the susceptibility on the frequency is neglected in the rate equations.

A possible solution consists of replacing the rate equations with a set of effective Maxwell–Bloch equations which are valid for semiconductor lasers, where a collective macroscopic polarization variable, P, is introduced. Several slightly different approaches can be found in the literature [59, 60, 61]. Our model is rather similar to that proposed in [59] and reads [62]

$$\dot{E} = E_I + P - (1 + \mathrm{i}\theta)E + \mathrm{i}\nabla_\perp^2 E\,, \tag{18}$$

$$\dot{P} = \Gamma(D)\left[1 + \mathrm{i}\Delta(D)\right]\left[(1 - \mathrm{i}\alpha)DE - P\right], \tag{19}$$

$$\dot{D} = \gamma\left[\mu - D - \left(EP^* + E^*P\right)/2 + \mathrm{d}\nabla_\perp^2 D\right]. \tag{20}$$

The meaning of the variables and parameters is the same as in (1) and (2). This model differs from the two-level Maxwell–Bloch equation in the equation for the macroscopic polarization P where, as in [59], the right-hand side of the equation is multiplied by a complex term which contains two real functions, $\Gamma(D)$ and $\Delta(D)$, that determine the shape of the effective susceptibility. The dependence on D can be obtained with a linear fit of the gain curves, calculated with a microscopic model. Here we set $\Gamma(D) = 6.9 + 25.4D$ and $\Delta(D) = -\alpha + 2\delta(D)/\Gamma(D)$, with $\delta(D) = -4.225 + 5.4D$. $\Gamma(D)$ is associated with the gain linewidth, while $\delta(D)$ is the detuning between the reference frequency (in our case that of the injected field) and the frequency where the gain is maximum.

We point out that a standard adiabatic elimination of P allows us to recover the rate equation models (1) and (2) in a straightforward manner. This makes a physical comparison with the amplifier configuration more direct. In particular, as regards the plane wave stationary solution and the MI, all the results presented in Sect. 3.1 remain valid. The only relevant difference is that, in a VCSEL above threshold, the plane wave stationary solution is Hopf unstable up to the injection locking point,

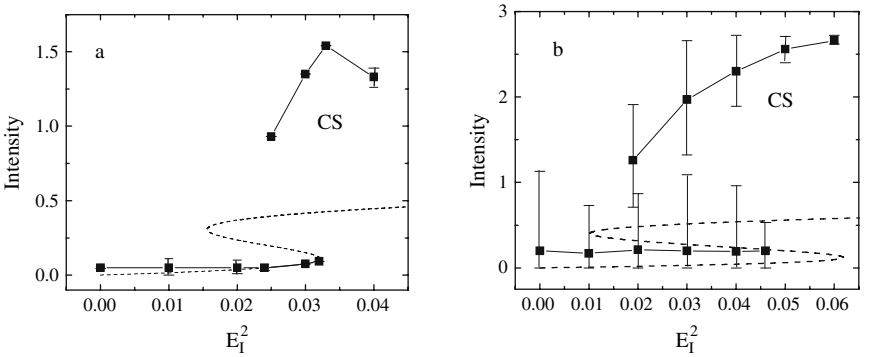

Fig. 15 The results of the dynamical simulations are superimposed on the stationary curves for (**a**) $\mu = 1.05$, $\theta = -2.3$ and (**b**) $\mu = 1.2$, $\theta = -2.5$. The other parameters are $\alpha = 3$, $\gamma = 0.0025$, and $d = 0.052$. The squares indicate the average intensity and the vertical bars the amplitude of the oscillations. In (**a**), CSs coexist with the stable part of the lower branch from the injection locking point to the right turning point. In (**b**), CSs coexist with the unstable lower branch in the interval from $E_I^2 = 0.019$ to $E_I^2 = 0.047$. Figure taken from [62]

$|E_S|^2 = \mu - 1$. The effective Maxwell–Bloch equations remove the unphysical short wavelength instability predicted by the rate equations, thus limiting the instability to a finite band of wave-vectors K.

Since the injection locking point moves toward higher intensity as the pump is increased, two different scenarios are possible, as shown in Fig. 15. For a VCSEL close to threshold ($\mu = 1.05$), a portion of the lower intensity homogeneous branch between the injection locking point and the right turning point is stable, as shown in Fig. 15a. A numerical integration of the dynamical equations shows that, as expected, a branch of stable CSs exists, corresponding to the stable part of the lower branch. Apart from the small oscillations observed before the injection locking point is met, the behavior is very similar to that found for the laser below threshold.

If the pump value is increased ($\mu = 1.2$), Fig. 15b shows that the whole lower intensity homogeneous branch of the steady-state curve is unstable. Nevertheless, the numerical simulations prove that CSs also exist in this case, and for a range of injected intensities even larger than in the previous case. The CSs display strong oscillations, and they are embedded in an oscillating background, but they are clearly visible, stable, and robust.

3.3.2 Experimental Results and Comparison with Theory

The experimental set-up used for the analysis of the VCSEL biased above threshold is the same as that in Fig. 4, except that the broad-area VCSEL is driven above the lasing threshold. The near-field time-averaged output profiles of the VCSEL above threshold, injected by the HB, are quite similar to the ones shown for the below-threshold device in Fig. 5 [62]. The theoretical prediction and the analogy with the

case below threshold indicate that the most favorable region in the transverse plane for finding a CS is close to the boundary of the MI. If we target this region with the WB, we are able to switch two bright spots on and off independently, and we obtain exactly the same sequence as that shown in Fig. 6 [62]. Then CSs do exist, even in the VCSEL above threshold, and they have the same shape and size as in the case of the VCSEL below threshold.

The most important difference between the two situations comes from the background on which the CS forms. Below threshold, the background solution is locked at the HB frequency, while above threshold the background is oscillating at a frequency that is close to the beat note between the solitary VCSEL emission frequency and the injection beam frequency.

In Fig. 16, we plot the local emission spectrum of the VCSEL without injection, the local emission spectrum of the injected VCSEL when the CS is off (background), and the local emission spectrum of the injected VCSEL when the CS is on. The HB wavelength is also marked.

When the VCSEL is biased at threshold or slightly above it (Fig. 16a), the local spectra of the background and of the CS have the same characteristics as those for the case below threshold – both are locked to the HB frequency. Moreover, both spectra are red detuned with respect to the peak of the solitary VCSEL.

For greater pumping currents (Fig. 16b), the local spectrum of the background shows the presence of two peaks, with one corresponding to the injection frequency, and the second close to the solitary VCSEL peak. The spectrum of the CS shows a narrow and high peak centered on the injection frequency and detuned with respect to the solitary VCSEL emission. The presence of a double peak structure in the optical spectrum of the homogeneous solution reveals that, when the injected VCSEL is operated well above threshold, the background oscillates in time at a frequency corresponding to the peak separation (35 GHz).

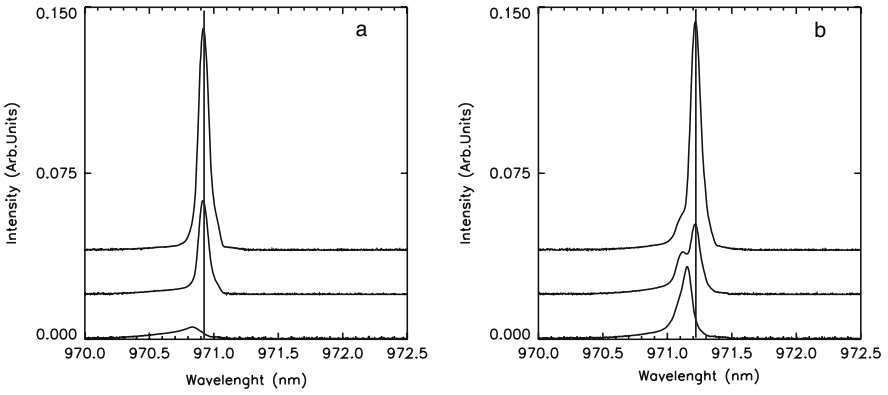

Fig. 16 Experimentally measured local optical spectra for a VCSEL slightly above threshold (**a**) and well above threshold (**b**). The region monitored is a spot of 15 μm around the point targeted by the WB. The lowest curve is the spectrum of the solitary VCSEL, the curve in the middle is the emission spectrum of the VCSEL with injection and the CS off, while the upper curve is the emission spectrum of the VCSEL with injection and CS on. Figure taken from [62]

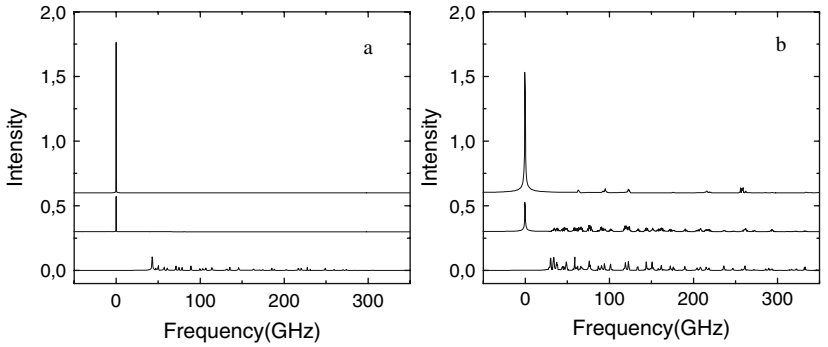

Fig. 17 Numerically calculated local optical spectra for the same parameters as in Fig. 15 ($\mu = 1.05$, $\theta = -2.3$ for panel (**a**) and $\mu = 1.2$, $\theta = -2.5$ for panel (**b**)), and $E_I^2 = 0.03$. The meaning of the three traces is the same as in Fig.16. Figure taken from [62]

These experimental findings are well supported by the results of the numerical simulations shown in Fig. 17a for a low pump value ($\mu = 1.05$) and in Fig. 17b for a higher pump value ($\mu = 1.2$).

In both figures, the lower traces (solitary laser) display a quite rich spectrum, where every peak is associated with a mode with transverse vector K, whose frequency, with respect to that of the plane wave, is K^2. The left-most peak is that associated with the plane wave $K = 0$, and it corresponds to the single peak that appears in the lower traces of Fig. 16. In making a comparison, one must remember that, in the experiment, the frequencies of modes with $K \neq 0$ are probably suppressed by the spatial filtering action of the fiber used in the detection apparatus, and this explains why the experimental spectrum presents a single peak.

As in Fig. 16, when the HB is on and the CS is off (middle traces), the spectrum of the solitary laser disappears only for the lower pump value (Fig. 17a). For the higher pump value (Fig. 17b), locking does not occur, and the peak associated with the HB, which has zero frequency in the model, appears together with the spectrum of the solitary laser. If the modes with $K \neq 0$ are neglected, the numerically calculated spectrum has a two-peak structure, as in Fig. 16b. The figure shows that the distance between the two peaks is very close to the experimental value of 35 GHZ.

4 VCSELs with Saturable Absorber: The Cavity Soliton Laser

In a laser with a saturable absorber (LSA), it is possible to achieve the optimal condition where a patterned stationary state coexists with a dark state of pure spontaneous emission corresponding to a laser below threshold. Under this condition, the contrast between the CSs and the homogeneous background is maximized. On the other hand, such a device, which will be able to generate CSs without an external HB, represents a remarkable step forward in the field because it is the realization of

a cavity soliton laser, i.e., a laser able to emit a beam whose properties are determined only by the characteristics of the radiation–matter interaction, independently of the boundary conditions. Moreover, the elimination of the HB makes the device simpler, more compact, and robust, and, more importantly, allows us to avoid the injection of considerable optical power and hence the occurrence of undesired thermal effects.

The formation of single-peaked structures in a laser with a saturable absorber has been demonstrated with a photorefractive material as the active medium, with an organic material being passive [63]. In this case, it was possible to excite just one intensity peak at a time, since, when a second one is created – even far away from the first – the first one disappears. For semiconductor materials, to the best of our knowledge, there exists only a preliminary result showing the existence of propagating spatial solitons (different from the CSs) in an optical amplifier [64].

A theoretical prediction of dissipative optical localized structures ("auto-solitons") in a laser with a saturable absorber was proposed by Rosanov [31, 65, 66, 67]. The theory, initially developed only in the limit of fast materials, was later generalized to account for finite relaxation times [68]. However, the case of slow materials, which applies to semiconductor lasers, was not considered.

The dynamical equations, suitable for describing the effects of diffraction in an LSA where both the active and the passive materials are semiconductors, are [69]

$$\dot{F} = [(1-\mathrm{i}\alpha)D + (1-\mathrm{i}\beta)d - 1 + \mathrm{i}\nabla_\perp^2]F, \tag{21}$$

$$\dot{D} = -\gamma_1[D(1+|F|^2) - \mu], \tag{22}$$

$$\dot{d} = -\gamma_2[d(1+s|F|^2) + \gamma], \tag{23}$$

where F is the slowly varying amplitude of the electric field, and D and d are related to the carrier densities in the active and passive material, respectively. Specifically, if N_1 (N_2) is the carrier density in the active (passive) material, and $N_{1,0}$ ($N_{2,0}$) is its transparency value, we have

$$D = \eta_1 (N_1/N_{1,0} - 1), \qquad d = \eta_2 (N_2/N_{2,0} - 1), \tag{24}$$

where the coefficients η_1 and η_2 have the same meaning as $2C$ in (3). Similarly, the pump and absorption parameters, μ and γ, are defined as

$$\mu = \eta_1 (I_1/I_{1,0} - 1), \qquad \gamma = -\eta_2 (I_2/I_{2,0} - 1), \tag{25}$$

where I_1 (I_2) is the current injected in the active (passive) material, and $I_{1,0}$ ($I_{2,0}$) is its transparency value. By definition, $I_1 > I_{1,0}$ (the active material is pumped above transparency) and $I_2 < I_{2,0}$ (the passive material is pumped below transparency) and both μ and γ are positive. The passive material may not be pumped at all - in that case we simply have $\gamma = \eta_2$. The parameters α and γ_1 (β and γ_2) are the linewidth enhancement factor and the ratio of the photon lifetime to the carrier lifetime in the active (passive) material. In VCSELs, $\gamma_1, \gamma_2 \ll 1$ because the material response is much slower than the electric field. Moreover, we will assume $\gamma_1 > \gamma_2$, which

should be valid when the same semiconductor material is used in the amplifier and in the absorber because the decay rate of carriers increases with the carrier density, and it is larger in the active material. Finally, the saturation parameter, s, is defined as

$$s = \frac{a_2 \gamma_1}{a_1 \gamma_2}, \tag{26}$$

where the differential gains a_1 and a_2 are related to the slope of the gain as a function of the carrier density. Since the growth of the gain with the carrier density is less than linear (it is typically logarithmic in quantum well devices), the differential gain will be larger in the passive material, i.e., $a_2 > a_1$. This inequality, together with $\gamma_1 > \gamma_2$, ensures that, in a semiconductor LSA, the saturation parameter s is larger than 1, which, as we shall soon see, is a necessary condition for bistability. Equations (21), (22) and (23) admit a trivial homogeneous steady-state (HSS) solution with

$$F_0 = 0, \quad D_0 = \mu, \quad d_0 = -\gamma, \tag{27}$$

and a non-trivial HSS solution with

$$F_0 = \sqrt{I_0} \mathrm{e}^{-\mathrm{i}\omega t}, \quad D_0 = \mu/(1+I_0), \quad d_0 = -\gamma/(1+sI_0), \tag{28}$$

where the stationary intensity, I_0, is related to the parameters s and γ by the equation

$$\mu/(1+I_0) - \gamma/(1+sI_0) = 1, \tag{29}$$

and the laser frequency

$$\omega = \alpha + \gamma(\alpha - \beta)/(1+sI_0) \tag{30}$$

is intensity dependent. Equation (29) shows that the laser threshold ($I_0 = 0$) is

$$\mu_{\mathrm{th}} = 1 + \gamma. \tag{31}$$

A closer inspection reveals that, if $s > 1 + 1/\gamma$, the nontrivial HSS has a C shape, as shown in the upper plot of Fig. 18. The value of the pump associated with the turning point is

$$\mu_{\mathrm{TP}} = (\sqrt{s-1} + \sqrt{\gamma})^2/s \tag{32}$$

In the plane wave approximation, i.e., if diffraction is neglected, the stability of the two HSSs does not depend on the parameters α and β because the dynamics of the phase can be decoupled from that of the intensity and of the populations. The stability analysis gives the following well-known results: (i) the trivial HSS is stable only for $\mu < \mu_{\mathrm{th}}$; (ii) the negative slope branch is always unstable; (iii) part of the upper branch can be unstable. In the limit $\gamma_1, \gamma_2 \ll 1$, the upper branch is Hopf unstable for $\mu < \mu_{\mathrm{H}}$, with

$$\mu_{\mathrm{H}} = (\gamma_2/\gamma_1)^2 \gamma s. \tag{33}$$

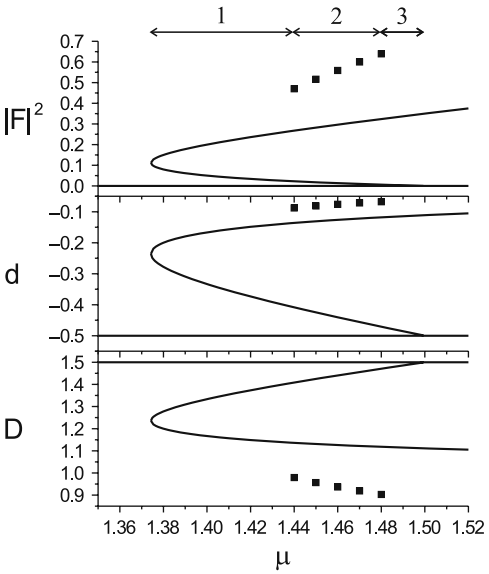

Fig. 18 The HSSs for $\gamma = 0.5$, $s = 10$. The bistability criterion, $s > 1 + 1/\gamma$, is fulfilled, and three HSSs coexist in the range $\mu_{TP} < \mu < \mu_{th}$, with $\mu_{TP} = 1.374$ and $\mu_{th} = 1.5$. The *upper plot* shows the field intensity, the *middle* shows absorber carrier density while the *lower* shows amplifier carrier density. The range of existence of the CS is indicated by plotting the peak intensity of the stable CSs (*squares*). Figure taken from [69]

Evidently, the instability disappears if $\mu_H < \mu_{TP}$, and, in this case, there is bistability between the upper branch of the nontrivial HSS and the trivial HSS over the full range $\mu_{TP} < \mu < \mu_{th}$. Taking into account (32) and (33), the condition $\mu_H < \mu_{TP}$ is equivalent to

$$\gamma_2/\gamma_1 < \left(\sqrt{s-1} + \sqrt{\gamma}\right)/\sqrt{\gamma}s\,. \tag{34}$$

With $s = 10$ and $\gamma = 0.5$, the theory predicts that the Hopf instability disappears for $\gamma_2/\gamma_1 < 0.524$, in very good agreement with the numerical calculations.

We can now ask how this scenario changes if the effects of diffraction are taken into account. Now, the dynamics of the phase can no longer be neglected, and the characteristic equation has the form $\lambda^4 + c_3\lambda^3 + c_2\lambda^2 + c_1\lambda + c_0 = 0$. As usual, the boundaries of the instability associated with a real eigenvalue are found by setting $c_0 = 0$, while the equation for the boundaries of the pattern-forming Hopf instabilities has the form $c_1^2 - c_1c_2c_3 + c_0c_3^2 = 0$.

With our choice of the parameters s, γ, γ_1, and γ_2, we found that a Hopf instability with transverse wave-vector $K \neq 0$ exists only if there is a Hopf instability with $K = 0$. Hence, if condition (34) holds, we can exclude the presence of any kind of Hopf instability.

Instead, the upper branch is unstable with respect to any transverse wave-vector, K, such that

$$0 < K^2 < \frac{2I_0}{1+sI_0}\left(\alpha\frac{1+sI_0+\gamma}{1+I_0} - \beta\frac{s\gamma}{1+sI_0}\right). \tag{35}$$

It can be shown that the whole upper branch is unstable as long as $\alpha \geq \beta$. We note that, if the absorber is eliminated by setting $\gamma = 0$, the instability condition becomes

$$0 < K^2 < \frac{2\alpha I_0}{1+I_0}, \tag{36}$$

which coincides with the pattern-forming instability discovered in [10] in the framework of two-level lasers, but with the remarkable difference that in [10], the atomic detuning Δ appeared instead of the parameter α. This circumstance implied that, in two-level lasers, the instability could exist only for $\Delta > 0$. This limitation does not exist in semiconductor lasers, where α is usually positive.

As in a driven VCSEL, CSs may be created by injecting a gaussian field for a brief period, τ_{inj}. The main difference with respect to the driven VCSEL is the absence of an HB which fixes a reference phase. Nevertheless, our numerical simulations showed that CSs can be excited and deleted by using the amplitude of the pulse, rather than its phase, as the control parameter.

In this way, we were able to demonstrate that the CSs are stable in the interval $1.44 \leq \mu \leq 1.48$, labeled as regime 2 in Fig. 18. In regime 1, the CSs can also be excited but they display undamped oscillations and finally they die out, leaving the system in a non-lasing condition. In regime 3, the transient oscillations are actually damped, but the CSs undergo a further instability and the system eventually evolves into filaments, similarly to what was previously observed in [41]. These filaments are also the structures observed beyond the bistability area for $\mu > 1.5$.

The stability of the CSs also strongly depends on the parameters α, β, γ_1, and γ_2. For these simulations, we adopted the values $\alpha = 2$, $\beta = 0$, $\gamma_1 = 0.01$, and $\gamma_2 = 0.005$. The simulations indicated that in order to excite a CS for a given injection time and gaussian width, the pulse amplitude, $|F_{\text{inj}}|$, must exceed a lower threshold and be smaller than an upper threshold. Not surprisingly, the upper threshold for exciting a CS is also the lower threshold for deleting it. In fact, in each case, when that threshold is crossed, the CS does not survive, which means failed excitation or successful deletion. The phase of the pulse does not seem to play any role.

The analysis of CS dynamics reveals that the existence of these thresholds for the pulse amplitude, $|F_{\text{inj}}|$, is related to the fact that whether a CS survives or not at the turn-off of the pulse depends on the values reached at that instant by the intensity, $|F|^2$, and the population, D, at the injection point. The results obtained for $\mu = 1.46$ are summarized in Fig. 19. The CS survives at turn-off only if $|F|^2$ and D lie between the two horizontal lines. The displayed data explain why, for the excitation process (upward triangles), there are both lower and upper thresholds for the amplitude $|F_{inj}|$, while, for the deletion process (downward triangles), there is only a lower threshold. The interpretation fails only for the value of $|F|^2$ obtained for $|F_{\text{inj}}| = 1.4$, which is below the dashed horizontal line, even though the CS survives. However, the corresponding value of D is well inside the two horizontal lines, which probably means that what determines the survival of the CS is mainly the depth of the hole burnt by the pulse, rather than the intensity of the intra-cavity field

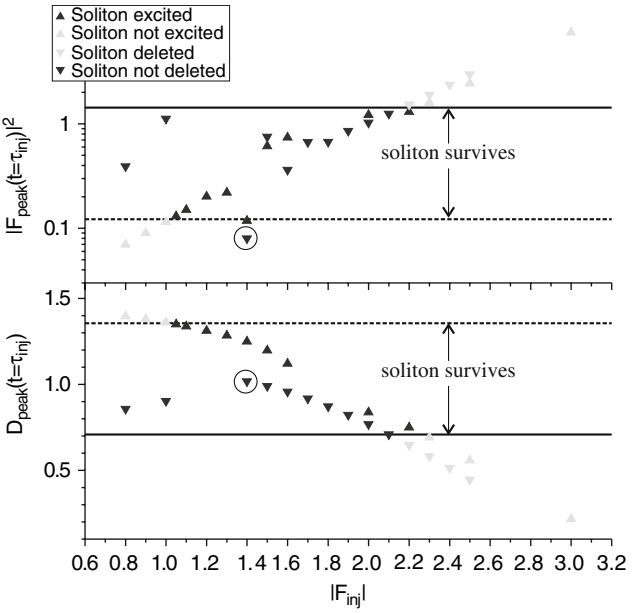

Fig. 19 Exciting and destroying a CS. The data are represented for both $|F|^2$ and D. The *light gray* symbols represent cases where the CS does not survive after turn-off, while the *dark gray* symbols indicate that the CS does survive. The *horizontal lines* denote the heuristic thresholds for the CS survival; the *solid lines* exist in both the exciting and destroying case, while indications for the *dotted lines* were found only when exciting a CS. Figure taken from [69]

at the injection point. This suggests that a CS could be written and erased in this device in a totally incoherent way, by using a local injection of carriers rather than photons [42].

5 Conclusions and Perspectives

As has been shown in Sect. 3, clear-cut experimental demonstrations of the generation of CSs in driven broad-area VCSELs have been obtained, both below and above threshold, and the results are in good agreement with theoretical models and numerics.

With the devices used in these experiments, an important role is played by the presence of local defects in the device. On the one hand, such defects are capable of pinning the position of CSs, which would otherwise quickly drift away because of the presence of a sizable gradient of cavity length along the sample. This pinning property has been valuable for the very observation of CSs. On the other hand, the presence of defects represents a problem for development. In the future, it will be desirable to operate with samples in which the gradient of cavity length is reduced

Fig. 20 The cavity soliton laser

as much as possible. This is necessary for controlling the position of CSs by means of gradients and for setting them in controlled motion, as predicted by the theory, and for realizing devices such as an optical delay line.

The possibility of doing without the HB is also quite interesting. This could allow the realization of semiconductor cavity soliton lasers in the future. These compact devices would correspond to lasers which emit one or more narrow beams, corresponding to the CSs, where their number and transverse positions could be controlled (Fig. 20). One can conceive of cavity soliton lasers which operate in a CW regime or in a pulsed regime.

A subject which has not been discussed in this chapter is that of cavity light bullets. CSs are confined with respect to the transverse dimensions, but are beams with respect to the longitudinal direction in which the light propagates. In contrast, cavity light bullets represent a full 3D confinement. They correspond to sequences of drops of light which have arbitrary positions with respect to all dimensions, and so they are not necessarily periodic. In recent years, there has been notable interest in this topic, see e.g. [70, 71, 72, 73, 74].

Acknowledgments The results described in this chapter have been obtained within the framework of the ESPRIT Basic research Action PIANOS (Processing of Information by Arrays of Nonlinear Optical Solitons) and the FET Open project FunFACS (Fundamentals, Functionalities and Applications of Cavity Solitons).

References

1. L.A. Lugiato, M. Brambilla, and A. Gatti, Optical pattern formation, in *Advances in Atomic, Molecular and Optical Physics*, (Academic Press, New York, 1999), Vol. **40**, p. 229. 52
2. W.J. Firth, in *Self-Organization in Optical Systems and Applications to Information Technology*, edited by M. Vorontsov and W.B. Miller, (Springer-Verlag, Berlin, 1995). 52
3. F.T. Arecchi, Il Nuovo Cimento **A 107**, 1111 (1998). 52
4. H. Haken, *Synergetics, an Introduction*, (Springer-Verlag, Berlin, 1977). 52
5. G. Nicolis and I. Prigogine, *Self-organization in Non-equilibrium Systems*, (Wiley, New York, 1977). 52
6. R. Bonifacio and L.A. Lugiato, Lett. Nuovo Cimento **21**, 505 (1987). 52
7. L.A. Lugiato and R. Lefever, Phys. Rev. Lett. **58**, 2209 (1987). 52, 53
8. L.A. Lugiato and C. Oldano, Phys. Rev. A **37**, 3896 (1988). 52
9. W.J. Firth and A.J. Scroggie, Europhys. Lett. **26**, 521 (1994). 52
10. L.A. Lugiato, C. Oldano, and L.M. Narducci, J. Opt. Soc. Am. B **5**, 879 (1988). 52, 88
11. G.L. Oppo, M. Brambilla, and L.A. Lugiato, Phys. Rev. A **49**, 2028 (1994). 52
12. W.J. Firth, J. Mod. Opt. **37**, 151 (1990). 52

13. G. D'Alessandro and W.J. Firth, Phys. Rev. A **46**, 537 (1992). 52
14. S. Fauve and O. Thual, J. Phys. France **49**, 1829 (1988). 53
15. L.Yu. Glebsky and L.M. Lerman, Chaos **5**, 424 (1995). 53
16. K.A. Gorshkov, L.N. Korzinov, M.I. Rabinovich, and L.S. Tsimring, J. Stat. Phys. **74**, 1033 (1994). 53
17. J. Dewel, P. Borkmans, A. De Wit, B. Rudovics, J.J. Perraud, E. Dulos, J. Boissonade, and P. De Kepper, Physica **213A**, 181 (1995) and references quoted therein. 53
18. L.S. Tsimring and I.S. Aranson, Phys. Rev. Lett. **79**, 213 (1997). 53
19. J.L. Kyoung, W.D. McCormick, Q. Ouyang, and H. L. Swinney, Science **261**, 192 (1993). 53
20. Y. Pomeau, Physica **23D**, 3 (1986). 53
21. N. Akhmediev and A. Ankiewicz (Eds), *Dissipative Solitons*, (Spinger-Verlag, Berlin, 2005). 53, 54, 91
22. Th. Ackemann and W.J. Firth, in Ref. [21], p. 55 ff. 53, 54
23. P. Coullet, C. Riera, and C. Tresser, Phys. Rev. Lett. **84**, 3069 (2000); see also P. Coullet, C. Riera, and C. Tresser, Chaos **14**, 193 (2004), and P. Coullet, Int. J. Bifurcat. Chaos **12**, special issue for the anniversary of Prof. Velarde, 2445 (2002). 53
24. N.N. Rosanov and G.V. Khodova, J. Opt. Soc. Am. B **7**, 1057 (1990). 53
25. M. Tlidi, P. Mandel, and R. Lefever, Phys. Rev. Lett. **73**, 640 (1994). 53
26. L.A. Lugiato, IEEE J. Quantum Electron. **39**, 193 (2003), and references therein. 53, 54
27. M. Segev and G. Stegeman, Physics Today, August 1998, p. 42. 53
28. P. Mandel, "Introduction to soliton theory", Notes for the Spring School on Solitons in Optical Cavities, May 8–12, 2006 Cargèse, Corsica (France). http://socaff.inln.cnrs.fr/IMG/pdf/introduction_to_soliton_theory.pdf 53
29. S. Barland, J.R. Tredicce, M. Brambilla, et al., Nature **419**, 699, (2002). 53, 54, 55, 58, 60, 70, 73
30. V.B. Taranenko, G. Slekys, and C.O. Weiss, in Ref. [21], 131ff. 54
31. N.N. Rosanov, in Ref. [21], 101ff. 54, 85
32. M. Brambilla, L.A. Lugiato, and M. Stefani, Europhys. Lett. **34**, 109 (1996). 55, 57, 63, 80
33. W.J. Firth and G. Harkness, Asian J. Phys. **7**, 665 (1998). 55, 80
34. B. Schaepers, M. Feldmann, T. Ackemann, and W. Lange, Phys. Rev. Lett. **85**, 748 (2000). 55
35. S. Barbay, Y. Menesguen, I. Sagnes, and R. Kuszelewicz, Appl. Phys. Lett. **86**, 151119 (2005). 55, 58
36. V.B. Taranenko, C.O. Weiss, and W. Stolz, Opt. Lett. **26**, 1574–1576 (2001). 56
37. I. Ganne, G. Slekys, I. Sagnes, and R. Kuszelewicz Phys. Rev. E **66**, 066613 (2002). 56
38. L. Spinelli, G. Tissoni, M. Brambilla, and L.A. Lugiato, Phys. Rev. A **66**, 023817 (2002). 56, 59, 77
39. X. Hachair, L. Furfaro, J. Javaloyes, et al., Phys. Rev. A **72**, 031815 (2005). 57, 75, 76, 77
40. D. Michaelis, U. Peschel, and F. Lederer, Phys. Rev. A **56**, R3366–R3369 (1997). 57
41. L. Spinelli, G. Tissoni, M. Brambilla, F. Prati, and L. A. Lugiato, Phys. Rev. A **58**, 2542 (1998). 57, 58, 60, 61, 65, 66, 77, 80, 88
42. S. Barbay, Y. Menesguen, X. Hachair, L. Leroy, I. Sagnes, and R. Kuszelewicz, Opt. Lett. **31**, 1504–1506 (2006). 58, 89
43. W.J. Firth and A. J. Scroggie, Phys. Rev. Lett. **76**, 1623 (1996). 58, 64, 77
44. G. Tissoni, L. Spinelli, M. Brambilla, T. Maggipinto, I.M. Perrini, and L.A. Lugiato, J. Opt. Soc. Am. B **16**, 2095–2105 (1999). 58, 80
45. T. Maggipinto, M. Brambilla, and W.J. Firth, Special Issue of IEEE J. Quantum Electron. **39**, 206 (2003). 58
46. X. Hachair, S. Barland, L. Furfaro, et al., Phys. Rev. A **69**, 043817, (2004). 58, 59, 67, 69, 70, 71, 74, 78, 80
47. F. Pedaci, Ph.D. Thesis, Institut Non-linéaire de Nice, CNRS–Université de Nice Sophia Antipolis. 58, 79
48. R. Kheradmand, L. Lugiato, G. Tissoni, M. Brambilla, and H. Tajalli, Opt. Express **11**, 3612–3621 (2003). 58, 59
49. A.J. Scroggie, J.M. McSloy, and W.J. Firth, Phys. Rev. E **66**, 036607 (2002). 59
50. L. Spinelli and M. Brambilla, Eur. Phys. J. D **15**, 257 (2001). 59
51. F. Pedaci, et al., All-optical delay lines using VCSEL Cavity Solitons, in preparation (2007). 60, 79, 81
52. J. Mørk, R. Kjær, M. van der Poel, and K. Yvind, Opt. Express **13**, 8136 (2005). 60
53. X. Zhao, P. Palinginis, B. Pesala, and C. Chang-Hasnain, Opt. Express **13**, 7899 (2005). 60
54. M. Grabherr, R. Jaeger, M. Miller, et al., IEEE Photon. Tech. Lett. **10**, 1061 (1998). 66
55. S. Barland, F. Marino, M. Giudici, et al., Appl. Phys. Lett. **83**, 2303 (2003). 70

56. R. Kuszelewicz, I. Ganne, G. Slekys, I. Sagnes, and M. Brambilla, Phys. Rev. Lett. **84**, 6006 (2000). 72, 80
57. U. Bortolozzo and S. Residori, Phys. Rev. Lett. **96**, 037801 (2006). 77
58. T. Maggipinto, M. Brambilla, G.K. Harkness, and W.J. Firth, Phys. Rev. E **62**, 8726 (2000). 80
59. J. Yao, G.P. Agrawal, P. Gallion, and C.M. Bowden, Opt. Commun. **119**, 246 (1995). 81
60. S. Balle, Opt. Commun. **119**, 227 (1995). 81
61. C.Z. Ning, R.A. Indik, and J.V. Moloney, IEEE J. Quantum Electron. **33**, 1543 (1997). 81
62. X. Hachair, F. Pedaci, E. Caboche, et al., IEEE J. Sel. Top. Quantum Electron. **12**, 339 (2006). 81, 82, 83, 84
63. V.B. Taranenko, K. Staliunas, and C.O. Weiss, Phys. Rev. A **56**, 1582 (1997). 85
64. E.A. Ultanir, G.I. Stegeman, D. Michaelis, C.H. Lange, and F. Lederer, Phys. Rev. Lett. **90**, 253903 (2003). 85
65. A.G. Vladimirov, S.V. Fedorov, N.A. Kaliteevski, G.V. Khodova, and N.N. Rosanov, J. Opt. B–Quantum Semicl. Opt. **1**, 101–106 (1999). 85
66. N.N. Rosanov, Transverse patterns in wide-aperture nonlinear optical systems, Prog. Optics **35**, 1–60 (1996). 85
67. S.V. Fedorov, N.N. Rosanov, A.N. Shatsev, N.A. Veretenov, and A.G. Vladimirov, IEEE J. Quantum Electron. **39**, 197–205 (2003). 85
68. S.V. Fedorov, A.G. Vladimirov, G.V. Khodova, and N.N. Rosanov, Phys. Rev. E **61**, 5814–5824 (2000). 85
69. M. Bache, F. Prati, G. Tissoni, R. Kheradmand, L.A. Lugiato, I. Protsenko, and M. Brambilla, Appl. Phys. B **81**, 913–920 (2005). 85, 87, 89
70. M. Tlidi and P. Mandel, Phys. Rev. Lett. **83**, 4995 (1999). 90
71. M. Le Berre, et al., J. Opt. B–Quantum Semicl. Opt. **1**, 153 (1999). 90
72. M. Brambilla, T. Maggipinto, G. Patera, and L. Columbo, Phys. Rev. Lett. **93**, 203901 (2004). 90
73. M. Brambilla, L. Columbo, and T. Maggipinto, J. Opt. B–Quantum Semicl. Opt. **6**, 197 (2004). 90
74. L. Columbo, I.M. Perrini, T. Maggipinto, and M. Brambilla, New J. Phys. **8**, 312 (2006). 90
75. F. Pedaci, P. Genevet, S. Barland, M. Giudici, and J. Tredicce, Positioning cavity solitons with a phase mask, Appl. Phys. Lett. **89**, (2006).

Dissipative Solitons in Laser Systems with Non-local and Non-instantaneous Nonlinearity

N.N. Rosanov, S.V. Fedorov, and A.N. Shatsev

Abstract Dissipative optical solitons (autosolitons) are considered, analytically and numerically, for a wide-aperture laser with saturable absorption in the case when nonlinearity relaxation and non-locality are important. Depending on the values of the relaxation times and diffusion coefficients for gain and absorption, we find stable stationary dissipative solitons which are similar to those in class A lasers, slowly moving dissipative solitons, and also a new type of "flying" soliton which is characterized by a high velocity of motion and a high peak intensity.

1 Introduction

Dissipative solitons, or autosolitons, first discovered in mechanics in 1831 [1] were further intensively investigated in the physics of electric discharge and in biology, chemistry, and many other fields of science [2, 3]. Mathematically, the governing equations were mainly of reaction–diffusion type for the dynamics of the nonlinear interactions of some "inhibitors" and "activators" in space and time [2]. The turn of optics began with the invention of lasers whose high-power radiation provides high nonlinearity and where different types of pumping are able to compensate for various types of energy losses. In addition to features in common with other dissipative solitons, the optical forms have some new ones. For example, diffraction

N.N. Rosanov
Vavilov State Optical Institute, Institute for Laser Physics, Birzhevaya Liniya 12, Saint-Petersburg 199034, Russia, nrosanov@yahoo.com

S.V. Fedorov
Vavilov State Optical Institute, Institute for Laser Physics, Birzhevaya Liniya 12, Saint-Petersburg 199034, Russia, sfedorov2006@bk.ru

A.N. Shatsev
Vavilov State Optical Institute, Institute for Laser Physics, Birzhevaya Liniya 12, Saint-Petersburg 199034, Russia, anshat@yahoo.com

Rosanov, N.N. et al.: *Dissipative Solitons in Laser Systems with Non-local and Non-instantaneous Nonlinearity.* Lect. Notes Phys. **751**, 93–111 (2008)
DOI 10.1007/978-3-540-78217-9_4

is typical for optics and replaces the traditional diffusion. With the corresponding diffractive oscillations of the electric field, these dissipative solitons could be called "diffractive dissipative solitons" [4]. In a sense, nonlinear optics and laser physics provide generally simpler and more tractable examples of dissipative solitons, and at the moment many of their features are best known in the area of optics.

Dissipative optical solitons, predicted first in the 1980s, are now objects of intensive research due to their rich and unusual physics and great potential for applications [3, 5, 6]. Due to the increase in the number of researchers and the diversity of laser systems, the actual definition of dissipative solitons varies in different publications. Here, to avoid misunderstanding, stable localized structures in homogeneous or weakly modulated nonlinear media or systems with essential energy exchange (energy sinks and sources) will be labeled as dissipative solitons or autosolitons [7]. The possibility of moderately weak modulation allows the possibility of dissipative Bragg or gap solitons [8]. A number of dissipative soliton features in this notion are especially important. First, it should be stable; unstable localized structures are well known, even for a single nonlinear diffusion equation, but there is no point in calling them "solitons". The second important feature is soliton localization. This is in time for temporal solitons, in the cross-section for spatial dissipative solitons, and in both time and space for 3D-dissipative solitons (so-called "laser bullets" in laser systems [5]). According to this definition, optical pulses in mode-locked lasers cannot be called temporal dissipative solitons, in the strict sense, because the temporal shape of the electric field at any fixed point is periodic (not localized) in this case. However, the concept of dissipative solitons can be useful even here as some approximation for the qualitative analysis. Further, we will follow the definition above and deal with "genuine" stable localized structures only.

In the theory of dissipative optical solitons, the main study was performed under the approximation of the medium nonlinearity being instantaneous and local. However, solitons in semiconductor vertical cavity surface emitting lasers [9, 10], where the medium relaxation times are much greater than the photon lifetime in the cavity (so-called class B lasers), are very promising for applications. And for spatial solitons in semiconductor optical amplifiers, where relaxation processes are not so critical, non-locality of the medium nonlinearity can be important [11]. Therefore, it is appropriate to find out what are the effects of non-locality of the nonlinearity, in space and time, on the features of laser solitons.

The goal of the present chapter is to study the effect of nonlinearity of non-instantaneous and non-local nature on the features of 1D and 2D laser solitons in wide-aperture lasers with saturable absorption. We will vary the relaxation rates and diffusion coefficients over a wide range, both for gain and absorption, to find the domain of stability of different types of laser solitons. Below, in Sect. 2, we introduce a model of a wide-aperture laser with saturable absorption and present the governing equations in the mean-field limit. In Sect. 3, the simplest regimes—with transversely independent radiation intensity—are discussed, and an analysis of their modulation instability is performed, taking into account processes of medium diffusion. Then, in Sect. 4, we present the simplest localized structures with symmetric intensity distributions and discuss their various complexes with weak and strong coupling of the constituent solitons. Section 5 is devoted to the generalization of

the description of the super-critical bifurcation from motionless dissipative soliton structures to slowly moving ones. Then we separately consider slowly moving solitons (Sect. 6) and non-stationary and soliton structures moving with high speed (Sect. 7). The conclusions are summarized in Sect. 8.

2 The Model and Initial Equations

The model is a wide-aperture laser with a large Fresnel number containing an intracavity saturable absorber. The cavity length is so small that only one longitudinal mode can be excited. We assume that the system includes an anisotropic element, which introduces sufficiently high polarization losses for one of the two field polarization components, and also losses which depend on the direction of the radiation propagation (e.g., reflection coefficients of the cavity mirrors which depend on the angle of radiation incidence). Therefore, laser radiation propagates predominantly in the longitudinal direction, along the z axis. The angular divergence of laser radiation is assumed to be small (diffraction limited), so the paraxial approach and use of the slowly varying envelope approximation is justified. Next, we assume that both linear and nonlinear variations of the electric field envelope E during one round trip of the laser cavity are small. Then we can use the mean-field model, averaging over the cavity length, resulting in the following governing equation for the electric field envelope:

$$\frac{\partial E}{\partial t} - (\mathrm{i} + d_\mathrm{s})\nabla_{\boldsymbol{r}}^2 E = (-1 + g - a)E, \tag{1}$$

where t is the dimensionless time normalized by t_c—the field lifetime in the empty cavity; $\nabla_{\boldsymbol{r}}^2 = \partial^2/\partial x^2$ (1D case) or $\nabla_{\boldsymbol{r}}^2 = \partial^2/\partial x^2 + \partial^2/\partial y^2$ (2D case) is the transverse Laplacian with dimensionless Cartesian transverse co-ordinates $\boldsymbol{r} = x$ or $\boldsymbol{r} = (x, y)$ normalized by the width of the effective Fresnel zone; and g and a are, respectively, the nonlinear gain and absorption of the medium inside the cavity normalized by the constant non-resonance losses. It is assumed that the effective field diffusion coefficient, d_s, is small, so $0 < d_\mathrm{s} \ll 1$, and also that it reflects the angular dependence of cavity losses. For the medium we use modified Bloch equations for gain and absorption in the form

$$\tau_g \frac{\partial g}{\partial t} - d_g \nabla_{\boldsymbol{r}}^2 g = g_0 - \left(1 + b_g |E|^2\right) g, \tag{2}$$

$$\tau_a \frac{\partial a}{\partial t} - d_a \nabla_{\boldsymbol{r}}^2 a = a_0 - \left(1 + b_a |E|^2\right) a, \tag{3}$$

where $d_{g,a}$ are diffusion coefficients, $\tau_{g,a}$ are relaxation times, g_0 and a_0 are real small-signal gain and absorption, and $b_{g,a}$ are saturation intensities for gain and losses, respectively. In the equations presented, in order to underline the purely dissipative nature of the structures, we neglect any frequency detunings and linewidth enhancement factors which arise.

3 Transversely Homogeneous Lasing

The trivial solution of (1), (2), (3) $E = 0$, $g = g_0$, $a = a_0$ corresponds to the non-lasing regime and is stable for $-1 + g_0 - a_0 < 0$. This condition coincides with the requirement of stability of the tails of the localized structures, and therefore it is fulfilled below.

Another simple solution of the governing equations corresponds to monochromatic radiation with a transversely homogeneous intensity distribution, I_s, with intensity $I = |E|^2$. For this regime, the stationary values of saturated gain and absorption are $g_\mathrm{s} = g_0/(1 + b_g I_\mathrm{s})$ and $a_\mathrm{s} = a_0/(1 + b_a I_\mathrm{s})$, respectively. Note that the parameters of medium relaxation and diffusion do not enter into these relations. However, they determine the regime stability. For the linear stability analysis, let us seek a solution of (1), (2), (3) in the form

$$\begin{aligned} E(\boldsymbol{r},t) &= \mathrm{e}^{\mathrm{i}\theta t}\sqrt{I_\mathrm{s}}\left(1 + u_1 \mathrm{e}^{\lambda t + \mathrm{i}\boldsymbol{k}\cdot r} + u_2^* \mathrm{e}^{\lambda^* t - \mathrm{i}\boldsymbol{k}\cdot r}\right), \\ g(\boldsymbol{r},t) &= g_\mathrm{s}\left(1 + 2\mathrm{Re}\, w_g \mathrm{e}^{\lambda t + \mathrm{i}\boldsymbol{k}\cdot r}\right), \\ a(\boldsymbol{r},t) &= a_\mathrm{s}\left(1 + 2\mathrm{Re}\, w_a \mathrm{e}^{\lambda t + \mathrm{i}\boldsymbol{k}\cdot r}\right), \end{aligned} \tag{4}$$

where I_s, g_s, a_s characterize the unperturbed regime of lasing with a transversely homogeneous intensity distribution, and a perturbation with small amplitudes $|u_{1,2}| \ll 1$, $|w_{g,a}| \ll 1$ has spatial frequency $\boldsymbol{k}$ and exponential temporal dependence with complex constant λ. Linearization of the governing equations results in a quartic algebraic equation for $\lambda_\mathrm{s} = \lambda + d_\mathrm{s} k^2$:

$$\tau_g \tau_a \lambda_\mathrm{s}^4 + c_{3\mathrm{s}} \lambda_\mathrm{s}^3 + c_{2\mathrm{s}} \lambda_\mathrm{s}^2 + c_{1\mathrm{s}} \lambda_\mathrm{s} + c_{0\mathrm{s}} = 0, \tag{5}$$

where

$$\begin{aligned} c_{3\mathrm{s}} &= \tau_g (1 + b_a I_k) + \tau_a (1 + b_g I_k), \\ c_{2\mathrm{s}} &= (1 + b_g I_k)(1 + b_a I_k) + 2\tau_a b_g I g_\mathrm{s} - 2\tau_g b_a I a_\mathrm{s} + \tau_g \tau_a k^4, \\ c_{1\mathrm{s}} &= 2 b_g I g_\mathrm{s} (1 + b_a I_k) - 2 b_a I a_\mathrm{s} (1 + b_g I_k) + c_{3\mathrm{s}} k^4, \\ c_{0\mathrm{s}} &= k^4 (1 + b_g I_k)(1 + b_a I_k), \end{aligned} \tag{6}$$

and $b_{g,a} I_k = b_{g,a} I_\mathrm{s} + (d_{g,a} - \tau_{g,a} d_\mathrm{s}) k^2$. The corresponding quartic equation for λ has the form

$$\tau_g \tau_a \lambda^4 + c_3 \lambda^3 + c_2 \lambda^2 + c_1 \lambda + c_0 = 0, \tag{7}$$

with

$$\begin{aligned} c_3 &= c_{3\mathrm{s}} + 4 d_\mathrm{s} k^2 \tau_g \tau_a = \tau_g (1 + b_a I_2) + \tau_a (1 + b_g I_2) + 2 d_\mathrm{s} k^2 \tau_g \tau_a, \\ c_2 &= c_{2\mathrm{s}} + 3 d_\mathrm{s} k^2 c_{3\mathrm{s}} + 6 d_\mathrm{s}^2 k^4 \tau_g \tau_a, \\ c_1 &= c_{1\mathrm{s}} + 2 d_\mathrm{s} k^2 c_{2\mathrm{s}} + 3 d_\mathrm{s}^2 k^4 c_{3\mathrm{s}} + 4 d_\mathrm{s}^3 k^6 \tau_g \tau_a, \\ c_0 &= c_{0\mathrm{s}} + d_\mathrm{s} k^2 c_{1\mathrm{s}} + d_\mathrm{s}^2 k^4 c_{2\mathrm{s}} + d_\mathrm{s}^3 k^6 c_{3\mathrm{s}} + d_\mathrm{s}^4 k^8 \tau_g \tau_a. \end{aligned} \tag{8}$$

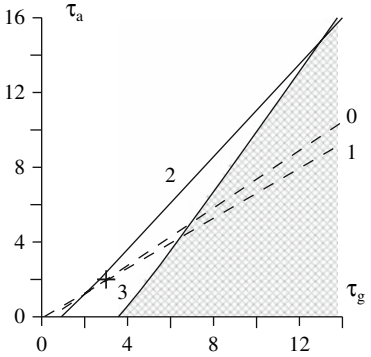

Fig. 1 Effect of relaxation times for active and passive media on the stability of different types of 1D laser solitons. To the left of line 1, motionless solitons are stable, and in the narrow zone to the right of this line, slowly moving solitons are stable. The line 0 indicates a similar boundary for zero values of the carrier diffusion coefficients. Flying solitons are stable to the right of line 2. The overlap of the parameter domains corresponding to motionless and flying dissipative solitons indicates hysteresis of these two regimes. The region of modulation instability of the transversely homogeneous regime is shaded. The cross indicates the parameters used for Fig. 2, $d_g = 60$, $d_a = 40$, $g_0 = 2.09$, $d = 0.06$

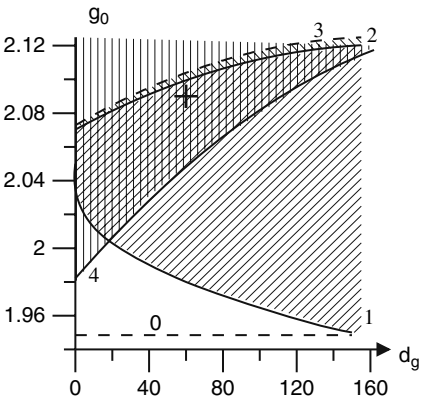

Fig. 2 Effect of carrier diffusion on the stability of different types of 1D laser solitons. Curves 1 and 2 define the region of stability of motionless and slowly moving solitons (*shaded obliquely*). Beyond the upper boundary 2, the Andronov–Hopf bifurcation occurs, and solitons become oscillatory. The oscillating regime corresponds to the narrow zone between curves 2 and 3. A further increase in the small-signal gain, g_0, results in the formation of a "flying" (fast-moving) soliton with locally unbalanced gain and absorption. The "flying" solitons are stable in the region between lines 3 and 4 (*shaded vertically*). Below line 4, these solitons either transform into slowly moving solitons or decay. Line 0 indicates the lower boundary of the branch of homogeneous states. The cross indicates the parameters used for Fig. 1, $d_g/d_a = 3/2$, $\tau_g = 3$, $\tau_a = 2$, $d = 0.06$

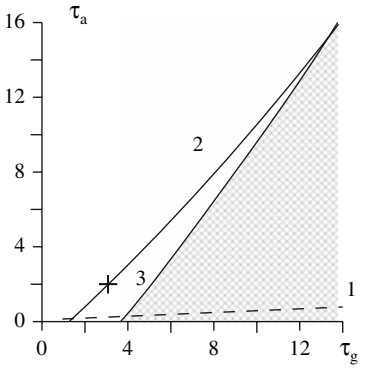

Fig. 3 Effect of relaxation times on regimes of 2D fundamental dissipative solitons. Motionless solitons are stable on the left of the straight line 1. Slowly moving solitons are stable in the narrow zone to the right of curve 1 for $\tau_a < 0.3$. Flying solitons are stable to the right of line 2. The cross indicates parameters used in Fig. 11 corresponding to a "flying" 2D soliton. The region of modulation instability of transversely homogeneous regime is to the right of line 3 (*shaded*). Here $d_g = 0.052$, $d_a = 0$, $g_0 = 2.11$, $d = 0.06$

On the boundary of the stability balloon, the value λ is purely imaginary: $\lambda = \mathrm{i}\gamma$. Then, it follows from the imaginary part of (7) that $c_1\gamma - c_3\gamma^3 = 0$, and therefore $\gamma^2 = c_1/c_3$. Substituting this value in the real part of (7), one obtains the conditions of the Andronov–Hopf instability:

$$c_{1,3} > 0, \quad \tau_g \tau_a c_1^2 - c_1 c_2 c_3 + c_0 c_3^2 > 0. \tag{9}$$

The explicit form of the condition of the Andronov–Hopf instability for $k^2 = 0$ is the following:

$$\tau_g > \tau_{g,\mathrm{cr}}(\tau_a) = \tfrac{1}{2}\tau_{g,\mathrm{cr}}(0)\sqrt{1 + \frac{4\tau_a}{1 + b_a I_\mathrm{s}}\left[1 + b_g I_\mathrm{s}\left(1 + \frac{2\tau_a g_\mathrm{s}}{1 + b_g I_\mathrm{s}}\right)\right]}, \tag{10}$$

where $\tau_{g,\mathrm{cr}}(0) = (1 + b_g I)(1 + b_a I)/2 b_a I a_\mathrm{s}$.

The results of the modulation instability analysis will be presented below in Figs. 1–3.

4 Single Motionless Dissipative Solitons and Their Complexes

For stationary localized structures with time-independent distributions of the electric field intensity, the radiation energy flows, gain, and absorption, the temporal derivatives in (2), (3) reduce to zero, and the values of relaxation times have no effect on the shape of the stationary distributions. If, additionally, we neglect the diffusion terms ($d_g = d_a = 0$), then we conclude that all stationary localized structures

known for class A lasers [5, 12, 13, 14, 15] exist for class B, too. However, depending on the values of the relaxation times, these localized structures can be stable or unstable, and new types specific to non-instantaneous nonlinearity can arise. In this section, we analyze the existence and stability of single motionless dissipative solitons and their complexes. These depend on the values of relaxation times and diffusion coefficients.

For 1D laser systems corresponding to planar waveguide lasers, the electric field envelope for a stationary symmetric dissipative soliton has the form

$$E(x,t) = A(x)\mathrm{e}^{-\mathrm{i}\nu t}, \quad g = g(x), \quad a = a(x), \tag{11}$$

where ν is the nonlinear frequency shift representing the spectral parameter or the eigenvalue of the nonlinear problem—Equations (1), (2), (3) with appropriate asymptotics at infinity. For diffusion coefficients equal to zero, $d_g = d_a = 0$, the dependence of the stability balloon boundaries on the relaxation times was studied in [16, 17, 18, 19]. Below, we generalize this analysis to include non-zero medium diffusion.

The domain of stability of the motionless 1D-dissipative soliton is given in Fig. 1 for the case of large values of the carrier diffusion coefficients. As in the case of zero carrier diffusion (line 0), it is necessary to deal with a relatively slow absorber for soliton stability. Comparison of lines 1 and 0 shows that the carrier diffusion increases the domain of stability of motionless solitons. This effect is demonstrated clearly in Fig. 2, where relaxation times are taken as indicated by the cross in Fig. 1. More exactly, this specific set of parameters corresponds to the regime of slowly moving solitons (see below), but the dependence has the same form for motionless solitons as well.

For 2D geometry, the simplest symmetric localized structures have electric field envelopes of the form

$$E(r,\varphi,t) = A(r)\exp(\mathrm{i}m\varphi - \mathrm{i}\nu t), \tag{12}$$

where (r,φ) are polar co-ordinates, and integer m is the topological charge. The spectral parameter ν plays the same role as it did in the 1D-case, viz. of an eigenvalue with a discrete spectrum, and it represents a nonlinear shift of frequency. At the dissipative soliton periphery, $r \to 0$, a transition to the non-lasing regime occurs: $A(r) \to 0$, $g(r) \to g_0$, and $a(r) \to a_0$. For fundamental dissipative solitons $m = 0$, and for vortex dissipative solitons $m = \pm 1, \pm 2, \ldots$. For class A lasers, the stability of fundamental and vortex solitons has been studied in [20]. Here, we investigate the effect of relaxation and diffusion on the stability of motionless fundamental solitons. The simulations show that they are again stable for a sufficiently slow absorber, to the left of the straight line 1 in Fig. 3. The stability has been confirmed up to fairly large relaxation times, $\tau_a = 400$, $\tau_g/\tau_a = 1/4$. In the narrow zone to the right of curve 1, $\tau_a < 0.3$, motionless fundamental solitons transform to slowly moving solitons (see below).

The results for vortex dissipative solitons presented in Fig. 4 are similar. They are motionless due to the symmetry of the transverse distributions of intensity and

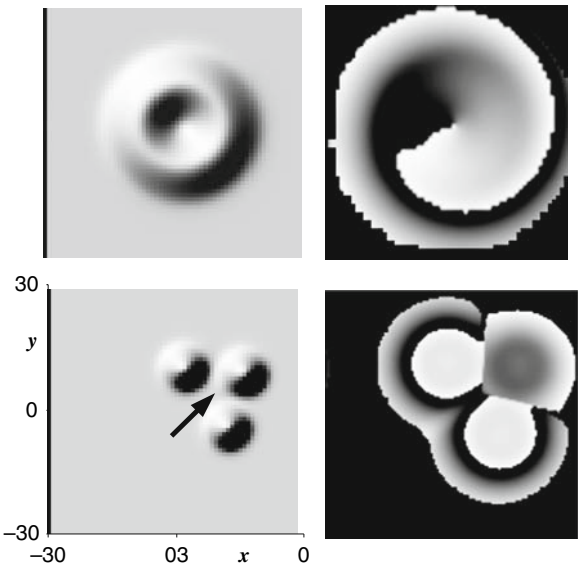

Fig. 4 Transverse distributions of intensity (*left*) and phase (*right*) of stable 2D-localized structures: vortex soliton (*upper row*) and triangle complex of weakly -coupled fundamental dissipative solitons (*lower row*). We have a regime of slow absorption and fast gain: $\tau_g = 100$, $\tau_a = 400$. Other parameters are the same as in Fig. 3

energy flows with respect to rotation at any angle [15]. The stability also occurs under conditions of relatively slow absorption and fast gain.

For laser class A systems, motion of complexes of solitons with weak inter-soliton coupling is determined by their symmetry, i.e., the symmetry of the transverse distributions of intensity and radiation energy flows [15]. For example, a complex does not move and rotate in the case of two axes of mirror symmetry of these two distributions, and its center of inertia moves in a straight line in the case of only one axis of symmetry [15]. The situation with class B laser solitons is similar, but then the distributions of gain and absorption should additionally be taken into account. In Fig. 4, a stable complex of three fundamental solitons in the form of an isosceles triangle is shown. There is zero phase difference between the two solitons on the base of the triangle and an anti-phase soliton at the third vertex of the triangle. It moves along the symmetry axis with constant velocity, even for fairly large relaxation times for gain and absorption. The velocity V is fairly small, $V = 0.07 L_{\mathrm{F}}/\tau_c \sim 0.0014c$, where $L_{\mathrm{F}} = \sqrt{\lambda L/4\pi(1-R)}$ is the effective width of the Fresnel zone, L is the cavity length, λ is the radiation wavelength, R is the product of the reflection coefficients of the cavity mirrors, and c is the light speed in vacuum. The velocity value depends only weakly on the relaxation times. In this case, the speed of motion decreases by a factor of 2 for an increase in $\tau_{g,a}$ by a factor of 100. Note that the constituent solitons are stable and motionless if they are

isolated; therefore this motion is not connected with any instability of the motionless structures and is just manifestation of the complex asymmetry. The triangle complex is stable up to relaxation times of hundreds of photon lifetimes in the cavity.

However, our simulations show that not all complexes of laser solitons are stable under conditions which are typical in experiments on VCSELs with integrated saturable absorption. So, we now give the results for the case of pairs of vortex laser solitons with strong coupling [21]. A pair of vortex solitons with the same topological charges, "the topological double" keeps stability even for the large relaxation times of $\tau_g = 100$ and $\tau_a = 400$. With a further increase in the relaxation times, destabilization and quasi-chaotic behavior take place, but the whole structure remains localized (Fig. 5).

A pair of vortex solitons with opposite topological charges, "the topological dipole" is not very stable in class B lasers; it is destabilized for $\tau_a > 10$. Then annihilation of vortices takes place with the final formation of a single fundamental dissipative soliton, as shown in Fig. 6.

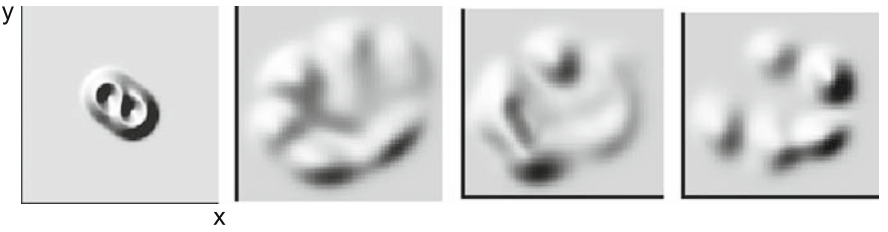

Fig. 5 Evolution of transverse distribution of intensity for the "the topological double"—a strongly coupled pair of two vortex dissipative solitons with equal topological charges. The radiation energy flows for the two vortices in the middle of the double have opposite directions. The destabilization which occurs for fairly large relaxation times ($\tau_g = 100$, $\tau_a = 400$) results in the formation of a quasi-chaotic, but localized, structure

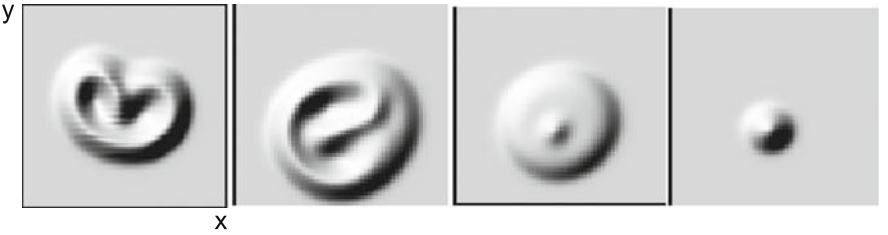

Fig. 6 Evolution of transverse distribution of intensity for the "the topological dipole"—i.e., a strongly coupled pair of two vortex dissipative solitons with opposite topological charges. The radiation energy flows of the two vortices in the middle of the dipole have the same direction. Destabilization takes place for fairly small relaxation times ($\tau_g = 10$, $\tau_a = 40$) and leads to the annihilation of the vortices and the formation of one fundamental soliton

5 Bifurcation from Motionless to Slowly Moving Structures

A general mechanism of destabilization of motionless localized structures, resulting in their slow motion, as determined by the finite response time of the nonlinearity, was first found for 1D systems without medium diffusion [16, 17, 18, 19]. Here, we generalize this analysis, taking into account carrier diffusion and the assorted geometries of structures under consideration. To include the case of structures without axial symmetry, e.g., a pair of two coupled fundamental dissipative solitons, we consider structures with two axes of symmetry, where (1), (2), (3) have solutions corresponding to motionless and non-rotating complexes.

To find the boundary of stability of motionless dissipative soliton structures, let us rewrite (1), (2), (3) in the system of co-ordinates moving with velocity $\boldsymbol{v}$: $\boldsymbol{\xi} = \boldsymbol{r} - \boldsymbol{v}t$, $\tau = t$. Assume that, in this system of co-ordinates, the field amplitude and medium gain and absorption do not depend on time, apart from the frequency nonlinear shift: $E = A(\boldsymbol{\xi})\exp(\mathrm{i}\boldsymbol{v}\boldsymbol{\xi}/2 - \mathrm{i}vt)$, $g = g(\boldsymbol{\xi})$, $a = a(\boldsymbol{\xi})$. Then one has the following equations for the stationary amplitudes:

$$
\begin{aligned}
&-\mathrm{i}d_s\boldsymbol{v}\nabla_{\boldsymbol{\xi}}A + d_s v^2 A/4 = (\mathrm{i}+d_s)\nabla^2_{\boldsymbol{\xi}}A + \mathrm{i}\alpha A + (-1+g-a)A,\\
&-\tau_g\boldsymbol{v}\nabla_{\boldsymbol{\xi}}g = d_g\nabla^2_{\boldsymbol{\xi}}A + g_0 - (1+b_g I)\,g, \quad \alpha = \nu + v^2/4,\\
&-\tau_a\boldsymbol{v}\nabla_{\boldsymbol{\xi}}a = d_a\nabla^2_{\boldsymbol{\xi}}A + a_0 - (1+b_a I)\,a, \quad I = |A|^2.
\end{aligned}
\tag{13}
$$

Near the point of bifurcation from motionless to moving structures, the speed is small $v^2 = |\boldsymbol{v}|^2 \ll 1$. Let us fix the bifurcation point $\tau_g^{(0)}(\tau_a)$ on the parameter plane τ_g, τ_a and decompose the unknown functions in a series with the small parameter being $\boldsymbol{v}$:

$$
\tau_g = \tau_g^{(0)}(\tau_a) + v^2\tau_g^{(2)} + \cdots, \qquad A = A_0(\boldsymbol{\xi}) + \boldsymbol{v}\boldsymbol{A}_1(\boldsymbol{\xi}) + \cdots, \tag{14}
$$

$$
g = g_0(\boldsymbol{\xi}) + \boldsymbol{v}\boldsymbol{g}_1(\boldsymbol{\xi}) + \cdots, \qquad a = a_0(\boldsymbol{\xi}) + \boldsymbol{v}\boldsymbol{a}_1(\boldsymbol{\xi}) + \cdots. \tag{15}
$$

In the specific case of a distribution with axially symmetrical intensity, (13) take the form

$$
\begin{aligned}
&\left[(\mathrm{i}+d_s)\nabla^2_{\boldsymbol{\xi}} + \mathrm{i}\alpha\right]A_0(\boldsymbol{\xi}) + [-1 + g_0(\boldsymbol{\xi}) - a_0(\boldsymbol{\xi})]A_0(\boldsymbol{\xi}) = 0,\\
&-d_g\nabla^2_0 g_0(\boldsymbol{\xi}) = g_0 - \left(1 + b_g|A_0(\xi)|^2\right)g_0(\boldsymbol{\xi}),\\
&-d_a\nabla^2_0 a_0(\boldsymbol{\xi}) = a_0 - \left(1 + b_a|A_0(\xi)|^2\right)a_0(\boldsymbol{\xi}),
\end{aligned}
\tag{16}
$$

where $\nabla^2_0 = \partial^2_r + nr^{-1}\partial_r$.

The equations for the first-order perturbations are deduced as a result of the linearization of (13) near the unperturbed solution:

$$
\boldsymbol{V}_0 = (A_0(\boldsymbol{\xi}), A_0^*(\boldsymbol{\xi}), g_0(\boldsymbol{\xi}), a_0(\boldsymbol{\xi}))^{\mathrm{Tr}}.
$$

In matrix form, they are as follows: $\hat{L}\boldsymbol{V}_1 = \boldsymbol{U}_1$, where

$$\boldsymbol{V}_1 = \left(A_1(\boldsymbol{\xi}), A_1^*(\boldsymbol{\xi}), g_1(\boldsymbol{\xi}), a_1(\boldsymbol{\xi})\right)^{\mathrm{Tr}},$$

and $\hat{L}$ is a matrix differential operator:

$$\hat{L} = \begin{pmatrix} L_{11} & 0 & -A_0(\boldsymbol{\xi}) & A_0(\boldsymbol{\xi}) \\ 0 & L_{11}^* & -A_0^*(\boldsymbol{\xi}) & A_0^*(\boldsymbol{\xi}) \\ -b_g A_0^* g(\boldsymbol{\xi})_0(\boldsymbol{\xi}) & -b_g A_0(\boldsymbol{\xi}) g_0(\boldsymbol{\xi}) & L_g & 0 \\ -b_a A_0^* a(\boldsymbol{\xi})_0(\boldsymbol{\xi}) & -b_a A_0(\boldsymbol{\xi}) a_0(\boldsymbol{\xi}) & 0 & L_a \end{pmatrix}, \tag{17}$$

where $L_{11} = \mathrm{i}\alpha + (\mathrm{i} + d_0)\nabla_{\boldsymbol{\xi}}^2 + f_0$, $L_{g,a} = 1 + b_{g,a}|A_0|^2 - d_{g,a}\nabla_{\boldsymbol{\xi}}^2$.

According to the Fredholm alternative, the condition of solvability of the linear inhomogeneous equation $\hat{L}\boldsymbol{V}_1 = \boldsymbol{U}_1$ is the orthogonality of its right-hand side to the null vector of the adjoint operator:

$$\hat{L}^\dagger \boldsymbol{\Psi}_1^\dagger = 0, \Rightarrow \left\langle \boldsymbol{\Psi}_1^\dagger, \boldsymbol{U}_1 \right\rangle = 0, \quad \boldsymbol{\Psi}_1^\dagger = \left(\boldsymbol{\psi}_1^\dagger, \boldsymbol{\psi}_1^{\dagger *}, \boldsymbol{g}_1^\dagger, -\boldsymbol{a}_1^\dagger\right)^{\mathrm{Tr}}, \tag{18}$$

where

$$\hat{L}^\dagger = \begin{pmatrix} L_{11} & 0 & -b_g A_0^* g(\boldsymbol{\xi})_0(\boldsymbol{\xi}) & -b_a A_0^*(\boldsymbol{\xi}) a_0(\boldsymbol{\xi}) \\ 0 & L_{11}^* & -b_g A_0(\boldsymbol{\xi}) g_0(\boldsymbol{\xi}) & -b_a A_0(\boldsymbol{\xi}) a_0(\boldsymbol{\xi}) \\ -A_0(\boldsymbol{\xi}) & -A_0^*(\boldsymbol{\xi}) & L_g & 0 \\ A_0(\boldsymbol{\xi}) & A_0^*(\boldsymbol{\xi}) & 0 & L_a \end{pmatrix}. \tag{19}$$

For a soliton structure of general type, without axial symmetry, the first-order equations for vectors $\boldsymbol{\psi}_1^\dagger = \boldsymbol{\psi}_1^\dagger(\boldsymbol{\xi}), \boldsymbol{g}_1^\dagger = \boldsymbol{g}_1^\dagger(\boldsymbol{\xi}), \boldsymbol{g}_1^\dagger = \boldsymbol{g}_1^\dagger(\boldsymbol{\xi})$ have the form

$$\begin{aligned} (\mathrm{i} + d_\mathrm{s})\nabla_{\boldsymbol{\xi}}^2 \boldsymbol{\psi}_1^\dagger + \mathrm{i}\alpha\boldsymbol{\psi}_1^\dagger + f(|A_0|^2)\boldsymbol{\psi}_1^\dagger &= A_0^*(\boldsymbol{r}) g_0(\boldsymbol{r}) \boldsymbol{g}_1^\dagger - bA_0^*(\boldsymbol{r}) a_0(\boldsymbol{r}) \boldsymbol{a}_1^\dagger, \\ -d_g \nabla_{\boldsymbol{\xi}}^2 \boldsymbol{g}_1^\dagger + \left(1 + b_g|A_0|^2\right)\boldsymbol{g}_1^\dagger &= 2\mathrm{Re}\, A_0(\boldsymbol{r})\boldsymbol{\psi}_1^\dagger, \\ -d_a \nabla_{\boldsymbol{\xi}}^2 \boldsymbol{a}_1^\dagger + \left(1 + b_a|A_0|^2\right)\boldsymbol{a}_1^\dagger &= 2\mathrm{Re}\, A_0(\boldsymbol{r})\boldsymbol{\psi}_1^\dagger. \end{aligned} \tag{20}$$

For the particular case of nonlinearity which is instantaneous and local, $\tau_{g,a} = d_{g,a} = 0$, it is sufficient to solve the following equation:

$$(\mathrm{i} + d_\mathrm{s})\nabla_{\boldsymbol{r}}^2 \boldsymbol{\psi}_1^\dagger + \mathrm{i}\alpha\boldsymbol{\psi}_1^\dagger + f(|A_0|^2)\boldsymbol{\psi}_1^\dagger + |A_0|^2 f'(|A_0|^2)\boldsymbol{\psi}_1^\dagger + A_0^{*2} f'(|A_0|^2)\boldsymbol{\psi}_1^{\dagger *} = 0. \tag{21}$$

For structures of general type,

$$\boldsymbol{g}_1^\dagger = \frac{2\mathrm{Re}\, A_0(\boldsymbol{r})\boldsymbol{\psi}_1^\dagger}{1 + b_g|A_0|^2}, \quad \boldsymbol{a}_1^\dagger = \frac{2\mathrm{Re}\, A_0(\boldsymbol{r})\boldsymbol{\psi}_1^\dagger}{1 + b_a|A_0|^2}. \tag{22}$$

Then, the resulting solvability condition can be written in the following general form:

$$\tau_g^{(0)} \int \boldsymbol{g}_1^{\dagger}(\boldsymbol{r})\,\nabla_{\boldsymbol{r}} g_0(\boldsymbol{r})\,\mathrm{d}^3\boldsymbol{r} = \tau_a \int \boldsymbol{a}_1^{\dagger}(\boldsymbol{r})\,\nabla_{\boldsymbol{r}} a_0(\boldsymbol{r})\,\mathrm{d}^3\boldsymbol{r} + 2\int d_{\mathrm{s}}\,\mathrm{Im}\left[\boldsymbol{\psi}_1^{\dagger}(\boldsymbol{r})\,\nabla_{\boldsymbol{r}} A_0(\boldsymbol{r})\right]\mathrm{d}^3\boldsymbol{r}. \quad (23)$$

Note that this general equation determines the linear function $\tau_g^{(0)}(\tau_a)$ and, due to the inequality $d_{\mathrm{s}} > 0$, the corresponding straight line in the parameter plane (τ_g, τ_a) does not cross the origin of the co-ordinates ($\tau_g = \tau_a = 0$).

For the specific case of single fundamental or vortex dissipative solitons, it is sufficient to consider only the radial equations in the zeroth order, substituting $A_0(\boldsymbol{\xi}) = A_0(\xi)\mathrm{e}^{\mathrm{i}m\varphi}$ in (16) and $\boldsymbol{\psi}_1^{\dagger}(\boldsymbol{\xi}) = \bar{\boldsymbol{\psi}}_1^{\dagger}(\boldsymbol{\xi})\mathrm{e}^{-\mathrm{i}m\varphi}$ in (18). These equations and the expressions for the matrices hold true after replacing $\boldsymbol{\xi} \to \xi$ and $\nabla_{\boldsymbol{\xi}}^2$ in the first equation for $\nabla_m^2 = \partial_\xi^2 + n\xi^{-1}\partial_\xi - m^2\xi^{-2}$ ($m = n = 0$ for 1D case) and in the other two equations for ∇_0^2. Then, introducing polar co-ordinates ($\xi_x = r\cos\varphi$, $\xi_y = r\sin\varphi$) and decomposing the differential operator $\nabla_{\boldsymbol{\xi}}$ into vector form

$$\begin{aligned} \bar{\boldsymbol{\psi}}_1^{\dagger}(\boldsymbol{\xi}) &= \boldsymbol{e}_r\psi_r^{\dagger}(r) + \boldsymbol{e}_\varphi\psi_\varphi^{\dagger}(r), & \psi_{\pm}^{\dagger}(r) &= -\psi_r^{\dagger}(r) \pm \mathrm{i}\psi_\varphi^{\dagger}(r), \\ \boldsymbol{g}_1^{\dagger}(\boldsymbol{\xi}) &= \boldsymbol{e}_r g_r^{\dagger}(r) + \boldsymbol{e}_\varphi g_\varphi^{\dagger}(r), & \boldsymbol{a}_1^{\dagger}(\boldsymbol{\xi}) &= \boldsymbol{e}_r a_r^{\dagger}(r) + \boldsymbol{e}_\varphi a_\varphi^{\dagger}(r), \end{aligned} \quad (24)$$

we get coupled linear equations for the components of the eigenfunctions of the operator $\hat{L}^{\dagger}$. It is more convenient to solve equations for the field perturbations $\psi_{\pm}^{\dagger}(r)$, defined in (24), and for $g_{\pm}^{\dagger}$, $a_{\pm}^{\dagger}$:

$$\begin{aligned} &\left[(\mathrm{i}+d_{\mathrm{s}})\nabla_{m\pm1}^2 + \mathrm{i}\alpha + f_0(r)\right]\psi_{\pm}^{\dagger}(r) = b_g A_0^*(r)\,g_0(r)\,g_{\pm}^{\dagger} - b_a A_0^*(r)\,a_0(r)\,a_{\pm}^{\dagger}, \\ &\left(-d_g\nabla_0^2 + 1 + b_g|A_0(r)|^2\right)g_{\pm}^{\dagger} = A_0\psi_{\pm}^{\dagger} + A_0^*\psi_{\mp}^{\dagger *}, \\ &\left(-d_a\nabla_0^2 + 1 + b_a|A_0(r)|^2\right)a_{\pm}^{\dagger} = A_0\psi_{\pm}^{\dagger} + A_0^*\psi_{\mp}^{\dagger *}, \end{aligned} \quad (25)$$

where $f_0(r) = -1 + g_0(r) - a_0(r)$, $\nabla_m^2 = \nabla_0^2 - m^2 r^{-2}$, and $\nabla_0^2 = \partial_r^2 + nr^{-1}\partial_r$ (for 1D case, $m = n = 0$). As a result, for symmetric structures, (23) takes the form

$$\begin{aligned} \tau_g^{(0)} \int_0^{\infty} g_r^{\dagger}(r)\,\partial_r g_0(r)\,r\,\mathrm{d}r &= \tau_a \int_0^{\infty} a_r^{\dagger}(r)\,\partial_r a_0(r)\,r\,\mathrm{d}r \\ &+ 2\int_0^{\infty} d_{\mathrm{s}}\left[\mathrm{Im}\left(\psi_r^{\dagger}\partial_r A_0\right) + mr^{-1}\mathrm{Re}\left(\psi_\varphi^{\dagger}A_0\right)\right]r\,\mathrm{d}r. \end{aligned} \quad (26)$$

The corresponding straight line in the parameter plane (τ_g, τ_a) is given in Figs. 1 and 3 as line 1. The result of the bifurcation considered is analyzed in the next section.

6 Slowly Moving Dissipative Solitons

The bifurcation found in the previous section is a super-critical bifurcation from motionless to slowly moving structures, and the instability of motionless dissipative solitons to the right of line 1 is confirmed by direct numerical simulations. In the close vicinity of line 1 in Figs. 1–3, slowly moving solitons are stable where their speeds tend to zero as the parameters approach line 1. This is surely valid if, on the left of line 1, there are no other instabilities which could destabilize motionless structures due to, e.g., an Andronov–Hopf bifurcation. Despite the weak asymmetry of these soliton shapes, the energy balance between radiation and the medium holds, and the spatial distributions of gain and absorption remain almost the same as those for an instantaneous nonlinearity. To characterize the bifurcation-induced asymmetry, let us introduce two functions, which, respectively, have the meaning of instantaneous total gain excess over unsaturated (δg) and saturated (δG) total gain:

$$\delta g = (g(\boldsymbol{r}) - a(\boldsymbol{r})) - (g_0 - a_0)\,, \tag{27}$$

$$\delta G = (g(\boldsymbol{r}) - a(\boldsymbol{r})) - \left(\frac{g_0}{1 + b_g I(\boldsymbol{r})} - \frac{a_0}{1 + b_a I(\boldsymbol{r})}\right). \tag{28}$$

In Figs. 7 and 8, radiation intensity profiles and profiles of the functions δg and δG for slowly moving 1D-dissipative solitons under conditions of zero (Fig. 7) and strong (Fig. 8) carrier diffusion are presented. One can see that the asymmetry is not very pronounced for radiation intensity profiles. It is connected with the low value of the speed. The gain function δg is practically symmetric, with a minimum at the maximum of the radiation intensity. The depth of the gain well decreases for strong diffusion. For the function δG, there are two minima located at two fronts of the intensity profile. The asymmetry is most pronounced for the function δG in the case

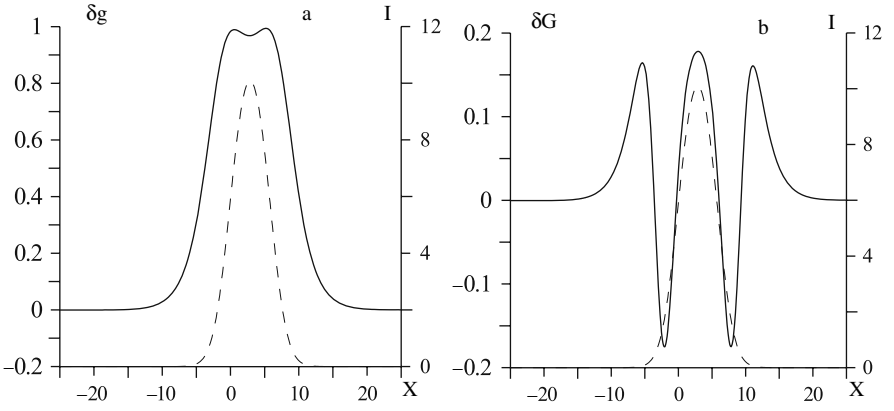

Fig. 7 Intensity profile (*dashed lines*) and profiles of instantaneous total gain δg (**a**) and δG (**b**) for slowly moving (from left to right) dissipative soliton for the case of local nonlinearity. The speed of motion $v = 0.0002 = 8 \times 10^{-6} c$, $d_g = 0$, $d_a = 0$, $\tau_g = 3$, $\tau_a = 2$, $g_0 = 2.06$, $d = 0.06$

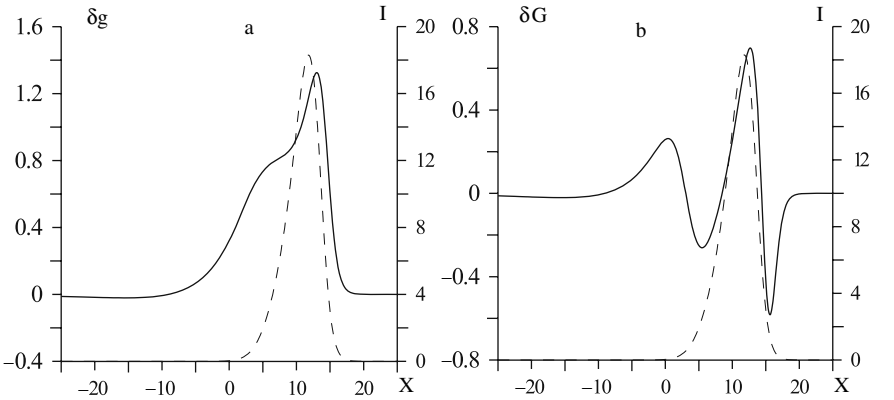

Fig. 8 Same as in Fig. 7, but for the case of strong carrier diffusion. The speed of motion $v = 0.002 = 4 \times 10^{-5}c$, $d_g = 78$, $d_a = 52$, $\tau_g = 3$, $\tau_a = 2$, $g_0 = 2.05$, $d = 0.06$

of zero carrier diffusion (Fig. 7b), but it is at a very low level value of this function. As can be seen from Fig. 8b, carrier diffusion decreases asymmetry, but increases the gain function δG maximum minus minimum difference. One can say that in this case, the energy flows between the radiation and the medium are balanced in the sense that characteristic changes of total gain functions are located in the center or at the fronts of the radiation intensity profile.

For 2D slowly moving dissipative solitons, the conclusions are similar, but a new issue arises. Though the speed of slowly moving symmetric solitons is fixed by the system parameters, their direction in the 2D geometry is arbitrary. However, in the general case of structures without axial symmetry, e.g., a pair of weakly coupled fundamental solitons, there is no isotropy for motion direction to be broken by the asymmetry of the unperturbed structure. Therefore, only the initial stage of the dynamics is characterized by an almost arbitrary direction of the structure motion, induced by the concrete noise realization. Then simulations demonstrate the tendency of two coupled dissipative solitons, under conditions of pair stability, to move in single file. This could be connected with the criterion of energy benefit, because the pair moves in a "hostile environment" where linear gain is smaller than linear losses.

7 Flying and Non-stationary Dissipative Solitons

Both motionless and slowly moving dissipative solitons lose stability for sufficiently large relaxation times. Then, in fairly narrow zones of parameters, various non-stationary regimes occur. However, in much wider range of parameters, a regime of "flying solitons" forms—with a much higher speed of motion and maximum intensity. For 1D-dissipative solitons without carrier diffusion, this regime was first

found in [16, 17, 18, 19]. Flying solitons arise as a result of a sub-critical bifurcation with characteristic hysteresis jumps in, e.g., structure speed with a slow variation of the system parameters. In this section, we present the results of a more detailed study of this regime, both for 1D- and 2D-dissipative solitons, taking into account non-locality of the medium nonlinearity.

Let us begin with 1D geometry. In Figs. 1, 2, the domain of existence of flying dissipative solitons is given as a function of relaxation times and carrier diffusion coefficients. According to Fig. 1, flying solitons exist under conditions where absorption is faster than gain. As one can see from Fig. 2, carrier diffusion increases the minimum gain necessary for the formation of flying solitons. The overlap of the domains of existence of the regimes of motionless, slowly moving, and flying solitons means that hysteresis phenomena will occur with an increase or decrease in the system parameters. The profiles of radiation intensity and medium gain functions are presented in Fig. 9. Comparing them with Fig. 7, one can see that the radiation maximum intensity for flying solitons is much higher, by about 5–7 times, than that for motionless and slowly moving solitons, while flying solitons are narrower. Again, asymmetry is more pronounced for total gain functions. There is a long tail of total gain in the region behind the intensity peak, where the intensity is close to zero; its origin is in carrier relaxation and diffusion. Due to the inequality $\tau_g > \tau_a$, gain dynamics is slower than that for absorption. One can say that there is now a local imbalance between gain and losses, resulting in fast motion of the dissipative soliton.

For certain sets of parameters, the regime of flying dissipative solitons loses stability, and some non-stationary regimes occur. In addition to the regimes of periodic or quasi-periodic oscillations which are typical for the Andronov–Hopf bifurcation, there are more interesting classes with non-conservation of dissipative soliton num-

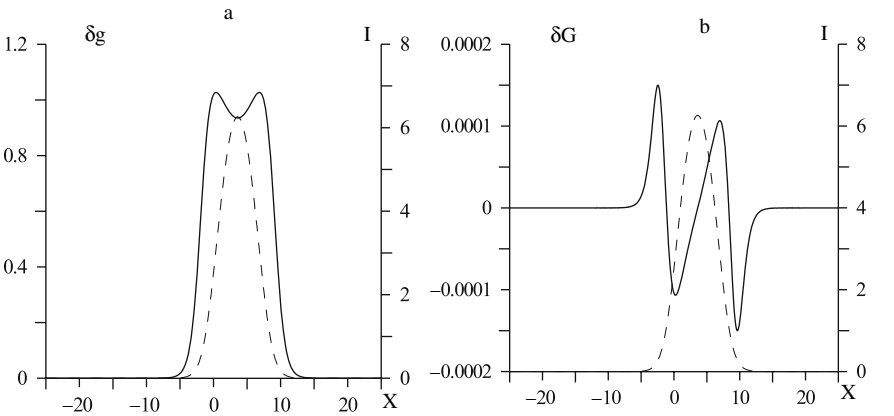

Fig. 9 Same as in Fig. 7, but for the case of a flying dissipative soliton and strong carrier diffusion. The speed of motion $v = 2.5 = 0.05c$, $d_g = 21$, $d_a = 14$, $\tau_g = 3$, $\tau_a = 2$, $g_0 = 2.05$, $d = 0.06$

ber. For class A lasers, such a regime of "leading center" was found in [22]. In Fig. 10, we present a different type which is specific to class B lasers. Here, a flying soliton periodically produces a new one on the pulse trailing edge. The new soliton propagates with a lower speed and finally stops by transforming into a motionless symmetric dissipative soliton. At the same time, the initial soliton recovers its shape, and the process repeats.

The structure of 2D flying dissipative solitons is similar to the 1D case and is presented in Figs. 11 and 12. From Fig. 11, it follows that the tail of the total gain (Fig. 11b) is much longer than that for intensity (Fig. 11a) and is located in the area where the radiation intensity is very low. However, it is possible to shorten the tail when relaxation times for gain and absorption are balanced (compare Fig. 12a and b).

For the conditions of Fig. 11, the dimensionless speed of the flying dissipative soliton is high, $v = 5$. Here are estimates of the corresponding physical values of parameters which are typical for VCSELs: radiation wavelength $\lambda = 1\,\mu\text{m}$, cavity length $L = 4\lambda$, and product of reflection coefficients of cavity mirrors $R \approx 0.999$, $\tau_c = (L/c)/(1-R) \sim 1\,\text{ps}$, which gives the fairly high speed $V = v(L_F/\tau_c) = vc\sqrt{(1-R)\lambda/4\pi L} \sim 0.1c$. This corresponds to a switching time 10 ps for a laser aperture 100 μm or a switching frequency of about 100 GHz. However, 2D flying solitons are very sensitive to perturbations in the direction transverse to the direction of their motion. For small changes of system parameters, widening of flying solitons and subsequent birth of new solitons is typical. This results in the formation of a chaotic combination of moving solitons and switching waves below the linear lasing threshold. Effective control of this dynamics is possible for laser cavities with moderately large Fresnel numbers. It is also important to use an absorber which is slow when compared with the gain.

8 Conclusions

In conclusion, we have investigated, theoretically and numerically, 1D- and 2D-dissipative solitons, or dissipative solitons, in wide-aperture lasers with saturable absorption, taking into account the non-instantaneous and non-local nature of the medium nonlinearity. This model is important for the following reasons. First, it describes semiconductor vertical cavity surface emitting lasers much better than class A models. These lasers are very promising for experiments and for potential applications of optical dissipative solitons to information processing [9, 5, 23]. Second, this model not only confirms most of the predictions of the simpler laser class A theory, but also provides evidence of new phenomena connected with the non-instantaneous and non-local nature of the optical nonlinearity. Third, this optical model is a step toward unification with the reaction–diffusion models used in many other fields of dissipative soliton theory [2, 24]. In fact, the Bloch equations for gain (an activator, or yang in the ancient Chinese philosophy—see also [25]) and absorber (an inhibitor, or Chinese yin) are quite similar to the equations of the

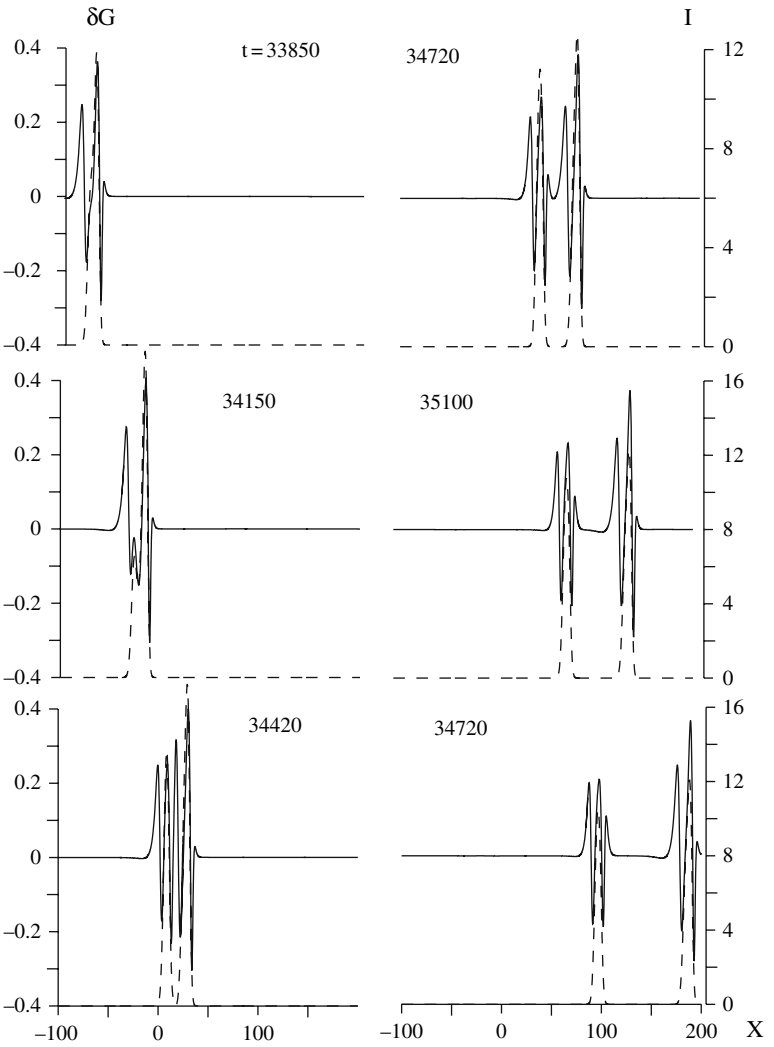

Fig. 10 Profiles of radiation intensity (*dashed lines*) and deviation of total gain from its value for fast saturation (*solid lines*) at different time moments, as indicated near the figures, demonstrating the regime of the shooting dissipative soliton. The dynamics corresponds to periodic birth of a new soliton on the trailing edge of a flying soliton with the later restoration of the initial soliton shape and the braking of the new soliton, which transforms into a motionless one. Here $d_g = 0.92483$, $d_a = 0.58333$, $g_0 = 2.09$, $d = 0.06$

reaction–diffusion theory, where the electromagnetic field envelope plays the role of some mediator. Depending on the parameters, by generalization of the model equations (1), (2), (3), it is possible to derive some simple particular cases describing laser class A systems, with diffraction and/or dispersion-dominated non-locality, or reaction–diffusion models where non-locality has a predominantly diffusive nature.

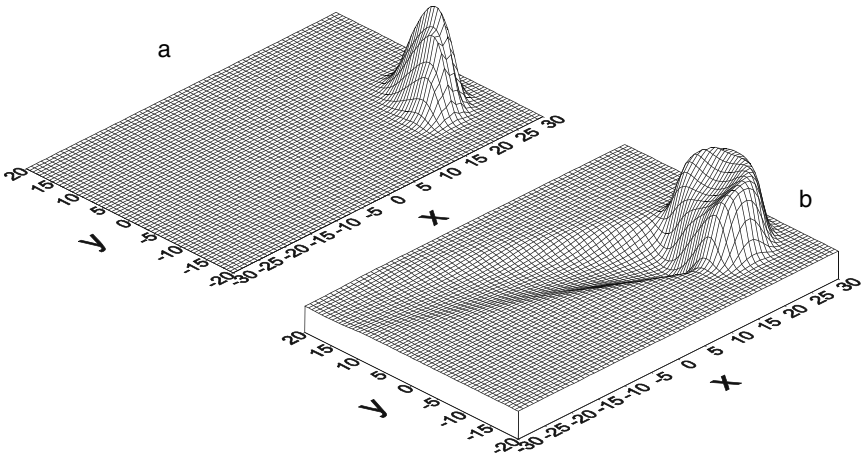

Fig. 11 Transverse distributions of radiation intensity (**a**) and total gain function δg (**b**) for 2D flying dissipative soliton, $v = 5$; $g_0 = 2.09$, $d_g = 0$, $d_a = 0$, $\tau_g = 3.077$, $\tau_a = 0$

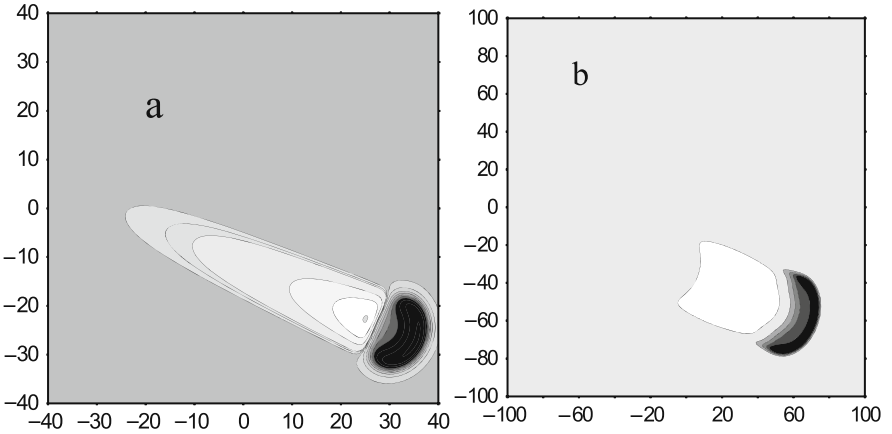

Fig. 12 Contour maps of total gain function δg for 2D flying dissipative soliton. Parameters are $g_0 = 2.09$, $d_g = 0.052$, $d_a = 0$, $\tau_g = 3$; (**a**) $\tau_a = 0$, (**b**) $\tau_a = 2$

Also, note that the main features of typhoons, including the threshold nature of their excitation, allow us to anticipate the possibility of classifying them as giant dissipative vortex solitons. Knowledge of laser vortex soliton instabilities and the laws of their motion can open up a new approach to controlling typhoon trajectories, and even their existence, with relatively weak artificial perturbations.

Acknowledgments This work was supported by grant RNP.2.1.1.1189 of the Russian Ministry of Education and Science. The authors are very grateful to V.E. Sherstobitov for fruitful discussions on the correspondence between dissipative solitons and typhoons.

References

1. M. Faraday, Philos. Trans. R. Soc. London **122**, Part II, 299 (1831). 93
2. B.S. Kerner and V.V. Osipov, *AutoSolitons* (Kluwer, Dordrecht, 1994). 93, 108
3. Akhmediev, N., A. Ankiewicz, *Dissipative Solitons*, Lect. Notes Phys.: **661**. Springer, Berlin (2005). 93, 94
4. N.N. Rosanov and G.V. Khodova, J. Opt. Soc. Am. B **7**, 1057 (1990). 94
5. N.N. Rosanov, *Spatial Hysteresis and Optical Patterns* (Springer, Berlin, 2002). 94, 99, 108
6. A.S. Desyatnikov, Yu.S. Kivshar, and L. Torner, Prog. Opt. ed. E. Wolf **47**, 291 (2002). 94
7. N.N. Rosanov, *Autosoliton* The Big Russian Encyclopedia, **1**, 171 (Moscow, 2005) (in Russian). 94
8. Yu.S. Kivshar and G.P. Agrawal, *Optical Solitons* (Academic Press, Amsterdam, 2003). 94
9. S. Barland, J.R. Tredicce, M. Brambilla, L.A. Lugiato, et al., Nature (London) **419**, 699 (2002). 94, 108
10. M. Bache, F. Prati, G. Tissoni, R. Kheradmand, et al., Appl. Phys. B **81**, 913 (2005). 94
11. Ultanir, E., Stegeman, G.I., Michaelis, D., Lange, C.H., Lederer, F.: In: Akhmediev, N., Ankiewicz, A. (eds.): *Dissipative Solitons*. Lect. Notes Phys. **661**, 37. Springer, Berlin (2005). 94
12. Rosanov, N.N.: In: Akhmediev, N., Ankiewicz, A. (eds.): *Dissipative Solitons*. Lect. Notes Phys. **661**, 101. Springer, Berlin (2005). 99
13. N.N. Rosanov, S.V. Fedorov, and A.N. Shatsev, Phys. Rev. Lett. **95**, 053903 (2005). 99
14. N.N. Rosanov, S.V. Fedorov, and A.N. Shatsev, Appl. Phys. B **81**, 937 (2005). 99
15. N.N. Rosanov, S.V. Fedorov, and A.N. Shatsev, JETP **102**, 547 (2006). 99, 100
16. S.V. Fedorov and N.N. Rosanov, Opt. Spectr. **84**, 767 (1998). 99, 102, 107
17. S.V. Fedorov, N.N. Rosanov, and A.G. Vladimirov, Opt. Spectr. **84**, 905 (1998). 99, 102, 107
18. N.N. Rosanov, S.V. Fedorov, and G.V. Khodova, Opt. Spectr. **88**, 790 (2000). 99, 102, 107
19. S.V. Fedorov, A.G. Vladimirov, G.V. Khodova, and N.N. Rosanov, Phys. Rev. E **61**, 5814 (2000). 99, 102, 107
20. S.V. Fedorov, N.N. Rosanov, A.N. Shatsev, N.A. Veretenov, and A.G. Vladimirov, IEEE J. Quantum Electron. **39**, 197 (2003). 99
21. N.N. Rosanov, S.V. Fedorov, and A.N. Shatsev, JETP **98**, 427 (2004). 101
22. N.N. Rosanov, S.V. Fedorov, G.V. Khodova, A.A. Zinchik, Opt. Spectr. **83**, 370 (1997). 108
23. Taranenko, V.B., Slekys, G., Weiss, C.O.: In: Akhmediev, N., Ankiewicz, A. (eds.): *Dissipative Solitons*. Lect. Notes Phys. **661**, 131. Springer, Berlin (2005). 108
24. Purwins, H.-G., Bödeker, H.U., Liehr, A.W.: In: Akhmediev, N., Ankiewicz, A. (eds.): *Dissipative Solitons*. Lect. Notes Phys. **661**, 267. Springer, Berlin (2005). 108
25. Akhmediev, N., Ankiewicz, A.: In: Akhmediev, N., Ankiewicz, A. (eds.): *Dissipative Solitons*. Lect. Notes. Phys. **661**, 1. Springer, Berlin (2005). 108

Excitability Mediated by Dissipative Solitons in Nonlinear Optical Cavities

P. Colet, D. Gomila, A. Jacobo, and M.A. Matías

Abstract Cavity solitons, which are dissipative solitons with a finite extension that appear in the transverse plane of nonlinear optical cavities, have been advocated for use in fast and compact optical information storage. We discuss the instabilities that can affect cavity solitons appearing in Kerr cavities. In particular, cavity solitons may exhibit a Hopf bifurcation leading to self-pulsating behavior, which is then followed by the destruction of the oscillation in a saddle-loop bifurcation. Beyond this point, there is a regime of excitable cavity solitons which appear when suitable perturbations are applied. Excitability is characterized by the nonlinear response of the system upon the application of an external stimulus. Only stimuli exceeding a threshold value are able to elicit a full and well-defined response in the system. In the case of cavity solitons, excitability emerges from the spatial dependence, since the system does not exhibit any excitable behavior locally. We demonstrate the existence of two different mechanisms which lead to excitability, depending on the profile of the pump field.

P. Colet
IFISC, Instituto de Física Interdisciplinar y Sistemas Complejos, (CSIC-UIB), Campus Universitat de les Illes Balears, E-07122 Palma de Mallorca, Spain, pere@ifisc.uib.es

D. Gomila
IFISC, Instituto de Física Interdisciplinar y Sistemas Complejos, (CSIC-UIB), Campus Universitat de les Illes Balears, E-07122 Palma de Mallorca, Spain, damia@ifisc.uib.es

A. Jacobo
IFISC, Instituto de Física Interdisciplinar y Sistemas Complejos, (CSIC-UIB), Campus Universitat de les Illes Balears, E-07122 Palma de Mallorca, Spain, adrian@ifisc.uib.es

M.A. Matías
IFISC, Instituto de Física Interdisciplinar y Sistemas Complejos, (CSIC-UIB), Campus Universitat de les Illes Balears, E-07122 Palma de Mallorca, Spain, manuel@ifisc.uib.es

Colet, P. et al.: *Excitability Mediated by Dissipative Solitons in Nonlinear Optical Cavities.* Lect. Notes Phys. **751**, 113–135 (2008)
DOI 10.1007/978-3-540-78217-9_5

1 Introduction

The concept of excitability was initially introduced in the context of biological systems, e.g., to describe neuron firing, and it has been found to be present in a wide variety of systems [1, 2], including optical systems [3, 4, 5, 6, 7]. Typically, a system is considered to be excitable if the response of the system to perturbations of the stationary state varies greatly, depending on whether the amplitude of the perturbation exceeds a threshold value. Thus, while small perturbations induce a smooth return to the fixed point, above-threshold perturbations induce a large phase space excursion (firing) before coming back to the rest state. Furthermore, after one firing, the system cannot be excited again within a refractory period of time. In phase space [8, 9], excitability occurs for parameter regions where a stable fixed point is close to a bifurcation in which an oscillation is created. A well-known example of an excitable system is the FitzHugh–Nagumo model, close to the Hopf bifurcation. One may also find excitable behavior mediated by a saddle point, in the form of either an Andronov (or saddle node on the invariant circle) bifurcation or a saddle-loop (or homoclinic) bifurcation. These three scenarios are the simplest possible, and they occur in systems that, minimally, can be characterized by two phase space variables. The first scenario is characterized by the fact that the response time to come back to the fixed point after a firing is basically constant. This is described as a Class II excitability. In the last two scenarios, where excitability is mediated by a saddle, the distribution of response times is unbounded and they are described as Class I excitability.

The concept of excitability has been extended to systems with spatial dependence by coupling several or many zero-dimensional excitable systems [1, 2]. Here, we consider a different situation – a system that does not show excitable behavior when there is no spatial dependence, but does show this behavior when the dissipative localized structures appear in an extended system with spatial dependence.

Dissipative solitons (DSs) are spatially localized structures that appear in certain dissipative media [10, 11], and, in particular, they have been found in a variety of systems, including chemical reactions [12, 13], gas discharges [14], and fluids [11]. They are also found in optical cavities due to the interplay of different effects, such as diffraction, nonlinearity, driving, and dissipation [15, 16, 17, 18, 19]. These structures, also known in this field as cavity solitons, have to be distinguished from conservative solitons which are found, for example, in propagation in fibers, and for which there is a continuous family of solutions, which can depend on the initial conditions. Instead, a cavity soliton is unique once the parameters of the system have been fixed. This fact makes these structures potentially useful in optical (i.e., fast and spatially dense) storage and processing of information [17, 19, 20, 21, 22].

DSs may develop various kinds of instabilities, as they may start moving, breathing, or oscillating. In the latter case, the amplitude of the DS oscillates in time, while its position remains stationary in space, like the “oscillons” found in a vibrating layer of sand [23]. Oscillating DSs are autonomous oscillons and have been reported in both optical [24, 25, 26] and chemical systems [27]. They appear when the DS exhibits a Hopf bifurcation. Here, we describe a route by which autonomous

oscillating DSs are destroyed, leading to an excitability regime [28, 29]. The excitable behavior may confer new computational capabilities, beyond information storage, to DSs in optical systems.

In particular, we consider the dynamics of DSs arising in optical cavities filled with a Kerr nonlinear medium. These are known as Kerr cavity solitons (KCS) as a consequence of a modulational (namely a pattern-forming) instability of a homogeneous solution. They exist in the parameter range where the homogeneous solution coexists with sub-critical (hexagonal) patterns. They share some properties with propagating spatial (conservative) solitons in a Kerr medium, but there are also interesting differences. While Kerr spatial solitons are stable in one transverse dimension (1D), it is well known that their 2D counterparts are unstable against self-focusing collapse [30]. The stability and dynamics of 2D Kerr cavity solitons are thus of particular interest, and their existence and stability have been studied in several papers [24, 25, 31].

Here, we show the existence of different mechanisms leading to excitability, depending on the profile of the pump field. For a homogeneous pump, the mechanism leading to excitable behavior is a saddle-loop bifurcation through which a stable oscillating DS collides with an unstable DS [28, 29]. For a system pumped by a localized Gaussian beam on top of a homogeneous background, the scenario is richer and one finds two different mechanisms leading to excitability. One is based on a saddle-loop bifurcation, as above, while the other takes place through a saddle node in an invariant circle (SNIC) bifurcation. Under the second mechanism, the excitability threshold can be tuned by changing accessible system parameters.

2 Model

An optical cavity filled with a nonlinear Kerr medium can be described by the model introduced by Lugiato and Lefever [32]. This prototype model, obtained by averaging the dependence of the field along the propagation direction, was first introduced to study pattern formation in this system. Later studies showed that this model also exhibits DSs in some parameter regions [24, 31]. In the paraxial limit, after suitably rescaling the variables, the dynamics of the intra-cavity slowly varying amplitude of the electromagnetic field $E(\boldsymbol{x},t)$, where $\boldsymbol{x} = (x,y)$ is the plane transverse to the propagation direction, is given by

$$\frac{\partial E}{\partial t} = -(1+\mathrm{i}\theta)E + \mathrm{i}\nabla^2 E + E_\mathrm{I} + \mathrm{i}|E^2|E. \tag{1}$$

The first term on the right-hand side describes cavity losses (which make the system dissipative), E_I is the input field, θ the cavity detuning with respect to E_I, and $\nabla^2 = \partial^2/\partial x^2 + \partial^2/\partial y^2$ is the transverse Laplacian which models diffraction. The sign of the cubic term indicates the so-called self-focusing case.

When neither loss nor input field is present, the intra-cavity field can be rescaled to $E \to E\mathrm{e}^{\mathrm{i}\theta t}$ to remove the detuning term and (1) becomes the nonlinear Schrödinger

equation (NLSE). For the NLSE in two spatial dimensions, an initial condition with sufficient energy collapses, so energy accumulates at a point in space, leading to the divergence of the solution at a finite time [33]. Dissipation, such as that originating from the cavity losses, can prevent this collapse [34]. In any case, in the parameter region in which DSs are stable, their dynamics is closely related to the collapse regime. In our system, the above mechanism, which combines collapse and cavity losses, is also responsible for various instabilities arising in regular patterns which lead to complex spatio-temporal dynamical behavior, including the existence of optical turbulence [35].

Firstly, we will consider the case in which the input field is homogeneous, viz. $E_{\mathrm{I}}(\boldsymbol{x}) = E_0$. In Sect. 10, we address the case in which the pump consists of a localized Gaussian beam on top of a homogeneous background. For a constant pump, Equation (1) has a homogeneous steady-state solution which is implicitly given by $E_{\mathrm{s}} = E_0/(1 + (\mathrm{i}(\theta - I_{\mathrm{s}}))$, where $I_{\mathrm{s}} = |E_{\mathrm{s}}|^2$ [32]. For convenience, we will use the intra-cavity background, I_{s}, together with θ, as our control parameters. It is well known that the homogeneous solution shows bistability for $\theta > \sqrt{3}$.

In the following sections, it is convenient to introduce the field $A(x,y)$ as $E = E_{\mathrm{s}}(1 + A)$, so that $A(x,y)$ describes the solution without the homogeneous background. Equation (1) can be rewritten as

$$\frac{\partial A}{\partial t} = -(1 + \mathrm{i}\theta)A + \mathrm{i}\nabla^2 A + \mathrm{i}I_{\mathrm{s}}\left(2A + A^{\star} + A^2 + 2|A|^2 + |A|^2 A\right). \tag{2}$$

Note that this equation is fully equivalent to (1), without any linear approximation.

For numerical simulations, we integrate (1) using a pseudo-spectral method where the linear terms in Fourier space are integrated exactly, while the nonlinear ones are integrated using an approximation which is second order in time [29, 36]. Periodic boundary conditions are used since they are convenient for the pseudo-spectral code. The system size is large enough to ensure that the electric field reaches the homogeneous steady state well inside the boundaries. A square lattice of size 512×512 points was used. The space discretization was taken as $\mathrm{d}x = 0.1875$, while the time step was $\mathrm{d}t = 10^{-3}$.

3 Dissipative Solitons for Homogeneous Pump

The homogeneous solution is stable for $I_{\mathrm{s}} < 1$. The so-called modulation instability takes place at $I_{\mathrm{s}} = 1$ and the homogeneous solution becomes unstable, leading to the formation of hexagonal patterns [32, 37]. For $I_{\mathrm{s}} > 1$, the homogeneous solution continues to exist, although it is unstable. The hexagonal patterns are sub-critical, viz. through an S-shaped branch, and thus, they coexist with the stable homogeneous solution for a certain parameter range. This bistability is at the origin of the existence of stable DSs that appear when suitable (localized) transient perturbations are applied. The DS can be seen as a solution connecting a cell of the pattern with the

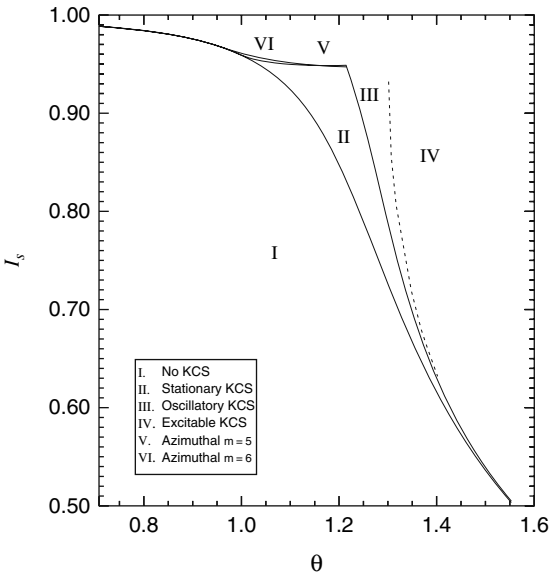

Fig. 1 Phase diagram of DSs in a Kerr cavity. KCSs are stable in region II and oscillate in III. (The line between these two regions indicates a Hopf bifurcation.) In the lower part, below the saddle-node bifurcation (*solid line*), there are no KCSs. When crossing from regions III to V (VI), one KCS develops azimuthal instabilities, with $m = 5$ ($m = 6$) which lead to an extended pattern. To the left of the saddle-loop bifurcation (*dashed line*), the system exhibits excitability

homogeneous solution. While the existence of DSs in this bistable regime is quite generic in extended systems, the stability of such DSs strongly depends on the particular system. The region of existence of DSs, also known as Kerr cavity solitons (KCSs), in parameter space is shown in Fig. 1 [25].

The mechanism by which KCSs appear is a saddle-node (or fold) bifurcation, as can be seen in Fig. 2 for $\theta = 1.34$ and $I_s \sim 0.655$ ($|E_0|^2 \sim 4.5$), where a pair of stable–unstable DSs are created [21, 38]. The middle-branch KCS is unstable and ends at the modulational instability point where it collides with the homogeneous solution. The middle-branch KCS then acts as a barrier. Thus, if an initial condition is somewhat above the middle branch in phase space, it will evolve to the upper branch (so that a DS is written), while it will decay to the homogeneous solution if below it. This role of the middle-branch DS, as a separatrix in phase space, is quite general and has been identified in a semiconductor model [39] and experimentally observed for solitons in a sodium cell with feedback [40, 41, 42] and in a semiconductor cavity [43].

The DSs are rotationally symmetric about their centers. Figure 2 shows the spatial shape of a typical upper- and middle-branch DS. The transverse profile can be accurately found by taking advantage of the symmetry. From (2), one obtains the radial equation for $A(r)$:

$$\frac{\partial A}{\partial t} = -(1+\mathrm{i}\theta)A + \mathrm{i}\left(\frac{\partial^2}{\partial^2 r} + \frac{1}{r}\frac{\partial}{\partial r}\right)A + \mathrm{i}I_\mathrm{s}\left(2A + A^\star + A^2 + 2|A|^2 + |A|^2 A\right). \tag{3}$$

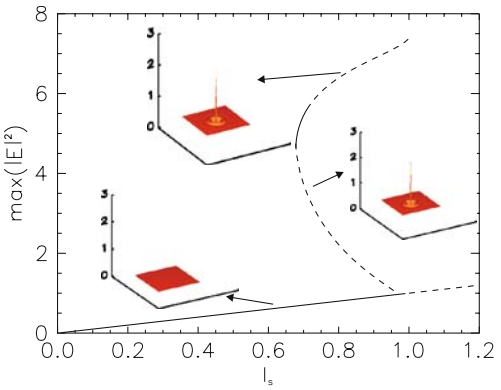

Fig. 2 Bifurcation diagram of stationary KCSs: $\max(|E|^2)$ vs. I_s for $\theta = 1.34$. *Solid lines* represent stable solutions and *dashed lines* unstable ones. The lowest branch corresponds to the homogeneous solution that becomes unstable at $I_s = 1.0$. The upper branch corresponds to the stable KCS, while the middle branch corresponds to the unstable KCS. Upper and middle branches originate at the saddle-node bifurcation. The upper branch becomes Hopf unstable for larger values of I_s. The 3D plots, from top to bottom, show the profiles of the upper-branch KCSs, the middle-branch KCSs, and the homogeneous solution

Steady-state DS solutions, both stable and unstable, are found by equating the left-hand side of (3) to zero. The boundary conditions for this problem are such that the derivatives are zero at the boundaries: $\partial A/\partial r(r=0) = \partial A/\partial r(r=L) = 0$, where the system size, L, is large enough to ensure that the electric field smoothly approaches the homogeneous solution ($A(r) \to 0$) before reaching the boundary. Discretizing the radial coordinate, one obtains a set of coupled nonlinear equations which can be solved using a Newton–Raphson method [44, 45]. Spatial derivatives are computed in Fourier space. The initial guess for the Newton method is obtained from a radial cut of a numerical integration of the 2D equation (1). After obtaining a precise solution for given parameter values, continuation techniques [46] are used to explore the region of existence of KCSs in the parameter space. This approach is extremely accurate, and it allows us to find both stable and unstable fixed point solutions.

The stability of the DS against radial and azimuthal perturbations is obtained, cf. [47], by linearizing equation (2) around the stationary DS, $A_{\mathrm{DS}}(r)$. This yields a linearized equation for the time evolution of the perturbations $\delta A(r,\phi,t) = A(r,\phi,t) - A_{\mathrm{DS}}(r)$. The solutions of the linear problem can be written as

$$\delta A = [R_+(r)\,\mathrm{e}^{\mathrm{i}m\phi} + R_-(r)\,\mathrm{e}^{-\mathrm{i}m\phi}]\exp(\lambda t)\ , \tag{4}$$

where m is the wavenumber of the azimuthal perturbation. This yields the eigenvalue problem

$$\mathbf{U}\boldsymbol{\Psi} = \lambda\boldsymbol{\Psi}, \tag{5}$$

where $\boldsymbol{\Psi} = (R_+, R_-^\star)^\top$ and $\mathbf{U} = \begin{pmatrix} U_+ & U_- \\ U_-^\star & U_+^\star \end{pmatrix}$ with

$$U_+ = -(1+\mathrm{i}\theta) + \mathrm{i}\left(\frac{\partial^2}{\partial^2 r} + \frac{1}{r}\frac{\partial}{\partial r} - \frac{m^2}{r^2}\right) + \mathrm{i}2I_\mathrm{s}\left(1 + A_\mathrm{DS} + A_\mathrm{DS}^\star + |A_\mathrm{DS}|^2\right)$$

$$U_- = \mathrm{i}I_\mathrm{s}\left(1 + 2A_\mathrm{DS} + A_\mathrm{DS}^2\right) . \tag{6}$$

For purely radial perturbations ($m = 0$), we have $R_- = R_+$. The matrix $\mathbf{U}$ is time independent, as it is evaluated at the stationary DS (stable or unstable) under study.

The problem thus reduces to finding the eigenvalues, λ, and eigenvectors, $\mathbf{\Psi}$, where it is important to mention that $\mathbf{U}$ is a complex matrix, so the eigenvectors are, in general, complex quantities. Due to the symmetry of $\mathbf{U}$, the eigenvalues are either real or pairs of complex conjugates. This last property stems from the fact that, considering the real and imaginary parts of A_s, $\mathbf{U}$ can be rewritten as a real matrix. Due to the discretization of the space, $\mathbf{\Psi}$ becomes a vector whose dimension is $2N$. The set of eigenvectors $\mathbf{\Psi}_i$ ($i = 1, 2N$) forms a basis, and their amplitudes define a natural phase space for studying the dynamics of DSs. Thus, the stability problem of stationary DSs, which, in principle, live in an infinite-dimensional phase space, is numerically reduced to the study of these stationary DSs in a finite, albeit large, dimensional phase space. However, we note that $\mathbf{U}$ is not self-adjoint, and these modes do not form an orthogonal basis. To find the components of a field profile on a mode $\mathbf{\Psi}_i$, one has to project it onto the corresponding eigenmode $\mathbf{\Phi}_i$ of the adjoint Jacobian matrix $\mathbf{U}^\dagger$.

The stability of the 2D KCS, as function of the two control parameters (θ, I_s), is displayed in Fig. 1. The lowest curve corresponds to the saddle-node bifurcation where the upper and middle KCS branches collide. There are no KCS solutions below this line. The area above the saddle-node curve shows where 2D KCSs exist, and region II corresponds to the parameter values for which they are stable. For a given detuning, KCSs only exist for a finite range of background intra-cavity intensities, $I_\mathrm{min} < I_\mathrm{s} < 1$. While the range of existence is broader when the detuning is increased, the range in which KCSs are stable is, in fact, narrower. For $\theta > 1.5$, it is so narrow that early studies missed the existence of stable KCSs altogether [31]. DSs can be unstable to perturbations at zero azimuthal number ($m = 0$), when crossing from regions II to III in Fig. 1, or to azimuthal perturbations ($m \neq 0$), when crossing from II to V or VI [25]. In the first case, the instability preserves the shape of the KCS and leads to an oscillatory DS. This case will be discussed in detail in Sect. 5. On the other hand, when the KCS undergoes an azimuthal instability, its radial symmetry is broken and a pattern arises, as discussed in the next section.

4 Azimuthal Instabilities

For the approximate range $\theta < 1.22$, shown in Fig. 1, the KCS become unstable as I_s is increased due to an azimuthal instability with $m = 5$ or $m = 6$, depending on the

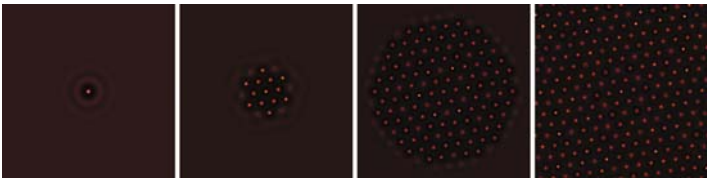

Fig. 3 Development of $m = 6$ azimuthal instability. From *left* to *right*: $t = 0, 100, 200, 300$. $\theta = 1.1$, $I = 0.97$

detuning. The ring surrounding the KCS core breaks into five or six spots, respectively. Numerical integration of (1) shows that the resulting structure then grows to invade the homogeneous background. For $\theta < 1.1$, the system is unstable to perturbations with azimuthal number $m = 6$, leading to a hexagonal pattern (Fig. 3). This pattern is not stationary but oscillates because of the values of I_s and θ [35]. For a narrow domain around $\theta = 1.2$ (Fig. 1), $m = 5$ dominates and the growing pattern, though locally hexagonal, retains its global five-fold symmetry (Figs. 4 and 5). Due to periodic boundary conditions, penta–hepta defects are created as soon as the pattern fills the whole system.

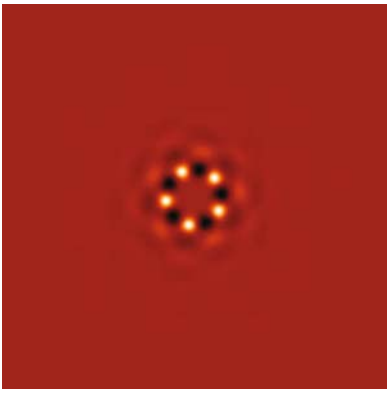

Fig. 4 Eigenmode corresponding to an azimuthal $m = 5$ instability. $\theta = 1.2$, $I = 0.95$

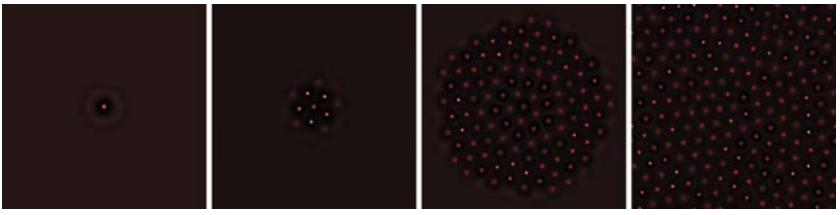

Fig. 5 Development of $m = 5$ azimuthal instability. From *left* to *right*: $t = 0, 200, 400, 600$. $\theta = 1.2$, $I = 0.95$

5 Oscillatory KCSs

The upper branch DS remains stable for a range of values of I_s, but undergoes a Hopf bifurcation when I_s is increased, leading to a limit cycle, and the DS oscillates autonomously [25, 31, 48]. The oscillatory regime is shown in parameter space in Fig. 1. Thus, in these conditions, a DS is an autonomous oscillon. An interesting connection to the conservative case is that the growth of the DS during the oscillations resembles the collapse regime observed for the 2D (or $2+1$) NLSE. In this case, however, dissipation arrests this growth after some value is attained for the electric field, E. For one spatial dimension, Equation (1) also has DSs in the appropriate parameter regime, but these structures never undergo any Hopf instability.

As either the intra-cavity intensity, I_s, or the detuning, θ, is increased, the limit cycle gets closer and closer to the middle-branch KCS and the period of oscillation increases. This is illustrated in Fig. 6 for an increase in the detuning θ. The time evolution of the KCS maximum, as obtained from numerical integration of (1), is plotted in the left column, while the dashed line shows the maximum of the middle-branch KCS for comparison. The evolution in phase space, projected onto two variables, is sketched in the right column. At a critical value, θ_c, a global bifurcation

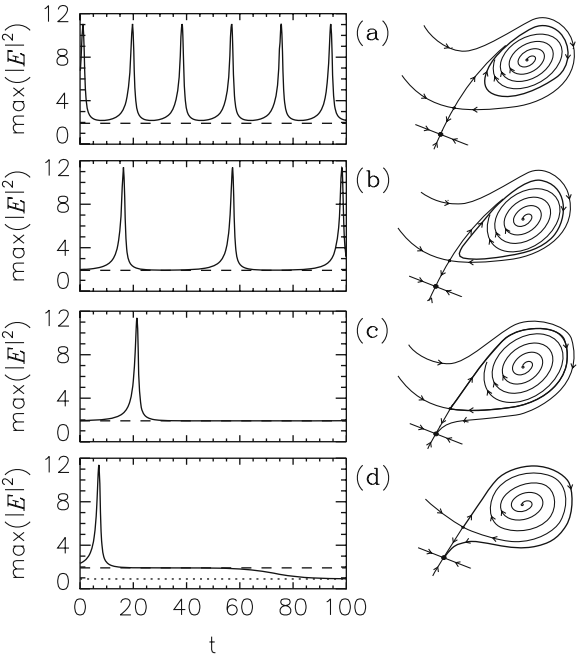

Fig. 6 *Left*: DS maximum intensity as a function of time for increasing values of the detuning parameter θ. From *top* to *bottom*: $\theta = 1.3, 1.3047, 1.30478592, 1.304788$. $I_s = 0.9$. *Right*: Sketch of the phase space for each parameter value. The *thick line* shows the trajectory of the DS in phase space

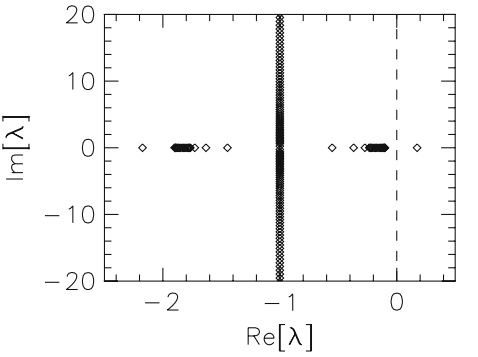

Fig. 7 Spectrum of the unstable (middle branch) DS for $\theta = 1.30478592$ and $I_s = 0.9$

takes place – the cycle touches the middle-branch KCS and becomes a homoclinic orbit [Fig. 6(c)].

It is perhaps surprising that the overall scenario can be understood qualitatively by resorting to a planar dynamical system, i.e., one with a 2D phase space. As we will show later, these two phase space variables correspond to the amplitude of localized modes of the system. The spectrum of eigenvalues for an unstable (middle) branch DS is shown in Fig. 7. There is only one positive eigenvalue, so this structure has a single unstable direction in the full phase space. The limit cycle corresponding to the oscillating KCS is such that it approaches the stable manifold of the middle-branch KCS and then escapes along the 1D unstable manifold. The middle-branch KCS is a saddle point in the reduced planar phase space. Once it is created, the middle-branch DS does not undergo any bifurcation for the parameter values explored here, and so remains a saddle point in phase space. When the limit cycle corresponding to the oscillating KCS touches the middle branch, the KCS undergoes a so-called *saddle-loop* bifurcation, and this is the subject of Sect. 6. An excitable regime, which will be described later in Sect. 8, emerges beyond this bifurcation.

6 Saddle-Loop Bifurcation

A saddle-loop bifurcation is a global bifurcation in which a limit cycle becomes bi-asymptotic to a (real) saddle point, or, in other words, becomes the homoclinic orbit of a saddle point (cf. [49, 50]), i.e., at criticality, a trajectory leaving the saddle point through the unstable manifold returns to it through the stable manifold. Thus, on one side of this bifurcation, one finds a detached limit cycle (stable or unstable), while on the other side, the cycle no longer exists, and only its *ghost* remains, as the bifurcation creates an exit slit that makes the system dynamics leave the region in phase space previously occupied by the cycle. (See the long plateau between $t = 15$ and $t = 60$ in Fig. 6(d).) Thus, after the bifurcation, the system dynamics jumps to another available attractor. In the present case, this alternative attractor is the homogeneous solution.

Let us take θ as the control parameter and assume that the saddle-loop bifurcation occurs for $\theta = \theta_{SL}$ and that $\theta < \theta_{SL}$ corresponds to the oscillatory side, where the limit cycle is detached from the saddle point, while, in turn, $\theta > \theta_{SL}$ corresponds to the side where the limit cycle is no longer present and there is only one stable solution, which is a fixed point. The fact that the bifurcation is global implies that it cannot be detected locally (a local eigenvalue passing through zero), but one can still resort to the Poincaré map technique[1] to analyze it, and, interestingly, the main features of the bifurcation can be understood from knowledge of the linear eigenvalues of the saddle.

The case studied here is the simplest: a saddle point with real eigenvalues, say $\lambda_s < 0$ and $\lambda_u > 0$, in a 2D phase space. Strictly speaking, in our case, the saddle has an infinite number of eigenvalues (Fig. 7), but only two eigenmodes take part in the dynamics close to the saddle. This will be studied in more detail in Sect. 7. It is convenient to define the so-called *saddle index* $\nu = -\lambda_s/\lambda_u$ and *saddle quantity* $\sigma = \lambda_s + \lambda_u$. It can be shown[2] that this cycle is stable for $\sigma < 0$, or $\nu > 1$, at the side of the saddle-loop bifurcation where one has a detached cycle, while for $\sigma > 0$ ($\nu < 1$), the cycle is unstable. Analogously, one can study the period of the cycle close to this bifurcation, and, to leading order, it is given by [51]

$$T \propto -\frac{1}{\lambda_u} \ln|\theta - \theta_{SL}| \,. \tag{7}$$

This expression is accurate for θ close enough to θ_{SL}. Interestingly, the transient time spent by a trajectory in the ghost region after the cycle has ceased to exist, close enough to the bifurcation point, also shows this scaling.

Numerically, the bifurcation point will be characterized by the fact that, on approaching it from the oscillatory side, the period will diverge to infinity (see Fig. 8 (a)) and also because, past this bifurcation point, the DS disappears and the system relaxes to the homogeneous solution, as shown in Fig. 6. For $I_s = 0.9$, the saddle loop takes place at $\theta_{SL} = 1.30478592$. In Fig. 6, the time evolution of the maximum of the DS is plotted for two values of the detuning, differing by 10^{-7}, with one just above and the other just below θ_{SL}. Figure 8 (b) displays a log-linear plot of the period versus a control parameter. As expected, it exhibits a linear slope. Furthermore, one can compare the value of the slope obtained from the simulations with its theoretical prediction, equation (7), namely $-1/\lambda_u$. The full spectrum of the

[1] The Poincaré map can be constructed through two cross-sections, i.e., two planes that are transversal to the limit cycle and that are placed slightly before and after the closest approach of the cycle to the saddle point. One can construct two maps from these two planes. The first is the so-called local (or linear or singular) map, T_0, that takes the flow from the plane before the saddle point to the plane after the saddle point, and is dominated by the saddle point. The second is the global (or nonlinear) map, T_1, that takes the flow all the way from the plane, past the saddle point through all of the limit cycle back to the plane before the saddle point. The complete Poincaré map is the composition of these two maps. It has to be remarked that the T_0 map is unbounded, as the return time is infinity at the onset of the global bifurcation.

[2] For details refer, e.g., to Sect. 12.3 of [49].

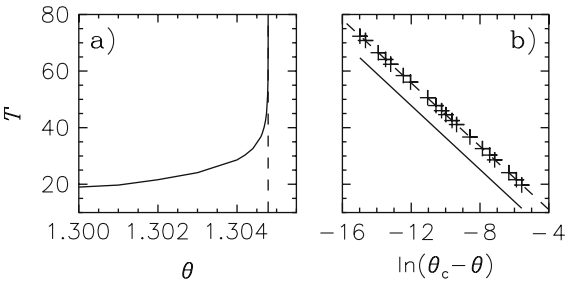

Fig. 8 (**a**) Period of the limit cycle, T, as a function of the detuning, θ, for $I_s = 0.9$. The *vertical dashed line* indicates the threshold of the saddle-loop bifurcation, $\theta_c = 1.30478592$. (**b**) Scaling of the period in the saddle-loop bifurcation. *Crosses* correspond to numerical simulations, while the *solid line*, arbitrarily positioned, has a slope $-1/\lambda_u$, with $\lambda_u = 0.177$, obtained from the stability analysis of the middle-branch KCS

middle-branch soliton for $\theta = \theta_{SL}$ is shown in Fig. 7. The agreement between the simulations and theoretical slopes is within 1%.

A comment is in place here regarding the spectrum shown in Fig. 7. The spectrum is formed by a stable continuous spectrum (although numerically discretized) and a discrete one with a positive ($\lambda_u = 0.177$) and a negative ($\lambda_s = -2.177$) eigenvalue. Having this spectrum in mind, it is perhaps surprising that one can describe the bifurcation route very well qualitatively, and to some extent quantitatively (cf. the observed scaling law, Fig. 8), by resorting to a planar dynamical system when many modes could, in principle, be involved. The first mode of the planar theory unequivocally corresponds to the positive (unstable) eigenvalue, $\lambda_u = 0.177$, while, in first approximation, the second mode should correspond to the second nearest to zero eigenvalue. However, this eigenvalue belongs to a continuum band, and the arbitrarily close eigenvalues of its band could play a role in the dynamics, modifying the planar theory. Moreover, considering this mode, $\lambda \sim -0.10$, the saddle index $\nu = -\lambda/\lambda_u < 1$, indicating that the cycle emerging from the saddle loop should be unstable, although we observe otherwise. The analysis of the modes of the unstable DS and dimensionality of the phase space is addressed in detail in the next section.

7 Quantitative Phase Space Projection

We now study the dynamics in terms of the modes obtained when performing the stability analysis of the middle-branch DS in a parameter region close to the saddle-loop bifurcation. By plotting the spatial profile of the modes, one obtains a clue to identifying the relevant modes for the dynamics. It turns out that most of the modes of the stable spectrum are delocalized. Figure 9 contains a representation of two such delocalized modes. The bands of extended modes correspond to modes of the homogeneous background, and are basically Fourier modes, apart from a radial dependence coming from the fact that we are using radial instead of

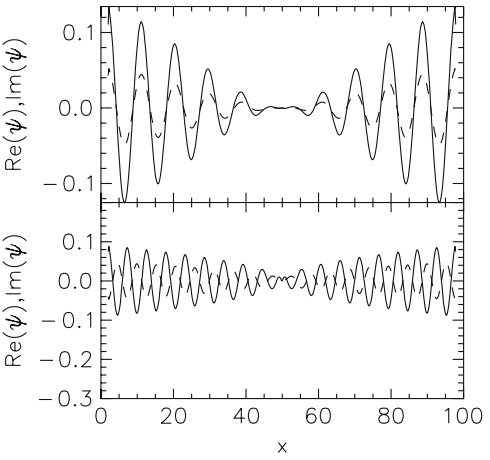

Fig. 9 Stable extended modes from the continuous band. The *top (bottom) panel* shows the transverse cut of the mode associated with the eigenvalue $\lambda = -0.1$ ($\lambda = -1 + \mathrm{i}0.24$) of Fig. 7. The *solid (dashed) line* indicates the real (imaginary) part of the eigenmode

Cartesian coordinates. As illustrated in Fig. 9, the basic difference between these modes is the wavenumber of their oscillations. There are, however, two exceptions, viz. two localized modes which are the one corresponding to the unstable direction and the most stable mode (which has eigenvalue $\lambda_s = -2.177$). Figure 10 displays the spatial profiles of these two modes. The fact that the dynamics of the DS remains localized in the space indicates that only these two localized modes take part in the dynamics.

Using this knowledge of the spectrum and the relevant eigenmodes, we can now explain the stability of the orbits emerging out of the bifurcation, specifically by employing the saddle index introduced above. Computing this index for the two modes that participate in the saddle-loop bifurcation, one obtains $\nu = 2.177/0.177 > 1$, and this fits perfectly with the fact that the cycle that detaches at one side of the

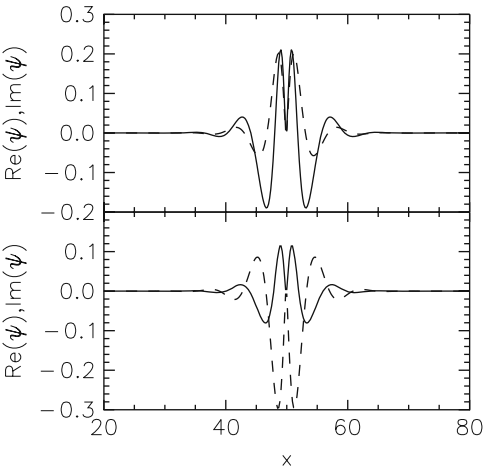

Fig. 10 Transverse cut of the unstable (*top*) and the most stable (*bottom*) modes of the unstable DS. These modes are associated with the eigenvalues $\lambda_u = 0.177$ and $\lambda_s = -2.177$ of Fig. 7, respectively. The *solid (dashed) line* indicates the real (imaginary) part of the eigenmode

bifurcation point is stable. Thus, one may understand that the whole dynamical instability scenario of the DS can be analyzed qualitatively in a planar dynamical system.

A closer inspection of the dynamics in the *linear* region, namely the region close to the saddle point, provides a justification of the role of the two participating localized modes – stable and unstable. Figure 6a contains a time trace of one such trajectory in the parameter region in which the limit cycle is stable, but close to the saddle-loop bifurcation. We project the deviation of the trajectory from the unstable DS onto the most stable and the unstable eigenvectors of the adjoint Jacobian matrix of the middle-branch KCS. These projections are the amplitudes of the unstable (β_1) and the most stable (β_2) modes, whose profiles are shown in Fig. 10. In the linear region close to the saddle point, the amplitudes of the other modes are negligible. The trajectory enters the linear region through the stable mode and leaves the region through the unstable one. This behavior is clear in the insets of Fig. 11. Next, we reconstruct the qualitative sketch of the bifurcation shown in Fig. 6 from our knowledge of the projections onto the modes, that is, we represent the trajectories before and after the saddle-loop bifurcation in mode space. Thus, Fig. 11 contains a quantitative, reconstructed, 2D phase space from the two localized modes involved in the transition for a set of parameter values in the oscillatory (a) and excitable (b) sides of the transition. The dynamics takes place on a plane when close to the saddle, but, away from it, the nonlinear dynamics bends the trajectory out of the plane into a higher-dimensional space which produces the apparent crossing of the trajectory in Fig. 11.

This is the final numerical confirmation that the infinite-dimensional dynamical system on which DSs live can be reduced to a 2D dynamical system with an excellent degree of precision, and that the picture is fully consistent with a saddle-loop bifurcation.

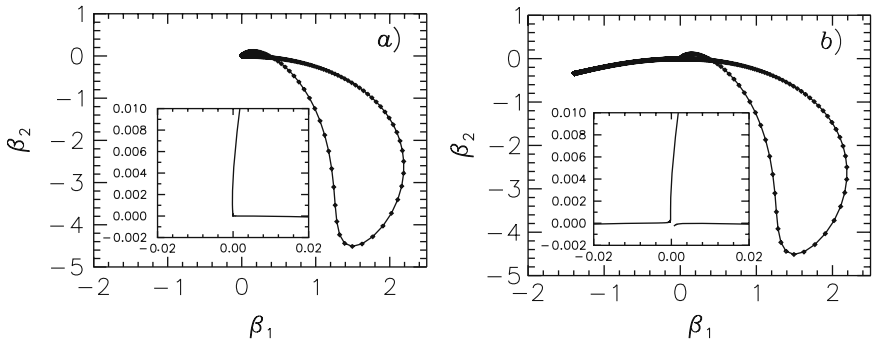

Fig. 11 Phase plane reconstructed by finding the amplitude of the deviation of the trajectory from the unstable DS in the unstable (β_1) and the most stable (β_2) modes of the middle-branch KCS. (**a**) Oscillatory trajectory ($\theta = 1.3047859$). (**b**) Excitable trajectory ($\theta = 1.3047860$). The symbols are equally time-spaced along the trajectory, so sparse symbols indicate fast dynamics while dense symbols indicate slow dynamics. The saddle point is at $(0,0)$. The inset is a close-up of the linear region around the saddle

8 Excitable Behavior

The saddle-loop bifurcation described above involves a fixed point (the homogeneous solution) on one side of the bifurcation and an oscillation on the other, so the system is a candidate for exhibiting excitability [9]. While excitability as a result of a saddle-loop bifurcation has been observed in different systems [7, 8, 9], it should be noted that it does not always appear. In particular, one needs a fixed point attractor that is close enough to the saddle point that destroys the oscillation. The excitability threshold in this type of system is the stable manifold of the saddle point, which implies that the observed behavior is formally "Class I excitability" [9]. This means that the excitability is characterized by response times that can be infinite (if a perturbation exactly hits the stable manifold of the fixed point), or, conversely, frequencies can start from zero. In our system, the excitable threshold reduces by increasing I_s (Fig. 2), since the middle-branch KCS (the saddle point) gets progressively closer to the homogeneous solution (fixed point).

This excitability scenario was first shown in [28], and, in parameter space, it is found in the region above the dashed line corresponding to the saddle-loop bifurcation shown in Fig. 1. Figure 12 shows the resulting trajectories after applying a localized perturbation in the direction of the unstable DS with three different amplitudes

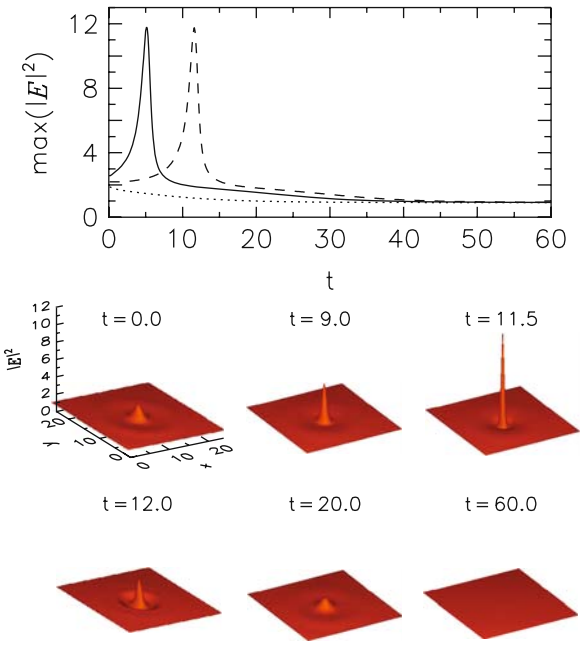

Fig. 12 *Top panel*: Time evolution of the maximum intensity, starting from the homogeneous solution ($I_s = 0.9$) plus a localized perturbation of the form of the unstable DS multiplied by a factor a. The *dotted*, *dashed*, and *solid lines* correspond to $a = 0.8$, $a = 1.01$, and $a = 1.2$, respectively. The 3D plots show the transverse profile at different times for $a = 1.01$

– one is below the excitability threshold (dotted line), while two are above it; of these, one is very close to threshold (dashed line) and the other is well above it (solid line). For the below-threshold perturbation, the system decays exponentially to the homogeneous solution, while, for the above-threshold perturbations, a long excursion in phase space is performed before returning to the stable fixed point. The refractory period for the perturbation just above the excitability threshold is appreciably longer, due to the effect of the saddle. The spatio-temporal dynamics of the excitable DS is also shown in Fig. 12. After an initial localized excitation is applied, the peak grows to a large value until the losses stop it. Then it decays exponentially until it disappears. A remnant wave dissipating the remaining energy is emitted out of the center.

It should be emphasized that, on neglecting the spatial dependence, equation (1) does not present any kind of excitability. The excitable behavior is an emergent property of the spatial dependence and it is strictly related to the dynamics of the 2D DS. The self-focusing collapse of the 2D NLSE is behind the long excursion in phase space. When a localized perturbation concentrates enough power, the self-focusing nonlinear mechanism induces a concentration of energy at that place. The presence of losses prevents collapse, the perturbation is finally dissipated, and the system returns to the homogeneous solution.

In parameter space, the excitable region is relatively large, as shown in Fig. 1. Therefore, it is potentially easy to observe experimentally. The excitable behavior belongs to Class I, as the period diverges to infinity when a perturbation hits the saddle. However, due to the logarithmic scaling law for the period, the parameter range over which the period increases dramatically is extremely narrow (see Fig. 8), so, from an operational point of view, systems exhibiting this scenario might not be classified as "Class I excitable", as the large period responses may easily be missed [52].

9 Takens–Bogdanov Point

The saddle-loop (or homoclinic) bifurcation is, in some sense, not *generic*, namely, a tangency between a limit cycle and a saddle point which occurs exactly so that it happens simultaneously at both sides of the stable and unstable manifolds is, in principle, not to be expected generically. In fact, also due to the fact that global bifurcations are not always easy to detect, the most convincing argument for the existence of such bifurcations is to show that a dynamical system exhibits a certain type of co-dimension-2 point.

A scenario in which the unfolding of a co-dimension-2 point yields a saddle-loop (or homoclinic) bifurcation is a Takens–Bogdanov (TB) point [46, 53]. This is a double-zero bifurcation point in which a saddle-node bifurcation line and the zero-frequency limit of a Hopf bifurcation line (hence no longer a Hopf line at the crossing point) meet in a two-parameter plane. The particular feature that the Hopf line has zero frequency at the TB point allows this co-dimension-2 bifurcation to

occur in a 2D phase space. This bifurcation has to be distinguished from the occurrence of a crossing between a saddle-node and a Hopf line at non-zero frequency, known as Gavrilov-Guckenheimer or saddle node-Hopf point, which requires a 3D phase space to take place. One can prove that, from the unfolding of a TB point, a saddle-loop line, apart from the saddle-node and Hopf lines, emerges [46, 53] from the TB point.

This can be checked in Fig. 1, where a two-parameter bifurcation plot is presented as a function of the two parameters of the system, I_s and θ. The problem here is that the saddle-node and Hopf lines tend to meet only asymptotically, namely when $\theta \to \infty$. We had previously checked, in [28], that the distance between the saddle-node and the Hopf lines decreases as one increases θ. (The same happens with the saddle-loop line.) By calculating the eigenvalues, it can be seen that the frequencies (viz. their imaginary parts) do indeed go to zero as one approaches the TB point. Figure 13 displays the two eigenvalues of the upper-branch DS, with largest real parts for parameter values corresponding to three vertical cuts of Fig. 1. Open symbols correspond to eigenvalues with a non-zero imaginary part, while filled symbols are associated with real eigenvalues. The point where the open symbols cross zero in the upper panel of Fig. 13 signals the Hopf bifurcation, while the point where the filled symbols cross zero signals the saddle-node bifurcation. The origin for the three plots is taken as the saddle-node bifurcation. At some point along the branch of the two complex conjugate eigenvalues associated with the Hopf bifurcation, the imaginary part vanishes, leading to two branches of real eigenvalues, the largest of which is precisely the one responsible for the saddle-node bifurcation. As detuning increases, the Hopf and saddle-node bifurcation points get closer and closer, but the structure of the eigenvalues remains unchanged, so that when the Hopf and saddle-node bifurcations finally meet, the Hopf bifurcation has zero frequency, signaling a TB point.

The TB point appears asymptotically in the limit of large detuning, θ, and small pump, E_0. In this limit, equation (1) becomes the conservative NLSE [31]. The Hopf instability in this limit was studied in [48], where evidence for a double-zero bifurcation point was given; however, the unfolding leading to the scenario presented here was not analyzed.

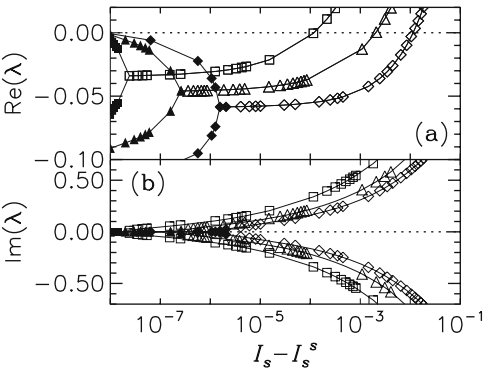

Fig. 13 Real part (*upper panel*) and imaginary part (*lower panel*) of the eigenvalues corresponding to the stable DS for three vertical cuts in Fig. 1, corresponding to three different values θ: *squares*, 1.7; *triangles*, 1.5; *rhombs*, 1.4, versus the difference between I_s and its value at the saddle-node bifurcation, $I_s^s(\theta)$

10 Effect of an Addressing Gaussian Beam

We now consider a pump consisting of a narrow Gaussian addressing beam on top of a homogeneous background. This is motivated by the fact that the common way to write and erase solitons in nonlinear cavities is by means of an addressing beam. This beam is customarily applied during a prescribed short interval of time. Here, we consider applying such a perturbation in a sustained way in order to control the spatial position of a soliton and its susceptibility to be excited. Hence, we consider a pump beam of the form $E_I(r) = E_0 + H\exp(-r^2/r_0^2)$, where E_0 is a homogeneous field, assumed real, H the height of the Gaussian perturbation, and r_0 its width. For convenience, we write the height of the Gaussian beam as

$$H = \sqrt{(I_s + I_{sh})\left[1 + (\theta - I_s - I_{sh})^2\right]} - E_0, \tag{8}$$

where $I_s + I_{sh}$ would correspond to the intra-cavity field intensity of a cavity driven by a homogeneous field with an intensity equal to the intensity at the top of the Gaussian beam, $E_I = E_0 + H$. This directly relates the height of the Gaussian beam, H, to a more intuitive quantity such as the equivalent intra-cavity intensity for a homogeneous pump.

The control parameters are the intra-cavity background intensity, I_s, the detuning, θ, and I_{sh}, which is associated with the Gaussian beam. Now the translational symmetry of the system (and also of its solutions) is broken, and the fundamental solution, which is no longer homogeneous, exhibits a bump which is small (when compared to the true DS), and this is the system response to the Gaussian perturbation. The bifurcation diagram for fixed I_{sh} and θ is given in Fig. 14.

On comparing Fig. 14 with the bifurcation diagram for a homogeneous pump (Fig. 2), it is clear that one feature which has changed is the region around the modulational instability point which signals the instability of the fundamental solution, i.e., the right end of the bistability region. In the homogeneous case, this instability occurs exactly at $I_s = 1$, but the introduction of a localized pump makes this point shift to a lower value (around $I_s = 0.7$ for these parameter values). One can also

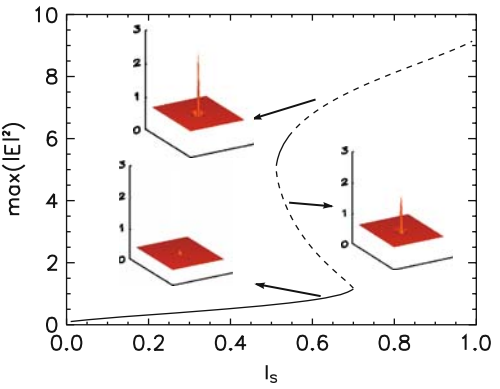

Fig. 14 Bifurcation diagram, $\max(|E|^2)$ vs. I_s, for homogeneous pump plus Gaussian addressing beam ($I_{sh} = 0.7$) for $\theta = 1.34$. *Solid lines* represent stable solutions and *dashed lines* unstable ones. The 3D plots show, from top to bottom, the profiles of the upper-branch KCS, the unstable middle-branch KCS, and the fundamental solution, which is no longer homogeneous

notice that no line is plotted for the localized pump case, while, in the homogeneous case, the fundamental branch continues to exist as an unstable branch. This is because, in the latter case, the bifurcation has changed to a saddle-node bifurcation, in which the stable and unstable branches that meet at this point coalesce and disappear. This bifurcation is, in fact, a saddle node on the invariant circle (SNIC).

Exploring now the upper branch, past the (left) saddle-node bifurcation, a pair of stationary (stable, upper branch and unstable, middle branch) solutions are found, and they are not qualitatively different from those found in the homogeneous pump case. These two DS solutions are now slightly modified and fixed spatially (in the transverse plane) by the localized Gaussian beam, but their localized nature mainly comes from the self-focusing feature of the model, which implies that the DSs are self-sustained. On increasing I_s, the stable high-amplitude DS undergoes a Hopf bifurcation, resulting in a periodically oscillating DS. The oscillation is, however, destroyed for larger I_s in a saddle-loop bifurcation, leading to an excitable regime, in an analogous manner to what happens with a homogeneous pump. The saddle loop occurs at a value of I_s which is below the SNIC. The excitable regime is possible only while the fundamental solution exists (I_s between the saddle loop and the SNIC). After the SNIC, both the fundamental and the upper-branch DS are unstable, and a new, oscillatory, regime appears. Figure 15 shows the temporal evolution

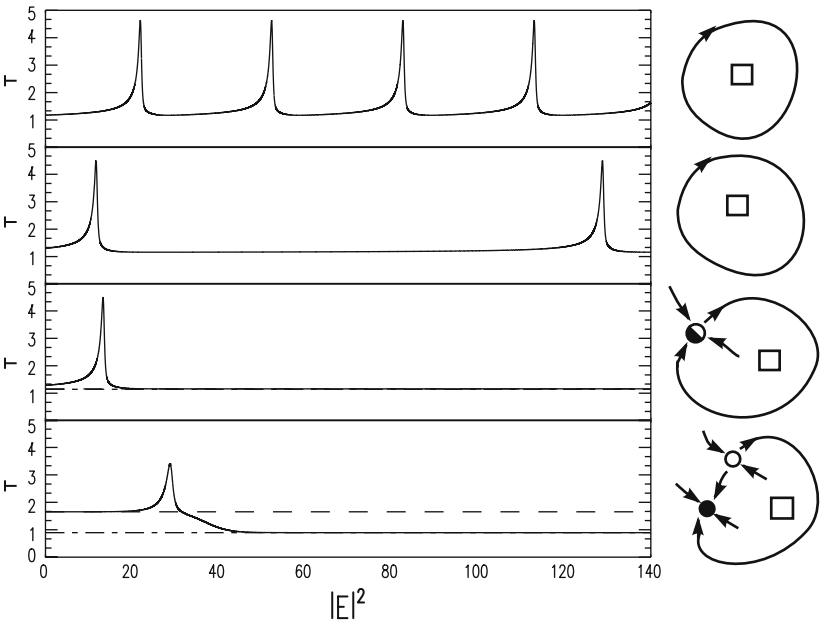

Fig. 15 *Left*: KCS maximum intensity, as a function of time, for decreasing values of I_s. From *top* to *bottom*, $I_s = 0.72, 0.7075, 0.707, 0.6$. $I_{sh} = 0.7$, $\theta = 1.34$. *Right*: sketch of the phase space for each parameter value. First two parameters correspond to region V (oscillating DS) in Fig. 16; the third one is very close to the SNIC bifurcation, while the fourth is in region IV (excitable), where this excitable behavior is dominated by the SNIC bifurcation

in the new oscillatory regime. As I_s is decreased, the period of the oscillations becomes longer and it finally diverges on reaching the SNIC. The scaling of the period of oscillation shows that this is, in fact, a saddle node on the invariant circle (SNIC). A SNIC bifurcation induces excitable behavior for I_s below the critical value. This scenario is different from the previous one, although both lead to a regime where DSs are excitable. Here the excitable threshold can be controlled by the intensity of the addressing Gaussian beam that effectively causes the saddle and the stable fixed point to approach each other in phase space.

A better understanding of these instabilities can be gained through a two-parameter bifurcation diagram, Fig. 16, in which just one parameter is kept fixed, namely $\theta = 1.34$. (On the other hand, however, the structure of the branches cannot be seen in this diagram, as the electric field is not plotted. In this sense, these two representations, Figs. 14–16, have to be seen as complementary.) A first remark on this diagram is that the $I_{sh} = 0$ line must match the homogeneous case (Fig. 1). In the diagram shown in Fig. 16, the one-parameter bifurcation diagram in Fig. 14 corresponds to a cut along a vertical line located at $I_{sh} = 0.7$, and the saddle-node, Hopf, and saddle-loop bifurcation lines are found when going upward, followed by a final bifurcation line, viz. the SNIC. The sequence of behaviors exhibited by the system is as follows. Below the (left) saddle-node (SN) line, region I, the system has a single stationary (fundamental) solution, which has a small bump at the spatial region where the Gaussian pump is applied. On increasing I_s, a saddle point is created in a saddle-node bifurcation, along with another fixed point which is a DS (region II). Further on, this fixed point becomes unstable in an Andronov-Hopf bifurcation, and a cycle is created (region III). At this point, the stable fundamental solution and a stable cycle (oscillating DS) coexist in the system, together with the

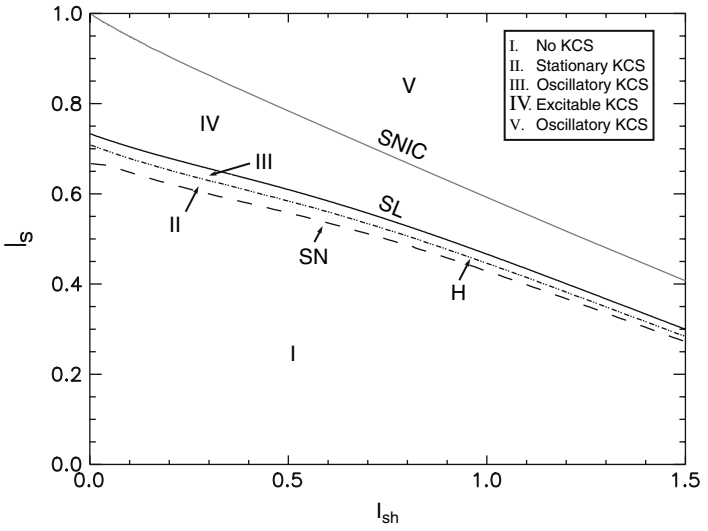

Fig. 16 Phase diagram I_s vs. I_{sh} for $\theta = 1.34$

unstable middle-branch KCS and the upper-branch KCS (which is now also unstable). If we further increase I_s, the limit cycle approaches the middle-branch KCS and collides in a saddle-loop bifurcation (SL line). Beyond this saddle loop, the fundamental solution becomes excitable in two possible ways (region IV). If the line indicated by SNIC is crossed, the fundamental solution (stable) and the lower DS stationary solution (saddle) annihilate each other inside an invariant circle, leading to oscillatory DS behavior (region V). Region IV is excitable in the sense that suitable perturbations of the fundamental solution lead to long excursions in phase space. This appears in two possible ways when changing system parameters depending on whether the SL or the SNIC bifurcation lines are crossed.

11 Concluding Remarks

We have analyzed the instabilities of dissipative solitons in a nonlinear Kerr cavity. Azimuthal instabilities lead to the destruction of the soliton, resulting in the formation of an extended pattern. On the other hand, instabilities occurring at zero azimuthal number lead to a localized structure whose amplitude oscillates in time, but in which the localized character of the soliton is preserved. More interestingly, beyond this oscillatory regime, an excitable regime, associated with the existence of dissipative structures, arises. This shows that, in order to exhibit excitability, extended systems do not necessarily require local excitable behavior. Instead, such phenomena can emerge because of spatial dependence through the dynamics of a coherent (localized) structure. This opens up the possibility of observing excitable behavior in a whole new class of systems where excitability was not thought to be present.

In Kerr cavities, there are two different mechanisms leading to excitability. One is based on a saddle-loop bifurcation in which a stable oscillating cavity soliton collides with an unstable one. The other occurs through a saddle node in the invariant circle (SNIC) bifurcation. The first one appears when either studying a homogeneous pump or considering a system pumped by a Gaussian beam on top of a homogeneous background, while the second mechanism appears only in the latter case. For both mechanisms, the excitability threshold is determined by the distance in phase space between the stable fixed point and the saddle. However, in the saddle-loop scenario, this distance cannot be easily tuned by changing system parameters, but, in the SNIC case, this distance vanishes precisely at the bifurcation point. By choosing to operate close to the SNIC bifurcation point, the threshold can be as low as desired. Therefore, it is possible to control the excitability threshold by changing a system parameter, e.g., the amplitude of the Gaussian addressing beam.

It has been shown that an excitable system can be used for computational purposes such as noise filtering or addition of input signals [54]. Thus, the excitable properties of cavity solitons open the possibility of optical information processing beyond the storage capabilities already suggested. This is a dynamical regime in which firing neuron-like structures could be generated at arbitrary points on the

transverse plane of a nonlinear optical cavity. By coupling several of these *optical neurons*, reconfigurable optical networks could be created with the aim of processing information in a similar way to networks of neurons.

References

1. D. Murray, *Mathematical Biology*, (Springer, New York, 2002), Chap. 11. 114
2. E. Meron, Phys. Rep. **218**, 1 (1992). 114
3. H.J. Wünsche, O. Brox, M. Radziunas, and F. Henneberger, Phys. Rev. Lett. **88**, 023901 (2002). 114
4. S. Barland, O. Piro, M. Giudici, J.R. Tredicce, and S. Balle, Phys. Rev. E **68**, 036209 (2003). 114
5. J.L.A. Dubbeldam, B. Krauskopf, and D. Lenstra, Phys. Rev. E **60**, 6580 (1999). 114
6. B. Krauskopf, K. Schneider, J. Sieber, S. Wieczorek, and M. Wolfrum, Optics Commun. **215**, 367 (2003). 114
7. F. Plaza, M.G. Velarde, F.T. Arecchi, S. Boccaletti, M. Ciofini, and R. Meucci, Europhys. Lett. **38**, 85 (1997). 114, 127
8. J. Rinzel and G.B. Ermentrout, in *Methods in Neuronal Modeling*, edited by C. Koch and I. Segev, (MIT Press, Cambridge, MA, 1989). 114, 127
9. E.M. Izhikevich, Int. J. Bif. Chaos **10**, 1171 (2000). 114, 127
10. Akhmediev, N., Ankiewicz, A. *Dissipative solitons*, Lect. Notes Phys. **661**. Springer, Berlin (2005) 114
11. O. Thual and S. Fauve, J. Phys. (France) **49**, 1829 (1988). 114
12. J.E. Pearson, Science **261**, 189 (1993). 114
13. K.J. Lee and H.L. Swinney, Science **261**, 192 (1993). 114
14. I. Müller, E. Ammelt, and H.G. Purwins, Phys. Rev. Lett. **82**, 3428 (1999). 114
15. N.N. Rosanov, *Progress in Optics*, (Elsevier, Amsterdam, 1996), Vol. **35**. 114
16. Feature Section on Cavity Solitons, edited by L.A. Lugiato, IEEE J. Quantum Electon. **39**, #2 (2003). 114
17. W.J. Firth and C.O. Weiss, Opt. Photon. News **13**, 55 (2002). 114
18. M. Tlidi, P. Mandel, and R. Lefever, Phys. Rev. Lett. **73**, 640 (1994). 114
19. S. Barland, et al., Nature (London) **419**, 699 (2002). 114
20. W.J. Firth and A.J. Scroggie, Phys. Rev. Lett. **76**, 1623 (1996). 114
21. P. Coullet, C. Riera, and C. Tresser, Phys. Rev. Lett. **84**, 3069 (2000). 114, 117
22. P. Coullet, C. Riera, and C. Tresser, Chaos **14**, 193 (2004). 114
23. P.B. Umbanhowar, F. Melo, and H.L. Swinney, Nature (London) **382**, 793 (1996). 114
24. W.J. Firth, A. Lord, and A.J. Scroggie, Physica Scripta **67**, 12 (1996). 114, 115
25. W.J. Firth, G.K. Harkness, A. Lord, J.M. McSloy, D. Gomila, and P. Colet, J. Opt. Soc. Am. B **19**, 747 (2002). 114, 115, 117, 119, 121
26. S. Longhi, G. Steinmayer, and W.S. Wong, J. Opt. Soc. Am. B **14**, 2167 (1997). 114
27. V.K. Vanag and I.R. Epstein, Phys. Rev. Lett. **92**, 128301 (2004). 114
28. D. Gomila, M.A. Matías, and P. Colet, Phys. Rev. Lett. **94**, 063905 (2005). 115, 127, 129
29. D. Gomila, A. Jacobo, M.A. Matías, and P. Colet, Phys. Rev. E, **75**, 026317 (2007). 115, 116
30. C. Sulem and P.L. Sulem, *The Nonlinear Schrödinger Equation*, (Springer, New York, 1999). 115
31. W.J. Firth and A. Lord, J. Mod. Optic. **43**, 1071 (1996). 115, 119, 121, 129
32. L.A. Lugiato and R. Lefever, Phys. Rev. Lett. **58**, 2209 (1987). 115, 116
33. J.J. Rasmussen and K. Rypdal, Phys. Scr. **33**, 481 (1986). 116
34. M.V. Goldman, K. Rypdal, and B. Hafizi, Phys. Fluids **23**, 945 (1980). 116
35. D. Gomila, and P. Colet, Phys. Rev. A **68**, 011801 (R) (2003). 116, 120
36. R. Montagne, E. Hernández-García, A. Amengual, and M. San Miguel, Phys. Rev. E **56**, 151 (1997). 116
37. A.J. Scroggie, Chaos, Soliton, Fract. **4**, 1323 (1994). 116

38. P.D. Woods, and A.R. Champneys, Physica D **129**, 147 (1999). 117
39. T. Maggipinto, M. Brambilla, G.K. Harkness, and W.J. Firth, Phys. Rev. E **62**, 8726 (2000). 117
40. B. Schäpers, M. Feldmann, T. Ackemann, and W. Lange, Phys. Rev. Lett. **85**, 748–751 (2000). 117
41. B. Schäpers, T. Ackemann, and W. Lange, Proc. SPIE **4271**, 130 (2001). 117
42. A. Schreiber, B. Thüering, M. Kreuzer, and T. Tschudi, Optics Commun. **136**, 415 (1997). 117
43. V.B. Taranenko, I. Ganne, R.J. Kuszelewicz, and C.O. Weiss, Phys. Rev. A **61**, 063818 (2000). 117
44. W.J. Firth, and G.K. Harkness, Asian J. Phys. **7**, 665 (1998). 118
45. G.-L. Oppo, A.J. Scroggie, and W. Firth, Phys. Rev. E **63**, 066209 (2001). 118
46. Y.A. Kuznetsov, *Elements of Applied Bifurcation Theory, 2nd ed.*, (Springer, New York, 1998). 118, 128, 129
47. J.M. McSloy, W.J. Firth, G.K. Harkness, and G.L. Oppo, Phys. Rev. E **66**, 046606 (2002) 118
48. D.V. Skryabin, J. Opt. Soc. Am. B **19**, 529 (2002). 121, 129
49. P. Glendinning, *Stability, Instability, and Chaos*, (Cambridge U.P., Cambridge, UK, 1994). 122, 123
50. S. Wiggins, *Global Bifurcations, and Chaos: Analytical Methods*, (Springer, New York, 1988). 122
51. P. Gaspard, J. Phys. Chem. **94**, 1 (1990). 123
52. E.M. Izhikevich, *Dynamical Systems in Neuroscience*, (MIT Press, Cambridge, MA, 2006). 128
53. J. Guckenheimer, and P. Holmes, *Nonlinear Oscillations, Dynamical Systems, and Bifurcations of Vector Fields*, (Springer, New York, 1983). 128, 129
54. C. Koch, *Biophysics of Computation: Information Processing in Single Neurons*, (Oxford U.P., New York, 1998). 133

Temporal Soliton "Molecules" in Mode-Locked Lasers: Collisions, Pulsations, and Vibrations

P. Grelu and J.M. Soto-Crespo

Abstract A few years after the discovery of the stable dissipative soliton pairs in passively mode-locked lasers, a large variety of multi-soliton complexes were studied in both experiments and numerical simulations, revealing interesting new behaviors. This chapter focuses on the following three subjects: collisions between dissipative solitons, pulsations of dissipative solitons, and vibrations of soliton pairs. Different outcomes of collisions between a soliton pair and a soliton singlet are discussed, showing possible experimental control in the formation or dissociation of "soliton molecules". Long-period pulsations of single and multiple dissipative solitons are presented as limit cycles and observed experimentally. Finally, one possible manifestation of long-period pulsation for a soliton pair results in a vibrational motion. All these behaviors that enrich the life of multi-soliton complexes make them akin to molecules. However, the analogy has clear limitations, since these "soliton molecules" are inherently strongly dissipative and require a sustained energy supply from the gain medium.

1 Introduction

Mode-locked lasers provide a fantastic playground for experiencing nonlinear dynamics of dissipative temporal solitons. The range of time scales in which field evolution can be observed typically spans over ten orders of magnitude, from nanoseconds to tens of seconds. Associated with a relatively simple experimental setup, the mode-locked laser possesses all the complexity required to observe a wide

P. Grelu
Institut Carnot de Bourgogne, UMR 5209 CNRS, Université de Bourgogne, BP 47 870, F-21078 Dijon Cedex, France, philippe.grelu@u-bourgogne.fr

J.M. Soto-Crespo
Instituto de Óptica, C.S.I.C., Serrano 121, 28006 Madrid, Spain,
iodsc09@io.cfmac.csic.es

Grelu, P., Soto-Crespo, J.M.: *Temporal Soliton "Molecules" in Mode-Locked Lasers: Collisions, Pulsations and Vibrations.* Lect. Notes Phys. **751**, 137–173 (2008)
DOI 10.1007/978-3-540-78217-9_6

range of dynamics, from stationary pulses to pulsating and chaotic waveforms, with single or multiple pulses. This dynamics can be triggered by control over a limited set of cavity parameters accessible to the experimentalist. These include the level of pump power, the amount of loss, and the average chromatic dispersion.

In most cases, a newly investigated form of dynamics can be associated with a tractable numerical model, such as the complex Ginzburg–Landau equation (CGLE) [1]. In the few cases studied in this chapter, the experimental observation either follows or precedes a numerical prediction based on an appropriate simplification of the field evolution problem and the use of realistic parameters. The related observation of several types of dynamics in a large variety of experimental setups is a valuable a posteriori justification of the use of simplified models that are able to reveal universal behavior more clearly and readily.

During the past few years, several works have shed new light on the understanding of the dynamics of mode-locked lasers, based on the concept of the dissipative soliton [2, 3]. A mode-locked laser uses nonlinear dissipation as a key mechanism to form and stabilize a pulse as it makes round-trips in a laser cavity. When it is obtained, the stable stationary pulse is the result of a stable balance between nonlinear gain and losses on the one hand, and between nonlinear and linear phase shifts on the other hand. Presented as the stable equilibrium point of a double nonlinear balance, the stationary pulse can be understood as a dissipative soliton. In the phase space of degrees of freedom, which is of infinite dimension, the stable stationary pulse can be represented by a point attractor, surrounded by a finite basin of attraction. For a given set of system parameters, the existence of a basin of attraction limits the number of stable solutions, while, at the same time, it guarantees a certain amount of stability and robustness with respect to environmental noise and drifts. This statement is in contrast to the case of Hamiltonian solitons, such as those derived from the nonlinear Schrödinger equation (NLSE), which belong to continuous families of solutions for a given set of equation parameters.

Although many definitions of a soliton can be proposed, they all encompass the notion of a localized structure, which should restore itself after it has been moderately perturbed. For instance, the perturbation can be linear noise – random fluctuations of small amplitude – or it can be an interaction with a neighboring soliton. These examples are typical of what can be studied with a mode-locked laser.

The interaction of two dissipative temporal solitons can lead to the formation of a stable stationary bound state, characterized by a phase difference of $\pm\pi/2$ between the components, as predicted semi-analytically and numerically in [4] and found experimentally in [5]. It is important to recall that such a soliton pair is *not* a second-order Schrödinger soliton: in a distributed propagation model such as the CGLE, the soliton pair is a stable stationary solution and it acts as an attractor for the interacting two solitons. That is why the image of a *molecule* can be useful in depicting a stable soliton pair, which is the result (the *product*) of the interaction (the *reaction*) between two separate single solitons (single *atoms*). Indeed, the formation of a molecule requires dissipation to stabilize the product with respect to the reactants.

Other stable soliton pairs were found in various fiber laser experimental configurations, in either anomalous or normal dispersion regimes of propagation [6, 7, 8, 9, 10, 11]. The existence of stable bright soliton pairs in both dispersion regimes affirms the pre-eminence of the dissipative soliton concept over the Schrödinger soliton concept in related experiments. However, the sign of the dispersion affects the detailed features of the soliton pair: for instance in the normal dispersion regime, the phase relationship between the two bound solitons is found to be close to π in most cases [12]. The consideration of a more complicated spectral response has proved to give rise to pairs which also have a π phase difference in the anomalous dispersion regime [13].

Quite logically, when the impact of nonlinear dissipation on propagation dynamics is stronger, then the stationary pulse will be further from a Schrödinger soliton. Among passively mode-locked lasers, and compared to bulk-medium cavity designs (based on titanium sapphire amplifiers for example), fiber lasers are generally characterized by large gain and losses. The main losses usually come from the mode-locking mechanism, which is either nonlinear polarization evolution [14] or saturable absorption in a fast-responding material (from saturable semiconductor mirrors to carbon nanotubes [15, 16]). In comparison, the Kerr-lens mode-locking mechanism (KLM, [17]) used in many bulk-medium cavity designs exhibits fewer losses. In fiber lasers, large losses (from 50% to more than 90% per round-trip when linear and nonlinear losses are summed up) do not create a major obstacle, since the doped-fiber medium can be arbitrarily long and efficiently pumped, so that the unsaturated gain can exceed 100 if required. Also, with respect to bulk-medium cavities, a fiber cavity is characterized by a considerable level of pulse re-shaping within one round-trip. Finally, multiple pulse operation can be easily achieved with a moderate pumping power of typically 100 mW. All these characteristics, which are more or less significant, depending on the specific cavity design, generally make the mode-locked fiber laser an ideal tool for testing various dissipative soliton dynamics. Of course, bulk mode-locked laser configurations are sufficiently versatile to allow various dynamics of dissipative soliton complexes to be observed as well [18, 19]. Even some earlier observations [20, 21, 22] could also be reinterpreted in the frame of dissipative solitons, although observations of purely Hamiltonian soliton dynamics of high-order Schrödinger solitons were initially reported in other setups [23, 24].

The case of the dissipative soliton pair has been extensively studied in [25]. The situation that we now consider is the case of three dissipative solitons interacting inside the cavity. As we shall see in Sect. 2, the three pulses can bind stably, forming a dissipative triplet *molecule*. However, there is also another scenario in which a soliton pair interacts with the third soliton. Depending on the cavity parameters and the initial conditions, the outcome can be either the observation of "pseudo-elastic" collisions that are repeated indefinitely inside the cavity or a clear manifestation of inelastic collisions that include the formation of a triplet soliton *molecule*.

In the space of the system parameters, the existence of stable dissipative soliton solutions can be found in a given domain. At the boundary of such a parameter

domain, the soliton solution becomes marginally stable. As predicted theoretically and numerically in [26], stable pulsating solutions are likely to be found near these boundaries. Section 3 details examples where various pulsating solutions that reveal even the existence of doubly periodic pulsations have been found in mode-locked fiber laser experiments and in numerical simulations. We shall see that pulsating solutions can be particularly stable when they are attributed to the existence of a limit cycle attractor, and therefore they can be labeled as "pulsating dissipative solitons". Pulsating solitons are, again, a distinct feature of propagation dynamics in the presence of nonlinear dissipation, since they do not exist in Hamiltonian systems.

Pulsating solutions are not restricted to the single pulse case. Double-pulse pulsating solutions can be found and can be called "pulsating soliton pairs". Interestingly, among pulsating soliton pairs, there exist pulsations in which the oscillation of the relative temporal separation and the relative phase of the two pulses are the major dynamical effects. These solutions can then be viewed as vibrating soliton pairs, fueling the analogy with a matter molecule which has internal vibrational states. This is presented in Sect. 4. Finally, Sect. 5 gives an overview of the present chapter and presents a few prospects. The molecular analogy, which served as a useful guide in the search for new multi-soliton complexes and their possible dynamics, is briefly discussed.

2 Collisions Between Dissipative Solitons Inside a Laser Cavity

In this section, we address the simplest situation relating to the collision between two different soliton complexes, namely that between a single soliton and a soliton pair. The soliton pair can itself be seen as the result of an inelastic collision between two identical single solitons, and has previously been studied extensively [25]. For the sake of clarity, we first recall the basic features of the soliton pair, as well as the fiber laser experimental setup in which it was observed.

2.1 The Soliton Pair, and Why It Can Move with Respect to a Single Soliton

2.1.1 The Dissipative Soliton Pair: Theory

The existence of stable soliton pairs was first predicted in 1997 [4], by using a continuous cubic–quintic CGLE model, which is a generic equation that has been used in many areas of nonlinear physics. In optics, it provides a distributed model for passively mode-locked lasers and optical transmission lines with nonlinear amplifiers. In this context, the CGLE takes the form of a normalized propagation equation, as follows:

$$\mathrm{i}\psi_z + \frac{D}{2}\,\psi_{tt} + |\psi|^2\psi + \nu|\psi|^4\psi = \mathrm{i}\delta\psi + \mathrm{i}\varepsilon|\psi|^2\psi + \mathrm{i}\beta\psi_{tt} + \mathrm{i}\mu|\psi|^4\psi, \qquad (1)$$

where z is the normalized distance of propagation, t is the time in the moving pulse frame, and ψ is the normalized envelope of the electric field. All the terms involved in (1) have clear physical significance in the context of mode-locked lasers. The left-hand part groups the conservative terms, including chromatic dispersion (with coefficient D), the nonlinear Kerr effect, and its possible saturation, if ν is taken as negative. In the normalized form, the dispersion coefficient is taken to be $D = +1$ for propagation in an anomalous dispersive medium, and $D = -1$ in the case of normal dispersion. The right-hand part of (1) comprises successively the linear loss term, with a negative coefficient δ, the nonlinear gain, with a positive coefficient ε, which is required to favor pulses over continuous waves, a Gaussian spectral filter with positive coefficient β, and a saturation of the nonlinear gain term which is required for the stabilization of the amplitude of pulses and is associated with a negative coefficient μ.

Stable bright soliton solutions of (1) can be found within a specific range of values of the above parameters. When all the parameters are fixed, the soliton solutions form a discrete set, which means that the amplitude and the width of solitons are fixed. The plain, bell-shaped soliton is the most common solution, since it exists over a wider range of parameters than other soliton profiles. During the interaction of two plain solitons, their temporal separation, ρ, and their phase relationship, ϕ, are practically the only two quantities that are allowed to change significantly, since the shape of each soliton is fixed by the double nonlinear balance. Although the evolution problem deals with an infinite number of degrees of freedom, they are mainly frozen, apart from these two, viz., ρ and ϕ. The evolution problem can be analyzed in a reduced two-dimensional phase space called the "interaction plane" [27]. At a given propagation distance, the two interacting pulses are represented by a dot in this plane, and while propagation takes place, the succession of dots creates a trajectory.

For a given set of parameters, two stable soliton pair solutions were found in [4]. In the interaction plane, they correspond to a precise temporal separation and a phase relationship which is either $+\pi/2$ or $-\pi/2$. These two stable solutions are attractors, since neighboring trajectories converge to them, as shown in Fig. 1.

2.1.2 The Fiber Laser Experimental Setup and Observation of Soliton Pairs

Here we detail the setup in which most of the experimental results presented in this chapter have been obtained. It consists of a dispersion-managed mode-locked fiber ring laser, similar to those used in [5, 28, 29]. The fiber laser, which emits ultrashort pulses at a wavelength of around 1.5 µm, is sketched in Fig. 2. The gain is provided by a 1.9-m long, 1400-ppm erbium-doped fiber (EDF) that features normal chromatic dispersion [$D = -40\,(\mathrm{ps/nm})/\mathrm{km}$]. The pumping source consists of four wavelength-multiplexed laser diodes operating at around 980 nm, providing a coupled power of up to 350 mW. The path-averaged cavity dispersion is adjusted

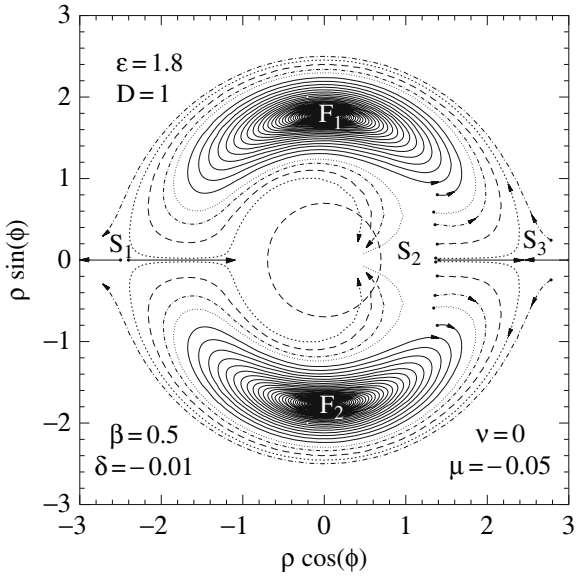

Fig. 1 Attractors for stable soliton pairs, as they appear in the interaction plane. They are located symmetrically (F_1 and F_2), corresponding to a phase relationship that is either $+\pi/2$ or $-\pi/2$. The parameters of the CGLE used for this simulation are marked inside the figure

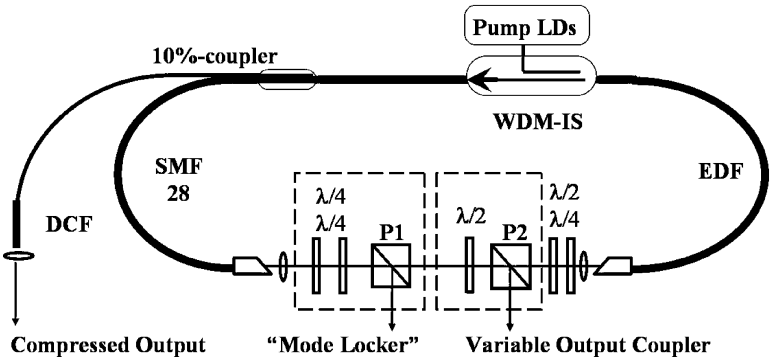

Fig. 2 Mode-locked fiber laser experimental setup

with the use of an appropriate length of a SMF-28 fiber that has anomalous dispersion [$D = +16.5\,(\mathrm{ps/nm})/\mathrm{km}$]. A 50-cm-long open-air section is used to insert polarization components. Due to the nonlinear polarization evolution that takes place along with propagation in the fibers, the transmission through the polarizer P1 is intensity dependent, and an appropriate adjustment of the preceding wave plates triggers the mode-locked laser operation. A polarization-insensitive optical isolator (WDM-IS) ensures uni-directional lasing. Depending on the length of the SMF, the cavity round-trip time is in the range 25–50 ns (repetition rate 20–40 MHz).

Two other optional outputs are implemented in the cavity, and these may be used according to which type of experiment is performed. First, a second polarizer (P2), preceded by a half-wave plate, provides a convenient variable output coupler. Second, a 10% fiber output coupler is inserted inside the cavity in order to splice in a small length of dispersion-compensation fiber (DCF). This gives a convenient way of compressing the chirped pulses that propagate in the cavity.

The cavity parameters that can be controlled quite easily are the following: the pumping power, the amount of linear losses, and the path-averaged dispersion. The tuning of the retarding wave plates, that precede the first polarizer, acts on both linear and nonlinear losses. Although the relationship between the wave plate angle, the amount of nonlinear losses, and the laser pulse features is a non-trivial issue, a semi-analytical study has been undertaken in [30, 31, 32].

In the anomalous dispersion regime, a pumping power of typically 80 mW is required to achieve mode-locking. The pulse duration is typically 300 fs, but can vary between 120 fs and 1 ps according to the choice of cavity parameters. Then, in dealing with ultra-short pulses, the main pulse features are obtained via the information provided by the recording of the optical auto-correlation and of the optical spectrum.

On further increasing the pumping power, multiple pulsing occurs. This involves the co-existence of several pulses inside the laser cavity. In general, additional pulses are formed, one by one, as the pumping power increases [33]. A large hysteresis between the number of pulses and the pumping power has been observed and modeled by several authors [34, 35, 36]. Sometimes, these pulses spread almost regularly along the cavity. This situation is called "harmonic mode-locking", since it multiplies the fundamental repetition rate (see discussion in [25]). However, in many cases, the interactions between these pulses produce bound states that are self-organized multi-soliton complexes.

In the simplest case of two bound pulses, the optical spectrum generally presents fringes of interference of high contrast. As the typical recording time of each spectral data point is 10 ms, it is averaged over more than 10^5 round-trips. That is why the observation of spectral fringes, with reflective experimental artifacts set apart, is possible only if the two bound pulses possess a precise and stable phase relationship, as well as a stable temporal separation. The spectral inter-fringe is inversely proportional to the temporal separation, and the location of the fringes inside the spectral envelope is dictated by the phase relationship between the two pulses. The spectral envelope is basically the optical spectrum profile of a single soliton. If the pulses are in phase, a bright spectral fringe will coincide with the center of the spectrum. If the pulses are out of phase, a dark spectral fringe will be in the center. In contrast, the $\pm\pi/2$ asymmetric phase relationships will provide asymmetric spectra. These were found in the fiber laser experiment, and Fig. 3 presents one example of a soliton pair with an asymmetric phase relationship, which is fitted to be very close to $\pi/2$ (91 degrees). In the case presented here, the pulse pair consists of two 610-fs FWHM pulses separated by 6.8 ps. As a secondary proof of the presence of a fixed phase relationship, the optical auto-correlation is performed interferometrically, and the crossed correlation is also characterized by temporal fringes. In the rest of this

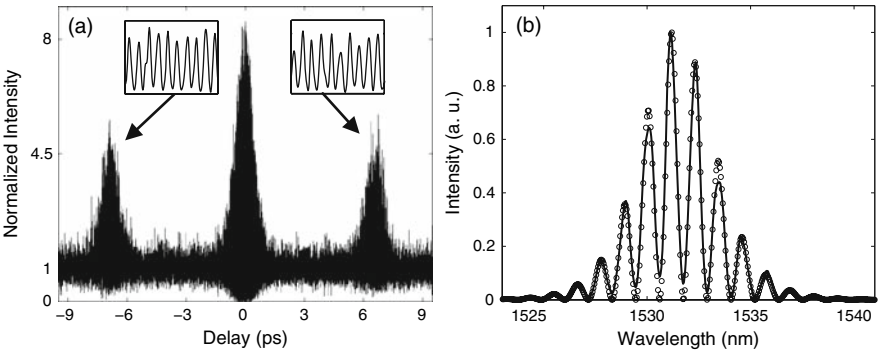

Fig. 3 Experimental observation of a soliton pair via (**a**) its interferometric auto-correlation trace, with coherent cross-correlations (insets), and (**b**) its optical spectrum, fitted for a $\pi/2$ phase relationship (circles)

chapter, the optical auto-correlations will be presented non-interferometrically, thus providing lower noise traces that are easily interpreted.

It should be emphasized that the $\pm\pi/2$ phase-locked soliton pairs play a central role, as they are the only stable soliton pairs found in the continuous cubic–quintic CGLE, in the regime of anomalous dispersion. To find them experimentally, the fiber laser was operated with a low pumping power (below 50 mW), yielding pulses which were moderately short (≈ 0.5 ps) and moderately energetic (≈ 30 pJ). In this context, the accuracy of the CGLE model is quite high, namely more refined propagation models that include higher-order effects or discretized propagation are not required here to retrieve the essential dynamical features of the laser.

However, in subsequent experiments, soliton pairs with different features were also been found. For example, in the normal propagation regime, there is stretched-pulse operation, which implies a large amount of frequency chirping [8, 12]. In these cases, a more detailed model, which took into account the discrete nature of different cavity segments, was required to prove the existence of stable soliton pairs with a phase relationship of π [12].

2.1.3 Basic Origin of the Relative Speed

In the case of an asymmetric phase relationship between the two bound dissipative solitons, the optical spectrum also acquires asymmetry. This spectral asymmetry results in a slightly modified center of gravity for the spectrum intensity, and this, in turn, provides a slightly modified group velocity due to the non-zero path-averaged chromatic dispersion. This implies that such a soliton pair has a group velocity which is different from the group velocity of a single soliton, and also that two soliton pairs with different phase relationships (namely $+\pi/2$ and $-\pi/2$) should also have distinct group velocities. If two different soliton species propagate simultaneously inside the laser cavity with a relative velocity, they will collide some

time later. The following analytic calculation will study the relationship between the phase asymmetry of a soliton pair and the relative velocity between the soliton pair and a single soliton.

Let $U(t)$ be the stationary field envelope of a single stable pulse solution. For simplicity of analysis, we assume that it has a Gaussian power spectrum, P_1, i.e.,

$$P_1(\omega) = A_o \exp\left(-(\omega/B)^2\right), \tag{2}$$

where A_o is a real constant, and $2\sqrt{\log 2} \times B$ is the FWHM spectral width. A doublet solution, formed by two of these pulses, separated by a distance T_o and with a fixed phase difference of ϕ, can be written as

$$V(t) = U(t) + U(t - T_o)\exp(\mathrm{i}\phi).$$

Its spectrum can be easily calculated and is

$$P_2(\omega) = A_o \exp\left(-(\omega/B)^2\right)[2 + 2\cos(\omega T_o + \phi)]. \tag{3}$$

The average frequency (or detuning from the central one) is defined by

$$\Delta\omega = \frac{\int_{-\infty}^{\infty} \omega P(\omega)\mathrm{d}\omega}{\int_{-\infty}^{\infty} P(\omega)\mathrm{d}\omega}. \tag{4}$$

This is clearly zero for the singlet, since $P_1(\omega)$ is an even function of ω. For the doublet, it becomes

$$\Delta\omega = \sin(\phi)\frac{T_o B^2}{2}\exp\left(\frac{-T_o^2 B^2}{4}\right). \tag{5}$$

Equation (5) is represented in Fig. 4 for two values of B. The group velocity difference between the soliton pair and the soliton singlet is linearly related to this frequency change. Experimental curves of relative speed, such as those in Fig. 4 of [10], are reproduced quite well, at least qualitatively, by formula (5).

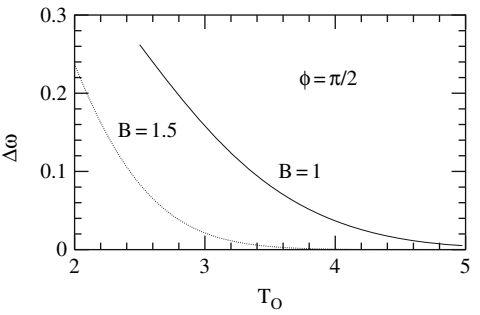

Fig. 4 Frequency change for a soliton pair as a function of the separation between the two solitons, with $\phi = \pi/2$ for two different spectral widths, B

There has also been speculation that other higher-order nonlinear effects, such as the Raman effect, could induce a relative group velocity between a single soliton and a soliton pair [37].

2.2 Collisions Between a Soliton Pair and a Soliton Singlet: Experiment

The discussion above should have convinced the reader that collisions between a soliton pair and a soliton singlet would naturally occur inside a mode-locked laser cavity. The following paragraphs present various outcomes of collisions, from the experimental point of view [10, 38]. The following section will present the results of numerical simulations [38, 39].

2.2.1 Observation of Periodic "Pseudo-elastic" Collisions Inside the Cavity

In the study presented here [38], three pulses are generated inside the cavity with a pumping power of 300 mW, with the variable output coupler set to extract around 40% of the intra-cavity energy. As the nonlinear losses of the cavity, measured from the "mode-locker" port, amount to nearly 50%, the total losses of the cavity amount to almost 90%, or 10 dB. Thus, the cavity operates in a strongly dissipative regime, in which we can expect dynamical effects to be ruled rather by nonlinear dissipation than by conservative nonlinearities, although the various physical effects at play cannot be separated.

With three mode-locked pulses, there are many "internal" degrees of freedom that can be affected by the fine tuning of cavity parameters. In our setup, the easiest parameters to change when the laser is running are the pumping power and the amount of linear loss. The latter can be tuned via a modification of the orientation of the half-wave plate which precedes polarizer P2 of Fig. 2. To analyze the dynamical changes, one output of the cavity is directed onto a fast photodiode, which is connected to a 500-MHz digital-phosphor oscilloscope, while another output is connected to the optical auto-correlator and to the optical spectrum analyzer.

The interest in having simple output monitoring is as follows: whereas the recording of the auto-correlation trace typically takes 1s, and that of the optical spectrum takes 10 s, the photodiode provides real-time monitoring of the intra-cavity energy, within the bandwidth limitation of the electronics. When a soliton-bound triplet is formed, the triplet state is not resolved by the photodiode, and the oscilloscope trace features one large peak per cavity round-trip time, as shown in Fig. 5(a).

However, within a small range of orientations (± 5 degrees) of the half-wave plate preceding P2, the oscilloscope traces can feature two peaks, which have a slow relative motion per cavity round-trip. The larger one is double the other one in intensity and appears stably on the screen, since its level is used for trace synchronization.

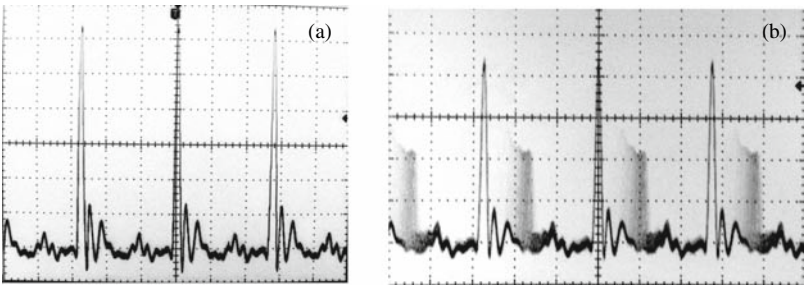

Fig. 5 (**a**) Oscilloscope trace showing stable pulse train generation at the fundamental repetition rate of the fiber laser cavity, i.e., 36.3 MHz. Each main peak consists of a soliton triplet whose structure is not resolved. The small sub-peaks of amplitude, about or less than one division, are electronic artifacts due to imperfect impedance matching. The time unit is 10 ns per division. (**b**) Oscilloscope trace of soliton pair and soliton "singlet" in relative motion

The second one always moves with a constant relative velocity on this scale of observation. This is illustrated by Fig. 5(b).

The motion in real time can be seen in the first movie of [38], available online from the website of *Optics Express*. The largest peak is identified as a soliton pair, or "doublet", whereas the second peak is identified as a single soliton, or "singlet". As presented below, this analysis is validated by the recordings of the optical spectra and of the auto-correlation traces.

As the singlet moves, it takes 0.64 s for it to be delayed by one round-trip with respect to the doublet. Here, as one round-trip represents 5.3 m of fiber length, the group velocity difference between the doublet and singlet is 8.3 m/s, which is less than 10^{-7} of each soliton's group velocity. Once it has been obtained, this relative motion can be stable for hours. A similar observation was reported in [10].

2.2.2 Synthesis and Decomposition of Triplet States

If the output coupling is slightly changed, a triplet soliton-bound state can be formed as a result of the interaction between the doublet and the singlet states. The triplet corresponds to the oscilloscope trace of Fig. 5(a). This is highly stable once obtained, but if the output coupling is changed back, the result is again a decomposition of the triplet into doublet and singlet solitons, as in Fig. 5(b). As the same cycle can be repeated many times over, the transition $2+1 \rightarrow 3$ is reversible, although it presents hysteresis. These switching cycles can be observed directly in the oscillograms, as presented in the second movie of [38]. At the same time, switching between the spectra (a) and (b) in Fig. 6 is observed: spectrum (a) is analyzed to be the incoherent superposition of singlet (dashed line) and doublet spectra, whereas spectrum (b) is clearly the spectrum of a stable bound triplet (with phase relationships of $+\pi/2$ and $-\pi/2$ between successive solitons, hence its symmetry).

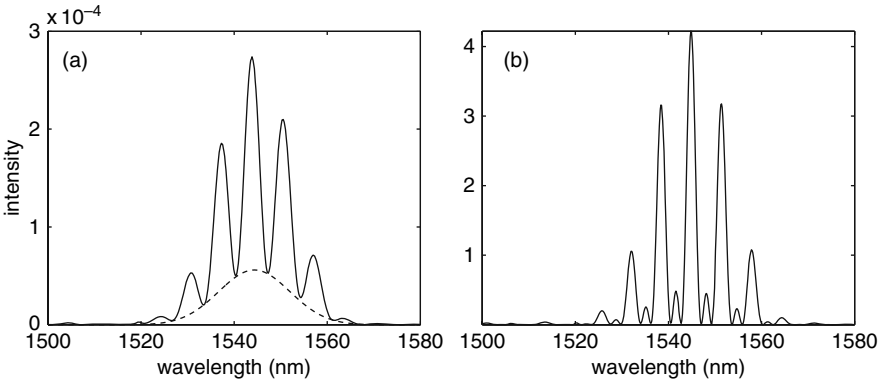

Fig. 6 (**a**) Recorded optical spectrum (solid line) and its baseline (dashed line), for the doublet and "singlet" solitons in continuous relative motion. (**b**) Optical spectrum when the soliton triplet is formed

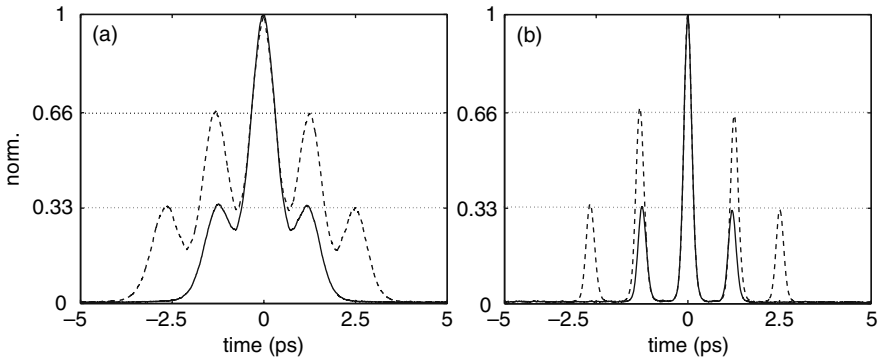

Fig. 7 Auto-correlation traces taken from (**a**) the variable output coupler and (**b**) the 10% coupler. Solid line is for doublet and singlet in continuous relative motion. Dashed line relates to time after the triplet soliton state has formed

The appearance of singlet, doublet, and triplet soliton states in the cavity finds complete justification when optical auto-correlation traces are considered. Figure 7(a) represents the auto-correlation traces recorded at the variable output coupler. The solid curve is taken when the soliton pair and the soliton "singlet" are moving with different group velocities, as in Fig. 6(a). The amplitude of the central peak is three times larger than the amplitude of the side peaks. This is compatible with the fact that the soliton pair is made of two equal pulses that have the same amplitude as the third moving pulse. The dashed curve is used when the triplet is formed, as in Fig. 6(b). This is clearly the auto-correlation function of three identical, equally separated pulses.

The same conclusion is confirmed by recording the auto-correlation function at a different location, namely after the erbium-doped fiber, at the 10% output of the fiber coupler. It is displayed in Fig. 7(b). Dispersion compensation allows for a

clearer identification of the pulses that produce either a doublet or a triplet state. The separation between the bound pulses is 1.2 ps, and this hardly changes during the round-trip, whereas individual pulse widths vary significantly due to the important frequency chirping effect inside the cavity. Similar collision behaviors have also been reported in the fiber laser experimental setup of [10].

2.3 Soliton Collisions in the Continuous CGLE Model

In the CGLE model, the bound state is an asymmetric solution because of the phase difference, $\pm\pi/2$, between the solitons. As a consequence, the soliton pair moves with respect to the single soliton, with non-zero group velocity, as proved by (5). When a two-soliton bound state and a single soliton exist simultaneously, they necessarily will collide at some point. The result of the collision depends mainly on the phase difference, ϕ, between the pair and the single soliton, as this is the only parameter in the initial condition provided that the soliton pair is exactly at one of the points F_i of Fig. 1. If a bound state is not reached before the collision, the result will also depend on where the point is located on the trajectory that converges to the bound state.

Below, we present numerical simulations of collisions between a soliton pair at the point F_1 and a single soliton, as they have been computed in [39]. Due to the symmetry of (1) relative to the transformation $t \rightarrow -t$, the same collision occurs when the soliton pair is at F_2. This simply requires a change from $\psi(t)$ to $\psi(-t)$. The pair denoted by F_1 moves to the right. Hence, in order to collide, the single soliton must be located at the right-hand side of the pair.

In all plots, the numbers 1, 2, and 3 are assigned to the solitons, labeling them from left to right (see Fig. 8). In this section, solitons 1 and 2 initially form the stable pair. Soliton 3 is initially well separated from the pair, so that there is no interaction

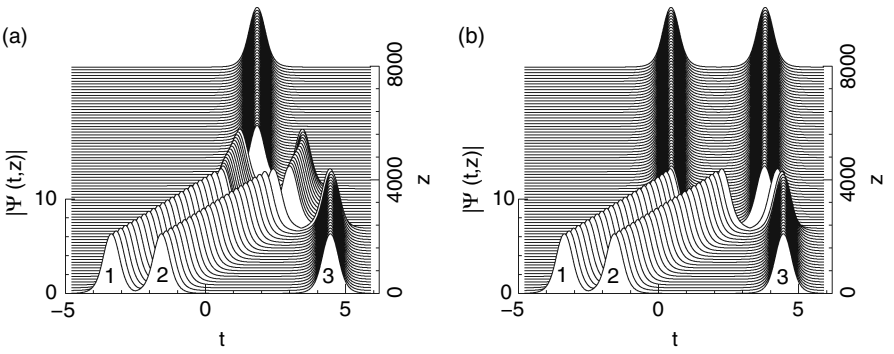

Fig. 8 Collision of a two-soliton bound state with a single soliton. This case illustrates "soliton fusion" or "annihilation". Depending on the initial phase difference between the bound state and the single soliton, the output is either (**a**) one or (**b**) two weakly interacting solitons

with it. Nevertheless, a plot of the separation between the solitons 2 and 3 and the phase difference between them on the interaction plane can be made in the same way as that for solitons 1 and 2. This plot will represent the interaction plane of the initial conditions for the pair and a single soliton before the collision. As the pair is initially located at the point F_1 of Fig. 1, the interaction plane of the solitons 2 and 3 is a convenient way to classify the collisions in the continuous model.

A few scenarios for the collision are possible. One possible scenario is the complete destruction of the bound state, resulting in soliton fusion. Of the three solitons in the initial condition, one or two may disappear. The result after the collision would be just one or two solitons at a separation where they interact weakly – as a result, they have zero velocity. These two examples of collisions are shown in Fig. 8.

The second scenario that can be observed is the merging of all solitons into a three-soliton bound state, which can be of two different types (which can be referred as "cis" and "trans" triplets [40]). They are shown in Fig. 9. In case (a), the phase differences between consecutive solitons are $-\pi/2$ and $\pi/2$, respectively. The resulting three-soliton bound state is an oscillatory solution, so each soliton changes its position and relative phase periodically around fixed values. After the collision, the corresponding resultant trajectory for solitons 1 and 2 on the interaction plane, as well as the trajectory for solitons 2 and 3, converges to a periodic orbit (limit cycle) around the points $(\rho, \phi) = (1.8, \pm\pi/2)$ respectively. In case (b), the phase differences between successive solitons are both $\pi/2$. In this case, the corresponding trajectories on the interaction plane, after the collision for solitons 1 and 2, and 2 and 3, converge to fixed points which are very close, but they do not coincide exactly with the point F_1. The bound state of three solitons moves with a velocity which is almost equal to the velocity of the pair.

The last possible scenario obtained in the continuous model is the destruction of the initial pair and the formation of a new soliton pair after the collision, with an exchange of the soliton in the middle. This case is shown in Fig. 10. This case is referred to as an "elastic-type collision". This scenario of collision may seem to correlate with the laws of classical mechanics, where two particles of the same mass moving in one direction collide with a third one, resulting in motion of the third

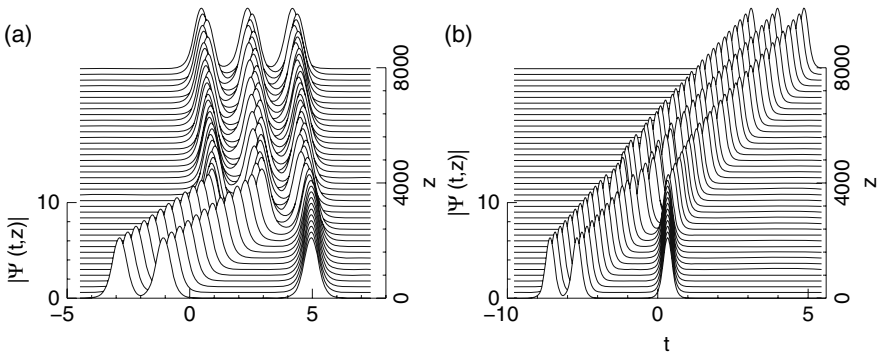

Fig. 9 Two possible cases of formation of a three-soliton bound state, or "triplet formation", after the collision of a soliton pair with a single soliton

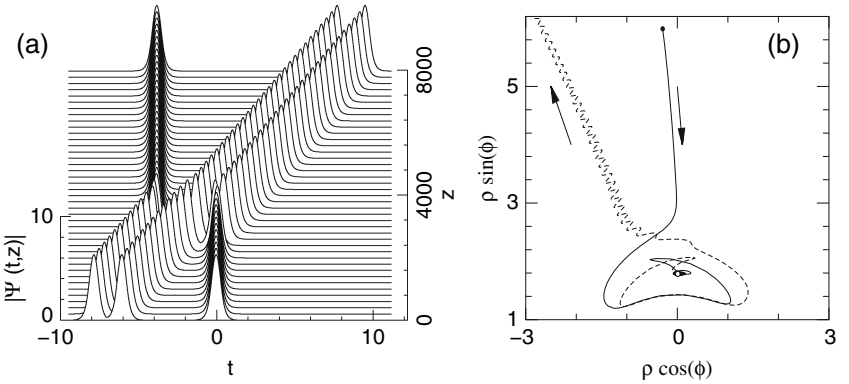

Fig. 10 (**a**) Exchange of a soliton in a bound state after the collision of a soliton pair with a single soliton. (**b**) Trajectories on the interaction plane for solitons 1–2 (dashed line) and 2–3 (solid line). The black solid dot represents the initial point for the separation and phase difference between the pulses 2–3. The circle at the point F_1 is the initial point for the pulses 1–2 and the final point for the pulses 2–3. The first trajectory is pushed out of the point of equilibrium after the collision. The second trajectory is attracted to the point of equilibrium after the collision

particle, along with one of the incident ones. However, there are no conserved quantities such as momentum or energy in a dissipative system. Moreover, the binding energy of solitons is non-zero. On the other hand, we know that stationary solutions must be fixed. Therefore, the difference in velocities between the pair and the singlet is fixed and must be the same before and after the collision. This is the main reason for the results with "elastic collisions" of dissipative solitons shown in Fig. 10.

Figure 10(b) shows the separations and phase differences between the solitons on the interaction plane, before, during, and after a collision. The solid line is for solitons 2 and 3, while the dashed line is for solitons 1 and 2. The solid curve ends up at the point F_1, while the dashed line starts at this point, thus indicating that the pair formed by solitons 2 and 3 is exactly the same as the initial pair formed by the solitons 1 and 2.

Due to the fact that dissipative solitons are fixed, the outcome is always an integer number of solitons with fixed amplitude and velocity. Therefore, qualitative considerations lead us to the conclusion that no other scenario of collision between a pair and a singlet is possible. This would be the conclusion for any other set of parameters of the CGLE where stable soliton pairs exist.

A summary of these results is presented in Fig. 11. Initially, the point on the interaction plane for solitons 2 and 3 is located far away from the origin at a fixed distance (≈ 6) in all our simulations. For the relative phase difference, ϕ, we choose 36 values, with 10 degrees angular difference between neighbors. All 36 initial points are shown as small dots in Fig. 11. In this way, we cover a circle of initial conditions on the interaction plane in a relatively dense way. Each of these initial conditions leads to one of the outcomes that we described above. The simulations allow us to establish a correspondence between the angular position of the initial point and the result of the collision.

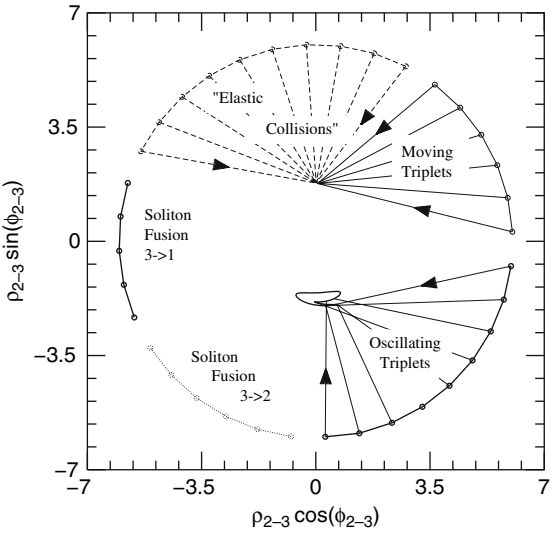

Fig. 11 Schematic of the evolution of solitons 2 and 3 on the interaction plane according to their initial phase relationship. The result of the collision of the soliton pair 1–2 with the single soliton 3 depends on the relative phase between the solitons 2 and 3 before the collision. This plot shows the outcomes of the collision for 36 initial conditions, which are represented by small dots on a circle of radius ≈ 6. The values of the equation parameters for these simulations are the same as those in Fig. 1

Specifically, the points in the lower left quadrant result in the annihilation (or fusion) of one or two solitons. This is indicated in the figure close to each set of initial conditions. This evolution is similar to the examples presented in Fig. 8. Fusion to a single soliton occurs when the initial point is in the upper part of this quadrant. Fusion of three solitons into two occurs when the initial point is in the lower part of this quadrant.

The rest of the circle of initial conditions can be divided into three arcs, depending on the collision outcome. The final and initial points in this plane are joined schematically by the straight lines. These are not the actual trajectories. The trajectory may rotate around the origin before the collision. We obtain oscillating soliton triplets (as in Fig. 9(a)) when the initial point is in the lower right quadrant of the interaction plane. As indicated in that figure and mentioned above, the final state in these cases is a limit cycle, rather than a point. Moving soliton triplets (as in Fig. 9(b)) are obtained when the initial point is in the upper right quadrant. Finally, an "elastic collision" (similar to that in Fig. 10(a)) occurs when the initial point is in the upper part of the circle. This last case is well illustrated by Fig. 10(b).

If we select an initial distance between the solitons 2 and 3 which is different from the value 6, the whole circle of initial conditions may rotate around the origin, thus moving our classification scheme around. However, the relative locations of the various outcomes of the collision will remain unchanged.

In [39], a comprehensive numerical study was also undertaken with a CGLE model with parameter management. In addition to the cases found with the distributed CGLE, as presented above, the existence of an additional type of soliton pair gave a few additional collision cases, such as reflection of a doublet by a singlet, thus clearly manifesting inelastic behavior. This reflection case was reported experimentally in [41].

3 Pulsations of Dissipative Solitons

The existence of pulsations is linked to dissipative nonlinear dynamics. The most direct example in optics is the passively mode-locked laser [42] which produces a train of ultra-short pulses. Other examples include parametric oscillators [43] and spatial soliton lasers. All of these devices, within certain approximations, can be well described by the complex Ginzburg–Landau equation. As discussed above, this equation has all the essential elements needed to describe the main influences on the optical field, namely dispersion (or diffraction), nonlinearity, linear and nonlinear gain/loss, and spectral filtering.

A comprehensive balance between all these effects results in solitons which have a wide variety of shapes and a rich dynamical evolution. This richness is in striking contrast to soliton dynamics in Hamiltonian systems, where the only balance is between nonlinearity and dispersion. This produces simple bell-shaped pulses or beams. One of the manifestations of this complexity is self-pulsations – pulses evolve in time, either periodically or in a more complex way [44]. However, they remain as localized solutions all the time, as required for solitons. The variety of these objects is considerable, and more examples are presented in [26].

At first glance, pulsating solutions may seem to be trivial generalizations of higher-order solitons, or "breathers" in integrable systems [45], but such a comparison is deceptive. Breathers are nonlinear superpositions of several solitons of an integrable system, and, with any disturbance, they tend to split into their constituents or transform into a single soliton [1]. On the other hand, in a dissipative system, a pulsating soliton can be considered as a single robust object, which nonetheless has its own internal dynamics.

Pulsations in a distributed model governed by a single CGLE [26, 44] occur with intrinsic periods that cannot be related to any cavity length. In order to overcome the limitation of the distributed model, we here consider a parameter-management CGLE model which explicitly incorporates the cavity periodicity of the laser. Thus, in the rest of Sect. 3, a simple laser model, composed basically of two parts, is used. Propagation in the first part is modeled by the full CGLE equation, which stands for the gain medium plus the passive mode-locking element. The dispersion in this section of the cavity is normal ($D < 0$) and the length of the section is L_D. The second part corresponds to dispersion compensation alone, and is ruled by linear propagation in a dispersive link of normal dispersion $d > 0$ and length L_d. The equation in this part is linear, and therefore the only relevant parameter is the product (dL_d).

3.1 Short-Period Pulsations

Short-period pulsations are pulsations whose period is comparable with the round-trip time. When this period coincides with the round-trip time, the laser is in a stable regime of pulse generation, i.e., it produces exactly the same pulse each round-trip,

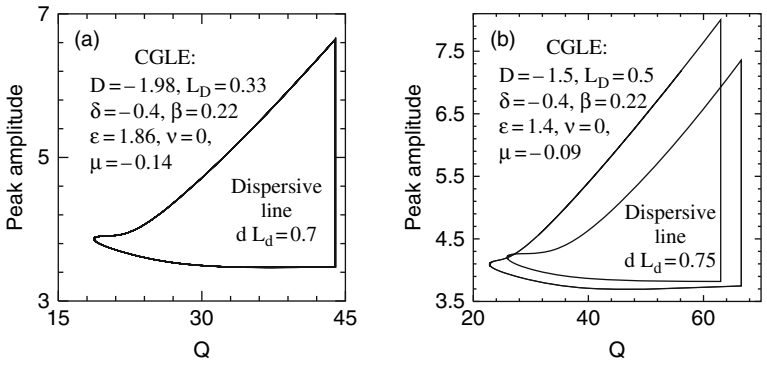

Fig. 12 Peak amplitude versus energy, Q, for (**a**) a period-1 solution as it evolves during one round-trip inside the cavity. The vertical part of this trajectory corresponds to the propagation during the purely dispersive stage. (**b**) Trajectory repeats after twice passing through the laser cavity. The parameters used in the simulation are written inside the figure

as illustrated numerically in Fig. 12(a). This figure shows the soliton peak amplitude versus the energy, Q, of the pulse as it evolves during one round-trip inside the cavity. After each round-trip, the trajectory returns exactly to the initial point. For any arbitrary initial soliton parameters, the trajectory is out of this loop, but converges to it after a number of round-trips. Hence, according to the common terminology used in nonlinear dynamics theory, the loop is a stable limit cycle. As in the rest of this section, any transitory evolution needed to reach the solution from arbitrary initial conditions has been removed from the plot.

In contrast to this dynamical evolution, which has the same periodicity as the cavity round-trip time, other regular dynamical forms may arise when one changes the cavity parameters. The case of a period equal to two round-trip times is shown in Fig. 12(b). The model parameters that cause such a transformation are shown in the figure. As a rule, the period-1 pulsation becomes unstable, but the cycle with two loops becomes stable instead. This phenomenon is known as a period-doubling bifurcation.

3.1.1 Bifurcations in the Parameter-Management CGLE Model

Phenomena known as period-doubling and period-tripling can occur in mode-locked lasers [46, 47]. In general, a "period-N" solution is one whose shape is restored after N round-trips. The model used here provides pulsating behaviors with virtually any integer number, N. The appearance of these dynamical types follows specific bifurcations, as presented below.

In the example shown in Fig. 12, several parameters were changed in order to obtain period-doubling. In many cases, only one of the parameters needs to be

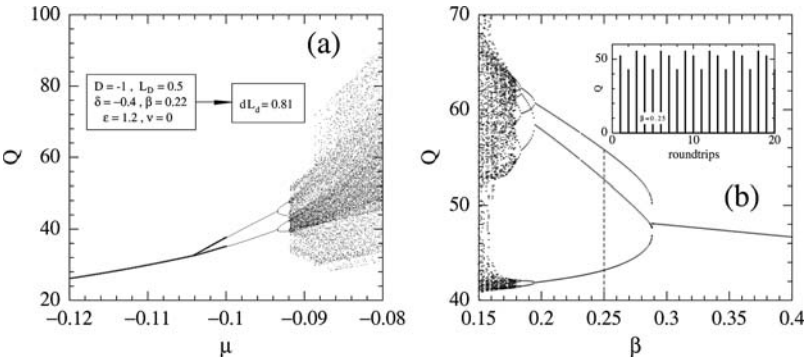

Fig. 13 Output energy, Q, monitored at the end of the amplifying stage as a function of (**a**) μ and (**b**) β. (**a**) shows a sequence of period-doubling bifurcations in the parameter-managed laser model. The parameters are shown in the inset. (**b**) shows a period-tripling bifurcation. The inset shows the pulse energy versus the number of round-trips for the period-3 solution at $\beta = 0.25$. The parameters of the simulations, apart from β, are shown in the inset in Fig. 14(a)

varied to have a bifurcation or even a sequence of bifurcations. For instance, if the gain saturation, μ, is chosen as a variable parameter, one can also observe period-quadrupling. A diagram showing a sequence of period-doubling bifurcations is presented in Fig. 13(a). Period-4 appears at a value of $\mu \approx -0.093$. A further change of μ gives period-8 solutions and chaotic evolution of pulses at around $\mu = -0.092$. The whole sequence of period-doubling bifurcations exists but cannot be resolved on the scale of Fig. 13(a). A similar evolution can be observed with a continuous change of other system parameters, but, depending upon the choice of the parameter used as a variable, one can get a more complicated sequence. In particular, a diagram with the period-tripling bifurcation is shown in Fig. 13(b). In this case, when changing the spectral filtering parameter, β, we have a transition directly to the period-3 solution, rather than to the period-2 one at the bifurcation point. The bifurcation occurs at $\beta \approx 0.288$. When further reducing the parameter β, we obtain a transition to a period-6 solution. A further reduction in β leads to chaotic solutions, after a series of bifurcations with period multiplication.

The trajectory in the (Q, *Peak Amplitude*) space for the case shown in the inset of Fig. 13(b) is presented in Fig. 14(a). It shows the evolution of a pulsating soliton whose period covers three cavity round-trip times.

The form of the bifurcation diagram depends on the trajectory in the parameter space chosen in the simulations. In the two cases presented above, all the parameters except one (μ or β) were fixed. This is the easiest way to change parameters in the simulations. Experimentally, changing the configuration may cause the simultaneous variation of several parameters. Then, the trajectory in the parameter space would be more complicated. Each route would create a specific bifurcation diagram, so that extensive mapping of all possible bifurcation diagrams does not seem possible.

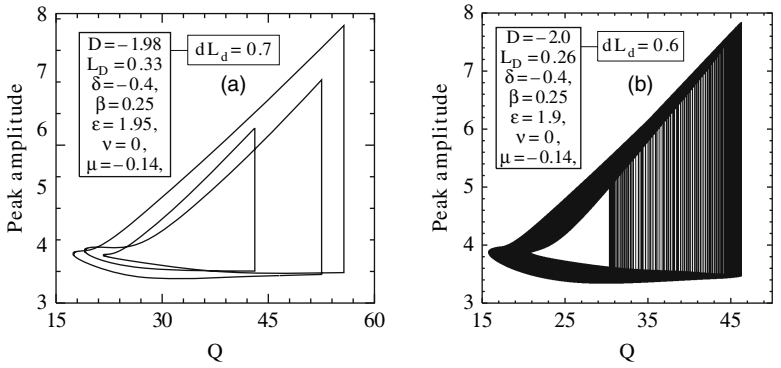

Fig. 14 (**a**) Period-3 pulsation. (**b**) Period-3 loop with an additional "long-period" modulation for multiple passes of the laser cavity

3.1.2 Experimental Observations and Additional Features

The aim is to observe "pulsating waveforms", namely pulsations of the intensity of the ultra-short pulses generated in the mode-locked laser. Starting from stable single pulse mode-locking, the experimentalist has the latitude to slightly vary one or several cavity parameters, so as to remain in the mode-locked regime while adding new dynamical features. If we consider the setup of Fig. 2, the experimentalist can, for instance, change the orientation of the mode-locking wave plates. This results in an alteration of the whole nonlinear transmission function of the open-air section. From a numerical point of view, this is different from varying one single parameter at a time. The experimentalist can also tune the amount of loss related to the orientation of the half-wave plate preceding polarizer P2. For example, starting from a stable, period-1, single pulse and a value of 20% loss due to the variable output coupler, a reduction of that loss leads to the sequence of period-2 and period-4 bifurcations represented in Fig. 15(a). The bifurcation points are resolved at transmission values of around 0.9 and 0.97. The real-time observation of a period-2 pulsation is displayed in Fig. 16(a).

Comparisons between experiment and numerical simulations are consistent when only a single pulse is circulating in the cavity. For two or more pulses, the model should be modified to take into account gain saturation, which depends upon the total energy inside the laser cavity [18]. It is well known that multiple pulsing and the formation of multi-soliton complexes can be favored in the cavity when the intracavity energy is increased [12, 28]. Multiple pulsing can be seen as a possible way of restoring the energy balance in the cavity and stabilizing the laser operation.

An example of this type, which relates a change of the mode of the laser operation to an increase in pump power, is shown in Fig. 15(b). When the pumping power is increased up to 140 mW, period-2 oscillations appear. These exist at higher power levels. However, at $P = 200\,\mathrm{mW}$, instead of a continuation of the period-doubling cascade, a bound soliton pair, or doublet, is formed, as revealed by the analysis of

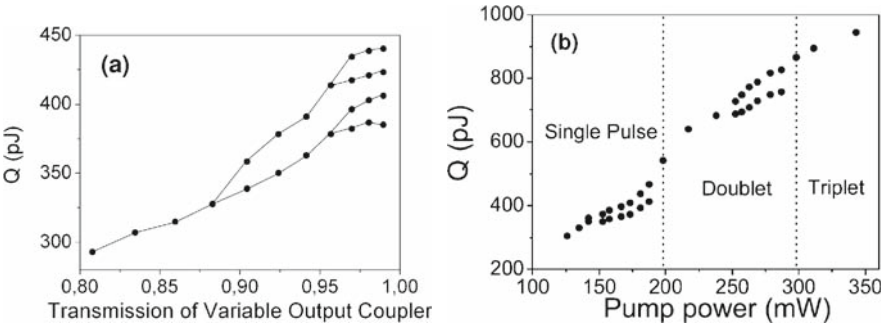

Fig. 15 (**a**) Experimental bifurcation diagram revealing period-2 and period-4 dynamics in the single pulse case. (**b**) Bifurcation diagram showing the formation of doublet and triplet multi-soliton states, in addition to period-doubling

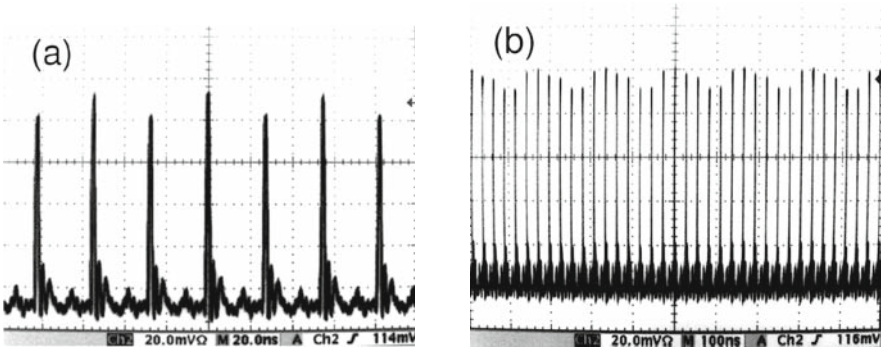

Fig. 16 Experimental observation of (**a**) period-2 and (**b**) period-6 pulsations in the single pulse case. The round-trip time is the same in the two figures, namely 27.5 ns, and the time interval per division is set at 20 ns on (**a**) and at 100 ns on (**b**)

the optical spectrum and optical auto-correlation (see Sect. 2). At the same time, period-2 oscillations disappear.

The interpretation of this phenomenon is as follows. The increase of the intra-cavity energy causes the instabilities described above. However, large instabilities are avoided due to the sharing of intra-cavity energy between several pulses that are bound together [33]. This observation of stabilization through additional pulse formation was also reported in [47], where a simple recursive model was given to explain that dynamical behavior.

Dynamical behavior with periods other than 2 and 4 can also be observed. Period-3 pulsations and period-6 pulsations are easily observed formations. Figure 16(b) shows an example of period-6 pulsations that appears in the sequence with a period-tripling bifurcation. This observation is a qualitative analog of the numerical solutions obtained for the values of β in the interval [$\approx 0.184, 0.196$] in Fig. 13 (b).

When several pulses per round-trip are involved, additional combinations of pulsations can be observed. For instance, when two pulses are regularly spaced in the

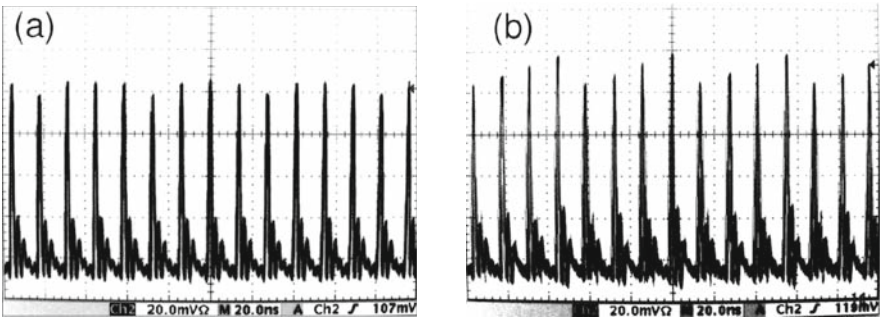

Fig. 17 Observation of two possibilities of period-4 pulsations for harmonically mode-locked laser regime with two pulses per round-trip. Compared with Fig. 16, the repetition rate has been doubled. The change from (**a**) to (**b**) is triggered by a slight adjustment of cavity losses

cavity, i.e., they are harmonically mode-locked, the cavity repetition rate is doubled and this situation can also lead to multiple-period pulsations. An example is provided in Fig. 17, with two options for period-4 pulsations.

It is almost impossible to perform a complete mapping of bifurcations with respect to cavity parameters. When one follows the bifurcation diagram with respect to the variation of a given cavity parameter, the type of bifurcation can be dramatically different after another parameter is changed. To give an example, starting from the bifurcation case displayed in Fig. 15(a), if the quarter-wave plate preceding the polarizer P1 is rotated by 5 degrees, the variation of the transmission of the output coupler leads to the new bifurcation diagram displayed in Fig. 18(a). An abrupt transition to a longer-period pulsation is found, instead of a period-doubling cascade. Then, at a transmission value of 0.88, these pulsations disappear, along with the creation of a soliton pair. An illustration of a real-time observation, corresponding to a transmission value of 0.8, is shown in Fig. 18(b). The period is close to 18 round-trips, which looks unusual. The explanation for the existence of such a pulsation is provided in Sect. 3.2.

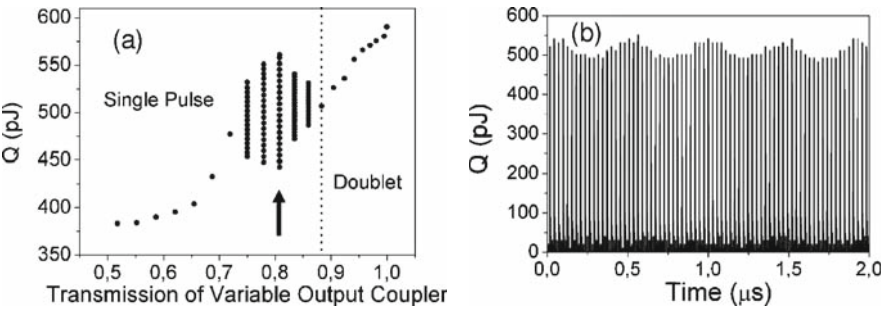

Fig. 18 (**a**) Experimental bifurcation diagram showing abrupt transition to pulsations of longer period. The pulsation that corresponds to the location of the arrow is illustrated in (**b**)

3.2 Long-Period Pulsations

"Long-period pulsations" are pulsating solutions that have a period much longer than the round-trip time. As a rule, the period in this case is not an integer multiple of the round-trip time, although it can become commensurate with it after a careful adjustment of the system parameters.

3.2.1 Pulsating Solitons in a Laser Model with Parameter Management

There are many types of long-period pulsations. One example is shown in Fig. 19(a). The pulse is asymmetric at any particular value of z. As a result, it moves with a velocity that changes sign over a pulsation period. The pulse profile also changes continuously – it splits into two but then these recombine. In spite of such complicated behavior, the pulse retains the same position in t, on average. The total period of the pulsations in this example is $N \approx 38$. The pulse changes its symmetry relative to the transformation $t \to -t$ after approximately 19 round-trips. As a consequence, the energy, Q, plotted versus the number of round-trips (presented in Fig. 19(b)) shows a periodicity that is ≈ 19. Despite complicated shape transformations, the evolution of the energy is almost harmonic. This means that the parameters of the system are not far from the bifurcation point where we have the transition from stationary to pulsating solitons.

Another example of a pulsation with a period of approximately 11 round- trips is shown in Fig. 20(a). This solution alternates between moving to the left and to the right, periodically changing its velocity and position. The evolution of its spectrum is shown in Fig. 20(b). The average velocity is zero in this case. However, if we choose different parameter values, we can observe a non-zero average velocity and then the pulsating soliton will permanently move in a certain direction [48].

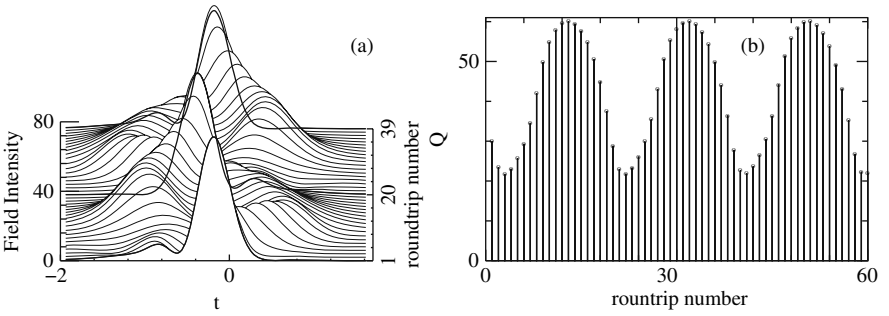

Fig. 19 (**a**) An example of long-period (≈ 38 round-trips) pulsation. The plot shows the evolution of the pulse profile. Pulse profiles at $N = 1$, 20, and 39 are plotted with thicker lines for the sake of comparison. The parameters for this simulation in the nonlinear section of the laser are: $L_D = 0.059$, $D = -3.0$, $\varepsilon = 2.0$, $\delta = -0.4$, $\beta = 0.25$, $\nu = 0$, and $\mu = -0.12$. In the linear section, $dL_d = 0.254$. (**b**) Pulse energy versus the round-trip number for the same case

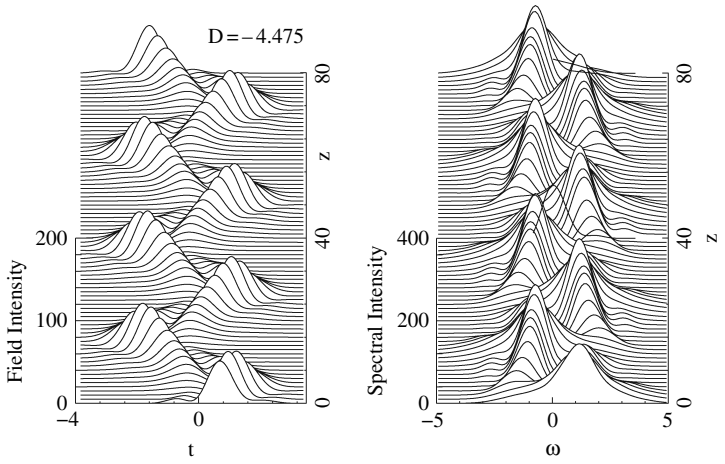

Fig. 20 (**a**) An example of soliton pulsations with velocity beating. (**b**) Evolution of the soliton spectrum. The parameters for this simulation in the nonlinear section of the laser are: $L_D = 0.3$, $D = -4.475$, $\varepsilon = 1.6$, $\delta = -0.4$, $\beta = 0.15$, $\nu = 0$, and $\mu = -0.18$. In the linear section, we have $dL_d = 1.6$

The variety of possible pulsating solutions is considerable, and they occupy appreciable regions of the seven-dimensional parameters space. The pulse can periodically change its profile, chirp, and group velocity and also oscillate back and forth relative to its average position in the moving frame of reference. All general types of pulsating solutions obtained with the continuous model [44, 26] can be obtained with the parameter-managed CGLE. However, in each model, each type of solution has its own specific characteristics. Pulsation periods of up to a few hundred round-trips can be obtained in the simulations. There is no doubt that pulsations with longer periods also exist. The pulse energy modulation can be changed over a wide range, reaching values of up to 60% (see Fig. 19(b) and Fig. 21 below).

At the point of transition, when the pulsations are weak, they are close to simple harmonics. However, when the amplitude of the pulsations become larger, they

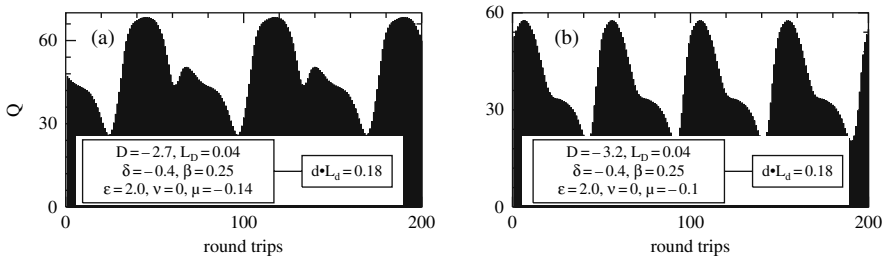

Fig. 21 Soliton energy, Q, versus the number of round-trips for two cases of pulsations with a large amplitude. Their set of parameter values are shown in the insets

contain higher-order harmonics. Two examples are shown in Fig. 21. These correspond to well-developed pulsations which are far above the bifurcation from stationary solitons.

3.2.2 Experimental Observations

In a mode-locked fiber laser with typical pulse duration below 500 fs at a repetition rate of several tens of MHz, it would be hard to observe all the features of the pulse transformation in z experimentally. It is a very difficult task to accurately characterize a pulse when it changes its parameters. However, one can follow the periodic changes of the pulse energy from oscilloscope traces, and these show that long-period pulsations certainly exist.

It is important to distinguish between long-period pulsations that develop in a medium with an instantaneous response, as simulated above, and pulsations that rely on finite relaxation times linked to the laser gain medium, since these are not taken into account in the model. Relaxation pulsations in the mode-locking regime, also called "Q-switch" mode-locking, are well known to laser physicists. In particular, they develop in cavity designs which incorporate semiconductor-based saturable absorbers, where they present a limitation to power scalability. These pulsations are indeed characterized by a long period, but also by a strong and asymmetric modulation of nearly 100%, and are accompanied by an excess of intensity noise [49].

Below are a few examples of long-period pulsations, recorded with the experimental setup of Fig. 2, that do not belong to the category of "Q-switch" mode-locking, although some interplay between the nonlinear dynamics, as simulated above, and the gain medium relaxation times cannot be strictly ruled out.

In a stable regime of laser operation, monitoring the output intensity displays the amplitude peaks that repeat at the cavity fundamental frequency of 36.6 MHz, as shown in Fig. 5(a). In order to observe long-period pulsations in the experiment, one of the four wave plates used to obtain mode-locking is shifted. This affects the whole nonlinear loss function in the cavity, since it is related to the values of the coefficients δ, ε, and μ in the CGLE model. In this way, single-pulse mode-locking is maintained, while significant pulse changes from one round-trip to the next are achieved.

Long-period modulation of the output pulse energy is thus obtained, and, after entering this regime, an increase of the soliton energy modulation can be achieved either by increasing the pumping power or by a subsequent tuning of the mode-locking wave plates. When the modulation amplitude is small, it appears as a sinusoidal modulation. This is illustrated by the recording in Fig. 22(a), which reveals a pulsation close to period-26. In the majority of the experimental arrangements, larger soliton energy modulations would correspond to longer periods.

When the soliton energy modulation is high, it follows a more complicated non-sinusoidal evolution. This is illustrated by the oscillogram in Fig. 22(b). These results are in qualitative agreement with numerical simulations that show complicated but periodic behavior. Much longer periods, of the order of 10^3 cavity round-trips, have been achieved experimentally. Two examples are shown in Fig. 23(a, b). It also shows the transition from a close-to-sinusoidal modulation to a non-sinusoidal modulation.

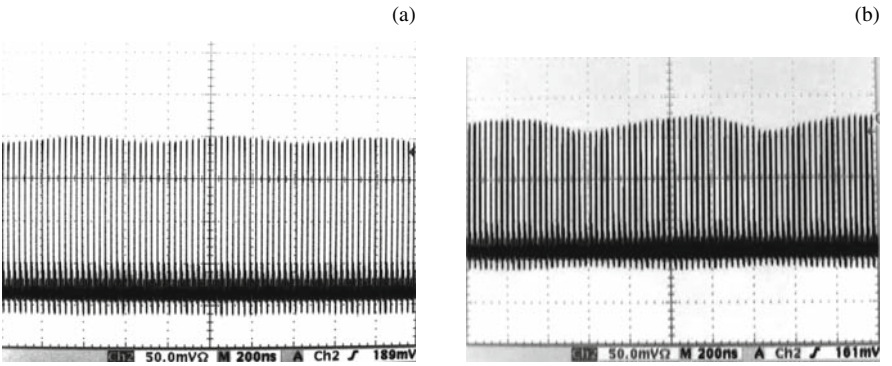

Fig. 22 Two examples of long-period pulsations for single pulse operation. (**a**) Pulsations with small energy modulation and with a period ≈ 26 round-trips. (**b**) Pulsations with a larger soliton energy modulation (with period ≈ 32 round-trips), which depart from a sinusoidal modulation

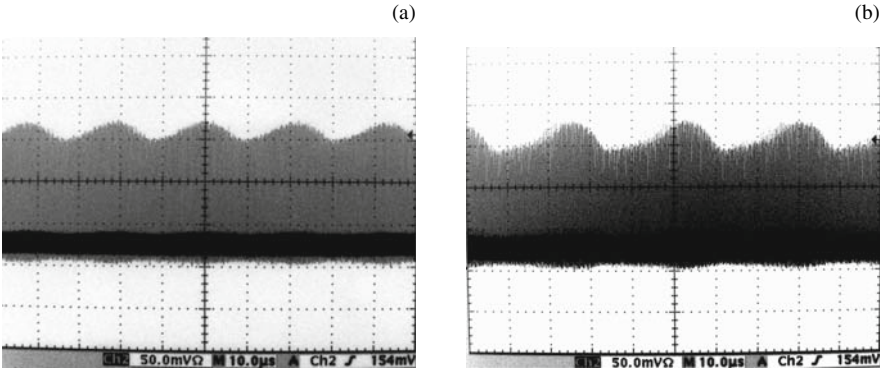

Fig. 23 Two more examples displaying pulsations of longer period. (**a**) The period is around 815 round-trips and (**b**) the period is around 910 round-trips

Very large soliton energy modulations lead to the complete disruption of the single pulse mode-locking regime. The laser either enters a multi-pulse regime of generation or the pulses in each round-trip become so unstable that mode-locking is disrupted. However, the range of parameters where periodically modulated pulse generation exists is very large, and it is comparable with the range where stable pulse generation exists.

3.3 Double Periodic Pulsations

Pulsations become complicated when two periods of oscillation are involved in the dynamics. A large variety of such solutions can be found numerically. In the following, only the simplest examples are provided.

3.3.1 Double Period Pulsations in the Model with Parameter Management

Figure 24(a) is an example of one of the possible bifurcation diagrams which leads to double periodic pulsations. It shows the values of the output energy, Q, as a function of ε. For the specified set of parameters shown in the inset of this figure, the period-1 solution is stable for $\varepsilon > 1.332$. A bifurcation to the period-2 solution occurs at around $\varepsilon \approx 1.332$. The period-2 solution exists below this value all the way down to $\varepsilon = 1.25$. There are two other bifurcations at $\varepsilon \approx 1.292$ and $\varepsilon \approx 1.33$, delimiting a wide area of seemingly chaotic solutions, where a diversity of Q values can be obtained, rather than two fixed values. In fact, in this latter region, we have quasi-periodic soliton evolution with two incommensurate periods.

The soliton energy versus the round-trip number for one of these solutions is plotted in Fig. 24(b) using thick vertical lines. This plot clearly shows the double periodic nature of the solution. After each round-trip, the Q value jumps from a low (high) value to a high (low) value, as it should for period-2 solutions. In addition, the upper and the lower Q-values oscillate with a longer period (approximately 18 round-trips). The longer period is not exactly a multiple of the round-trip time, thus creating the region of seemingly chaotic motion in Fig. 24(a). The additional period and the amplitude of pulsations vary in the interval between the two bifurcations.

Virtually any imaginable combination of long and short periods in the dynamics can be realized with a proper choice of system parameters. New periods appear and disappear at bifurcation points which are similar to those in Fig. 24(a). Figure 25(a) is another example of a bifurcation diagram. It shows a bifurcation from a single period to a short period-3 solution. In fact, the period-1 can be seen clearly in the region below $D \approx -1.32$. A period-3 solution exists in the interval $-1.05 < D < -0.92$. In

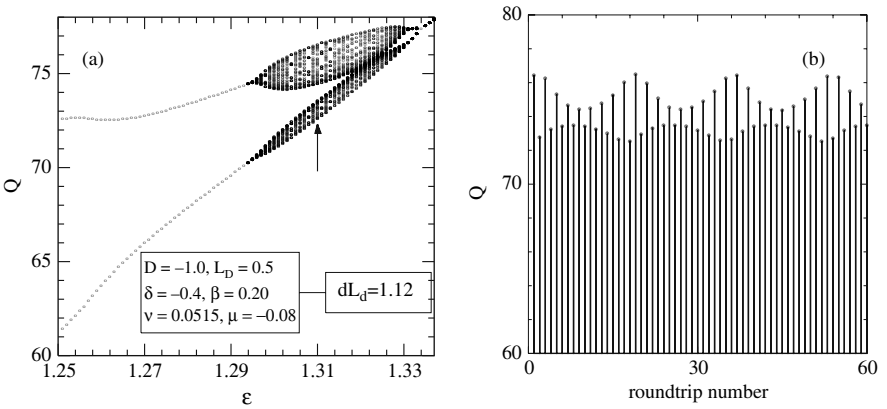

Fig. 24 (**a**) The total soliton energy, Q, versus ε. The inset gives the values of other parameters used for the simulations. This diagram shows the period-doubling bifurcation at $\varepsilon \approx 1.332$. Bifurcations leading to additional long-period pulsations occur at $\varepsilon \approx 1.33$ and $\varepsilon \approx 1.292$. (**b**) Q versus round-trip time for the period-2 solution with an additional long-period pulsation. The value of ε chosen for this case is 1.31 (marked by the arrow in (**a**))

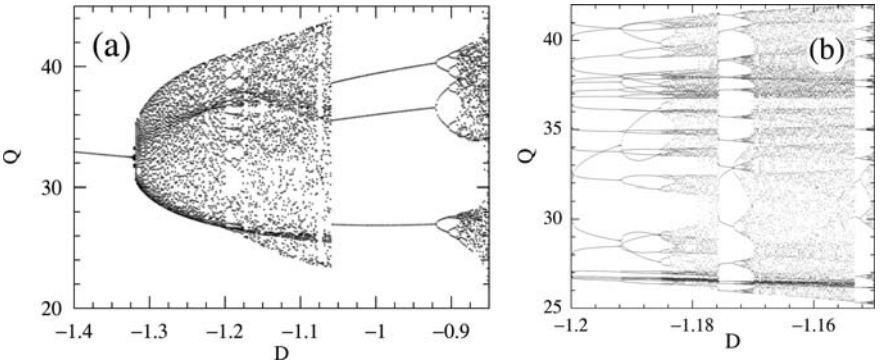

Fig. 25 (**a**) Bifurcation diagram showing a period-tripling bifurcation with an additional long-period pulsation. The parameters of the simulation are $L_D = 0.35$, $\beta = 0.25$, $\delta = -0.4$, $\varepsilon = 1.8$, $\nu = 0$, $\mu = -0.15$, and $dL_d = 0.6$. (**b**) Part of the bifurcation diagram that shows "synchronization"

between these two regimes, we can see a wide area of soliton evolution with a continuous range of output energies, Q. This area corresponds to quasi-periodic soliton evolution, with two incommensurate periods involved in the dynamics.

Double periodicity also appears in Fig. 14(b). This plot was calculated for a different set of parameters but had the same properties – pulsations occur with a combination of a period-3 and a long-period modulation. The triple limit cycle, similar to the one shown in Fig. 14(a), is shifted each round-trip by a small amount defined by the longer period of pulsations. The final result is this "attractor" which fills the triangular "donut". We stress that such motion is not chaotic, but quasi-periodic.

The long periods are generally incommensurate with the short ones. However, for some range of parameters, a "synchronization" of the two frequencies may occur. Then, a period which is an integer multiple of 3 can be observed. An example of such synchronization can be seen in Fig. 25(a) in a small window in the region $-1.2 < D < -1.19$. The soliton energy takes discrete values, rather than an arbitrary value from the continuous range. This can be seen clearly if we plot the same figure with a higher resolution (see Fig. 25(b)).

3.3.2 An Experimental Observation of a Double-Period Pulsation

Not every dynamical form obtained numerically can be easily observed in the experiment. This is related, in part, to the fact that some external parameters of the laser system cannot be changed continuously. As a result, some of the regions of parameter space cannot be reached in the fixed arrangement of the setup. Nevertheless, some of the double periodic motions have been experimentally observed in [50]. Figure 26 illustrates period-doubling with an additional pulse energy modulation. Here, the same pattern is repeated every ≈ 32 round-trips. This long-period pulsation exists on the top of the period-doubling modulation and is generally incommensurate with the period-2.

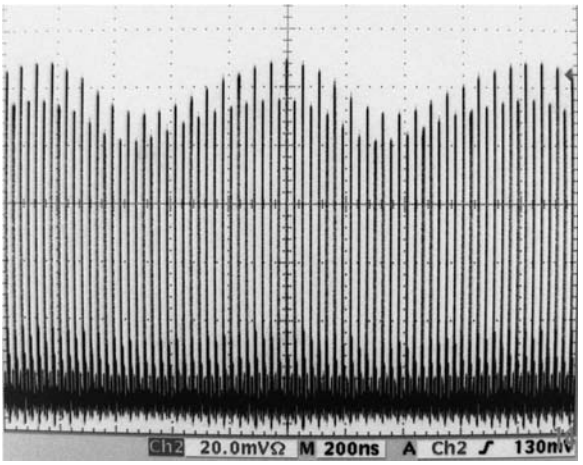

Fig. 26 Experimental oscillogram showing a sequence of laser output pulses with combined period-doubling and long-period (≈ 32) pulsations

4 Vibrations of a Soliton Pair

While the previous section essentially dealt with pulsations of single dissipative solitons, we may wonder if pulsations of multi-soliton complexes are possible, and what forms they could take. In fact, in the case of three solitons, oscillating triplets were already predicted by the CGLE laser model, as mentioned in Sect. 2.3 (see Figs. 9(a) and 11). If we start with a soliton pair, the simplest pulsation that can be imagined can be seeded by the image of the natural pulsations of a diatomic molecule, namely, the vibrational states.

4.1 Indirect Experimental Evidence

A vibrating soliton pair would consist of two bound solitons, whose temporal separation and phase relationship oscillate with time. From the experimental point of view, this should be observable, at least indirectly, when considering the optical spectrum and the optical auto-correlation function. Indeed, as was shown in Sect. 2, these measurements are particularly sensitive to both the separation and phase relationship of the bound pulses. If the period of the oscillation, which is large compared to the cavity round-trip time, is small compared to the acquisition time of a data point, then the experimental recordings will present an averaging effect, which will reduce the contrast of spectral fringes and widen the cross-correlation peaks. This has recently been observed experimentally, as presented in Fig. 27, adapted from [51]. In the reported experiment, there were no visible oscillations of the total cavity energy, since the recording of the output pulses showed a similar aspect to that in Fig. 5(a). This is in marked contrast to the results of Sect. 3, where all pulsations had major influences on the function $Q(z)$. Compared with the single pulse

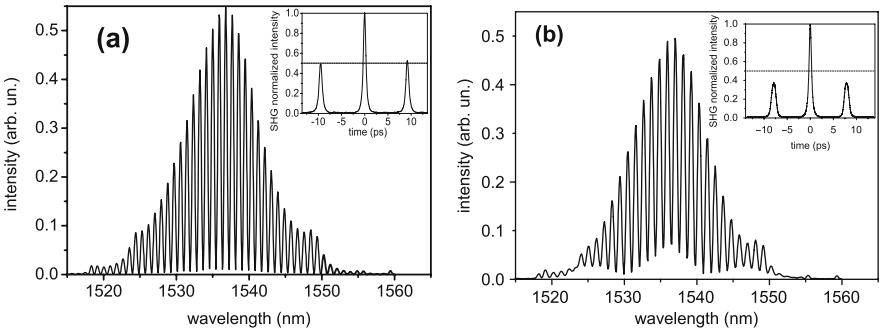

Fig. 27 Transition from (**a**) a stable soliton pair (pump power: 210 mW) to (**b**) a soliton pair with relaxed separation and phase relationships (pump power: 220 mW). The blurring of fringe contrast and the widening of auto-correlation side peaks are attributed to a vibrational motion of the soliton pair

case, a weakly bound soliton pair has internal degrees of freedom (separation ρ and relative phase θ) that could oscillate significantly without having much of an effect on the total energy, if the binding energy is relatively weak.

A loss of contrast in the spectral fringes can have several different origins. If pumping power is significantly increased, a wandering third pulse, with no phase relationship to the soliton pair, could be created. The contrast of fringes would then jump from nearly 100 to 67%, as in Fig. 6(a) [38]. A second possibility is that the two bound pulses become unequal. This would be detected from analysis of the auto-correlation trace and would also be in contradiction to the expected properties of dissipative solitons, which, in principle, have fixed energies for a given set of propagation parameters. A third possibility is that the phase relationship between the two solitons is loosened, and this would correspond to the case of dissipative solitons which are more weakly bound. It is very likely that Fig. 27(b) corresponds to this third possibility. Indeed, the auto-correlation trace (inset) shows a reduction of the amplitude of the side peaks, with, at the same time, a broadening of the side peaks. As the side peaks represent the cross-correlation between the two pulses, the broadening should correspond to time variation of the relative distance between the two solitons, as expected in the case of an oscillating soliton pair. Following this first experimental evidence, which is an indirect integrated measurement, time-resolved studies of the internal vibrational motions of soliton pairs could be designed. In the meantime, it is highly desirable to gain more insight from numerical simulations, as in the next section.

4.2 Vibrating Soliton Pair in the CGLE Model

Single pulse solutions of the CGLE are stable over wide regions of the parameter space. Stationary stable soliton pairs occupy sub-regions of considerably smaller

size inside the previous one [52]. The region of existence of pulsating solitons is also relatively small. In this respect, oscillating pairs seem to exist stably in very narrow areas in the 6D parameter space of the equation parameters.

Figure 28(a) presents a set of parameters of the CGLE where single-frequency oscillating soliton pairs are obtained. It shows the final state of the trajectories for two different pairs that start at the locations of the two black dots. Both trajectories converge to the central loop in the (ρ, θ) plane, after passing through either the darker region or the lighter one. This central loop represents the asymptotic limit cycle, and is located at the boundary between the light and dark gray regions. Once the limit cycle has been reached, the energy, or any other relevant quantity, evolves periodically, as Fig. 28(b) shows. The pulse profile evolution is displayed in Fig. 28(c). These oscillating pairs can be represented quite reasonably in a two-parameter space, as only the phase difference and the relative distance change in a visible way during evolution, while each pulse essentially keeps a fixed profile. There is no doubt that many other types of non-stationary, but stable, pairs can be found.

Various oscillating and vibrating soliton pairs have been found numerically very recently in the continuous CGLE model [53, 54], as well as in the more involved case of a (3+1) CGLE model [55].

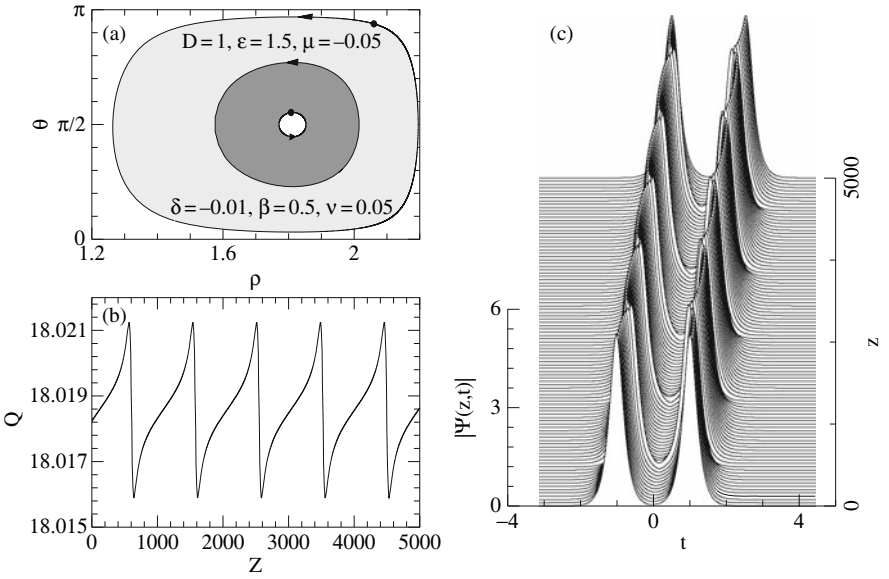

Fig. 28 (**a**) Trajectories in the (ρ, θ) space for two soliton pairs initially located at the black dots. After many loops, both trajectories converge to the closed orbit in the middle. (**b**) Evolution of the energy, Q, when the central loop is reached. (**c**) Pulse profile which more clearly shows the periodic vibration of the soliton pair asymptotic solution

4.3 Vibrating Soliton Pair in a Detailed Laser Model

The CGLE model, due to its simplicity, tracks the physical essence of the vibration of the soliton pair. However, to make a more precise comparison with the experimental results, one may need a more specific model that provides a better match with the experimental setup used in each case and whose parameters are directly related to the experimental control parameters. Therefore, more complete laser models, such as those in [25, 56], have been developed.

The aim is to understand how the relaxation of the time separation and the phase relationship between bound solitons can arise in the experiment, when a control parameter is changed. A previously developed laser propagation model, which is detailed in [56], has been used as the basis for the numerical simulations that have been performed in [51]. The model retains the essential features of the passively mode-locked fiber ring laser, namely nonlinear polarization evolution for passive mode-locking, as well as dispersion management with two types of fibers. The periodicity of the cavity is thus taken into account in an accurate way.

4.3.1 Hopf Bifurcations and Limit Cycles

Vibrating soliton pairs are observed numerically close to the domain of existence of the phase-locked soliton pairs that were obtained in [56]. The stationary regime consists of two solitons for which the temporal separation and the phase relationship oscillate. Qualitatively, the motion is an analog of that in Fig. 28(c), but the time scale of its dynamics, relative to the cavity round-trip time, is now revealed. Indeed, the period of the pulsation is much larger than the cavity round-trip time, being in the range of 10^3–10^4 cavity round-trips. In addition, the existence of quantized vibrational states is revealed, instead of there being just one vibrational state for each given set of cavity parameters. This is clearly shown in Fig. 29 – there is not one, but a full "necklace" of limit cycle attractors that correspond to different allowed averaged separations for the vibrating states for the same set of cavity parameters. This is a remarkable extension of the quantization of allowed separations found for soliton pairs in laser cavities [57].

In Fig. 29, the model parameters are the same as those used in creating Fig. 2 of [51], but the phase space has been enlarged to allow for the appearance of six limit cycle attractors. To create the picture, various initial conditions of soliton pairs (denoted by the large dots) were used. For all these initial conditions, the stationary regime corresponds to a given vibrating pair.

Such long-period pulsations are thus analogous to the long-period pulsations predicted and observed in Sect. 3, and do not need to rely on the gain relaxation dynamics. However, observation of a vibrating soliton pair is more difficult, since the vibrational motion is not associated with significant variations of the total cavity energy, in contrast to the case of a single pulse long-period pulsation. Indeed, the oscillation of the total energy has an amplitude which is typically lower than 10^{-4} times the average total energy. Due to technical 1/f noise in the sub-30 kHz domain,

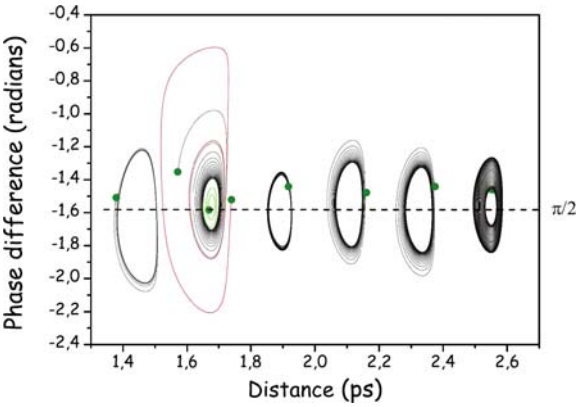

Fig. 29 Set of vibrational states that are simultaneously allowed in the laser model of [51], with $Q_{sat} = 0.6$ and $\theta = 64$ degrees. The diagram represents the phase relationship versus the temporal separation of the two solitons. Each vibrational state acts as a limit cycle that attracts neighboring initial conditions of soliton pairs. Initial conditions are represented by large dots

no corresponding peak in the RF spectrum could be clearly isolated in the experiment, although there was evidence of higher frequency vibrations. On the other hand, the vibrational motion has a direct influence on the averaged optical spectra and auto-correlation traces that can be recorded, since the limit cycle is stable.

As suggested by the experiments, the transition from a phase-locked soliton pair to a vibrating soliton pair is almost continuous when we change a model parameter such as the saturation energy (which corresponds to the pumping power in the experiment) or the polarizer angle. Indeed, Fig. 30(a) presents a super-critical Hopf bifurcation from a stable stationary soliton pair to a vibrating soliton pair, when the polarizer angle (which corresponds to polarizer P1 in Fig. 2) is decreased. Figure 30(a) was plotted following the first attractor on the left of Fig. 29, but the evolution of other attractors would present the same transition feature. An averaging of the optical spectra over the limit cycle for $\theta = 66$ degrees is shown in Fig. 30(c) – partial blurring of spectral fringes is clearly observed, in accordance with the experimental observation.

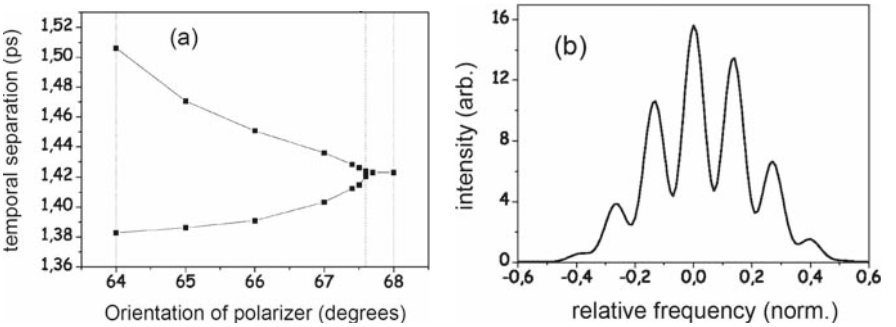

Fig. 30 (**a**) Super-critical Hopf bifurcation from stable stationary soliton pair to vibrating soliton pair, when decreasing the polarizer angle. (**b**) Averaging of the optical spectra over the limit cycle for $\theta = 66$ degrees, showing the fringe blur

5 Conclusion and Prospects

The nonlinear dynamics of dissipative multi-soliton complexes seems to offer an unlimited range of cases. Furthermore, most of these cases are not marginal, with each one occurring for a given range of parameters and initial conditions. This allows them to be classified in terms of their existence domains. This is very important from the perspective of applications. In this chapter, we have dealt with two main dynamical classes: stable temporal multi-soliton complexes, akin to optical soliton linear molecules in their fundamental state, and pulsating solitons, which also include the class of vibrating soliton molecules.

5.1 The Molecule Analogy: Similarities and Differences

Several authors have explicitly used the term "optical soliton molecule" in the title of recent papers [58, 59] in various contexts of nonlinear optics. It should be noted that in other areas of nonlinear physics, such as reaction–diffusion systems, the "soliton molecule" analogy was used earlier [60]. Let us briefly discuss the legitimacy of the analogy. A molecule is a localized group of atomic constituents that are stably bound together. The notion of stability, although very relative, is the central point. It means that a given molecule can be observed in the same state in repeated measurements, within a given lifetime. If the lifetime is short, it can be viewed as an unstable molecule, but the main interest lies on stable molecules. The stability of a matter molecule can be addressed at different levels, linked to the existence of the following physical features: a local minimum of potential energy, discrete energy levels, and dissipation during the formation process. In nonlinear optics, the use of conservative nonlinearities could lead to various unstable molecules, initially called "multi-mode solitons" [61, 62, 63], but in order to form a long-lived stable optical soliton molecule, nonlinear dissipation seems to be required. Indeed, most of the various multi-soliton complexes presented in this chapter are stable for extremely long propagation distances, which, in experimental terms, means minutes or hours at the speed of the light. Such stability appears possible only if the internal degrees of freedom of the molecule are constrained by the existence of dynamical attractors.

If the molecule analogy proves to be a useful guide in the search for new dissipative multi-soliton complexes and their associated internal dynamics, one should not forget the fundamental limitations of the comparison. A matter molecule, although always coupled to a bath of radiation in reality, inherently has Hamiltonian internal dynamics. The matter molecule does not need a constant energy supply from the outside to survive intact, and when it is in an excited state, its vibrational and rotational motions occur while maintaining energy conservation of the molecule. Of course, these basic conditions are not met with dissipative soliton "molecules". For the latter, there are no known conserved quantities. As we saw in this chapter,

any pulsation or vibration is associated with an oscillation of the total field energy (Sects. 3 and 4). In Sect. 2, we presented explicit cases in which the momentum and even the number of "particles" are not conserved. This is why the observation of an "elastic"-type collision was remarkable, as it is an "exception to the violation rule".

However, up to a point, the molecule analogy should still be useful for the study of dissipative multi-soliton complexes.

5.2 Are Soliton "Macro-molecules" Observable?

The perspective of using soliton "molecules" as upper bits in digital all-optical communication is attracting attention [59]. The possibility of stabilizing a long series of bits in a sort of data "macro-molecule" could also be investigated, whether for the improvement of the quality of transmission in a long-haul transmission line or for the creation of optical buffer memories via stable recirculating loops [64]. In practice, there are two main issues – the stability of a large soliton molecule and its possible manipulation to place or convert data. The stability itself is a major concern, since, when the soliton molecule becomes larger, the internal degrees of freedom appear to be less stable [9]. Obviously, this subject would require further investigation, along with new analytical tools based on statistical mechanics [65].

5.3 Toward Spatio-temporal Soliton Molecules?

The principles that made possible the observation of stable temporal soliton "molecules" in mode-locked lasers could be extended to the spatio-temporal case, at least in principle. Theoretically, the CGLE model can be easily extended to (3+1)dimensions with the inclusion of the transverse Laplacian operator to take into account spatial diffraction in the paraxial approximation. Although numerical computation is a much harder task than in the temporal domain, the existence of stable (3+1)D dissipative solitons [3, 66], or "light bullets", as well as stable double bullet complexes [55], have been demonstrated numerically. Nonlinear dissipation is thus able to efficiently overcome the problem of field confinement in higher dimensions. However, experimental evidence of a (3+1)D dissipative light bullet is an even more challenging task and is yet to be demonstrated.

Acknowledgments We are indebted to our invaluable collaborator Prof. N. Akhmediev, for stimulating and participating in the studies discussed in this chapter, as well as for giving us the opportunity to relate the work of several years in a condensed way. Ph. G. acknowledges the work of his former PhD student M. Grapinet in the discovery of vibrating soliton pairs, as well as institutional support from *Agence Nationale de la Recherche* since 2005. The work of J.M.S.C. was supported by the M.C.y T. under contracts BFM2003-00427 and FIS2006-03376.

References

1. N.N. Akhmediev and A. Ankiewicz, *Solitons: Nonlinear Pulses and Beams*, (Chapman & Hall, London, 1997). 138, 153
2. N.N. Akhmediev and Ankiewicz, A. (eds.): *Dissipative Solitons*. Lect. Notes Phys. Springer, Berlin (2005) 138
3. Nikolay N. Rosanov. *Spatial Hysteresis and Optical Patterns*, (Springer, Berlin, 2002). 138, 171
4. N. Akhmediev, A. Ankiewicz, and J.M. Soto-Crespo, Phys. Rev. Lett. **79**, 4047 (1997). 138, 140, 141
5. Ph. Grelu, F. Belhache, F. Gutty, and J.M. Soto-Crespo, Opt. Lett. **27,** 966 (2002). 138, 141
6. D.Y. Tang, W.S. Man, H.Y. Tam, and P.D. Drummond, Phys. Rev. A, **64,** 033814 (2001). 139
7. N.H. Seong and D.Y. Kim, Opt. Lett. **27,** 1321 (2002). 139
8. A. Hideur, B. Ortaç, T. Chartier, M. Brunel, H. Leblond, and F. Sanchez, Opt. Commun. **225,** 71 (2003). 139, 144
9. Ph. Grelu and J.M. Soto-Crespo, J. Opt. B: Quantum Semiclass. Opt. **6,** S271 (2004). 139, 171
10. M. Olivier, V. Roy, M. Piché, and F. Babin, Opt. Lett. **29,** 1461 (2004). 139, 145, 146, 147, 149
11. B. Ortaç, A. Hideur, M. Brunel, C. Chédot, J. Limpert, A. Tünnermann, and F. Ilday, Opt. Express **14,** 6075 (2006). 139
12. Ph. Grelu, J. Béal, and J.M. Soto-Crespo, Opt. Express **11,** 2238 (2003). 139, 144, 156
13. J.M. Soto-Crespo and N. Akhmediev, Phys. Rev. E **66,** 066610 (2002). 139
14. V.J. Matsas, T.P. Newson, D.J. Richardson, and D.N. Payne, Electron. Lett. **28,** 1391 (1992). 139
15. B.C. Barnett, et al., Opt. Lett. **20**, 471 (1995). 139
16. S. Yamashita, Y. Inoue, S. Maruyama, Y. Murakami, H. Yaguchi, M. Jablonski, and S.Y. Set, Opt. Lett. **29**, 1581 (2004). 139
17. D.E. Spence, J.M. Evans, W.E. Sleat, and W. Sibbett, Opt. Lett. **16,** 1762 (1991). 139
18. M.J. Lederer, B. Luther-Davies, H.H. Tan, C. Jagadish, N.N. Akhmediev, and J.M. Soto-Crespo, J. Opt. Soc. Am. B **16**, 895 (1999). 139, 156
19. S.T. Cundiff, J.M. Soto-Crespo, and N. Akhmediev, Phys. Rev. Lett. **88**, 073903 (2002). 139
20. Ch. Spielmann, P.F. Curley, T. Brabec, and F. Krausz, IEEE J. Quantum Electron. **30,** 1100 (1994). 139
21. H. Kitano and S. Kinoshita, Opt. Commun. **157,** 128 (1998). 139
22. B. Chassagne, G. Jonusauskas, J. Oberlé, and C. Rullière, Opt. Commun. **150,** 355 (1998). 139
23. F. Salin, P. Grangier, G. Roger, and A. Brun, Phys. Rev. Lett. **56,** 1132 (1986). 139
24. T. Tsang, Opt. Lett. **18,** 293-295 (1993). 139
25. J.M. Soto-Crespo and Grelu, Ph.: Temporal multi-soliton complexes generated by passively mode-locked lasers, In: Akhmediev, N.N., Ankiewicz, A. (eds.): Dissipative Solitons. Lect. Notes Phys. Springer, Berlin (2005) 139, 140, 143, 168
26. N. Akhmediev, J.M. Soto-Crespo, and G. Town, Phys. Rev. E **63** 056602 (2001). 140, 153, 160
27. V.V. Afanasjev and N. Akhmediev, Phys. Rev. E **53**, 6471 (1996). 141
28. K. Tamura, E.P. Ippen, H.A. Haus, and L.E. Nelson, Opt. Lett. **18**, 1080 (1993). 141, 156
29. K. Tamura and M. Nakazawa, Appl. Phys. Lett. **67,** 3691 (1995). 141
30. M. Salhi, H. Leblond, and F. Sanchez Phys. Rev. A **68**, 033815 (2003). 143
31. A. Komarov, H. Leblond, and F. Sanchez Phys. Rev. E **72**, 025604 (2005). 143
32. A. Komarov, H. Leblond, and F. Sanchez Phys. Rev. A **72**, 063811 (2005). 143
33. F. Gutty, Ph. Grelu, N. Huot, G. Vienne, and G. Millot, Electron. Lett. **37,** 745 (2001). 143, 157
34. A.K. Komarov and K.P. Komarov, Opt. Commun. **183**, 265–270 (2000). 143
35. S. Namiki, E.P. Ippen, H.A. Haus, and C.X. Yu, J. Opt. Soc. Am. **B 14**, 2099 (1997). 143
36. D.Y. Tang, W.S. Man, and H.Y. Tam, Opt. Commun. **165**, 189 (1999). 143
37. M. Olivier, V. Roy, and M. Piché, Opt. Express **14,** 9728 (2006). 146
38. Ph. Grelu and N. Akhmediev, Opt. Express **12,** 3184 (2004). 146, 147, 166
39. N. Akhmediev, J.M. Soto-Crespo, M. Grapinet, and Ph. Grelu, Opt. Fib. Technol. **11**, 209 (2005). 146, 149, 152
40. H. Leblond, A. Komarov, M. Salhi, A. Haboucha, and F. Sanchez, J. Opt. A **8**, 319 (2006). 150
41. V. Roy, M. Olivier, and M. Piché, Opt. Express **13,** 9217 (2005). 152
42. H. Haus, J. Appl. Phys. **46**, 3049 (1975). 153

43. P.-S. Jian, W.E. Torruellas, M. Haelterman, S. Trillo, U. Peschel, and F. Lederer, Opt. Lett. **24**, 400 (1999). 153
44. J.M. Soto-Crespo, N.N. Akhmediev, and A. Ankiewicz, Phys. Rev. Lett. **85**, 2937 (2000). 153, 160
45. J. Satsuma and N. Yajima, Progr. Theor. Phys. Suppl. **55**, 284–306 (1974). 153
46. K. Tamura, C.R. Doerr, H.A. Haus, and E.P. Ippen, IEEE Phot. Technol. Lett. **6**, 697 (1994). 154
47. F. Ilday, J. Buckley and F. Wise, Proceedings of the Nonlinear Guided Waves Conference (OSA, Washington, DC 2004), Toronto, March 28–31, (2004), Paper MD9. 154, 157
48. N. Akhmediev, J.M. Soto-Crespo, M. Grapinet, and Ph. Grelu, J. Nonlin. Opt. Phys. Mat. **14**, 177 (2005). 159
49. C. Honninger, R. Paschotta, F. Morier-Genoud, M. Moser, and U. Keller, J. Opt. Soc. Am. B **16**, 46–56 (1999). 161
50. J.M. Soto-Crespo, M. Grapinet, Ph. Grelu, and N. Akhmediev, Phys. Rev. E, **70**, 066612 (2004). 164
51. M. Grapinet and Ph. Grelu, Opt. Lett. **31,** 2115 (2006). 165, 168, 169
52. N.N. Akhmediev, A. Ankiewicz, and J.M. Soto-Crespo, J. Opt. Soc. Am. B **15**, 515 (1998). 167
53. J.M. Soto-Crespo, Ph. Grelu, N. Akhmediev, and N. Devine, Phys. Rev. E **75**, 016613 (2007). 167
54. N. Akhmediev, J.M. Soto-Crespo, and Ph. Grelu, Phys. Lett. A, Phys. Lett. A **364**, 413–416 (2007). 167
55. J.M. Soto-Crespo, N. Akhmediev, and Ph. Grelu, Phys. Rev. E **74**, 046612 (2006). 167, 171
56. Ph. Grelu, F. Belhache, F. Gutty, and J.M. Soto-Crespo, J. Opt. Soc. Am. **B 20,** 863 (2003). 168
57. J.M. Soto-Crespo, N. Akhmediev, Ph. Grelu, and F. Belhache, Opt. Lett. **28,** 1757 (2003). 168
58. L.C. Crasovan, Y.V. Kartashov, D. Mihalache, Ll. Torner, Y.S. Kivshar, and V.M. Pérez-García, Phys. Rev. E **67**, 046610 (2003). 170
59. M. Stratmann, T. Pagel, and F. Mitschke, Phys. Rev. Lett. **95**, 143902 (2005). 170, 171
60. C. Schenk, P. Schütz, M. Bode, and H.-G. Purwins, Phys. Rev. E **57**, 6480–6486 (1998). 170
61. M. Haelterman and A.P. Sheppard, Phys. Rev. E **49**, 3376–3381 (1994). 170
62. M. Mitchell, M. Segev and D. Christodoulides, Phys. Rev. Lett. **80**, 4657 (1998). 170
63. C. Cambournac, T. Sylvestre, H. Maillotte, B. Vanderlinden, P. Kockaert, Ph. Emplit, and M. Haelterman, Phys. Rev. Lett. **89**, 083901 (2002). 170
64. K.L. Hall, J.D. Moores, K.A. Rauschenbach, W.S. Wong, E.P. Ippen, and H.A. Haus, IEEE Phot. Technol. Lett. **7**, 1093–1095 (1995). 171
65. A. Schwache and F. Mitschke, Phys. Rev. E **55**, 7720 (1997). 171
66. Ph. Grelu, J.M. Soto-Crespo, and N. Akhmediev, Opt. Express **13**, 9352 (2005). 171

Compounds of Fiber-Optic Solitons

F. Mitschke

Abstract The concept of solitons is making inroads into industrial applications. In optical telecommunications, we see the beginning of the commercial utilization of temporal solitons – short pulses of light traveling down an optical fiber which are stabilized by nonlinearity. This technology is very successful, and yet the data-carrying capacity of optical fiber, even though it is enormous, is on the verge of reaching a fundamental limit. Concepts beyond individual soliton pulses might be helpful in pushing beyond, or working around, that limit. Several ways of creating soliton compounds will be discussed, among them soliton molecules which have already been experimentally demonstrated and recently discovered chains of dark solitons.

1 Introduction

Solitons exist in a vast variety of nonlinear wave phenomena; the collection of contributions in this book alone lends powerful support to that point. In the field of optics, fiber-optic (temporal) solitons were the first type to be discussed [1] and experimentally demonstrated [2]. Light pulses which possess robustness in the presence of perturbations naturally hold great promise for optical telecommunications, and their further evolution has been driven mostly by this possible application. Due to intense research, our understanding of these solitons has matured considerably over the last quarter century. Meanwhile, several textbooks have been written [3, 4, 5, 6] on the subject. Recently, soliton-based telecommunication systems have finally entered the commercial market. In this situation, one may wonder whether the subject, at this degree of maturity, can still provide new and unexpected

F. Mitschke
Universität Rostock, Institut für Physik, 18059 Rostock, Germany,
fedor.mitschke@uni-rostock.de

Mitschke, F.: *Compounds of Fiber-Optic Solitons.* Lect. Notes Phys. **751**, 175–194 (2008)
DOI 10.1007/978-3-540-78217-9_7

phenomena – apart perhaps from petty technicalities. Amazingly, the fiber-optic solitons continue to amaze researchers with new, rather fundamental, questions about the underlying physics.

Among the recent considerations is the following. Fiber-optic telecommunication begins to get hemmed in by its own success. There are limits on the information-carrying capacity of a telecommunications channel. As was first formulated by Shannon [7], the rate of information flow through a channel is bounded by the channel capacity which is given by the available bandwidth times a factor which depends on the signal-to-noise ratio or, as is more appropriate for digital transmission, on the coding format. If progress continues at a rapid pace which is similar to what occurred for many years (with the exception of 2001–2005), transmission using binary encoding – the commercial standard to date – will soon reach the Shannon limit. One might object that Shannon only considered linear channels. Indeed, several refinements for the nonlinear case given in optical fibers have been presented recently [8, 9, 10, 11]; however, these corrections provide only moderately higher estimates of the ultimate limit.

Several other attempts have been undertaken to find a way around the limitation, including phase shift-keying of information (rather than encoding in power) [12] or the use of higher-order solitons [13, 14]. Any successful approach to improving the data-carrying capacity would certainly be preferable to the obvious, but costly, possibility of deploying more fibers in parallel.

The present contribution illustrates how several new variants, which might collectively be called soliton ensembles, become possible. Research on an ensemble of solitons generated in a nonlinear feedback system will be reviewed in Sect. 3. Section 4 describes soliton molecules in dispersion-managed fiber, i.e., bound states of molecules which exploit the mutual interaction of solitons and may allow better use of the communication channel. Section 5 will show that dispersion-managed fiber also supports bound states of dark solitons.

2 General

2.1 Schrödinger Solitons

Solitons in optical fibers are pulses of light which are basically specified as solutions of the underlying wave equation, the nonlinear Schrödinger equation (NLSE) [3, 15]

$$\frac{\partial A}{\partial z} = -\frac{\mathrm{i}}{2}\beta_2 \frac{\partial^2 A}{\partial T^2} + \mathrm{i}\gamma |A|^2 A \,. \tag{1}$$

Here $A = A(T,z)$ is the pulse envelope, z is the co-ordinate in the propagation direction, T is time in the co-moving frame, and β_2 and γ are the coefficients for dispersion and nonlinearity, respectively.

For negative dispersion, $\beta_2 < 0$, there is the fundamental bright soliton solution

$$A(T,z) = \sqrt{\hat{P}}\,\mathrm{sech}\left(\frac{T}{T_0}\right)\exp\left(\frac{\mathrm{i}}{2}\,\gamma\hat{P}z\right)\ . \tag{2}$$

This is a stable solution of (1). Stability implies self-correcting effects after perturbation, hence the appeal of solitons as the natural 'bits' for optical telecommunication. In (2), the peak power $\hat{P} = |A(0,0)|^2$ and the pulse duration T_0 cannot be chosen independently; rather, both are linked by the 'condition of constant action':

$$T_0^2\,\hat{P} = \frac{|\beta_2|}{\gamma} = \text{const.} \tag{3}$$

For the opposite sign, $\beta_2 > 0$, a stable solution is given by the dark soliton

$$A(z,T) = \sqrt{\hat{P}}\tanh\left(\frac{T}{T_0}\right)\exp\left(\mathrm{i}\,\gamma\hat{P}z\right)\ , \tag{4}$$

subject to the same constraint (3). Its hyperbolic-tangent envelope shape gives rise to a $\tanh^2$, or 'inverted sech-squared', power profile. This is a dark notch appearing in a constant-power bright wave. In other words, dark solitons are dark pulses on a c.w. bright background. (More precisely, there is a whole family of dark solitons with varying levels of depth of the minimum. They are known as grey solitons. It has become customary, however, to refer to the 'black soliton' of (4) which dips to zero as the 'dark soliton' where no confusion can arise [3].) While the first experimental demonstrations of dark solitons [16, 17] followed soon after that of the bright soliton, the number of experimental studies devoted to the dark soliton case [16, 17, 18, 19] is quite limited.

A description of fiber-optic solitons, both bright and dark, in terms of the nonlinear Schrödinger equation already captures many of their basic properties. Many finer points, however, were only understood after various corrections to the simple equation, including higher-order dispersion, the Raman effect, and others, had been investigated. It was shown many years ago that, in the presence of Hamiltonian deformations, solitons of the NLSE remain stable, but they may decay when non-Hamiltonian deformations are present [20]. In the present context of this book about dissipative solitons, gain and loss are important, and this statement requires a further comment. Dissipative solitons derive their stability from a balanced flow of energy into and out of the soliton [21]. Their description requires generalized versions of the NLSE, e.g., the Ginzburg–Landau equation.

However, for now, terms added to (1) will be disregarded. The single extension considered here is that the NLSE can be applied only piecewise, either because there is a repetitive perturbation (Sect. 3) or because the dispersion parameter is made to vary in a piecewise-constant fashion (Sects. 4, 5). Even with this seemingly mild modification, the NLSE allows a variety of solutions other than the bright soliton.

3 Soliton Ensembles in a Feedback System

It is a broad general rule that nonlinear processes, when subject to feedback, can give rise to qualitatively new features. Bistable, self-oscillating, or chaotic systems are cases in point [22]. It is therefore interesting to discuss a nonlinear feedback system involving an optical fiber which is essentially closed upon itself. Figure 1 shows the conceptual set-up. The ring resonator is driven by a sequence of external pulses of light from a mode-locked laser, which we will call feed pulses. The round-trip time T_{rt} is carefully chosen so that it equals the repetition time of the feed pulses T_{rep} or an integer multiple thereof. This way, the feed pulse train is in synchronism with the circulating pulses: Whenever the circulating pulse reaches the input coupler, it meets with a fresh feed pulse, and both will interfere.

Consider feed pulses which are wide enough so that dispersion does not appreciably alter their shape during a single round-trip. This statement can be cast in more definitive form by using the characteristic dispersion length, commonly defined as [3]

$$L_{\mathrm{D}} = T_0^2/|\beta_2| \tag{5}$$

and comparing it with the round-trip distance L_{rt}. Here, we choose the initial pulse width T_{init} to be large enough so that $L_{\mathrm{D}} = T_{\mathrm{init}}^2/|\beta_2| \gg L_{\mathrm{rt}}$. Then, during the first round-trip, the pulse will basically experience only self-phase modulation. Depending on the amount of phase modulation, interference will yield a pulse with a more complicated structure, as sketched in Fig. 2. Then, this more complicated pulse starts the next round-trip, during which it will experience a more involved chirp, so that upon the second interference, the pulse shape will get even more complicated. Rapidly, a more complex structure is formed until, after very few round-trips, the shortest sub-structures in the pulse will be limited by dispersion when $T_{\mathrm{min}}^2/|\beta_2| \approx L_{\mathrm{rt}}$. Sub-structures will then cover all time scales from T_{init} down to

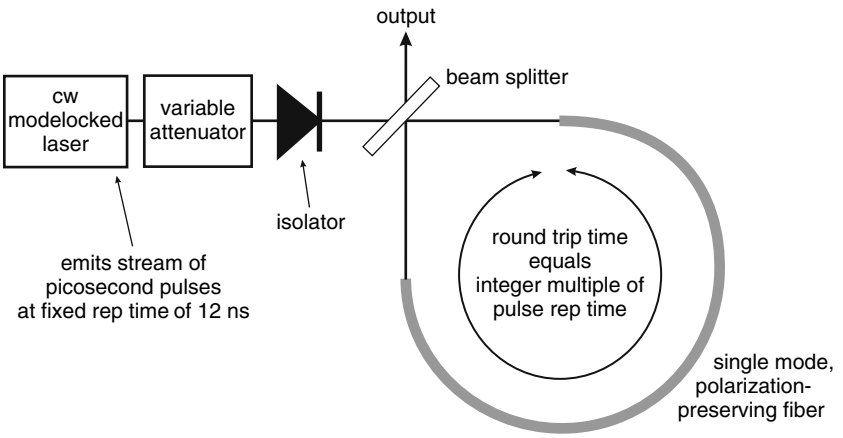

Fig. 1 Schematic set-up of the synchronously driven ring resonator experiment

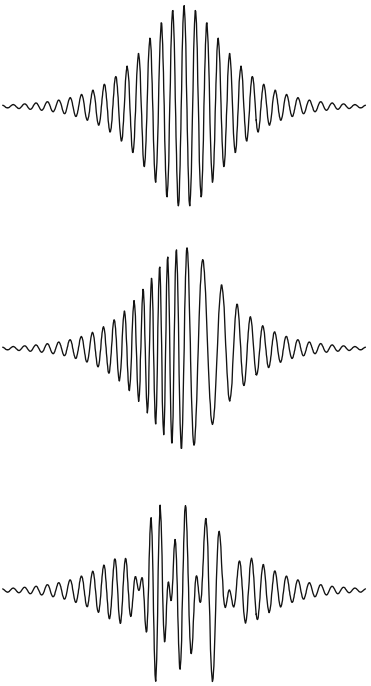

Fig. 2 Schematic representation (not to scale) of the earliest phase of the structure formation process for the set-up of Fig. 1. Time is plotted horizontally; vertical directions represent electric field strength. The unchirped laser pulse (*top*) acquires self-phase modulation during its first round-trip (*middle*). Then it interferes with the next laser pulse; depending on the amount of phase modulation, the result may have complex structure (*bottom*)

$T_{\min}$. The actual structure, however, is not stationary [23], but may become chaotic [24, 25] or turbulent [26, 27].

Numerical modeling of the process is straightforward. There is unperturbed fiber propagation which is modeled using (1) and a split-step Fourier algorithm, alternating with interference which is just a complex addition in mathematical terms. Figure 3 shows two subsequent round-trips after the initial transients have died down. Both round-trip plots are separated graphically for better clarity. There are well-defined sub-pulses on a minimal background; they move around during fiber propagation and they are rearranged at the interference moment.

Closer examination of the simulation data reveals a remarkable fact – the highest spikes are also the narrowest. This correlation is shown in Fig. 4, where the sub-pulse peak power P is plotted versus τ^{-2}, the square of the inverse sub-pulse width.[1] Many data points occur at very low values of P and can have any value of τ over the range shown and beyond it. This branch consists mostly of linear waves, possibly in the far wings of the pulse. Some data points may also be caused by numerical noise. The other branch corresponds to nonlinear pulses and displays a linear trend in this plot, indicating $\tau^2 \hat{P} \approx \text{const}$. For comparison, the constraint (3) is shown as the solid line for the fiber parameters used here. The agreement is remarkably close, considering that for the system as a whole (propagation *plus* interference),

[1] Here the pulse width is given as the full-width at half-maximum τ. Earlier (see, e.g., (2)), we used T_0, the half-width at $\text{sech}^2(1)$ of maximum. To convert, $\tau = 2\,\text{arcosh}(\sqrt{2})\,T_0 \approx 1.76\,T_0$.

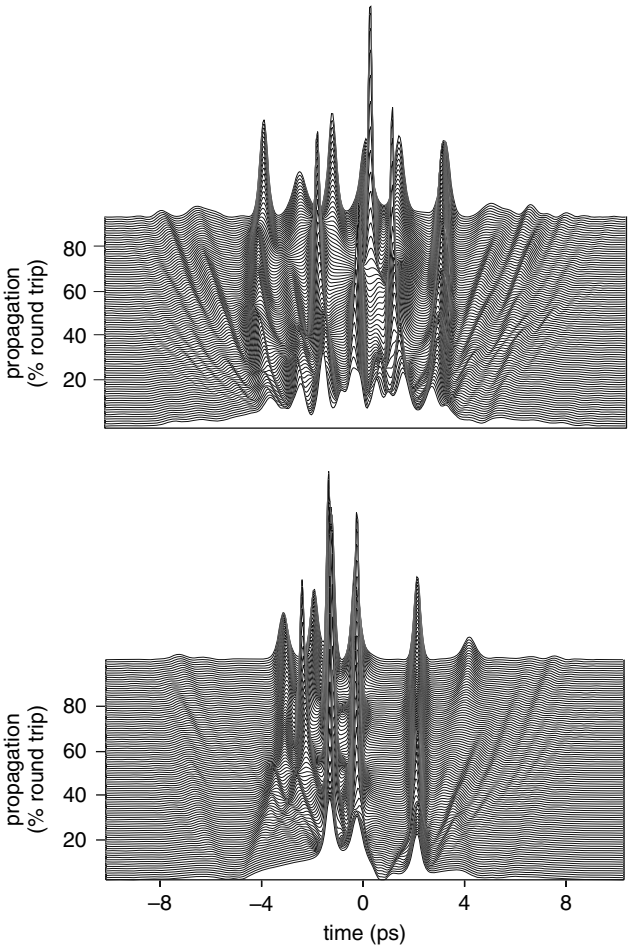

Fig. 3 Numerically generated picture of a soliton gas. Propagation is from bottom to top. Two complete consecutive round-trips are shown; for clarity they are plotted with a vertical gap in between

one can certainly not speak of unperturbed propagation. The fact that the sub-pulses are subject to a constraint of the type (3) justifies identifying them as soliton-like pulses.

It is no surprise that at the moment of interference, the ensemble of solitons is strongly perturbed and modified; however, it is also obvious from the simulation that, during unperturbed fiber propagation, the individual solitons move relative to each other. This must be attributed to their mutual interaction, so that the whole ensemble resembles a fluid of particles – hence the name ‘soliton gas’.

When we varied the parameters, we noticed that, below a certain threshold value of input power, the solitons in the gas cease to move (after a long transient has died out). As shown in Fig. 5, they then sit in fixed, essentially equi-distant positions

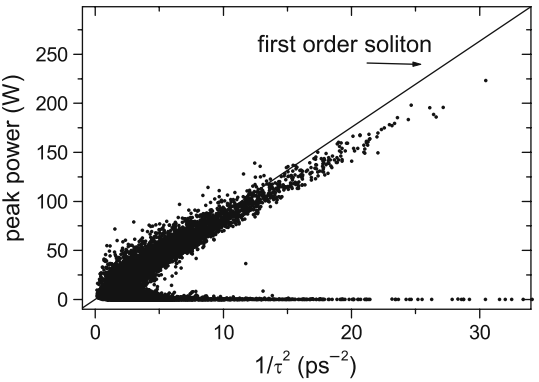

Fig. 4 Correlation of the peak power (*vertical*) with the inverse square of the half-width (*horizontal*) for all maxima in a soliton gas, taken from many round-trips similar to those shown in Fig. 3. The straight solid line represents condition (3)

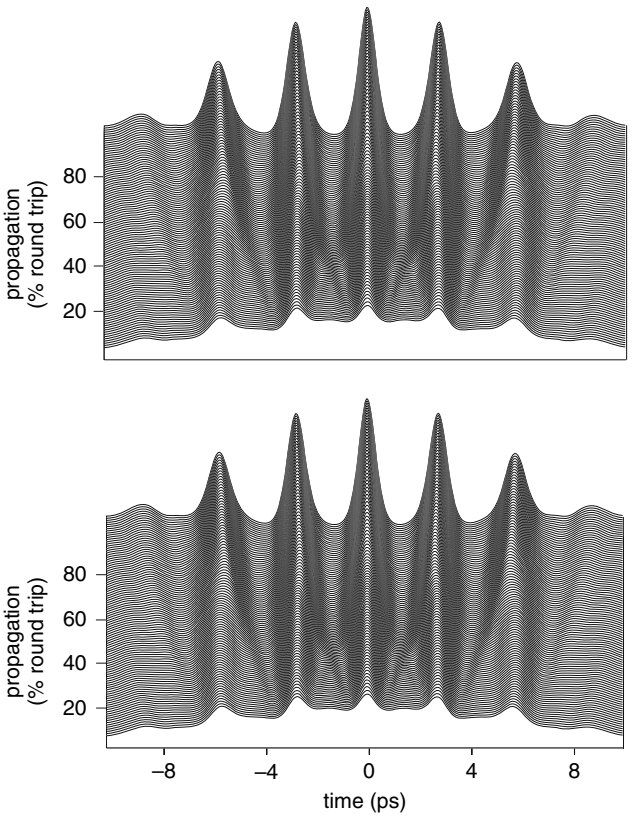

Fig. 5 Numerically generated picture of a soliton crystal. When compared with the gas in Fig. 3, the only parameter difference here is reduced input power. The vertical scale has been expanded

[28, 29] which were examined in more detail in [30]. In keeping with the analogy to a soliton gas in Fig. 3, it is consistent to call the regular lattice of Fig. 5 a soliton crystal. It occurs when the perturbation through interference is not sufficient to overcome the order created by modulational instability during propagation. It should be mentioned, in passing, that the transition from gas to crystal can be triggered by spectral filters in a manner which is analogous to evaporative cooling [31, 32].

The numerical work described so far was accompanied by extensive experiments. Polarization-preserving fiber was used to render the ring truly single mode in the strictest sense. For experiments with $\beta_2 < 0$, a color center laser at $\lambda = 1.6\,\mu\text{m}$ was used. (We also conducted experiments at $\beta_2 > 0$ with a Nd:YAG laser at $\lambda = 1.32\,\mu\text{m}$.) Since no direct photodetection on the sub-picosecond time scale of the experiment is feasible, we acquired optical spectra from a scanning Fabry–Perot interferometer and timing information from auto-correlation measurements. This may appear somewhat indirect. Nevertheless, there was irrefutable experimental evidence for the existence of both soliton gas and crystal, and they occurred at the predicted parameter values. Moreover, characteristics like the typical sub-structure width in the gas and its scaling with β_2, the lattice constant of the crystal, etc., could be confirmed experimentally. The reader is referred to [23, 25, 28, 29, 33] for detailed accounts.

4 Soliton Molecules: Bound States in Dispersion-Managed Fiber

Both this section and Sect. 5 deal with solitons in dispersion-managed fiber. Section 4.1 serves to remind the reader of that concept and of its known soliton solutions.

4.1 Dispersion-Managed Fiber and Its Solitons

Increasingly, the telecom industry now uses fiber lines with periodically alternating dispersion. Such fibers, commonly called dispersion-managed, allow better transmission of data for several reasons. Not the least among the advantages is that phase-matching of four-wave mixing products is destroyed. With this technique, the build-up of channel cross-talk is thwarted.

In such fibers, the dispersion allocation is basically characterized by two dispersion values ($\beta_2^+ > 0$ and $\beta_2^- < 0$) and their respective segment lengths (L^+ and L^-). After a distance $L_{\text{map}} = L^+ + L^-$, called the map period, the pattern repeats periodically. The effect on pulses of duration τ (full-width at half-maximum) is best described by using the path-average dispersion

$$\beta_2^{\text{ave}} = (\beta_2^+ L^+ + \beta_2^- L^-)/L_{\text{map}} \tag{6}$$

and the map strength

$$S = \frac{\left|\beta_2^+ - \beta_2^{\text{ave}}\right| L_+ + \left|\beta_2^- - \beta_2^{\text{ave}}\right| L_-}{\tau^2} \,. \tag{7}$$

(Several slightly different definitions of S appear in the literature. It seems advantageous to use the difference with β_2^{ave} in both terms in the numerator, because this gives a particularly nice transition to the homogenous fiber for $S \to 0$.) It is also useful to define a characteristic length in analogy with (5), where β_2 is replaced by β_2^{ave}.

It is not immediately obvious that solitons would exist at all in dispersion-managed fiber. However, it has been established that bright pulses deserving to be called dispersion-managed solitons do exist. While their shape and width 'breathe' over one map period, both are stable in a stroboscopic sense (i.e., when sampled at intervals equaling L_{map}). Fiber nonlinearity is responsible for the stabilization. Their shape is more closely Gaussian than sech-squared, i.e., it approximates the solution of the *linear* problem. This is easy to understand because during the breathing of the pulse shape, dispersion acts all the time while nonlinearity is only appreciable over that partial segment where the peak power is high [6]. It was also pointed out that their existence is not strictly limited to the regime of $\beta_2^{\text{ave}} < 0$. In fact, they also exist in a small parameter range where $\beta_2^{\text{ave}} \geq 0$ [34, 35, 36, 37, 38]. Again, this can be understood by realizing that the soliton 'sees' a weighted average which is different from (6).

Corresponding statements for dark solitons were established in [39]: Dark dispersion-managed solitons breathe, but are stable in a stroboscopic sense. Their shape differs from tanh-squared mainly because of the presence of oscillatory tails. Also, they exist beyond the zero-dispersion point. Results for both cases taken together imply that the regimes of existence of bright and dark solitons overlap.

4.2 Soliton Molecules

In the parameter range where the regimes of bright and dark dispersion-managed solitons overlap, we found that they can actually co-exist and form a stable bound state in which a bright pulse sits on either side of a dark soliton (see Fig. 6). A first report containing both numerical and experimental results was given in [40].

It should be clear that such a structure in a constant-dispersion fiber would definitely be unstable; dispersion-alternating fiber is an absolute necessity for this compound to exist. It is also clear that this soliton compound is very different from the well-known 'higher-order solitons' of the unmodified NLSE which have no binding energy [4] and therefore decay under infinitesimal perturbation. The possibility of bright soliton pairs was theoretically pointed out, however, in terms of Hermite–Gaussian functions in [41]. It appears that the structure we investigate is the same, but we prefer to describe it as a compound of one dark and two bright solitons.

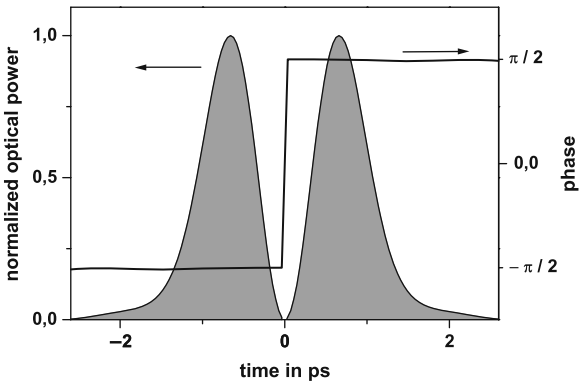

Fig. 6 A soliton molecule consists of two bright pulses with opposite phases; the π phase jumps occur at the central power zero. Alternatively, the central notch can be thought of as a dark soliton

Maruta et al. also found compounds of two (and more) solitons [42]; we believe that, in spite of slight differences, they discuss the same structure. However, no experimental study has been reported so far other than ours [40].

Dispersion-managed solitons have pulse shapes approximating a Gaussian, and the compound can in fact be approximated by the sum of two Gaussian pulses in anti-phase. This is a convenient prescription for the launch condition; a better approximation is obtained numerically from this by using the convergence-enhancing procedure described in [34]. We then let the compound propagate and obtain data as in Fig. 7. One sees stable propagation over long distances, with no change in shape, even on a logarithmic scale.

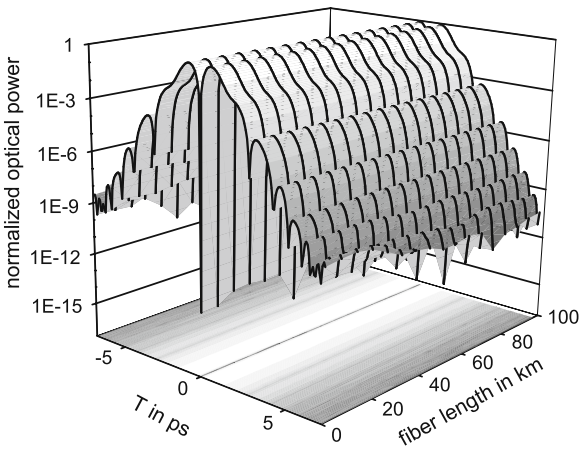

Fig. 7 Numerical simulation of long-distance propagation of the soliton molecule. Here $S = 7.2$ was assumed; the maximum distance shown corresponds to $77\,L_{\mathrm{D}}$

We then found, numerically, that the separation between the maxima (in units of pulse width) is a characteristic of the compound which is restored after perturbation. The bright pulses repel each other if the spacing is too narrow, whereas they mutually attract if the spacing is too wide. In either case, after a sufficient propagation distance, they return to their equilibrium distance. This is reminiscent of the equilibrium separation of the two constituents of a diatomic molecule; we therefore call this structure a *soliton molecule*. Very recently, and based on our first report on this research, an analytical approach for the 'restoring force' has been found, and our result was independently confirmed [43].

We performed experiments to verify the numerical predictions regarding the soliton molecule. To this end, we set up a scale model of a real telecom system (see Fig. 8). Pulses of width ≈ 300 fs were taken from a mode-locked TiSa laser/OPO system. The pulses were split into pairs with a Mach–Zehnder interferometer – note that fine tuning of the path length difference affords tuning of the relative phase. For 300 fs pulse width, the required fiber length is scaled down from tens or hundreds of kilometer to just tens of meter of fiber. Note that this scaling actually exacerbates problems from the Raman effect and from higher-order dispersion, therefore the success of our experiment allows a safe conclusion about its viability in any full-scale system. To show the principle, Figs. 6, 7 were calculated without these perturbations, but, in the interests of greater realism, from now on results from an extended model, including these effects, will be used for comparison with experimental data.

The useable fiber length was restricted mainly for the reason that the two types of fiber in the dispersion-managed line had differing mode field sizes, so that the line suffered from impedance mismatch losses at every junction. In order to keep things clean and simple, we did not want to add amplifiers (with their own gain dynamics) in this proof-of-principle experiment. In the first report [40] we therefore used a fiber line which was just three dispersion periods long. In subsequent experiments, we doubled this by using the fiber twice. We introduced a full reflector at the fiber end and a beam splitter in front of the input, so that the pulses could travel down the fiber and back again before being coupled out for data acquisition. We could

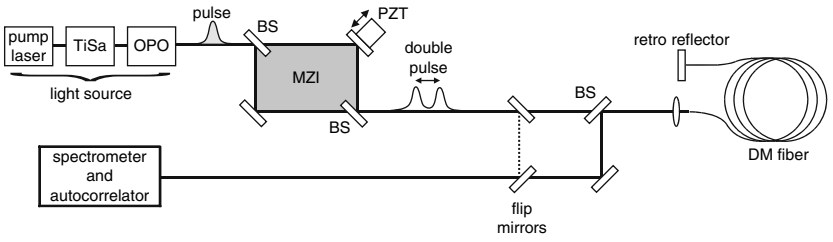

Fig. 8 Set-up of experiment to demonstrate soliton molecules. Pulses from the light source (TiSa: mode-locked titanium sapphire laser, OPO: optical parametric oscillator) are split into pairs (MZI: Mach–Zehnder interferometer, PZT: piezoelectric transducer, BS: beam splitter) and sent into the fiber. After traveling back and forth through the fiber, signals are sent on to data acquisition. Flip mirrors: inserting them into the beam path as shown allows us to assess the fiber input signals

immediately compare fiber input and output signals at all times by using the flipping mirrors. This was an important safeguard against, e.g., drift in the relative phase of the two bright pulses. For further technical details, the reader is referred to [40].

We performed systematic experiments, varying all the relevant parameters. Consider Fig. 9, left column, which shows results from a systematic variation of the initial separation, σ, between the bright pulses for the case of a π phase difference. The horizontal axis is σ, as derived from the path difference in the Mach–Zehnder interferometer. The top panel shows the result of numerical simulation – the vertical axis is time at the fiber output. A grey scale is used to indicate the power level. For large initial separations, the final separation equals the initial separation. In other words, at large distance between the bright pulses, there is no interaction between them. As the separation is reduced, the bright pulses are pulled in and, over a small range of initial separations, the final separation is almost constant. There is a certain 'capture range' at $\sigma \approx 0.4$–0.8 ps. For larger separations, there is too little interaction, while for smaller initial separation, the (anti-phase!) pulses tend to mutually cancel by destructive interference.

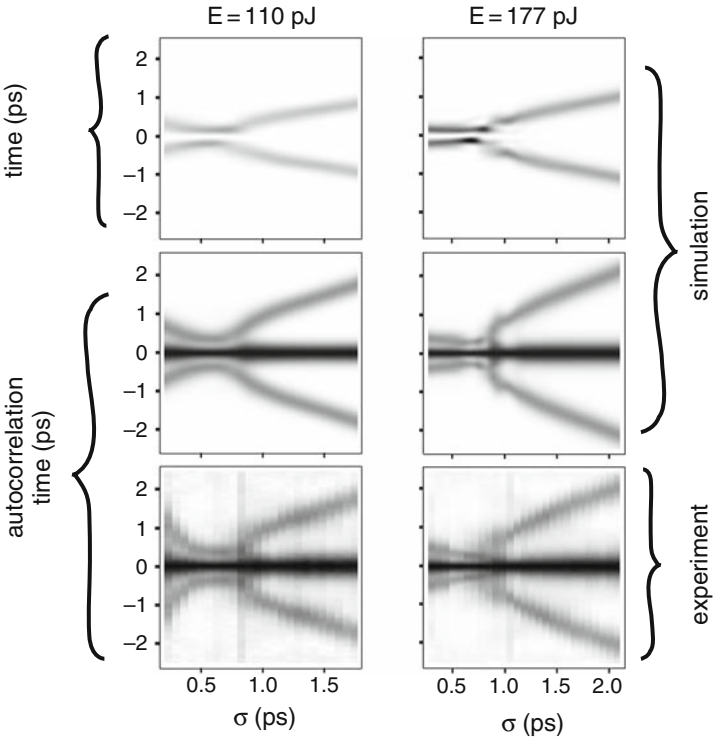

Fig. 9 Comparison of numerical and experimental results at relative phase π; (*top*): direct simulation, (*center*): auto-correlation constructed from simulation, (*bottom*): experimental result. See text

From these data, it is straightforward to calculate the corresponding auto-correlation trace (middle panel). Note that the auto-correlation of a pulse pair is a triplet with 1:2:1 power ratio, and that the positions of the side lobes allow for direct reading of the pair separation. The computed auto-correlation data finally allow direct comparison with the compilation of experimental auto-correlation data in the lower panel. The agreement between calculation and observation is convincing.

The right column of Fig. 9 presents the situation at somewhat higher power. The overall similarity indicates that there is some liberty in the choice of power level used to generate the soliton molecule. There is a certain capture range in terms of power, roughly bracketed by the values in the two columns, while no molecule is formed outside the capture range.

Figure 10 shows the corresponding results for in-phase bright pulses. As expected, nothing indicates a formation of a stable pulse pair anywhere. It is quite obvious that a stable molecule is achieved only in the anti-phase case, as predicted. Anti-phase implies a dark soliton in the middle, which – in a manner of speaking – acts as a 'gluon'.

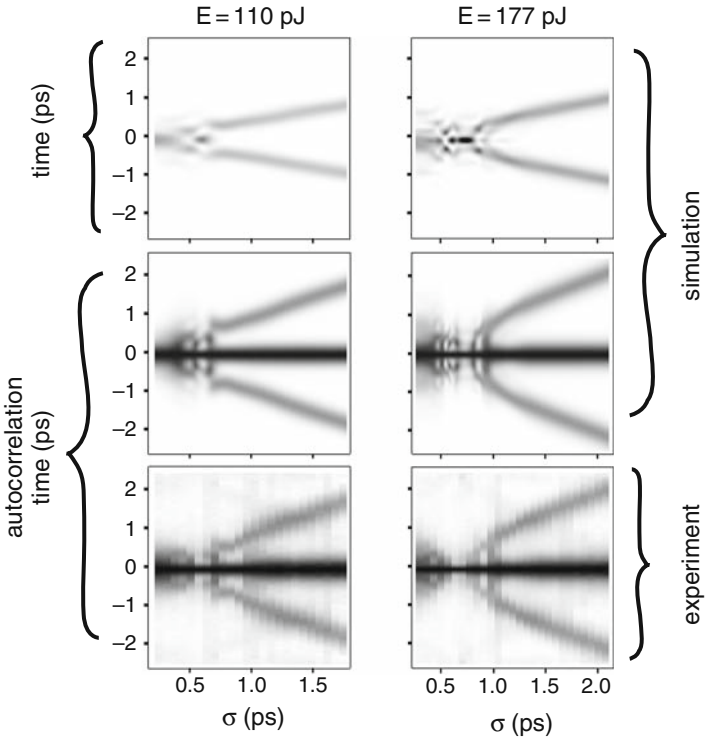

Fig. 10 Comparison of numerical and experimental results at zero relative phase, but otherwise as in Fig. 9

All experimental results confirm the numerical predictions to a high degree of precision. The existence of soliton molecules has therefore been proven beyond doubt. They can improve fiber-optic telecommunications by allowing us to pack the transmitted data more closely. For example, one could go beyond 'dark'=0 and 'pulse'=1 in a binary return-to-zero format by using the molecule as a further symbol (e.g., 'molecule'=2). Longer chain molecules (bright-dark-bright-dark-bright, etc.) could then extend the alphabet to more letters. Such a coding format would enhance the amount of information transmitted per clock cycle. Alternatively, one could reduce the temporal spacing between adjacent bit slots to the molecule's equilibrium distance, rather than retaining the current routine wide safety margin. Either way, soliton molecules could help pushing toward, or beyond, the binary Shannon limit of information-carrying capacity. Only the future will tell whether they become successful in tomorrow's commercial environment.

5 Bound States of Dark Solitons in Dispersion-Managed Fiber

In this section, a new family of soliton solutions in dispersion-managed fiber is described. It is based on the discovery [44] that dark solitons in dispersion-managed fiber lines can exhibit not only repulsive, but also attractive interaction. In conventional constant-dispersion fibers, it has been known since [45] that dark (black) fiber solitons always repel; [46] extended this conclusion to both black and grey solitons. Attraction between same-frequency, same-polarization dark solitons was previously considered impossible in fiber optics, and to the best of our knowledge, prior to [44], no attractive force between such solitons had been reported.

After a demonstration of this attractive interaction, the existence of stable bound states of dark dispersion-managed solitons will be shown. Finally, it will be demonstrated that these bound states can take the form of chains of several dark solitons. For details, the reader is referred to [44].

In simulations of dark solitons, one needs to replace the infinite c.w. background with a finite background pulse. This background pulse has to be much wider than the dark pulse, and indeed so broad that no artifacts from its wings become noticeable. Here an unchirped super-Gaussian (with exponent 6) background pulse, 200 times wider than the dark soliton, was used in order to ensure an almost constant background level in a computational window which is another factor of 4 wider than that. By varying the width of the background, we convinced ourselves that, for these parameters, we had avoided artifacts caused by the finite width of the background pulse. For consistency, all dark pulse widths will henceforth be referred to τ_{sol}, defined as the full-width at half-maximum which a single dark soliton attains after the initial transients have died down. The nonlinearity parameter, γ, is assumed to be equal for both fiber types in the line. Higher-order effects, gain, or polarization effects are not included.

We simulated transmission lines consisting of a few hundreds of map periods with map strength $S = 1.8$. This corresponds to a total span length of almost a

hundred L_D. For dark pulses of about $\tau_{sol} = 1$ ps, this translates to nearly 60 km. Over the first $\approx 10 L_D$ or so, the launch pulse, taken here as a $\tau = 1$ ps tanh-squared pulse, sheds radiation, and the asymptotic shape of a true dark dispersion-managed soliton with a width of $\tau_{sol} = 1.43$ ps becomes visible.

5.1 Dark Soliton Pairs

Now the interaction between two such dark pulses is investigated. The product of two position-shifted dark pulses is launched. During numerical propagation, there is again an evolution to a final dark soliton pair shape. Figure 11 shows the separation between the centers as a function of their position along the transmission line. The figure combines data for initial separations ranging from 0.9 τ_{sol} to 9.8 τ_{sol}. The result is remarkable in that a few curves diverge, but most curves tend to one out of five fixed final separations. These preferred values are highlighted by arrows in Fig. 11 and are labeled with $\Delta T/\tau_{sol}$. These labels constitute a set of 'magic numbers' which will be referred to below. The data assert that bound pairs of dark solitons exist at separations corresponding to one of the 'magic numbers'.

Figure 11 also reveals that individual traces approach these equilibrium positions in an oscillatory fashion. From this observation, one has to conclude that the trajectories experience not only repulsion but also attraction. Oscillation around a stable position suggests some kind of binding force, and the oscillation period is then a

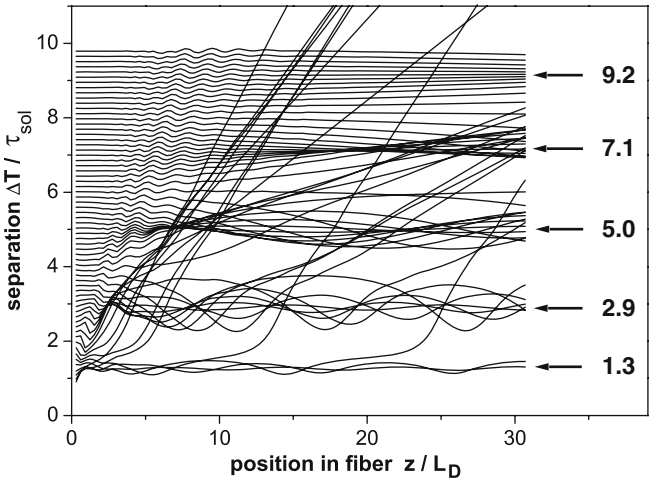

Fig. 11 Interaction of two dark dispersion-managed solitons: separation $\Delta T/\tau_{sol}$ as a function of propagation distance z/L_D. The separations evolve toward a discrete set of equilibrium values (*arrows*)

rough indicator of the strength of this binding force. Since oscillations are longer for larger separation, one concludes that the binding force falls with distance, as is physically intuitive. At separations more than $10\,\tau_{\mathrm{sol}}$, the binding force has practically vanished.

The bound dark soliton pair undergoes some breathing over a dispersion map period L_{map}, but the separation of the centers is modulated only very slightly. The mechanism of the binding force is related to the oscillating tails of dark dispersion-managed solitons, as was pointed out in [39] and alluded to above in Sect. 4.1. These oscillatory tails can lock on to each other and provide a mutually stabilizing force, resulting in a stable bonding.

5.2 Dark Soliton Chains

The whole discussion about dark soliton pairs contained nothing that would prevent more than two solitons forming a bond. One concludes that chains of dark solitons should be possible.

Pursuing this thought, we used the product of several position-shifted hyperbolic-tangent pulses as a launching condition, thus approximating the structure that finally emerges and which is well described as a comb of dark pulses.

Figure 12 shows the propagation of a 12-soliton chain over a very long distance. Here the second 'magic number', 2.9, was chosen for the mutual separation. Since

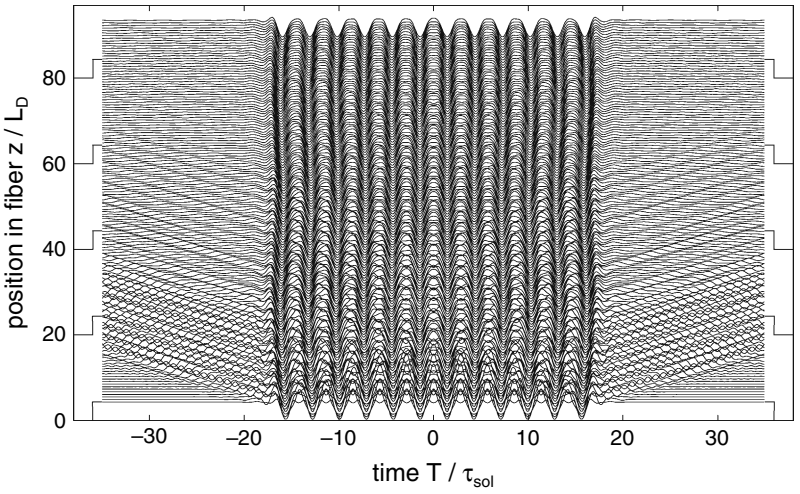

Fig. 12 Stable propagation of a chain of 12 dark solitons. The separation was chosen to be 2.9 (compare Fig. 11). Propagation (from bottom to top trace) is shown over 300 dispersion map periods or $93\,L_{\mathrm{D}}$

our launch condition only approximates the shape of the chain, some radiation is shed in the transition phase. This is easily visible in Fig. 12 as small waves radiating out on both sides. Nevertheless, the chain is remarkably stable.

Stable propagation over the distance considered is also found for the other separations ('magic numbers'). The exception is the smallest number, 1.3, for which longer chains tend to break apart after some propagation distance. Our interpretation is that, in this situation, the separation wiggles too much (a few percent) in the course of one dispersion period. This is inconsequential for soliton pairs, but, in longer chains, one soliton pushes the next in the row, and the outermost solitons must undergo a correspondingly larger oscillation around their average position. Eventually the perturbation seems to be so large that stability is lost. For all other 'magic numbers' the positions wiggle much less, and we did not encounter instabilities.

It is not necessary that all nearest-neighbor distances in the chain be the same. We tested many randomly chosen selections of different 'magic number' nearest-neighbor separations, and in most cases we obtained a stable chain. One example is shown in Fig. 13 which depicts propagation of a chain of 8 dark solitons in which the separations of three are 2.9 and of the others are 5.0. Exceptions – chains with compromised stability – were found when several occurrences of the smallest possible separation were involved, as described previously.

Combination of various separations in a long chain provides an enormous number of different chain arrangements. To the extent that, through further investigation, their stability can indeed be guaranteed, these different chain arrangements, reminiscent of bar codes, may constitute yet another way to encode information.

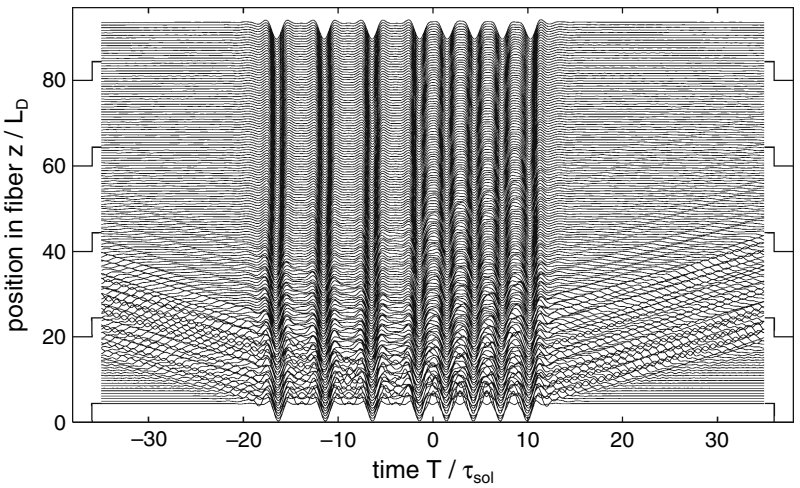

Fig. 13 Chain of dark solitons with unequal separations: In contrast to Fig. 12, the separation is 5.0 in the left half, and 2.9 in the right half

6 Discussion and Conclusion

In the driven-resonator experiment of Sect. 3, the crucial deviation from pure, unperturbed NLSE solitons is brought about by the repetitive interference with laser pulses. This interference acts in two ways: It transforms phase modulation to amplitude modulation and it restores energy to the circulating pulse. Considerable energy loss occurs during each round-trip (chiefly at coupling into the fiber and at the beam splitter), and the cavity finesse is extremely low. Only the continued supply of feed pulses makes it possible for signals traveling around the ring to have a constant power level, at least on average.

Can the constituents of the soliton gas and crystal then be considered as dissipative solitons? Several criteria of the definition are fulfilled: There is an ongoing energy flow in and out, so that the average energy level is maintained. Dissipation causes a rapid loss of memory of the initial conditions, so that the set-up, not the initial condition, is responsible for the emerging structure. On the other hand, not all criteria are met.

For example, the generated solitons are not uniquely shaped, but constitute a one-parameter family, as Fig. 4 shows. Moreover, there are peculiarities in that the loss is discontinuous – it occurs mostly in a localized, not distributed, manner. The energy input is also not continuous but rather has the form of periodically recurring kicks. Moreover, the energy restoration is a coherent process, not an incoherent one as in typical amplifiers. Mathematically, one has to consider a NLSE with a periodic perturbation, not something like a Ginzburg–Landau equation, etc. Whether the resulting soliton ensemble is called a dissipative ensemble or not is probably a matter of taste, or maybe for more discussion.

The soliton molecules in Sect. 4 might easily be confused with structures in fiber lasers described by several authors [47, 48, 49, 50]. However, there are important distinctions. For example, our soliton molecules have π phase difference and a separation of about 1.6 pulse widths, not $\pi/2$ and a separation of 3–6 pulse widths, as predicted in [51] and observed in [48, 49]. The situation regarding gain and loss is somewhat more complex – in our experiment, there was no gain, but there was also only a short fiber so that the loss was kept at tolerable levels. For soliton molecules – and also for the dark soliton chains in Sect. 5 – one can consider that, in dispersion-managed fibers, all propagating signals always suffer from power loss due to the periodic perturbation.

Speaking in the strictest sense, signals in dispersion-managed fibers are not stable. In the periodic dispersion structure, they are resonantly coupled to the radiation background, therefore energy is drained away from the soliton all the time [52, 53]. The rate of loss may be small, but it is non-zero (with the possible exception of singular cases [53]). Continued trickling away of energy will cause the solitons to deform considerably, and, in this sense, they are unstable. It stands to reason, though, that stability can be obtained in the presence of a suitable gain mechanism, so that the power level is maintained – perhaps only on average. If this is true, dispersion-managed solitons and all derivative entities, as described above, are stable only in the presence of a balance between loss and gain, a property which they share with

dissipative solitons. Is it therefore meaningful to list the dispersion-managed soliton compounds described above as dissipative solitons? This author would exercise caution, and hope for further refinements to the definition of dissipative solitons.

In conclusion, this presentation describes some unusual soliton compounds in optical fibers. In each case, one can discuss the role of loss and gain; it is not necessarily obvious which structure qualifies as a dissipative soliton and which does not. That decision would depend on the finer points of the definition of dissipative solitons. In that sense, this chapter may help in clarifying that definition.

Acknowledgments This research has been conducted over several years; financial support came from Deutsche Forschungsgemeinschaft and from the 'DIP' program (German–Israeli project partnership) and is gratefully acknowledged. Many people have contributed, and I cannot possibly list them all in the confines of this space. I just wish to highlight the following: I enjoyed stimulating discussions with Andreas Sizmann, Falk Lederer, Boris Malomed, Moti Segev, and Linn Mollenauer. Günter Steinmeyer, Andreas Schwache, Soeren Rutz, Michael Böhm, Martin Stratmann, and Haldor Hartwig have been involved as members of my group. Also, I especially thank Nail Akhmediev for inviting me to write this chapter.

References

1. A. Hasegawa and F. Tappert, Appl. Phys. Lett. **23**, 142 (1973). 175
2. L.F. Mollenauer, R.H. Stolen, and J.P. Gordon, Phys. Rev. Lett. **45**, 1095 (1980). 175
3. G.P. Agrawal, *Nonlinear Fiber Optics*, (Academic Press, San Diego, 1995). 175, 176, 177, 178
4. A. Hasegawa and Y. Kodama, *Solitons in Optical Communications*, (Oxford University Press, Oxford, 1995). 175, 183
5. A. Hasegawa and M. Matsumoto, *Optical Solitons in Fibers*, (Springer, Berlin, 2003). 175
6. L.F. Mollenauer and J.P. Gordon, *Solitons in Optical Fibers: Fundamentals and Applications*, (Elsevier Academic Press, Burlington, MA, 2006). 175, 183
7. C.E. Shannon, The Bell Syst. Tech. J. **27**, 379 and 623 (1948). 176
8. J.M. Kahn and K.-P. Ho, Nature (London) **411**, 1007 (2001). 176
9. P.P. Mitra and J.B. Stark, Nature (London) **411**, 1027 (2001). 176
10. K.-P. Ho and J.M. Kahn, Channel capacity of WDM systems using constant-intensity modulation formats. In: *Proc. of Optical Fiber Commun. Conf. 2002* paper ThGG85 (Optical Society of America, Washington, DC, 2002). 176
11. J. Tang, J. Lightwave Technol. **24**, 2070 (2006). 176
12. C. Xu, X. Liu, and X. Wei, IEEE J. Sel. Topics Quant. El. **18**, 281 (2004). 176
13. N.N. Akhmediev, G. Town, and S. Wabnitz, Opt. Commun. **104**, 385 (1994). 176
14. N.N. Akhmediev and A. Ankiewicz, Chaos **10**, 600 (2000). 176
15. V.E. Zakharov and A.B. Shabat, Sov. Phys. JETP **34**, 62 (1971). 176
16. P. Emplit, J.P. Hamaide, F. Reynaud, C. Froehly, and A. Barthelemy, Opt. Comm. **62**, 374 (1987). 177
17. D. Krökel, N.J. Halas, G. Giuliani, and D. Grischkowsky, Phys. Rev. Lett. **60**, 29 (1988). 177
18. A.M. Weiner, J.P. Heritage, R.J. Hawkins, R.N. Thurston, E.M. Kirschner, D.E. Leaird, and W.J. Tomlinson, Phys. Rev. Lett. **61**, 2445 (1988). 177
19. M. Haelterman and P. Emplit, Electron. Lett. **29**, 356 (1993). 177
20. C.R. Menyuk, J. Opt. Soc. Am. B **10**, 1585 (1993). 177
21. N. Akhmediev, A. Ankiewicz, (eds.): *Dissipative Solitons*, Springer Lect. Notes Phys. **661**. Springer, Berlin, Heidelberg (2005). 177

22. A. Mees Chaos in feedback systems, In: *Chaos*, edited by A.V. Holden (Princeton University Press, Princeton, 1986). 178
23. A. Schwache and F. Mitschke, Phys. Rev. E **55**, 7720 (1997). 179, 182
24. G. Steinmeyer, D. Jaspert, and F. Mitschke, Opt. Comm. **104**, 379 (1993). 179
25. G. Steinmeyer, A. Buchholz, M. Hänsel, M. Heuer, A. Schwache, and F. Mitschke, Phys. Rev. A **52**, 830 (1995). 179, 182
26. F. Mitschke, G. Steinmeyer, and A. Schwache, Physica D **96**, 251 (1996). 179
27. G. Steinmeyer, A. Schwache, and F. Mitschke, Phys. Rev. E **53**, 5399 (1996). 179
28. F. Mitschke, I. Halama, and A. Schwache, Chaos, Solitons, Fract. **10**, 913 (1999). 182
29. F. Mitschke and A. Schwache, Quantum Semicl. Opt. **10**, 779 (1998). 182
30. B. Malomed, A. Schwache, and F. Mitschke, Fiber Integrated Opt. **17**, 267 (1998). 182
31. S. Rutz and F. Mitschke, J. Optics B: Quant. Semiclass. Opt. **2**, 364 (2000). 182
32. S. Rutz, T. Körösi, and F. Mitschke, Appl. Phys. B **72**, 101 (2001). 182
33. G. Steinmeyer and F. Mitschke, Appl. Phys. B **62**, 367 (1996). 182
34. J.H.B. Nijhof, N.J. Doran, W. Forysiak, and F.M. Knox, Electron. Lett. **33**, 1726 (1997). 183, 184
35. Y. Chen and H.A. Haus, Opt. Lett. **23**, 1013 (1998). 183
36. S.K. Turytsin and E.G. Shapiro, Opt. Lett. **23**, 682 (1998). 183
37. J.N. Kutz and S.G. Evangelides, Opt. Lett. **23**, 685 (1998). 183
38. V.S. Grigoryan and C.R. Menyuk, Opt. Lett. **23**, 609 (1998). 183
39. M. Stratmann, M. Böhm, and F. Mitschke, Electron. Lett. **37**, 1182–1183 (2001). 183, 190
40. M. Stratmann, T. Pagel, and F. Mitschke, Phys. Rev. Lett. **95**, 143902 (2005). 183, 184, 185, 186
41. C. Paré and P.-A. Bélanger, Opt. Commun. **168**, 103 (1999). 183
42. A. Maruta, T. Inoue, Y. Nonaka, and Y. Yoshika, IEEE J. Selec. Top. Quant. Electron. **8**, 640 (2002). 184
43. J.P. Gordon and L.F. Mollenauer: *personal communication*; see also I. Gabitov, R. Indik, L. Mollenauer, M. Stepanov, P.M. Lushnikov, Opt. Lett. **32**, 605 (2007). 185
44. M. Stratmann and F. Mitschke, Phys. Rev. E **72**, 066616 (2005). 188
45. K.J. Blow and N.J. Doran, Physics Lett. **107A**, 55 (1985). 188
46. D. Foursa and P. Emplit, Phys. Rev. Lett. **77**, 4011 (1996). 188
47. D.Y. Tang, W.S. Man, H.Y. Tam, and P.D. Drummond, Phys. Rev. A **64**, 033814 (2001). 192
48. D.Y. Tang, B. Zhao, D.Y. Chen, C. Lu, W.S. Man, and H.Y. Tam, Phys. Rev. A **68**, 0013816 (2003). 192
49. Ph. Grelu, F. Belhache, F. Gutty, and J.-M. Soto-Crespo, Opt. Lett. **27**, 966 (2002). 192
50. N.H. Seong and D.Y. Kim, Opt. Lett. **27**, 1321 (2002). 192
51. N.N. Akhmediev, A. Ankiewicz, and J.M. Soto-Crespo, J. Opt. Soc. Am. B **15**, 515 (1998). 192
52. Y. Kodama, S. Kumar, and A. Maruta, Opt. Lett. **22**, 1689 (1997). 192
53. T.-S. Yang and W.L. Kath, Physica D **149**, 80 (2001). 192

Dissipative Nonlinear Structures in Fiber Optics

S.K. Turitsyn and S. Boscolo

Abstract Optical fiber materials exhibit a nonlinear response to strong electric fields, such as those of optical signals confined within the small fiber core. Fiber nonlinearity is an essential component in the design of the next generation of advanced optical communication systems, but its use is often avoided by engineers because of its intractability. The application of nonlinear technologies in fiber optics offers new opportunities for the design of photonic systems and devices. In this chapter, we make an overview of recent progress in mathematical theory and practical applications of temporal dissipative solitons and self-similar nonlinear structures in optical fiber systems. The design of all-optical high-speed signal processing devices, based on nonlinear dissipative structures, is discussed.

1 Introduction

Fiber optics is particularly known because of its enormous contribution to telecommunication applications, underpinning the never-ending development of the Internet and the growth in global data traffic. There are, however, many other interesting applications of fiber optics, especially in nonlinear science. An optical fiber waveguide that can trap relatively high-intensity electromagnetic fields inside a small core area presents a natural nonlinear medium with the additional advantages of low loss and cost. Note also that in fiber optic geometry, transversal field distribution does not change on propagation, so the field evolution problem is essentially one-dimensional, making it very attractive for mathematical modeling. As a result,

S.K. Turitsyn
Photonics Research Group, School of Engineering and Applied Science, Aston University, Birmingham B4 7ET, UK, s.k.turitsyn@aston.ac.uk

S. Boscolo
Photonics Research Group, School of Engineering and Applied Science, Aston University, Birmingham B4 7ET, UK, s.a.boscolo@aston.ac.uk

Turitsyn, S.K., Boscolo, S.: *Dissipative Nonlinear Structures in Fiber Optics.* Lect. Notes Phys. **751**, 195–220 (2008)
DOI 10.1007/978-3-540-78217-9_8

nonlinear fiber optics has attracted a great deal of attention in the applied mathematics community, making this field truly inter-disciplinary. Nonlinear fiber optics is a fast-developing area of research with a rich variety of nonlinear phenomena such as super-continuum generation, solitons, stimulated Raman effect and many others. Loss is a dominant effect on optical signal propagation along a fiber. However, historically in soliton theory optical fibers have been commonly treated as media where conservative solitons do occur [1, 2, 3, 4]. This is justified by consideration of average pulse dynamics along long fiber links, where the signal evolution is averaged over many amplification periods. To the leading order, only fiber loss and periodic amplification are significant factors affecting the pulse evolution between two consecutive amplifiers. These factors cause oscillations of the signal power, while the form of the pulse remains approximately unchanged. On larger scales, nonlinearity and dispersion come into play and the pulse propagation in such communication systems is described by the well-established path-average (guiding-center) soliton theory [5, 6, 7]. In this case, to the leading order, the average dynamics of the optical signal is given by the integrable [2] nonlinear Schrödinger (NLS) equation. In this chapter, however, we would like to draw attention to examples of dissipative (non-conservative) nonlinear structures in fiber-optic systems.

The emergence of temporal and/or spatial localized, particle-like structures that are called solitary waves, or solitons, is a widespread phenomenon occurring in a variety of physical problems. From a mathematical viewpoint, a soliton is a self-localized solution of a nonlinear partial differential equation describing the evolution of a nonlinear dynamical system with an infinite number of degrees of freedom. Since the discovery of the inverse scattering transform technique, a lot of emphasis has been put on solitons in so-called "integrable" conservative systems. The theory of nonlinear integrable systems is a remarkable and inspiring area of mathematical research. However, reductions to integrable systems are often a particular simplification of more complex physical models. Additionally, very often gain/loss effects make essential contributions to the dynamics of nonlinear waves. In recent years, the notion of solitons has been extended to dissipative systems in which gain and loss are important factors determining the system dynamics (see, e.g., [8, 9, 10, 11] and references therein). Dissipative localized structures or auto-solitons are of particular interest because they form a new paradigm for the investigation of phenomena involving self-organization into stable structures in nonlinear environments far from equilibrium. The term "auto-solitons" or "dissipative solitons" here and throughout the chapter means robust localized pulses, with parameters prescribed by properties of the system, which often occur in nonlinear dissipative models [12, 13, 14, 15, 16]. Mathematically, dissipative solitary waves are nonlinear modes of non-integrable non-Hamiltonian physical systems. Dissipative solitons have been observed in different areas of physics, such as hydrodynamics, plasmas, solid-state physics and nonlinear optics. In optics, the notion of a dissipative soliton is mainly associated with ultra-short pulses generated in laser systems, spatial solitons in wide aperture lasers, cavity solitons [10] and solitons in active optical media [13, 17, 18]. The term "dissipative", in contrast to "conservative", underlines the key role of energy flows in systems with radiation sinks (losses) and sources (pumping). While conservative

solitons (e.g., solitons of the NLS equation) have a continuous spectrum of their parameters, i.e., they form families, the balance between losses and pumping in dissipative systems results in solitary wave solutions that usually do not form families and whose parameters are entirely fixed by the system. Therefore, the physics of dissipative solitons is essentially different from that of the much better-known and more-studied conservative solitons. Thus, the development of appropriate mathematical and physical models to describe dissipative solitons and the characterization of the properties of such objects in various physical systems represent one of the most challenging and fundamental problems of modern nonlinear science. In addition to their fundamental interest, dissipative solitons also exhibit a remarkable potential for applications, particularly in nonlinear optics.

In this chapter, we discuss recent progress in the theory of nonlinear dissipative structures in fiber optics, focusing on two particular examples: dissipative solitons in high-speed optical transmission lines and self-similar parabolic pulses. We would like to note that the main attention in this chapter will be focussed on results obtained in our group, and that it is not our intention here to comprehensively cover all the possible examples of nonlinear dissipative structures in fiber optics.

2 Dissipative Solitons in High-Speed Fiber Communication Systems

An increase in the capacity of digital communication systems can be achieved by an increase in the channel bit rate – the speed at which information is transmitted. Increasing the channel rate assumes the utilization of shorter time slots allocated for each information bit and, consequently, of shorter signal pulses. The propagation of ultra-short pulses is strongly affected by the fiber dispersion, which results in large temporal broadening of the signal pulses. Because of the temporal broadening during propagation, the signal pulse power spreads over many time slots and so the accumulated effect of the instantaneous fiber nonlinearity tends to get averaged out. Signal transmission using very short optical pulses is often referred to as the quasi-linear regime [19]. This regime is, in some sense, the opposite of soliton [4] or dispersion-managed (DM) soliton [20] transmission, where the fiber nonlinearity plays an important role in preserving the pulse shapes during propagation. Note that, in the quasi-linear regime, the in-line Kerr nonlinearity is almost a "negative" factor contributing to the destabilization and distortion of signal pulses. Therefore, a certain amount of "constructive" nonlinearity is required to stabilize ultra-short pulse propagation and, thus, to improve the system performance. Recently, the periodic in-line deployment of nonlinear optical devices (NODs), such as nonlinear optical loop mirrors (NOLMs), semiconductor saturable absorbers and semiconductor amplifier-based devices, has been demonstrated to be an effective technique for all-optical signal regeneration [21, 22, 23, 24], which may achieve stable pulse propagation and virtually unlimited transmission distances in high-speed, strongly DM optical fiber communication systems [22, 23]. It has numerically been shown

in [21, 22, 23] that, under certain conditions, the interplay between fiber dispersion, the lumped nonlinearity provided by in-line NOLMs and the action of linear control elements, such as optical filters, leads to the formation of dissipative solitons. These are periodically reproduced at the output of each segment of the transmission line.

The use of ultra-short optical pulses in fiber-optic communication leads to new interesting physical regimes. Novel mathematical models should be introduced to adequately describe such transmission systems. Here, we present a theory of optical signal transmission in DM fiber transmission systems in the quasi-linear regime, with periodically placed in-line point NODs [25]. We present a fundamental discrete mapping equation governing signal pulse propagation in a unit cell of the transmission line. As a particular example of an approach to the solution of this basic model, we apply a variational method to determine the steady-state pulse characteristics. Without loss of generality, as a specific practical application of the general theory, we consider a system with in-line NOLMs.

2.1 Theoretical Model

Optical pulse propagation in a cascaded transmission system with periodic variations of dispersion and nonlinearity, frequency filtering and NOD management can be described by

$$\mathrm{i}\psi_z - \frac{1}{2}\beta_2(z)\psi_{tt} + \sigma(z)|\psi|^2\psi = \mathrm{i}G(z,|\psi|^2)\psi, \tag{1}$$

where $\psi(z,t)$ is the slowly varying pulse envelope in the co-moving system of coordinates, $\beta_2(z)$ represents the variation in the group-velocity dispersion (GVD) due to dispersion compensation, and is assumed to be a periodic function of z with the period L, $\beta_2(z) = \beta_2(z+L)$, and σ is the fiber nonlinear coefficient. It is customary to express β_2 in terms of the associated dispersion coefficient D via $\beta_2 = -\lambda^2 D/(2\pi c_0)$, where λ is the carrier wavelength, c_0 is the speed of light and D is measured in ps/(nm km). The function $G(z,|\psi|^2)$ accounts for the signal attenuation due to fiber loss, the signal amplification by optical amplifiers, the action of filters and the nonlinear gain at the NODs. It can be represented by

$$\begin{aligned} G(z,|\psi|^2) = &-\gamma(z) + \sum_k \delta(z-kZ_\mathrm{a})\left\{\exp\left[\int_{(k-1)Z_\mathrm{a}}^{kZ\mathrm{a}} \mathrm{d}z\,\gamma(z)\right] - 1\right\} \\ &+ \sum_k \delta(z-kZ_\mathrm{f})[h(t) * -1] + \sum_k \delta(z-kZ_0)[f(|\psi|^2) - 1]. \end{aligned} \tag{2}$$

In (2), we have assumed that amplifiers, filters and NODs are placed periodically in the system with respective periods Z_a, Z_f, and Z_0. $\gamma = 0.05\ln(10)\alpha$ is the fiber loss coefficient that accounts for the signal attenuation along the fiber span before the kth amplifier, α is given in dB/km and $\exp\left[\int_{(k-1)Z_\mathrm{a}}^{kZ_\mathrm{a}} \mathrm{d}z\,\gamma(z)\right] - 1$ is the

amplification coefficient after the fiber span between the $(k-1)$th and kth amplifiers. $h(t)$ is the inverse Fourier transform of the filter transfer function and $*$ represents the Fourier convolution. The NODs are specified by their power-dependent transfer function $f(P)$. Henceforth, we will focus on loss (gain)-unbalanced fiber NOLMs. The transfer function for such devices can be written in the form

$$f(P) = a\sin(bP)\exp(\mathrm{i}cP), \tag{3}$$

with $a,b,c \in \Re^+$ some given constants.

To simplify the full model given by system (1), we make some justified physical assumptions. Here, we analyze the case of linear propagation in fiber, when we can neglect the nonlinear term in (1). Such a propagation regime corresponds to the case where the nonlinear length $L_{\mathrm{NL}} = (\sigma P_0)^{-1}$ (P_0 is the signal peak power) in the fiber is much longer than the local dispersion length $L_{\mathrm{D}} = T^2/|\beta_2|$ (T is the pulse width). The transformation of a pulse after propagation in one segment of the transmission line can be considered as the mapping of an input pulse into an output one. If we consider an element of the transmission line that includes a NOD given by (3), a piece of linear fiber of length Z_0 and m filters, the mapping of the signal, defined up to a phase factor μ, can be represented by

$$\mathrm{e}^{\mathrm{i}\mu}U_{n+1}(t) = \int_{-\infty}^{+\infty} \mathrm{d}t'\, K(t-t';Z_0) f(|U_n(t')|^2)U_n(t'), \qquad n = 0,1,\ldots. \tag{4}$$

The derived equation is one of the central results of the theory presented in this section [25]. This mapping problem plays a fundamental role in the description of fiber communication systems at high bit rates. To obtain (4), we have assumed that each NOD is placed immediately after an amplifier, and we have applied the transformation $U(z,t) = Q^{-1}(z)\psi(z,t)$, where $Q(z) = \exp\left[-\int_{(k-1)Z_{\mathrm{a}}}^{z} \mathrm{d}z'\,\gamma(z')\right]$ for $(k-1)Z_{\mathrm{a}} < z < kZ_{\mathrm{a}}$ and $Q(z) = 1$ for $z = kZ_a^+$. In (4), the signal is taken at the input point nZ_0^- to the NOD after any device prior to the NOD. The kernel K describes signal propagation in the unit cell Z_0. In the case where Gaussian filters are used, K can be written in the form

$$K(t-t';Z_0) = \sqrt{G}\sqrt{\frac{\mathrm{i}}{2\pi\left(B_0 + \mathrm{i}m/\Omega_{\mathrm{f}}^2\right)}}\exp\left[-\frac{\mathrm{i}(t-t')^2}{2\left(B_0+\mathrm{i}m/\Omega_{\mathrm{f}}^2\right)}\right], \tag{5}$$

where $\Omega_{\mathrm{f}} = \pi\delta\nu_{\mathrm{f}}/\sqrt{\ln 2}$ is the filter bandwidth ($\delta\nu_f$ denotes the full-width at half-maximum (FWHM) bandwidth) and $B_0 = \int_{nZ_0}^{(n+1)Z_0} \mathrm{d}z\,\beta_2(z)$ is the total accumulated dispersion. In (5), the excess gain, G, accounts for compensation of the signal energy losses introduced by the NODs and filters in the system. From a transmission point of view, it is desirable to find a steady-state propagation regime (if it exists) in which an optical pulse propagating along the transmission line reproduces itself periodically at the output of each element of the line. That corresponds to determining a fixed point of the mapping (4). Therefore, in order to find the steady-state pulse shape, $U(t)$, one has to solve the nonlinear integral equation which stems from (4)

if we put $U_{n+1}(t) = U_n(t) = U(t)$. If the steady-state pulse is stable, then any initial signal within the basin of attraction of the fixed point will gradually evolve toward it after some mapping intervals.

2.2 Dissipative Soliton Solutions

In this subsection, we demonstrate the feasibility of stable dissipative soliton propagation guided by in-line NOLMs, by direct numerical simulations of the basic propagation model (1). The sample transmission scheme used in the numerical integration of (1) is depicted in Fig. 1. The transmission line is composed of an equal number of positive (anomalous) dispersion fiber (PDF) segments and negative (normal) dispersion fiber (NDF) segments. The dispersion map consists of an alternation of a PDF–NDF block and a mirror NDF–PDF block. Fiber parameters of practical importance are used for the PDF and the NDF [22]. We note that fiber nonlinearity is included in the calculations. An optical amplifier (OA), which compensates for the fiber loss, follows each of the two blocks. The high values of the local dispersion of the fibers, together with the short pulse widths that are typically used to operate the system at high data transmission rates, result in considerable broadening of the pulses during propagation. These regimes are beyond the range where stable propagation of DM solitons has been observed [26]. A NOLM is placed into the transmission line at every integer number, p, of dispersion map periods, $Z_0 = pL$. We note that, in this case, $B_0 = \langle\beta_2\rangle Z_0 = -\lambda^2\langle D\rangle Z_0/(2\pi c_0)$ ($\langle\cdot\rangle$ denotes the average over the dispersion compensating period, L). In the sample configuration used here, $Z_0 = 391$ km and $p = 5$. A single ($m = 1$) Gaussian optical filter (OF) is placed after the amplifier prior to the NOLM location. The loss-unbalanced NOLM configuration is employed as an example, and pre-amplification of the input pulses to the NOLM is used (see [22] for details). Parameters a, b and c in (3) have the respective values: 0.06369, 1.823 and 1.839. Following [22, 23], the system is operated such that the peak power of the steady-state pulses (if any exist) is in the region slightly past the first peak of the continuous-wave power characteristic of the NOLM.

Figure 2 shows an example of pulse evolution in the system, measured stroboscopically at the NOLM input point. In this example, an unchirped Gaussian pulse is

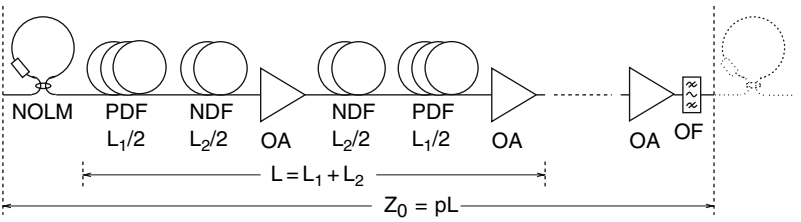

Fig. 1 One element of the periodic transmission system

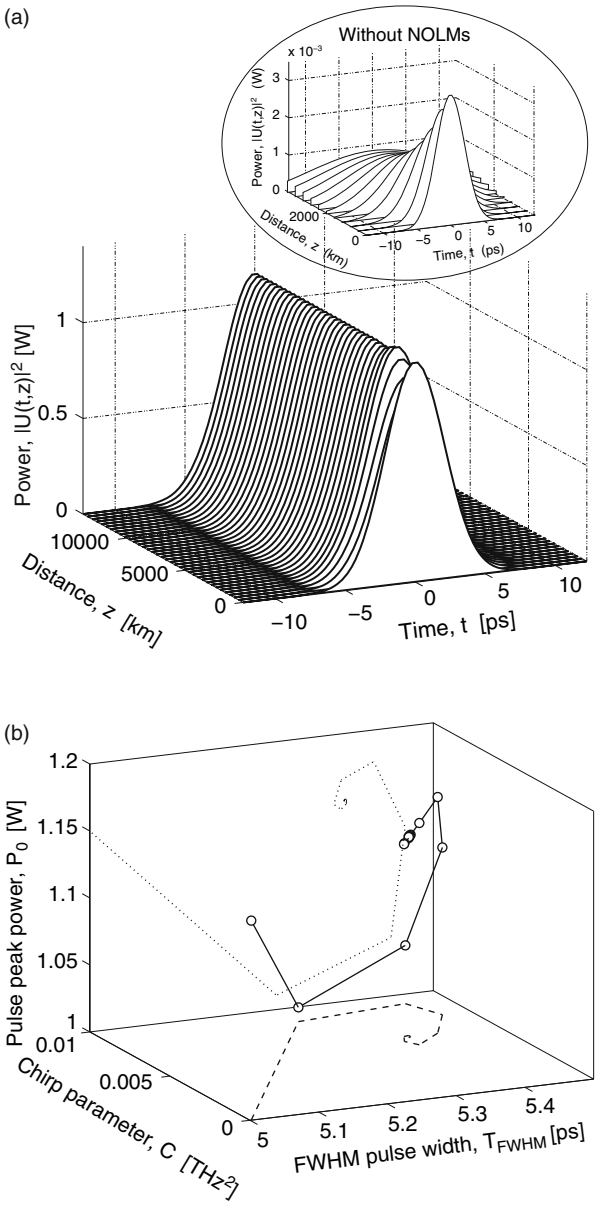

Fig. 2 Stroboscopic pulse evolution, as viewed at the NOLM input: (**a**), evolution of the intensity profile; inset, intensity profile evolution in the system without NOLMs; (**b**), acquisition of the steady state in the space FWHM pulse width–chirp parameter–peak power

launched into the system, with peak power $P_0 = 1.15\,\mathrm{W}$ (corresponding to 3.5 mW at the starting point of the transmission) and an FWHM pulse width $T_{\mathrm{FWHM}} = 5\,\mathrm{ps}$. The system parameters are: $\langle D \rangle = 0.009\,\mathrm{ps}/(\mathrm{nm\,km})$, $\delta\nu_{\mathrm{f}} = \sqrt{\ln 2}\Omega_{\mathrm{f}}/\pi = 0.1\,\mathrm{THz}$ and $G = 627.0$ (28.0 dB). Here the pulse chirp parameter is calculated

$$C = \mathrm{Im} \int_{-\infty}^{+\infty} \mathrm{d}t\, U^2 (U_t^*)^2 / \int_{-\infty}^{+\infty} \mathrm{d}t\, |U|^4.$$

Figure 2 is the key demonstration of the dissipative nature of the considered nonlinear structures. In contrast to conservative Hamiltonian solitary waves, where the pulse power is a continuous function of the width, here the dissipative soliton parameters are fixed by the system characteristics. The solution is an attractor that provides robustness and stability of these signal pulses. One may see, from Fig. 2, that the pulse settles down to a steady state after a short initial transient, in contrast to the case without NOLMs, where the pulse peak power decays and the pulse width broadens with distance. This result demonstrates the feasibility of stable pulse propagation in the system, and indicates that the use of in-line NOLMs converts the quasi-linear transmission regime into a dissipative soliton transmission regime, which is strictly nonlinear [22, 23]. We note that the same stroboscopic picture as that in Fig. 2 can be obtained by simply iterating the mapping equation (4). Figure 3 shows the basin of attraction of the steady-state solution of Fig. 2 in the plane (T_{FWHM}, C). To calculate Fig. 3, the initial pulse peak power has been set to its steady-state value. It is seen that there is a large tolerance to the initial pulse width and chirp, which indicates a high degree of stability of the steady-state solution.

We have also defined the tolerance limits of stable pulse propagation to the filter bandwidth and the path-averaged dispersion of the line. The results are shown in Fig. 4, where $\delta\nu_{\mathrm{f}}$ and $\langle D \rangle$ are varied within a practical range of values. In Fig. 4, the excess gain, G, is chosen so that the stationary pulse peak power is approximately 1.15 W at the NOLM input. Figure 4 illustrates how the system parameters can be used to select desirable stable regimes with a particular average dispersion. Note that this is a feature that is not always possible in conservative fiber transmission systems. Specifically, it means that the use of dissipative solitons as information carriers provides more freedom and opportunities in the design of transmission systems.

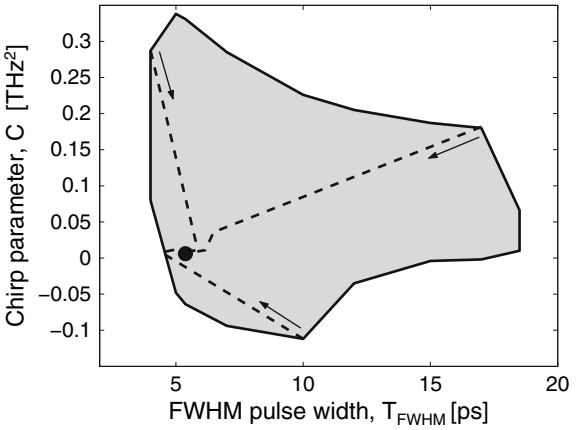

Fig. 3 Basin of attraction of the steady-state solution of Fig. 2 in the plane (FWHM pulse width vs. chirp parameter)

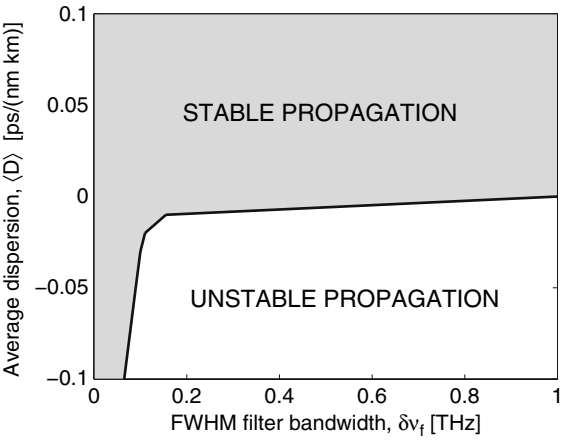

Fig. 4 Limits of stable pulse propagation in the plane (filter bandwidth vs. average dispersion)

2.3 Approximate Mapping Using Integral Characteristics

Following [25], here we present a simplified approximate method to describe the characteristics of the dissipative soliton solutions found in the previous subsection. As we pointed out previously, in order to find a steady-state pulse propagation regime, one has to solve a mapping integral equation (4) for the fixed points. While this can be done numerically, it is very useful to have a simplified approximate method to find solutions of the basic model for massive optimization of the system parameters. Therefore, here we apply a simple variational approach. We notice, from full numerics, that the steady-state pulse shape at the NOLM input point can always be fitted well by a Gaussian profile. Thus, we choose a trial input pulse $U(t)$ for the map as a Gaussian-shaped pulse with (yet unknown) peak power P_0, root-mean-square (RMS) width T_{RMS} and RMS chirp parameter C_{RMS}: $U_n(t) = \sqrt{P_0}\exp[-t^2/(4T_{\mathrm{RMS}}^2) + \mathrm{i}C_{\mathrm{RMS}}t^2]$. The output of the map $U_{n+1}(t)$ given by (4) will be non-Gaussian in general, but it will have a similar shape and will depend on the parameters of the input signal, $U_{n+1} = U_{n+1}(t; P_0, T_{\mathrm{RMS}}, C_{\mathrm{RMS}})$. Let us now demand that the peak power, pulse width and chirp of the output signal coincide with those of the input Gaussian signal. This provides a system of transcendental equations for the required parameters P_0, T_{RMS} and C_{RMS}:

$$
\begin{aligned}
P_0 &= \frac{1}{\sqrt{2\pi}T_{\mathrm{RMS}}}\int_{-\infty}^{+\infty}\mathrm{d}t\,|U_{n+1}(t;P_0,T_{\mathrm{RMS}},C_{\mathrm{RMS}})|^2,\\
T_{\mathrm{RMS}}^2 &= \frac{\displaystyle\int_{-\infty}^{+\infty}\mathrm{d}t\,t^2|U_{n+1}(t;P_0,T_{\mathrm{RMS}},C_{\mathrm{RMS}})|^2}{\displaystyle\int_{-\infty}^{+\infty}\mathrm{d}t\,|U_{n+1}(t;P_0,T_{\mathrm{RMS}},C_{\mathrm{RMS}})|^2},\\
C_{\mathrm{RMS}} &= \frac{\mathrm{Im}\displaystyle\int_{-\infty}^{+\infty}\mathrm{d}t\,U_{n+1}^2(t;P_0,T_{\mathrm{RMS}},C_{\mathrm{RMS}})(\partial_t U_{n+1}^*(t;P_0,T_{\mathrm{RMS}},C_{\mathrm{RMS}}))^2}{\displaystyle\int_{-\infty}^{+\infty}\mathrm{d}t\,|U_{n+1}(t;P_0,T_{\mathrm{RMS}},C_{\mathrm{RMS}})|^4}.
\end{aligned}
\tag{6}
$$

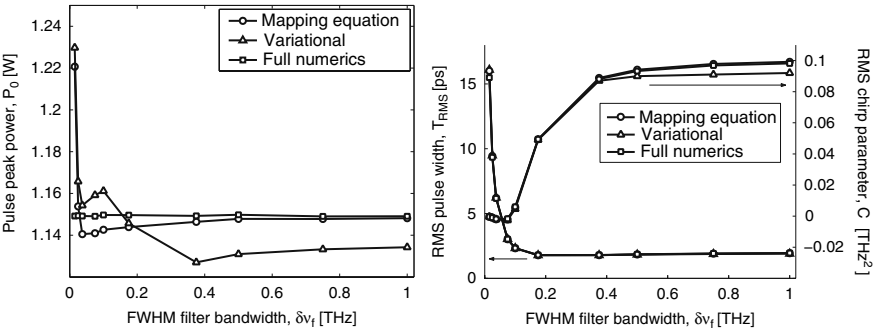

Fig. 5 Steady-state pulse parameters at the NOLM input vs. filter bandwidth: *left*, peak power; *right*, RMS width (*left axis*) and RMS chirp parameter (*right axis*)

If the solution of system (6) exists, then it provides a variational approximation for the parameters of the steady-state pulse [25]. In particular, one may use the Gaussian *ansatz* with the resultant values of P_0, T_{RMS} and C_{RMS} as an approximation of the steady-state pulse shape.

The theoretical predictions from the variational model (6) have been compared with the results of full numerical simulations. The steady-state pulse peak power, RMS width and RMS chirp parameter are plotted in Fig. 5 as functions of the filter bandwidth, for $\langle D \rangle = 0.009\,\mathrm{ps}/(\mathrm{nm\,km})$ and the same values of G as those used in Fig. 4. The results agree well, especially for the pulse width and the chirp parameter. As for the pulse amplitude, the discrepancies between the solutions of (4) and the full numerics (of the order of 6% at maximum) occurring at small values of $\delta\nu_{\mathrm{f}}$ can be attributed to the fact that, for small filter bandwidths, the effect of the nonlinearity in the transmission fibers becomes important, whereas it is neglected in model (4). For larger $\delta\nu_{\mathrm{f}}$, the deviation of model (4) from the full numerics result does not exceed 0.6%. This fully justifies the linear assumption underlying (4) in this filter bandwidth range. The deviation of the variational model from either full numerics or model (4) does not exceed 2% in the bandwidth range where the linear assumption is entirely justified. The steady-state intensity profile and chirp (first time derivative of the phase) of the input pulse to the NOLM are plotted in Fig. 6, for $\delta\nu_{\mathrm{f}} = 0.1\,\mathrm{THz}$. The results from the variational model are in good agreement with the full numerical results and the results from (4) in the central part of the pulse. We observe that although the pulse chirp obtained from the full numerics and (4) is linear across the entire pulse duration, it exhibits a small change in slope in the pulse tails.

We note that the dissipative soliton solutions presented here are only a particular example of nonlinear dissipative structures that occur in high-speed fiber communication systems. An increase in the channel rate and corresponding decrease in carrier pulse width lead to a considerable overlap of the bits during transmission, and corresponding patterning effects. To combat these effects some "positive" nonlinearity is required to provide for stability of the carrier signals. Dissipative solitons are attractive candidates for use as carriers of information in high-speed, high-capacity fiber systems.

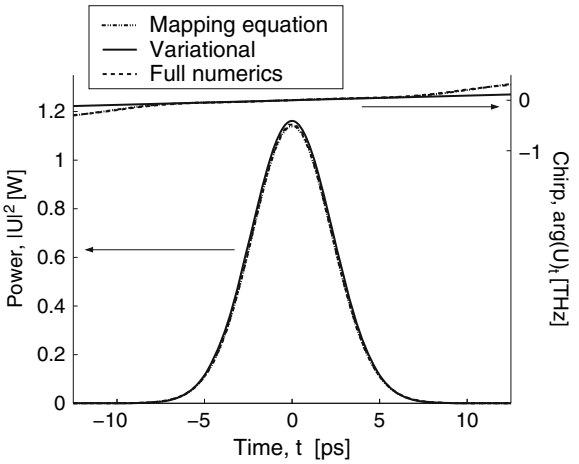

Fig. 6 Intensity (*left axis*) and chirp (*right axis*) of the steady-state pulse at the NOLM input

3 Self-Similar Parabolic Pulses in Active Fibers

In this section, we consider an interesting and important type of dissipative nonlinear structure in fiber optics, viz., self-similar parabolic pulses. Self-similar behavior occurs in a variety of physical systems and has been extensively studied in diverse areas of science [27]. A theory of self-similar propagation of short pulses of parabolic intensity profile in optical fibers with normal GVD and strong nonlinearity has been developed in [28]. Recently, this concept has been extended to a fiber amplifier [29, 30, 31, 32, 33]. In addition to their fundamental scientific interest, self-similar pulses or similaritons are of great practical significance, because their intrinsic resistance to optical wave-breaking allows them to be scaled up to the high-power regime, and their linear chirp facilitates efficient pulse compression [28]. Moreover, a combination of a similariton amplifier and optical feedback recently resulted in a new regime of laser mode-locking that is likely to have major implications for the development of high-power ultra-short pulse laser oscillators [34].

Analytically, self-similar parabolic pulses can be found as approximate solutions of the NLS equation in a gain medium in the high-intensity limit [29]. The derivation of such solutions is based on the assumption that the linear dispersive term in the equation for the field amplitude is negligible compared with the nonlinear term. This is similar to the semi-classical approximation in quantum mechanics. Here, we present a detailed mathematical analysis of the solutions of the NLS equation with gain [30]. We construct a semi-classical self-similar solution with a parabolic temporal variation that corresponds to the energy-containing core of the asymptotically propagating pulse in the gain medium. We match the self-similar core through Painlevé functions to the solution of the linearized equation that corresponds to the low-amplitude tails of the pulse.

3.1 Basic Equations

Optical pulse propagation in a fiber gain medium can be described by

$$\mathrm{i}\psi_z - \frac{\beta_2}{2}\psi_{tt} + \sigma|\psi|^2\psi = \mathrm{i}\frac{g(z)}{2}\psi, \tag{7}$$

where $g(z)$ is the gain profile along the fiber. Following [30], we seek a solution of (7) of the form

$$\psi(z,t) = a(z)F(\eta,\xi)\mathrm{e}^{\mathrm{i}C(z)t^2}, \tag{8}$$

where new self-similar variables are introduced as $\xi = t/\tau(z)$ and $\mathrm{d}\eta/\mathrm{d}z = \sigma a^2(z)$. Here, $a(z)$ describes the evolution of the pulse peak amplitude with distance, $\tau(z)$ is a characteristic width, $C(z)$ is a chirp parameter and $F(\eta,\xi)$ is a normalized, dimensionless function that describes the evolution of the temporal profile through its ξ dependence, and accounts for contributions to the peak amplitude and the phase through its η dependence. These transformations yield coupled equations for a, τ, C and F:

$$\frac{a_z}{a} = \beta_2 C + \frac{g}{2}, \tag{9}$$

$$\frac{\tau_z}{\tau} = -2\beta_2 C, \tag{10}$$

$$(C_z - 2\beta_2 C^2)\tau^2 = -\lambda\sigma a^2, \tag{11}$$

$$\mathrm{i}F_\eta + (|F|^2 + \lambda\xi^2)F - \frac{1}{c(\eta)}F_{\xi\xi} = 0, \tag{12}$$

where λ is an arbitrary parameter related to the pulse power, and $c = 2\sigma a^2\tau^2/\beta_2$. Equations (9), (10), (11) can be re-written to yield the relation between a and τ (the energy equation) and a second-order equation for τ, from which one may calculate the scaling of the pulse amplitude and width from their initial values. In (12), we separate F into a real amplitude A and a phase Φ as $F(\eta,\xi) = A(\eta,\xi)\mathrm{e}^{\mathrm{i}\Phi(\eta,\xi)}$ to obtain the "hydrodynamic" system of equations:

$$\begin{aligned} (A^2)_\eta - \frac{2}{c(\eta)}(A^2\Phi_\xi)_\xi &= 0, \\ \Phi_\eta + \frac{1}{c(\eta)}\left(\frac{A_{\xi\xi}}{A} - (\Phi_\xi)^2\right) - (A^2 + \lambda\xi^2) &= 0. \end{aligned} \tag{13}$$

3.2 High-Intensity Parabolic Pulses

We first consider the possibility of an approximate description of the central part of the pulse where most of the energy is concentrated. We define a parameter ε as the ratio of the linear dispersive term to the nonlinear term in the second equation in (13),

$$\varepsilon(\eta,\xi) = \left| \frac{A_{\xi\xi}}{c(\eta)A^3} \right|. \tag{14}$$

In the pulse core, the condition $\varepsilon \ll 1$ is satisfied. This corresponds to the so-called semi-classical limit of (7). Using this condition in (13), it is easy to find a self-similar solution with a parabolic distribution of the intensity:

$$A(\xi) = [\lambda(1-\xi^2)]^{1/2}, \quad |\xi| \le 1, \qquad \Phi(\eta) = \lambda\eta. \tag{15}$$

This solution yields the dependence of the pulse energy on the pulse parameters: $U = \int_{-\infty}^{\infty} \mathrm{d}t\, |\psi|^2 = 4\lambda a^2 \tau/3$.

The theoretical predictions from (9), (10), (11), (15) have been compared with the results of numerical simulations of (7). We modeled the propagation of a Gaussian pulse with energy 70 pJ and a FWHM pulse width 0.5 ps in a fiber amplifier of length 4 m, integrated gain 25 dB, $\sigma = 6 \times 10^{-3}\,(\mathrm{W\,m})^{-1}$ and $\beta_2 = 35 \times 10^{-3}\,\mathrm{ps}^2/\mathrm{m}$ [29]. Here, we focus on the case of a constant gain profile, $g(z) = g_\mathrm{a}$, with $g_\mathrm{a} = 1.44\,\mathrm{m}^{-1}$, because the functional form of $g(z)$ determines only the self-similar scaling of the propagating pulse in the amplifier (see (9), (10), (11)). This is without loss of generality.

Figure 7 shows the evolution of the pulse intensity profile in the amplifier obtained from simulation of the NLS equation. We can see that, as the incident Gaussian pulse is amplified to a high intensity, it evolves into a parabolic pulse in the second half of the amplifier. It can also be seen that the asymptotic pulse presents a self-similar energy-containing core surrounded by low-amplitude wings. These tails start developing on the pulse near the points $t = \pm\tau$, i.e., in the region where the linear term, neglected in the theory, becomes important. Therefore, the description of these tails requires a more detailed analysis of the pulse shape, and we will present this in the next subsection. Considering the asymptotic parabolic regime that occurs after some initial transition stage (here after a distance of 2.5 m), we

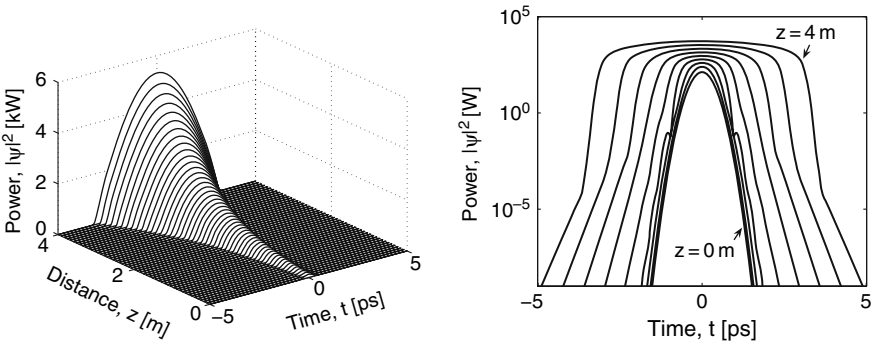

Fig. 7 Pulse evolution in the amplifier: *left*, evolution of the intensity profile, shown on a linear scale; *right*, intensity profiles plotted on a logarithmic scale in 0.5 m increments

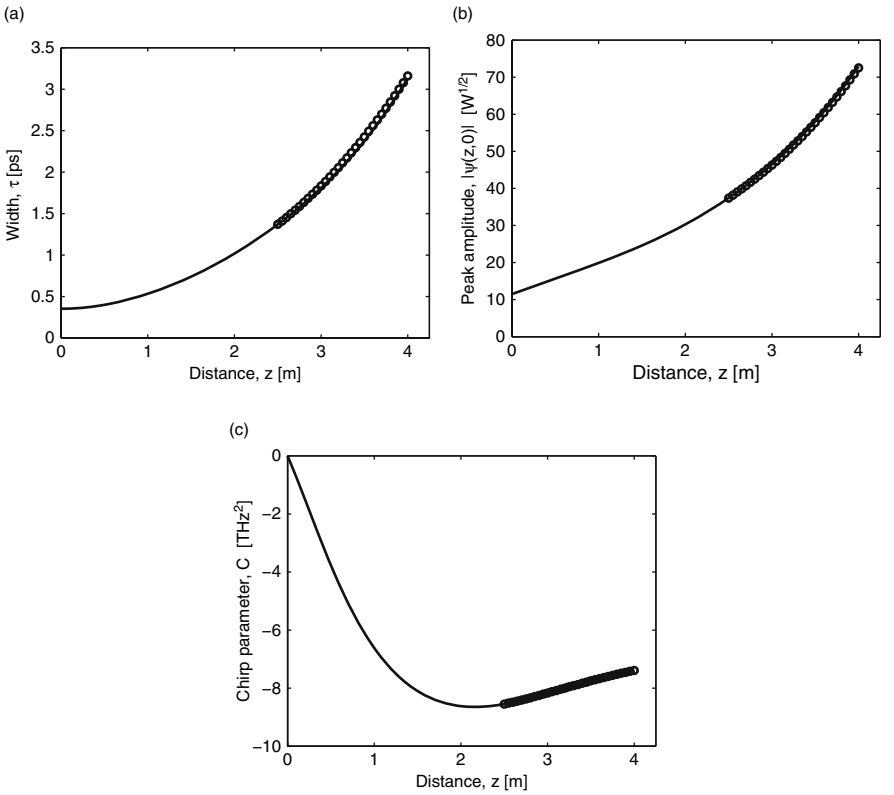

Fig. 8 Evolution of effective pulse width $\tau(z)$ (*top left*), peak amplitude $|\psi(z,0)|$ (*top right*) and chirp parameter $C(z)$ (*bottom*): solid curves, simulation results; circles, theoretical predictions for $z \geq 2.5\,\mathrm{m}$

can quantitatively compare the evolution of the pulse parameters from simulations with the theory. Figure 8 shows the evolution of the effective width $\tau(z)$, the peak amplitude $|\psi(z,0)|$ and the chirp parameter $C(z)$ obtained by fitting to the propagating pulse from simulations. These values are in good agreement with the expected results obtained from the solutions of (9), (10), (11), calculated for $z \geq 2.5\,\mathrm{m}$.

3.3 Matching Problem

In the previous subsection, we demonstrated that the parabolic approximation for the pulse shape can describe the central part of the asymptotically propagating pulse in the gain medium. Now, our aim is to include the pulse tails in the description [30]. For this, we first study the evolution in the time vs. distance plane of the parameter ε defined in (14). Figure 9 shows the variation of ε in the asymptotic regime, starting

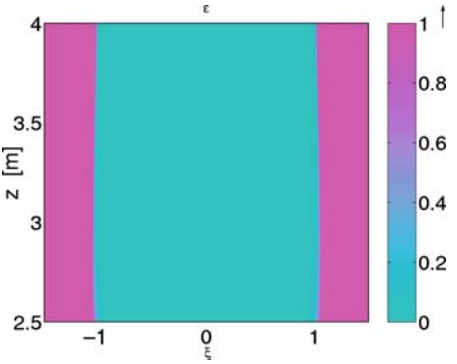

Fig. 9 Evolution of ε with distance, z, and normalized time, ξ, for $z \geq 2.5\,\text{m}$ and $-1.5 \leq \xi \leq 1.5$

from a propagation distance of 2.5 m. The entire color map is used for values ranging from 0 to 1, with values greater than 1 rendered with the same color associated with 1. It is clear from Fig. 9 that the transition of ε from values smaller than 1 to values greater than 1 occurs in a narrow region around the points $\xi = \pm 1$; this agrees with our intuitive expectations. We can also see that, in the asymptotic regime, the transition region does not move with distance (when presented in self-similar variables).

Based on these results, we define three regions on the ξ axis, as the schematic in Fig. 10 shows. We can limit our considerations to the semi-axis $\xi \geq 0$, because the problem is symmetric in ξ. Region (I), $0 \leq \xi \leq 1-\Delta_1$, corresponds to the central part of the asymptotic pulse, where $\varepsilon \ll 1$. Region (III), $\xi \geq 1+\Delta_2$, corresponds to the pulse tails, where $\varepsilon \gg 1$. Finally, region (II), $1-\Delta_1 \leq \xi \leq 1+\Delta_2$, is a transition zone, where $\varepsilon \approx 1$. The size of the transition zone is parametrized by $\Delta_1, \Delta_2 \ll 1$. We introduce two different Δ-intervals for the region around the point $\xi = 1$ because of an obvious asymmetry of the solutions with respect to this point. In each of the regions, we construct an approximate solution of (12) or, equivalently, of system (13) at fixed η. We then match the solutions at the boundaries. Here, we outline the procedure and the main results. The reader is referred to [30] for details.

In region (I), we consider the semi-classical solution derived in the previous subsection, namely,

$$A = A_{\text{I}}(\xi) = [\lambda(1-\xi^2)]^{1/2}, \quad \Phi = \Phi_{\text{I}}(\eta) = \lambda\eta, \quad 0 \leq \xi \leq 1-\Delta_1. \tag{16}$$

In region (II), we seek the solution

$$A = A_{\text{II}}(\eta,\xi), \quad 1-\Delta_1 \leq \xi \leq 1+\Delta_2,$$
$$\Phi = \Phi_{\text{II}}(\eta,\xi) = \begin{cases} \lambda\eta, & \xi = 1-\Delta_1, \\ \lambda\eta + \Phi_1(\eta,\xi), & 1-\Delta_1 < \xi \leq 1+\Delta_2. \end{cases} \tag{17}$$

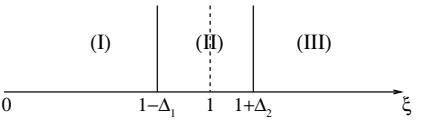

Fig. 10 Schematic of the ξ regions where (12) is solved

Following [35], the equation for the field amplitude (the second equation in (13)) can be reduced to

$$[2\lambda(\xi-1)+A_{\rm II}^2]A_{\rm II}-\frac{1}{c(\eta)}\frac{\partial^2 A_{\rm II}}{\partial\xi^2}=0, \tag{18}$$

where we have neglected terms of order ≥ 2 in $\Delta_{1,2}$. Such an equation corresponds to a special case of the second Painlevé equation with the change of variables $x=(2\lambda c)^{1/3}(\xi-1)$, $\phi=(c/(4\lambda^2))^{1/6}A_{\rm II}/\sqrt{2}$. The boundary conditions for (18) can be formulated in terms of the asymptotic behaviors of the second Painlevé transcendent. For a particular choice of the free parameters [36], these boundary conditions read

$$A_{\rm II}=[-\lambda(\xi^2-1)]^{1/2}\simeq[-2\lambda(\xi-1)]^{1/2},\quad \xi=1-\Delta_1,$$

$$A_{\rm II}=\frac{1}{\sqrt{\pi}}\left(\frac{\lambda}{2c}\right)^{1/4}\frac{{\rm e}^{-2(2\lambda c)^{1/2}(\xi-1)^{3/2}/3}}{(\xi-1)^{1/4}},\quad \xi=1+\Delta_2. \tag{19}$$

The solution of the boundary value problem specified by (18) and (19) gives $A_{\rm II}(\eta,\xi)$ (at fixed η). Using $A_{\rm II}(\eta,\xi)$ in

$$\Phi_1(\eta,\xi)=\frac{c(\eta)}{2}\int_{1-\Delta_1}^{\xi}{\rm d}\xi'\,\frac{1}{A_{\rm II}^2(\eta,\xi')}\int_{1-\Delta_1}^{\xi'}{\rm d}\xi''\,\frac{\partial A_{\rm II}^2}{\partial\eta}(\eta,\xi''), \tag{20}$$

which follows from the first equation in (13) (with the assumption that $A_{\rm II}^2$ never approaches zero), we obtain $\Phi_{\rm II}(\eta,\xi)$. In region (III), we seek a solution of the linearized equation of (12) with the form

$$F(\eta,\xi)=A_{\rm III}(\eta,\xi){\rm e}^{{\rm i}\Phi_{\rm III}(\eta,\xi)}=\alpha(\eta)G(\eta,\theta){\rm e}^{{\rm i}R(\eta)\xi^2},$$

$$\theta=\beta(\eta)\xi,\quad \xi\geq 1+\Delta_2. \tag{21}$$

We then obtain

$$\frac{\beta_\eta}{\beta}=\frac{4R}{c},\qquad \frac{\alpha_\eta}{\alpha}=\frac{2R}{c},\qquad R_\eta=\frac{4R^2}{c}+\lambda, \tag{22}$$

and a parabolic equation for $G(\eta,\theta)$ which is subject to the boundary condition coming from region (II) (see (19)), where we apply phase matching. The parabolic equation, together with the boundary condition, is solved by the double potential formula [37]

$$G(\eta,\theta)=\frac{1}{2\sqrt{\pi}}\int_0^{b(\eta)}{\rm d}\eta'\,G(\eta',\beta(\eta)(1+\Delta_2))\frac{\theta}{(b(\eta)-\eta')^{3/2}}{\rm e}^{-{\rm i}\theta^2/(4(b(\eta)-\eta'))}, \tag{23}$$

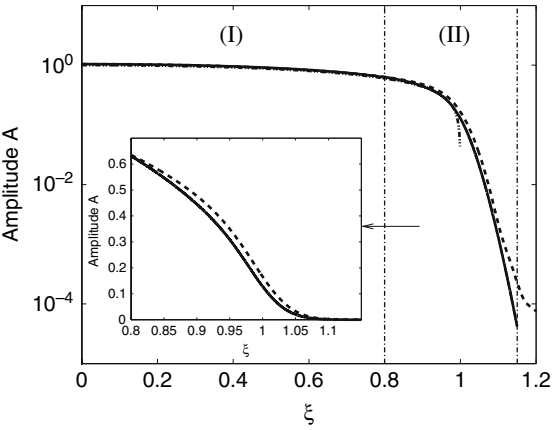

Fig. 11 Variation of the amplitude A with ξ at the amplifier output: *dashed curve*, numerical solution; *solid curve*, solution of the matching problem for $\Delta_1 = 0.2$ and $\Delta_2 = 0.15$; *dotted curve*, parabolic solution for $\Delta_1 = 0$. Inset: numerical solution and solution of the matching problem shown on a linear scale

where $\mathrm{d}b(\eta)/\mathrm{d}\eta = \beta^2(\eta)/c(\eta)$. This completes the construction of the function $F(\eta,\xi)$ for all ξ at fixed η. Parameters Δ_1 and Δ_2 must be sufficiently small to ensure matching between regions (I) and (II) and between regions (II) and (III): $(2\lambda c(\eta))^{1/3}|\xi - 1| \gg 1$, and $|\xi - 1| \ll 1$. We therefore choose $\Delta_{1,2}$ in the interval $0 < \Delta_{1,2} < (2\lambda c(\eta))^{-1/3+\varepsilon}$, with $0 < \varepsilon < 1/3$.

We compared the solution of the matching problem with the numerical solution of (7). An example is given in Fig. 11, which shows the amplitude A of F as a function of ξ for $0 \le \xi \le 1+\Delta_2$ at the final distance in the amplifier. The numerical solution is compared with the solution of the matching problem specified by (16) and the solution of (18). The parabolic solution of (16) is also plotted for $\Delta_1 = 0$. We note that Δ_1 must be chosen so that the parabolic solution of (16) does not deviate from the numerical solution at the point $\xi = 1 - \Delta_1$. The example in Fig. 11 corresponds to $\Delta_1 = 0.2$. In Fig. 11, $\Delta_2 = 0.15$. It can be seen that there is a good agreement between the analytic and numerical results. As the inset clearly shows, the difference between the analytic and the numerical curves is in fact of the order of $\Delta_{1,2}^2$, and the lowest-order terms neglected in (18) are $\mathrm{O}(\Delta_{1,2}^2)$.

3.4 Simple Approximate Description of the Pulse Shape

In theoretical studies, one of the technical problems in using the pure parabolic pulse approximation in (15) is that the time derivatives of the amplitude for such an approximation are singular functions at the borders $|t| = \tau$. Therefore, applying the results of the previous subsections, we propose here the next-level approximation for the description of parabolic pulses, so that we remove the problem of singularities. As can be seen from (18) and Fig. 11, the amplitude of the true asymptotic pulse solution does not vanish at the points where the parabolic approximation tends to zero. Equation

$$A_0(\xi) = \begin{cases} [\lambda(1-\xi^2)]^{1/2}, & |\xi| \le 1-\delta, \\ [\lambda\delta(2-\delta)]^{1/2} \mathrm{e}^{-|\xi|+1-\delta}, & 1-\delta \le |\xi| \le 1 \end{cases} \tag{24}$$

yields an approximation that coincides with the parabolic pulse shape in the central core area and, at the same time, approximates the smooth decrease of the pulse amplitude in the pulse tails. Parameter δ, with $0 < \delta < 1$, can be adjusted to achieve a good approximation for some particular properties – local or integral – of the pulse. The accuracy of the approximation in (24) can be estimated by introducing the quantity $I = \int_{-1}^{1} \mathrm{d}\xi \, (|\psi_{\mathrm{num}}| - |\psi_{\mathrm{th}}|)^2 / \int_{-1}^{1} \mathrm{d}\xi \, |\psi_{\mathrm{num}}|^2$, which represents the integral relative amplitude deviation of the theoretical pulse solution ψ_{th} from the numerical one ψ_{num} (obtained from direct simulation of (7)). Here, $|\psi_{\mathrm{th}}| = aA_0$ with A_0 specified by (24). Figure 12 shows the variation of I as a function of parameter δ and the propagation distance. In the example of Fig. 12, the evolution of a parabolic pulse with a FWHM pulse width 1.9 ps and energy 2562 pJ is modeled. It is seen that I reduces with decreasing δ, as would be expected. However, even for values of δ as large as 0.2, the relative amplitude deviation of the theoretical solution from the numerical one does not exceed 1%. Figure 12 also shows the quantity $I^* = \int_{-1}^{1} \mathrm{d}\xi \, (|\psi_{\mathrm{num}}| - |\psi_{\mathrm{th}}|)^2 / \int_{-1}^{1} \mathrm{d}\xi \, (|\psi_{\mathrm{num}}| - |\psi_{\mathrm{th,p}}|)^2$ plotted as a function of δ and the propagation distance. Here, $\psi_{\mathrm{th,p}}$ is the pure parabolic pulse solution with A_0 given by (15). I^* gives a measure of the accuracy of the approximation (24) in describing the true pulse shape compared with the pure parabolic approximation. In Fig. 12, the values of I^* greater than 10 are rendered with the same color as that associated with 10. It can be seen that, for values of δ close to zero, approximation (24) and the pure parabolic approximation are comparable. For larger values of δ, the pure parabolic approximation gives a better description of the true pulse shape. However, there exists a relatively large range of δ values for which the deviation of approximation (24) from the true amplitude is less than one order greater than the corresponding deviation of the pure parabolic approximation.

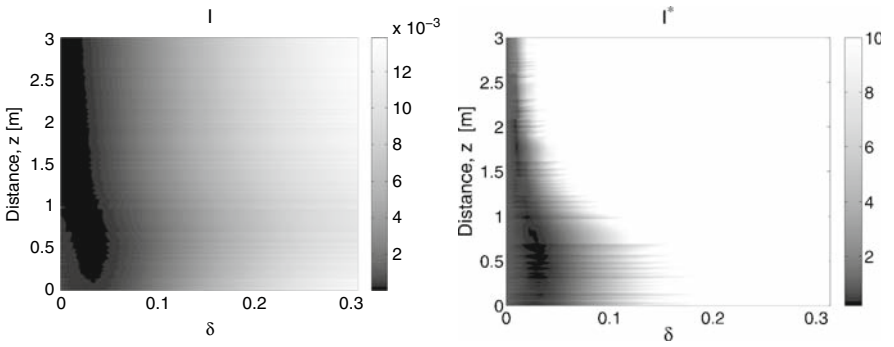

Fig. 12 *Left*: relative amplitude deviation of the approximate parabolic solution (A_0 given by (24)) from the numerical solution, and *right*: ratio of the amplitude deviations of the approximate parabolic solution and the pure parabolic solution (A_0 given by (15)) from the numerical solution vs. parameter δ and propagation distance

4 Application of Parabolic Pulses to Optical Signal Processing

Signal processing is an attractive technique for further improvement of the performance of fiber transmission systems. The full potential of all-optical data processing is still to be realized in a variety of possible applications. An attractive approach to the design of the optical receiver for high-speed optical fiber communication systems using return-to-zero (RZ) data formats is based on employing an additional all-optical decision element (ODE) just before the conventional receiver. In this way, the first decision is carried out in the optical domain, thus improving the quality of the signal which is received. A number of nonlinear ODE schemes have been proposed recently [38, 39, 40, 41, 42]. The improvement in the bit error rate (BER) – the key characteristic of the performance of telecommunication systems – by optical devices in the context of optical regeneration was discussed recently in [43]. The BER of a signal cannot be intrinsically improved by optical regenerators that are characterized by a transfer function solely determined by the signal power, i.e., the BERs before and after such devices are identical. However, it was argued that regenerators that can discriminate the noise from the signal by processing logical ones and logical zeros with distinct power transfer functions are capable of improving the BER of a signal passing through them. Actually, the conceptual basis of the BER improvement by optical devices is more general and comes from information theory: an intrinsic BER improvement is possible whenever the decision performed by the device in the optical domain is based on information that is different from the information used by the decision circuit of the receiver in the electrical domain. Here, we demonstrate an application of this general concept by presenting a novel approach to the improvement of the BER in an optical communication system that utilizes a design of an advanced optical receiver enhanced by a nonlinear ODE [44]. We discuss the technical implications of the approach in the particular case of RZ systems limited by timing jitter (i.e., fluctuations of the pulse position in time), but the proposed concept is not limited to the improvement of the performance of a particular transmission system. The example of an ODE scheme presented in this chapter exploits the nonlinear mechanism that leads to the formation of parabolic pulses and the resultant flattening of the signal waveform. The method is based on nonlinear temporal pulse broadening and flattening in an NDF and subsequent slicing of the pulse temporal waveform by an optical temporal gate (e.g., an amplitude modulator with a sharp nonlinear transfer function or a NOLM provided with a clock) [39, 41].

4.1 Receiver Model and Operation Principle

The structure of the proposed ODE-enhanced receiver is shown in Fig. 13. The receiver is constructed from an optical band-pass filter (OBPF)/demultiplexer, a photodetector with a square-law characteristic, an electrical low-pass filter (ELPF) and a threshold detector at the decision point. The ODE, which is placed in front of

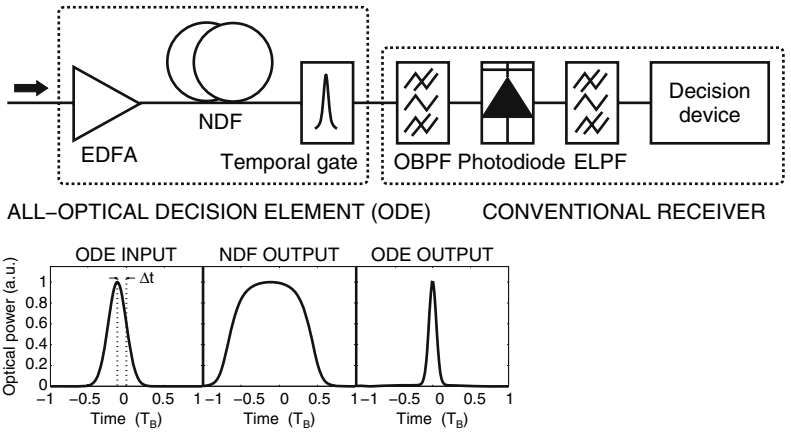

Fig. 13 Schematic of the RZ optical receiver

the receiver, consists of an erbium-doped fiber amplifier (EDFA), a section of NDF and an optical temporal gating device [39]. The principle of the decision function in the optical domain is as follows [40]: an input optical pulse to the ODE is first amplified by the optical amplifier to enhance the effect of nonlinearity in the NDF. During transmission along the NDF, the temporal waveform of the pulse is changed to a rectangular-like profile by the combined action of GVD and Kerr nonlinearity [45]. Note that, if we use distributed amplification in the NDF instead of lumped amplification by the EDFA, then the pulse temporal waveform will be changed to a parabolic profile by dispersion, nonlinearity and gain. After propagation in the NDF, the pulse width is broadened and the central portion of the pulse changes to become flat. The phase margin of a RZ pulse train is improved by utilizing this property [38]. This in turn reduces the influence of the displacement of pulse position in time caused by timing jitter. Indeed, broadening of the pulse width to approximately a 1-bit duration causes the center-of-mass of the pulse portion contained in the bit slot to move toward the top of the pulse, where timing jitter is less than in the tails, as a result of flattening of the pulse envelope. Moreover, temporal broadening and flattening permits the pulse portions containing most of the pulse energy to recover the bit slot for those pulses that are significantly shifted from the center of the bit slot in the input pulse train, as Fig. 14 schematically shows. Note that strongly time-shifted pulses in the optical domain, once they are converted into electrical pulses and arrive at the decision point, might be missed by the threshold detector in a conventional receiver. In contrast, the temporal broadening and flattening-induced bit slot recovery in the NDF enables such pulses, which were originally strongly shifted, to be recognized as marks in the proposed receiver. This is the basic mechanism that is responsible for BER improvement in the ODE-enhanced receiver. Following the NDF, the pulse enters the temporal gating device. The gate slices the central portion of the broadened pulse temporal profile. Such an effective discrimination of the pulse tails against the central portion enables efficient suppression of the timing jitter of a pulse

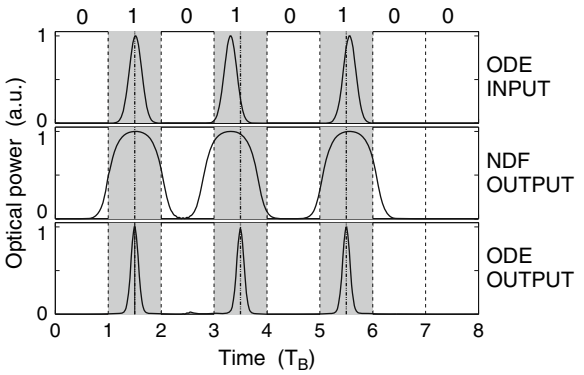

Fig. 14 Schematic of the optical decision

train. The suppression of timing jitter in the optical domain improves the receiver sensitivity. Indeed, once the detected electrical signal arrives at the decision circuit, the reduced fluctuations of the sampling time from bit to bit, which result from the reduction of the optical timing jitter, lead to reduced fluctuations of the bit sampled values and, consequently, to an improved signal-to-noise ratio. The required temporal gate can be implemented in various ways. For instance, one can exploit an amplitude modulator with a nonlinear transfer function given by [39, 41]

$$f(t) = x + (1-x)\cos^{2m}\left(\frac{\pi(t-t_0)}{T_\mathrm{B}}\right), \quad m = 1, 2, \ldots. \tag{25}$$

In (25), x is the extinction ratio, t_0 is the center of the modulation, T_B is the bit period and parameter m controls the degree of narrowing and sharpening of the modulation peaks (see Fig. 15) and, thus, the degree of slicing of the pulse temporal profile. We would like to stress that (25) is only a particular example of a sharp nonlinear response function, and obviously, other devices may be used for temporal gating.

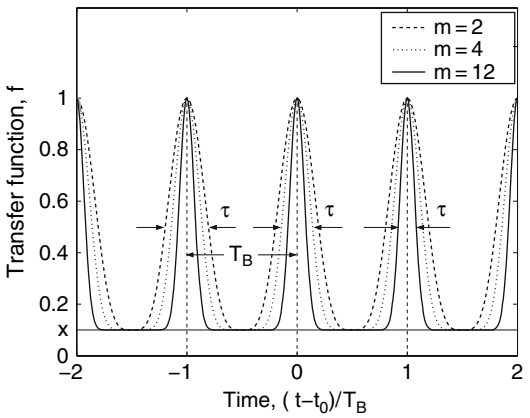

Fig. 15 Temporal gate transfer function

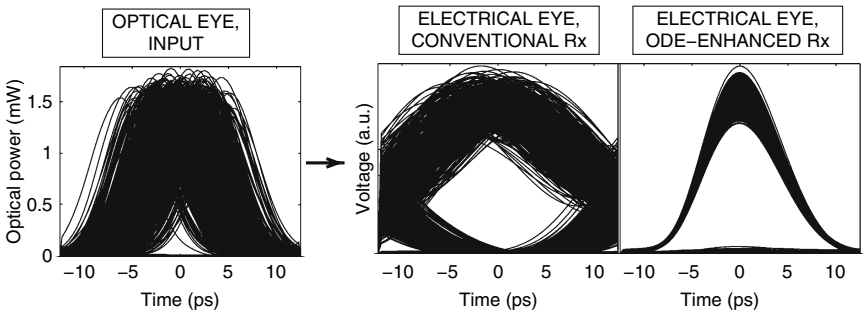

Fig. 16 Signal eye diagrams in the receiver

The essential property of the temporal gate response function must be that it opens a narrow window in time τ with periodicity T_B.

The improvement of signal quality that can be achieved in the ODE-modified receiver with respect to the conventional receiver is illustrated with the so-called eye diagrams in Fig. 16 [40]. An eye diagram overlays the signal waveform over many cycles (time slots). Each cycle waveform is aligned to a common timing reference, typically a clock. The eye diagram provides a visual indication of the power (amplitude variation) and timing (timing jitter) uncertainty associated with the signal at the detector. The eye of the optical input 40 Gb/s RZ signal closes mainly because of significant timing jitter with the pulses. When the pulses are detected with the conventional scheme, the pulse width is broadened by the ELPF, and this yields an increase in eye opening. The eye opening detected with the proposed scheme is larger than that in the conventional receiver. This is due to a substantial suppression of the timing jitter, which results from temporal slicing of the NDF-broadened and flattened pulse waveforms by the amplitude modulator.

4.2 Receiver Performance Computation

We now analyze quantitatively the performance of the nonlinear ODE-enhanced receiver [44]. For systems using ODEs, the inherent nonlinearity of the optical devices employed causes the received-voltage probability density functions (PDFs) of the marks and spaces to have essentially non-Gaussian shapes. This invalidates the use of standard estimates of the BER in terms of the well-known Q-factor of the signal, as it is based on the Gaussian approximation for the statistics [46]. Therefore, here we apply the multi-canonical Monte Carlo (MMC) simulation technique [47] to accurately evaluate the receiver performance. The MMC method is widely recognized for its efficiency in determining the complete PDFs, while fully accounting for the system nonlinearity [48], insofar as it iteratively biases Monte Carlo simulations, so

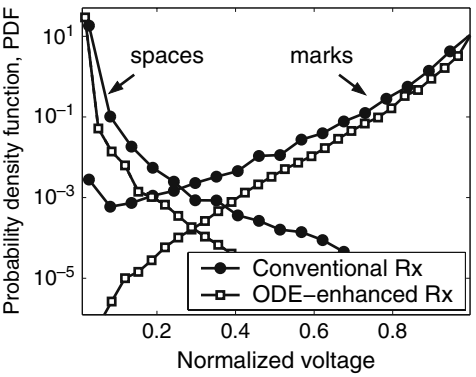

Fig. 17 PDFs for the voltage of the marks and spaces in the conventional and ODE-enhanced receivers

that a priori knowledge of how to bias the simulation is not needed. This contrasts with most other important sampling-based techniques.

We refer to [40] for details of the system and notations. In particular, we use the modulator transfer function given by (25) with control parameter $m = 12$, and the bandwidths of the OBPF and ELPF are set to the respective (optimal) values of 400 and 20 GHz for the conventional receiver, and of 400 and 40 GHz for the ODE-enhanced receiver. In our simulations, we model the signal to be received by an 8-bit random binary sequence with a bit period of $T_B = 25$ ps (corresponding to the 40 Gb/s bit rate). The signal pulses are Gaussian shaped and have a FWHM duration of 7 ps and a peak power of 1.6 mW at the input of the ODE. Timing jitter in the signal is modeled by a superposed Gaussian-distributed random shift of the pulse temporal position. The timing jitter standard deviation is 3 ps. When the signal passes the EDFA in the modified receiver, complex Gaussian random noise is appended to the complex signal field. By applying the MMC method, we calculate the distribution of the voltage of the marks and spaces at the decision point in the receiver.

Our key result is presented in Fig. 17 [44], which shows the PDFs of the voltage for the marks and the spaces in the conventional and ODE-enhanced receivers. The voltage is normalized to the statistical average of signal voltages in each of the two receiver types. The BER, as measured from the common surface under the PDFs of marks and spaces, is 4×10^{-4} for the conventional receiver and 10^{-5} for the ODE-enhanced receiver. This result demonstrates that significant improvement of the BER can be obtained in the proposed receiver compared with that of the conventional scheme. We stress the fact that BER improvement is achieved here by making a decision in the optical domain, which is based effectively on using additional information about the signal distortion (timing jitter) with respect to the conventional receiver.

5 Conclusion

We have presented some examples of nonlinear dissipative structures in fiber optics. First, we have introduced a theoretical model to describe ultra-short pulse

propagation in fiber transmission systems in the quasi-linear regime with periodic in-line deployment of nonlinear optical devices. In the particular application to NOLMs, we have demonstrated numerically that dissipative soliton formation can be observed in such systems as a result of a balance between the effects of dispersion in the transmission fibers, linear control by optical filters and nonlinear focusing in the NOLMs. We have applied an approximate variational approach to determine the steady-state pulse characteristics and have shown that the theoretical analysis accurately reproduces the results of full numerical simulations.

Second, we have revisited a theory of nonlinear dissipative structures having the form of self-similar parabolic pulses in a fiber gain medium. Semi-classical solutions of the NLS equation in a gain medium with a parabolic temporal profile in the energy-containing core have been accurately analyzed, theoretically and numerically. We have presented matching of the parabolic solution to the linear low-amplitude tails of the pulse. The theoretical analysis has been shown to accurately reproduce the solution obtained from numerical simulation of the NLS equation. We have also introduced a simple approximation to describe the shape of parabolic pulses. It may be useful for problems involving time derivatives of the pulse amplitude.

Third, we have discussed possible applications of parabolic-like nonlinear dissipative structures in optical communication systems. In particular, we have presented a new approach to the improvement of the BER in optical communications. We have proposed a design for an advanced RZ receiver enhanced by a nonlinear all-optical decision element. As a particular example, we have exploited an ODE scheme based on an optical temporal gate enhanced by the effect of Kerr nonlinearity in an NDF. Significant improvement in the BER compared with the conventional receiver at a channel rate of 40 Gb/s has been demonstrated.

Acknowledgments We would like to acknowledge and thank our co-authors of the publications that form a basis for the mini-review chapter presented here, viz., Dr. Stanislav A. Derevyanko, Prof. Alexander S. Kovalev, Prof. Mikhail M. Bogdan, Prof. Victor Yu. Novokshenov, Dr. Jeroen H. B. Nijhof, Prof. Keith J. Blow and Mrs. Irina O. Nasieva.

References

1. A. Hasegawa and F.D. Tappert, Appl. Phys. Lett. **23**, 142–144 (1973). 196
2. V.E. Zakharov and A.B. Shabat, Zh. Eksp. Teor. Fiz. **60**, 136 (1971); [Sov. Phys. JETP **33**, 77–81 (1971).] 196
3. S.V. Manakov, Zh. Ekp. Teor. Fiz. **65**, 505–516 (1973); [Sov. Phys. JETP **38**, 248–253 (1973). 196
4. A. Hasegawa and Y. Kodama, *Solitons in Optical Communications*, (Clarendon, Oxford University Press, Oxford, (1995). 196, 197
5. L.F. Mollenauer, S.G. Evangelides, and H.A. Haus, IEEE J. Lightwave Technol. **9**: 194–196 (1991). 196
6. A. Hasegawa and Y. Kodama, Opt. Lett. **15**, 1443–1445 (1990); Phys. Rev. Lett. **66**:161–164 (1991). 196
7. K.J. Blow and N.J. Doran, IEEE Photon Technol. Lett. **3**, 369–371 (1991). 196

8. Akhmediev, N. and Ankiewicz, A. (eds.): *Dissipative Solitons*, Lect. Notes Phys. **661**. Springer, Berlin (2005) 196
9. N.N. Rozanov, PHYS-USP **43**, 421–424 (2000). 196
10. W.J. Firth, Theory of cavity solitons. in: Soliton-Driven photonics, edited by A.D. Boardman and A.P. Sukhorukov, (Kluwer, Amsterdam, (2001), pp. 459–485. 196
11. A.V. Yulin, D.V. Skryabin, and P.St.J. Russell, Opt. Express **13**, 3529–3534 (2005). 196
12. B.S. Kerner and V.V. Osipov, Autosolitons, (Kluwer Academic Publ, Dordrecht, 1994). 196
13. V.S. Grigoryan, Phys. Lett. A **149**, 371–380 (1990). 196
14. A.G. Vladimirov, G.V. Khodova, and N.N. Rosanov, Phys. Rev. E **63**, 056607(6) (2001). 196
15. I. Gabitov, D.D. Holm, B.P. Luce, and A. Mattheus, Opt. Lett. **20**, 2490–2492 (1995). 196
16. I. Gabitov, D.D. Holm, and B.P. Luce, J. Opt. Soc. Am. B. **14**, 1850–1855 (1997). 196
17. E.V. Vanin, A.I. Korytin, A.M. Sergeev, D. Anderson, M. Lisak, and L. Vasquez, Phys. Rev. A **49**, 2806–2811 (1994) 196
18. A.M. Sergeev, E.V. Vanin, D. Anderson, M. Lisak, and M. Quiroga Teixeiro, J. Opt. Soc. Am. B **15**, 1641–1646 (1998). 196
19. P.V. Mamyshev and N.A. Mamysheva, Opt. Lett. **24**, 1454–1456 (1999). 197
20. I. Gabitov and S.K. Turitsyn, Opt. Lett. **21**, 327–329 (1996). 197
21. S. Boscolo, J.H.B. Nijhof, and S.K. Turitsyn, Opt. Lett. **25**, 1240–1242 (2000). 197, 198
22. S. Boscolo, S.K. Turitsyn, and K.J. Blow, Electron. Lett. **37**, 112–113 (2001); IEEE Photon Technol. Lett. **14**, 30–32 (2002). 197, 198, 200, 202
23. K.J. Blow, S. Boscolo, and S.K. Turitsyn, Patent GB2371160 A (17/07/2002); Patent GB2371160 B (30/06/2004); Patent WO02056506 A2 (18/07/2002); Patent WO02056506 A3 (01/05/2003); Patent EP1356612 A2 (29/10/2003); Patent US2004076373 A1 (22/04/2004). 197, 198, 200, 20
24. D. Rouvillain, et al. Electron Lett. **38**, 1113–1114 (2002). 197
25. S. Boscolo, S.A. Derevyanko, S.K. Turitsyn, A.S. Kovalev, and M.M. Bogdan, Phys. Rev. E **72**, 016601(4) (2005); Theor. Math. Phys. **144**, 1117–1127 (2005). 198, 199, 203, 204
26. J.H.B. Nijhof, N.J. Doran, W. Forysiak, and A. Berntson, Electron. Lett. **34**, 481–482 (1998). 200
27. G.I. Barenblatt, Scaling, Self-Similarity, and Intermediate Asymptotics, (Cambridge University Press, Cambridge, 1996). 205
28. D. Anderson, M. Desaix, M. Karlsson, M. Lisak, and M.L. Quiroga-Teixeiro, J. Opt. Soc. Am. B **10**, 1185–1190 (1993). 205
29. M.E. Fermann, V.I. Kruglov, B.C. Thomsen, J.M. Dudley, and J.D. Harvey, Phys. Rev. Lett. **84**, 6010–6013 (2000); V.I. Kruglov, A.C. Peacock, J.M. Dudley, and J.D. Harvey, Opt. Lett. **25**, 1753–1755 (2000). 205, 207
30. S. Boscolo, S.K. Turitsyn, V.Yu. Novokshenov, and J.H.B Nijhof, Theor. Math. Phys. **133**, 1647–1656 (2002). 205, 206, 208, 209
31. C. Finot, G. Millot, C. Billet, and J.M. Dudley, IEEE J. Sel. Top. Quantum Electron. **10**, 1211–1218 (2004). 205
32. C. Finot, G. Millot, and J.M. Dudley, Opt. Lett. **29**, 2533–2535 (2004). 205
33. C. Finot, F. Parmigiani, P. Petropoulos, and D.J. Richardson, Opt. Express **14**, 3161–3170 (2006). 205
34. F.Ö. Ilday, J.R. Buckley, W.G. Clark, and F.W. Wise, Phys. Rev. Lett. **92**, 213902(4) (2004). 205
35. V.E. Zakharov, and E.A. Kuznetsov, Sov. Phys. JETP **64**, 773–780 (1986). 210
36. A.R. Its and V.Yu. Novokshenov, *The Isodromic Deformation Method in the Theory of Painlevé Equations* (Lect Notes Math 1191), (Springer, Berlin, 1986); S.P. Hastings and J.B. McLeod, Arch. Ration Mech. Anal. **73**, 31–51 (1980). 210
37. O.A. Ladyzhenskaya, V.A. Solonnikov, and N.N. Ural'tseva, *Linear and Quasi-Linear Equations of Parabolic Type* (Transl Math Monographs 23), (Amer Math Soc, Providence, RI, 1968). 210
38. M. Suzuki, H. Toda, A.H. Liang, and A. Hasegawa, IEEE Photon Technol. Lett. **13**, 1248–1250 (2001). 213, 214
39. S. Boscolo and S.K. Turitsyn, IEEE Photon Technol. Lett. **16**, 1912–1914 (2004). 213, 214, 215
40. S. Boscolo, S.K. Turitsyn, and K.J. Blow, Opt. Express **13**, 6217–6227 (2005). 213, 214, 216, 217
41. K.J. Blow, S. Boscolo, and S.K. Turitsyn, Patent GB2421382 A (21/06/2006); Patent WO2006064240 A1 (22/06/2006). 213, 215

42. P. Ghelfi, M. Scaffardi, M. Secondini, F. Fresi, M.F. Matchouani, A. Bogoni, and L. Potí, in *Proceedings of 31st European Conference on Optical Communication:We1.2.2*, (Glasgow, United Kingdom, 2005). 213
43. M. Rochette, J.N. Kutz, J.L. Blows, D. Moss, J.T. Mok, B.J. Eggleton, IEEE Photon. Technol. Lett. **17**, 908–910 (2005). 213
44. Nasieva I.O, S. Boscolo, and S.K. Turitsyn (2006) Opt. Lett. 31:1205–1207 213, 216, 217
45. H. Nakatsuka, D. Grischkowsky and A.C. Balant, Phys. Rev. Lett. **47**, 910–913 (1981). 214
46. GP. Agrawal, *Fiber-Optic Communication Systems*. 3rd ed, (Wiley, New York, 2002). 216
47. B.A. Berg and T. Neuhaus Phys. Rev. Lett. **68**, 9–12 (1992). 216
48. R. Holzlöhner and C.R. Menyuk, Opt. Lett. **28**, 1894–1896 (2003). 216

Three-Wave Dissipative Brillouin Solitons

C. Montes

Abstract Stimulated Brillouin backscattering of an electromagnetic c.w. pump wave into a red-shifted Stokes wave through a dissipative material acoustic wave, as governed by the nonlinear space–time three-wave resonant model, gives rise to backward-traveling solitary pulses, which are experimentally obtained in long fiber-ring cavities. Stability analysis of the inhomogeneous stationary *Brillouin mirror* solution in a c.w.-pumped cavity exhibits a one-parameter Hopf bifurcation. Below a critical feedback, a time-dependent oscillatory regime occurs, and we get self-organization of a localized pulsed regime. Experimental results and a dynamical simulation confirm this scenario. A stable continuous family of super-luminous and sub-luminous backward-traveling dissipative solitary pulses is obtained through a single control parameter. A parallel analysis in an unbounded one-dimensional medium shows that the integrable three-wave super-luminous symmetrical soliton is unstable for small dissipation, and that it cascades to a turbulent multi-peak structure. The general non-symmetrical and non-integrable case is dependent only on the exponential slope of the wave front of the backscattered Stokes wave, thus providing the stable super- and sub-luminous dissipative solitary attractors. An overview of the experimental results for a large set of input pump powers and Stokes feedback conditions shows a remarkable agreement with the numerical simulations of the three-wave coherent, partial differential equations model.

1 Introduction

Stimulated Brillouin scattering (SBS) experiments in liquids [1], gases [2], plasmas [3], and optical fiber-ring resonators [4, 5, 6, 7, 8] give rise to localized

C. Montes
Laboratoire de Physique de la Matière Condensée, Centre National de la Recherche Scientifique, Université de Nice - Sophia Antipolis, Parc Valrose, F-06108 Nice Cedex 2, France, carlos.montes@unice.fr

Montes, C.: *Three-Wave Dissipative Brillouin Solitons.* Lect. Notes Phys. **751**, 221–260 (2008)
DOI 10.1007/978-3-540-78217-9_9

backward-traveling Stokes pulses. The space–time dynamics in one spatial dimension, resulting from the resonant three-wave nonlinear interaction between the pump wave A_p, the material acoustic wave A_a, and the backscattered Stokes wave A_S, is governed by the nonlinear three-wave partial differential equations (PDE) model within the slowly varying envelope approximation. This model is particularly appropriate for describing the dynamics in single-mode optical fibers [4, 5, 6, 7, 8, 9, 10, 11]. SBS is responsible for a large class of dynamical behaviors in c.w.-pumped single-mode optical fiber cavities. Steady state, periodic and quasi-periodic oscillations, and even chaotic dynamics, may arise in single-mode Fabry–Perot cavities with weak external feedback [12, 13, 14, 15].

In c.w.-pumped fiber-ring cavities, our group has obtained stable-pulsed regimes at a round-trip repetition rate for moderate feedback in unpolarized fiber-ring lasers [7] and in an Nd:YAG polarization-maintaining fiber-ring laser [8]. A continuous set of super- and sub-luminous dissipative solitons is obtained through a single control parameter, viz. the Stokes feedback, R, for a given gain-length $G = gI_pL$, where g is the SBS gain coefficient, I_p the c.w.-pump intensity, and L the length of the cavity, or G for a given feedback, R. Stability analysis of the inhomogeneous stationary solution, made by using a $(1+1)D$ space–time coherent three-wave model [6], proves the scenario of solitonic pulse generation via a generic single-parameter Hopf bifurcation. For a given gain-length G, and below a critical feedback R_{crit}, the steady *Brillouin mirror* regime gives rise to a time-dependent oscillatory regime, and for lower feedback (i.e., higher dissipation), spontaneous mode-locking of several cavity-longitudinal modes generates stable-pulsed regimes at the round-trip repetition rate. The single-parameter bifurcation is also obtained, for a given feedback R, by decreasing the input pump intensity, I_p, from the steady Brillouin mirror regime down to the threshold.

The length, L, of the fiber cavity must be long enough to allow a large number of longitudinal modes, $N = nL\Delta\nu_B/c$, under the Brillouin gain curve of spectral width (FWHM) $\Delta\nu_B$. For a convenient length scale, typically for $10 < L(\mathrm{m})/[\lambda_p(\mu\mathrm{m})]^2 < 400$, where λ_p is the pump wavelength, stable-pulsed regimes occur below R_{crit} and above R_{thres} in low-finesse c.w.-pumped Brillouin fiber-ring lasers [7, 8]. If $N \sim 1$, the dynamics can be only stationary [11], and if N is very high, as occurs for very long fibers, the fiber noise [7] or the transverse guided-acoustic wave Brillouin scattering (GAWBS) [16, 17] induces decoherence between consecutive pulses. However, the GAWBS transverse resonances, within finite frequency ranges, may co-operatively couple with the acoustic longitudinal modes of the cavity, giving rise to compressed Brillouin solitons [18]. Active mode-locking of all the cavity-longitudinal modes under the Brillouin gain curve is obtained by using an intra-cavity phase modulator; this allows controllable pulse compression in a polarization-maintaining fiber-ring laser [19]. The temporal width of these compressed pulses is included in Table 1, in order to compare it with the analytical formulae obtained from the unlimited SBS line dynamics.

The three-wave interaction problem has been the object of many theoretical studies and numerical simulations [20]. Here, we are concerned with nonconservative SBS in the presence of a continuous pump. This model has been integrated by

Table 1 Numerical pulse characteristics [from (1)] for the Nd:YAG c.w.-pumped Brillouin fiber-ring laser, 260 m in length, at different amplitudes of feedback $\rho_S = \sqrt{R}$ [Series **(1)**–**(4)** of Fig. 20] and different gains, G, around the narrowest pulse width (in bold numerals). The particular analytic solutions are inserted in column 7, evaluated from formulae (46), (47), and (48)

Series **(1)** $R = 0.15$; $\rho_S = \sqrt{R} = 0.3872$						
G	P(mW)	$\lvert A_S\rvert_{max}$	Δ_t/t_r	$\delta_t\lvert A_S\rvert/t_r$	$\delta_t\lvert A_S\rvert^*/t_r$	Analytic
3.00	17.07	2.0525	1.0016	0.1655	0.0676	$\Delta\zeta = \mathbf{0.0508}$
3.20	18.21	2.2347	1.0003	0.1565	0.0640	
3.40	19.35	2.3576	0.9989	0.1543	0.0631	
3.60	**20.49**	**2.4121**	**0.9970**	**0.1563**	**0.0639**	$\Delta\sigma = \mathbf{0.0719}$
3.80	21.63	2.3555	0.9944	0.1708	0.0698	$S = \mathbf{4.0123}$
Series **(2)** $R = 0.0593$; $\rho_S = \sqrt{R} = 0.2435$						
G	P(mW)	$\lvert A_S\rvert_{max}$	Δ_t/t_r	$\delta_t\lvert A_S\rvert/t_r$	$\delta_t\lvert A_S\rvert^*/t_r$	Analytic
5.00	28.46	2.4495	1.0022	0.1245	0.0509	$\Delta\zeta = \mathbf{0.0383}$
5.20	29.60	2.5317	1.0011	0.1221	0.0499	
5.40	**30.74**	**2.5901**	**0.9999**	**0.1215**	**0.0496**	
5.60	31.88	2.6211	0.9984	0.1237	0.0505	$\Delta\sigma = \mathbf{0.0693}$
5.80	33.02	2.6180	0.9967	0.1277	0.0522	$S = \mathbf{3.3803}$
Series **(3)** $R = 0.0225$; $\rho_S = \sqrt{R} = 0.04405$						
G	P(mW)	$\lvert A_S\rvert_{max}$	Δ_t/t_r	$\delta_t\lvert A_S\rvert/t_r$	$\delta_t\lvert A_S\rvert^*/t_r$	Analytic
6.50	37.00	2.4184	1.0061	0.1142	0.0467	$\Delta\zeta = \mathbf{0.0414}$
7.00	**39.85**	**2.6017**	**1.0038**	**0.1086**	**0.0444**	
7.50	42.69	2.7014	1.0011	0.1088	0.0445	
8.00	45.54	2.6899	0.9973	0.1169	0.0478	$\Delta\sigma = \mathbf{0.0607}$
8.50	48.39	2.4605	0.9905	0.1430	0.0584	$S = \mathbf{3.2002}$
Series **(4)** $R = 8.23\times10^{-3}$; $\rho_S = \sqrt{R} = 0.0907$						
G	P(mW)	$\lvert A_S\rvert_{max}$	Δ_t/t_r	$\delta_t\lvert A_S\rvert/t_r$	$\delta_t\lvert A_S\rvert^*/t_r$	Analytic
8.50	48.39	2.5399	1.0081	0.1047	0.0428	$\Delta\zeta = \mathbf{0.0383}$
9.00	**51.23**	**2.6645**	**1.0058**	**0.1022**	**0.0418**	
9.50	54.08	2.7280	1.0031	0.1029	0.0420	
10.00	56.93	2.7126	0.9996	0.1088	0.0445	$\Delta\sigma = \mathbf{0.0554}$
10.50	59.77	2.5750	0.9944	0.1252	0.0511	$S = \mathbf{3.0301}$

The amplitudes are normalized to the input pump amplitude: $\lvert A_S\rvert_{max}/\lvert A_{cw}\rvert$ [numerical from (1), column 3] and $S = \lvert A_S\rvert_{sym}/\lvert A_{cw}\rvert$ [analytic super-luminous symmetric solution from (48), column 7]. The nonlinear round-trip time, Δ_t, is normalized to the linear flight time, $t_r = nL/c \simeq 1.26$ μm, as well as to the respective amplitude widths (FWHM): spontaneous width, $\delta_t\lvert A_S\rvert/t_r$, active mode-locking width, $\delta_t\lvert A_S\rvert^*/t_r$ [19], and, in column 7, analytic luminous asymptotic width, $\Delta\zeta = \ln(2+\sqrt{3})\delta\zeta/t_r$ (46), and analytic super-luminous symmetric width, $\Delta\sigma = \ln(2+\sqrt{3})\delta\sigma/t_r$ (47).

the inverse scattering transform (IST) in the non-dissipative case [21], giving rise to backscattered solitons. Our aim is to study the nonconservative problem in the presence of material damping and Stokes dissipation, in order to shed light on the nonlinear dynamics in the c.w.-pumped optical fiber-ring laser, where the periodic round-trip interaction in the long lossy cavity can be associated with a nonconservative unlimited interaction.

We present, for the unlimited line problem, a continuous family of dissipative solitary structures which result from the three-wave interaction of the c.w. pump in the presence of dissipative Stokes and material waves [22]. The dissipation then introduces the concept of an attractor, yielding solitary structures which are extremely robust with respect to noise perturbations, for example. These attractors support the experimental observation of the large variety of solitary Stokes pulses observed in Brillouin fiber-ring cavities.

From a theoretical point of view, two types of initial and/or boundary conditions for the A_a or A_S envelopes will yield two classes of localized traveling backscattered structures:

1. The c.w. pump interacting with initially *bounded* Stokes or material wave fluctuations yields a *sub-luminous* backscattered three-wave solitary structure, whose constant velocity is uniquely determined by the damping coefficients and the c.w.-pump level, and which is an universal attractor for any initial conditions with compact support. This *Cauchy problem* of an initially bounded Stokes wave-packet cannot yield a super-luminous asymptotic traveling structure, since the front of the bounded wave-packet propagates at the velocity of light. The linear asymptotic Kolmogorov–Petrovskii–Piskunov (KPP) assertion [23] allows us to analytically determine the wave-front slope and the sub-luminous velocity, and, when the dynamics attains the asymptotic steady regime [20], they are in remarkably good agreement with the numerical results of the nonlinear PDE model. However, this initially bounded problem will not be considered here because it cannot account for the continuous family of sub-luminous and super-luminous dissipative solitons generated in the fiber-ring Brillouin laser.
2. Initially *unbounded* Stokes conditions in a line present well-known analytical *super-luminous* [24] three-wave soliton solutions [25, 26], and they are also available for dissipative A_a and A_S envelopes [5, 27, 28]. Perturbative IST has been considered in the small dissipation case [29], but the soliton solution is unstable and is accompanied by a turbulent tail at finite times. Such turbulent behavior is reached via a bifurcation cascade from the stable dissipative one-soliton solution by decreasing the dissipation. It begins with a bi-solitary structure and is followed by a space–time-dependent multi-peak solitary regime for very small dissipation. We determine a stability criterion for such structures by using an extension of the KPP asymptotic procedure used for the initially bounded case [20]. It is shown that the sub-luminous attractor obtained in the initially bounded case also belongs to the set of dissipative soliton solutions for unbounded conditions. In addition to this bifurcation scenario of the super-luminous soliton solution, we have obtained a stable family of asymmetric dissipative solitons for the general non-integrable problem, resulting from the unlimited interaction at any dissipation [22]. This family constitutes a continuous set of solitary attractors, traveling backward with respect to the continuous pump, at velocities running from super- to sub-luminous, and with the dynamics only being dependent on the wave-front slope, p, of the backscattered Stokes wave. These stable solitary structures, generated by the backscattering three-wave instability, attain their nonlinear steady regime through dynamic compensation between the wave-front

slope dispersion and the pump depletion. In the well-known bright optical NLS (nonlinear Schrödinger) soliton case, compensation is achieved between the linear group velocity dispersion and the nonlinear Kerr effect [30], and here there is a similar balance between *velocity dispersion steepening* and *nonlinear pump depletion flattening*.

We present experimental and numerical results for a c.w.-pumped Brillouin fiber-ring cavity, showing trains of dissipative solitons at different velocities having different slopes, in order to point out its resemblance to the theoretical unlimited interaction.

The bifurcation in the cavity is responsible for the time-dependent oscillatory and pulsed regimes which have been observed in a systematic experimental and numerical exploration of the whole soliton localization domain. This was for a large set of (G,R) parameters in a polarization-maintaining Nd:YAG Brillouin fiber-ring laser with the best conditions of stability and coherence. An excellent quantitative agreement of the coherent three-wave model simulations and the experiments was obtained [8]. The explicit solution for the integrable luminous velocity case of the unbounded problem allows us to relate this selected dissipative soliton to that obtained in the actual stable Brillouin fiber-ring experiment, which corresponds to one of the best localized pulses.

2 SBS Kerr Model Equations

In single-mode fibers, which are considered to be uni-dimensional media, the nonlinear SBS process resonantly couples a pump wave, $A_\mathrm{p}(\omega_\mathrm{p},\ k_\mathrm{p})$, and a backscattered Stokes wave, $A_\mathrm{S}(\omega_\mathrm{S},\ k_\mathrm{S})$, with an acoustic wave, $A_\mathrm{a}(\omega_\mathrm{a}=\omega_\mathrm{p}-\omega_\mathrm{S},\ k_\mathrm{a}=k_\mathrm{p}+k_\mathrm{S})$, through electrostriction. Neglecting the acoustic propagation, which has speed $c_\mathrm{a} \ll c$, and including the optical Kerr effect, we obtain three coupled SBS Kerr equations for the complex amplitudes [4, 7], within the slowly varying envelope approximation,

$$\begin{aligned}
(\partial_t + \frac{c}{n}\partial_x + \gamma_\mathrm{p})A_\mathrm{p} &= -KA_\mathrm{S}A_\mathrm{a} + \mathrm{i}K_\mathrm{r}\left[|A_\mathrm{p}|^2 + 2|A_\mathrm{S}|^2\right]A_\mathrm{p},\\
(\partial_t - \frac{c}{n}\partial_x + \gamma_\mathrm{S})A_\mathrm{S} &= KA_\mathrm{p}A_\mathrm{a}^* + \mathrm{i}K_\mathrm{r}\left[2|A_\mathrm{p}|^2 + |A_\mathrm{S}|^2\right]A_\mathrm{S},\\
(\partial_t + \gamma_\mathrm{a})A_\mathrm{a} &= KA_\mathrm{p}A_\mathrm{S}^* + f_\mathrm{n},
\end{aligned} \tag{1}$$

where $\gamma_{\mathrm{p,S}}$ are the damping coefficients for the optical waves, $\gamma_\mathrm{a} = \pi\Delta\nu_\mathrm{B}$ is the damping coefficient for the acoustic wave, $K_\mathrm{r} = n_2\omega/2n$ is the perturbative optical Kerr constant, and n is the effective linear index. The electrostrictive field, A_a, is defined from the perturbative density at the acoustic frequency $\rho_\mathrm{a} = \mathrm{i}(\rho_0 n^3\varepsilon_0/2cc_\mathrm{a})^{1/2}A_\mathrm{a}$ [4]. The SBS coupling constant for optical materials, K, is related to the usual SBS gain coefficient, g, by $K = (g\gamma_\mathrm{a}\varepsilon_0 c^2/4)^{1/2}(\int\int F^4\mathrm{d}^2\sigma_\perp/\int\int F^2\mathrm{d}^2\sigma_\perp)^{1/2}$

[19]. This includes the overlap integrals of the transverse field distribution, $F(\sigma_\perp)$, and it may also be defined [31] by

$$K = \frac{1}{\sigma}\left(\frac{\varepsilon_0 n^7}{8\rho_0 c c_a}\right)^{1/2} \omega_p p_{12}, \tag{2}$$

where the elasto-optic coefficient $p_{12} = (\rho_0/n^4)(\partial\varepsilon/\partial\rho) = 0.286$ for silica can be evaluated through the Lorentz–Lorenz relation $\left[p_{12} = (n^2-1)(n^2+2)/(3n^4)\right]$. The constant σ accounts for both the overlap between optical and acoustic modes in optical fibers [32, 33] and for phase mismatch which is related to the transverse material gradient [34]; it is typically less than 2. The best value of K is obtained in steady conditions at threshold from the experimentally measured Brillouin gain coefficient, g, for the intensities $I_{p,S} = (n\varepsilon_0 c/2)|A_{p,S}|^2$. The dimensionless gain-length is defined by $G = gI_pL$. For a polarization-maintaining optical fiber-ring resonator at $\lambda_p = 1.319\,\mu m$, whose results are presented in Sect. 10, the experimental SBS threshold is obtained for $g = 1.65\times10^{-11}\,m/W$. Consider a fiber with refractive index $n = 1.44$, mode radius $r = 2.8\,\mu m$, time optical damping $\gamma_{p,S} = \gamma_e = 2.4\times10^4\,s^{-1}$ [optical attenuation 1 dB/km (Fiber-core Ltd)], and time acoustic damping $\gamma_a = \pi\Delta\nu_B = 7.2\times10^7\,s^{-1}$. These parameters yield an SBS coupling constant $K = 15\,ms^{-1}\,V^{-1}$. This is obtained from (2) for $\sigma = 1.2$, acoustic velocity $c_a = 5960\,m/s$, and unperturbed silica fiber density $\rho_0 = 2.21\times10^3\,kg\,m^{-3}$. The perturbative optical Kerr constant yields $K_r = 6.26\times10^{-8}\,m^2\,V^{-2}\,s^{-1}$.

We include, in the acoustic equation, the Langevin noise source f_n with space and time averages such that $\langle f_n(x,t)\rangle = 0$ and $\langle f_n(x,t)f_n^*(x',t')\rangle = Q\delta(x-x')\delta(t-t')$; Q is estimated from the Brillouin threshold [35], so $f_n(x,t)/|KA_p(0)|^2 \sim 10^{-5}-10^{-6}$. Thus, we take into account the spontaneous Brillouin scattering through thermally excited acoustic noise. This will be negligible for the length scales chosen in our experiments, but it should play an important role for de-correlating the pulses in much longer cavities, rendering the dynamics unstable [7].

The dynamics in the cavity is governed by the complex three-wave equations system (1) with the boundary conditions

$$A_p(0,t) = A_{cw}, \qquad A_S(L,t) = \rho_S A_S(0,t), \tag{3a}$$

where A_{cw} is the c.w.-pump input amplitude and $\rho_S = |\rho_S|\exp\left[i\Phi_S\right]$ is the complex feedback control parameter for the single Stokes resonator. Interaction between the backward pump and the forward Stokes waves is avoided in the ring cavity. The simplest configuration to improve control of the input pump phase is a ring cavity with an intra-cavity isolator, as this avoids pump reflections and yields a simple Stokes resonator. When N is large enough, a constant Stokes detuning $\Phi_S \neq 0$ has no significant effect [36], but active phase modulation turns out to be very effective in locking all the longitudinal cavity modes under the Brillouin gain curve in order to compress the Brillouin solitons [19]. The temporal width of these solitons, compressed due to active mode-locking, is in Table 1, in order to compare it with the analytical formulae obtained for the unlimited SBS line problem. Here, we consider

a single Stokes resonator [6, 7] having the Stokes intensity feedback $R = |\rho_S|^2$ as its only control parameter. Therefore, the amplitude boundary conditions will be given by:

$$A_p(0,t) = A_{cw}, \qquad A_S(L,t) = \sqrt{R}\, A_S(0,t). \tag{3b}$$

In the numerical computations, the optical Kerr contribution is systematically included, or its absence is tested. Some authors have argued that the optical Kerr effect may be responsible for chaotic behavior of SBS line lasers [13, 10]. This is not realistic for actual Brillouin fiber-ring lasers, but may be crucial for its sister mechanism, namely stimulated Raman backscattering [37].

3 Three-Wave Dissipative Model

For the purpose of stability analysis, we may neglect the Kerr effect and the noise term and consider only the standard three-wave coherent model [6]. Introducing the dimensionless units

$$E_{p,S,a} = \frac{A_{p,S,a}}{A_{cw}}; \qquad \mu_{p,S,a} = \gamma_{p,S,a}\tau_0; \qquad \tau = \frac{t}{\tau_0}; \qquad \xi = \frac{x}{\Lambda_0};$$
$$\tau_0 = \frac{1}{|KA_{cw}|}; \qquad \Lambda_0 = \frac{c\tau_0}{n}; \tag{4}$$

where A_{cw} is the constant pump input amplitude, and τ_0 and Λ_0 are the nonlinear characteristic time and length; the dimensionless three-wave model, in the slowly varying envelope (SVE) approximation, reads

$$\begin{aligned}(\partial_\tau + \partial_\xi + \mu_p)E_p &= -E_S E_a,\\ (\partial_\tau - \partial_\xi + \mu_S)E_S &= E_p E_a^*,\\ (\partial_\tau + \mu_a)E_a &= E_p E_S^*.\end{aligned} \tag{5}$$

We obtain the instantaneous acoustic response model from (5) by neglecting the acoustic dynamics ($\partial_\tau E_a \ll \mu_a E_a$) through the adiabatic approximation $E_a = E_p E_S^*/\mu_a$; this then yields the intensity equations:

$$\begin{aligned}\left[\partial_\tau + \partial_\xi + 2\mu_p\right)\right]I_p &= -\frac{2}{\mu_a} I_p I_S,\\ \left[\partial_\tau - \partial_\xi + 2\mu_S\right)\right]I_S &= \frac{2}{\mu_a} I_p I_S,\end{aligned} \tag{6a}$$

where $I_{p,S} = |E_{p,S}|^2$. In a non-detuned Stokes ring cavity, the boundary conditions (3b) are given by

$$I_p(0,\tau) = I_{cw}\,, \qquad I_S(L/\Lambda_0,\tau) = R\, I_S(0,\tau). \tag{6b}$$

The stability analysis is performed for $\mu_p = \mu_S = 0$ by solving the linear perturbative equations around the inhomogeneous stationary Brillouin mirror solution which is common to both systems (5) and (6). For the dimensionless $I_{p,S}$ dynamics, let us renormalize the dimensionless time and length variables through $t = 2\tau/\mu_a$, $x = 2\xi/\mu_a$ and define the dimensionless gain-length product by

$$G = gI_pL = \frac{2L}{\Lambda_0\mu_a}.$$

The stationary Brillouin mirror solution is

$$I_p^{st}(x) = \frac{2DI_p^0}{(2D - I_p^0)\exp(-2Dx) + I_p^0},$$

$$I_S^{st}(x) = I_p^{st}(x) - 2D, \tag{7}$$

where the monotonic depletion of the forward-propagating c.w. pump in the optical medium saturates the monotonic amplification of the backscattered Stokes wave. Here, $I_p^0 \equiv I(x=0) = I_{cw}$ is normalized to unity and $D = \text{const}$ is related to R through the boundary conditions (6b):

$$R\exp(2DG) = R + 2(1-R)D. \tag{8}$$

By taking into account the time-dependent optical and acoustic responses of (5) through $I_j(x,t) = I_j^{st}(x) + \delta I_j(x)\exp(-i\omega t)$, $(j = p, S, a)$, where $I_a^{st} = I_p^{st}(x)I_S^{st}(x)/\mu_a^2$, we reduce the stability analysis to the study of a complex eigenvalue equation for ω [6] [7], namely

$$\frac{d^2Y}{dx^2} + \left[(\omega - ifD)^2 + \frac{f(1-f)D^2}{\sinh^2[D(x_0+x)]}\right] Y = 0; \qquad f(\omega) = \frac{1 - i(\omega/\mu_a^2)}{1 - 2i(\omega/\mu_a^2)}, \tag{9}$$

where

$$Y = \frac{1}{2}\left[(1-D)\sinh Dx + D\cosh Dx\right]^{f(\omega)}(\delta I_p - \delta I_B),$$

$$\frac{d(\delta I_p - \delta I_B)}{dx} = i\omega(\delta I_p + \delta I_B).$$

We obtain the characteristic equation for ω by integrating (9) over x and imposing the boundary conditions (6b). The discrete set of frequencies Re ω, which are solutions of the eigenvalue problem, define the longitudinal modes of the SBS ring cavity, and these are unstable if Im $\omega > 0$. By assuming that $f(\omega)$ is real in the potential term in (9), and that $D \to 0$ so $\sinh^2[D(x_0+x)] \sim [D(x_0+x)]^2$, we arrive at a solution that is given by a combination of Airy functions Ai and Bi (C_1 and C_2 are constants):

$$Y(x) = z^{1/4}[\mathrm{C}_1\mathrm{Ai}(-z) + \mathrm{C}_2\mathrm{Bi}(-z)];$$
$$z = [3\Omega(x+1)/2]^{2/3}; \quad \Omega = \omega - \mathrm{i}fD. \tag{10}$$

Within this approximation, the complex characteristic equation that expresses ω as a function of R, D, and G is given by

$$A(\omega) + B(\omega)\,\sin(\Omega G) + C(\omega)\,\cos(\Omega G) = 0, \tag{11}$$

where the functions $A(\omega)$, $B(\omega)$, and $C(\omega)$ are given in [7]. This generalizes the analysis already performed for the case where the inhomogeneous potential is absent [6].

Intensity model (6) corresponds to $f = 1$ (because $\omega/\mu_a^2 \to 0$), and (9) becomes a harmonic oscillator equation at frequency $\Omega = \omega - \mathrm{i}D$, yielding simple coefficients for the Stokes ring cavity. Its anomaly has been discussed in [6]. Nevertheless, it provides simple expressions for the critical parameters at the bifurcation:

$$D_{\mathrm{crit}} = 1/6\,, \qquad (I_S^{\mathrm{st}})_{\mathrm{crit}}/I_p^0 = 2/3\,, \qquad R_{\mathrm{crit}}^{\mathrm{int}} = \frac{1}{3\,\exp(G/3) - 2}.$$

Let us define R_{pulse} as the lower bound of the transition region ΔR_{tran}. Self-pulsing is always observed below it. The value $R_{\mathrm{crit}}^{\mathrm{int}}$ is a fair first approximation, always by default ($R_{\mathrm{crit}}^{\mathrm{int}} < R_{\mathrm{pulse}}$), of this bound. The transition region shrinks to a simple line ($\Delta R_{\mathrm{tran}} = 0$) within the instantaneous model.

No analytic solution of (9) is available, and we plot the marginal stability curve (Im $\omega = 0$) in Fig. 1 in the (G, log R) plane that delimits the stable (Im $\omega < 0$) and unstable (Im $\omega > 0$) domains.

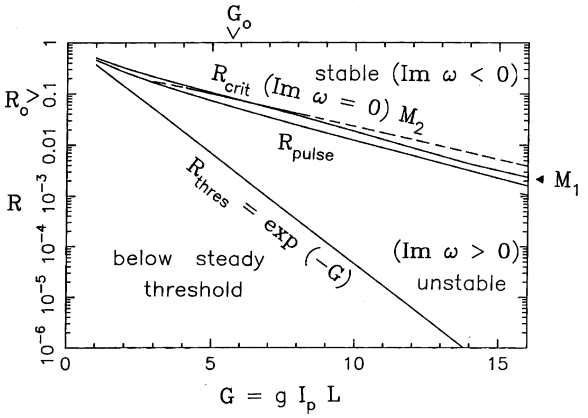

Fig. 1 SBS marginal stability for modes M_1 and M_2 in the (G, log R) plane. The curve R_{crit} (Im $\omega = 0$) separates the stable (Im $\omega < 0$) and the unstable (Im $\omega > 0$) domains. The point (G_0, R_0) delineates the sub-critical and super-critical bifurcations. At $R = R_{\mathrm{crit}}$, the first destabilized mode is M_1 when $G < G_0$ (or $R > R_0$), but it is M_2 when $G > G_0$ (or $R < R_0$). Below R_{pulse} and above R_{thres}, a great number of longitudinal modes N of the cavity, under the Brillouin gain curve, spontaneously lock together, giving rise to a solitonic pulse

Analysis of the non-instantaneous model still reveals a regular Hopf bifurcation. A time-dependent oscillatory regime appears at $R = R_{\mathrm{crit}} > R_{\mathrm{crit}}^{\mathrm{int}}$. The transition region has a finite width. The upper bound (R_{crit}) is accurately given by the solution of the complete characteristic equation (11), while upper and lower bounds are dynamically determined from analysis of the asymptotic behavior of the coherent three-wave dynamics. We numerically analyze the stability of the cavity modes M_{m} at frequencies near multiples, $\mathrm{mf_r}$, of the round-trip frequency which measures the cavity's free spectral range (FSR), i.e., of periods near sub-multiples of the cavity flight time, $t_{\mathrm{r}} = nL/c$. For critical values of the control parameter R, and for different values of G, we have shown [7] that either the fundamental oscillation, M_1, with period close to t_{r} (for low G), or the second mode oscillation, M_2, with period close to $t_{\mathrm{r}}/2$ – associated with the round-trip collision frequency of the counter-propagating pump and Stokes perturbations (for high G) – becomes unstable. For $G > G_0$, it is M_2 which is first destabilized at R_{crit}, but for $G < G_0$, the first destabilized mode is M_1. This stability scenario is confirmed by experiments performed in Brillouin fiber-ring lasers. In Figs. 2 and 3, we show the experimental results for the Nd:YAG experiments of [7, 8], taking the pump input power as the control parameter.

Even higher order modes should be destabilized at the bifurcation point in longer cavities [38], but such a high gain-length product would cause the total depletion of the pump through amplified spontaneous emission in much less than the cavity length, yielding a trivial dynamics.

In all the cases considered, and depending on the control parameter chosen [low enough feedback R for a given G (horizontal travel in Fig. 1), or low enough G for a given R (vertical travel in Fig. 1)], a large number of longitudinal modes of the long fiber cavity spontaneously lock together, giving rise to a backward Stokes pulse of some nanoseconds. This was predicted as a super-luminous soliton solution of the three-wave model [39, 27], and afterwards was observed as spontaneous structuring in Brillouin fiber-ring experiments [5, 6, 7, 8]. We may approach their characteristics by comparing them to the dissipative solitons of the unlimited line problem.

4 Asymptotic Three-Wave Dynamics in the Ring Cavity

Beyond the linear stability analysis, the numerical nonlinear dynamics of the three-wave coherent model (1) for the ring cavity (3b) yields the transient evolution, and finally the asymptotic state. We determine the resolution by following the *characteristics method* [9, 20, 40] and using a standard fourth-order Runge–Kutta algorithm, which has proved to be remarkably stable for long interaction times [7]. The morphogenesis of a Brillouin soliton, starting from the stationary Brillouin mirror in the unstable domain is shown in Fig. 4 (cf. [6]).

The periodic counter-propagating amplification of the Brillouin pulse in the asymptotic pulsing stage is shown in Fig. 5, where the spatial envelopes of the pump, Stokes and acoustic waves inside the cavity are plotted at successive time intervals, $\Delta t/t_{\mathrm{r}} = 1/8$, during one round-trip period. The pump, already depleted from

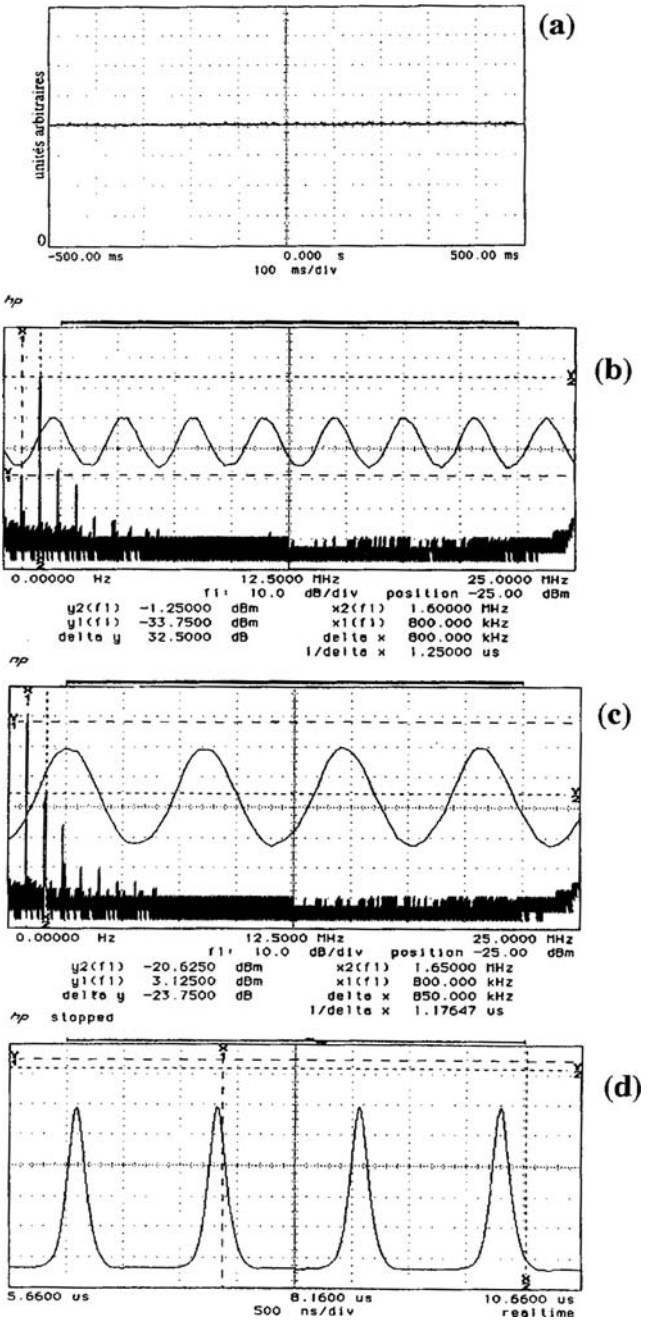

Fig. 2 Experimental results for the Nd:YAG experiment of [7] at $\lambda_p = 1319$ nm for $R \simeq 8\%$. By decreasing the input pump power (control parameter) from the stationary Brillouin mirror regime (**a**) at $P \simeq 100$ mW, successive time-dependent regimes appear below critical bifurcation; (**b**) oscillatory regime at M_2 ($P \simeq 75$–80 mW); (**c**) oscillatory regime at M_1 ($P \simeq 70$–75 mW); and (**d**) stable-pulsed regime ($P \simeq 30$) mW. The spectrum is included in (**b**) and (**c**)

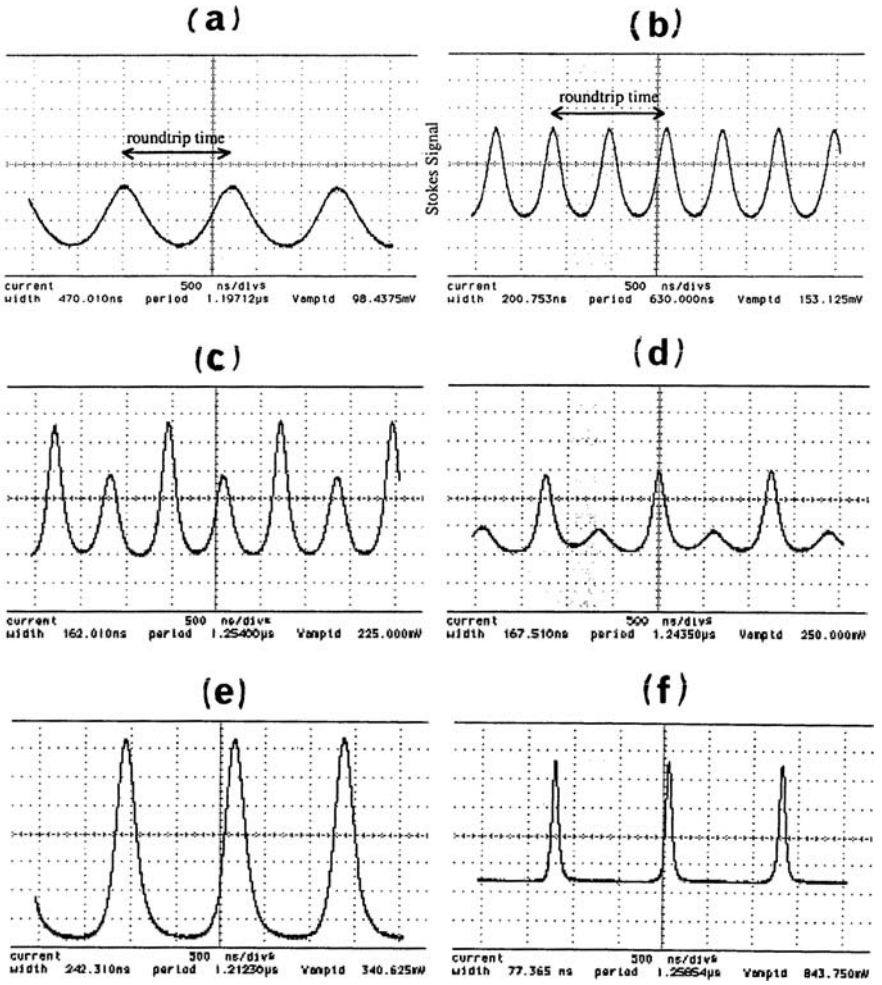

Fig. 3 Experimental results for the polarization-maintaining Nd:YAG experiment of [8] at $\lambda_p = 1319$ nm. (**a**) Destabilization of the stationary Brillouin mirror regime through mode M_1 at $R_{crit} = R_a$; (**b**) destabilization of the stationary Brillouin mirror regime through mode M_2 at lower $R_{crit} = R_b < R_a$; (**c**) and (**d**) building of the Stokes pulse from mode M_2; (**e**) and (**f**) simultaneous strengthening and narrowing of the Stokes pulse when the pump power decreases from the bifurcation point between the stationary Brillouin mirror regime and the pulsed regime

the preceding round-trip [Fig. 5(a)], encounters a small reinjected Stokes pulse up to the middle of the cavity length [Fig. 5(d)]. Then, the un-depleted fresh pump rapidly amplifies the backward pulse [Fig. 5(e, f)], exhibiting a novel localized depletion, which now accompanies the pulse during the second half of the round-trip [Fig. 5(f, g, h)]. The three-wave envelope distribution approaches the asymptotic three-wave solitary structure [22] during this last stage, even if the periodic truncation process and continuous amplification prevent the actual achievement of a stable invariant form. The precise pulse characteristics are obtained by numerical integration of the dynamical model (1). They depend on *G, R, L* and K_r, as will be shown in Sect. 10,

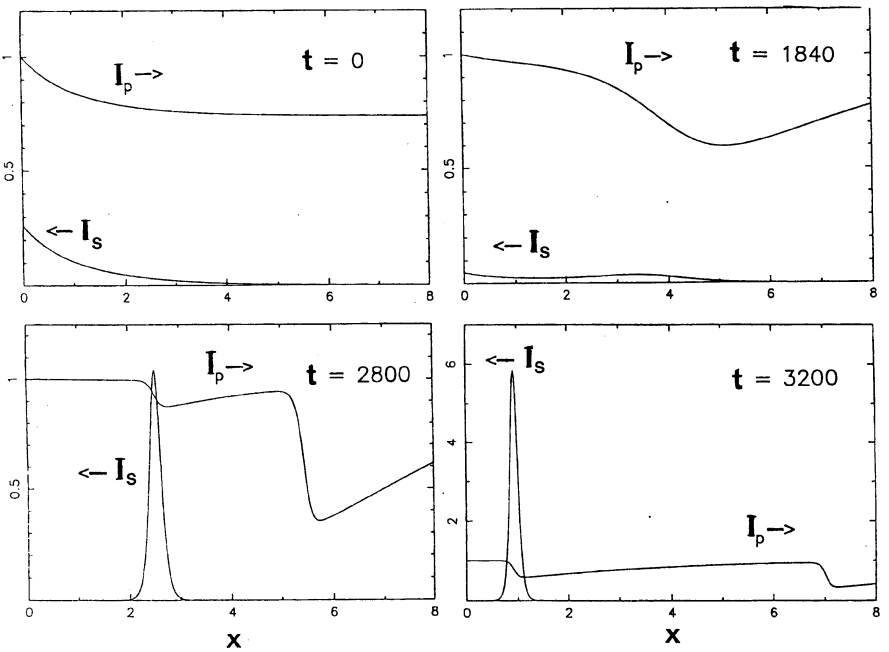

Fig. 4 Morphogenesis of the Brillouin soliton. For R below a critical value, the steady SBS mirror becomes unstable and the system bifurcates toward the time-dependent localized pulse regime for the backscattered Stokes wave (spatial distributions inside the optical medium at different times)

where a systematic experimental and numerical exploration of the whole soliton localization domain for a large set of (G,R) parameters in the polarization-maintaining fiber-ring laser [8] will be presented.

4.1 Asymptotic Mean Reflectivities

After lengthy numerical simulation, the regimes can be considered asymptotic. In Fig. 6, we plot the numerical results for the asymptotic mean reflectivities corresponding to the argon ion Brillouin fiber-ring experiment of [7]. The mean reflectivities were obtained after 1800 round-trips (not fully asymptotic in the transition region), and after 7200 round-trips, where all regimes can be considered asymptotic. The steady and pulsed asymptotic regimes are attained rapidly for values of R outside the transition region. However, we can remark that this region itself is modified and exhibits long transients, so the mean reflectivity computed over a set of round-trips evolves over a long time. The dramatic change in the squared mean amplitude, $\langle |A_S(x=0)| \rangle^2$, of the backscattered Stokes wave indicates the localization process. It is interesting to note that the mean-squared amplitude (or mean Stokes intensity), $\langle |A_S(x=0)|^2 \rangle$, which is the measure of the overall SBS efficiency, varies smoothly,

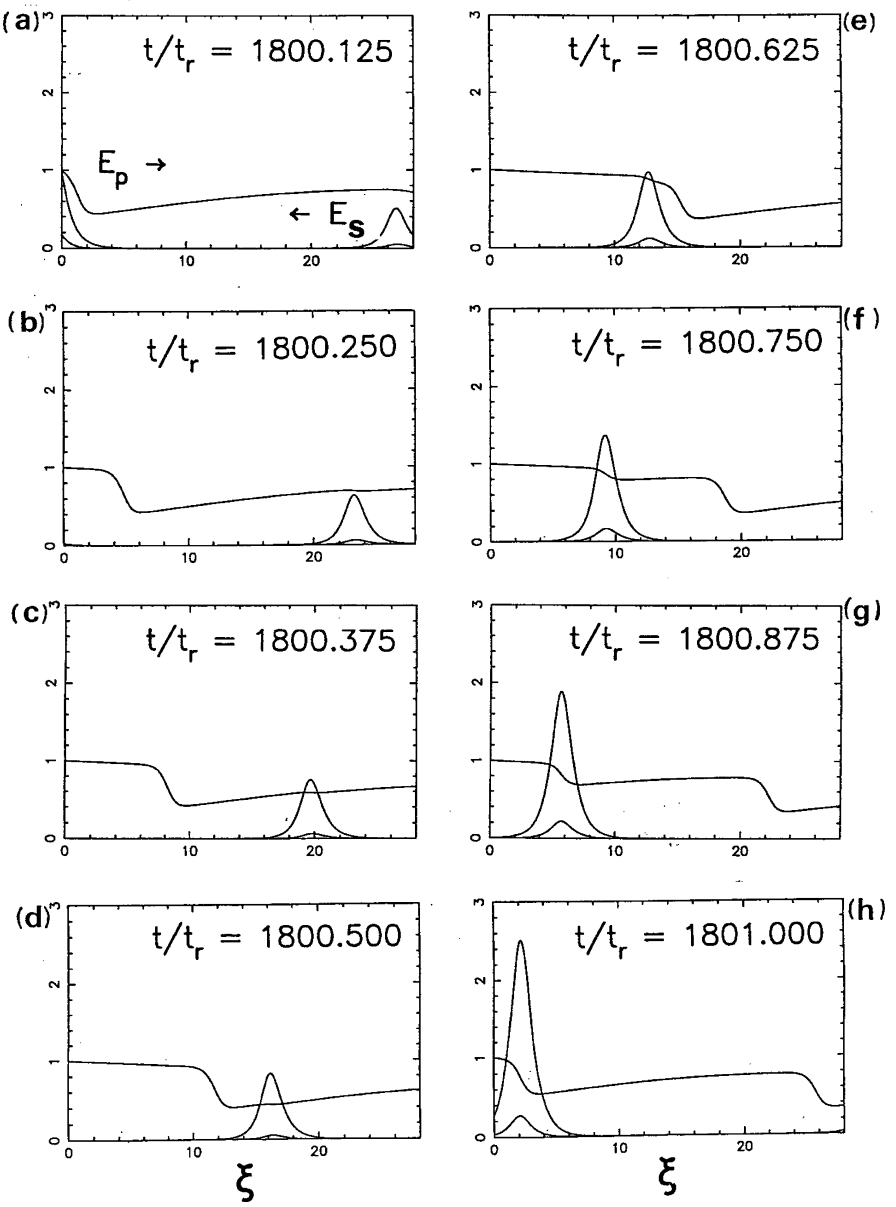

Fig. 5 Space–time dynamics in the ring cavity during one round-trip, showing the periodic counter-propagating process in the asymptotic pulsed regime. Spatial distributions of the locally depleted pump, E_{p}, the amplified Stokes, E_{S}, and acoustic E_{a} wave envelopes inside the cavity at successive time intervals $\Delta t/t_{\mathrm{r}} = 1/8$

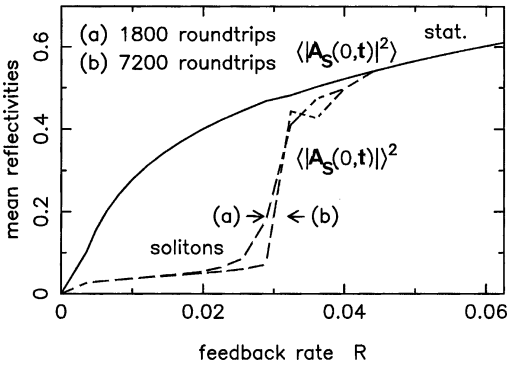

Fig. 6 Mean reflectivities computed from (1) obtained : (a) after 1800 round-trips and (b) after 7200 round-trips, showing the long transient evolution in the transition region. For low R, the small value of the squared mean amplitude, $\langle |A_S(0,t)| \rangle^2$, (*dashed lines*) with respect to the mean instantaneous intensity, $\langle |A_S(0,t)|^2 \rangle$, (*solid curve*) accounts for the solitonic localization. Both quantities are normalized to $|A_{cw}|^2$. (Computation parameters: $G = 8$, $L/\Lambda_0 = 28$, $\mu_a = 10^3 \mu_{p,S} = 7$, $K_r A_{cw}/K = 2.5 \times 10^{-3}$)

and its value is almost attained from the transient stage of the high amplitude Stokes response. The optical Kerr effect does not significantly affect the asymptotic dynamics, as we can see by comparing Fig. 6, computed with the entire SBS Kerr system of (1), with Fig. 7, computed without the Kerr effect (5). As expected from the pioneering work of [4] on SBS Kerr dynamics, the Kerr effect remains perturbative in the mono-stable super-critical localization domain.

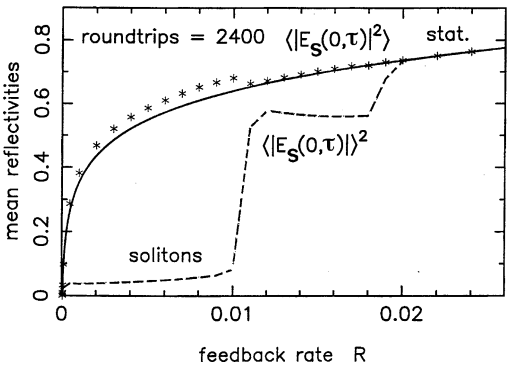

Fig. 7 Mean reflectivity, $\langle |E_S(0,\tau)|^2 \rangle$, computed from the dynamical three-wave model (5) for $\mu_{p,S} = 0$ (asterisks), compared with the analytical stationary output, $I_S(0)^{st} = |E_S(0)|^2$, given by (7) (*solid curve*). This shows the discrepancy, in the pulsed region, ($R < 0.01$), between the mean and stationary intensities. The *dashed curve* $\langle |E_S(0,\tau)| \rangle^2$ is for the model (5). The intensities are normalized to $|E_{cw}|^2$. (Computation parameters: $G = 10$, $L/\Lambda_0 = 32$, $\mu_a = 6.4$, $\mu_{p,S} = 0$, $K_r = 0$)

Another interesting result obtained from the three-wave dynamic simulations is the enhancement, for the same input intensity, I_{cw}, and feedback values, of the mean Stokes reflectivity, $\langle|E_S(x=0)|\rangle^2/I_{cw}$, in the pulsed regime with respect to the pure stationary solution, whose analytical expression (7) is obtained from the intensity model (6). This allows us to interpret the discrepancy observed for low gain values [41], between the measured experimental Brillouin gain coefficient, g, and that computed from the stationary intensity model. Figure 7 compares the mean Stokes reflectivities for each model.

5 Backward-Traveling Three-Wave Solutions

In order to obtain dissipative traveling three-wave solutions of (5) in the unbounded line problem (without cavity boundary conditions), we must assume a constant pump input ($E_p = 1$) compensating for the Stokes and material losses. Therefore, assuming that the threshold condition is satisfied

$$\mu_S \mu_a \equiv \frac{\gamma_S \gamma_a}{|KA_{cw}|^2} < 1, \tag{12}$$

the E_S and E_a waves are unstable, and they grow exponentially in the linear parametric regime until a nonlinear stage is reached, where the depletion of the pump E_p saturates the instability. The problem will be to determine the nonlinear three-wave solitary structures. In order to look for backward-traveling wave solutions of (5), let us change to a frame moving in the backward direction $\zeta = \xi + \mathrm{V}\tau,\ \tau = \tau$

$$\begin{aligned}
\left[\partial_\tau + (1+V)\partial_\zeta\right]E_p &= -E_S E_a - \mu_p E_p,\\
\left[\partial_\tau + (V-1)\partial_\zeta\right]E_S &= E_p E_a^* - \mu_S E_S,\\
\left[\partial_\tau + V\partial_\zeta\right]E_a &= E_p E_S^* - \mu_a E_a.
\end{aligned} \tag{13}$$

We define the a_i fields as

$$a_p = |1+V|^{1/2}E_p; \quad a_S = |\mathrm{V}-1|^{1/2}E_S; \quad a_a = |\mathrm{V}|^{1/2}E_a; \tag{14}$$

and look for stationary solutions in the new frame. This reduces the PDE problem to an ordinary differential equation (ODE) dynamical system, where we have

$$\begin{aligned}
\partial_X a_p &= -s_1 a_S a_a - s_1 \Gamma_p a_p,\\
\partial_X a_S &= s_2 a_p a_a^* - s_2 \Gamma_S A_S,\\
\partial_X a_a &= s_3 a_p a_S^* - s_3 \Gamma_a a_a,
\end{aligned} \tag{15}$$

where $X = \zeta/|(V-1)(1+V)V|^{1/2}$; $\Gamma_p = \mu_p|V-1|^{1/2}|V|^{1/2}/|1+V|^{1/2}$; $\Gamma_S = \mu_S|1+V|^{1/2}|V|^{1/2}/|V-1|^{1/2}$; $\Gamma_a = \mu_a|1+V|^{1/2}|V-1|^{1/2}/|V|^{1/2}$; and $s_1 = \mathrm{sgn}(1+V)$, $s_2 = \mathrm{sgn}(V-1)$, $s_3 = \mathrm{sgn}(V)$. Since $\mu_p \sim \mu_S \ll \mu_a$ and $V \sim 1$, we also

have $\Gamma_p \ll \Gamma_a$, but Γ_S and Γ_a are of the same order, so then we can neglect the electromagnetic pump damping. This is necessary in order to define a local three-wave traveling solution [5]. Moreover, for the pure resonance problem, the relation between the three phases remains fixed, and the whole dynamics is governed by real E_i or a_i fields, with negative amplitude standing for a π-phase shift.

6 Dissipative Symmetric Three-Wave Solution

First, let us recall the dissipationless case [25, 26], which has been integrated by the inverse scattering transform [21]. The concept of self-induced transparency has been associated with this soliton solution Fig. 8(a) because all of the pump is reconstructed after the interaction. This self-similar Stokes pulse can travel at any super-luminous velocity. In order to introduce the family of dissipative traveling wave structures, our starting point will be the only known analytic super-luminous soliton solution which accounts for the presence of dissipative Stokes ($\mu_S \neq 0$) and material ($\mu_a \neq 0$) waves [5]. This particular solution of system (15), here called *symmetric* since it is obtained for

$$\Gamma_S = \Gamma_a = \Gamma, \tag{16}$$

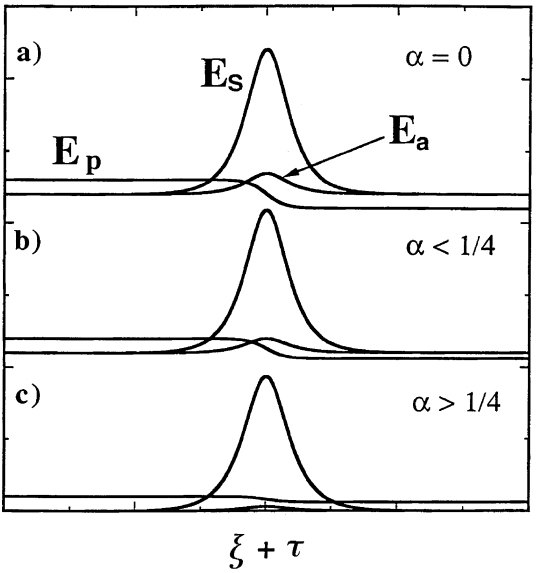

Fig. 8 Symmetric three-wave soliton solution: (**a**) Total self-induced transparency: non-dissipative ($\alpha = 0$) IST integrable soliton solution. (**b**) and (**c**) Partial self-induced transparency: dissipative soliton solution (20). In (**b**), the pump wave exhibits a phase change ($\alpha < 1/4$), while in (**c**), the pump wave is weakly depleted without changing its phase ($\alpha > 1/4$)

is given by

$$a_{\rm p}^0 = -a\tanh aX + \Gamma; \qquad a_{\rm S}^0 = a_{\rm a}^0 = a\,\mathrm{sech}\,aX, \tag{17}$$

where the limit conditions $[E_{\rm p}(\zeta \to -\infty) = 1$ and $E_{\rm S,a}(\zeta \to -\infty) \to 0]$ determine the constant

$$a = (1+V)^{1/2} - \Gamma \tag{18}$$

and fix the velocity $V = V_{\rm sym}$ as a function of $(\mu_{\rm a},\ \mu_{\rm S})$,

$$V_{\rm sym} = \frac{1}{1-\mu_{\rm S}/\mu_{\rm a}}. \tag{19}$$

Let us write this *symmetric* solution, of slope $p_{\rm sym}$, in terms of the variables of (5) [42]:

$$\begin{aligned} E_{\rm p} &= (\mu_{\rm S}\mu_{\rm a})^{1/2} - [1-(\mu_{\rm S}\mu_{\rm a})^{1/2}]\tanh[p_{\rm sym}(x+V_{\rm sym}t)], \\ E_{\rm S} &= S\,\mathrm{sech}[p_{\rm sym}(x+V_{\rm sym}t)], \\ E_{\rm a} &= S\left(\frac{\mu_{\rm S}}{\mu_{\rm a}}\right)^{1/2}\mathrm{sech}[p_{\rm sym}(x+V_{\rm sym}t)], \end{aligned} \tag{20}$$

where

$$\begin{aligned} S &= [1-(\mu_{\rm S}\mu_{\rm a})^{1/2}]\ [2(\mu_{\rm a}/\mu_{\rm S})-1]^{1/2}, \\ p_{\rm sym} &= \frac{[1-(\mu_{\rm S}\mu_{\rm a})^{1/2}](1-\mu_{\rm S}/\mu_{\rm a})}{(\mu_{\rm S}/\mu_{\rm a})^{1/2}}. \end{aligned} \tag{21}$$

In the presence of weak dissipation, $(\alpha \equiv \mu_{\rm S}\mu_{\rm a} < 1/4)$, the behavior is reminiscent of the self-induced transparency case, with the pump wave being partially restored with an opposite phase after the interaction Fig. 8(b). A property of this structure is then the possibility for the pump wave to change its phase, and this is the key argument in the following stability discussion. When the Stokes and material waves are heavily damped, with $\alpha > 1/4$, the pump is weakly depleted Fig. 8(c) without changing its phase.

Before describing the continuous family of three-wave dissipative solitary structures whose nonlinear dynamical behavior is obtained by the numerical treatment of (5) for any dissipation and any initial wave-front slope conditions, let us look at the stability of the super-luminous symmetric soliton solution.

6.1 Instability of the Symmetric Solution

6.1.1 Pitchfork Bifurcation

Equation (5) has been integrated through perturbative IST in the small dissipation case [29], but the symmetric soliton structure is unstable at finite times. We show

here that it decays through a cascade of bifurcations toward a turbulent-tail structure for small dissipation, when the transmitted pump is still strong enough to stimulate the Stokes and material waves. We study the stability of solution (17), satisfying the ODE system (15), and being a particular traveling solution of the PDE (5), by looking at what happens in its neighborhood. Defining

$$\begin{aligned}\Gamma_{\mathrm{a}} &= \Gamma + \varepsilon/2,\\ \Gamma_{\mathrm{S}} &= \Gamma - \varepsilon/2,\end{aligned}$$

with $\varepsilon \ll \Gamma$ and $2\Gamma = \Gamma_{\mathrm{a}} + \Gamma_{\mathrm{S}}$, we can linearize (15) (with $s_i = 1$ for $i = 1,2,3$ because $V_{\mathrm{sym}} > 1$) around the analytic solution

$$a_{\mathrm{i}}(X) = a_{\mathrm{i}}^0(X) + \delta_{\mathrm{i}}(X), \tag{22}$$

where $\delta_{\mathrm{i}} \ll a_{\mathrm{i}}^0$ and a_{i}^0 ($i = \mathrm{p},\mathrm{S},\mathrm{a}$) are given by (17). Substituting (22) into (15), defining $\delta = \delta_{\mathrm{S}} - \delta_{\mathrm{a}}$, and subtracting the last two equations of system (15), we obtain

$$\partial_X \delta = -\delta(a_{\mathrm{p}}^0 + \Gamma) + \varepsilon a_{\mathrm{S}}^0,$$

whose solution is

$$\delta(X) = \varepsilon K(X) \exp(-2\Gamma X) \cosh(aX), \tag{23}$$

where $K(X)$ is the following positive function:

$$K(X) = A \int_{-\infty}^{X} \exp(2\Gamma x) \operatorname{sech}^2(ax)\, \mathrm{d}x.$$

The two main points here are (i) δ has the same sign as ε and (ii) for X large (but not too large, in order to remain in the linear regime), there is an exponential dependence of δ on X:

$$\delta(X) \propto \exp(\lambda X), \tag{24}$$

where λ, obtained from expressions (16), (17), (18) with $\alpha = \mu_{\mathrm{S}}\mu_{\mathrm{a}}$, is given by

$$\lambda = 1 - \left(\frac{\alpha}{\alpha_{\mathrm{c}}}\right)^{1/2}, \qquad \alpha_{\mathrm{c}} = 1/9. \tag{25}$$

For $\alpha > \alpha_{\mathrm{c}}$, the perturbation decreases exponentially and the *symmetric* solution is stable. Otherwise, $\lambda > 0$ for $\alpha < \alpha_{\mathrm{c}}$, and the Stokes and material wave trajectories diverge exponentially at the trailing end of the pulse. This result has a simple physical interpretation in that the pump wave is reconstructed with the opposite phase ($\alpha < 1/4$) and is once again able to stimulate the Stokes and material waves.

We look at the nonlinear evolution of this instability up to its saturation by numerically solving the spatio-temporal PDE (5) in the co-moving E_{S} frame ($\zeta = \xi + \tau,\ \tau = \tau$), following the "characteristics" algorithm [9, 20, 22, 41]. Starting from

the unbounded *symmetric* solution, two asymptotic stable traveling wave structures are reached after a transient Fig. 9(a, b). These correspond to the two possible paths for the development of the instability, depending on the sign of ε in (23). If $\varepsilon > 0$, then $\delta_S > \delta_a$, and the effective material wave damping Γ_a is greater than the Stokes one Γ_S ($\Gamma_a > \Gamma_S$), accounting for the phase change of the material amplitude Fig. 9(a). The instability is saturated by exciting a second Stokes-material pulse. Otherwise, if $\Gamma_a < \Gamma_S$, the second pulse is also generated with the Stokes and material envelopes having opposite phases Fig. 9(b), but now undergoes a change of sign for the Stokes wave. The symmetry $a_S = a_a$, available for any $\alpha > \alpha_c$, is now broken. These properties are the characteristic features of a pitchfork bifurcation, where the order parameter is $\delta = \delta_S - \delta_a$ and the control parameter is α. Therefore, for $\alpha < \alpha_c$, the *symmetric* solution is unstable and the nonlinear spatio-temporal dynamics reveals an interesting class of stable bi-solitary solutions.

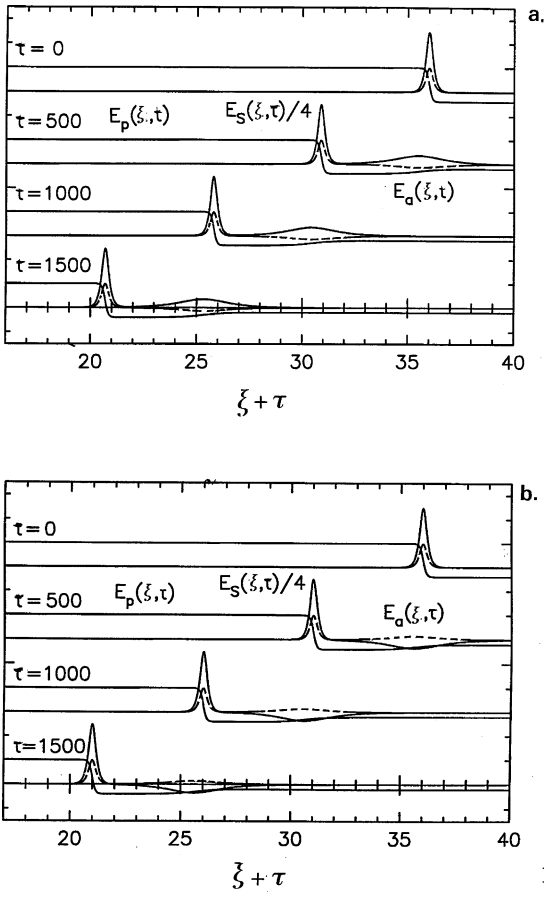

Fig. 9 Space–time evolution of the symmetric three-wave soliton solution for small dissipation ($\mu_a = 3$, $\mu_S = 3 \times 10^{-2}$, $\alpha = 9 \times 10^{-2}$), obtained by numerical computation of (5) in the co-moving Stokes frame $\zeta = \xi + \tau$, and giving rise to an asympotically stable bi-solitary structure: (**a**) For $\Gamma_a > \Gamma_S$, the material envelope exhibits a π-phase change for the second peak; (**b**) For $\Gamma_a < \Gamma_S$, the Stokes envelope exhibits a π-phase change for the second peak

A parameter which characterizes the bi-solitary structure is the distance, d, between the two pulses. As we can see from Fig. 9(a, b), it is always conserved. In fact, it characterizes the growth rate of the instability, as is shown by expression (24). This distance is therefore proportional to λ^{-1}:

$$d \propto \frac{1}{1-(\alpha/\alpha_c)^{1/2}}. \tag{26}$$

For $\alpha \lesssim \alpha_c$, the pump wave restored after the first pulse is just above threshold (12), while the second pulse will be stimulated at infinity. This critical behavior of the ODE system is in excellent agreement with the numerical simulation of the nonlinear PDE system.

6.1.2 Cascading Toward Turbulence

As the damping term, α, decreases, the pump wave – having generated the second Stokes-material pulse – may be sufficiently reconstructed (with two successive π-phase shifts) to yet stimulate a third pulse, with the process repeating for smaller values of α. Therefore, a set of peaks may be stimulated in cascade until the pump is exhausted. A linear stability analysis, assuming the peaks to be independent of each other, yields the following formula for the critical value necessary for stimulation of the $(n+1)$ multi-peak structure:

$$\alpha_{c,n} = \frac{1}{(2n+1)^2}, \tag{27}$$

where $\alpha_{c,1}$ is the critical value of the pitchfork bifurcation. Therefore, just below $\alpha_{c,n}$, the $(n+1)$th pulse is excited at infinity and will rejoin the n-peak structure for $\alpha < \alpha_{c,n}$, following the critical behavior expressed in (26). A typical example of the evolution of the *symmetric* solution for a rather small α ($\mu_a = 1$; $\mu_S = 10^{-3}$) is plotted in Fig. 10. The Stokes envelope exhibits a set of large peaks, but no steady solitary behavior is reached. We can interpret this dynamics in the phase plane representation, where a two-dimensional projection is shown schematically in Fig. 5 of [22]. The distortion and spreading of the trajectories are related to the homoclinic orbit corresponding to the analytic *symmetrical* solution (17).

We may point out that, in Fig. 10, *symmetric* solutions seem to escape from the turbulent tail of the structure. This behavior is very evident as we approach the non-dissipative integrable problem ($\alpha = 0$) where super-luminous solitons leave from the radiative envelope (π-pulse type structure) propagating at the light velocity [39]. Here the word *radiation* is used in contrast to *soliton*. Therefore, *weak dissipation traps the radiation leading to turbulent-tail solitary structures*. This turbulence limits the analytic perturbative approach [29] obtained for $\alpha \ll 1$ to a description for short-time evolution.

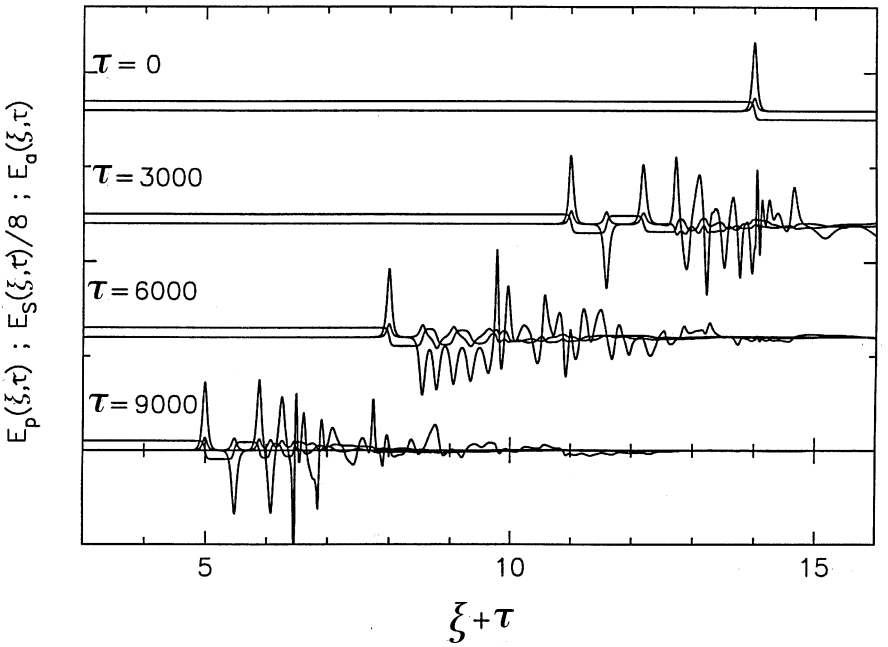

Fig. 10 Space–time evolution of the symmetric three-wave soliton solution for smaller dissipation than Fig. 9 ($\mu_a = 1$, $\mu_S = 10^{-3}$, $\alpha = 10^{-3}$), giving rise to a multi-peak turbulent-tail structure. (The characteristic time, τ_0, for SBS is nanoseconds)

7 Asymmetric Three-Wave Dissipative Solitons

In the previous section, we explored the spatio-temporal behavior for any damping value α, while still remaining in the vicinity of the *symmetric* solution (17) and (20). This satisfies (16), characterized by its wave-front slope, p_{sym}, (21) and its velocity, V_{sym} (19). This solution is the only localized backward-traveling three-wave structure in the dissipationless case [25, 26], so our aim here is to show how the damping reveals a family of asymmetric solitary structures when condition (16) is no longer satisfied. Moreover, even for small damping values ($\alpha \ll \alpha_c$, $p \neq p_{\text{sym}}$), the Stokes and material trajectories in the phase plane representation swerve from the sensitive homoclinic orbit [22], which causes turbulence, and a steady solitary attractor is once again reached. In order to summarize the complex spatio-temporal dynamics, the domain of stability has been drawn schematically in the (p, α) plane in [22] as well.

7.1 Luminous Backward-Traveling Solution

For the particular case of a three-wave backward-traveling solution with the velocity of light ($V = 1$), the non-integrable three-wave PDE equations system (13) reduces

to a problem of two ODE equations, and we are able to integrate these. Indeed, the second equation (13) yields

$$E_{\mathrm{S}} = \frac{E_{\mathrm{p}} E_{\mathrm{a}}^{*}}{\mu_{\mathrm{S}}}, \tag{28}$$

and we obtain a two-equation system for the pump and material wave intensities ($I_{\mathrm{p,a}} = |E_{\mathrm{p,a}}|^2$), where the Stokes wave plays the role of a slave variable:

$$\frac{\mathrm{d}I_{\mathrm{p}}}{\mathrm{d}X} = -I_{\mathrm{p}} I_{\mathrm{a}}, \tag{29a}$$

$$\frac{\mathrm{d}I_{\mathrm{a}}}{\mathrm{d}X} = 2I_{\mathrm{p}} I_{\mathrm{a}} - 2\alpha I_{\mathrm{a}}, \tag{29b}$$

with $X = \zeta/\mu_{\mathrm{S}}$ and $\alpha = \mu_{\mathrm{S}}\mu_{\mathrm{a}}$. Upon introducing the change

$$I_{\mathrm{p}} = \exp(W - 1/\alpha), \tag{30}$$

Equation (29a) verifies that

$$I_{\mathrm{a}} = -\frac{\mathrm{d}W}{\mathrm{d}X}, \tag{31}$$

and the equation system (29a) and (29b) is reduced [cf. [22]] to the integral

$$\frac{\mathrm{d}W}{\mathrm{d}\eta} = \exp W - \mathrm{a}W, \tag{32}$$

where $\eta = 2X \exp(-1/\alpha)$, and the constant $a = \alpha \exp(1/\alpha)$ is determined by the limit condition $I_{\mathrm{p}}(X \to -\infty) = 1$. Equation (32) is in a "separation of variables" form, but no analytic solution is available. It may easily be integrated by a numerical Runge–Kutta algorithm. For $a > e$ (i.e., for the localization threshold condition $\alpha = \mu_{\mathrm{S}}\mu_{\mathrm{a}} < 1$), we obtain two finite values of W, say W_1 and W_2, which are solutions of

$$\exp W - aW = 0 \qquad \Rightarrow \ (W_1, W_2) \ \text{ for } \ \mathrm{a} > \mathrm{e},$$

where all the derivatives of W vanish for $\eta \to \pm\infty$. For $I_{\mathrm{p}}(X \to -\infty) = 1$, we have $W_2 = 1/\alpha$. Knowing $W = W(\eta)$, (30) yields a traveling localized structure of kink type for I_{p}, and, from (31), of the asymmetric pulse type for I_{a} and I_{S}

$$I_{\mathrm{a}} = \frac{-\mathrm{d}W}{\mathrm{d}\eta}\frac{\mathrm{d}\eta}{\mathrm{d}X} = -2\exp(-1/\alpha)\big(\exp W - aW\big), \tag{33}$$

$$I_{\mathrm{S}} = \frac{I_{\mathrm{p}} I_{\mathrm{a}}}{\mu_{\mathrm{S}}^2}, \tag{34}$$

which are represented in Fig. 11(a).

The maximum of I_{a}, obtained from $\mathrm{d}I_{\mathrm{a/d}}X = 0$, at $W_{\mathrm{a,max}} = a$, is given by

$$I_{\mathrm{a,max}} = 2\alpha(\log \alpha + 1/\alpha - 1), \tag{35}$$

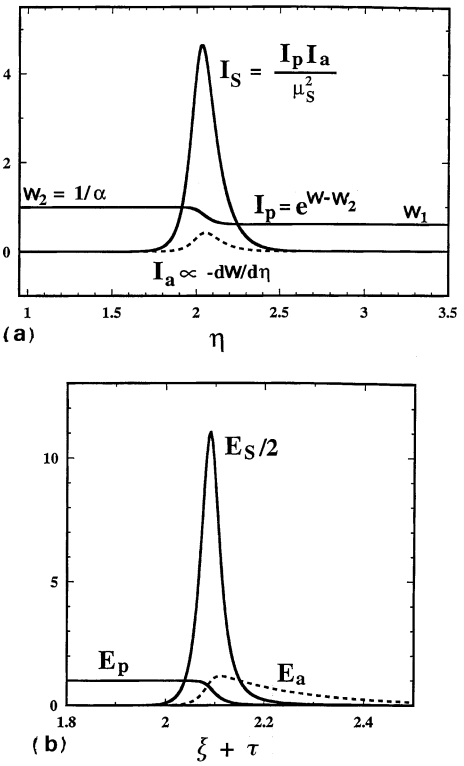

Fig. 11 Luminous three-wave backward-traveling solution: (**a**) Shape of the analytical solutions (30), (33), and (34) for $\alpha = 0.625$. (**b**) Asymptotic three-wave (luminous) amplitude structure for $\mu_a = 3$ and $\mu_S = 3 \times 10^{-2}$ ($\alpha = 9 \times 10^{-2}$), resulting from the space–time dynamical evolution

and the maximum of the Stokes pulse, I_S [obtained from $dI_S/dX = 0$, at $W_{S,max}$, the solution of $\exp W_{S,max} = (1 + a)W_{S,max/2}$], is given by

$$I_{S,max} = \frac{1}{2\mu_S^2}[\alpha^2 - \exp(-2/\alpha)]W_{S,max}^2. \tag{36}$$

For example, let us take $\alpha = \mu_S \mu_a = 0.625$; then we have $a = \alpha \exp(1/\alpha) = 3.09564$, $W_2 = 1/\alpha = 1.6$, $W_1 = 0.5724$, $I_p(\zeta \to +\infty) = \exp(W_1 - W_2) = 0.3578$, which is in perfect agreement with the space–time numerical simulation of (13), namely $E_p(\zeta \to \infty) = \sqrt{I_p(\zeta \to +\infty)} = 0.5983$.

Even if this luminous solution is a particular one, it turns out to be one of the most interesting attractors, since we can approach it in an actual Brillouin fiber-ring experiment, as we shall see in Sects. 9 and 10. In Fig. 11(b), we show the three-amplitude luminous structure for $\alpha = 9 \times 10^{-2}$ ($\mu_a = 3$; $\mu_S = 3 \times 10^{-2}$), which are values associated with an actual experiment.

8 Stability Criterion: Asymptotic Procedure

In Sect. 7, we announced the existence of a family of asymptotically stable three-wave dissipative solitary structures whose velocity can be super-luminous or sub-luminous, depending on the wave-front slope, p, of the backscattered or material wave. An explicit solution for the particular integrable luminous velocity case was also given. The object here is to determine a stability criterion for all these structures by using an extension of the Kolmogorov, Petrovskii, and Piskunov (KPP) asymptotic procedure [23] used in [20] for the bounded problem to this unbounded problem [22], in order to find the long-term evolution of initially unbounded Stokes or material envelopes in the presence of a c.w. pump. The main property found is the existence of a particular solution (coinciding with the sub-luminous attractor of [20]), corresponding to the minimum possible velocity V_0, which turns to be the frontier of stability for the entire family of backward-traveling wave structures.

Assuming that the threshold condition (12) is satisfied ($\mu_S \mu_a < 1$), the Stokes and material waves are unstable and they grow exponentially in the linear parametric regime. The instability is then saturated by pump depletion, and the three envelopes self-organize into a solitary wave. For an initially unbounded Stokes or material condition, the asymptotic procedure analytically determines the velocity and the slope of the wave front in the linear regime of un-depleted pump, which turns out to be the value of the velocity in the nonlinear steady state of strong pump depletion, since the front edge of the whole three-wave steady structure always remains in the linear un-depleted pump regime.

Thus, assuming an un-depleted pump wave ($E_p = 1$) throughout the whole linear interaction range, we obtain, from (5), a set of linearized equations

$$(\partial_\tau - \partial_\xi + \mu_S)(\partial_t + \mu_a) E_{S,a} = E_{S,a}, \tag{37}$$

whose characteristic equation for an exponential dependence [$E_{S,a} \propto \exp(\gamma\tau + p\xi)$] reads

$$(\gamma - p + \mu_S)\,(\gamma + \mu_a) = 1, \tag{38}$$

where we only keep the unstable root (Re $\gamma > 0$)

$$\gamma = \frac{p - \mu_a - \mu_S}{2} + \frac{\sqrt{(p + \mu_a - \mu_S)^2 + 4}}{2}. \tag{39}$$

The solution of this linear problem can be found by means of the Fourier transform (with $p = -ik$ and k complex):

$$E_{S,a}(\xi, \tau) = \int_{-\infty}^{\infty} \widetilde{E_{S,a}}(p) \exp(\gamma(p)\tau) \exp(p\xi)\, dp,$$

where $\widetilde{E_{\mathrm{S,a}}}(p)$ is the Fourier transform of the initial condition $E_{\mathrm{S,a}}(x,t=0)$. Let us look for backward-traveling waves with velocity V,

$$\zeta = \xi + V\tau,$$

yielding

$$E_{\mathrm{S,a}}(\zeta,\tau) = \int_C \widetilde{E_{\mathrm{S,a}}}(p)\exp[\gamma(p) - pV]\tau\,\exp(p\zeta)\mathrm{d}p. \tag{40}$$

This linear solution applies for long times τ, allowing us to obtain the asymptotic behavior of the far pulse wave front where the linear un-depleted pump approximation always remains valid. As a result of the parametric instability, the asymptotic wave-front structure grows exponentially. Here, since we are interested in characterizing the whole family of backward-traveling wave structures, we will only consider the exponential head-front dependence; then the corresponding Fourier transform $\widetilde{E_{\mathrm{S,a}}}(p)$ has a pole. Moreover, the function $f(p) = \gamma(p) - pV$ has a saddle point, and the integral can then be calculated by the steepest descent method. Using this, it was shown in Appendix C of [22], that the pole asymptotically dominates over the saddle point for any slope, p, smaller than a critical value, p_0 ($p < p_0$). The stationarity of the three-wave structure in its backward-traveling frame then imposes

$$V(p) = \frac{\gamma(p)}{p} = \frac{1}{2} - \frac{\mu_{\mathrm{S}} + \mu_{\mathrm{a}}}{2p} + \frac{\sqrt{(\mu_{\mathrm{a}} - \mu_{\mathrm{S}} + p)^2 + 4}}{2p}, \tag{41}$$

where the *amplitude velocity* of the traveling wave structure is then defined as the quotient of the temporal (γ) and spatial (p) growth rates. We plot this velocity dispersion relation (41) in Fig. 12.

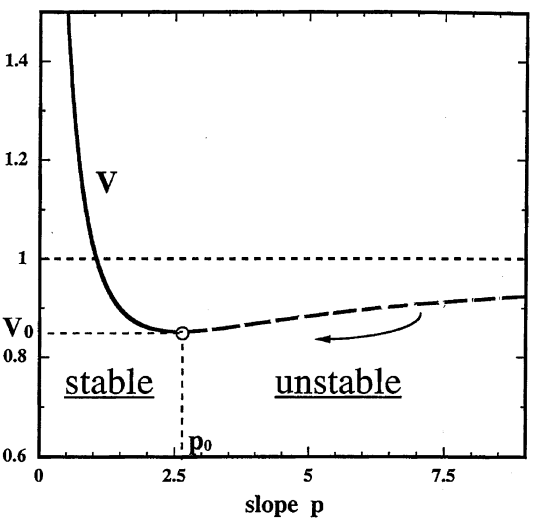

Fig. 12 Velocity dispersion: amplitude velocity $V = \gamma/p$ of the dissipative three-wave structure versus the exponential slope, p, of the backscattered wave front, showing the stable ($p < p_{\mathrm{sym}}$) and unstable ($p > p_{\mathrm{sym}}$) domains

In the other case, $p > p_0$, it is the saddle point which dominates the long-term behavior, and, following the steepest descent method [43], the supplementary condition is

$$V = [\partial\gamma(p)/\partial p]_{p=p_0}. \tag{42}$$

The velocity and the head-front slope then become fixed by (41) and (42):

$$V_0 = \frac{2+\mu_a^2-\mu_S\mu_a+2\sqrt{1-\mu_S\mu_a}}{4+(\mu_a-\mu_S)^2}, \tag{43}$$

$$p_0 = \frac{1}{\mu_S}+\mu_S-\frac{1}{\mu_a}-\mu_a+\frac{\sqrt{1-\mu_S\mu_a}}{\mu_a}+\frac{\sqrt{1-\mu_S\mu_a}}{\mu_S}. \tag{44}$$

Hence, this particular solution, which stands at the bottom of the $V(p)$ curve of Fig. 12, separates the stable ($p < p_0$) and the unstable ($p > p_0$) domains. Moreover, such a solution is an attractor for any initial condition having a wave-front slope $p > p_0$.

Let us finally point out the strength of this method, which allows us to determine the nonlinear stage of the interaction by simply looking at the linear asymptotic evolution of its wave front, and characterizes the continuous family of three-wave solitary attractors analyzed in Sects. 6 and 7. In order to test this statement with an additional example, we considered an initial Gaussian condition for the Stokes envelope. Since the slope of its frontal tail is greater than any exponential one, it is expected from the theory that only the saddle point will contribute to the integral (40). The numerical evolution confirms this prediction and shows that the corresponding fundamental sub-luminous attractor is reached asymptotically (see Fig. 13).

The reader may now wonder how an initially bounded condition [20] can yield the same asymptotic solution as that obtained for a particular sub-luminous case of an initially unbounded condition. This can occur due to the sub-luminous velocity of the structure formed from the initially bounded condition, since it becomes asymptotically de-correlated from its luminous tip of the foot at the beginning of the interaction.

8.1 Balance Between Velocity Dispersion and Pump Depletion

In fact, this stability problem has fundamental physical significance. Let us point out its resemblance to the well-known bright optical NLS soliton [30], where compensation between the linear dispersion and the nonlinear Kerr effect is only possible for negative dispersion of the group velocity ($\partial\omega/\partial k$). Here, for the three-wave soliton, the *amplitude velocity* γ/p stands for the group velocity, the linear effect is the backscattering instability characterized by its growth rate, p, and the nonlinear effect is the pump depletion. Figure 12 shows that the velocity dispersion now depends on the slope (instead of the NLS soliton wave-number). In our case, if the velocity dispersion ($\partial V/\partial p < 0$) allows the smaller slopes to rejoin the higher ones

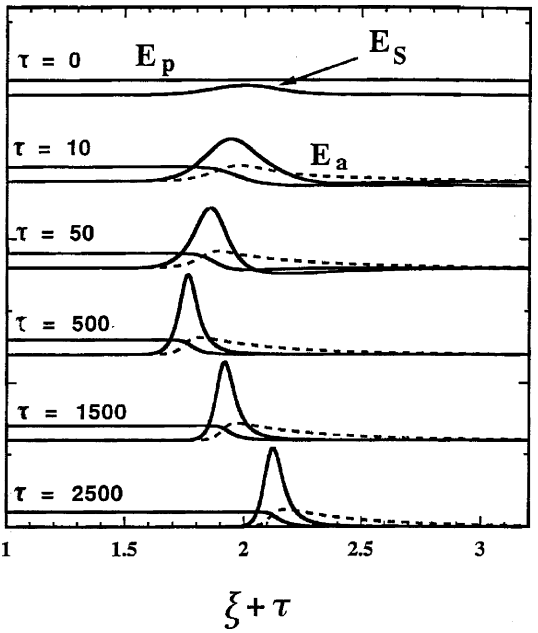

Fig. 13 Space–time evolution of an initial Gaussian Stokes condition. Since the wave-front tail profile is steeper than any exponential slope, the solitary structure is attracted by the sub-luminous (p_0, V_0) solution

(since their velocity is greater), a balance may be achieved between *velocity dispersion steepening* and *nonlinear pump depletion flattening*. This case corresponds to stable soliton solutions ($p < p_0$). For the opposite case ($p > p_0; \partial V/\partial p > 0$), both effects act in the same way and tend to flatten the three-wave structure, which then spreads until it reaches the sub-luminous attractor, (p_0, V_0), which is given by (43) and (44), and described in [20].

9 Brillouin Fiber-Ring Laser Pulses

The theoretical study for the unlimited interaction in Sects. 4, 5, 6, 7, 8 is useful because it sheds light on the nonlinear dynamics of the c.w.-pumped Brillouin fiber-ring laser, where solitonic pulses are obtained in the feedback range $R_{\text{thres}} < R < R_{\text{crit}}$. They are interpreted via a Hopf bifurcation process from the steady Brillouin mirror solution (Sect. 3). We have performed long-time numerical simulations of (5) and made systematic tests by numerical computation of the entire SBS Kerr model (1) for a ring configuration of length L, corresponding to the experiments of [6, 7, 8], with periodic boundary conditions (3b) for the Stokes wave.

However, we note from Fig. 5 that, in spite of the time-dependent amplification process, the pulse width remains almost constant throughout the fiber round-trip. Thus, we suggest going further with a comparison of the actual pulses in the ring

cavity with the invariant three-wave dissipative solitary structure of the unbounded system. Here we may consider an average dissipative solitary wave which is similar to the concept of an average soliton [44] in optical fiber transmission. In the second case, the sharp localized lumped amplification is assumed to be distributed through the whole fiber length between two consecutive amplifiers, in order to compensate for the distributed loss, while in our case, we are looking to distribute the sharp localized feedback action throughout the cavity length by means of an effective Stokes damping rate in order to compensate for the amplification. The effective damping will be given by

$$\gamma_{\text{eff}} \simeq \frac{c}{nL}\,\ln\frac{1}{\sqrt{R}}\,, \qquad \mu_{\text{eff}} = \frac{\gamma_{\text{eff}}}{|KA_{\text{cw}}|} = \frac{\Lambda_0}{L}\ln\frac{1}{\sqrt{R}}, \tag{45}$$

which is much greater than the optical wave damping $\gamma_{\text{S}} = \gamma_{\text{e}}$, as required for a satisfactory comparison of the unbounded three-wave dissipative structure with the actual pulse obtained in a finite length cavity. It will correspond to the dimensionless Stokes damping rate, μ_{S}, introduced in Sect. 3, together with $\mu_{\text{a}} = \gamma_{\text{a}}/|KA_{\text{cw}}|$ in order to analyze the whole family of three-wave dissipative sub-luminous and superluminous solitary structures in unbounded systems determined by the Stokes front slope, $p = p(\mu_{\text{a}}, \mu_{\text{S}})$. Now, the slope, p, and the amplitude pulse width, $\delta\zeta = p^{-1}$, are associated with R and L through $\mu_{\text{S}} = \mu_{\text{eff}}$ and μ_{a}. Simple analytical expressions are obtained for special cases. For the luminous case $(V = 1)$, we have, from (41)

$$\delta\zeta = \frac{1}{p} = \left(\frac{1}{\mu_{\text{S}}} - \mu_{\text{a}}\right)^{-1}, \tag{46}$$

which exhibits the right dependence $\propto 1/\gamma_{\text{a}}$, but only yields an approximate value of the numerical width obtained from the dynamical simulations (cf. Table 1).

Another value for the amplitude width is provided by the symmetric solution (21)

$$\delta\sigma = \frac{(\mu_{\text{S}}/\mu_{\text{a}})^{1/2}}{\left[1 - (\mu_{\text{S}}\mu_{\text{a}})^{1/2}\right](1 - \mu_{\text{S}}/\mu_{\text{a}})}, \tag{47}$$

but this also only yields an approximate value for the width. Nevertheless, it provides an analytic expression for the Stokes amplitude [45], namely

$$S \equiv A_{\text{S,max}}/A_{\text{cw}} = \left[1 - (\mu_{\text{S}}\mu_{\text{a}})^{1/2}\right]\left[2\mu_{\text{a}}/\mu_{\text{S}} - 1\right]^{1/2}, \tag{48}$$

which yields a good estimate for the maximum amplitude obtained from (1), as we can also seen in Table 1. For the unpolarized Ar-ion fiber-ring experiment of [7], we obtain $S = 1.10\, A^{\text{dyn}}_{\text{S,max}}/A_{\text{cw}} = 3.16$. In Fig. 14, we plot the numerical backscattered asymptotic pulses at the output of this ring cavity. Each pulse corresponds to one round-trip, and the time interval between them measures the nonlinear mean round-trip period, Δ_t, normalized to the linear photon flight time, $t_{\text{r}} = nL/c$. We can see

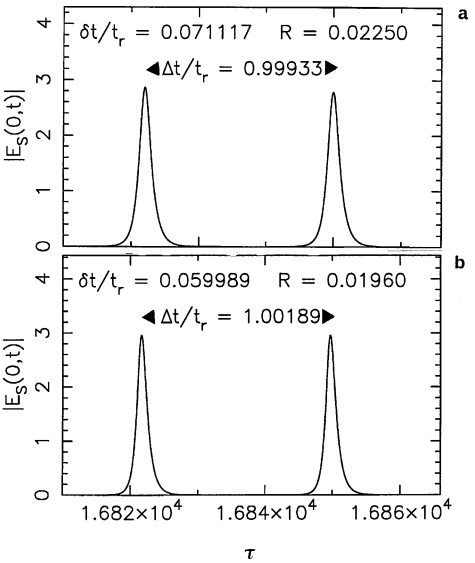

Fig. 14 Backscattered asymptotic pulses at the output of the Brillouin fiber-ring cavity of [7], obtained from numerical integration of (1) with boundary conditions (3b) for a SBS gain-length $G = gLI_{cw} = 8$. (**a**) Super-luminous regime ($\Delta t/t_r = 0.99933, V > 1$) corresponding to a Stokes intensity feedback $R = 0.0225$. (**b**) Sub-luminous regime ($\Delta t/t_r = 1.00189, V < 1$) for $R = 0.0196$

that both slightly super-luminous ($\Delta_t/t_r < 1$) and sub-luminous ($\Delta_t/t_r > 1$) regimes can be obtained for the same configuration, by just varying the feedback control parameter, R, for the same gain-length, $G = gLI_p = 8$. Moreover, the width, δt, of the pulses, which is inversely proportional to the exponential slope p, is narrower for smaller velocities, in agreement with the dispersion curve of Fig. 12. A more complete comparison can be seen in Table 1.

9.1 Experimental Results

In Fig. 15(a, b), we plot the experimental recording of different trains of solitary Stokes pulses at the output of the 250 m fiber-ring cavity. Fig. 15(a) shows a pair of solitary pulses for a feedback just below R_{crit}, and a gain-length of $G = 4 (P \simeq 70\,\text{mW})$, corresponding to one of the experimental results of the unpolarized Nd: YAG fiber-ring experiment of [22]. Their shape shows a strong resemblance to the asymmetric luminous dissipative soliton shown in Fig. 11(b). We can measure a time width $\delta t = 153 \pm 0.004$ ns, which is inversely proportional to the exponential slope, p, and a mean round-trip period of $\Delta t = 1.087 \pm 0.004$ µs, which is inversely proportional to the velocity. In Fig. 15(b), we show two superimposed trains of solitons in order to compare the different round-trip periods for different slopes in a better way. In the experiment, these are controlled by varying the feedback between R_{crit} and R_{thres}. We note that the lower slopes correspond to the faster train.

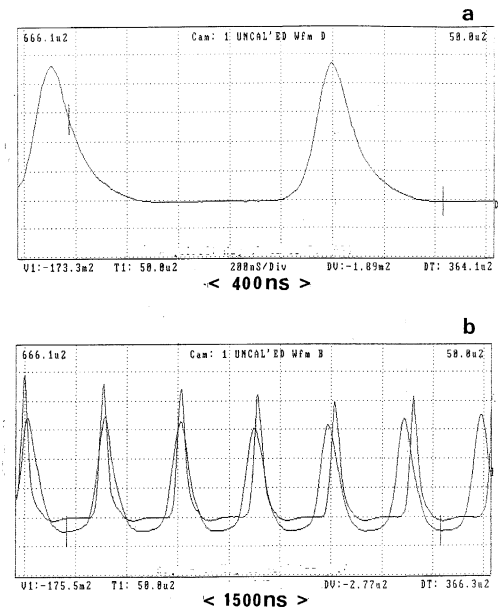

Fig. 15 Experimental recording of different trains of solitary Stokes pulses at the output of the 250 m Nd:YAG fiber-ring experiment of [22], corresponding to a feedback near R_{crit} and a gain-length of about $G = 4$. (**a**) The shape shows a strong resemblance to the asymmetric luminous dissipative soliton shown in Fig. 13. (**b**) Comparison of two superimposed trains of pulses in order to show that the lower slopes correspond to the faster train, as predicted by the theory

10 Systematic Experimental and Numerical Exploration of the Whole Soliton Localization Domain

In order to test the universality of our results, we perform systematic experimental and numerical exploration of the whole soliton localization domain for a large set of (G,R) parameters in the polarization-maintaining fiber-ring laser experiments of [8].

The experiment is built around a $L = 253$ m single-mode, polarization-preserving fiber of 800 kHz free spectral range. The characteristics are given in Sect. 2. In order to enhance the Brillouin scattering coherent features – which increase with the acoustic damping length – we have chosen to work in the infrared range, at $\lambda_{\text{p}} = 1.319\ \mu$m. This is associated with a *low* acoustic frequency (equal to the Stokes spectral shift) of 13 GHz, with a homogeneous broadening width $\Delta\nu_{\text{B}} =$ 23 MHz, i.e., a *long* damping time of 14 ns. The description of the experimental set-up (Fig. 16) is given in [8].

Following Fig. 1, the generic features of such a ring are summarized in Fig. 17, with the horizontal axis being the gain parameter $G = g_{\text{B}} I_0 L$. (Here, g_{B} is the fiber Brillouin gain coefficient, I_0 is the pump intensity at the entrance (15) of the fiber, and L is its effective length.) The vertical axis is the ring energetic Stokes feedback coefficient R (on a logarithmic scale). Under the straight line determined by $R = \text{e}^{-G}$, Stokes losses exceed the gain, and the pump propagates along the fiber in the linear regime. For the highest values of R and G, the Brillouin laser works in a stationary regime, i.e., in a single longitudinal mode. Between these two domains, other longitudinal modes are involved and are phase-locked: the Stokes wave is

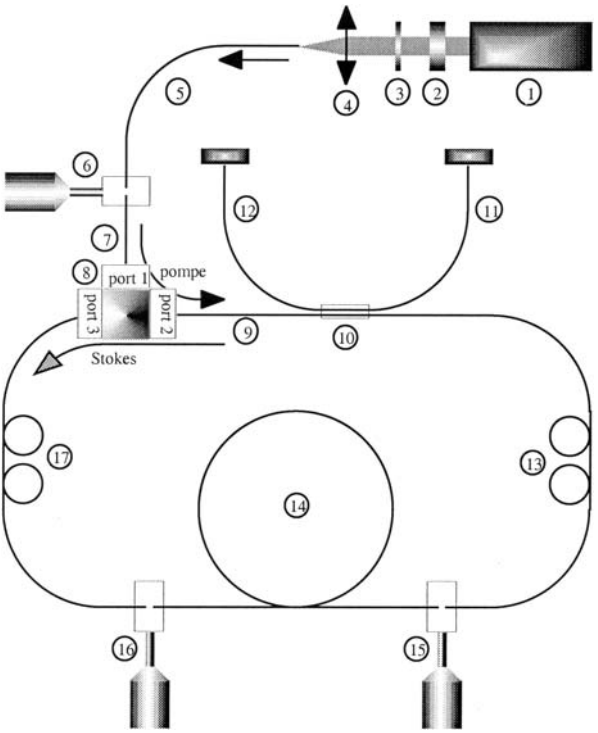

Fig. 16 Experimental set-up: (1): diode-pumped YAG:Nd^{+++} c.w. laser (1.319 μm, 340 mW); (2): Faraday isolator; (3): half-wave plate; (4): coupling lens; (5): coupling fiber; (6): micro-handler; (7): input fiber; (8): three-port optical circulator; (9): up-stream fiber; (10): 10/90 coupler; (11): pump signal detection; (12): Stokes signal detection; (13): polarization controller; (14): single-mode polarization-maintaining fiber; (15, 16): micro-handlers; (17): polarization controller

then structured in pulses of roughly 100 ns width. Note that, in going from the c.w. regime to the pulse regime, it is not the adjacent mode which is first destabilized for $G < 7$, but the following second longitudinal mode beyond this limit, as is shown in Fig. 3.

We have experimentally explored six zones (the tinted areas in Fig. 17). Each of them corresponds to a particular adjustment of the micro-handler (16) (cf. Fig. 16), as determined by the feedback values **(1)** $R = 0.15$, **(2)** $R = 0.0593$, **(3)** $R = 0.0225$, **(4)** $R = 0.00823$, **(5)** $R = 0.00194$, and **(6)** $R = 2.62 \times 10^{-4}$.

The experimental pulses, characterized by a width between 70 and 250 ns, exhibit shapes that are almost independent of experimental conditions. They always present a slight asymmetry, with the trailing edge being longer than the leading one. Generic Stokes behavior is observed when the pump power decreases from the c.w. zone toward the Brillouin threshold. This is qualitatively independent of the re-coupling factor R_{eff}. A periodic modulation of the Stokes signal appears at the bifurcation point, either at a frequency equal to the cavity FSR for the large values of R_{eff}, or

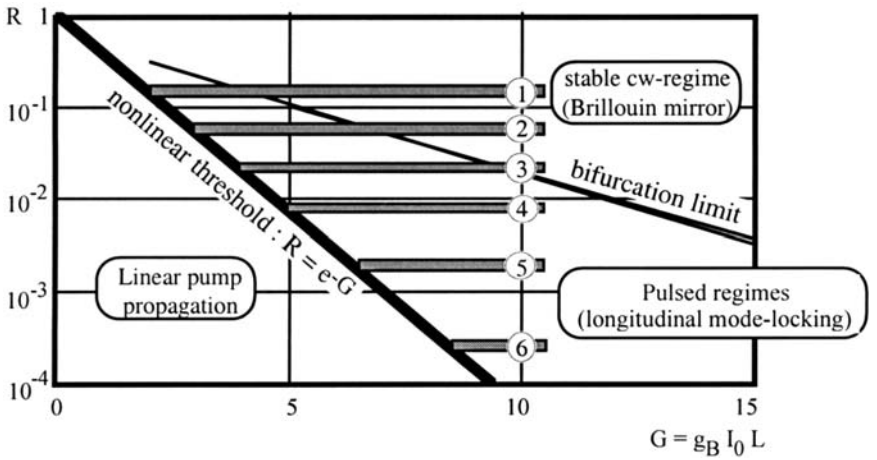

Fig. 17 Bifurcation diagram for the Brillouin fiber-ring laser with the experimentally explored areas (tinted areas)

at twice this frequency when R_{eff} is lower [cf. Fig. 3(a, b)], in agreement with the stability analysis. When the pump power decreases further, these oscillating regimes are replaced by a pulsed regime with a frequency close to the ring FSR. In particular, Fig. 3(c, d) show how these pulses build up from the second mode destabilization. When the pump power decreases still further, there is a rapid strengthening of the Stokes pulses, and they become much narrower. Fig. 3(e, f) illustrates this scenario.

We present, on the same graphs, the results relative to each value of R_{eff} (referenced by circled numbers), in order to get a quantitative view of them. In each case, experimental data have been fitted by a fourth-order polynomial which minimizes the mean square-root error. In order to show the excellent agreement between the experimental results and the results obtained by numerical simulation of (1), we perform a parallel systematic numerical study for the same six feedback series by taking the pump power as the control parameter, and increasing it from threshold to the Brillouin stationary regime value. Figure 18 shows the experimental Stokes peak amplitude versus pump power (left) compared with the numerical results (right). Note that the strongest experimental pulses are obtained for the weakest values of R_{eff}, taking into account that curves (4)–(6) cannot reach the bifurcation due to experimental pump power constraints. The numerical study (right) is not limited by pump power for small feedback values, and we can explore the whole bifurcation domain between pulsing and stationarity for all of the above six feedback values.

Figure 19 groups all the experimental results obtained in the pulsed range [series (1)–(6)] and in the stationary (or c.w.) range [series (1)–(3)] versus pump power at point (15) of the experimental set-up. This is done in order to quantitatively appreciate the optical energy localization associated with the Stokes pulses. Each R_{eff} value is associated with two curves – the top curve corresponds to the Stokes amplitude

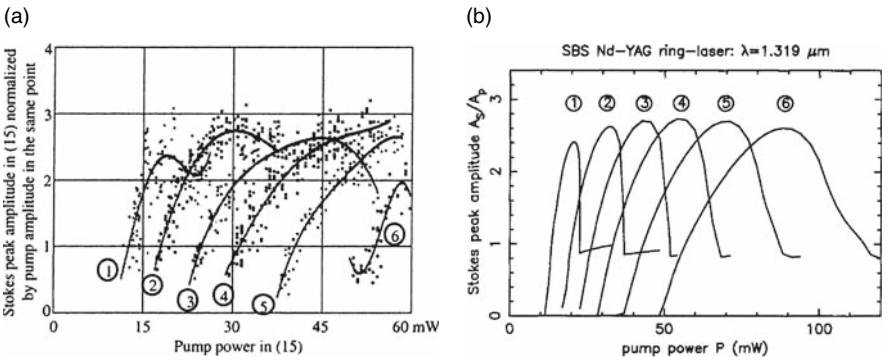

Fig. 18 *Left figure*: Experimental normalized Stokes peak amplitude in (15) for different values of R_{eff} versus input pump power at this point. *Right figure*: Numerical simulation of (1) showing the normalized Stokes peak amplitude at the fiber entry versus input pump power in mW.

squared value, averaged over a round-trip time; this is therefore proportional to the averaged power at this point. In accordance with the notation of Sect. 4 (Fig. 6), it is labeled by $\langle |A_S|^2 \rangle$. The lower curve gives the variation of the square of the averaged Stokes amplitude, $\langle |A_S| \rangle^2$, at (15) [cf. Fig. 16] and is a measure of the pulse confinement. For stationary conditions, we obviously have $\langle |A_S|^2 \rangle = \langle |A_S| \rangle^2$, but in the best pulsed regime, we roughly have

$$\frac{\langle |A_S| \rangle^2}{\langle |A_S|^2 \rangle} \simeq \frac{\text{round-trip time}}{\text{pulse width}} \simeq 10.$$

The corresponding numerical results are plotted in Fig. 20, where the whole localization domain can now be explored by the numerical model, from threshold to the stationary state for the six feedback values (1)–(6). In Table 1, we give the maximum amplitudes for series (1)–(4). Curves (1) and (2) show a sharper bifurcation from stationary to pulsed regime, since numerical simulations have been performed for up to 16384 round-trips (in the transition region) in order to better approach the asymptotic regime. The mean reflectivity, $\langle |A_S(0,t)|^2 \rangle / |A_{cw}|^2$, (top curve) even presents an appreciable jump at the bifurcation for both curves (1) and (2), but this is smoothed out for curves (3)–(6), since simulations have been performed only up to 4096 round-trips.

Another interesting Brillouin pulse parameter is its width (Fig. 21). The minimum value reached is roughly 100 ns. It is the same for the different R_{eff} values and covers a large domain of pump power or of Stokes pulse energy; this means that between 10 and 15, longitudinal modes are then spontaneously locked. This width increases near the nonlinear threshold, since the pump is too weak to excite the side modes far from the center of the Brillouin gain curve. Increasing width is also observed near the bifurcation toward the stationary regime, since the Brillouin solitary pulses become super-luminous (lower p), as we can see in Table 1, where the

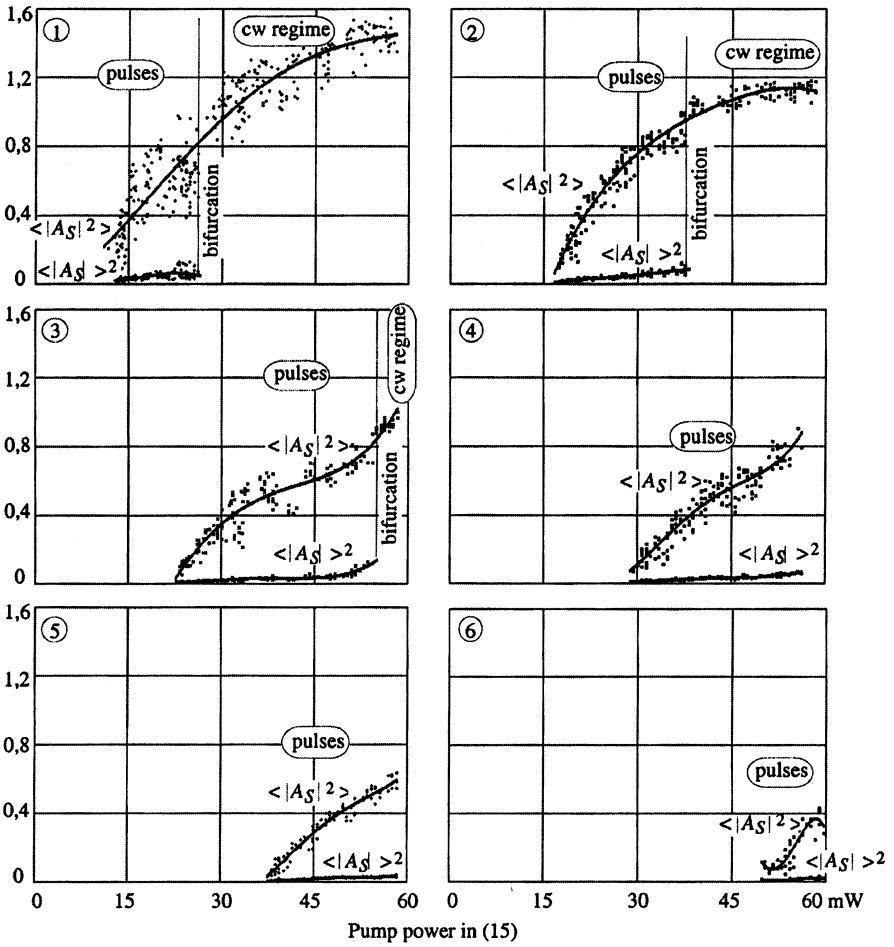

Fig. 19 Comparison (experimental) between the averaged normalized Stokes amplitude squared and the square of the averaged normalized Stokes amplitude in (15) *versus* pump power at this point for different values of R_{eff}

nonlinear pulse's round-trip time, Δ_t, becomes shorter than the linear photon flight time, t_{r}. These features are shown in Fig. 22, where the round-trip time, plotted *versus* pump power, decreases uniformly. This corroborates our theoretical prediction that the pulses are sub-luminous in the vicinity of the nonlinear threshold but are super-luminous near the bifurcation. The lack of a flat zone (at $\Delta_t/t_{\text{r}} = 1$) in these curves clearly shows that the nonlinear interaction can never be neglected. Note also that, for a given energy per pulse, the round-trip time decreases when R_{eff} (experimental) or R (numerical) increases.

Table 1 summarizes the numerical pulse characteristics [from (1)] for the series (1)–(4) of Fig. 20 around the narrowest pulse width (respective line in bold numerals). In column 6, we give the compressed width obtained through active

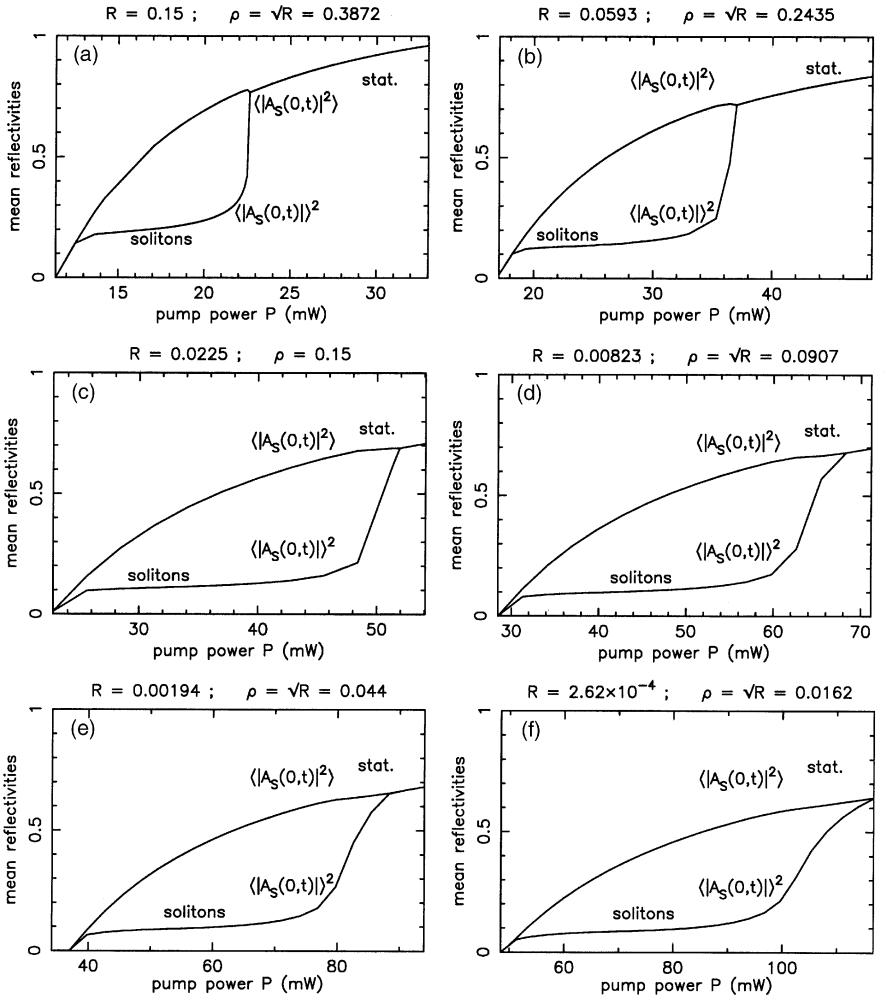

Fig. 20 Mean reflectivities, $\langle|A_S(0,t)|^2\rangle/|A_{cw}|^2$ and $\langle|A_S(0,t)|\rangle^2/|A_{cw}|^2$, as functions of c.w.-pump power, obtained by numerical simulation of (1), for (**a**) $R = 0.15$; (**b**) $R = 0.0593$; (**c**) $R = 0.0225$; (**d**) $R = 0.00823$; (**e**) $R = 0.00194$; and (**f**) $R = 2.62 \times 10^{-4}$. The soliton localization domain of the bifurcation map is characterized by a low value of the squared averaged Stokes amplitude, $\langle|A_S(0,t)|\rangle^2$, with respect to the averaged squared Stokes amplitude, $\langle|A_S(0,t)|^2\rangle$

mode-locking by phase modulation [from [19]]; this benefits from the entire Brillouin gain curve. The particular analytic solutions, evaluated from formulae (46), (47), and (48) are inserted into column 7. We remark that the analytic luminous widths are close to the compressed widths, while the analytic super-luminous symmetric widths move apart to some extent, since they correspond to the super-luminous zone toward the bifurcation. Nevertheless, the analytic amplitudes yield an adequate approximation to the maximum numerical amplitudes.

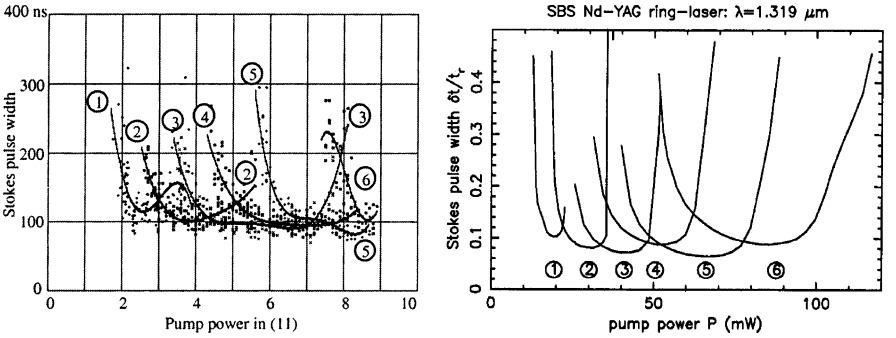

Fig. 21 *Left figure*: Experimental Stokes pulse width (FWHM), in ns, for various R_{eff} *versus* input pump power. *Right figure*: Numerical simulation of (1) showing the Stokes intensity width normalized to the linear flight time $\delta_t|A_S(0,t)|^2/t_r$ *versus* input pump power in mW

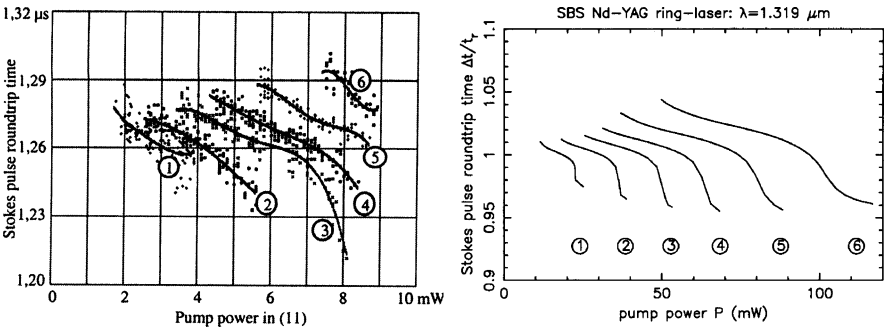

Fig. 22 *Left figure*: Experimental Stokes peak round-trip (in μs) for various values of R_{eff} *versus* input pump power. *Right figure*: Numerical simulation of (1) showing the Stokes pulse round-trip time, normalized to the linear flight time $\delta_t|A_S(0,t)|^2/t_r$ *versus* input pump power in mW

11 Conclusion

We have found, experimentally and numerically, a continuous set of asymptotically stable super-luminous and sub-luminous dissipative three-wave Brillouin solitons in fiber-ring cavities, and we have attempted to associate them with the attractors of the unbounded Stokes problem in the presence of a continuous pump wave. These attractors only depend on the wave-front exponential slope, p, of the backscattered Stokes envelope, while the continuous family of Stokes pulses in the Brillouin fiber-ring cavity can be displayed via a single control parameter, viz. the Stokes feedback (R) or the pump power (G).

It appears that the experimental results fit the numerical predictions very accurately. The good quantitative agreement for all the experimentally accessible values shows that the homogeneous broadening model (1) remains the relevant Brillouin model for a c.w.-pumped fiber-ring cavity, regardless of some recent criticisms [46]. However, despite our numerous precautions, the experiments exhibit

large remaining fluctuations. Obviously, this cannot be surprising near the bifurcation, where numerical simulations show the huge asymptotic regime sensitivity to the slightest variations of the experimental parameters, as well as the extreme length of the transient regimes [cf. Fig. 6]. However, we expected much more stable behavior elsewhere. A first explanation is, of course, related to the intrinsic pump laser instability, which results in non-negligible fluctuations of the nonlinear regime, added to the fact that not every part of the set-up is polarization-maintaining. However, there is probably a more fundamental reason due to the interaction with the guided-acoustic wave Brillouin scattering (GAWBS) effect. We have indeed observed that the most stable-pulsed regimes remained unchanged for some 10 or 100 ms only. Trains of some 10 pulses appear randomly, and they are much stronger and narrower (by a typical factor of $\simeq 10$). We attribute these new features to the interaction with the fiber transverse acoustic GAWBS resonances through cladding Brillouin scattering (CBS). The coupling of the Brillouin transverse resonator with the Brillouin axial resonator is responsible for unstable dynamics, since all kinds of transverse resonances may be excited [16, 17]. The pulses can be compressed for certain co-operative frequencies, while they may widen and/or be destabilized for other frequencies [18].

In Ref. [19], we overcame the experimentally unstable behavior by the action of an axial intra-cavity phase modulator, whose frequency and strength can be controllably tuned. The resulting controlled coupling then reveals a rich dynamics which is comparable with the SBS–CBS dynamics, but which is still described by the coherent three-wave model. Besides the compressed and/or unstable frequency domains, we have obtained – within finite frequency bands – a splitting of the Brillouin solitons into N stable pulses by tuning the phase modulator to *a little less* than N times the round-trip frequency.

In Table 1, we have found it relevant to include the temporal widths of these compressed pulses resulting from active mode-locking through phase modulation because they are closer to the analytic formulae obtained for the unlimited SBS line interaction developed in Sects. 5, 7, and 8.

Acknowledgments The author thanks D. Bahloul, I. Bongrand, J. Botineau, G. Cheval, J. Coste, D.J. Kaup, O. Legrand, A. Mamhoud, A. Mikhailov, A. Picozzi, and E. Picholle for fruitful collaborations.

References

1. D. Pohl and W. Kaiser, Phys. Rev. B **1**, 31 (1970). 221
2. V.A. Gorbunov, S.B. Papernyi, and V.R. Startsev, Sov. J. Quantum Electron **13**, 900 (1983). 221
3. B. Gellert and B. Kronast, Appl. Phys. B **32**, 175 (1983); Appl. Phys. B **33**, 29 (1984). 221
4. J. Botineau, C. Leycuras, C. Montes, and E. Picholle, J. Opt. Soc. Am. **B 6**, 300 (1989). 221, 222, 225, 235
5. E. Picholle, C. Montes, C. Leycuras, O. Legrand, and J. Botineau, Phys. Rev. Lett. **66**, 1454 (1991). 221, 222, 224, 230, 237, 260
6. C. Montes, A. Mamhoud, and E. Picholle, Phys. Rev. A **49**, 1344 (1994). 221, 222, 227, 228, 229, 230, 248

7. C. Montes, D. Bahloul, I. Bongrand, J. Botineau, G. Cheval, A. Mamhoud, E. Picholle, and A. Picozzi, J. Opt. Soc. Am. B **16**, 932 (1999), and references therein. 221, 222, 225, 226, 227, 228, 229, 230,
8. J. Botineau, G. Cheval, and C. Montes. Opt. Commun. **257** 319 (2006). 221, 222, 225, 230, 232, 233, 248, 251
9. J. Coste and C. Montes, Phys. Rev. A **34**, 3940 (1986). 222, 230, 239
10. W. Lu and R.G. Harrison, Europhys. Lett. **16**, 655 (1991); W. Lu, A. Johnstone, and R.G. Harrison, Phys. Rev. A **46**, 4114 (1992). 222, 227
11. S. Randoux, V. Lecoeuche, B. Ségard, and J. Zemmouri, Phys. Rev. A **51**, R4345–R4348 (1995). 222
12. I. Bar-Joseph, A.A. Friesem, E. Lichtman, and R.G. Waarts, J. Opt. Soc. Am. B **2**, 1606–1611 (1986). 222
13. R.G. Harrison, J.S. Uppal, A. Johnstone, and J.V. Moloney, Phys. Rev. Lett. **65**, 167 (1990). 222, 227
14. A.L. Gaeta and R.W. Boyd, Internat. J. Nonlinear Opt. Phys. **1**, 581 (1992). 222
15. M. Dämmig, G. Zinner, F. Mitschke, and H. Welling, Phys. Rev. A **48**, 3301 (1993). 222
16. E. Picholle and A. Picozzi, Opt. Commun. **135**, 327 (1997). 222, 258
17. I. Bongrand, E. Picholle, and C. Montes, Eur. Phys. J. **D 20**, 121 (2002). 222, 258
18. I. Bongrand, C. Montes, E. Picholle, J. Botineau, A. Picozzi, G. Cheval, and D. Bahloul, Opt. Lett. **19**, 1475 (2001). 222, 258
19. J. Botineau, G. Cheval, and C. Montes. Opt. Commun. **257**, 311 (2006). 222, 223, 226, 256, 258
20. C. Montes, A. Mikhailov, A. Picozzi, and F. Ginovart, Phys. Rev. E **55**, 1086 (1997) and references therein. 222, 224, 230, 239, 245, 247, 248
21. S.C. Chiu, J. Math. Phys. **19**, 168 (1978). 223, 237
22. C. Montes, A. Picozzi, and D. Bahlouol, Phys. Rev. E **55**, 1092 (1997). 224, 232, 239, 241, 242, 243, 245, 246
23. V.G. Kolmogorov, I.G. Petrovskii, and N.S. Piskunov, Bull. Moscow State University, Math. and Mechanics **1**, 1 (1937). 224, 245
24. Super-luminous motion of the three-wave localized structure does not contradict the special theory of relativity in any way. This motion can be viewed as the result of the convective amplification of the leading edges of the Stokes and material pulses, whereas their tails are attenuated, since the pump wave is depleted during the interaction, and then totally or partially restored afterwards. This deformation process can only occur if a sufficiently extended background of Stokes light is available, and no transportation of information can occur because of it. 224
25. J.A. Armstrong, S.S. Jha, and N.S. Shiren, IEEE J. Quant. Elect. **QE-6**, 123 (1970). 224, 237, 242
26. K. Nozaki and T. Taniuti, J. Phys. Soc. Jpn. **34**, 796 (1973); Y. Oshawa and K. Nozaki, J. Phys. Soc. Jpn. **36**, 591 (1974). 224, 237, 242
27. S.F. Morosov, L.V. Piskunova, M.M. Sushik, and G.I. Freidman, Sov. J. Quant. Electron. **8**, 576 (1978). 224, 230
28. E. Gaizauskas and K. Staliunas, Opt. Commun. **114**, 463 (1995). 224
29. D.J. Kaup, J. Nonlinear Sci. **3**, 427 (1993). 224, 238, 241
30. A. Hasegawa, in *Optical Solitons in Fibers* (Springer-Verlag, Berlin, 1990). 225, 247
31. Note that the coherent SBS coupling coefficient, K, in Ref. [7], Eq.(1b), contains two errors. 226
32. B. Ya Zel'dovich and A.N. Pilipetskii, Sov. J. Quantum Electron. **183**, 818 (1988). 226
33. C.K. Jen, J.E.B. Oliveira, N. Goto, and K. Abe, Electron. Lett. **24**, 1419 (1988). 226
34. J. Botineau, E. Picholle, and D. Bahloul, Electron. Lett. **23**, 2032 (1995). 226
35. R.W. Boyd and K. Rzazewsky, Phys. Rev. A **42**, 5514 (1990). 226
36. J. Botineau, C. Leycuras, C. Montes, and E. Picholle, Opt. Commun. **109**, 126 (1994). 226
37. A. Picozzi, C. Montes, J. Botineau, E. Picholle, J. Opt. Soc. Am. B **15**, 1309 (1998); A. Picozzi, C. Montes, and E. Picholle, Phys. Rev. E **58**, 2548 (1998). 227
38. V. Lecoeuche, B. Ségard, and J. Zemmouri, Opt. Commun. **134**, 547–558 (1997). 230
39. C. Montes and O. Legrand, in *Electromagnetic and Acoustic Scattering: Detection and Inverse Problem*, edited by C. Bourrely, P. Chiappetta, and B. Torresani, (World Scientific, Singapore, 1989), pp. 209–221; O. Legrand and C. Montes, *J. Phys. Colloq. France* **50**, C3–147 (1989). 230, 241
40. D.J. Kaup, A. Reiman, and A. Bers, Rev. Mod. Phys. **51**, 275 (1979). 230
41. L. Chen and X. Bao, Opt. Commun. **152**, 65 (1998). 236, 239
42. Note that Eq.(11) in Ref. [22] contains an error. The first line stands for S and the second line is the expression for p_{sym}. 238, 260

43. Ph.M. Morse and H. Feshbach, in *Methods of Theoretical Physics*, (Mc Graw-Hill, New York, 1953) p. 437. 247
44. A. Hasegawa and Y. Kodama, Opt. Lett. **15**, 1443 (1990). 249
45. Note that Eq.(15) in Ref. [7] contains an error; it must be written $E_B/E_p^0 = [1-(\mu_s\mu_a)^{1/2}](2\mu_a/\mu_S - 1)^{1/2}$. according to Eq.(3) of Ref. [5] or as the corrected expression (11) of Ref.[22] (*cf.* [42]). 249
46. V.I. Kovalev and R.G. Harrison, Phys. Rev. Lett. **85**, 1879 (2000); V.I. Kovalev and R.G. Harrison, Opt. Lett. **27**, 2022 (2002). 257

Spatial Dissipative Solitons Under Convective and Absolute Instabilities in Optical Parametric Oscillators

S. Coulibaly, C. Durniak, and M. Taki

Abstract Optical parametric oscillators are sources for producing coherent and frequency-tunable light beams by using three-wave interaction in a nonlinear crystal. These are nonlinear optical cavities, in which spatial dissipative solitons can form spontaneously. In the first part, we show that patterns of periodic dissipative solitons are continuously generated in a regime of absolute instability, i.e., they spontaneously develop from localized perturbations of the unstable homogeneous steady state that separates the two stable states of an hysteresis cycle. The bifurcation occurs in a regime far from any modulational instability (Turing instability) and emphasizes the crucial role of localized perturbations in the formation of solitons. This constitutes the counterpart of Turing spontaneous modulations initiated by extended perturbations. In the second part, taking into account the coupling of non-local effects (walk-off) and diffraction leads to the appearance of an original nonlinear gradient term in the amplitude equation in a bistable regime, and this describes the near-threshold dynamics of intra-cavity fields. Our analytical investigations show the utmost importance of non-local effects in the nonlinear dependence of the frequency and velocity of dissipative solitons on their intensity. This makes it possible to explain the self-frequency shift, the slowing down and the nonlinear

S. Coulibaly
Laboratoire de Physique des Lasers, Atomes et Molécules, UMR CNRS 8523 IRCICA, Centre d'Etudes et de Recherches Lasers et Applications (CERLA) FR CNRS 2416, Université des Sciences et Technologies de Lille, 59655 Villeneuve d'Ascq Cedex, France

C. Durniak
Laboratoire de Physique des Lasers, Atomes et Molécules, UMR CNRS 8523 IRCICA, Centre d'Etudes et de Recherches Lasers et Applications (CERLA) FR CNRS 2416, Université des Sciences et Technologies de Lille, 59655 Villeneuve d'Ascq Cedex, France
Optical Sciences Group, Research School of Physical Sciences and Engineering, Australian National University, Canberra, ACT 0200, Australia, taki@phlam.univ-lille1.fr

M. Taki
Laboratoire de Physique des Lasers, Atomes et Molécules, UMR CNRS 8523 IRCICA, Centre d'Etudes et de Recherches Lasers et Applications (CERLA) FR CNRS 2416, Université des Sciences et Technologies de Lille, 59655 Villeneuve d'Ascq Cedex, France

Coulibaly, S., et al.: *Spatial Dissipative Solitons Under Convective and Absolute Instabilities in Optical Parametric Oscillators.* Lect. Notes Phys. **751**, 261–287 (2008)
DOI 10.1007/978-3-540-78217-9_10

symmetry-breaking observed in the envelope of dissipative solitons emitted by the optical parametric oscillator.

1 Introduction

Dissipative spatial solitons and, more generally, pattern formation in extended systems have attracted much attention in fields as different as physics [1], hydrodynamics [2], chemistry [3] and biology [4]. Nonlinear optics, in particular, represents a fruitful area of research activity [5]. This is due to the fact that patterned states, leading to dissipative solitons, arise naturally in many optical devices from the coupling of diffraction, nonlinearities and dissipation. More importantly, the ability of the soliton to self-confine light beam power makes it a promising candidate for future applications in information technology [6] and image processing [7, 8]. In large-area devices, this coupling triggers the Turing instability [9], which leads to the spontaneous formation of 2D dissipative structures [10]. These structures can be stationary or time-dependent, periodic or localized in the plane orthogonal to the propagation direction of the beam [11]. In optics, most of the previous studies have pointed out that the Turing type of instability is responsible for the transition to self-organized or ordered states by a translational symmetry-breaking along one or more transverse directions. So far, however, such systems are often subject to successive instabilities and mode interaction may alter the self-organization process. In particular, it has been shown that both Turing and Hopf branches of solutions lose their stabilities under their mutual interaction [12]. It has also been shown, in passive and frequency conversion systems, that the interaction between Turing and saddle-node bifurcations modifies the stability, as well as the existence, of the emerging structures [13]. The link between sub-critical Turing bifurcations and the formation of localized structures (often called cavity solitons) was first established in passive media [14]. This link was experimentally proved in a variety of nonlinear optical system devices [15]. This demonstrates the importance of pattern-forming instabilities and their interactions when studying complex spatio-temporal dynamics or the formation of optical dissipative solitons in spatially extended systems. This subject has been abundantly discussed in a number of overviews [16], for example in the review paper by Mandel and Tlidi [17] that reports very recent progress on transverse instabilities in nonlinear optics.

Among the possible devices, optical parametric oscillators (OPOs) have recently appeared as one of the most promising systems, not only for the richness in their nonlinear dynamics [18], but also for their potential applications [19], including low noise measurements and detection [20]. Indeed, frequency conversion by means of optical parametric oscillators is a fundamental phenomenon for the generation of tunable coherent radiation in quadratic crystals. In OPOs, the phase-matching between waves of different optical frequencies is achieved by using anisotropic crystals, in which birefringence allows us to compensate for the unavoidable chromatic dispersion. However, this generation is often accompanied by walk-off, i.e., spatial

separation of the interacting beams. Walk-off alters the spontaneous pattern formation by producing a lateral drift of one beam, as was observed experimentally [21]. It was recently shown that in the presence of walk-off, the standard theoretical approach of pattern formation must be extended [22]. More specifically, a homogeneous state may be unstable with respect to localized perturbations, but the resulting state which is reached depends on the relative values of the amplification and the drift. This is the basis of the difference between convective and absolute regimes. In the former, the perturbation grows in time but decreases locally because it is advected away. In the latter, it increases locally and not only in the moving frame, so that it eventually extends over all the available space.

There is currently considerable interest in understanding the role of *convection* (walk-off, drift) in pattern-forming systems in such diverse fields as hydrodynamics [23], plasma physics [24], traffic flow [25], crystal growth [26] and nonlinear optics [27]. In these studies, the most important and common result is that convection, modeled by gradient terms ($\boldsymbol{\alpha}\cdot\boldsymbol{\nabla}$ with $\boldsymbol{\alpha}$ group velocity), breaks the transverse reflection symmetry ($\boldsymbol{r}\rightarrow-\boldsymbol{r}$) and dramatically affects pattern selection in spatially extended systems. This is *linear* symmetry-breaking, where convection terms are generally considered to have the effect of inducing a traveling character onto selected patterns, as well as leading to a peculiar regime of convective instability. Many studies have shown how the existence, type and dynamics of the selected pattern are closely related to the linear transition from convective instability (where propagation overcomes amplification of perturbations) to absolute instability (where amplification dominates) [28].

The purpose of this chapter is first to report on the continuous generation of spatially periodic dissipative solitons with an intrinsic wavelength in a modulationally stable regime, i.e., in a regime far from any modulational instability (Turing instability [9]). These modulations develop spontaneously from *localized* perturbations of the *unstable* homogeneous steady state that separates the two stable states of a hysteresis cycle. This constitutes the counterpart of Turing spontaneous modulations initiated by *extended* perturbations. They occur in the wings of 2D traveling flat-top solitons (fronts, domain walls or kink-anti-kink) and eventually give rise to ring-shaped propagating dissipative solitons. Analytical expressions for their wavelengths and velocities have been derived explicitly. Such non-Turing periodic dissipative solitons have been predicted in some 1D models in fluid mechanics [29] and, very recently, for a liquid crystal light valve nonlinear optical cavity [30]. Second, in contrast to previous studies, we discuss an unforeseen effect of convection, which does not rely on a linear convective/absolute transition, in the dynamics of spatially extended systems [31]. Here, we show how convection, which is a linear phenomenon, actually modifies the intrinsic nonlinearity of the system and hence the main characteristics of dissipative solitons. More precisely, we show that convection affects the interaction of solitons in both regimes of convective and absolute instabilities. It results in *nonlinear symmetry-breaking* in the generated, otherwise symmetrical, dissipative flat-top (fronts) and localized (pulses) solitons. Our analytical investigations of this mechanism reveal, to our knowledge for the first time in optics, the existence of a nonlinear gradient term in the amplitude equation describing the

near-threshold behavior of the optical parametric oscillator. More importantly, the nonlinear gradient term is obtained as a function of convection (walk-off), leading to a novel dependence of the frequency and velocity of dissipative solitons on their intensity. This demonstrates the utmost importance of convection in above-threshold nonlinear dynamics and, therefore, makes it possible to explain the self-frequency shift, the slowing down and the nonlinear symmetry-breaking observed in the envelope of dissipative solitons emitted by the optical parametric oscillator.

The chapter is organized as follows. In Sect. 2, we recall the OPO governing equations, including walk-off and diffraction effects. Linear stability analysis of these equations is performed as an initial-value problem to obtain both the pump thresholds for the onset of convective and absolute instabilities, and the response of the system to 2D localized perturbations. This approach allows us to investigate, in Sect. 3, the evolution of wave packets in the modulationally stable region of a degenerate OPO. The characteristics of the transition from ground states to flat or spatially periodic dissipative solitons, such as the thresholds, the critical wave-numbers and the frequencies, are analytically obtained. Section 4 is devoted to non-degenerate OPOs that involve three-wave, instead of two-wave, mixing process in the degenerate case. Here, the combined action of convection and diffraction additionally produces non-variational effects that strongly influence the nonlinear dynamics. The underlying role of convection on the formation and characteristics of dissipative solitons is investigated. Numerical simulations of the full OPO model are carried out in order to check the range of validity of the analytical studies. Finally, concluding remarks form a summary in the final section.

2 Convective Versus Absolute Instabilities in OPOs

2.1 Full Three-Wave Model of Optical Parametric Oscillators

Optical parametric oscillators are sources capable of producing coherent, frequency-tunable light beams by nonlinear interaction in a crystal. This process takes place in a quadratic ($\chi^{(2)}$) crystal inserted inside an optical cavity. An external coherent beam, E, at a frequency ω_p is injected into the cavity where it undergoes a down-conversion process: one photon with frequency ω_p is annihilated and two photons with frequencies ω_s and ω_i are emitted (see Fig. 1). In the triply resonant configuration, the OPO is non-degenerate and its spatio-temporal dynamics, in the mean-field approximation, including diffraction ($\nabla_\perp^2$) and walk-off (∂_x) effects, is governed by [32]

$$\begin{aligned}
\partial_t A_\mathrm{p} &= \gamma_\mathrm{p}[-(1+\mathrm{i}\Delta_\mathrm{p})A_\mathrm{p} + E(x,y) - A_\mathrm{s}A_\mathrm{i} + \mathrm{i}a_\mathrm{p}\nabla_\perp^2 A_\mathrm{p}],\\
\partial_t A_\mathrm{s} &= \gamma_\mathrm{s}[-(1+\mathrm{i}\Delta_\mathrm{s})A_\mathrm{s} + A_\mathrm{p}A_\mathrm{i}^* + \mathrm{i}a_\mathrm{s}\nabla_\perp^2 A_\mathrm{s} - \alpha_\mathrm{s}\partial_x A_\mathrm{s}],\\
\partial_t A_\mathrm{i} &= \gamma_\mathrm{i}[-(1+\mathrm{i}\Delta_\mathrm{i})A_\mathrm{i} + A_\mathrm{p}A_\mathrm{s}^* + \mathrm{i}a_\mathrm{i}\nabla_\perp^2 A_\mathrm{i} - \alpha_\mathrm{i}\partial_x A_\mathrm{i}],
\end{aligned} \tag{1}$$

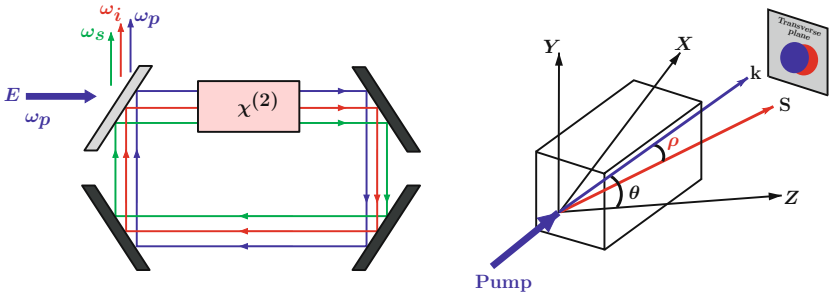

Fig. 1 Schematic set-up of a ring cavity, triply resonant optical parametric oscillator (left) and sketch of walk-off effect on beam propagation in the crystallographic co-ordinates system (X,Y,Z) for an anisotropic $\chi^{(2)}$ crystal (right). θ indicates the phase-matching angle between the optical axis, Z, and the longitudinal direction of wave propagation vector **k**. The walk-off angle then corresponds to a tilt of the Poynting vector direction, **S**, of the extraordinary polarized electric field with respect to the direction of its wave propagation vector, **k**

where A_j, with $j = \mathrm{p,s}$ and i are the normalized slowly varying envelopes for pump, signal and idler fields. The parameters Δ_j, γ_j and a_j are the detunings, the cavity decay rates and the diffraction coefficients, respectively. E is the normalized external pump and $\alpha_{\mathrm{s,i}}$ are the signal and idler walk-off coefficients.

Equations (1) have a uniform steady-state solution (OPO OFF) $A_\mathrm{p} = E/(1+\mathrm{i}\Delta_\mathrm{p}) = \mu$, $A_\mathrm{s} = 0$, $A_\mathrm{i} = 0$. A linear stability analysis [32] shows that it becomes unstable if the intensity of the normalized pump (μ) is such that $\left|\mu(k_x,k_y)\right|^2 \geq 1 + \left[-D/4a + a(k_x + \alpha/2a)^2 + ak_y^2\right]^2/(\gamma_\mathrm{s}+\gamma_\mathrm{i})^2$ where we have set $a = \gamma_\mathrm{s}a_\mathrm{s} + \gamma_\mathrm{i}a_\mathrm{i}$, $\Delta = \gamma_\mathrm{s}\Delta_\mathrm{s} + \gamma_\mathrm{i}\Delta_\mathrm{i}$, $\alpha = \gamma_\mathrm{s}\alpha_\mathrm{s} - \gamma_\mathrm{i}\alpha_\mathrm{i}$ and $D = \alpha^2 - 4a\Delta$.

2.2 *Linear Stability Analysis, Dispersion Relation and Normal Modes*

The linear stability analysis is performed by linearizing (1) around the basic state (OPO OFF) and considering normal mode solutions of the form $\mathrm{e}^{\mathrm{i}k_x x + \mathrm{i}k_y y - \mathrm{i}\omega t}$, where $\mathbf{k} = (k_x, k_y)$ is the **real** transverse wave vector and ω is the complex frequency of the linear problem.

The linear pump perturbation is decoupled from those of the signal and the idler, and the dispersion relation obtained after straightforward calculations is

$$\mathscr{D}(k_x, k^2, \omega) = \omega^2 + \mathrm{i}(b_\mathrm{s} + b_\mathrm{i})\omega - b_\mathrm{s}b_\mathrm{i} + \gamma_\mathrm{s}\gamma_\mathrm{i}\left|\mu\right|^2 = 0, \tag{2}$$

where we have set

$$b_\mathrm{s} = \gamma_\mathrm{s}[1 + \mathrm{i}(\Delta_\mathrm{s} + a_\mathrm{s}k^2 + \alpha_\mathrm{s}k_x)],$$

$$b_{\mathrm{i}} = \gamma_{\mathrm{i}}[1 - \mathrm{i}(\Delta_{\mathrm{i}} + a_{\mathrm{i}}k^2 - \alpha_{\mathrm{i}}k_x)],$$
$$k^2 = k_x^2 + k_y^2.$$

The dispersion relation yields the neutral stability surface ($\Im(\omega) = 0$) in the 2D plane of the wave vector components (k_x, k_y) in the form

$$\left|\mu(k_x, k_y)\right| = \left(1 + \frac{(\Delta - \alpha^2/4a + a(k_x + \alpha/2a)^2 + ak_y^2)^2}{(\gamma_{\mathrm{s}} + \gamma_{\mathrm{i}})^2}\right)^{1/2} \tag{3}$$

with frequency

$$\omega(k_x, k_y) = \frac{\gamma_{\mathrm{s}}\gamma_{\mathrm{i}}}{\gamma_{\mathrm{s}} + \gamma_{\mathrm{i}}}\left[\Delta_{\mathrm{s}} - \Delta_{\mathrm{i}} + (a_{\mathrm{s}} - a_{\mathrm{i}})k^2 + (\alpha_{\mathrm{s}} + \alpha_{\mathrm{i}})k_x\right].$$

In the presence of walk-off, the critical surface (3) depends on both components of the wave vector (k_x, k_y) and cannot be reduced to a simple dependence on the wave vector modulus, k^2, as is the case without walk-off. (See Fig. 2(a) for a projection of this surface onto the plane (μ, k_x).) The stability analysis for the case $\Delta > 0$ has been carried out in [32]. Note that, in this case, the bifurcating solution is homogeneous as a result of the absence of Turing instability at threshold. In this section, we will mainly focus on the case $\Delta < 0$. Thus, we will develop the concept of convective and absolute instabilities in the more general situation of pattern-forming.

The onset of instability at critical threshold, $\mu = \mu_{\mathrm{th}} = 1$, is obtained for wave vectors minimizing μ in (3) and are given by

$$(k_x^{\mathrm{c}} + \alpha/2a)^2 + k_y^{\mathrm{c}2} = \frac{\alpha^2 - 4a\Delta}{4a^2}. \tag{4}$$

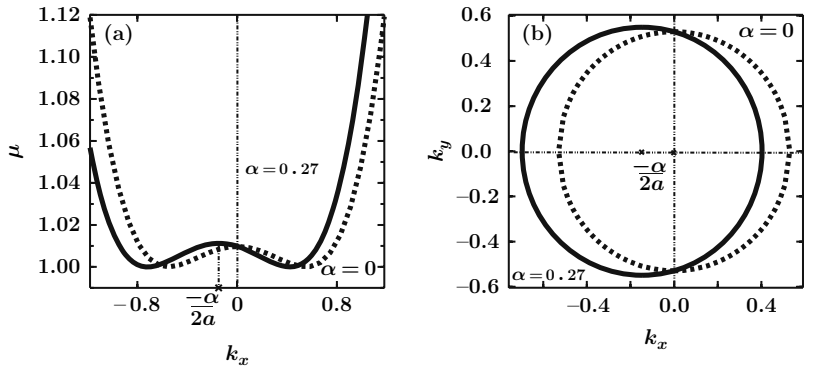

Fig. 2 (**a**) Projection of the neutral stability surface (3) onto the (μ, k_x) plane. (**b**) Plot of the critical wave vector components at the onset of instability, ($\mu = \mu_{\mathrm{th}} = 1$). Walk-off shifts the circle of unstable transverse wave vectors. Signal walk-off parameter is $\alpha_{\mathrm{s}} = 0.27$ for the solid curves and $\alpha_{\mathrm{s}} = 0$ for the dashed ones. For both figures, the values of the other parameters are fixed and equal to $\gamma_{\mathrm{s}} = \gamma_{\mathrm{i}} = 1$, $\Delta_{\mathrm{s}} = \Delta_{\mathrm{i}} = -0.14$, $a_{\mathrm{s}} = 0.5$, $a_{\mathrm{i}} = 0.42$ and $\alpha_{\mathrm{i}} = 0$

The critical real wave vectors, $\mathbf{k}^{\mathrm{c}} = (k_x^{\mathrm{c}}, k_y^{\mathrm{c}})$, belong to a circle (solid curves in Fig. 2) centered at $(k_x = -\alpha/2a, k_y = 0)$ with a radius $R = \sqrt{D}/(2a)$ and $D = \alpha^2 - 4a\Delta$. As indicated by the non-zero value of k_x, the rotational symmetry is broken by the amount $-\alpha/2a$, depending on the competition between walk-off and diffraction weighted by the cavity losses. Note that when walk-off vanishes, the circle (4) of critical wave vectors is centered on $\mathbf{k} = 0$, with $(k^{\mathrm{c}})^2 = k_x^{\mathrm{c}2} + k_y^{\mathrm{c}2} = -\Delta/a$ (dashed curves in Fig. 2). The basic state (OPO OFF) is linearly unstable to all 2D transverse modes lying on the circle (4). In contrast to the case of positive effective detuning Δ, where walk-off selects a 1D structure expanding in its direction at threshold [32], this 1D selection mechanism fails for $\Delta < 0$.

2.3 Response to Localized Perturbations

The linear stability analysis, given above, is based on the normal mode theory i.e., it checks the stability with respect to extended perturbations. Such an approach is insufficient to determine the linear response of the system to any localized perturbation. This is provided by solving the linear initial-value problem:

$$\begin{aligned}
&\partial_t A_{\mathrm{s}} - \gamma_{\mathrm{s}}[-(1+\mathrm{i}\Delta_{\mathrm{s}})A_{\mathrm{s}} + \mu A_{\mathrm{i}}^* + \mathrm{i}a_{\mathrm{s}}\nabla_\perp^2 A_{\mathrm{s}} - \alpha_{\mathrm{s}}\partial_x A_{\mathrm{s}}] = A_{\mathrm{s}}^{(0)}\delta(x)\delta(y)\delta(t),\\
&\partial_t A_{\mathrm{i}}^* - \gamma_{\mathrm{i}}[-(1-\mathrm{i}\Delta_{\mathrm{i}})A_{\mathrm{i}}^* + \mu A_{\mathrm{s}} - \mathrm{i}a_{\mathrm{i}}\nabla_\perp^2 A_{\mathrm{i}}^* - \alpha_{\mathrm{i}}\partial_x A_{\mathrm{i}}^*] = A_{\mathrm{i}}^{*(0)}\delta(x)\delta(y)\delta(t). \qquad (5)
\end{aligned}$$

The left-hand side is a part of (1) linearized around the steady-state solution (OPO OFF). The forcing terms added to the right-hand side of (5) represent a localized initial impulse for A_{s} and A_{i}^*, with δ being the Dirac function. Problem (5) can be solved using Fourier transforms in space (x, y) and Laplace transform in time t, defined by

$$\widehat{\Phi}(k_x, k_y, \omega) = \int_{-\infty}^{+\infty}\int_{-\infty}^{+\infty}\int_{0}^{+\infty} \Phi(x,y,t)\mathrm{e}^{\mathrm{i}(\omega t - k_x x - k_y y)}\mathrm{d}x\,\mathrm{d}y\,\mathrm{d}t, \qquad (6)$$

where we have defined the four-component vector $\Phi = (A_{\mathrm{s}}, A_{\mathrm{i}}^*, A_{\mathrm{s}}^{(0)}, A_{\mathrm{i}}^{*(0)})^{\mathrm{T}}$. After solving the problem in Fourier space and performing the Laplace transform by using the Residue Theorem, the solution, $A_{\mathrm{s}}(x,y,t)$, may be written as

$$A_{\mathrm{s}}(x,y,t) = -\frac{\mathrm{i}}{4\pi^2}\sum_{n=1}^{2}\int_{-\infty}^{+\infty}\int_{-\infty}^{+\infty} \frac{S_n(\omega_n, k_x, k_y)}{\dfrac{\partial D}{\partial \omega}(\omega_n, k_x, k_y)}\mathrm{e}^{-\mathrm{i}(\omega_n t - k_x x - k_y y)}\mathrm{d}k_x\,\mathrm{d}k_y, \qquad (7)$$

where $S_n(\omega_n, k_x, k_y) = \widehat{A}_{\mathrm{s}}^{(0)}[\mathrm{i}\omega_n + \gamma_{\mathrm{i}}(-(1-\mathrm{i}\Delta_{\mathrm{i}}) + \mathrm{i}a_{\mathrm{i}}k^2 - \mathrm{i}\alpha_{\mathrm{i}}k_x)] - \gamma_{\mathrm{s}}\mu\widehat{A}_{\mathrm{i}}^{*(0)}$ and ω_n $(n = 1, 2)$ are the two complex frequency mode solutions of the dispersion relation (2). The mode with the largest growth rate is the first one to absolutely destabilize the system. Thus, we shall now consider only this most destabilizing mode,

whose frequency will be referred to as ω. The emerging signal pattern, $A_s(x,y,t)$, is obtained by the asymptotic evaluation, as t tends to infinity, of the solution (7) along the rays $x/t = U$, $y/t = V$ for all constant values of U and V. Note that it is necessary to include x/t and y/t terms in order to allow the transverse point (x,y) to be large as t becomes large, so that one may follow a propagating perturbation. If the solution $A_s(x,y,t)$ is unbounded as $t \to \infty$, then the system is linearly unstable, and we have to distinguish between two types of instabilities. Any instability along a ray with $(U,V) = (0,0)$ which grows in time in situ and invades the whole spatial domain is called "absolute". Any instability which grows in time along a ray with $(U,V) \neq (0,0)$ but drifts away is called "convective". A summary of the various transitions is illustrated in Fig. 3, in a 1D configuration for clarity. The growth rate in this figure is defined, for 1D perturbations, as $\lambda = \Im(\omega)$. Asymptotic expansions of the integral (7) can be obtained by applying the method of the steepest descent [33]. It consists, to be specific, in deforming the real wave vector k-contour of integration in (7) into the two complex planes k_x and k_y, without changing the value of the integral. The dominant part of the integrand arises in the region of the saddle point (k_x^s, k_y^s), defined by

$$\frac{\partial \omega}{\partial k_x} = U \quad \text{and} \quad \frac{\partial \omega}{\partial k_y} = V. \tag{8}$$

The asymptotic form of the shape of the signal response to the initial pulse perturbation is given by

$$A_s(x,y,t) \sim -\frac{\mathrm{i}}{2\pi t} \frac{S(\omega(k_x^s,k_y^s),k_x^s,k_y^s))\mathrm{e}^{\mathrm{i}(k_x^s U + k_y^s V - \omega)t}}{\dfrac{\partial D}{\partial \omega}(k_x^s,k_y^s,\omega(k_x^s,k_y^s)) \left[\left(\dfrac{\partial^2 \omega}{\partial k_x \partial k_y} \right)^2 - \dfrac{\partial^2 \omega}{\partial k_x^2} \dfrac{\partial^2 \omega}{\partial k_y^2} \right]^{1/2}_{(k_x^s,k_y^s)}}.$$

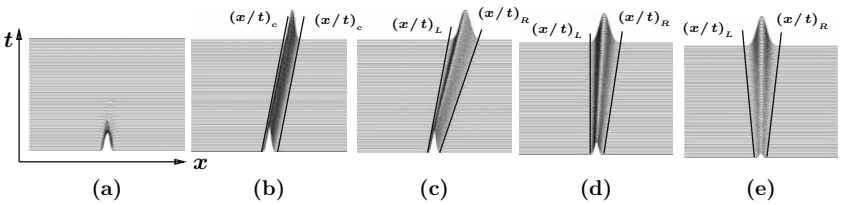

Fig. 3 Schematic diagram of the different types of wave-packet time evolution from an initial perturbation localized at the origin for (**a**) stable, (**c**) convectively unstable and (**e**) absolutely unstable regimes in a 1D configuration. The cases (**b**) and (**d**) correspond to the thresholds of the last two regimes. The control parameter is increased from (**a**) to (**e**). The convective threshold is observed when the global maximum of the growth rate, λ (defined in Sect. 2.3), reaches zero [case (b)], whereas the absolute threshold is reached when the growth rate of the wave packet having a vanishing group velocity reaches zero [case (d)]. $(x/t)_L$ and $(x/t)_R$ correspond to the slow and fast frontiers of the wave packets defined by $\lambda((x/t)_{L \text{ or } R}) = 0$, which are the dissipative flat solitons or front solutions limiting the wave packets

The necessary, but not sufficient, condition for absolute instability is the existence of a saddle point of frequency $\omega = \omega(k_x^s, k_y^s)$ in the two complex k_x and k_y planes for some complex $\omega^{(0)}$ with $\Im(\omega^{(0)}) > 0$ and $U = V = 0$. However, for sufficiency, it is required that the spatial branches in each of the complex k_x and k_y planes, which are the solutions of the dispersion relation (2), originate from the real k_x-axis and k_y-axis. This is the so-called "pinching" condition [34]. These two points are investigated in the following. First, we look for the necessary condition, which provides us with possible values for the absolute instability threshold, and then we check the pinching condition for sufficiency.

3 Degenerate Optical Parametric Oscillators

In degenerate optical parametric oscillators (DOPO), the energy conversion process is frequency and polarization degenerate – the signal and the idler are identical. As a consequence, the three-wave equations of the OPO (1) lead to a two-wave mixing system describing the spatio-temporal evolution of the pump, (A_p), and the signal, (A_s). Hence, the governing equations (1) reduce to

$$\begin{cases} \partial_t A_\mathrm{p} = \gamma_\mathrm{p}[-(1+\mathrm{i}\Delta_\mathrm{p})A_\mathrm{p} + E(x,y) - A_\mathrm{s}^2 + \mathrm{i}a_\mathrm{p}\triangle_\perp A_\mathrm{p}], \\ \partial_t A_\mathrm{s} = \gamma_\mathrm{s}[-(1+\mathrm{i}\Delta_\mathrm{s})A_\mathrm{s} + A_\mathrm{p}A_\mathrm{s}^* + \mathrm{i}a_\mathrm{s}\triangle_\perp A_\mathrm{s} - \alpha_\mathrm{s}\partial_x A_\mathrm{s}]. \end{cases} \tag{9}$$

The homogeneous steady states are

$$\left(A_\mathrm{p}^0, A_\mathrm{s}^0\right) = \left(\frac{E(1-\mathrm{i}\Delta_\mathrm{p})}{1+\Delta_\mathrm{p}^2} \equiv \mu, 0\right), \tag{10}$$

$$\left(A_\mathrm{p}^0, A_{\mathrm{s}\pm}^0\right) = \left(\frac{E - C_\pm^2 \mathrm{e}^{2\mathrm{i}\beta}}{1+\mathrm{i}\Delta_\mathrm{p}}, C_\pm \mathrm{e}^{\mathrm{i}\beta}\right), \tag{11}$$

where

$$C_\pm^2 = \Delta_\mathrm{s}\Delta_\mathrm{p} - 1 \pm \sqrt{E^2 - \left(\Delta_\mathrm{p} + \Delta_\mathrm{s}\right)^2} \tag{12}$$

and

$$\cos(2\beta) = \frac{C_\pm^2 + 1 - \Delta_\mathrm{s}\Delta_\mathrm{p}}{E}. \tag{13}$$

The first solution (10) is the OPO OFF solution, corresponding to the absence of signal emission, while the second one, called OPO ON, characterizes the signal emission. To investigate the transverse distributions of the interacting fields above threshold, it is convenient to analyze the linear stability of the OPO OFF solution with respect to perturbations of the form $A_\mathrm{p} = \mu + \delta A_\mathrm{p}\exp[-\mathrm{i}(\omega t - \mathbf{k}.\mathbf{r})]$, $A_\mathrm{s} = \delta A_\mathrm{s}\exp[-\mathrm{i}(\omega t - \mathbf{k}.\mathbf{r})]$, where $\mathbf{k}$ is the (real) wave vector of the perturbation and ω is its complex frequency. Keeping only linear contributions in $\delta A_{\mathrm{p,s}}$, we soon find that ω and $\mathbf{k}$ must satisfy

$$\omega = \mathrm{i}\gamma_\mathrm{s}\left[-1+\sqrt{|\mu|^2-\left(\Delta_\mathrm{s}+a_\mathrm{s}k^2\right)^2}\right]+\gamma_\mathrm{s}\alpha_\mathrm{s}k_x\,, \tag{14}$$

where k^2 stands for the squared modulus of $\mathbf{k}$. Since the pump remains stable, only the above signal dispersion relation is relevant. Note that, in this section, we set the walk-off parameter, α_s, to zero. Its effect on the existence domains of dissipative solitons will be investigated in the last subsection.

3.1 Bifurcation Types at Threshold of Degenerate OPO Emission

The spatial distribution above threshold of degenerate OPO signal emission strongly depends on the nature of the bifurcation at threshold. This bifurcation is completely determined by the signal detuning, Δ_s, and the physical effective detuning parameter, $\Delta_\mathrm{s}\Delta_\mathrm{p}-1$. For $\Delta_\mathrm{s}\Delta_\mathrm{p}-1<0$, there is one stationary stable solution for each value of the incident pump field. Therefore, the degenerate OPO is then operating in a mono-stable regime with a super-critical bifurcation at its threshold emission, as shown in Fig. 4(a). When $\Delta_\mathrm{s}\Delta_\mathrm{p}-1>0$, the bifurcation is sub-critical, characterized by the existence of the hysteresis cycle displayed in Fig. 4(b). The size of the bistability region is also shown in the figure [vertical arrows in Fig. 4(b)]. A modulational instability (Turing instability) occurs in both regimes when $\Im(\omega)=0$ and $\mathrm{d}\Im(\omega)/\mathrm{d}k=0$ for a finite and real k. It is well known, and one can easily show, that this can never happen for the trivial steady state (10) when $\Delta_\mathrm{s}>0$. In what follows, we consider positive values of the signal detuning (Δ_s), so that the system is stable to Turing bifurcations, and no spatially extended modulations can grow in the system at threshold.

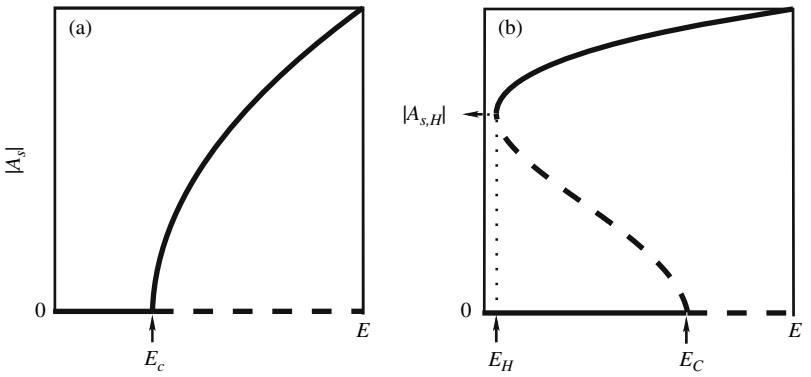

Fig. 4 Bifurcation diagram of a degenerate OPO operating in mono-stable (**a**) and bistable regimes (**b**). $E_\mathrm{c}=\sqrt{(1+\Delta_\mathrm{p}^2)(1+\Delta_\mathrm{s}^2)}$, $E_\mathrm{H}=(\Delta_\mathrm{p}+\Delta_\mathrm{s})$ and $A_{\mathrm{s,H}}=\sqrt{\Delta_\mathrm{s}\Delta_\mathrm{p}-1}$. E_c is the threshold for the destabilization of the OPO OFF solution. The solid line corresponds to stable state and the dashed line to unstable state

3.2 Optical Parametric Dissipative Solitons

It has been shown that, in the mono-stable regime with $\Delta_s > 0$, degenerate OPOs exhibit a transition from the unstable state, OPO OFF, to the stable stationary solution (11), giving rise to a switching front or flat dissipative soliton. It has also been shown that the final state depends on the extended or localized nature of the initial perturbations. The degenerate OPO response to extended perturbations (in the form of plane waves) has widely been investigated in previous works [18, 35]. Here, our analytical investigations deal with 2D-localized perturbations of the OPO OFF solution (10). In all the numerical simulations, the 2D spatio-temporal evolution of the signal field is initiated by using the form of radially symmetric Gaussian impulsions, as could be physically produced by a laser beam. In order to determine the linear response of the system to a localized perturbation, it is necessary to include a finite band of modes in the dynamical description. This can be achieved by reformulating the linear stability analysis as an initial-value problem. In Sect. 2, we have outlined a detailed description of the concept and techniques of stability analysis in terms of an initial-value problem analysis that allows us to obtain, in what follows, absolute and convective thresholds. Near the onset of the instability, the dispersion relation can be approximated by

$$\omega = \mathrm{i}\frac{\gamma_s}{2}\left[|\mu|^2 - 1 - \Delta_s^2 - 2a_s\Delta_s k^2 - a_s^2 k^4\right].$$

After lengthy calculations based on the method of Sect. 2, we find that, at absolute threshold,

$$\begin{cases} k_x^r = 0, \\ k_y^r = 0, \end{cases} \tag{15}$$

$$\begin{cases} (k_x^r)^2 = (k_x^i)^2\left(3 - \dfrac{\Delta_s}{a_s[(k_x^i)^2 + (k_y^i)^2]}\right), \\ (k_y^r)^2 = (k_y^i)^2\left(3 - \dfrac{\Delta_s}{a_s[(k_x^i)^2 + (k_y^i)^2]}\right), \\ \text{with} \quad k_y^r k_x^i = k_x^r k_y^i. \end{cases} \tag{16}$$

The above relations provide, via the steepest method, the co-ordinates of the complex 2D wave vector that dominates the asymptotic behavior of the wave packet generated from the initial localized perturbations. The value of k^r characterizes the spatial modulations of the wave packet and k^i determines its spatial decay. As can be seen from the above equations, a degenerate OPO can exhibit both flat (15) as well as periodic (16) dissipative solitons. Therefore, it is worthwhile to (i) examine the transition from flat to periodic dissipative solitons and (ii) determine their characteristics. Since the system is radially symmetric, the periodic ones necessarily must be organized in the form of ring-shaped structures.

3.2.1 Flat-Top Dissipative Solitons

Let us first examine the case of relations (15) where no modulation is predicted. By using the conditions defined in Sect. 2, one can determine the range of parameters for the existence of flat-top dissipative solitons and their characteristics. It turns out that they exist only if

$$E^2 \leq E_c^2 = \left(1+\Delta_p^2\right)\left(1+\frac{4}{3}\Delta_s^2\right) \quad \text{or} \quad |\mu|^2 \leq |\mu|_c^2 = \left(1+\frac{4}{3}\Delta_s^2\right) \tag{17}$$

$$\text{with} \quad (k_x^i)^2+(k_y^i)^2 = \frac{\Delta_s}{3a_s}\left(1-\sqrt{\frac{E_c^2-E^2}{E_c^2-E_{th}^2}}\right). \tag{18}$$

These solutions have a radial velocity $v^* = \sqrt{(v_x^*)^2+(v_y^*)^2}$ that only exists when E is larger than $E_{th} = \sqrt{(1+\Delta_p^2)(1+\Delta_s^2)}$. It is defined as

$$(v_x^*)^2+(v_y^*)^2 = \frac{16}{27}\gamma_s^2\Delta_s^3 a_s\left\{1-\sqrt{\frac{E_c^2-E^2}{E_c^2-E_{th}^2}}\right\}\left\{1+\frac{1}{2}\sqrt{\frac{E_c^2-E^2}{E_c^2-E_{th}^2}}\right\}^2. \tag{19}$$

When $E < E_{th}$, then $(k_x^i)^2+(k_y^i)^2 = 0$ and $v^* = 0$. This clearly indicates the appearance of flat-top dissipative solitons at the instability threshold, $E = E_{th}$, of the trivial solution. However, when $E > E_c$, the spatial decay (18) becomes infinite, leading to the disappearance of solutions with the form of flat-top types.

3.2.2 Generation of Ring-Shaped Dissipative Solitons

Periodic dissipative solitons are defined by (16), which show a simple and interesting relation between the real and imaginary parts of the wave vector components. One may then substitute (16) into the equations defining their velocity (8) to find

$$(k_x^i)^2+(k_y^i)^2 = \frac{\Delta_s}{12a_s}\left\{1+\sqrt{7+2\frac{E^2-E_{th}^2}{E_c^2-E_{th}^2}}\right\}. \tag{20}$$

These periodic solitons exist for $E > E_c$, and their velocity is given by the following expression:

$$(v_x^*)^2+(v_y^*)^2 = \frac{4}{27}\gamma_s^2\Delta_s^3 a_s\left\{1+\sqrt{7+2\frac{E^2-E_{th}^2}{E_c^2-E_{th}^2}}\right\}\left\{-2+\sqrt{7+2\frac{E^2-E_{th}^2}{E_c^2-E_{th}^2}}\right\}^2 \tag{21}$$

while their intrinsic wavelength is defined by $\frac{2\pi}{k_m}$ with

$$k_m = \frac{3}{8}\sqrt{\frac{\Delta_s}{a_s}}\frac{\left[-3+\sqrt{7+2\dfrac{E^2-E_{th}^2}{E_c^2-E_{th}^2}}\right]^{3/2}}{-2+\sqrt{7+2\dfrac{E^2-E_{th}^2}{E_c^2-E_{th}^2}}}. \tag{22}$$

Note that, although the diffraction is necessary for the existence of both types of dissipative solitons, the transition threshold from flat-top to periodic dissipative solitons is independent of diffraction.

To summarize, there exist two types of 2D dissipative solitons that emerge above the threshold emission of the degenerate OPO, where they are continuously generated from localized initial perturbations. When $1+\Delta_s^2 \le |\mu|^2 \le 1+\frac{4}{3}\Delta_s^2$, they are flat, while for $|\mu|^2 \ge 1+\frac{4}{3}\Delta_s^2$, they exhibit spatial modulations. The parameter range of their existence and the transitions curves are shown in Fig. 5, where we have plotted the normalized incident pump power versus the signal detuning. The main characteristics of both types of solitons, such as the effective decay rate (steepness) $R = \sqrt{(k_x^i)^2+(k_y^i)^2}$, the wave-number k_m and the radial velocity $v^* = \sqrt{(v_x^*)^2+(v_y^*)^2}$, are plotted versus the incident pump intensity in Fig. 6.

To validate our approach, we have checked these analytical predictions by numerically solving the full 2D model (9) with $\alpha_s = 0$ and starting from localized Gaussian initial conditions. Our numerical method is as follows. We fix the values of all parameters and take the incident pump amplitude, E, as a control parameter. We have carried out several numerical investigations with various sets of parameter values. Figure 7 shows a typical solution just above the transition from flat-top to periodic dissipative solitons, and it is in excellent agreement with analytical predictions. Moreover, the characteristics, including the spatial frequency, k_m, and the velocity, v^*, are displayed in Figs. 8 and 9 as functions of the normalized incident

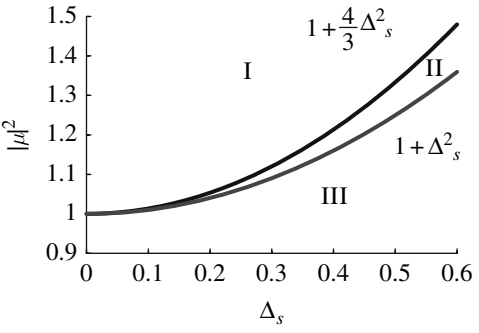

Fig. 5 Domains of existence of flat and periodic dissipative solitons for $\Delta_s \ge 0$. **I**: periodic solitons, **II**: flat solitons, **III**: OPO OFF

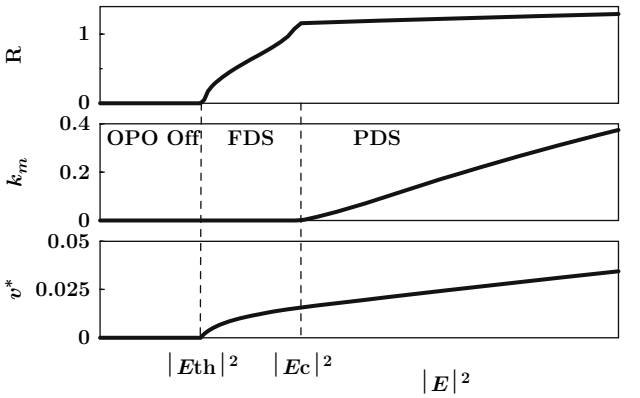

Fig. 6 Velocity v^*, wave-number k_m and steepness R of flat (FDS) and periodic (PDS) solitons with respect to pump intensity for $\Delta_\mathrm{p} = 0$, $\Delta_\mathrm{s} = 0.2$ and $a_\mathrm{s} = 0.05$

pump amplitude and signal detuning, respectively. As can be seen from the two figures, the evolution of k_m and v^* again shows excellent agreement between predictions (solid lines) and numerical results (dots). The dependence of the intrinsic spatial frequency, k_m, upon the incident pump amplitude is also illustrated in Fig. 9(a). This constitutes the main difference with respect to Turing instability. For the latter, the wavelength at threshold does not depend on the incident pump amplitude, and it is fixed by the signal diffraction and detuning coefficients ($k_\mathrm{T} = \sqrt{-\Delta_\mathrm{s}/a_\mathrm{s}}$). Here, the wavelength is almost doubled when $E = |\mu|\sqrt{1+\Delta_\mathrm{p}^2}$ increases from 1.1 to 1.2 [see Fig. 9(a)].

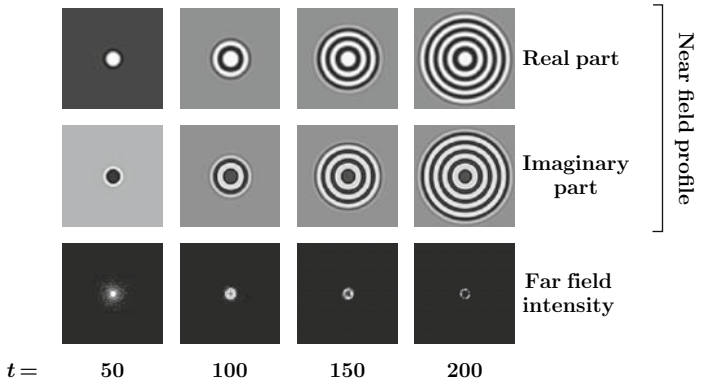

Fig. 7 Snapshots in the transverse plane of the signal time evolution resulting from numerical integration of the original equations of the degenerate OPO (9). The parameters are $E = 1.2$, $\Delta_\mathrm{p} = 0$, $\Delta_\mathrm{s} = 0.2$, $a_\mathrm{p} = \frac{a_\mathrm{s}}{2} = 0.0375$, $\gamma_\mathrm{p} = \gamma_\mathrm{s} = 1$, $L_x = L_y = 60$ and $N_x = N_y = 256$

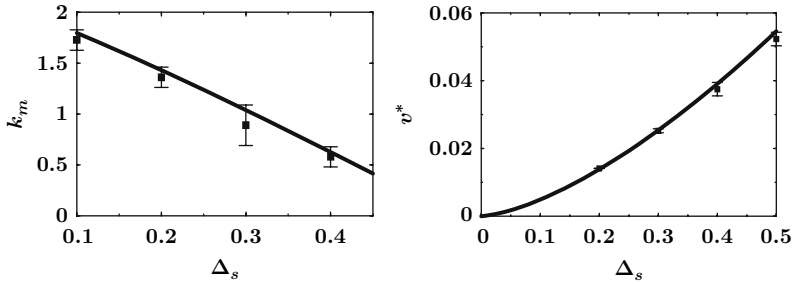

Fig. 8 Spatial frequency, k_{m}, and velocity, v^*, of periodic solitons (PDS) with respect to the detuning, Δ_{s}, for $E = 1.2$, $\Delta_{\mathrm{p}} = 0$, $a_{\mathrm{s}} = 0.05$ and $\gamma_{\mathrm{s}} = \gamma_{\mathrm{p}} = 1$. The solid lines correspond to the analytical predictions, while squares are the estimated values from numerical integration of the degenerate OPO equations (9)

3.2.3 Walk-Off Effect on Dissipative Solitons

The walk-off effect on the dynamics of the degenerate OPO can be described by taking into account the transverse propagating term $\alpha_{\mathrm{s}}\partial_x A_{\mathrm{s}}$ in (9). The main characteristics of dissipative solitons were determined in previous subsections. The whole procedure can be repeated, provided that one writes the governing equations (9) in the moving reference frame of the signal field. The result, in the laboratory frame (the rest frame attached to the incident pump field), is that the velocity of both types of dissipative solitons satisfies

$$(v_x^* - \alpha_{\mathrm{s}})^2 + (v_y^*)^2 = (v^*)^2,$$

where v^* is the velocity of the solitons determined in (19) and (21). Therefore, in the walk-off direction [x-axis in (9)], the two limiting flat solitons (fronts) have different

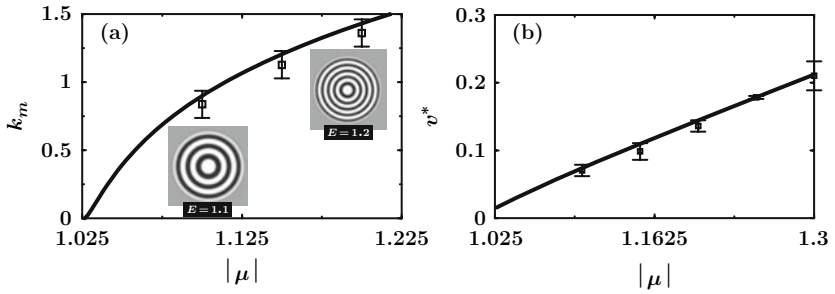

Fig. 9 Spatial frequency, k_{m}, and velocity, v^*, of periodic solitons (PDS) versus the control parameter μ, for $\Delta_{\mathrm{p}} = 0$, $\Delta_{\mathrm{s}} = 0.2$, $a_{\mathrm{s}} = 0.05$ and $\gamma_{\mathrm{s}} = \gamma_{\mathrm{p}} = 1$. The solid lines correspond to analytical predictions, while squares are the estimated values from numerical integration of the degenerate OPO equations (9). Let us note the dependence of the wavelength on the incident pump amplitude (inserts)

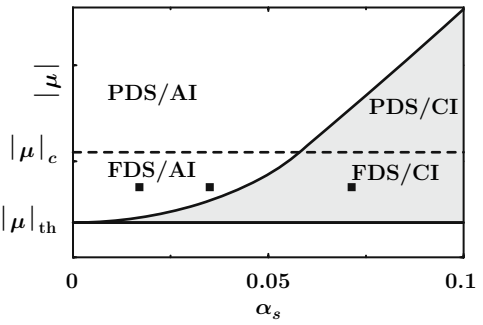

Fig. 10 Absolute (AI) and convective (CI) instabilities of periodic (PDS) and flat (FDS) solitons versus the walk-off parameter, $\alpha_{\rm s}$. Squares correspond to $\alpha_{\rm s}$ values in Fig. 11. Left square [Fig. 11 (a)], middle square [Fig. 11 (b)] and right square [Fig. 11 (d)]

velocities ($v_x^* = \alpha_{\rm s} \pm v^*$). As a consequence, the degenerate OPO enters a convective regime when they have the same sign, and otherwise an absolute regime occurs. The transition from convective to absolute regime is determined by the vanishing of one of the two velocities. As mentioned in Sect. 2, this necessary condition is not sufficient for an actual convective/absolute transition to occur. For sufficiency, we numerically investigated the pinching condition. Figure 10 shows the transition curve from convective to absolute instabilities, defined as $v^*(|\mu|) = \alpha_{\rm s}$. As a comparison, thresholds for the appearance of flat-top dissipative solitons and for their transition to periodic ones, $|\mu|_{\rm th}$ and $|\mu|_{\rm c}$, respectively, are also indicated in this

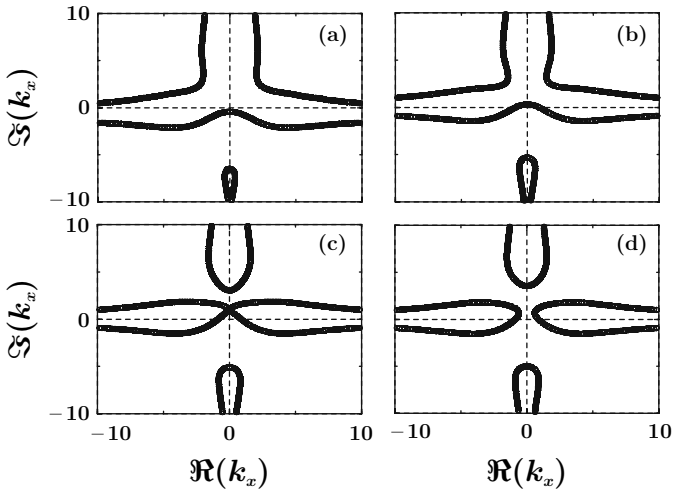

Fig. 11 Example of realization of the pinching condition in a degenerate OPO (9). Paths represent the contours satisfying $\Im(\omega) = 0$, plotted in the plane $(\Re(k_x), \Im(k_y))$, for increasing values of the walk-off parameter, $\alpha_{\rm s}$. (**a**) $\alpha_{\rm s} = 0.017$ and (**b**) $\alpha_{\rm s} = 0.035$ (absolute regime), (**d**) $\alpha_{\rm s} = 0.071$ (convective regime). Note the intersection of paths occurring for $\alpha_{\rm s} = 0.044$ (**c**) at the threshold of absolute instability according to analytical predictions

figure. Moreover, the pinching condition has been checked and the results are depicted in Fig. 11. In this figure, we have plotted the marginal stability condition $\Im(\omega) = 0$ in the (k_x^r, k_x^i) plane for various values of the walk-off parameter. The instability is absolute in Fig. 11(a, b) (left and right squares in Fig. 10), while it is convective in Fig. 11 (d) (middle square in Fig. 10). The pinching condition occurs for $\alpha_s = v^* = 0.044$ [Fig. 11(c)], which is in excellent accord with analytical predictions.

4 Walk-Off Nonlinear Effects in Parametric Optical Oscillators

As mentioned in Sect. 2, the existence of a non-zero angle between the energy propagation (Poynting vectors) axes of the pump and the signal is responsible for the instability splitting into two instability domains (absolute and convective). This follows from the translational symmetry-breaking induced by walk-off. In a previous work [36], we demonstrated that when a degenerate OPO is operating in the sub-critical regime, the spatio-temporal behavior of the slowly varying envelope of the signal/idler pair is modeled by a quintic–cubic Ginzburg–Landau equation [36, 37]. In this case, it has been shown that both nonlinear and linear fronts can exist and compete. The selected front satisfies the velocity criterion according to the predictions of [38, 39]. However, when the nonlinear fronts are selected, they appear as a compensation between higher-order nonlinear terms (quintic here), instead of cubic ones, and the *linear* translation induced by the walk-off [36]. Although the transition thresholds between linear and nonlinear fronts, together with their velocities, are satisfactorily predicted, there still exists a large discrepancy regarding their spatial shapes [36]. As a consequence, the underlying *nonlinear* symmetry-breaking cannot be explained within this model. Here, we derive a new model that takes into account walk-off *nonlinear* effects. The model is first derived in the way that provides the most general amplitude equations describing the weakly nonlinear dynamics of the slowly varying envelope of the fields in the OPO cavity, when operating in the sub-critical regime. Secondly, and for clarity, we separately investigate the degenerate and non-degenerate situations, respectively. So, in the OPO governing equations (1), by setting $A_p = \mu + \left(1 - i\Delta_p\right) B$, $A_s = \sqrt{1+\Delta_p^2}\, A_1$, $A_i = \sqrt{1+\Delta_p^2}\, A_2$ and after lengthy and cumbersome calculations, the amplitude equation is obtained as a complex quintic–cubic generalized Ginzburg–Landau equation (CQCGLE):

$$\tau \partial_t \psi = d\,(\mu - \mu_{th})\,\psi + c\nabla_\perp^2 \psi - v_g \partial_x \psi + v_{nl}\,\psi \partial_x(|\psi|^2) + b_3\,|\psi|^2\,\psi - b_5\,|\psi|^4\,\psi, \tag{23}$$

where

$$\begin{pmatrix} B \\ A_1 \\ A_2 \end{pmatrix} = \begin{pmatrix} -|\psi|^2\, e^{-i\theta} \\ \psi e^{i(\omega_c t + k_c x)} \\ \psi e^{-i\theta} e^{-i(\omega_c t + k_c x)} \end{pmatrix}. \tag{24}$$

The coefficients appearing in the above equation are defined from the physical parameters of the OPO (1) as

$$\begin{cases} \tau &= \dfrac{(\gamma_s+\gamma_i)^2+(\gamma_s-\gamma_i)^2\Delta_e^2}{2\gamma_s\gamma_i(\gamma_s+\gamma_i)}, \\ v_g &= \dfrac{1}{2}\left[\alpha_s+\alpha_i-(a_s-a_i)\dfrac{\alpha}{a}\right]+\dfrac{(\gamma_s-\gamma_i)}{2(\gamma_s+\gamma_i)}\left[\alpha_i-\alpha_s+(a_s+a_i)\dfrac{\alpha}{a}\right], \\ d &= d_r+\mathrm{i}d_i=\left[1-\mathrm{i}\dfrac{(\gamma_s-\gamma_i)}{(\gamma_s+\gamma_i)}\Delta_e\right]\mu_{th}, \\ c &= c_r+\mathrm{i}c_i=a\Delta_e+\dfrac{\mathrm{i}}{2}\left[(a_s-a_i)-\dfrac{(\gamma_s-\gamma_i)}{(\gamma_s+\gamma_i)}(a_s+a_i)\Delta_e^2\right], \\ v_{nl} &= v_{nl}^{r}+\mathrm{i}v_{nl}^{i}=\gamma v_g\left[1-\mathrm{i}\dfrac{(\gamma_s-\gamma_i)}{(\gamma_s+\gamma_i)}\Delta_e\right], \\ b_3 &= b_3^r+\mathrm{i}b_3^i=\left(\Delta_p\Delta_e-1\right)\left[1-\mathrm{i}\dfrac{(\gamma_s-\gamma_i)}{(\gamma_s+\gamma_i)}\Delta_e\right], \\ b_5 &= b_5^r+\mathrm{i}b_5^i=\dfrac{\mu_{th}^2}{2\Delta_e^2}\left[1-\mathrm{i}\dfrac{(\gamma_s-\gamma_i)}{(\gamma_s+\gamma_i)}\Delta_e\right], \\ \mathrm{e}^{\mathrm{i}\theta} &= \dfrac{1+\mathrm{i}\Delta_e}{\mu_{th}}, \\ \omega_c &= -\dfrac{\gamma_s\gamma_i}{\gamma_s+\gamma_i}\left[\Delta_s-\Delta_i+(a_s-a_i)\dfrac{\alpha^2}{4a^2}-(\alpha_s+\alpha_i)\dfrac{\alpha}{2a}\right], \\ k_c &= -\dfrac{\alpha}{2a}. \end{cases} \tag{25}$$

We have set $\gamma=1/\tau\gamma_p$, $\Delta_e=\alpha^2-4a\Delta/(\gamma_s+\gamma_i)$ and $\mu_{th}=\sqrt{1+\Delta_e^2}$. Without the term $v_{nl}\psi\partial_x\left(|\psi|^2\right)$ (corresponding to an absence of the walk-off), (23) is simply the sub-critical Ginzburg–Landau equation. The ability of this equation to generate a great variety of solutions does not need to be demonstrated here [39]. The most famous ones are the front and the pulse-like solutions. If both solutions can be stable in the complex case (where all or some coefficients are complex), then only fronts are stable when all coefficients are real. This is the case when the OPO is degenerate. The aim of this section is to point out the effects of the walk-off on these structures. Therefore, the formation and dynamics of flat-top dissipative solitons, as states of bounded fronts, will be considered first through the degenerate OPO. Secondly, we will show that the non-degenerate case is likely to exhibit localized dissipative solitons in the form of pulses.

4.1 Asymmetric Flat-Top Dissipative Solitons

When OPOs are operating in the degenerate configuration, the complex generalized amplitude equation (23) reduces to a real Ginzburg–Landau equation (RGLE), but with a *nonlinear gradient* term:

$$\partial_t \psi = \lambda\psi + d\nabla_\perp^2 \psi - \alpha_s \partial_x \psi + v_{nl}\psi^2 \partial_x \psi + b_3 \psi^3 - b_5 \psi^5, \tag{26}$$

where $\lambda = \mu_{th}(\mu - \mu_{th})$, $b_3 = \left(\Delta_p \Delta_s - 1\right) > 0$, $b_5 = \frac{\mu_{th}^2}{2\Delta_s^2} > 0$, $v_{nl} = 2\gamma_s\alpha_s/\gamma_p$ and $d = a_s\Delta_s$. Beyond the threshold of degenerate OPO emission, the expected signal transverse profile will correspond to the solutions of this equation. The only stable ones (fronts) are found by applying the Weiss–Tabor–Carnevale (WTC) method [40]. Therefore, any localized initial condition evolves into a flat-top dissipative soliton given by

$$\begin{cases} \psi(z = x - v_{nl}t) = \psi_s \sqrt{\dfrac{1 + \tanh\left[\kappa_+\left(z - z_+^0\right)\right]}{2}} \sqrt{\dfrac{1 + \tanh\left[\kappa_-\left(z - z_-^0\right)\right]}{2}}, \\ \kappa_\pm = \left(\dfrac{v_{nl}}{6d}\right)\left[1 \pm \sqrt{1 + \dfrac{12 d b_5}{v_{nl}^2}}\right]\psi_s^2, \end{cases} \tag{27}$$

with velocities

$$v_{\kappa_\pm} = \alpha_s - \frac{\lambda + d\kappa_\pm^2}{\kappa_\pm}. \tag{28}$$

z_+^0 and z_-^0 denote the *center-of-mass* co-ordinates of the kink and the antikink bounded states, respectively, and $\psi_s = \pm\sqrt{\frac{b_3 \pm \sqrt{b_3^2 + 4b_5\lambda}}{2b_5}}$ are the stationary steady-state solutions of (26). Let us now consider the case of small values of the nonlinear gradient coefficient. In this case, the steepness parameters $\kappa_\pm$ read

$$\kappa_\pm \simeq \left(\frac{v_{nl}}{6d} \pm \sqrt{\frac{b_5}{3d}}\right)\psi_s^2. \tag{29}$$

These expressions make it clear that, in the absence of walk-off, the kink (κ_+) and anti-kink (κ_-) have the same steepness. Then, the signal profile resulting from a localized initial condition corresponds to a symmetric flat-top dissipative soliton, as shown in Fig. 12 (left). In this figure, we have plotted the asymptotic solution obtained by numerically integrating the degenerate OPO (9) with $\alpha_s = 0$ in the 2D transverse plane. As a comparison, we have also displayed the resulting numerical signal for a non-zero walk-off parameter in Fig. 12 (right), where an asymmetry in the direction of the walk-off is clearly shown. Indeed, the presence of walk-off leads to a non-vanishing nonlinear gradient coefficient (v_{nl}) in (29), and this induces a difference in the steepness of the kink and anti-kink. So, for a localized initial condition, the signal profile takes the form of an asymmetric flat-top dissipative soliton where the kink always remains steeper than the anti-kink, as can be seen from Fig. 12 (right). This nonlinear effect involves an effective parameter, viz. the signal-to-pump relaxation rates ratio, $\frac{\gamma_s}{\gamma_p}$, that is usually absent in OPO amplitude equations. Here it emphasizes the key role of the pump relaxation time in the formation of dissipative solitons. In fact, this leads to the main nonlinear walk-off effect that drastically influences degenerate OPO dynamics. This impact leads to a nonlinear

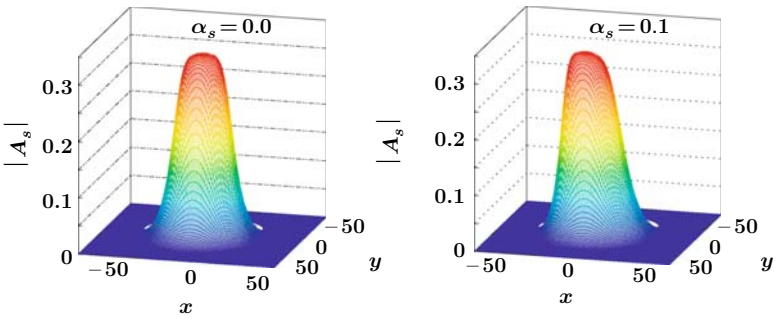

Fig. 12 2D transverse dissipative flat solitons, computed from the degenerate OPO (9) operating in sub-critical regime without walk-off (left, symmetric solitons), and with walk-off (right, asymmetric solitons). The other parameters are $a_s = 2a_p = 0.025$, $\Delta_s = 1.1$, $\Delta_p = 1$, $\mu = 1.486$ $(E = 2.101)$

symmetry-breaking that can quantitatively be evaluated by using the ratio η of the steepness of the kink and anti-kink bounded states forming the soliton:

$$\eta = \left| 1 - \frac{2v_{\rm nl}}{v_{\rm nl} + \sqrt{v_{\rm nl}^2 + 12db_5}} \right|. \tag{30}$$

Figure 13 illustrates the role of the walk-off nonlinear effect in the observed nonlinear symmetry-breaking of degenerate OPOs. Three curves are plotted in Fig. 13

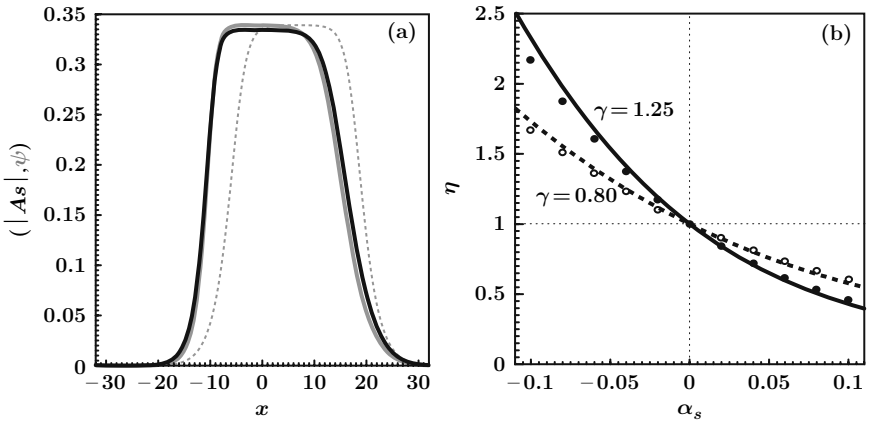

Fig. 13 (**a**) Transverse section of the signal solution displayed in Fig. 12, with $\alpha_s = 0.1$, along the walk-off direction (x-axis) (black solid line) compared with numerical solutions obtained by integration of (26) with the same conditions (gray solid line). The reference curve (dotted line) is the numerical solution from (26) with $v_{\rm nl}$ being set to zero. (**b**) Variation of the asymmetry coefficient versus the walk-off parameter for two values of the $\gamma = \frac{\gamma_s}{\gamma_p}$ ratio. Solid and dashed lines are predictions from (30). Dots represent estimated values obtained from numerical simulations of (9)

(a), viz. (i) the black curve which reproduces a cut of the signal solution on Fig. 12 (right) along the x-axis, showing the signal asymmetry in the walk-off direction, (ii) the grey curve which is the result of the numerical integration of the reduced model (26) with the same parameters and (iii) the dashed curve which shows what the results would be if the nonlinear gradient term were omitted in the model (26). A quantitative measure of the walk-off-induced nonlinear symmetry-breaking is provided by the η ratio that we have plotted against the walk-off parameter in Fig. 13 (b). To emphasize the impact of the pump relaxation rate in the observed signal asymmetry, we have plotted η for two values of γ_p and a fixed value of the signal relaxation rate, γ_s. (In the figure, γ_s/γ_p is labeled γ, as η is actually a function of this ratio). As can be seen from the figure, the estimated values from numerical simulations (dots) of the governing equation (9) are in excellent agreement with analytical predictions (solid and dotted lines) from the expression (30). Moreover, the relation (28) shows that the presence of the nonlinear gradient term causes the kink and anti-kink to move more slowly than is the case in its absence. This slowing down is also illustrated in Fig. 14, where the effective velocity-estimated values (dots) from numerical simulations of (9) are compared with the predicted ones (solid line) from (28). An indication of the results obtained when setting the coefficient $v_{nl} = 0$ in (26) is plotted with the dashed curve for comparison.

4.2 Static and Pulsating Dissipative Solitons of the Triply Resonant OPO

In the non-degenerate configuration, all of the three intra-cavity fields are involved in the OPO dynamics. When the pump, signal and idler are resonant in the cavity, giving rise to a triply resonant OPO, all the coefficients appearing in (23) can take

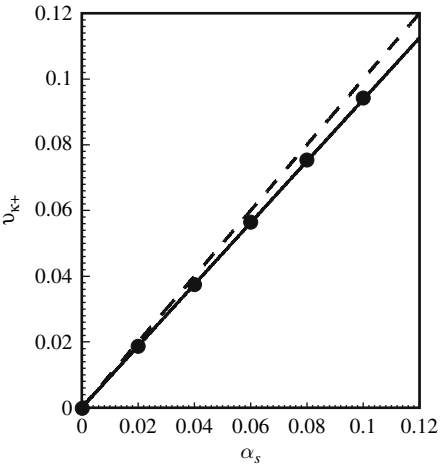

Fig. 14 Predicted velocity (28) of the kink-anti-kink bounded state, without (dashed line) and with (solid line) the nonlinear gradient term versus the walk-off parameter. The points are the estimated numerical values from the governing equations (9). The parameters are the same as in Fig. 12

non-zero values. However, in the absence of walk-off, the effective group velocity $v_g = 0$, leading to vanishing linear and nonlinear gradient terms. This gives the well-known complex cubic–quintic Ginzburg–Landau equation (CQCGLE). It has been shown, both analytically and numerically, that it can exhibit stable pulse-like solutions [41, 42, 43, 44, 45, 46]. Our goal in this section is twofold. First we prove that, even near threshold, where (23) governs the spatio-temporal dynamics of the intracavity fields, the OPO is able to generate a variety of stable dissipative pulse-like solutions. Some of them have not yet been reported in the OPO literature, where almost all investigations on localized structures are devoted to *degenerate* OPOs. Here, dissipative pulse-like solitons result from a three-wave interaction, and thus have no counterpart in the degenerate configuration. Second, we focus on the effect of the walk-off on these solutions through the linear and nonlinear gradient terms. We start by integrating the OPO equations (1) without any walk-off effect ($\alpha_s = \alpha_i = 0$). There is numerical evidence for two types of dissipative solitons, viz. static and pulsating solitons. Indeed, the temporal evolution of the profile of the signal/idler pair, with one transverse co-ordinate, is plotted in Fig. 15, showing that a static pulse-like solution remains stable according to the predictions of the reduced model (23). In addition to this solution, and for a set of parameters, we have observed that the real and imaginary parts present a phase mismatch and that they start oscillating and asymptotically converge to a fixed frequency. As a consequence, the envelopes of the signal/idler pair emitted by the OPO become time-periodic, as illustrated in Fig. 16. Both the spatio-temporal diagram of the signal envelope and the time evolution of its real and imaginary components are displayed in the figure.

Let us now investigate the walk-off effect on the formation and the dynamics of these localized OPO solitons. For this purpose, it is worthwhile to examine the terms appearing with the walk-off in (23). It is obvious that the linear gradient term ($v_g \partial_x \psi$) will only induce a drift in the direction of the walk-off. More importantly, the nonlinear gradient term $(v_{nl} \psi \partial_x (|\psi|^2))$ gives rise to a nonlinear coupling of the real and imaginary components. This allows us to qualitatively point out the effects of the real and imaginary parts of the coefficient v_{nl}. Note that when the degeneracy occurs ($A_s \equiv A_i$), the real part of this coefficient is similar to the

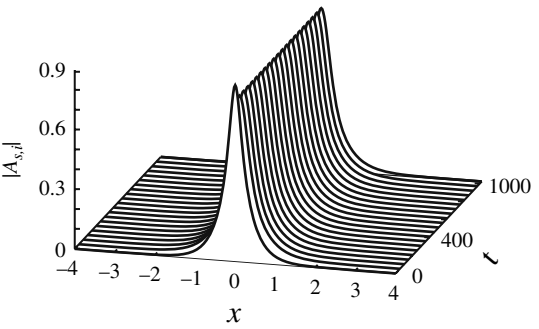

Fig. 15 Spatio-temporal evolution of the static soliton obtained by numerically solving (1) for the non-degenerate OPO . The parameters are $E = 1.51$, $a_p = 0.02$, $a_s = 0.01$, $a_i = 0.01$, $\gamma_p = 1.0$, $\gamma_s = 1.0$, $\gamma_i = 0.8$, $\Delta_p = 1.5$, $\Delta_s = 1.2$ and $\Delta_i = 1.20$

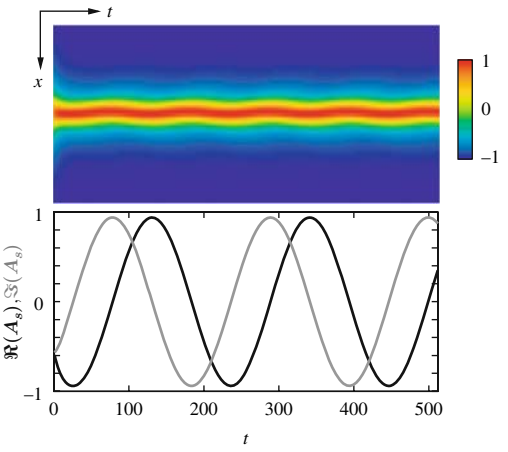

Fig. 16 Spatio-temporal evolution of the OPO (1) pulsating soliton envelope and time evolution of its real ($\Re(A_s)$) and imaginary ($\Im(A_s)$) parts. The parameters are the same as in Fig. 15, except: $a_i = 0.0025$ and $\gamma_i = 1.0$

nonlinear gradient term of (26). In the previous subsection, we have shown that it is responsible for a self-steepening in the envelope profile and a slowing down of its motion. So, one can expect the same effects on pulsating solitons. The imaginary part, however, characterizes *non-degenerate* OPOs and has, in space, a similar effect to that of the self-frequency shift term which appears in the modeling of the Raman-like process which occurs in the propagation of sub-picosecond pulses in an optical fiber [47].

To summarize, we expect to observe three nonlinear effects on the pulse solutions of the OPO which are due to the walk-off, viz. a self-steepening, a self-frequency shift and a slowing down of motion. In what follows, only static dissipative solitons (see Fig. 15) will be considered. Similar effects have been observed on pulsating solitons (Fig. 16) but they will not be reported here. We have numerically investigated the walk-off effect by varying the value of the coefficient v_{nl} and then observing the consequences of this variation on the behavior of the static pulse soliton. An examination of the expression for v_{nl} shows that it is the walk-off and the pump relaxation rate (γ_p) that characterize the importance of the nonlinear gradient term in the OPO dynamics. This is evidenced in Fig. 17(a), where we have assigned two typical values to γ_p, whereas the value of the walk-off is fixed. Two effects are emphasized: (i) the actual velocity of the pulse is not simply the group velocity, v_g (dotted line), but it is sensitive to the ratio $\gamma = \frac{1}{\gamma_p \tau}$ via the nonlinear gradient term coefficient, and (ii) this dependence is responsible for the slowing down of the pulse, which is more pronounced when decreasing [point (1)] γ_p values. A space–time diagram, showing the slowing down of the pulse motion corresponding to points (1) and (2) in Fig. 17(a), is displayed in Fig. 17(b), starting from the same initial pulse. The subsequent time evolution leads to two pulses that become separated as they drift. The second important nonlinear effect of the walk-off on static pulses is illustrated in Fig. 18. It displays the spatio-temporal diagram of the OPO signal envelope (upper figures) and the corresponding temporal evolution of the maximum of its real part (lower ones). Starting in (1) from the static pulse in the absence of

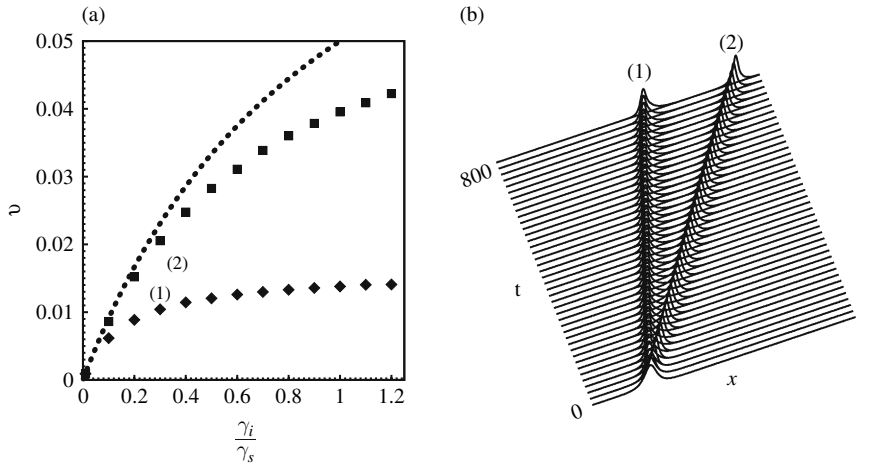

Fig. 17 (**a**) Velocity of the pulse-like soliton of the non-degenerate OPO (1) versus the idler-to-signal relaxation rates ratio, γ_i/γ_s, for $\gamma_p = 0.1$ and 1.0 (■). Dashed curve represents the group velocity in (23) defined by (25). (**b**) Spatio-temporal evolutions of pulses corresponding to points (1) and (2). The parameters are those of Fig. 12 (right)

walk-off [Fig. 18(a)], we increased the walk-off value up to $\alpha_s = \alpha_i = 0.1$ and observed the pulse time oscillations with a fixed frequency, as shown in Fig. 18(b). Note that the frequency of oscillation increases with the nonlinear gradient coefficient ratio, $\gamma = \frac{1}{\gamma_p \tau}$. Indeed, we have doubled the γ_p value, but use a fixed value of the walk-off. In this case, the frequency decreases by a factor of about $2/3$. We then conclude that, since the walk-off value is fixed, the observed frequency variation is a *pure* nonlinear effect of the walk-off, stemming from the nonlinear gradient term.

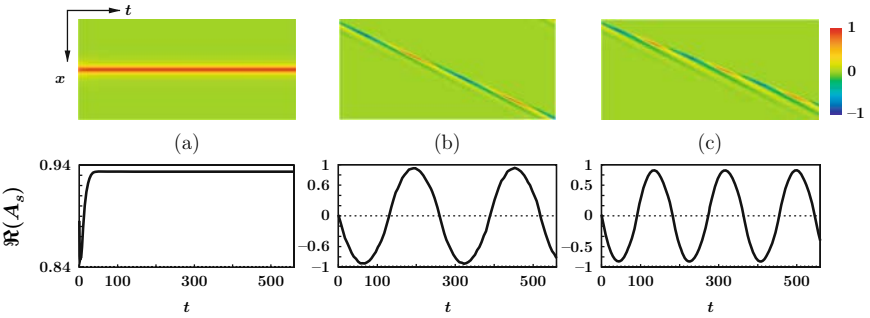

Fig. 18 Spatio-temporal diagram of the OPO soliton and the time evolution of its real part. The parameters are [(**a**) $\gamma_p = 0.3, \alpha_{s,i} = 0.0, E = 1.487$], [(**b**) $\gamma_p = 0.6, \alpha_{s,i} = 0.1, E = 1.487$], [(**c**) $\gamma_p = 0.3, \alpha_{s,i} = 0.1, E = 1.490$]. The remaining parameters are $a_p = 0.03$, $a_{s,i} = 0.0075$, $\gamma_p = 1.0$, $\gamma_s = 1.0$, $\gamma_i = 0.36$, $\Delta_p = 1.5$ and $\Delta_{s,i} = 1.2$

5 Concluding Remarks

We have presented an analytical and numerical study of the occurrence and the dynamics of dissipative solitons in optical parametric oscillators under the combined effects of diffraction and walk-off. We have shown that it is necessary to take into account the nonlinear effects of walk-off to capture the full spatio-temporal dynamics of the system. In particular, the derivation of a reduced model (of Ginzburg–Landau type), describing the weakly nonlinear (near-threshold) dynamics, reveals the appearance of a nonlinear gradient term induced by the walk-off. We have evidence that the latter strongly affects the dynamics and the shape of static and pulsating dissipative solitons. More precisely, we were able to explain the self-frequency shift, the slowing down and the nonlinear asymmetry observed in the envelopes of the signal/idler pair emitted by the non-degenerate optical parametric oscillator. Although we present our investigations in the context of optics, we believe that our result is generic for spatially extended systems with convection (drift effects) and that it characterizes the key role of convection in the nonlinear dynamics of such systems.

Acknowledgments This work was partially supported by the Interuniversity Attraction Pole program of the Belgian government. The IRCICA and CERLA are supported in part by the *Ministère Chargé de la Recherche*, the *"Conseil Régional Nord Pas de Calais"* and the *"Fonds Européen de Développement Economique des Régions"*.

References

1. Akhmediev, N., Ankiewicz, A.: *Dissipative Solitons*, Lect. Notes Phys. **66**. Springer, Heidelberg (2005). 262
2. M.C. Cross and P.C. Hohenberg, Rev. Mod. Phys. **65**, 851 (1993). 262
3. Y. Kuramoto, Chemical oscillations, *Waves and Turbulence*, (Springer, Berlin, 1984). 262
4. J.D. Murray, *Mathematical Biology,* 3rd ed. (Springer-Verlag, Berlin, 2002). 262
5. L.A. Lugiato, M. Brambilla, and A. Gatti, in *Advances in Atomic, Molecular and Optical Physics,* edited by B. Bederson and H. Walters (Academic, New York, 1998), vol. 40; W. Lange and T. Ackermann (ed), J. Opt. B **2**(3), 347–456 (2000); N.N. Rosanov, in *Spatial hysteresis and Optical Patterns,* (Springer, Berlin, 2002); K. Staliunas and V.J. Sanchez-Morcillo, *Transverse Patterns in Nonlinear Optical Resonators*, (Springer-Verlag, Berlin, 2003). 262
6. Y. Kivshar, Nat. Phys. **2**, 729 (2006). 262
7. S. Barland, J.R. Tredicce, M. Brambilla, L.A. Lugiato, S. Balle, M. Guidici, T. Maggipinto, L. Spinelli, G. Tissoni, T. Knödl, M. Miller, and R. Jäger, Nature **419**, 699 (2002). 262
8. A.W. Snyder and D.J. Mitchell, Science **276**, 1538 (1997). 262
9. A.M. Turing, Philos. Trans. R. Soc. London, Ser. B **237**, 37 (1952); L.A. Lugiato and R. Lefever, Phys. Rev. Lett. **58**, 2209 (1987). 262, 263
10. A. Barsella, C. Lepers, M. Taki, and P. Glorieux J. Opt. B: Quantum Semiclass. Opt. **1**, 64 (1999); M. Vaupel, A. Maître, and C. Fabre, Phys. Rev. Lett. **83**, 5278 (1999); R. Kuszelewicz, et al., Phys. Rev. Lett. **84**, 6006 (2000); T. Ackemann, et al., Opt. Lett. **25**, 814 (2000). 262
11. P.L. Ramazza, S. Ducci, and F.T. Arecchi, Phys. Rev. Lett. **81**, 4128 (1998); S. Ducci, P.L. Ramazza, W. Gonzàlez-Viñas, and F.T. Arecchi, Phys. Rev. Lett. **83**, 5210 (1999); F.T. Arecchi, S. Boccaletti, and P.L. Ramazza, Phys. Rep. **318**, 1 (1999). 262

12. M. Tlidi, A.G. Vladimirov, and P. Mandel, IEEE J. Quantum Electron. **39**, 216 (2003). 262
13. M. Tlidi and M. Taki, Phys. Rev. Lett. **91**, 023901 (2003). 262
14. M. Brambilla, L.A. Lugiato, and M. Stefani, Europhys. Lett. **34**, 109 (1996); W.J. Firth and A.J. Scroggie, Phys. Rev. Lett. **76**, 1623 (1996). 262
15. V.B. Taranenko, K. Staliunas, and C.O. Weiss, Phys. Rev. A **56**, 1582 (1997); Yu.A. Logvin, B. Schäpers, and T. Ackemann, Phys. Rev. E **61**, 4622 (2000); S. Residori, T. Nagaya, and A. Petrossian, Europhys. Lett. **63**, 531 (2003). 262
16. J. Lega, J.V. Moloney, and A.C. Newell, Phys. Rev. Lett. **73**, 2978 (1994); S. Longhi and A. Geraci, Phys. Rev. A **54**, 4581 (1996); G.J. de Valcarcel, K. Staliunas, E. Roldán, and V.J. Sánchez-Morcillo, Phys. Rev. A **54**, 1609 (1996); Z.H. Musslimani, Physica A **249**, 141 (1998); C. Etrich, U. Peschel, and F. Lederer, Phys. Rev E **56**, 4803 (1997); P. Lodahl, M. Bache, and M. Saffman, Opt. Lett. **25**, 654 (2000); M. Le Berre, E. Ressayre, and A. Tallet, J. Opt. B: Quantum Semiclass. Opt. **1**, 107 (1999); G.-L. Oppo, A.J. Scroggie, and W.J. Firth, J. Opt. B: Quantum Semiclass. Opt. **1**, 133 (1999); A. Barsella, C. Lepers, M. Taki, and M. Tlidi, Opt. Comm. **232**, 381 (2004). 262
17. P. Mandel and M. Tlidi, J. Opt. B: Quantum Semiclass. Opt. **6**, R60 (2004). 262
18. S. Longhi, Phys. Rev. A **59**, 4021 (1999); G.-L. Oppo, A.J. Scroggie, and W.J. Firth, Phys. Rev. E **63**, 066209 (2001); M. Tlidi, M. Taki, M. Le Berre, E. Ressayre, A. Tallet, and L. Di Menza, J. Opt. B: Quantum Semiclass. Opt. **6**, S421 (2004). 262, 271
19. See e.g. A.P. Piskarskas, Opt. Photon. News **7**, 25 (1997); R.L. Byer and A.S. Piskarskas, feature issue on optical parametric oscillators, J. Opt. Soc. Am. **B10**, 1656 (1993). 262
20. H.J. Kimble, *Fundamental Systems in Quantum Optics* (J. Dalibard, J.M. Raimond, J. Zinn-Justine, Elsevier Sc., Amsterdam), 545 (1992). 262
21. M. Lassen, P. Tidemand-Lichtenberg, and P. Buchehave, Phys. Rev. A **72**, 023817 (2005); S. Ducci, N. Treps, A. Maître, and C. Fabre, Phys. Rev. A **64**, 023803 (2001). 263
22. M. Santagiustina, P. Colet, M. San Miguel, and D. Walgraef, Phys. Rev. E **58**, 3843 (1998); G. Izús, M. Santagiustina, M. San Miguel, and P. Colet, J. Opt. Soc. Am. B **16**, 1592 (1999); J.N. Kutz, T. Erneux, S. Trillo, and M. Haelterman, J. Opt. Soc. Am. B **16**, 1936–1941 (1999); M. Taki, M. San Miguel, and M. Santagiustina, Phys. Rev. E **61**, 2133 (2000). 263
23. L. Pastur, M.T. Westra, and W. van de Water, Physica D **174**, 71 (2003); P. Gondret, P. Ern, L. Meignin, and M. Rabaud, Phys. Rev. Lett. **82**, 1442 (1999); P. Büchel and M. Lücke, Phys. Rev. E **61**, 3793 (2000); X. Nicolas, A. Mojtabi, and J.K. Platten, Phys. Fluids **9**, 337 (1997); H.R. Brand, R.J. Deissler, and G. Ahlers, Phys. Rev. A **43**, 4262 (1991); P. Huerre and P.A. Monkewitz, Ann. Rev. Fluid. Mech. **22**, 473 (1990). 263
24. A. Couairon and J.M. Chomaz, Phys. Rev. Lett. **79**, 2666 (1997); R.J. Briggs, *Electron-Stream Interaction with Plasmas*, (MIT Press, Cambridge, MA, 1964). 263
25. N. Mitarai and H. Nakanishi, Phys. Rev. Lett. **85**, 1766 (2000). 263
26. N. Israeli, D. Kandel, M.F. Schatz, and A. Zangwill, Surf. Sci. **494**, L735 (2001). 263
27. G. Agez, P. Glorieux, M. Taki, and E. Louvergneaux, Phys. Rev. A **74**, 043814 (2006); S. Trillo, M. Haelterman, and A. Sheppard, Opt. Lett. **22**, 970 (1997); T. Nishikawa and N. Uesugi, Opt. Comm. **140**, 277 (1997); J. Appl. Phys. **77**, 4941 (1995); A.V. Smith, W.J. Alford, T.D. Raymond, and M.S. Bowers, J. Opt. Soc. Am. B **12**, 2253 (1995). 263
28. R. Zambrini and F. Papoff, Phys. Rev. E **73**, 016611 (2006); F. Papoff and R. Zambrini, Phys. Rev. Lett. **94**, 243903 (2005); E. Louvergneaux, C. Szwaj, G. Agez, P. Glorieux, and M. Taki, Phys. Rev. Lett. **92**, 043901 (2004); H. Ward, M. Taki, and P. Glorieux, Opt. Lett. **27**, 348 (2002); M. Santagiustina, P. Colet, M. San Miguel, and D. Walgraef, Phys. Rev. Lett. **79**, 3633 (1997). 263
29. W. van Saarloos, Phys. Rep. **386**, 29 (2003); I.S. Aranson, B.A. Malomed, L.M. Pismen, and L.S. Tsimring, Phys. Rev. E **62**, R5 (2000); G.T. Dee and W. van Saarloos, Phys. Rev. Lett. **60**, 2641 (1988). 263
30. C. Durniak, M. Taki, M. Tlidi, P.L. Ramazza, U. Bortolozzo, and G. Kozyreff, Phys. Rev. E **72**, 026607 (2005). 263
31. R. Zambrini, M. San Miguel, C. Durniak, and M. Taki, Phys. Rev. E **72**, 025603 (2005). 263
32. H. Ward, M.N. Ouarzazi, M. Taki, and P. Glorieux, Eur. Phys. J. D **3**, 275 (1998). 264, 265, 266, 267

33. C.M. Bender and S.A. Orszag, *Advanced Mathematical Methods for Scientists and Engineers*, (Springer-Verlag, New York, 1999). 268
34. L. Brevdo, J. Appl. Math. Phys. (ZAMP) **42**, 911 (1991).
35. K. Staliunas and V.J. Sanchez-Morcillo, Phys. Rev. A **57**, 1454 (1998). 269
36. M. Taki, N. Ouarzazi, H. Ward, and P. Glorieux, J. Opt. Soc. Am B **17**, 997 (2000). 271
37. S. Longhi, Opt. Commun. **149**, 335 (1998). 277
38. J.A. Powell and A.C. Newell, Phys. Rev. A **44**, 997 (1991). 277
39. W. van Saarloos and P.C. Hohenberg, Phys. Rev. Lett. **64**, 749 (1990); W. van Saarloos, Physica D **56**, 303 (1992). 277
40. J.A. Powell and A.C. Newell, Phys. Rev. A **44**, 3636 (1991). 277, 278
41. S. Fauve and O. Thual, Phys. Rev. Lett. **64**, 282 (1996). 279
42. J.M. Soto-Crespo, N.N. Akhmediev, V.V. Afanasjev, J. Opt. Soc. Am. B **13**, 1439 (1996). 282
43. J.M. Soto-Crespo, N.N. Akhmediev, V.V. Afanasjev, and S. Wabnitz, Phys. Rev. E **55**, 4783 (1997). 282
44. O. Descalzi, Phys. Rev. E **72**, 046210 (2005). 282
45. R.J. Deissler and H.R. Brand, Phys. Rev. Lett. **72**, 478 (1994). 282
46. H.P. Tian, Z.H. Li, J.P. Tian, G.S. Zhou, J. Zi, Appl. Phys. B **78**, 199 (2004). 282
47. G.P. Agrawal, *Nonlinear Fiber Optics*, 3rd ed. (Academic Press, New York, 2001). 282
283

Discrete Breathers with Dissipation

S. Flach and A.V. Gorbach

Abstract The interplay between discreteness and nonlinearity leads to the emergence of a new class of nonlinear excitations, viz. discrete breathers. These time-periodic and spatially localized excitations correspond to generic exact solutions of the underlying nonlinear lattice models. Discrete breathers are not confined to certain lattice dimensions, nor are they sensitive to the particular type of nonlinearity in the system. They are usually dynamically and structurally stable and emerge in a variety of physical systems, ranging from lattice vibrations and magnetic excitations in crystals to light propagation in photonic structures and cold atom dynamics in periodic optical traps. Basic properties of discrete breathers, including spatial localization and stability, are briefly discussed in this chapter. Special focus is placed on a subclass of dissipative discrete breathers. Dissipation eliminates extended waves and allows for various resonances of discrete breathers with damped cavity modes. We discuss applications of the discrete breather concept in systems where dissipation is not only unavoidable but essential in order to observe and manipulate discrete breathers, and in order to use them for spectroscopic tools, amongst others.

1 Introduction

This chapter is about localized excitations in spatially extended discrete systems, i.e. lattices. These systems are translationally invariant, implying the absence of disorder and defects. The common expectation – throw a stone into the water of a

S. Flach
Max-Planck-Institut für Physik komplexer Systeme, Nöthnitzer Str. 38, D-01187 Dresden, Germany, flach@mpipks-dresden.mpg.de

A.V. Gorbach
Centre for Photonics and Photonic Materials, Department of Physics, University of Bath, Bath BA2 7AY, UK

Flach, S., Gorbach, A.V.: *Discrete Breathers with Dissipation.* Lect. Notes Phys. **751**, 289–320 (2008)
DOI 10.1007/978-3-540-78217-9_11

lake and follow the evolution of the localized surface wave perturbation – is that an initially localized excitation would distribute its energy over the entire system in the course of time. What could stop such a delocalization process? It needs just two ingredients – the above-mentioned discreteness of the system and evolution equations which are nonlinear. As a result, a new paradigm of nonlinear science has recently emerged – the concept of *discrete breathers* (DB), equally labelled *intrinsic localized modes* (ILM) in solid state physics and *discrete solitons* (DS) in nonlinear optics. These exact solutions of a huge variety of underlying nonlinear lattice models are typically characterized by being *time periodic* and *spatially localized*, independent of the actual (assumed to be large) size of the lattice, independent of the spatial dimension of the lattice, mostly independent of the actual choice of nonlinear forces acting on the lattice, and so on. Mastering their mathematical properties in *Hamiltonian* lattices allows us to also include the effects of dissipation, driving and quantization with relative ease, just to name a few important ones. We will especially focus on dissipative discrete breathers.

Nonlinearity is inherent in many systems in nature. Discreteness is common as well – e.g. solids (crystals) and molecules provide a natural underlying lattice, while artificial systems, e.g. those based on Bose–Einstein condensates in optical lattices, Josephson junction networks, optical devices, or micro-mechanical devices, also involve lattice structures. It thus makes perfect sense to understand the mechanisms of localization in nonlinear lattices and to apply that knowledge to various fields of physics, chemistry, biology, and mechanics.

The first report by Ovchinnikov on localized excitations in one-dimensional chains of coupled anharmonic oscillators dates back to 1969 [1]. After a long time span, Sievers and Takeno took the issue up again, considering the famous Fermi–Pasta–Ulam (FPU) chain and obtaining localized excitations, starting from 1988 [2, 3, 4]. From the beginning of the 1990s, a large number of research groups began to study these localized excitations with great mathematical rigour and detail (see, e.g. [5] for a review). Since then, a considerable amount of further mathematical beauty was (and still is being) added to the theory of localized excitations. In addition to this, it is most important to note that, since 1998, experimental studies have been carried out on a large variety of very different systems, demonstrating the fruitfulness of the concept of localization by discreteness and nonlinearity. In the following, we will discuss the basic aspects and some of the more recent developments, including the effect of dissipation.

1.1 Spatial Discreteness and Nonlinearity

Let us study the combined effect of nonlinearity and discreteness on the spatial localization of a discrete breather at a basic level. To do this, we look into the dynamics of a one-dimensional chain of interacting (scalar) oscillators or atoms with the Hamiltonian

$$H = \sum_n \left[\frac{1}{2} p_n^2 + V(x_n) + W(x_n - x_{n-1}) \right]. \tag{1}$$

The integer n marks the lattice site number of a possibly infinite chain, and x_n and p_n are the canonically conjugated coordinate and momentum of a degree of freedom associated with site number n. The on-site potential, V, and the interaction potential, W, satisfy $V'(0) = W'(0) = 0$, $V''(0), W''(0) \geq 0$. This choice ensures that the classical ground state $x_n = p_n = 0$ is a minimum of the energy H. The equations of motion read

$$\dot{x}_n = p_n, \ \dot{p}_n = -V'(x_n) - W'(x_n - x_{n-1}) + W'(x_{n+1} - x_n). \tag{2}$$

Let us linearize the equations of motion around the classical ground state. We obtain a set of linear coupled differential equations whose solutions are small amplitude plane waves:

$$x_n(t) \sim \mathrm{e}^{\mathrm{i}(\omega_q t - qn)}, \ \omega_q^2 = V''(0) + 4W''(0) \sin^2\left(\frac{q}{2}\right). \tag{3}$$

These waves are characterized by a wave number, q, and a corresponding frequency, ω_q. All allowed plane wave frequencies fill a part of the real axis which is called the linear spectrum. Due to the underlying lattice, the frequency ω_q depends periodically on q, and its absolute value has always a *finite upper bound*. The maximum (Debye) frequency of small amplitude waves is $\omega_\pi = \sqrt{V''(0) + 4W''(0)}$. The dispersion relation, ω_q, is shown in Fig. 1. Depending on the choice of the potential

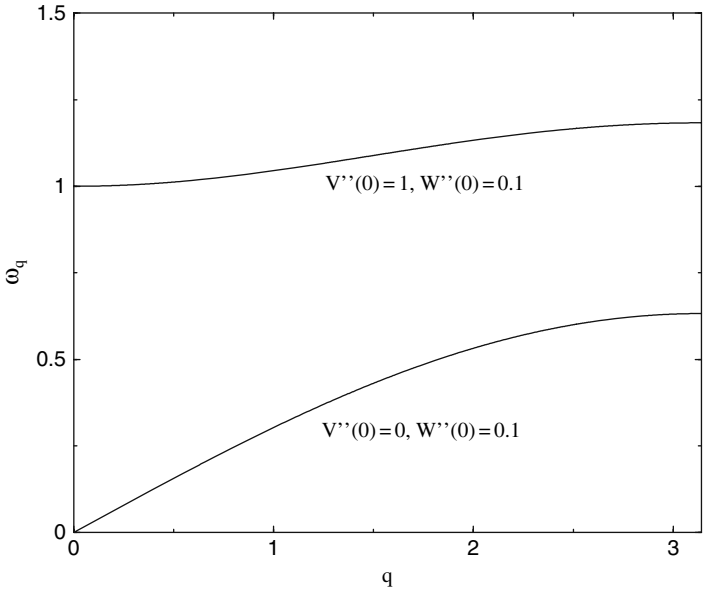

Fig. 1 The dispersion relation for small amplitude plane waves of the model (1)

$V(x)$, it can be either acoustic or optic-like, for $V(0)=0$ and $V(0)\neq 0$, respectively. In the first case, the linear spectrum covers the interval $-\omega_\pi \leq \omega_q \leq \omega_\pi$, which includes $\omega_{q=0}=0$. In the latter case, an additional (finite) gap opens for $|\omega_q|$ below the value $\omega_0=\sqrt{V''(0)}$. Two further characteristics of the linear spectrum are the group velocity, $v_{\rm g}$, and the phase velocity, $v_{\rm ph}$. The group velocity $v_{\rm g}(q)={\rm d}\omega_q/{\rm d}q$ is a periodic function of q and describes the propagation speed of a wave packet centred at q. At the edge of the linear spectrum, $v_{\rm g}=0$. Otherwise its absolute value has a finite upper bound. The phase velocity $v_{\rm ph}=\omega_q/q$ is a non-periodic oscillating function of q. It covers the whole real axis for an optic-like linear spectrum, since $\omega_{q=0}\neq 0$. Its absolute value has a finite upper bound, $|v_{\rm ph}|\leq v_{\rm g}(q=0)$, for acoustic-like linear spectra.

For large amplitude excitations, the linearization of the equations of motion is no longer correct. As in the case of a single anharmonic oscillator, the frequency of possible time-periodic excitations will depend on the amplitude of the excitation and thus may be located outside the linear spectrum. Let us assume that a time-periodic and spatially localized state, i.e. a *discrete breather*, $\hat{x}_n(t+T_{\rm b})=\hat{x}_n(t)$ exists as an exact solution of (2) with the period $T_{\rm b}=2\pi/\Omega_{\rm b}$. Due to its time periodicity, we can expand $\hat{x}_n(t)$ into a Fourier series:

$$x_n(t)=\sum_k A_{kn}{\rm e}^{{\rm i}k\Omega_{\rm b}t}. \tag{4}$$

The Fourier coefficients are, by assumption, also localized in space:

$$A_{k,|n|\to\infty}\to 0. \tag{5}$$

Inserting this ansatz into the equations of motion (2) and linearizing the resulting algebraic equations for Fourier coefficients in the spatial breather tails (where the amplitudes are, by assumption, small), we arrive at the following linear algebraic equations:

$$k^2\Omega_{\rm b}^2 A_{kn}=V''(0)A_{kn}+W''(0)(2A_{kn}-A_{k,n-1}-A_{k,n+1}). \tag{6}$$

If $k\Omega_{\rm b}=\omega_q$, the solution of (6) is $A_{k,n}=c_1{\rm e}^{{\rm i}qn}+c_2{\rm e}^{-{\rm i}qn}$. Any non-zero (however small) amplitude $A_{k,n}$ will thus oscillate without further spatial decay, contradicting the initial assumption. However, if

$$k^2\Omega_{\rm b}^2\neq\omega_q^2 \tag{7}$$

for any integer k, then the general solution of (6) is given by $A_{k,n}=c_1\kappa^n+c_2\kappa^{-n}$, where κ is a real number which depends on ω_q, $\Omega_{\rm b}$, and k. It always admits an (actually exponential) spatial decay by choosing either c_1 or c_2 to be non-zero. In order to satisfy (7) for at least one real value of $\Omega_{\rm b}$ and any integer k, we require that $|\omega_q|$ be bounded from above. This is precisely the reason why the spatial lattice is needed. In contrast, most spatially continuous field equations will have linear spectra which are unbounded. Then, resonances of higher-order harmonics of a localized excitation with the linear spectrum become unavoidable. The non-resonance condition (7)

is thus an (almost) necessary condition for obtaining a time-periodic localized state on a Hamiltonian lattice [6, 7].

The existing analysis can be extended to more general classes of discrete lattices, including, e.g. long-range interactions between sites, more degrees of freedom per site, and higher-dimensional lattices. But the resulting non-resonance condition (7) maintains its generality, illustrating the key role of discreteness and nonlinearity for the existence of discrete breathers.

As with any rule, the non-resonance condition may also have exceptions. However, as with any exception, there is a price to pay. When staying within the class of spatially continuous Hamiltonian systems, the price is imposing additional symmetries. While that may be of particular interest for a given application, the additional symmetries usually restrict the richness of possible solutions. And losing the symmetries leads to a loss of localized excitations – in contrast to the nonlinear lattice case, where no further symmetries are required.

While the nonlinear lattice appears to be a natural mathematical path to avoid resonances with plane waves which occur in spatially continuous nonlinear Hamiltonian field equations, there are other ways things can evolve. If resonances with plane waves are an obstacle, then we either remove the resonances or simply remove the plane waves! The first possibility can be realized by using a lattice, or restricting ourselves to equations which either do not contain linear terms or where at least the linear interaction terms vanish, making the linear spectrum degenerate – no matter whether for a lattice or a continuum. The second possibility – removing the plane waves – can be achieved by considering dissipative systems. Indeed dissipation will prevent the persistence of plane waves travelling over infinite distances. Thus, delocalization by itself is then not a problem. The loss of energy inside a breather core due to dissipation has to be taken care of by properly pumping more energy into the breather. We will discuss examples and note that a recently rapidly developing branch of *dissipative solitons* appears to follow exactly this latter path.

1.2 Why Only Time-Periodic Orbits?

In the previous section, we demonstrated how the interplay between nonlinearity and discreteness supports time-periodic and spatially localized solutions, i.e. discrete breathers. What can we say about the existence of more general types of localized solutions with dynamical behaviour which is not time periodic? An analogous approach shows that for a quasi-periodic DB with N incommensurate frequencies $\{\Omega_1, \Omega_2, ..., \Omega_N\}$, the non-resonance condition (7) transforms into [7]

$$\{k_1\Omega_1 + k_2\Omega_2 + \cdots + k_N\Omega_N\}^2 \neq \omega_q^2, \tag{8}$$

with k_i being arbitrary integers. In other words, none of the principal frequencies $\{\Omega_1, \Omega_2, ..., \Omega_N\}$ nor any linear combination of their multiples should resonate with the linear spectrum. However, any incommensurate pair of frequencies Ω_1 and Ω_2,

with irrational ratio Ω_1/Ω_2, will generate an infinite number of pairs k_1, k_2 which violate the non-resonance condition (8) [7]. Therefore, in general, quasi-periodic DBs are not expected to exist as exact spatially localized solutions.

Another question concerns the possibility of existence of moving DBs. A rather general definition of a moving DB assumes a localized object which translates n sites in a certain direction after m periods of internal oscillations, with the ratio n/m being irrational in general. In a one-dimensional chain, such a moving DB corresponds to a solution of (2) with the form

$$x_n(t) = \phi(\xi, t), \qquad \xi = n - Vt, \tag{9}$$

$$\phi(\xi, t + T_\mathrm{b}) = \phi(\xi, t), \qquad \phi(\xi \to \pm\infty, t) \to 0. \tag{10}$$

A detailed analysis of possible resonances has been carried out in [8, 9]. It follows that one has to avoid resonances of the velocity V with *phase velocities* v_ph of small amplitude plane waves (where the linear spectra which have been modified, as compared with the original underlying one). The essence is that these resonances cannot be avoided, so that moving DBs are not expected to be exact solutions for a general nonlinear lattice. Hence, moving DBs face the obstacle of resonances with phase velocities of plane waves. By removing the plane waves (e.g. by adding dissipation) we can again try to escape from the above-mentioned resonances and construct quasi-periodic DBs and even moving DBs.

1.3 Examples of Discrete Breather Solutions

Let us now present discrete breather solutions for various lattices. We start with a chain (1) with the functions

$$V(x) = x^2 + x^3 + \frac{1}{4}x^4, \; W(x) = 0.1x^2. \tag{11}$$

The spectrum, ω_q, is optic-like and is shown in Fig. 2. Discrete breather solutions can have frequencies Ω_b which are located either below or above the linear spectrum. The time-reversal symmetry of (2) allows us to search for DB displacements, $x_n(t=0)$, when all velocities $\dot{x}_n(t=0)$ are zero. These initial displacements are computed with high accuracy and plotted in the insets in Fig. 2 [10]. We show solutions for two DB frequencies located above and below ω_q – their actual values are marked with the green arrows. For each DB frequency, we show two different spatial DB patterns among an infinite number of other possibilities. The high-frequency DBs ($\Omega_\mathrm{b} \approx 1.66$) occur for large-amplitude, high-energy motion, with adjacent particles moving out of phase. Low-frequency DBs ($\Omega_\mathrm{b} \approx 1.26$) occur for small-amplitude motion, with adjacent particles moving in phase.

In Fig. 3, we show two DB solutions for a Fermi–Pasta–Ulam chain of particles coupled via anharmonic springs, $V(x) = 0, W(x) = \frac{1}{2}x^2 + \frac{1}{4}x^4$ (cf. (1)) which is of acoustic type [11]. The DB frequency in both cases is $\Omega_\mathrm{b} = 4.5$. Again, the

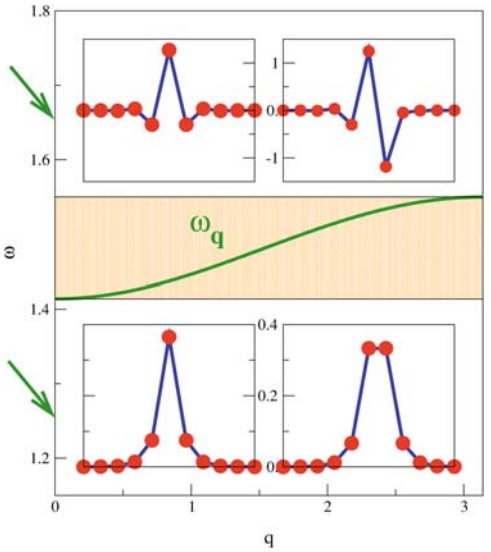

Fig. 2 The frequency versus wave-number dependence of the linear spectrum for a one-dimensional chain of anharmonic oscillators with potentials (11). The chosen DB frequencies are marked with green arrows and they lie outside the linear spectrum, ω_q. Red circles indicate the oscillator displacements for a given DB solution, with all velocities equal to zero. Lines connecting circles are guides for visualization (Figure adapted from [10])

displacements x_n are shown for an initial time when all velocities vanish. In the inset, we plot the strain $u_n = x_n - x_{n-1}$ on a log-normal scale. The DB solutions are exponentially localized in space.

Finally, we show DB solutions for a *two-dimensional* square lattice of anharmonic oscillators with nearest-neighbour coupling. The equations of motion read

$$\ddot{x}_{i,j} = k(x_{i+1,j} + x_{i-1,j} - 2x_{i,j}) + k(x_{i,j+1} + x_{i,j-1} - 2x_{i,j}) - x_{i,j} - x_{i,j}^3 \qquad (12)$$

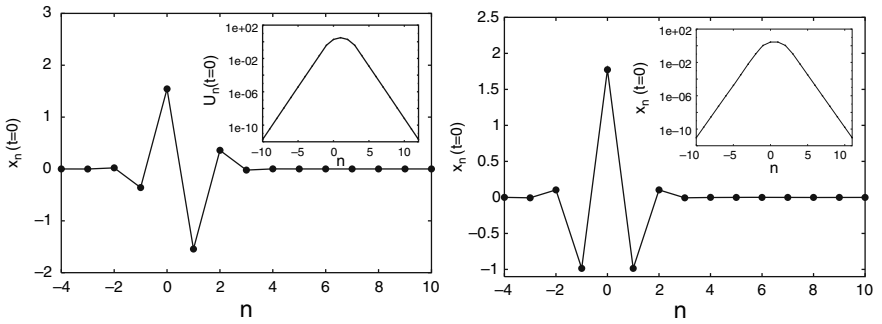

Fig. 3 Discrete breather solutions for a Fermi–Pasta–Ulam chain (see text) (Figure adapted from [11])

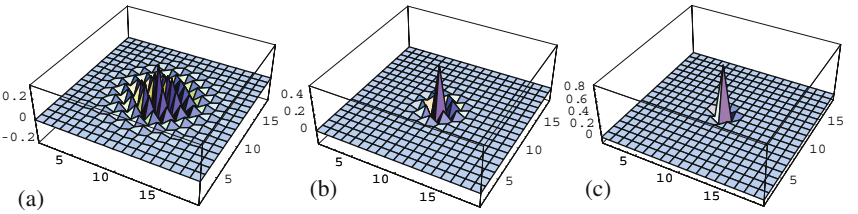

Fig. 4 Displacements of DBs on a two-dimensional lattice (12) with $k = 0.05$, with all velocities equal to zero. (**a**) $\Omega_b = 1.188$; (**b**) $\Omega_b = 1.207$; (**c**) $\Omega_b = 1.319$ (Figure adapted from [12])

which corresponds to oscillator potentials $V(x) = \frac{1}{2}x^2 + \frac{1}{4}x^4$. In Fig. 4, we plot the oscillator displacements with all velocities equal to zero for three different DB frequencies and $k = 0.05$ [12]. Adjacent oscillators move out of phase for all these cases.

We conclude this section by emphasizing that DB solutions can typically be localized on a few lattice sites, regardless of the lattice dimension. Thus, little overall coherence is needed to excite a state nearby – just a few sites have to oscillate coherently, while the rest of the lattice does not participate strongly in the excitation.

2 Basic Properties of Discrete Breathers

2.1 Spatial Localization

Discrete breathers are generic solutions on nonlinear lattices. As for their localization properties in space, we can consider both the profile inside the core of the DB and the decay properties in its spatial tails. The former aspect is the hardest one, since it needs mastery of the full nonlinear equations. The latter one is more accessible since breather amplitudes become small in their tails. A linearization of the equations of motion in the tails is then usually expected to correctly describe the tail asymptotics. Furthermore, one can even systematically go beyond such a linearization and treat nonlinear corrections as well.

To be specific, we will consider a model with one degree of freedom per unit cell. Generalizations to more complicated cases should be straightforward. The Hamiltonian reads

$$H = \sum_l \left[\frac{1}{2} P_l^2 + V(X_l) + \sum_{l'} W_{l,l'}(X_l - X_{l'}) \right]. \tag{13}$$

The hyper-cubic lattice has dimension d, and the lattice index l is a d-dimensional vector with integer components. The interaction potential $W_{l,l'} = W_{l+m,l'+m}$, and hence the model, is translationally invariant. All zero and first derivatives of the

potential functions vanish for zero arguments. By the virtue of the discreteness, the frequency spectrum, ω_q, of small amplitude plane waves is bounded in absolute value.

A discrete breather solution is given by

$$X_l(t) = \sum_k A_{kl} \mathrm{e}^{\mathrm{i}k\Omega_\mathrm{b} t}. \tag{14}$$

Here the Fourier number, k, is a scalar integer which is independent of the lattice dimension, d. The breather is localized in space, which implies

$$A_{k,|l|\to\infty} \to 0. \tag{15}$$

Assuming that the potential functions have non-zero second derivatives at their origin, i.e. $V''(0) = v_2 \neq 0$ and $W''_{0,l} = w_{0,l} \neq 0$ for some l, we may try to linearize the algebraic equations for the Fourier coefficients A_{kl}:

$$k^2\Omega_\mathrm{b}^2 A_{kl} = v_2 A_{kl} + \sum_{l'} w_{l,l'}(A_{kl} - A_{kl'}). \tag{16}$$

Since the Fourier amplitude equations decouple after linearization, we can solve each of these equations on its own. Recalling that the necessary condition for the possible localization of each Fourier amplitude is the non-resonance condition $k\Omega_\mathrm{b} \neq \omega_q$, the spatial decay of the k th amplitude is then given by the lattice Green's function [13]

$$G_\lambda(l) = \int_{1.\mathrm{BZ}} \frac{\cos(ql)}{\omega_q^2 - \lambda} \mathrm{d}^d q,\ \lambda = k^2\Omega_\mathrm{b}^2. \tag{17}$$

Here, the integration extends over the first Brillouin zone of the reciprocal wave-number space, q. We note that the spectrum, ω_q, is periodic in q, with its irreducible multi-dimensional period residing exactly in the first Brillouin zone. Fixing the direction of l and changing its absolute value, (17) will then generate the Fourier coefficients of the periodic function $(\omega_q^2 - \lambda)^{-1}$. The spatial decay of the breather is thus characterized by the convergence properties of the corresponding Fourier series, and the convergence properties of the Fourier series are defined through the analytical properties of the corresponding periodic function.

We describe a lattice as having short-range interactions if the corresponding squared spectrum, ω_q^2, is an analytic function on the extended wave-vector space q, i.e. where all its derivatives, at any point q, exist and are finite. Examples are lattices with nearest-neighbour interactions, and more general lattices with finite-size interactions where $w_{0,l} = 0$ for $|l| > r$, with r being a positive real number. However, we can even generalize this by considering lattices where the harmonic interaction potential extends over the whole lattice, with exponentially decaying amplitudes [14] $w_{0,l} \sim \mathrm{e}^{-|l|/r}$ for $|l| \gg r$. For all these cases, the denominator $(\omega_q^2 - \lambda)^{-1}$, which appears in (17), is an analytic periodic function of q, and thus the convergence of its Fourier series and the spatial localization of a DB are bound by exponential tails [15]. The exponent will depend on $\lambda = k^2\Omega_\mathrm{b}^2$. The localization length will grow whenever any of the multiples $k\Omega_\mathrm{b}$ come close to an edge of the spectrum ω_q.

In the insets in Fig. 3, the exponentially localized profiles of two DBs are shown for a one-dimensional FPU chain with nearest-neighbour interaction. A comparison between the numerically obtained localization length and the prediction from (17) has been made for various one-dimensional lattices in [7, 16] and is discussed extensively in [5].

Here, we also present the amplitude distribution of a DB solution for a three-dimensional cubic DNLS lattice with nearest-neighbour interaction:

$$\dot{\Psi}_l = \mathrm{i}(\Psi_l + |\Psi_l|^2\Psi_l + 0.1\sum_{m\in N_l}\Psi_m), \tag{18}$$

where N_l denotes the set of nearest neighbours of l. On making the substitution $\Psi_l = A_l e^{i\Omega_b t}$, the algebraic equations are solved for the real amplitudes A_l [17] for a lattice with size 31^3. To visualize the solution, we place the DB centre at the lattice site $l = (16,16,16)$ and plot its amplitude distribution as a function of the (x,y) coordinates in a plane with fixed coordinate $z = 16$, which contains the lattice site with the maximum breather amplitude. Note that the DB is strongly localized on a few lattice sites (see left plot in Fig. 5). The same solution, when displayed on a logarithmic amplitude scale, shows a conical structure (see right plot in Fig. 5), as expected from the predicted exponential decay in space.

We describe a lattice as having long-range interactions if the corresponding squared spectrum, ω_q^2, is a non-analytic function on the extended wave-vector space q, i.e. some of its derivatives, at some points q, diverge or do not exist. That happens, for example, when a harmonic interaction potential extends over the whole lattice and decays algebraically with increasing distance $w_{0,l} \sim |l|^{-s}$, with some positive exponent, s. Despite the slow decay of interactions, discrete breathers still exist, but now their localization will be slower than exponential. In fact, what matters is

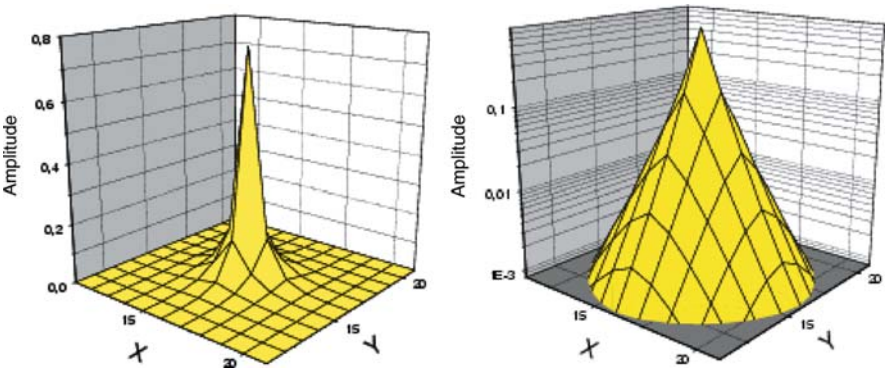

Fig. 5 Amplitude distribution of a breather solution of the three-dimensional DNLS system (18) with size $N = 31^3$. Actually, only a distribution in a cross-section $(x;y)$ plane is shown. (Here, the plane cuts the centre of the breather.) The intersections of the grid lines correspond to the actual amplitudes, while the rest of the grid lines are only guides for visualization. *Left panel* – amplitudes are shown on a linear scale. *Right panel* – the same solution with amplitudes plotted on a logarithmic scale. Data are from Fig. 2 in [17]

the analysis of the degree of non-analyticity of ω_q^2, which straightforwardly gives a power-law convergence of the Fourier series (17) (see [15]), and thus an algebraic spatial localization of DBs. As shown in [18], more complicated spatial decay laws apply, with crossovers from exponential to algebraic decay.

In the case of a purely nonlinear interaction [7, 19, 20, 21, 22, 23, 24, 25], the spatial decay of a breather is super-exponential, e.g.

$$\ln|\ln|A_n|| \approx n\ln(2m-1). \tag{19}$$

Such solutions are also called quasi-compact.

Other studies concern resonances with Goldstone modes [26] and nonlinear corrections [16].

2.2 Dynamical Stability of Perturbed Discrete Breathers

Once a DB solution is found, an important question arises regarding its stability. One has to study the problem of evolution of a perturbation, $\varepsilon_n(t)$, added to the DB solution, $\hat{x}_n(t)$. If the perturbation amplitude is large enough, one may expect generic dynamical features of a non-integrable system, which are usually rather complicated and hard to address analytically. However, by imposing certain restrictions on the size of perturbation, one may linearize the resulting equations for $\varepsilon_n(t)$ [27, 28]:

$$\ddot{\varepsilon}_n = -\sum_m \left.\frac{\partial^2 H}{\partial x_m \partial x_n}\right|_{\{\hat{x}_l(t)\}} \varepsilon_m, \tag{20}$$

where H is the Hamiltonian of the system. Within the linear approximation in the perturbation amplitude $\varepsilon_n(t)$, the DB acts as a parametric time-periodic driver, and the problem (20) corresponds to a time-dependent Hamiltonian, $\widetilde{H}(t)$:

$$\widetilde{H}(t) = \sum_n \left[\frac{\pi_n^2}{2} + \frac{1}{2}\sum_m \left.\frac{\partial^2 H}{\partial x_n \partial x_m}\right|_{\{\hat{x}_l(t)\}} \varepsilon_n \varepsilon_m\right], \tag{21}$$

$$\dot{\varepsilon}_n = \frac{\partial \widetilde{H}}{\partial \pi_n},\ \dot{\pi}_n = -\frac{\partial \widetilde{H}}{\partial \varepsilon_n}. \tag{22}$$

The specific structure of the Hamiltonian, $\widetilde{H}$, ensures the conservation law $\dot{I} = 0$ [27, 29] for the symplectic product

$$I = \sum_n \left[\varepsilon_n(t)\pi_n'(t) - \varepsilon_n'(t)\pi_n(t)\right] \tag{23}$$

of any two trajectories $y = \{\varepsilon_n, \pi_n\}$ and $y' = \{\varepsilon_n', \pi_n'\}$. It can be written as the scalar product

$$I = (Jy, y'), \tag{24}$$

where J is the $2N \times 2N$ matrix

$$J = \begin{pmatrix} 0 & \mathrm{I} \\ -\mathrm{I} & 0 \end{pmatrix}, \tag{25}$$

and I is the $N \times N$ unit matrix. The conservation of the symplectic product I implies that the evolution matrix, $U(t)$, which maps the linearized phase space flow around the given periodic orbit (corresponding to the DB solution) onto itself

$$\begin{Bmatrix} \varepsilon(t) \\ \pi(t) \end{Bmatrix} = U(t) \begin{Bmatrix} \varepsilon(0) \\ \pi(0) \end{Bmatrix}, \tag{26}$$

is symplectic:

$$U^{\mathrm{T}} J U = J. \tag{27}$$

Due to the time periodicity of all the coefficients on the right-hand side of (20), the dynamics of the small-amplitude perturbation $\varepsilon_n(t)$ is fully determined by the Floquet matrix $\mathscr{F} \equiv U(T_{\mathrm{b}})$, i.e. by the evolution matrix over the DB period, T_{b}. Thus, the problem is reduced to the determination of eigenvalues and eigenvectors of the symplectic Floquet matrix $\mathscr{F}$.

The condition of linear (marginal) stability of the DB solution is that all perturbations remain bounded in time. This implies that all the Floquet eigenvalues λ_ν are located on the unit circle in the complex plane: $|\lambda_\nu| = 1$ (see Fig. 6, left picture).

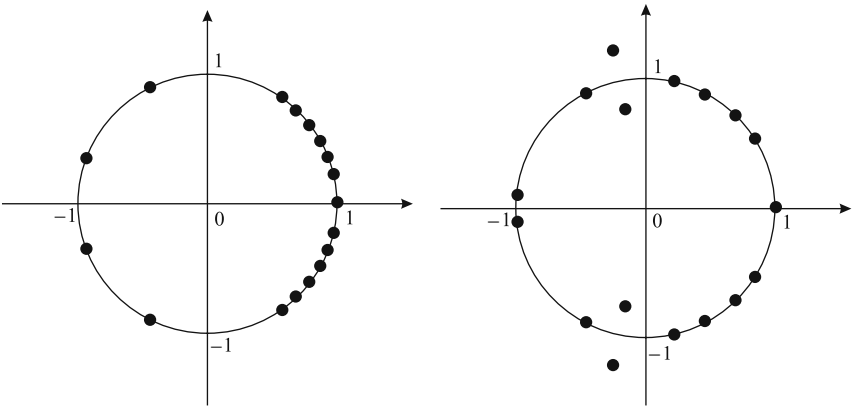

Fig. 6 Schematic view of an outcome of the Floquet analysis of a breather in a Hamiltonian system, Floquet eigenvalues (*filled circles*), and the unit circle in the complex plane. *Left picture*: stable breather (all eigenvalues are located on the unit circle). *Right picture*: unstable breather (two pairs of eigenvalues have collided on the unit circle, and one eigenvalue per pair departs outside it). Note that the group of eigenvalues in proximity on the unit circle correspond to the plane wave continuum (extended Floquet eigenstates), while the separated eigenvalues on the unit circle correspond to localized Floquet eigenstates

All Floquet eigenvalues for a typical DB solution can be divided into two groups, depending on whether the eigenvectors are spatially localized or spatially extended (over the lattice). Since the DB is exponentially localized in a finite region of the lattice, the extended eigenvectors are locally deformed linear modes (standing waves) of the system. Their number is proportional to the size of the system. In contrast, the number of eigenvalues, corresponding to spatially localized perturbations (internal modes of the DB), depends solely on the DB parameters and is finite, even for infinite system size.

For Hamiltonian systems, there are always two isolated eigenvalues, located at $+1$, which correspond to localized Floquet modes [27, 8] – the phase mode describing a rotation of the overall phase of the breather (i.e. sliding along the periodic orbit in phase space) and the growth mode describing a change of DB frequency/energy (i.e. sliding along the DB family).

On changing the model parameters, as well as the DB solution parameter (its frequency or energy), the Floquet eigenvalues will move in the complex plane. However, the only way a particular eigenvalue can leave the unit circle is through a collision with another eigenvalue (see Fig. 6, right picture). To conclude this discussion, the details of the scenario of switching between linearly stable and unstable DB states can be quite complicated. While that may seem a strange complication of the rather straightforward picture of the emergence of DB solutions, it is a consequence of the fact that we deal with periodic orbits in a high-dimensional phase space of non-integrable systems.

2.3 Energy Thresholds of Discrete Breathers

DB solutions come in one-parameter families. The parameter can be the amplitude (measured at the site with maximum amplitude), the energy, E, or the breather frequency, Ω_b. The amplitude can be decreased to arbitrarily small values, at least for some of the families in an infinite lattice. In this zero-amplitude limit, the DB frequency, Ω_b, approaches an edge of the phonon spectrum, ω_q. This happens because the non-resonance condition, $\omega_q/\Omega_\mathrm{b} \neq 0, 1, 2, 3, \ldots$, has to hold for all solutions of a generic DB family. In the limit of zero amplitude, the DB solutions have to approach solutions of the linearized equations of motion, so the frequency Ω_b has to approach some ω_q, but at the same time it must not coincide with any phonon frequency. This is possible only if the breather's frequency tends to an edge, ω_E, of the phonon spectrum in the limit of zero breather amplitude. If we consider the family of nonlinear plane waves which yields the corresponding band edge plane wave in the limit of zero amplitude A, then its frequency, ω, will depend on A as

$$|\omega - \omega_\mathrm{E}| \sim A^z \tag{28}$$

for small A, where the detuning exponent, z, depends on the type of nonlinearity of the Hamiltonian (13) and can be calculated using standard perturbation theory [30].

Here we closely follow the line of argument of [17]. Let us assume that we have a system with short-range interactions and estimate the discrete breather energy in the limit of small amplitudes. Define the amplitude of a DB to be the largest of the amplitudes of the oscillations over the lattice. Denote it by A_0, where we define the site $l = 0$ to be the one with the largest amplitude. The amplitudes decay in space away from the breather centre, and by linearizing around the equilibrium state and making a continuum approximation, the decay is found to be given by $A_l \sim CF_{\rm d}(|l|\delta)$ for $|l|$ large, where $F_{\rm d}$ is a dimension-dependent function:

$$F_1(x) = {\rm e}^{-x},\ F_3(x) = \frac{1}{x}{\rm e}^{-x}, \tag{29}$$

$$F_2(x) = \int \frac{{\rm e}^{-x\sqrt{1+\zeta^2}}}{\sqrt{1+\zeta^2}}{\rm d}\zeta, \tag{30}$$

δ is a spatial decay exponent, and we shall assume that the constant C is of order A_0. To estimate the dependence of the spatial decay exponent, δ, on the frequency of the time-periodic motion, $\Omega_{\rm b}$ (which is close to the edge of the linear spectrum), it is sufficient to consider the dependence of the frequency of the phonon spectrum, ω_q, on the wave vector, q, close to the edge. Generically, this dependence is quadratic $(\omega_{\rm E} - \omega_q) \sim |q - q_{\rm E}|^2$, where $\omega_{\rm E} \neq 0$ marks the frequency of the edge of the linear spectrum and $q_{\rm E}$ is the corresponding edge wave vector. Then analytical continuation of $(q - q_{\rm E})$ to ${\rm i}(q - q_{\rm E})$ yields a quadratic dependence, $|\Omega_{\rm b} - \omega_{\rm E}| \sim \delta^2$. Finally, we must insert the manner in which the detuning of the breather frequency from the edge of the linear spectrum, $|\Omega_{\rm b} - \omega_{\rm E}|$, depends on the small breather amplitude. If we assume that the frequency of the weakly localized breather detunes with amplitude as the weakly nonlinear band edge plane wave frequency, then this is $|\Omega_{\rm b} - \omega_{\rm E}| \sim A_0^z$. Then $\delta \sim A_0^{z/2}$.

Now we are able to calculate the scaling of the energy of the discrete breather as its amplitude goes to zero by replacing the sum over the lattice sites by an integral:

$$E_{\rm b} \sim \frac{1}{2}C^2 \int r^{d-1} F_{\rm d}^2(\delta r){\rm d}r \sim A_0^{(4-zd)/2}. \tag{31}$$

This is possible if the breather persists for small amplitudes and is slowly varying in space. We find that, if $d > d_c = 4/z$, the breather energy diverges for small amplitudes, whereas for $d < d_c$, the DB energy tends to zero with the amplitude. Inserting $z = 2$, we obtain $d_c = 2$, which is in accord with the exact results on plane wave stability [31], and thus strengthens the conjecture that discrete breathers bifurcate through tangent bifurcations from band edge plane waves. Note that, for $d = d_c$, logarithmic corrections may apply to (31), and these can lead to additional variations of the energy for small amplitudes.

An immediate consequence is that if $d \geq d_c$, the energy of a breather is bounded and is not zero. This is because for any non-zero amplitude, the breather energy cannot be zero, and as the amplitude goes to zero, the energy approaches a positive limit

($d = d_c$) or diverges ($d > d_c$). Thus, we obtain an energy threshold for the creation of DBs for $d \geq d_c$. This new energy scale is set by combinations of the expansion coefficients in (13). We assume $z = 2$ with $|\Omega - \omega_{\mathrm{E}}| \sim \beta A^2$ for the nonlinear plane waves and that the energy per oscillator $E \sim gA^2$. Then the relation $|\Omega_{\mathrm{b}} - \omega_{\mathrm{E}}| \sim \kappa\delta^2$ applies for the spatial decay exponent, δ. Furthermore, the energy threshold, E_{min}, is of the order of $\kappa g/\beta$, and the minimum energy breather in three dimension has a spatial size which is of the order of the lattice spacing and is independent of κ, g, and β. One should allow for a factor of $(2+d)$ for underestimating the true height of the minimum and the contributions of nearest neighbours.

Many numerical results have since confirmed the above results. For the d-dimensional DNLS model (18), the left panel in Fig. 7 shows the variation of the DB energy with its central amplitude, and a clear notion of an energy threshold, starting with $d = 2$ [17]. Note that $n = 1$ in that case. The minimum energy DB profile for $d = 3$ is the one plotted in Fig. 5; it is indeed strongly localized on the lattice. It was also observed that energy thresholds even appear in one-dimensional systems, if the lowest-order nonlinear term in the equations of motion has a large enough power. We present results for a modified DNLS system in one spatial dimension, $d = 1$:

$$\dot{\Psi}_l = \mathrm{i}\left(\Psi_l + |\Psi_l|^{\mu-1}\Psi_l + C\sum_{m\in N_l}\Psi_m\right). \tag{32}$$

By tuning μ, we can cross over from zero to non-zero energy thresholds. We show results for $d = 1$ and $\mu = 3, 5, 7$ in the right panel of Fig. 7. Again, we find full agreement with the predictions from above. Thus, even one-dimensional lattices

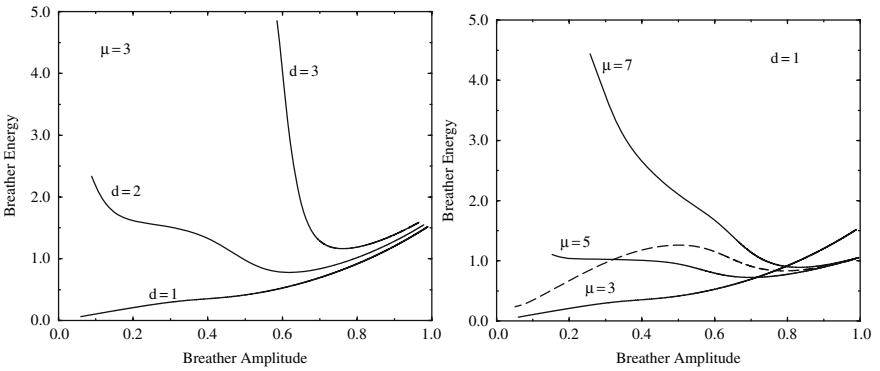

Fig. 7 *Left panel*: Breather energy versus amplitude for the DNLS system in one, two, and three lattice dimensions. System sizes for $d = 1, 2, 3$: $N = 100$, $N = 25^2$, and $N = 31^3$, respectively. *Right panel*: Breather energy versus maximum amplitude for the DNLS system in one lattice dimension for three different exponent values: $\mu = 3, 5, 7$ (*solid lines*). The system size is $N = 100$ and the parameter $C = 0.1$. The *dashed line* is for the modified system (cf. text) (Figure adapted from [17])

exhibit positive lower bounds on breather energies if $\mu \geq 5$. Weinstein has obtained rigorous proofs of these results for any value of μ [32].

We can predict that a modified DNLS system with an additional term $v_{\mu'}|\Psi_l|^{\mu'-1}\Psi_l$ will exhibit complex curves $E_\mathrm{b}(A_0)$. For example, for $d=1$, $\mu=7$, $\mu'=3$, and $v_{\mu'}=0.1$, the $E_\mathrm{b}(A_0)$-dependence will be nearly identical to the case $v_{\mu'}=0$ already considered, if the amplitude A_0 is not too small. Then $E_\mathrm{b}(A_0)$ will show a minimum at a non-zero value of A_0. For small A_0, however, the energy of the breather will ultimately decay to zero, so the curve has a maximum for smaller amplitudes! The dashed line in the right panel in Fig. 7 shows the numerical calculation, which coincides with our prediction.

Another example is a two-dimensional lattice system (12) where $d=2$ is the critical dimension. The energy thresholds have been computed and reported in [12]. The profiles of DB solutions in Fig. 4 correspond to (A) a low-amplitude DB, (B) the minimum energy DB, and (C) a high-amplitude DB.

2.4 Dissipative Discrete Breathers

So far we have been discussing breathers in Hamiltonian lattices. However, any experiment will show up with some dissipation. When this dissipation is of a fluctuating nature, it can be simulated using a heat bath. However, it is also possible to consider simple deterministic extensions to the above problems. In Josephson junction systems, this is actually even implemented experimentally. Let us mention the basic new features one is faced with when studying dissipative breathers and their properties [22, 33, 34].

2.4.1 Obtaining Dissipative Breathers

Consider the following set of equations of motion:

$$\ddot{x}_l = -\frac{\partial H}{\partial x_l} - \gamma \dot{x}_l - I, \tag{33}$$

with

$$H = \sum_l \left[1 - \cos x_l - C\left(1 - \cos(x_l - x_{l-1})\right)\right]. \tag{34}$$

For $\gamma = I = 0$, this system is Hamiltonian and it corresponds to the Takeno–Peyrard model of coupled pendula [22, 35]. This model allows for the usual discrete breathers, and also for the so-called 'roto-breathers'. Now $x_l(t+T_\mathrm{b}) = x_l(t)$ for all l for a usual breather, but for the simplest version of a roto-breather, one pendulum performs rotations:

$$x_0(t+T_\mathrm{b}) = x_0(t) + 2\pi m. \tag{35}$$

Here m is a winding number characterizing the roto-breather (again the simplest realization is $m = 1$). Note that, in contrast to a usual breather ($m = 0$), roto-breathers are not invariant under time reversal.

For non-zero γ and $I = 0$, the non-zero dissipation will lead to a decay of all breather and roto-breather solutions. However, for a time-independent $I \neq 0$, roto-breathers may still exist. The reason is that the rotating pendulum will both gain energy due to the non-zero torque, I, and dissipate energy due to the non-zero friction, γ, so an energy balance is possible (whereas this is impossible for breathers with $m = 0$).

Instead of families of breather periodic orbits in Hamiltonian systems, dissipative roto-breathers will be attractors in the phase space. Attractors are characterized by a finite-volume basin of attraction surrounding them. Any trajectory which starts inside this basin will ultimately be attracted by the roto-breather. Thus, dissipative breathers form a countable set of solutions.

To compute such a dissipative roto-breather, we can simply make a good guess for the initial conditions and then integrate the equations of motion until the roto-breather is reached. This method is very simple, but may suffer from long transient times and also from complicated structures of the boundaries of the basin of attraction.

The Newton method can be applied here as well. Although we do not know the precise period of the roto-breather, we do not actually need it. Instead of defining a map which integrates the phase space over a given time, T_b, we may define a map which integrates the phase space of all but the rotating pendulum coordinate from the initial value $x_0(t = 0) = 0$ to $x_0(t_\mathrm{map}) = 2\pi m$. Different trajectories will have different values of t_map, but this is not a problem. The only two things we have to worry about are finding a trajectory which leads to a rotation of x_0 and, as usual, being sufficiently close to the desired solution for the Newton map to converge. Once the solution is found, $T_\mathrm{b} = t_\mathrm{map}$.

2.4.2 Perturbing Dissipative Breathers

If a dissipative roto-breather is stable, then the volume of its basin of attraction is finite, so small deviations will return the perturbed trajectory back to the breather. Upon a change of some control parameter, the breather may still persist but become unstable. Consider the linearized phase space flow around a roto-breather of (33, 34):

$$\ddot{\varepsilon}_l = -\sum_m \frac{\partial^2 H}{\partial x_l \partial x_m}\Big|_{\{x_{l'}(t)\}} \varepsilon_m \; - \gamma \dot{\varepsilon}_l . \tag{36}$$

In analogy with Sect. 2.2, we may introduce a (quasi-symplectic) matrix $\mathscr{R}$ which maps the phase space of the perturbations onto itself by integration of (36) over one breather period [34]. By using the transformation

$$\varepsilon_l(t) = \mathrm{e}^{-\frac{1}{2}\gamma t}\, \kappa_l(t), \tag{37}$$

we obtain

$$\ddot{\kappa}_l = -\sum_m \frac{\partial^2 H}{\partial x_l \partial x_m}|_{\{x_{l'}(t)\}} \kappa_m - \frac{1}{4}\gamma^2 \kappa_l. \tag{38}$$

Equation (38) defines a Floquet problem with a symplectic matrix $\mathscr{F}$ with the properties discussed above. By transforming back to $\mathscr{R}$, we find that those eigenvalues which are located on the unit circle for $\mathscr{F}$ now reside on a circle with a smaller radius

$$R(\gamma) = \mathrm{e}^{-\gamma T_\mathrm{b}/2}. \tag{39}$$

If μ is an eigenvalue of $\mathscr{R}$, then so are

$$\mu^*, \mathrm{e}^{-\gamma T_\mathrm{b}} \frac{1}{\mu}, \mathrm{e}^{-\gamma T_\mathrm{b}} \frac{1}{\mu^*}. \tag{40}$$

There is still one eigenvalue, $\mu = 1$, which corresponds to perturbations tangent to the breather orbit. The related second eigenvalue is located at $\mathrm{e}^{-\gamma T_\mathrm{b}}$, in contrast to the Hamiltonian case. A schematic outcome of a Floquet analysis of a dissipative breather is shown in Fig. 8. We close by noting that the above properties of the quasi-symplectic matrix $\mathscr{R}$ follow directly from (36), and thus apply to many other situations in the study of the stability of periodic orbits in dissipative systems.

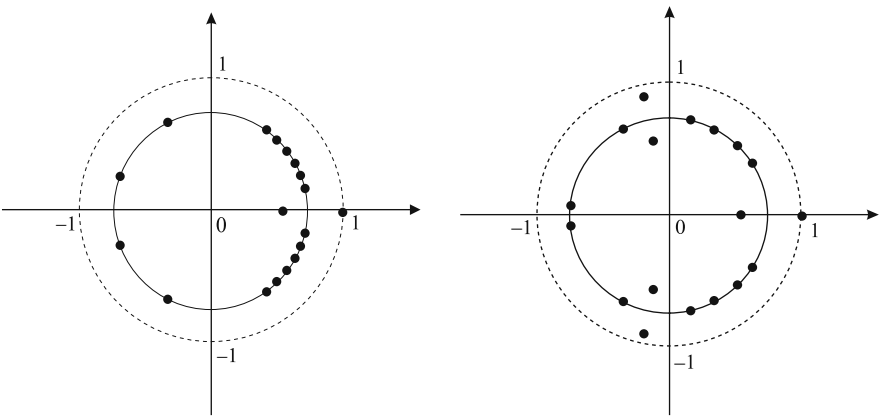

Fig. 8 Schematic view of an outcome of the Floquet analysis of a dissipative breather. Floquet eigenvalues (*filled circles*), the unit circle (*large radius*), and the inner circle of radius R (39) are plotted in the complex plane. *Left picture*: stable breather (all eigenvalues are located on the circle with radius R). *Right picture*: stable breather close to instability (two eigenvalues have collided on the inner circle, and one is departing outside towards the unit circle). Note that the group of eigenvalues in proximity on the unit circle correspond to the plane wave continuum (extended Floquet eigenstates), while the separated eigenvalues on the inner circle correspond to localized Floquet eigenstates

3 Applications

In the following, we will discuss in detail two recent applications of the concept of discrete breathers in systems where dissipation is not only unavoidable but essential in order to observe and manipulate DBs in a way which is impossible for a conservative case.

3.1 Josephson Junction Networks

Arrays of Josephson junctions are perfect laboratory objects to study various nonlinear phenomena. An anisotropic ladder of dc-biased Josephson junctions, as shown in Fig. 9, is perhaps the simplest structure which supports discrete breathers. The dynamics of a single Josephson junction is described by the time evolution of the difference of the phases of the wave function between adjacent superconducting islands, ϕ. It may support two stable states – a superconducting state and a resistive state. In the superconducting state, the average value of $\dot{\phi}$ vanishes. In the resistive state, it is non-zero and proportional to the voltage drop across the junction.

3.1.1 Basic Principles and Modelling

We denote the phase differences across the lth vertical junction and its right upper and lower horizontal neighbours by $\phi_l^v, \phi_l^h, \tilde{\phi}_l^h$. Then, the dimensionless equation of motion for each junction, with current I_l flowing through it, is given by the Josephson equation with its phase difference ϕ_l:

$$\ddot{\phi}_l + \alpha\dot{\phi}_l + \sin\phi_l \ = I_l. \tag{41}$$

The time is normalized to $t_0 = \sqrt{C\Phi_0/(2\pi I_c)}$, with Φ_0 being a magnetic flux quantum, C the capacitance, and I_c the critical current of the corresponding junction.

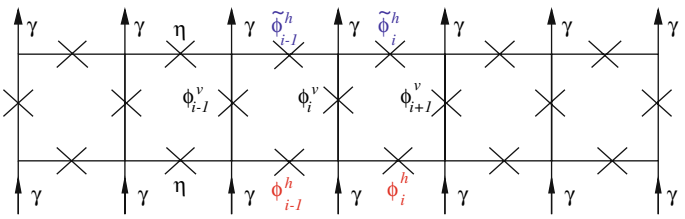

Fig. 9 A schematic view of a Josephson junction ladder (JJL). *Crosses* indicate the locations of junctions, while the *arrows* show the direction of external current flow, γ

The dimensionless damping parameter is $\alpha = \sqrt{\Phi_0/(2\pi I_c C R_N^2)}$ (where R_N is the junction resistance) and $\eta = I_{cH}/I_{cV}$ is the anisotropy constant, i.e. the ratio of the critical horizontal and vertical currents. Note that, due to the sin term, for a resistive junction $\phi = \Omega t + g(t)$, where the zero mean periodic function $g(t) = g(t + 2\pi/\Omega)$ describes periodic modulations of the resistive state. This a.c. Josephson effect also imposes a corresponding oscillation on nearby coupled junctions, which, when time-averaged, are in the superconducting state.

Using the Kirchhoff laws and the self-inductance relation for one elementary cell of the ladder (see [36]), one arrives at the following set of equations:

$$\begin{aligned}
\ddot{\phi}_l^v + \alpha\dot{\phi}_l^v + \sin\phi_l^v &= \gamma + (\Delta\phi_l^v - \nabla\tilde{\phi}_{l-1}^h + \nabla\phi_{l-1}^h)/\beta_L,\\
\ddot{\phi}_l^h + \alpha\dot{\phi}_l^h + \sin\phi_l^h &= -(\phi_l^h - \tilde{\phi}_l^h + \nabla\phi_l^v)/(\eta\beta_L),\\
\ddot{\tilde{\phi}}_l^h + \alpha\dot{\tilde{\phi}}_l^h + \sin\tilde{\phi}_l^h &= (\phi_l^h - \tilde{\phi}_l^h + \nabla\phi_l^v)/(\eta\beta_L),
\end{aligned} \tag{42}$$

where γ is the dimensionless d.c. bias in units of I_{cV}, $\beta_L = 2\pi L I_{cV}/\Phi_0$ is the dimensionless discreteness parameter, and L is the self-inductance of the elementary cell of the ladder. The discrete operators are given by $\nabla\phi_l = \phi_{l+1} - \phi_l$, $\Delta\phi_l = \phi_{l+1} - 2\phi_l + \phi_{l-1}$. The dispersion law for the plasmon plane waves for the weakly damped case ($\alpha \ll 1$) can be obtained by omitting the damping and linearizing the system (42):

$$\omega_0^2 = 1,\ \omega_\pm^2 = \frac{1}{2}\left[1 + \xi \pm \sqrt{(1-\xi)^2 + 8(1-\sqrt{1-\gamma^2})/(\eta\beta_L)}\ \right],$$

where $\xi = \sqrt{1-\gamma^2} + 2[1 + \eta(1-\cos q)]/(\eta\beta_L)$. The branch ω_0 corresponds to non-active vertical junctions and in-phase (symmetric) oscillations of the phases of upper and lower horizontal junctions. The branch $\omega_+ > \omega_0$ is characterized by anti-symmetric oscillations of the horizontal phases for all qs. For $q = 0$, only the horizontal junctions are excited. The branch $\omega_- < \omega_0$ becomes dispersionless for $\gamma = 0$. For $q = 0$, it corresponds to the excitation of only the vertical junctions, while the horizontal ones are not active.

For a finite-size ladder with open boundary conditions and N cells, i.e. $N+1$ vertical junctions, the spectrum of linear waves is discrete and is characterized by the following choice of allowed wave-number values:

$$q_l = \frac{l\pi}{N+1},\ l = 0, 1, 2, ..., N. \tag{43}$$

These plasmon waves are the *cavity modes* of the JJL. Odd values of l correspond to anti-symmetric eigenvectors (with respect to reflections at the centre of the ladder), whereas even values correspond to symmetric ones.

3.1.2 Roto-Breather Solutions and Their Current–Voltage Dependencies

The breather states (roto-breathers in this case) correspond to a few junctions being in the resistive state, with all other junctions oscillating around the superconducting state. These oscillations are induced by coupling to the resistive junctions.

Experiments [37, 38] have revealed different breather structures, as depicted in Fig. 10: (a) up–down symmetry, (b) left–right symmetry, (c) inversion symmetry, (d) no symmetry. Each group of breathers can also have an arbitrary number, n_r, of vertical resistive junctions. Experimentally, each discrete breather is characterized by its current–voltage dependence [37]. Such a time-averaged measurement does not resolve the details of the oscillatory dynamics of a state. This is almost impossible to do, due to the absence of spectroscopic tools at plasma frequencies of the order of 100 GHz. The average voltage drop on the lth vertical junction equals $V = (1/T_\mathrm{b}) \int_0^{T_\mathrm{b}} \dot{\phi}_l^v \mathrm{d}t$. For the type (a, d) breathers, $V = 2\omega_\mathrm{b}$, while for the type (b, c), $V = \omega_\mathrm{b}$.

Using the approximation $\phi \sim t$ for resistive junctions, one can compute the dependence of the average voltage drop on the d.c. bias:

$$V = \frac{k\gamma}{\alpha[k + (3 - \frac{1}{2}\delta)\eta]} \,, \tag{44}$$

where k is the number of vertical rotating junctions and δ denotes the number of resistive horizontal junctions. Note that $\delta = 4$ for breathers with up–down symmetry, $\delta = 2$ for left–right or inversion symmetry, and $\delta = 3$ for no symmetry. Numerical calculations of the current–voltage characteristics (Fig. 11) showed very good qualitative agreement with experiments. In addition, numerical studies allow us to directly access the tricky details of the nonlinear dynamics of the obtained states. Note that the variation of the parameters allows for breathers with frequencies located above the entire plasmon spectrum, as well as in its gaps.

The presence of dissipation leads to a temporal decay of plasmon waves, if excited homogeneously in the ladder. In addition, it also leads to a spatial decay of plasmon waves if a local resonant source is generating them. Thus, a roto-breather in the JJL can be brought into resonance with plasmon waves. The tuning parameter is simply the d.c. bias, which is the main control parameter in the experiments. When the breather frequency is tuned into resonance, the breather starts to generate plasmons, which will localize in space. Their localization length, though finite, will grow with decreasing dissipation constant, α. In a finite ladder, one expects to observe a resonant breather tail, which extends to the end of the ladder, and appears

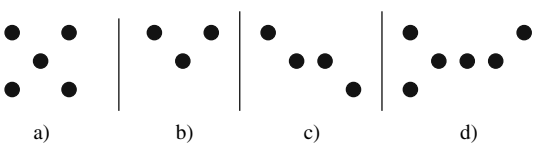

Fig. 10 Possible realizations of discrete breathers in a linear ladder. *Black spots* indicate the positions of resistive junctions. Ladders with periodic boundary conditions do not support (**c**) or (**d**) states

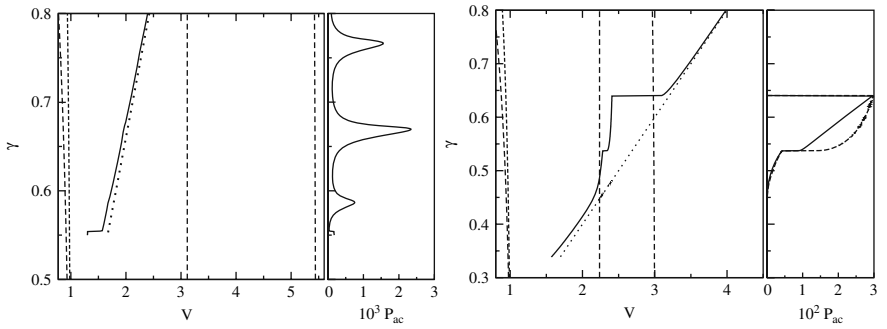

Fig. 11 Current–voltage dependence and the edge average power $P_{\rm ac} = \frac{1}{2}\langle \dot{\phi}_N^{\nu^2} \rangle$ dependence for breathers of type (b) in a ladder with $N = 10$ vertical Josephson junctions. *Solid lines* – numerical results. *Dotted lines* – approximation (44). *Vertical dashed lines* – band edges of the plasmon wave spectrum. *Left picture* – $\alpha = 0.1$, $\beta_L = 0.2$, $\eta = 1.15$. *Right picture* – $\alpha = 0.1$, $\beta_L = 1.0$, $\eta = 0.5$ (Figure adapted from [36])

at discrete values of the bias, due to the discrete set of cavity mode frequencies. This indeed can be observed, e.g. in the left picture in Fig. 11, where the cavity modes resonate with the second harmonics of the breather frequency. At the same time, almost no indication for that resonance is observable in the current–voltage characteristics.

In the right picture in Fig. 11, the breather frequency itself resonates with the plasmon waves. Still, the breather survives, due to the presence of dissipation. However, the resonant breather–plasmon interaction is now strong, and this leads to a considerable change in the current–voltage characteristics. Almost vertical resonant steps are observed, and these correspond to a locking of the breather frequency to a particular cavity mode frequency. These resonances allow us to use the tunable roto-breather as a spectroscopic tool to study the properties of cavity modes in a JJL.

The strong interaction of breathers with cavity modes in JJLs leads to the possibility of studying resonant scattering of cavity modes by roto-breathers [39]. Again, the dissipation helps in stabilizing the breather during the scattering process. The transmission for plasmons is strongly dependent upon their wave numbers. In addition, strong resonances can be obtained in the scattering, ranging from resonant transmission to resonant reflection. By changing the d.c. bias, the roto-breather is changed, and thus so is the scattering potential. Consequently, roto-breathers may serve as tunable frequency filters for plasmon waves in the 100 GHz frequency domain.

Another consequence of the presence of dissipation is the possibility of exciting genuine quasi-periodic breathers. This has been achieved, both theoretically and experimentally, by using the fact that not all resistive junctions have to lock to the cavity mode when a breather is driven into a resonance [40]. In such a case, the breather becomes an object where different resistive junctions rotate at various incommensurate frequencies. Due to the interaction, the final state is quasi-periodic in time.

3.1.3 Laser Scanning Microscopy

The technique of laser scanning microscopy finally allowed visualization of the experimentally obtained breather states [37]. To do this, the ladder is prepared in a given state, and the voltage drop across the ladder is monitored. Then, the probe is scanned with a laser beam with a moderate intensity and a cross-section diameter of few micrometres. The laser beam locally heats the probe. If it hits a resistive junction, the local temperature change will induce a change of the junction characteristics, and finally a change in the measured voltage drop. Otherwise, the voltage drop will show no response. In Fig. 12, the outcome of such experiments and the corresponding schematics are shown for the case of annular ladders. Both delocalized resistive states and roto-breather states are clearly visible. In the schematics, Josephson junctions (each about 3 μm wide) lie at the midpoints of each of the line segments that signify superconducting leads connecting the junctions. A homogeneous ladder in the schematic and a homogeneous background in the data would signal a superconducting state of all junctions at low d.c. current, i.e. the linear regime. However, a large d.c. current switches some of the junctions into a resistive state that supports a voltage across the junctions; in the schematic, dots depict resistive junctions having different voltages. The resistive junctions belong to discrete breather excitations localized at various sites of the ladder.

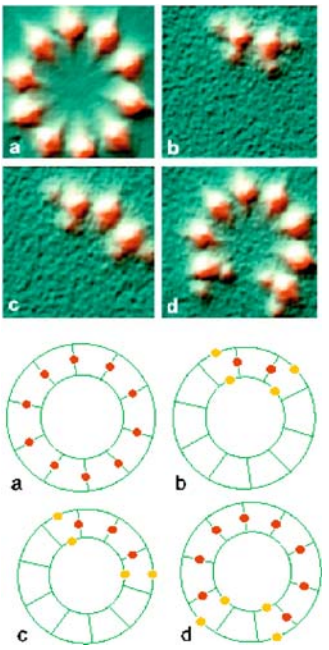

Fig. 12 Experimental and schematic images of roto-breathers in an annular Josephson ladder driven by a d.c. current. Among the many possible DB states, the data show four: (**a**) a highly excited, spatially homogeneous resistive state and (**b–d**) localized states corresponding to several distinct DBs (Figure adapted from [41])

3.2 Coupled Nonlinear Optical Waveguides and Resonators

Another experimental set-up used to observe discrete breathers is associated with coupled optical waveguides, which form periodic structures in one and two dimensions [42, 43, 44]. These structures represent generalizations of the nonlinear optical coupler, introduced by Jensen [45]. There are generally two different approaches to the experimental realization of coupled waveguide arrays. One is the etching of fixed waveguides in nonlinear materials, such as semiconductors [46], and the other is induction of periodic structures in compliant media, such as optical induction in photorefractive crystals [43] or periodic voltage biasing in liquid crystals [47]. Figures 13 and 14 illustrate typical one- and two-dimensional waveguide arrays produced by each of the two methods.

3.2.1 Basic Principles and Modelling

The standard theoretical approach for studying light propagation in waveguide arrays is based on the concept of coupled waveguide modes – see Fig 13(b) – which is similar to the tight-binding approximation used in solid state theory. Typical propagation distances in waveguide arrays are rather short, so that the effects of dispersion and diffraction in each individual waveguide are usually neglected.[1] With this assumption, and also only considering Kerr-type nonlinearity, the corresponding set of equations for the amplitudes of the waveguide modes, E_n, reduces to the DNLS model [44]:

$$\mathrm{i}\frac{\mathrm{d}E_n}{\mathrm{d}z} + \beta E_n + C(E_{n-1} + E_{n+1}) + \gamma |E_n|^2 E_n = 0, \tag{45}$$

where β is the linear propagation constant (taken to be the same in each waveguide), C is the coupling coefficient between adjacent waveguide modes, and γ is the

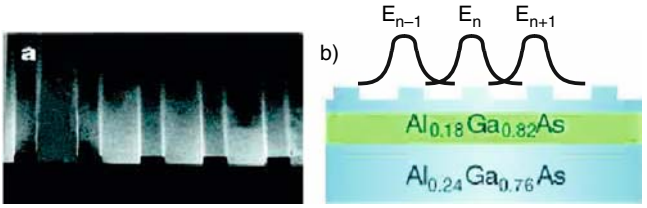

Fig. 13 A one-dimensional AlGaAs waveguide array. It is composed of three layers of AlGaAs material: the substrate and cladding with a lower refractive index and the guiding layer with the higher refractive index. Periodic etching of the cladding forms coupled waveguides. (**a**) A snapshot of the waveguide array. (**b**) Schematic structure of the waveguide array with illustration of modal overlap (Figure adapted from [42])

[1] Glass- and semiconductor-based waveguide arrays usually require picosecond or sub-picosecond pulsed lasers in order to achieve high-enough intensities for a nonlinear response. This can introduce spatio-temporal effects [48].

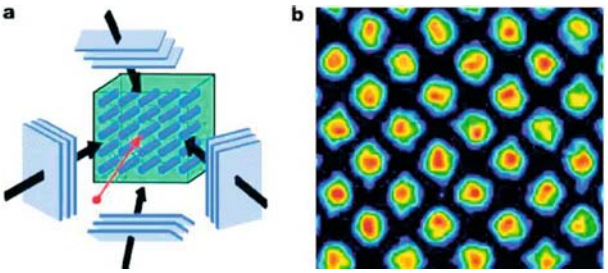

Fig. 14 (**a**) Diagram of an experimental set-up for observing two-dimensional discrete localized structures with the use of a photorefractive crystal – two interfering pairs of ordinarily polarized plane waves induce the photonic array, while the extraordinarily polarized probe beam is focused into a single waveguide and eventually forms a discrete soliton. (**b**) Typical observation of a waveguide array at the exit face of the crystal for low-probe beam power (no soliton formation). Each waveguide is approximately 7 μm in diameter, with an 11 μm spacing between nearest neighbours (Figure adapted from [52])

nonlinear parameter [49, 50, 44]. To the lowest-order approximation, only coupling between nearest neighbours is taken into account, while nonlinear coupling terms are neglected. For waveguide arrays created by optical induction in photorefractive materials [43], the nonlinear term in (45) is usually modified to account for saturation effects, and then takes the form $\gamma E_n/(1+|E_n|^2)$ [51]. Generalization to higher-dimensional problems is straightforward, cf. (18). In the above model, the actual evolution coordinate is the propagation distance z, which plays the role of an effective time. For that reason, we will refer to wave propagation constants along the z-axis as spatial frequencies, in analogy with other discrete models introduced earlier.

3.2.2 Discrete Solitons: Stationary DBs in One- and Two-Dimensional Coupled Waveguide Structures

The DNLS model (45) represents a very specific type of discrete nonlinear system which supports time-periodic solutions (space periodic in the z coordinate) where only one frequency is excited:

$$E_n(z) = A_n \exp(-\mathrm{i}\Omega_\mathrm{b} z). \tag{46}$$

Using a suitable rescaling of spatial frequencies Ω_b, the propagation constant β in (45) can be set to zero without loss of generality. Figures 15 and 16 illustrate basic types of stationary DBs in one- and two-dimensional DNLS models, while experimentally observed localized excitations in the corresponding waveguide array set-ups are presented in Fig. 17. Due to the stationary character of such excitations, they are often referred to as *discrete solitons*, rather than breathers.

The DNLS model is used as a convenient playground for analysing basic nonlinear phenomena because of its relative simplicity. On the other hand, DNLS

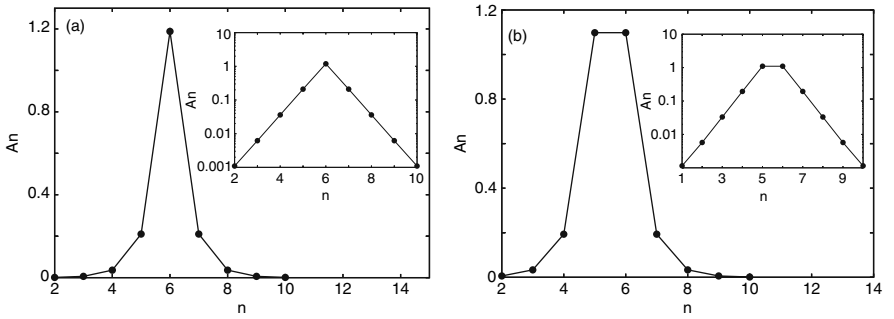

Fig. 15 Profiles of single-site (**a**) and two-site (**b**) stationary DB solutions (46) of the one-dimensional DNLS model, (45), using normal and log-normal (insets) plots. Parameter values are $\Omega_b = 1.0, C = 0.25, \gamma = 1$. Lines are to help visualization

equations can be derived as approximate small-amplitude models of more general nonlinear lattice models with on-site nonlinear potential (Klein–Gordon lattices) [5, 53, 54, 55, 56], inter-site nonlinear interaction (Fermi–Pasta–Ulam lattices). [57, 58, 59], and mixed-type nonlinearities [60]. One essentially uses the rotating wave approximation (RWA), which neglects the effect of the generation of higher harmonics. In this respect, coupled optical waveguides provide one with effective tools to test numerous theoretical predictions.

One of the obvious advantages of using optical waveguide arrays, as compared to many other experimental realizations of DBs, is that no special technique is needed to observe the localized states that are obtained. A snapshot, taken with a

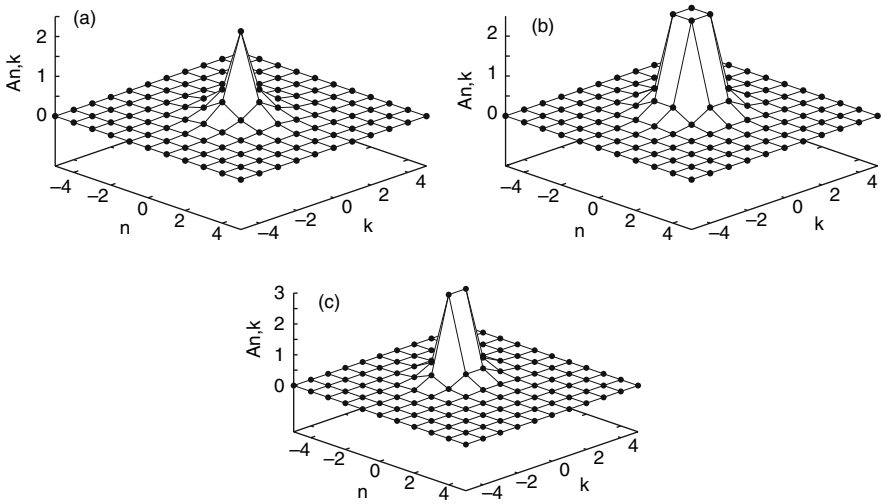

Fig. 16 Different types of DBs in the two-dimensional DNLS model with $\gamma = 1$ and $C = 4$: (**a**) single-site DB, $\Omega_b = 5.5$; (**b**) inter-site DB, $\Omega_b = 8$; (**c**) 'hybrid'-type DB, $\Omega_b = 9$

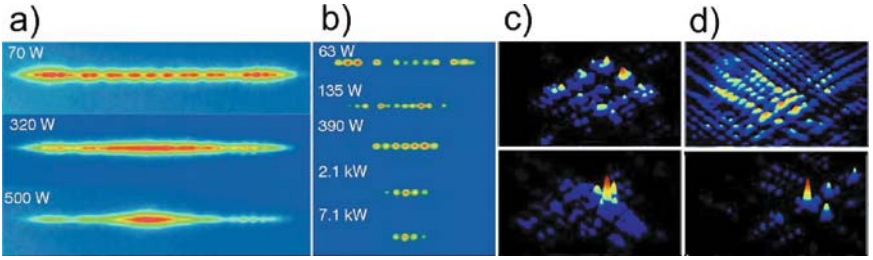

Fig. 17 Experimental observation of discrete diffraction in the linear regime (small input power) and localization in the nonlinear regime (high input power). (**a**) Experimental images of a Kerr-type AlGaAs one-dimensional waveguide array with waveguide spacing $D = 8\,\mu\text{m}$, operated at a wavelength of $\lambda = 1.53\,\mu\text{m}$ [61]. (**b**) The same for a periodically poled lithium niobate array with $D = 15\,\mu\text{m}$, operated at a wavelength of $\lambda = 1.56\,\mu\text{m}$ [42]. (**c**) and (**d**) The same for a two-dimensional optically induced waveguide array, shown in Fig. 14, with the input beam at normal incidence and at an angle of 0.55° to the lattice plane (at the edge of the first Brillouin zone), respectively. The signs of the voltage applied to the photorefractive crystal in (**c**) and (**d**) are opposite, corresponding to focusing and defocusing nonlinearities, respectively (Figure adapted from [52])

high-resolution infrared camera at the output facet of the array, provides full information about the light intensity distribution among the coupled waveguides. In addition, optical set-ups provide a unique opportunity for observing the actual dynamics of a discrete system by monitoring the light intensity evolution along the propagation direction. For example, this can be done by scanning the evanescent light from the top of the waveguide array [62]. As a result, the formation of various types of one- and two-dimensional DBs has been successfully observed in optical experiments, and, additionally, different intriguing aspects of the DB dynamics have been tested. In particular, interactions between highly localized discrete solitons and propagating broad wave packets have recently been observed experimentally in AlGaAs waveguide arrays [63, 64]. Also, possible experimental set-ups for the direct observation of resonant linear wave scattering by DBs and associated spectral hole-burning effects have been developed on the basis of optical waveguides [65, 66].

We also note that DNLS models can support more general types of time-periodic solutions, with several harmonics excited [6, 67, 68, 69]. Similar optical breathers were recently observed experimentally [70].

3.2.3 Coupled Resonators

A closely related and intensively developing subfield of nonlinear optics deals with coupled optical resonators. A straightforward generalization of the above waveguide array set-ups is given by a set of coupled zero-dimensional resonators [71], where mirrors are applied to the input and output facets of the array – see Fig. 18(a). Other possible set-ups include periodically arranged defect cavities in photonic crystals and coupled micro-ring resonators – see Fig. 18(b) and (c), respectively.

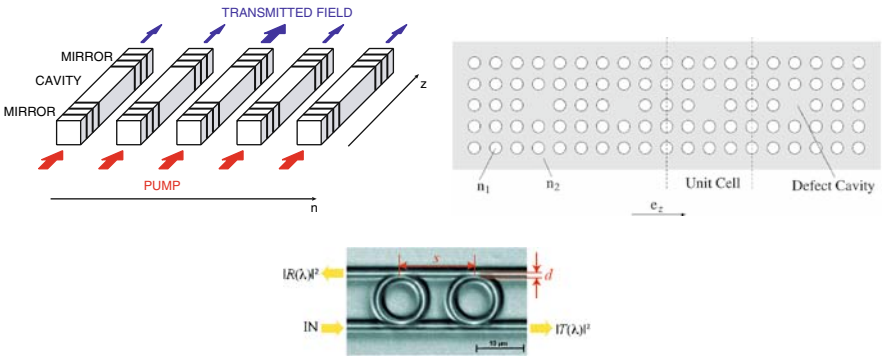

Fig. 18 Different set-ups of coupled optical resonators. *Top left*: coupled semiconductor resonators with mirrors applied at the input and output facets of waveguides (After [71]). *Top right*: periodically arranged defect cavities in a photonic crystal (After [72]). *Bottom*: coupled micro-ring resonators (After [73])

The corresponding theoretical models should account for dissipation, which is one of the principal ingredients in any resonator system. One of the simplest models is given by the driven and damped DNLS system [71], in which dissipative terms are taken to be linear in the field amplitude:

$$\left(\mathrm{i}\frac{\partial}{\partial\tau}+\Delta+\mathrm{i}+\gamma|E_n|^2\right)E_n+C(E_{n+1}+E_{n-1}-2E_n)=A_n^{(\mathrm{in})}. \tag{47}$$

Here, τ is the effective evolution coordinate, E_n is the field amplitude in the n th resonator, C is the coupling between adjacent resonators, Δ is the detuning from linear resonance, γ is the nonlinear Kerr coefficient, and the damping term is rescaled to unity. The amplitudes $A_n^{(\mathrm{in})}$ originate from the input field (pump), which can be non-homogeneous across the array.

In the case of a homogeneous pump, $A_n^{(\mathrm{in})}=\mathrm{const.}$, (47) supports different types of bright and dark stationary DBs – see Fig. 19. Due to dissipation, these objects no longer form families of solutions, but correspond to attractors in phase space. All the characteristics of such DBs, including their amplitude and phase, are fully determined by the model parameters and the parameters of the pump (its amplitude and phase). To a certain extent, this makes the dynamics of the driven-damped DNLS less rich than that of its Hamiltonian analogue. However, dissipation also brings certain new features to the dynamics of localized excitations. It can suppress some resonances with extended states of the system, which otherwise do not allow for quasi-periodic and moving DBs. Earlier, we mentioned the observation of quasi-periodic DBs in coupled Josephson junction systems. Here we will focus on moving DBs.

A tilted pump, $A_n^{(\mathrm{in})}=a\exp(\mathrm{i}\phi_{\mathrm{in}}n)$, which corresponds, for example, to an inclination of the incidence field in the set-up of Fig. 18(a), induces a transverse force acting on a DB. This, in turn, can cause the DB to move across the array – see

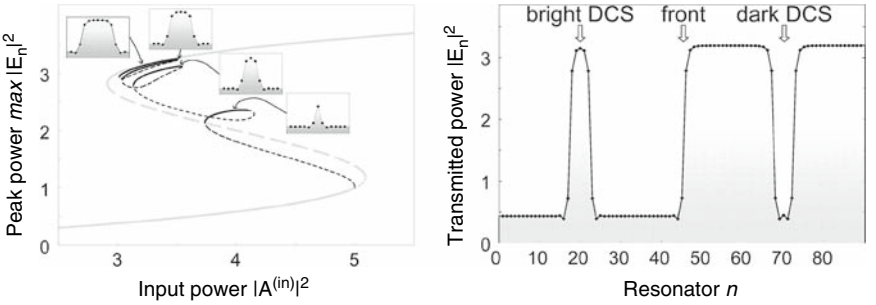

Fig. 19 *Left*: bifurcation diagram for the bistable homogeneous ground state of (47) (*grey lines*), and different types of bright stationary DBs (*black lines*). *Solid curves* indicate stable solutions, while *dashed curves* indicate unstable ones. Parameter values are $\gamma = 1$, $\Delta = -3$, $C = 0.25$. *Right*: co-existence of different types of stationary DBs. Parameter values are $\gamma = -1$, $\Delta = 3$, $C = 0.25$, $|A^{(\mathrm{in})}|^2 = 3.3$ (Figure adapted from [71])

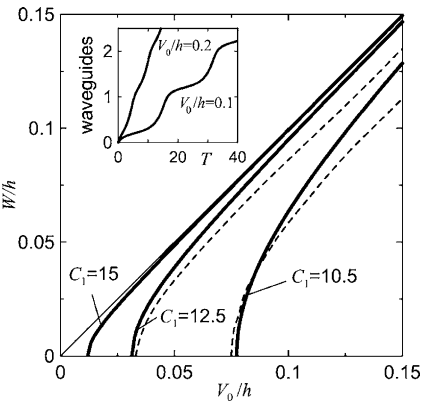

Fig. 20 Average velocity of a DB (W/h) versus normalized tilt (V_0/h) for various coupling constants. The inset illustrates the position of the centre of moving DBs for various tilts (Figure adapted from [74])

Fig. 20. It is important that the discreteness of the system hinders such motion and, in some cases, even prevents it [74]. Generally, there exists a critical value of the tilt, $\phi_{in}^{(\mathrm{cr})}$, below which a given type of DB cannot move – see Fig. 20. This is in contrast to continuous systems, where the resulting velocity of a cavity soliton is linearly proportional to the tilt [75].

The inherent nonlinearity of the DB velocity as a function of the tilt, $V(\phi_{\mathrm{in}})$, in the vicinity of the critical point, $\phi_{\mathrm{in}}^{(\mathrm{cr})}$, gives rise to the effect of DB ratchet motion under the influence of a periodically changing tilt with zero average value [76] – see Fig. 21. A necessary condition for the observation of such a DB ratchet effect is the violation of certain symmetries of the system, and this can be achieved, for example, by applying a bi-harmonic variation of the tilt, or by a superposition of two pumps with varying tilts at different frequencies [76]. For adiabatically changing tilt(s), the average velocity of the resulting net motion of a DB can be estimated to be

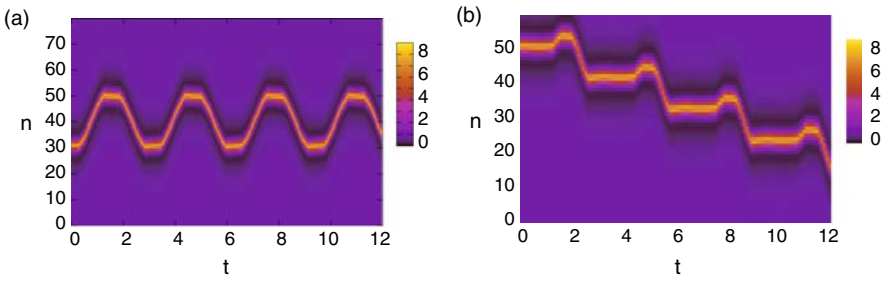

Fig. 21 Density plots of $|E_n|^2$ for DB motion under a periodically changing tilt of the input field. (**a**) Periodic motion of a DB under the influence of a single-harmonic periodically changing tilt. (**b**) Ratchet motion of a DB under the influence of superimposed pumps with varying tilts at different frequencies (Figure adapted from [76])

$\bar{V} = \frac{1}{T}\int_0^T V[\phi_{\rm in}(\tau)]\mathrm{d}\tau$, where T is the period of the tilt. Obviously, the ratchet effect vanishes in the continuous limit, where the function $V(\phi_{\rm in})$ becomes linear.

3.3 Other Examples

Dissipation is unavoidable in any experiment. Nevertheless, it is characterized by some time scale, and experiments which probe a system on shorter time scales are not influenced by the dissipation. In the above examples, the experimental time scales were much larger than the dissipation time scale, so the properties of the discrete breathers were strongly influenced by it. Let us briefly mention two more examples, from recent studies, which fall into this category.

Sato, Hubbard, and Sievers studied the generation of breathers in driven micromechanical cantilever arrays [77]. The frequency of the a.c. drive is chosen to be close to the linear cavity mode spectrum, but not resonant with it. Discrete breathers are spontaneously generated and stabilized by the a.c. drive. Once a DB is generated, laser beams are used to guide it along the cantilever lattice.

Sato and Sievers performed several experiments with anti-ferromagnets. A sophisticated set of different electromagnetic pulses are used to excite localized spin excitations [78]. Further pulses are used to stabilize DBs and finally to observe their decay in a controlled way. Although they are indirect, these experiments are an impressive example of controlling the excitation and properties of DBs at nanometre scales.

4 Summary

The rapidly growing field of the theory and applications of discrete breather excitations is too large to be covered in one chapter. As we pointed out here, a subclass of experimental studies makes a focus on the particular case of nonlinearity,

discreteness, and dissipation. While dissipation is not crucial here for the mere existence of DBs, it has a profound impact on many of their properties. A DB can be brought into resonance with cavity modes, without destroying the DB itself. Also DBs can become quasi-periodic in time, which again, in general, is impossible in the absence of dissipation. DBs can start to move along the lattice, in contrast to the case without dissipation. Finally, control over the strength of dissipation naturally introduces new, and sometimes easily accessible, control parameters which can be used in experiments.

References

1. A.A. Ovchinnikov, Zh. Eksp. Teor. Fiz. / Sov. Phys. JETP **57 / 30**, 263/147 (1969/1970). 290
2. A.J. Sievers and S. Takeno, Phys. Rev. Lett. **61**, 970 (1988). 290
3. S. Takeno and A. Sievers, Solid State Commun. **67**, 1023 (1988). 290
4. S. Takeno, K. Kisoda, and A. J. Sievers, Prog. Theor. Phys. Suppl. **94**, 242 (1988). 290
5. S. Flach and C. R. Willis, Phys. Rep. **295**, 182 (1998). 290, 298, 314
6. R.S. MacKay and S. Aubry, Nonlinearity **7**, 1623 (1994). 293, 315
7. S. Flach, Phys. Rev. E **50**, 3134 (1994). 293, 294, 298, 299
8. S. Aubry and T. Cretegny, Physica D **119**, 34 (1998). 294, 301
9. S. Flach and K. Kladko, Physica D **127**, 61 (1999). 294
10. D. Campbell, S. Flach, and Y. Kivshar, Phys. Today **57**, 43 (2004). 294, 295
11. S. Flach and A. Gorbach, Chaos **15**, 015112 (2005). 294, 295
12. M. Eleftheriou and S. Flach, Physica D **202**, 142 (2005). 296, 304
13. E.N. Economou, *Green's Functions in Quantum Physics*, (Springer-Verlag, Berlin, 1990). 297
14. C. Baesens and R. S. MacKay, Nonlinearity **10**, 931 (1997). 297
15. A. Zygmund, *Trigonometric Series*, (Cambridge University Press, Cambridge, 1968). 297, 299
16. S. Flach, Phys. Rev. E **51**, 3579 (1995). 298, 299
17. S. Flach, K. Kladko, and R. S. MacKay, Phys. Rev. Lett. **78**, 1207 (1997). 298, 302, 303
18. S. Flach, Phys. Rev. E **58**, R4116 (1998). 299
19. Y.S. Kivshar, Phys. Rev. E **48**, R43 (1993). 299
20. F. Fischer, Ann. Physik **2**, 296 (1993). 299
21. S. Flach, Phys. Rev. E **51**, 1503 (1995). 299
22. J. L. Marín and S. Aubry, Nonlinearity **9**, 1501 (1996). 299, 304
23. A. A. Ovchinnikov and S. Flach, Phys. Rev. Lett. **83**, 248 (1999). 299
24. B. Dey, M. Eleftheriou, S. Flach, and G.P. Tsironis, Phys. Rev. E **65**, 017601 (2001). 299
25. A. Gorbach and S. Flach, Phys. Rev. E **72**, 056607 (2005). 299
26. S. Flach, K. Kladko, and S. Takeno, Phys. Rev. Lett. **79**, 4838 (1997). 299
27. S. Aubry, Physica D **103**, 201 (1997). 299, 301
28. J.L. Marín and S. Aubry, Physica D **119**, 163 (1998). 299
29. V.I. Arnold, *Mathematical Methods of Classical Mechanics*, (Springer-Verlag, New York, 1989), 2nd ed. 299
30. A.H. Nayfeh, *Introduction to Perturbation Techniques*, (John Wiley and Sons, New York, 1993). 301
31. S. Flach, Physica **D91**, 223 (1996). 302
32. M. I. Weinstein, Nonlinearity **12**, 673 (1999). 304
33. L. M. Floria, J. L. Marin, P. J. Martinez, F. Falo, and S. Aubry, Europhys. Lett. **36**, 539 (1996). 304
34. J.L. Marín, F. Falo, P.J. Martínez, and L.M. Floría, Phys. Rev. E **63**, 066603 (2001). 304, 305
35. S. Takeno and M. Peyrard, Phys. Rev. E **55**, 1922 (1997). 304
36. A. Miroshnichenko, S. Flach, M. Fistul, Y. Zolotaryuk, and J.B. Page, Phys. Rev. E **64**, 066601 (2001). 308, 310
37. P. Binder, D. Abraimov, A.V. Ustinov, S. Flach, and Y. Zolotaryuk, Phys. Rev. Lett. **84**, 745 (2000). 309, 311
38. E. Trias, J.J. Mazo, and T. Orlando, Phys. Rev. Lett. **84**, 741 (2000). 309
39. A.E. Miroshnichenko, M. Schuster, S. Flach, M.V. Fistul, and A.V. Ustinov, Phys. Rev. B **71**, 174306 (2005). 310

40. M.V. Fistul, A.E. Miroshnichenko, S. Flach, M. Schuster, and A.V. Ustinov, Phys. Rev. B **65**, 174524 (2002). 310
41. A.V. Ustinov, Chaos **13**, 716 (2003). 311
42. D.N. Christodoulides, F. Lederer, and Y. Silberberg, Nature **424**, 817 (2003). 312, 315
43. J.W. Fleischer, G. Bartal, O. Cohen, T. Schwartz, O. Manela, B. Freedman, M. Segev, H. Buljan, and N.K. Efremidis, Opt. Express **13**, 1780 (2005). 312, 313
44. Y.S. Kivshar and G.P. Agrawal, *Optical Solitons: From Fibers to Photonic Crystals*, (Elsevier Science, Amsterdam, 2003). 312, 313
45. S.M. Jensen, IEEE J. Quant. Electronics **18**, 1580 (1982). 312
46. P. Millar, J.S. Aitchison, J.U. Kang, G.I. Stegeman, A. Villeneuve, G.T. Kennedy, and W. Sibbett, J. Opt. Soc. Am. B **14**, 3224 (1997). 312
47. A. Fratalocchi, G. Assanto, K.A. Brzdakiewicz, and M.A. Karpierz, Opt. Lett. **29**, 1530 (2004). 312
48. D. Cheskis, S. Bar-Ad, R. Morandotti, J.S. Aitchison, H.S. Eisenberg, Y. Silberberg, and D. Ross, Phys. Rev. Lett. **91**, 223901 (pages 4) (2003). 312
49. D.N. Christodoulides and R.I. Joseph, Opt. Lett. **13**, 794 (1988). 313
50. M.J. Ablowitz and Z.H. Musslimani, Physica D: Nonl. Phen. **184**, 276 (2003). 313
51. M. Stepic, D. Kip, L. Hadzievski, and A. Maluckov, Phys. Rev. **E 69**, 066618 (2004). 313
52. J. Fleischer, M. Segev, N. Efremidis, and D. Christodoulides, Nature **422**, 147 (2003). 313, 315
53. A. Morgante, M. Johansson, G. Kopidakis, and S. Aubry, Physica **D 162**, 5394 (2002). 314
54. I. Daumont, T. Dauxois, and M. Peyrard, Nonlinearity **10**, 617 (1997). 314
55. Y.S. Kivshar and M. Peyrard, Phys. Rev. **A46**, 3198 (1992). 314
56. Y.S. Kivshar, Phys. Lett. **A173**, 172 (1993). 314
57. V.M. Burlakov, S.A. Kisilev, and V.I. Rupasov, JETP Lett. **51**, 544 (1990). 314
58. C. Claude, Y.S. Kivshar, O. Kluth, and K.H. Spatschek, Phys. Rev. **B47**, 14228 (1993). 314
59. Y. Kivshar, Phys. Rev. **E 48**, 4132 (1993). 314
60. M. Johansson, Physica **D 216**, 62 (2006). 314
61. H.S. Eisenberg, Y. Silberberg, R. Morandotti, A.R. Boyd, and J.S. Aitchison, Phys. Rev. Lett. **81**, 3383 (1998). 315
62. Y. Linzon, I. Ilsar, D. Cheskis, R. Morandotti, J.S. Aitchison, and S. Bar-Ad, Phys. Rev. E **72**, 066607 (2005). 315
63. J. Meier, G.I. Stegeman, D.N. Christodoulides, Y. Silberberg, R. Morandotti, H. Yang, G. Salamo, M. Sorel, and J.S. Aitchison, Opt. Lett. **30**, 1027 (2005). 315
64. J. Meier, G.I. Stegeman, D.N. Christodoulides, R. Morandotti, G. Salamo, H. Yang, M. Sorel, Y. Silberberg, and J.S. Aitchison, Opt. Lett. **30**, 3174 (2005). 315
65. S. Flach, V. Fleurov, A.V. Gorbach, and A.E. Miroshnichenko, Phys. Rev. Lett. **95**, 023901 (2005). 315
66. A. Gorbach, V. Fleurov, S. Flach, and A. Miroshnichenko, in *Topical Problems of Nonlinear Wave Physics*, edited by A. Sergeev, (Proceedings of SPIE, Bellingham, 2006), Vol. **5975**, pp. 297–306. 315
67. M. Johansson, S. Aubry, Y.B. Gaididei, P.L. Christiansen, and K.O. Rasmussen, Physica D **119**, 115 (1998). 315
68. M. Johansson and S. Aubry, Nonlinearity **10**, 1151 (1997). 315
69. M. Johansson and A. V. Gorbach, Phys. Rev. E **70**, 057604 (2004). 315
70. D. Mandelik, H.S. Eisenberg, Y. Silberberg, R. Morandotti, and J.S. Aitchison, Phys. Rev. Lett. **90**, 253902 (2003). 315
71. U. Peschel, O. Egorov, and F. Lederer, Opt. Lett. **29**, 1909 (2004). 315, 316, 317
72. A. Yariv, Y. Xu, R.K. Lee, and A. Scherer, Opt. Lett. **24**, 711 (1999). 316
73. Q. Xu, S. Sandhu, M.L. Povinelli, J. Shakya, S. Fan, and M. Lipson, Phys. Rev. Lett. **96**, 123901 (2006). 316
74. O. Egorov, U. Peschel, and F. Lederer, Phys. Rev. E **72**, 066603 (2005). 317
75. S. Fedorov, D. Michaelis, U. Peschel, C. Etrich, D.V. Skryabin, N. Rosanov, and F. Lederer, Phys. Rev. E **64**, 036610 (2001). 317
76. A. Gorbach, S. Denisov, and S. Flach, Opt. Lett. **31**, 1702 (2006). 317, 318
77. M. Sato, B.E. Hubbard, and A.J. Sievers, Rev. Mod. Phys. **78**, 137 (2006). 318
78. M. Sato and A.J. Sievers, Nature **432**, 486 (2004). 318

Anharmonic Oscillations, Dissipative Solitons and Non-Ohmic Supersonic Electric Transport

M.G. Velarde, W. Ebeling, and A.P. Chetverikov

Abstract We consider the Toda lattice with exponentially repulsive interactions between the units and view these units as Brownian elements capable of pumping energy from a surrounding heat bath or reservoir, and we show that solitons can be excited and maintained in the presence of dissipation. Then, we endow these Toda lattice units with electric charge, i.e., we make them positive ions and add free electrons to the system. We use this to show that, in the presence of an external electric field, following an instability of the base linear Ohm conduction state, the electromechanical Toda lattice is able to maintain a non-Ohmic soliton-driven supersonic electric current, and we then discuss its striking characteristics. Thus the lattice appears very much like a versatile neural transmission line.

1 Introduction

The soliton concept, and the coinage of the word soliton, originates from the work of Zabusky and Kruskal [1] (see also [2, 3, 4]). They dealt with the dynamics of one-dimensional (1D) anharmonic lattices and their (quasi) continuum approximation [5] provided by the Boussinesq–Korteweg-de Vries (BKdV) equation [6, 7]. That work followed research done by Fermi et al. [8] (see also [9]) who tried to understand equi-partition in a lattice by adding anharmonic forces. They used 1D lattices with 16, 32 and 64 units interacting with springs obeying x^2 and x^3 anharmonic

M.G. Velarde
Instituto Pluridisciplinar, Universidad Complutense de Madrid, Paseo Juan XXIII, 1, E-28040 Madrid, Spain, mgvelarde@pluri.ucm.es

W. Ebeling
Institut für Physik, Humboldt-Universität Berlin, Newtonstr. 15, D-12489 Berlin, Germany, ebeling@physik.hu-berlin.de

A.P. Chetverikov
Faculty of Physics, Chernychevsky State University, Astrakhanskaya 83, 410012 Saratov, Russia, chetverikovAP@info.sgu.ru

Velarde, M.G. et al.: *Anharmonic Oscillations, Dissipative Solitons and Non-Ohmic Supersonic Electric Transport.* Lect. Notes Phys. **751**, 321–335 (2008)
DOI 10.1007/978-3-540-78217-9_12

forces and another described by a nonlinear but "piecewise linear" function. The significant achievements of Visscher and collaborators are also worth mentioning. While trying to understand heat transfer, they used the Lennard-Jones potential [10] to explore the role of anharmonicity and of impurities (i.e., doping a given lattice with different masses, thus generating isotopically disordered lattices). More recently, Heeger, Schrieffer and collaborators have used solitons to explain the electrical conductivity of polymers [11]. Finally, we ought to highlight the work done by Toda (1967) on the lattice (which he invented) with a peculiar exponential interaction [12, 13], since here we build upon the results obtained by Toda. [N.B. We make no claim of completeness in the list of references offered here. For a thorough, albeit now a bit old, review of solitons in condensed matter, see Bishop et al. [14]; for an in-depth discussion of heat transfer see Toda [15].]

In one limit, the Toda interaction yields the hard rod/sphere impulsive force (a gas), while in another limit, it becomes a harmonic oscillator (the ideal solid lattice crystal). When the force is proportional to displacement or elongation (x), we have Hooke's law, and this defines the realm of linear oscillations (harmonic in Fourier space), or phonons in the quantum terminology. Through a suitable Taylor expansion, the Toda interaction provides the aforementioned x^2 and x^3 anharmonic forces beyond Hooke's law. Figure 1 illustrates Toda's interaction (with its exponential-repulsive and linear-attractive parts) relative to the Lennard-Jones and Morse interactions. As the latter is a combination of exponentials, both the Toda and Morse interactions are easy to implement electronically. The mechanical–electrical analogy has been fruitfully exploited by researchers [13, 16, 17, 18].

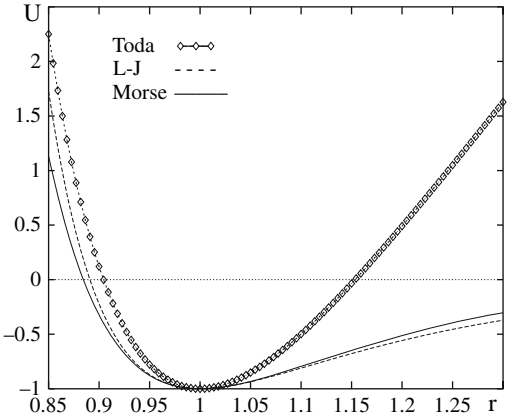

Fig. 1 Toda potential $(U = U^{\mathrm{T}} = \frac{a}{b}[\mathrm{e}^{-b\sigma(r-1)} - 1 + b\sigma(r-1)])$, Morse potential $(U = U^{\mathrm{M}} = \frac{a}{2b}[(\mathrm{e}^{-b\sigma(r-1)} - 1)^2 - 1])$ and Lennard-Jones potential $\left(U = U^{\text{L-J}} = U_0\left[\frac{1}{r^{12}} - \frac{1}{r^6} - 1\right]\right)$. In order to have all three minima of the potential functions at the same location, i.e., $(1, -1)$, we have suitably adjusted the free parameters, while keeping the same basic frequency; r is a suitably rescaled length quantity. It clearly appears that Toda's interaction captures the repulsive core in a good way, whereas its attractive part becomes unphysical for large values of the displacement. Both the Toda and Morse potentials are easily implemented with present-day electronics, as they contain exponentials

The concept of *dissipative* solitons extends the classical theory to non-conservative systems where energy (rather than being conserved) is pumped and dissipated in an appropriate balance, thus exciting and, eventually, sustaining a localized structure (or a periodic nonlinear wave) beyond an instability threshold [19, 20, 21]. The concept of *dissipative* solitons is also the natural generalization of a dynamical system consisting of maintained *dissipative* linear waves with an underlying *dissipative* harmonic oscillator [22, 23, 24, 25, 26, 27].

In this text, we limit ourselves entirely to one-dimensional (1D) lattice systems in classical (not quantum) mechanics. In Sect. 2, we recall how solitons (and nonlinear periodic cnoidal waves) appear in the Toda lattice and give a few other results needed in the subsequent sections of this chapter. Section 3 is devoted to a description of a first generalization of Toda's lattice, made by adding an energy pumping–dissipation balance. In Sects. 4 and 5, we add electric charges and we discuss the electric currents that our generalized driven-dissipative Toda lattice can exhibit in the presence of an external electric field. In particular, we discuss the recent striking discovery [28] of the onset and eventual sustenance of electron–soliton dynamic bound states (solectrons) and the "truth and consequences" that follow: a form of (purely classical) "high"-temperature supersonic current following a transition from the linear (Ohm–Drude) conduction state. Section 6 provides conclusions and suggestions for future research.

2 Solitons and Cnoidal Waves in a Toda Lattice

Let us consider a 1D lattice with Toda interactions between nearest-neighbor units (Fig. 1). Here, relative to the harmonic case, we replace Hooke's law by the force corresponding to

$$U_i^{\mathrm{T}}(r_i) = \frac{a}{b}\left[\exp(-br_i) - 1 + br_i\right]. \tag{1}$$

The relative mutual displacement between the mass i and the mass $i+1$ is $r_i = x_{i+1} - x_i - \sigma$. Then (in the infinite case), there is an exact solution of the corresponding dynamical system (the system is integrable), as found by Toda [12, 13]. As mentioned earlier, if we expand (1) in a Taylor series

$$U^{\mathrm{T}}(r) = \frac{ab}{2}\left(r^2 - \frac{b}{3}r^3 + \cdots\right), \tag{2}$$

for small values of the displacements, r_i, from equilibrium positions, we recover, to lowest-order, the harmonic oscillator. Subsequent terms in the series (r^3, r^4) reproduce the aforementioned interactions used by Fermi, Pasta and Ulam. Apart from an external periodic forcing term, these define the (asymmetric nonlinear) Helmholtz oscillator [29] and the (symmetric nonlinear) Duffing oscillator, respectively. We see from the expansion (2) that, for the Toda potential, the parameter ab controls the basic oscillation frequency and the parameter ab^2 controls the anharmonicity of the forces acting between the particles, so that b can be interpreted as the stiffness

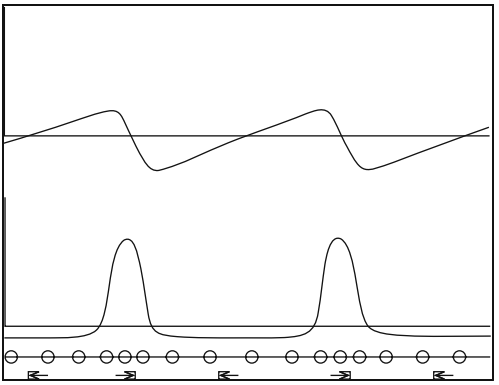

Fig. 2 Toda lattice. Lattice compressions (*bottom*) create solitons (pulse-like disturbances, solitary waves or periodic cnoidal wave peaks); momentum distribution along the lattice is shown at the top. Note that, taking into account the sign of the velocity (left to right motion), the former is the (negative) derivative of the latter

parameter of the springs. The solitary waves and (periodic) cnoidal waves found by Toda are the new "degrees of freedom" of the lattice, corresponding to Fourier modes in the linear approximation. For a uniform lattice $b_n = b(-\infty < n < \infty)$, the exact solutions are the cnoidal waves (Fig. 2)

$$\exp(-br_n) - 1 = m\frac{(2K\nu)^2}{ab}\left(\mathrm{dn}^2\left[2\left(\frac{n}{\lambda} \pm \nu t\right)K\right] - \frac{E(k)}{K(k)}\right), \tag{3}$$

where the wavelength λ and the frequency ν are related by the dispersion relation

$$\nu(\lambda) = \frac{\sqrt{\dfrac{ab}{m}}}{2K(k)\sqrt{\mathrm{sn}^{-2}(2K(k)/\lambda) - 1 + E(k)/K(k)}}. \tag{4}$$

Here $\mathrm{sn}(u)$ and $\mathrm{dn}(u)$ are elliptic functions with modulus k $(0 < k \leq 1)$. $K(k)$ and $E(k)$ are complete elliptic integrals [12, 13, 30].

When the modulus k is close to zero (i.e., for small values of the displacement), $E/K \simeq 1 - k^2/2$ and

$$r_n \simeq -\frac{\pi^2\nu^2k^2}{2ab^2}\cos 2\pi\left(\nu t \pm n/\lambda\right), \tag{5}$$

then the wave profile and dispersion of cnoidal waves in the Toda lattice are similar to those of harmonic (sinusoidal) waves in a linear lattice.

In the limit $k \to 1$, the cnoidal wave approaches a sequence of equally spaced delta functions. For $\lambda \approx K \to \infty (k \to 1)$, the result is a solitary wave

$$\exp\left(-b(r_{n+1} - r_n)\right) = 1 + \sinh^2(\chi)\,\mathrm{sech}^2\left(\chi n - t/\tau\right). \tag{6}$$

These "solitonic" excitations correspond to local compressions of the lattice with the characteristic compression time

$$\tau_{\mathrm{sol}} = (\omega \sinh\chi)^{-1} \tag{7}$$

and with a spatial "width" χ^{-1}. The energy of the soliton is related to this quantity by

$$\varepsilon_{\mathrm{sol}} = 2\frac{a}{b}(\sinh\chi\cosh\chi - \chi), \tag{8}$$

with σ taken as the unit of length. The soliton velocity is given by

$$v_{\mathrm{sol}} = \sigma\sqrt{\frac{ab}{m}}\frac{\sinh\chi}{\chi}, \tag{9}$$

which is supersonic, since the sound velocity in the corresponding linear lattice is $\sigma\sqrt{ab/m}$, with both velocities being given in common appropriate units [$\omega_0\sigma = \sigma\sqrt{ab/m}, \sigma = 1$ and even $\omega_0 = 1$ in most of the text]. Figure 2 illustrates how compressions create the solitonic peaks and the wave motion along the Toda lattice.

3 Self-Organization with an Input–Output Energy Balance

Driving, forcing and hence maintaining nonlinear oscillations in a Toda lattice can be achieved using the following Langevin equations:

$$\begin{aligned} \frac{\mathrm{d}}{\mathrm{d}t}x_i &= v_i, \\ m\frac{\mathrm{d}}{\mathrm{d}t}v_i + \frac{\partial U}{\partial x_i} &= F_i(v_i) + m\sqrt{2D}\,\xi_i(t), \end{aligned} \tag{10}$$

governing the evolution of the *i*th particle viewed as a Brownian element on the lattice. Here, the stochastic forces mimic embedding the system in a thermal bath or reservoir, from where the lattice units can pump energy in a kind of self-organization, obtaining order out of the noise. They have zero mean and are delta-correlated:

$$\begin{aligned} \langle\xi_i(t)\rangle &= 0, \\ \langle\xi_i(t)\xi_j(t)\rangle &= \delta_{ij}\delta(t'-t). \end{aligned}$$

Note that if we go back to the deterministic description ($D = 0$) and set $F_i = 0$, we get Newton's equations for the original Toda lattice [12, 13].

In order to introduce an input–output energy balance into the system, we define a force, F_i, including its *passive* and *active* components. Following Lord Rayleigh [22, 23], (an alternative is Van der Pol's approach [24]) we define a velocity-dependent friction force by

$$F(v) = F_0(v) + F_{\mathrm{a}}(v) = -m\gamma(v)\,v, \tag{11}$$

with

$$\gamma(v) = \gamma_0 + \gamma_{\mathrm{a}}(v), \tag{12}$$

where the first term, γ_0, describes the standard friction between the particles and the surrounding heat bath. For this *passive* friction, we assume the validity of the Einstein fluctuation–dissipation theorem [31, 32]. However, for simplicity, we assume that the *active* (non-equilibrium) part of the friction force, γ_a, does not fluctuate.

The balance for the total energy, ε, of the system (10) is

$$\frac{d\varepsilon}{dt} = -m\gamma_0 \sum_i v_i^2 - m \sum_i \gamma_a(v_i) v_i^2 + m\sqrt{2D} \sum_i v_i \xi_i. \tag{13}$$

Since $\gamma_0 > 0$, the sign of the active term, $\gamma_a(v)$, is crucial for the energy balance of our lattice if we wish to have a steady state ($d\varepsilon/dt = 0$). As noted earlier, this contribution to the friction function may describe *active* forces, which, due to their energy pumping effect, can drive the system away from equilibrium. Retaining Lord Rayleigh's law, we set

$$F_a(v) = -m\gamma_a(v)v = -m\left(-\hat{\gamma}_1 + \gamma_2 v^2\right) v;\ \hat{\gamma}_1,\ \gamma_2 > 0, \tag{14}$$

and hence, for $\hat{\gamma}_1 > \gamma_0$, we re-write the complete dissipative force as

$$F(v) = m\gamma_0 \left(\mu - v^2/v_d^2\right) v, \tag{15}$$

with

$$\mu = (\hat{\gamma}_1 - \gamma_0)/\gamma_0, \qquad v_d^2 = \gamma_0/\gamma_2. \tag{16}$$

Instead of the Rayleigh law, we may use a more refined law for the dissipative force by introducing the expression [31, 32]

$$\gamma_1 = -\gamma_0 \frac{\delta}{1 + v^2/\hat{v}_d^2}. \tag{17}$$

Then the total friction force acting on a particle may be represented as

$$F(v) = -m\gamma_0 \left[1 - \frac{\delta}{1 + v^2/\hat{v}_d^2}\right] v. \tag{18}$$

Note that (18) yields (15) for low velocity values when we replace $(\delta - 1)$ with μ and $\hat{v}_d^2$ with δv_d^2. For simplicity, we shall continue with (15).

The parameters μ and δ control the conversion of the energy taken up from the reservoir into kinetic energy. One or the other is the bifurcation parameter of our model. The values $\mu = -1$ and $\delta = 0$ correspond to equilibrium, the region $-1 < \mu < 0$, or $0 < \delta < 1$, stands for nonlinear *passive* friction and $\mu > 0$, or $\delta > 1$, corresponds to an *active* friction force. The bifurcation from one regime to the other occurs at $\mu = 0$, or $\delta = 1$. For the *passive* regime, the friction force vanishes at $v = 0$, which is the only attractor of the deterministic motion, i.e., with no noise, all particles come to rest at $v = 0$. For the *active* case, the point $v = 0$ becomes unstable, but we then have two additional zeros at

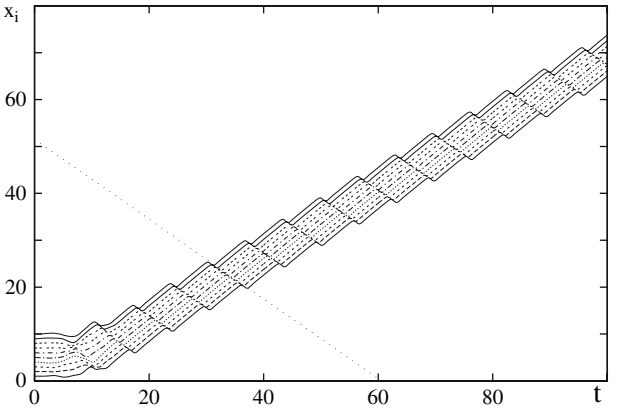

Fig. 3 Active Toda lattice. Trajectories (x, t) of 10 particles with added *active* Rayleigh friction force. Solitons (peaks of the cnoidal waves) appear traveling (*dotted line*) along the lattice in the direction which is opposite to that of the mean motions of the lattice particles. The single soliton is genuine solitary wave appearing in the lattice. It was obtained by suitably adjusting the randomly distributed initial velocities of the particles. The soliton velocity is given by the slope of the dotted line. Parameter values: $\omega_0 = 1$, $\sigma = 1$, $\gamma_0 = 0.8$, $\mu = 1$, $b = 1$ and $D = 0$

$$v = \pm v_0,\ v_0 = \hat{v}_\mathrm{d}\sqrt{\delta - 1} = \sqrt{\delta - 1},\ \text{as } \hat{v}_\mathrm{d} = 1 \text{ or } v_0 = v_\mathrm{d}\sqrt{\mu} = \sqrt{\mu},\ \text{as } v_\mathrm{d} = 1. \tag{19}$$

The two velocities, $\pm v_0$, are the new "attractors" of the free deterministic motion.

We look for a description with universality using dimensionless equations through an appropriate choice of scales. In the light of earlier comments, and for illustrative computational purposes, we set $m = 1$, $\sigma = 1$, and $\omega_0 = 1$. In Fig. 3, we show the result of a numerical integration of (10) for 10 lattice units without forcing and with no noise, but with an *active* friction force. The Toda lattice units are moving clockwise, while the excited soliton is moving counter-clockwise (as illustrated by the dotted line).

4 Electromechanical Toda Lattice

Let us consider the role of *dissipative* solitons in the *active* Toda lattice endowed with electric charges (ions and electrons). Hence, we now view the Toda lattice units as ions (charge $+e$ and mass m_i; $m_\mathrm{i} = m$) interacting with *free* electrons (charge $-e$ and mass $m_\mathrm{e} << m_\mathrm{i}$, $m_\mathrm{i} \approx 10^3 m_\mathrm{e}$; we expect no confusion regarding the subscripts "e" and "i", which here refer to electrons and ions, respectively). If we approximate the repulsion of the ions with a simple exponential law (see Fig. 1), then the 1D ion system on a lattice is equivalent to a 1D Toda lattice (1),

$$U(r_k) = \frac{m\omega_0^2}{b^2}\exp(-br_k) \tag{20}$$

(recall that $a/b = m\omega_0^2/b^2,\ \sigma = 1$). Thus, for small displacements, an ion moves in the harmonic potential of its nearest neighbors, while for larger values of the displacement, it feels a stiff (exponential) repulsion on each side. In principle, the stiffness, b, is a tunable parameter. Let us study the influence of the dynamics of the system on its electrical conductivity.

Let us place the N electrons at positions y_j (thus having electro-neutrality) and allow them to move freely in the non-uniform and, in general, time-dependent, electric field generated by the positive lattice particles (ions) located at lattice positions x_k. For simplicity, we describe the electron–ion interaction with a pseudo-potential with an appropriate cut-off [33]:

$$U_{\mathrm{e}}(y_j) = \sum_k \frac{(-e)e}{\sqrt{(y_j - x_k)^2 + h^2}}. \tag{21}$$

This potential avoids the pole (a Coulomb singularity) by introducing a cut-off at $U_{\min} = -e^2/h$; $h \approx \sigma/2$ is the cut-off distance and, as previously noted, σ is the equilibrium inter-ion mean distance. [N.B. Quantum mechanically, (21) is justified by the fact that, in a real solid, the ion core is a region of high electronic density and finite size, and so it can hardly be penetrated by a *free* electron.] Figure 4 illustrates, using suitable dimensionless quantities, the role of the cut-off, h, and of the compression of the Toda springs in the lattice.

To avoid Coulomb singularities in 1D or 2D geometry in (21), we consider the *free* electrons to be moving along the lattice in 3D. Accordingly, the electrons are able to move from one side of an ion to the other. Also, for simplicity, the interaction between electrons is neglected. Thus, with N ions placed at co-ordinates x_k, moving

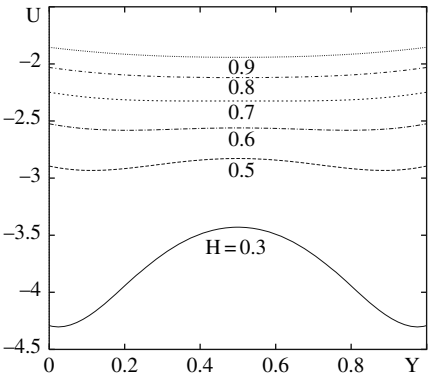

Fig. 4 Electromechanical Toda lattice. Pseudo-potential (21) experienced by an electron placed midway between two nearby ions. The graphs here appear in universal forms, since we use $H \equiv h/r, Y \equiv y/r, X \equiv x/r$, hence $x_1 = 0 \to X = 0, x_2 = r \to X = 1$ and $0 < y < r \to 0 < Y < 1$. Also, $U(Y)/e^2 = -\left[Y^2 + H^2\right]^{-1/2} - \left[(Y-1)^2 + H^2\right]^{-1/2}$. As H grows, either because h grows (cut-off length increases) or r decreases (compression increases), the maximum yields to a minimum midway between the two ions

on a lattice of length $L = N\sigma$, and in view of the evolution assumed for the ions (10), we now make use of Langevin dynamics for electrons, which are also taken to be Brownian elements:

$$\begin{aligned} \frac{\mathrm{d}}{\mathrm{d}t} y_j &= v_j, \\ m_\mathrm{e}\frac{\mathrm{d}v_j}{\mathrm{d}t} + \sum_k \frac{\partial U_\mathrm{e}(y_j, x_k)}{\partial y_j} &= -eE - m_\mathrm{e}\gamma_{\mathrm{e}0} v_j + m_\mathrm{e}\sqrt{2D_\mathrm{e}}\ \xi_j(t). \end{aligned} \tag{22}$$

We assume periodic boundary conditions. For further simplicity, we may, on occasion, consider just one electron located at a position y, rather than N (non-interacting) electrons at co-ordinates y_j. Note that the friction of the electrons is assumed to be purely *passive* (i.e., we have standard damping for all velocities). As for the ions (10), the stochastic force in (22) also models a surrounding heat bath (Gaussian white noise), but, following Einstein's relation [31, 32], temperatures need not be equal (as we disregard issues of thermal equilibrium). Note also that the friction force acting on the electron is small relative to that on the ions, $m_\mathrm{e}\gamma_{\mathrm{e}0} \ll m_\mathrm{i}\gamma_{\mathrm{i}0}$ (the subscript "0" denotes passive friction).

As we have now "ions" and "electrons", (1) must be replaced by

$$U = \sum_{k=1}^{N} [U_\mathrm{i}^\mathrm{T}(r_k) + U_\mathrm{e}(r_k)], \tag{23}$$

with $U_\mathrm{i}^\mathrm{T}(r_k)$ denoting the Toda exponential potential (1) and $U_\mathrm{e}(r_k)$ the electron–ion potential (21). The external electric field E also acts on the charge $e_\mathrm{i} = +e$ of the Toda particles (ions). Making the Rayleigh-like velocity-dependent force explicit, the Langevin equation in (10) becomes

$$m\frac{\mathrm{d}}{\mathrm{d}t} v_k + m\gamma_0 v_k + \frac{\partial U}{\partial x_k} = eE + F_\mathrm{a}(v_k) + m\sqrt{2D}\ \xi_k(t), \tag{24}$$

where k denotes the kth ion on the lattice ring. Our evolution problem is now the combined set of (22) and (24). These equations have been integrated by means of a fourth-order Runge–Kutta algorithm adapted for solving stochastic problems like the Langevin equation [34]. All computer runs begin with a state where the distances between ions are equal and their velocities are taken randomly from a normal distribution with amplitude v_in, $v_k(0) = v_\mathrm{in}\xi(k)$. Each electron is placed at rest, $v_j = 0$, midway between two ions. Heavy ions are not affected much by light electrons, and hence (free) electrons move on the background/landscape of the pseudo-potential profile created by the ions (Fig. 5). The integration step is chosen to correctly describe the fastest component of the process, viz. oscillations of electrons in a potential well. The parameters of both Toda and Coulomb potentials, the mass ratio and the particle charges are all held fixed in order to reduce the number of parameters of the problem. Thus, the damping rates, γ_0 and $\gamma_{\mathrm{e}0}$; the values of the parameters characterizing the driving forces, $F_\mathrm{a}(v_k)$; the initial velocity, v_in, chosen to select a

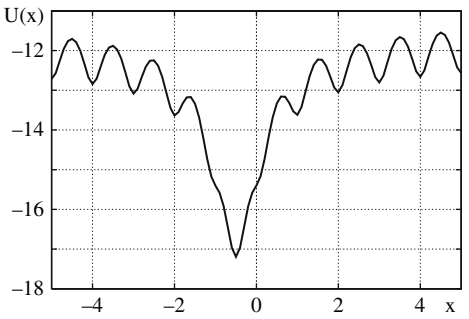

Fig. 5 Electromechanical Toda lattice. Snapshot of the effective potential/landscape acting on an electron moving in a lattice with a solitonic excitation which creates a locally deeper potential well. In a lattice which is sufficiently long, the solitonic (negative) peaks define a new periodicity (cnoidal waves) which is different from the other (quasi) harmonic one. Parameter values: $\sigma = 1$, $b = 1$ and $h/\sigma = 0.3$

solitonic mode; the value of the external field; and the electron temperature, T, are varied in the computer integrations.

5 From Ohm's Law to a Soliton-Mediated Supersonic Current

Due to the above-mentioned large difference in the masses of the charged particles, by far the major contribution to the current comes from the electrons moving on the nonlinear ion lattice. The current density (per unit length) of the electrons is obtained by taking average of the electron velocities. Hence, the electric current density (per unit length) is

$$j_{\mathrm{e}} = -n_{\mathrm{e}} e \sum_j \langle v_j^{\mathrm{e}} \rangle, \tag{25}$$

($n_{\mathrm{e}} = 1$ with 10 electrons and 10 ions). The average should be taken over sufficiently long trajectories. We are interested in the interaction of the electrons with the previously discussed (rather deep) solitonic excitations in the lattice (Fig. 5).

Before embarking on a study of electric currents, we study the effect of solitonic excitations generated through quenching by numerically finding the corresponding solutions of the coupled Langevin equations (22) and (24). Let us first discuss what happens if $E = F = 0$ in (24). The numerical integration was conducted by starting from a Gaussian distribution of the ion velocities, corresponding to a high-temperature Maxwellian as the initial condition. This temperature was of the order of 200–300 in units of $m\omega_0^2\sigma^2$, the energy of harmonic oscillations with amplitude σ (for clarity we make all variables and parameters explicit). At this rather high temperature, solitons should also be generated in addition to other elementary excitations. However, they are difficult to identify due to the seemingly chaotic motions

of the particles. Then, we quench to a temperature near zero. The solitons survive, since they have a longer lifetime than other excitations.

In another set of computer integrations, we combined quenching with active friction ($F \neq 0$) to overcome the dissipation. Again, the numerical integration started with a high-temperature initial condition, then, after quenching, the solitonic excitations were maintained by feeding in energy with Rayleigh's *active* friction force. In this case, and as noted earlier, the system develops solitons moving oppositely to the field. The electrons which are coupled to the charged Toda lattice units (ions) form rather stable dynamic bound states with the solitons (solectrons). For illustration, we take (unless otherwise specified) $\mu = 1$. Most of the time, the electrons will be located near local ion clusters, since they seek the deepest nearby minimum of the potential (see Fig. 4). Note that we have a dynamic process which does not lead to a static cluster, as the ions participating in the local compression are changing all the time. In other words, the electrons continually have new partners (a kind of promiscuity) in forming the bound states.

[N.B. An active Toda lattice (with Rayleigh's *active* friction force) with N particles possesses $(N+1)$ basic attractors. Of these, $(N-1)$ are oscillatory and two are non-oscillatory. (As a whole, the lattice moves to the right or left or clockwise/counter-clockwise in a lattice ring.) For N even, there is also an "optical" mode, corresponding to anti-phase oscillations. Here, we opt not to discuss this wealth of possibilities and hence, once more, refer the reader to recent publications on the subject [17, 18, 35].]

In Fig. 6, we show the evolution of 10 Toda lattice units (ions) creating 1 dissipative soliton which moves in the opposite direction and 10 *free*, non-interacting electrons. After a sufficient time interval, most of the electrons bind to the soliton, one after another, and move with a velocity which is approximately that of the

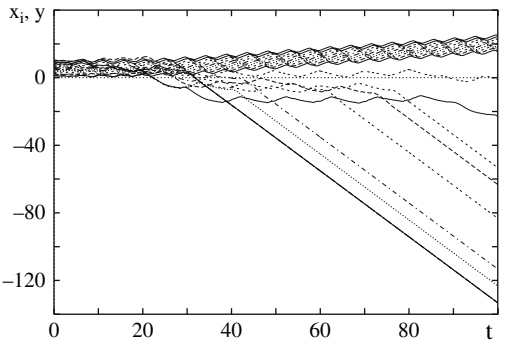

Fig. 6 Active electric Toda lattice. Trajectories are shown for 10 particles (ions) moving left to right, creating one fast dissipative soliton moving in the opposite direction, and for 10 electrons (ending, generally, as *sloped lines*) captured, one after another, by the soliton. Three electrons seem to be traveling together (*thicker sloped line*), while the 10th electron still moves almost freely (trajectory around $y = 0$). Parameter values: $h = 0.3$, $\mu = 0.25$, $\gamma_0 = \gamma_{e0} = 0.5$, $D = D_e = 0$ and $m/m_e = 10^3$. Unit time along abscissa: $t/\sqrt{5}$

soliton in a direction opposite to that of the ions. Needless to say, this is possible in the context of pure classical mechanics with the free non-interacting electron approximation that we have used here.

We have seen in the computer simulations that, when $\mu > 0$ for $E \neq 0$, the ions execute a slow drift following the direction of the external field. If the field strength is stronger than the decay imposed by the thermal fluctuations, then the electrons proceed in opposite direction. After a sufficient time interval, the ion compressions create solitonic excitations moving with the soliton velocity, v_{sol}, and opposite to the mean drift of the ions. As discussed in the earlier case, the electrons "like" the potential well formed by the local compression connected with the soliton (Fig. 5). After a while, the electrons are captured by the local compressions and move with the soliton velocity and opposite to the ion drift.

The magnitudes of both the electron and ion currents do not depend on the value of the external field over a wide range. Figure 7 shows both currents versus field strength. The scale, E_0, corresponds to the field imparting a velocity v_0 to an electron which is not interacting with the ions. It clearly appears that the stationary currents corresponding to the case of dissipative solitons are indeed stabilized, thanks to the *active* friction force that is due to energy pumping or, more precisely, to the input–output energy balance. At very low values of the field strength, we observe an apparent gap in the values for the current. In this narrow region, around zero, we could not obtain reliable data from the computer simulations. For very low electric field strengths, we cannot specify the running direction for solitons, and they may travel in either direction. On the other hand, intense field values do not allow electrons to be trapped easily by a potential well. In particular, at the upper boundary of the range, electrons are only captured by the soliton for a very limited domain of initial conditions for ions and electrons.

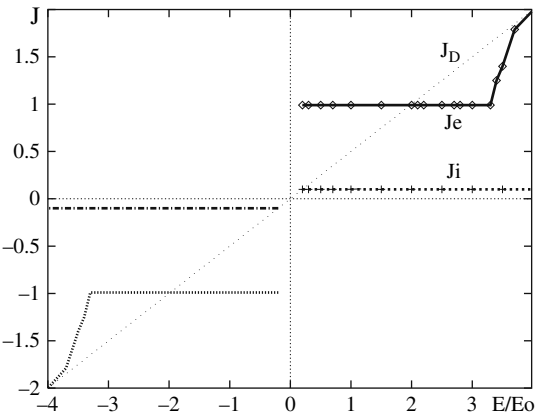

Fig. 7 Active electric Toda lattice. Current-field characteristics displaying the steady current densities (j_{D}, Ohm–Drude; j_{i}, ion current; and j_{e}, electron current). We see nonlinear current-field characteristics with a region of constant current. We observe an apparent gap in the values for the current at very small field values. Parameter values: $h = 0.3$, $\mu = 0.25$, $\gamma_0 = \gamma_{\mathrm{e}0} = 0.5$, $D = D_{\mathrm{e}} = 0$, $m/m_{\mathrm{e}} = 10^3$ and $b = 1$. E_0 is defined in the main text

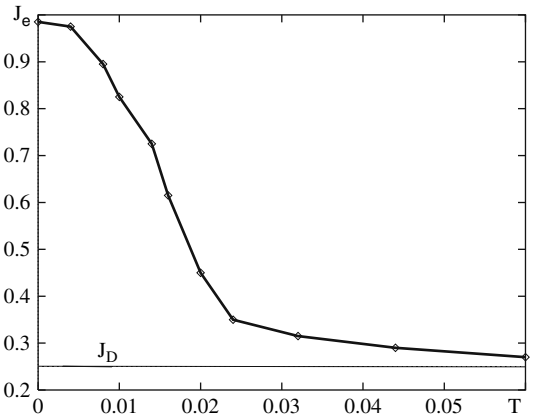

Fig. 8 Active electric Toda lattice. Current-temperature (electron noise) characteristics. The *solid line* (j_e, electron current) shows a significant increase as the temperature decreases and approaches the soliton range. The *horizontal straight dotted line* (ordinate 0.5) corresponds to the Ohm (Drude) current ($j_D = 0.25$). The value at $T = 0$ is the same as that of the plateau in Fig. 7. Parameter values: $b = 1$, $\mu = 0.25$, $h = 0.3$, $\gamma_0 = \gamma_{e0} = 0.5$, $T = D_e$, $D = 0$, $m/m_e = 10^3$ and $E/E_0 = 0.5$. E_0 is defined in the main text

Figure 8 illustrates the behavior of the electron current as a function of the temperature (electron noise). We see that, on lowering the temperature, the electron current driven by the solectrons grows significantly relative to the Ohm (Drude) current.

6 Final Remarks

The excitation of *dissipative* solitons in a Toda lattice has been discussed. In particular, we have studied the evolution of the lattice with added dissipation and "activity" in the form of energy pumping, following an idea put forward by Lord Rayleigh to maintain vibrations. We have considered the Toda lattice units as *active* Brownian elements. Then, we have studied the electrically charged (with ions and electrons) active Toda lattice and we have shown how the electric field triggers electric currents with striking properties. For such an active Toda lattice, we have shown how a (non-equilibrium) transition occurs beyond an instability threshold. This is from the linear Ohm (Drude) conduction (that can be viewed as defining a "disordered" state) to a form of "super-current" (that can be viewed as characterizing a more "ordered" state). The underlying mechanism of such a non-Ohmic supersonic current is the formation of electron–soliton dynamic bound states (solectrons) due to the role played by the compressions in the Toda springs. One of the most interesting properties of the phenomena studied here appears to be that, for a wide plateau, the strength of the external field is nearly irrelevant, and that what matters is its symmetry-breaking

role. On the other hand, it seems pertinent to point out that an electromechanical active Toda lattice can be seen as a versatile, two-speed neural-like cable. Recall that action potential propagation in axons, as in the case of the squid, proceeds at about 400 km/h [36]. This is the typical velocity of a super-critical ocean solitary wave and is equivalent to supersonic in the lattice studied here.

The study provided here is based on purely classical dynamics (i.e., no quantum mechanics is involved). Recent quantum mechanical calculations using the tight binding approximation for the electron–lattice interaction support the results reported in [37, 38, 39]. The results found, first reported in a 2005 letter [28], share common (formal) features with the experimental curves obtained in measurements of the characteristics of high-T superconductors [40, 41]. We are aware of pictures that look alike, yet refer to different objects. Hence, linking the predictions made using the purely classical analysis of a 1D Toda lattice model with data about real systems, or discussing any quantum effects, is beyond the scope of this discussion [42, 43].

Acknowledgments This research was, in part, supported by the EU under Grant SPARK.

References

1. N.J. Zabusky and M.D. Kruskal, Phys. Rev. Lett. **15**, 57 (1965). 321
2. A.C. Scott, F.Y.F. Chu and D.W. McLaughlin, Proc. IEEE **61**, 1443 (1973). 321
3. A.C. Scott, *Nonlinear Science: Emergence & Dynamics of Coherent Structures*, 2nd edn (Oxford University Press, New York, 2003). 321
4. N.J. Zabusky, Chaos **15**, 015102 (2005). 321
5. C.I. Christov, G.A. Maugin and M.G.Velarde, Phys. Rev. E **54**, 3621 (1996). 321
6. J.V. Boussinesq, Mém. présentés par divers savants à l'Acad. Sci. Inst. France (Paris) **23**, 1 (1877). J.V. Boussinesq, Mém. présentés par dıvers savants à l'Acad. Sci. Inst. France (Paris) **24**, No. 2, 1 (1978). 321
7. D.J. Korteweg and G. de Vries, Phil. Mag. **39**, 442 (1895). 321
8. E. Fermi, J.R. Pasta and S.M. Ulam, *Studies of Nonlinear Problems* (Los Alamos Nat. Lab. Report LA-1940, 1955); Reprinted in *Collected Papers of Enrico Fermi*, (Univ. Chicago Press, Chicago, 1965) pp. 978–988. 321
9. G.P. Berman and F.M. Izrailev, Chaos **15**, 015104 (2005). 321
10. D.N. Payton III, M. Rich and W.M. Visscher, Phys. Rev **160**, 706 (1967). 322
11. A.J. Heeger, S. Kivelson, J.R. Schrieffer and W.P. Su, Rev. Mod. Phys. **60**, 781 (1988) (and references therein). 322
12. M. Toda, *Theory of Nonlinear Lattices*, 2nd edn (Springer-Verlag, New York, 1989a). 322, 323, 324, 325
13. M. Toda, *Nonlinear Waves and Solitons* (KTK Scientific Publishers, Tokyo, 1989b). 322, 323, 324, 325
14. A.R. Bishop, J.A. Krumhansl and S.E. Trullinger, Physica D **1**, 1 (1980). 322
15. M. Toda, Phys. Scripta **20**, 424 (1979). 322
16. M. Remoissenet, *Waves Called Solitons*, 3rd edn (Springer, Berlin, 1999). 322
17. V.A. Makarov, E. del Rio, W. Ebeling and M.G. Velarde, Phys. Rev. E **64**, 036601 (2001). 322, 331
18. E. del Rio, V.A. Makarov, M.G. Velarde and W. Ebeling, Phys. Rev. E **67**, 056208 (2003). 322, 331
19. C.I. Christov and M.G. Velarde, Physica D **86**, 323 (1995). 323
20. A.A. Nepomnyashchy, M.G. Velarde and P. Colinet, *Interfacial Phenomena and Convection* (CRC-Chapman & Hall, London, 2002), Chapter 5. 323

21. V.I. Nekorkin and M.G. Velarde, *Synergetic Phenomena in Active Lattices. Patterns, Waves, Solitons, Chaos* (Springer, Berlin, 2002). 323
22. J.W. Strutt (Lord Rayleigh), Phil. Mag. **15**, 229 (1883). 323, 325
23. J.W. Strutt (Lord Rayleigh), *The Theory of Sound*, (original, 1894, reprinted by Dover, New York, 1945), vol. I, Sect. 68a. 323, 325
24. B. Van der Pol, Phil. Mag. **2**, Ser. 7, 978 (1926). B. Van der Pol, Phil. Mag. **3**, Ser. 7, 65 (1927). 323, 325
25. M.G. Velarde and X.-L. Chu, Phys. Lett. A **131**, 430 (1988). 323
26. X.-L. Chu and M.G. Velarde, Il Nuovo Cimento D **11**, 709 (1989). 323
27. M.G. Velarde, Benard layers, overstability and waves. In *Dynamics of Spatio-Temporal Cellular Structures-Henri Benard Centenary Review*, (Springer, New York, 2006, Springer Tracts in Modern Physics), Vol. 207, pp. 129–145. 323
28. M.G. Velarde, W. Ebeling and A.P. Chetverikov, Int. J. Bifurcat. Chaos **15**, 245 (2005). 323, 334
29. E. del Rio, A. Rodriguez-Lozano and M.G. Velarde, Rev. Sci. Instrum. **63**, 4208 (1992). 323
30. M. Abramowitz and I.A. Stegun (eds.), *Handbook of Mathematical Functions, with Formulas, Graphs, and Mathematical Tables*, (Dover, New York, 1965). 324
31. F. Schweitzer: *Brownian Agents and Active Particles. Collective Dynamics in the Natural and Social Sciences* (Springer, Berlin, 2003). 326, 329
32. W. Ebeling and I.M. Sokolov, *Statistical Thermodynamics and Stochastic Theory of Nonequilibrium Systems*, (World Scientific, Singapore, 2005). 326, 329
33. V. Heine, M.L. Cohen and D. Weaire, *The Pseudopotential Concept*, (Academic Press, New York, 1970). 328
34. A.P. Chetverikov and J. Dunkel, Eur. Phys. J. B **35**, 239 (2003). 329
35. V.A. Makarov, M.G. Velarde, A.P. Chetverikov and W. Ebeling, Phys. Rev. E **73**, 066626 (2006). 331
36. J. Cronin, *Mathematical Aspects of Hodgkin-Huxley Neural Theory*, (Cambridge University Press, Cambridge, 1987). 334
37. M.G. Velarde, W. Ebeling, D. Hennig, and C. Neissner, Int. J. Bifurcat. Chaos **16**, 1035 (2006). 334
38. D. Hennig, C. Neissner, M.G. Velarde and W. Ebeling, Phys. Rev. B **73**, 024306 (2006). 334
39. A.P. Chetverikov, W. Ebeling, G. Röpke and M.G. Velarde, Contrib. Plasma Phys. **47**, 465 (2007). 334
40. P. Chaudhari, J. Mannhart, D. Dimos, C.C. Tsuei, J. Chi, M.M. Oprysko and M. Scheuermann, Phys. Rev. Lett. **60**, 1653 (1988). 334
41. J. Mannhart, P. Chaudhari, D. Dimos, C.C. Tsuei and T.R. McGuire, Phys. Rev. Lett. **61**, 2476 (1988). 334
42. D. Hennig, A.P. Chetverikov, M.G. Velarde and W. Ebeling, Phys. Rev. E **76**, 046602 (2007). 334
43. M.G. Velarde, W. Ebeling, A.P. Chetverikov and D. Hennig, Int. J. Bifurcat. Chaos **18**, 521 (2008). 334

Coherent Optical Pulse Dynamics in Nano-composite Plasmonic Bragg Gratings

I.R. Gabitov, A.O. Korotkevich, A.I. Maimistov, and J.B. McMahon

Abstract The propagation of solitary waves in a Bragg grating formed by an array of thin nanostructured dielectric films is considered. A system of equations of Maxwell–Duffing type, describing forward- and backward-propagating waves in such a grating, is derived. Exact solitary wave solutions are found, analyzed, and compared with the results of direct numerical simulations.

1 Introduction

The last decade has been a period of rapid progress in the field of photonic crystals [1, 2, 3, 4, 5, 6, 7, 8, 9, 10]. In particular, the one-dimensional case of a *resonant Bragg grating* [1, 2, 3, 4, 5] or a *resonantly absorbing Bragg reflector* (RABR) [6, 7, 8] has been studied extensively. In the simplest case, a resonant Bragg grating consists of a linear homogeneous dielectric medium containing an array of thin films with resonant atoms or molecules. The thickness of each film

I.R. Gabitov
Department of Mathematics, University of Arizona, 617 North Santa Rita Avenue, Tucson, AZ 85721, USA, gabitov@math.arizona.edu
L.D. Landau Institute for Theoretical Physics, Russian Academy of Sciences, 2 Kosygin Street, Moscow, 119334, Russian,

A.O. Korotkevich
L.D. Landau Institute for Theoretical Physics, Russian Academy of Sciences, 2 Kosygin Street, Moscow, 119334, Russian, kao@itp.ac.ru

A.I. Maimistov
Department of Solid State Physics, Moscow Engineering Physics Institute Moscow, 115409, Russian, maimistov@pico.miphi.ru

J.B. McMahon
Program in Applied Mathematics, University of Arizona, 617 North Santa Rita Avenue, P.O. Box 210089, Tucson, AZ 85721-0089, USA, jmcmahon@math.arizona.edu

Gabitov, I.R. et al.: *Coherent Optical Pulse Dynamics in Nano-composite Plasmonic Bragg Gratings.* Lect. Notes Phys. **751**, 337–360 (2008)
DOI 10.1007/978-3-540-78217-9_13

is much less than the wavelength of the electromagnetic wave propagating through such a structure. The interaction of ultra-short pulses and films embedded with two-level atoms has been studied by Mantsyzov et al. [1, 2, 3, 4, 5] in the framework of the two-wave reduced Maxwell–Bloch model and by Kozhekin et al. [6, 7, 8]. These works demonstrated the existence of a 2π-pulse of self-induced transparency in such structures [1, 4, 6]. It was also found [8] that bright solitons, as well as dark ones, can exist in the prohibited spectral gap, and that bright solitons can have arbitrary pulse area.

If the density of two-level atoms is very high, then the near-dipole–dipole interaction is noticeable and should be accounted for in the mathematical model. The effect of the dipole–dipole interaction on the existence of gap solitons in a resonant Bragg grating was studied in [10]; details can be found in [9]. Recent numerical simulations have yielded unusual solutions known as *zoomerons* [11]. The optical "zoomeron" was discovered and investigated recently [12] in the context of the resonant Bragg grating. These works also contain careful construction of the underlying mathematical model, which is derived from first principles. A "zoomeron" is a localized pulse which is similar to an optical soliton, except that its velocity oscillates around some mean value.

Recent advances in nano-fabrication have allowed for the creation of nanocomposite materials, and these have the ability to sustain nonlinear plasmonic oscillations. These materials have metallic nano-particles embedded in them [13, 14, 15]. In this chapter, we consider a dielectric material, into which thin films containing metallic nano-particles have been inserted. These thin films are spaced periodically along the length of the dielectric, so that the Bragg-prohibited spectral gap is centered at the plasmonic resonance frequency of the nano-particles. We derive governing equations for the slowly varying envelopes of two counter-propagating electromagnetic waves and of the plasmonic oscillation-induced medium polarization. We find that this system of equations has the form of the two-wave Maxwell–Duffing model. We find exact solutions of this system and demonstrate that, in contrast to conventional 2π-pulses, they have nonlinear phase. We show that the stability of these solutions is sensitive to perturbation of this phase. We also study the collisions of these pulses and find that the outcomes of such collisions are highly dependent on relative phase.

There are three natural mechanisms of dissipation of energy in nanostructured Bragg gratings. The first mechanism is damping of the plasmonic oscillations, occurring within metallic nano-particles. In our work, we assume that the characteristic pulse duration is shorter than the characteristic time for these losses, and therefore, this type of loss can be neglected. The second source of dissipation is the result of irregularities in realistic gratings. Due to these irregularities, there is incomplete return of energy from the grating to the optical field during the field-grating interaction. As a result, non-returned energy that remains in the grating will be dissipated. The third mechanism is due to the presence of inhomogeneous broadening of the absorption line. In this case, the energy of the field is absorbed and redistributed among oscillators due to the phase modulation of the pulse. The range

of resonant frequencies of these excited oscillators is broader than the bandwidth of the optical field pulse. The energy of the oscillating particles which are outside that bandwidth will be dissipated. The material presented here is an essential starting point for work toward understanding the physics of these last two dissipation mechanisms for solitary pulses (dissipative solitons) in Bragg gratings with embedded nano-particles.

2 Basic Equations

We consider a grating formed by an array of thin films which are embedded in a linear dielectric medium. In our derivation of the governing equations, we follow [1, 2, 3, 4, 5, 6, 7, 8], wherein Bragg resonance arises if the distance between successive films is $a = (\lambda/2)\,m$, $m = 1,2,3,\ldots$. To obtain the governing equations, we apply the transfer-operator approach, as presented below.

2.1 Transfer-Operator Approach

Let us consider ultra-short optical pulse propagation along the X-direction of a periodic array of thin films, which are placed at points $\ldots, x_{n-1}, x_n, x_{n+1}, \ldots$ (Fig. 1). The medium between the films has dielectric permittivity ε. Hereafter, to be definite, we consider a TE-wave whose electric field component is parallel to the layers. All results can be easily generalized to the case of TM-polarized waves.

It is convenient to represent the electric and magnetic strengths $\boldsymbol{E}, \boldsymbol{H}$ and the polarization of the two-level atoms ensemble $\boldsymbol{P}$ in the form of Fourier integrals

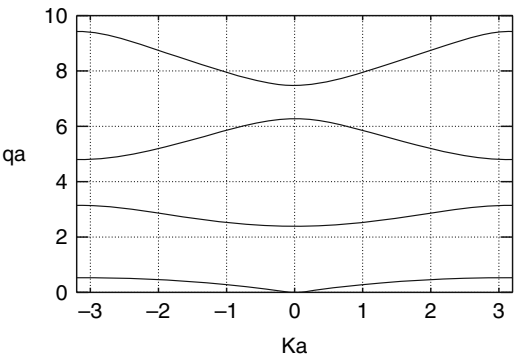

Fig. 1 An example of band structure, where inclusions are linear oscillators

$$\mathbf{E}(x,z,t) = (2\pi)^{-2} \int_{-\infty}^{\infty} \exp[-\mathrm{i}\omega t + \mathrm{i}\beta z]\boldsymbol{E}(x,\beta,\omega)\mathrm{d}t\ \mathrm{d}z,$$

$$\mathbf{H}(x,z,t) = (2\pi)^{-2} \int_{-\infty}^{\infty} \exp[-\mathrm{i}\omega t + \mathrm{i}\beta z]\boldsymbol{H}(x,\beta,\omega)\mathrm{d}t\ \mathrm{d}z,$$

$$\mathbf{P}(x_n,z,t) = (2\pi)^{-2} \int_{-\infty}^{\infty} \exp[-\mathrm{i}\omega t + \mathrm{i}\beta z]\boldsymbol{P}(x_n,\beta,\omega)\mathrm{d}t\ \mathrm{d}z.$$

Outside the films, the Fourier components of the vectors $\boldsymbol{E}(x,\beta,\omega)$ and $\boldsymbol{H}(x,\beta,\omega)$ are defined by the Maxwell equations. At points x_n, these values are defined from continuity conditions. Thus, the TE-wave propagation can be described by the following system:

$$\frac{\mathrm{d}^2E}{\mathrm{d}x^2} + \left(k^2\varepsilon - \beta^2\right)E = 0, \tag{1}$$

$$H_x = -(\beta/k)E, \quad H_z = -(\mathrm{i}/k)\mathrm{d}E/\mathrm{d}x, \quad E_y = E,$$

with boundary conditions [16, 17]

$$E(x_n - 0) = E(x_n + 0), \quad H_z(x_n + 0) - H_z(x_n - 0) = 4\mathrm{i}\pi k P_y(x_n,\beta,\omega), \tag{2}$$

where $k = \omega/c$. The solutions of (1) in the intervals $x_n < x < x_{n+1}$ can be written as

$$E(x,\beta,\omega) = A_n(\beta,\omega)\exp[\mathrm{i}q(x-x_n)] + B_n(\beta,\omega)\exp[-\mathrm{i}q(x-x_n)],$$

$$H_z(x,\beta,\omega) = qk^{-1}\left\{A_n(\beta,\omega)\exp[\mathrm{i}q(x-x_n)] - B_n(\beta,\omega)\exp[-\mathrm{i}q(x-x_n)]\right\},$$

where $q = \sqrt{k^2\varepsilon - \beta^2}$. Hence, the amplitudes A_n and B_n completely determine the electromagnetic field in a RABR. Let us consider the point x_n. The electric field at $x = x_n - \delta$ ($\delta << a$) is defined by amplitudes $A_n^{(L)}$ and $B_n^{(L)}$, and the field at $x = x_n + \delta$ is defined by $A_n^{(R)}$ and $B_n^{(R)}$. Continuity conditions (1) result in the following relations between these amplitudes:

$$A_n^{(R)} + B_n^{(R)} = A_n^{(L)} + B_n^{(L)},$$

$$A_n^{(R)} - B_n^{(R)} = A_n^{(L)} - B_n^{(L)} + 4\pi\mathrm{i}k^2q^{-1}P_{\mathrm{S},n},$$

where $P_{\mathrm{S},n} = P_{\mathrm{S}}(A_n^{(R)} + B_n^{(R)})$ is the surface polarization of a thin film at point x_n. This is induced by the electrical field inside the film. Thus we find

$$A_n^{(R)} = A_n^{(L)} + 2\pi\mathrm{i}k^2q^{-1}P_{\mathrm{S},n}, \quad B_n^{(R)} = B_n^{(L)} - 2\pi\mathrm{i}k^2q^{-1}P_{\mathrm{S},n}. \tag{3}$$

Taking into account the strength of the electric field outside the films, we write

$$A_{n+1}^{(L)} = A_n^{(R)} \exp(\mathrm{i}qa), \quad B_{n+1}^{(L)} = B_n^{(R)} \exp(-\mathrm{i}qa). \tag{4}$$

If the vectors $\psi_n^{(L)} = (A_n^{(L)}, B_n^{(L)})$ and $\psi_n^{(R)} = (A_n^{(R)}, B_n^{(R)})$ are introduced, then the relations (3) can be represented as

$$\psi_n^{(R)} = \widehat{U}_n \psi_n^{(L)},$$

where $\widehat{U}_n$ is the *transfer-operator* of the vector $\psi_n^{(L)}$ through the film located at point x_n. In the general case, $\widehat{U}_n$ is a nonlinear operator. The relations (4) are represented in the vectorial form

$$\psi_{n+1}^{(L)} = \widehat{V}_n \psi_n^{(R)},$$

where the linear operator $\widehat{V}_n$ transfers the vector $\psi_n^{(R)}$ between adjacent thin films and is represented by the diagonal matrix

$$\widehat{V}_n = \begin{pmatrix} \exp(\mathrm{i}qa) & 0 \\ 0 & \exp(-\mathrm{i}qa) \end{pmatrix}.$$

In this manner, we define the nonlinear transfer-operator of the vector $\psi_n^{(L)}$ through an elementary cell of RABR:

$$\psi_{n+1}^{(L)} = \widehat{V}_n \widehat{U}_n \psi_n^{(L)} = \widehat{T}_n \psi_n^{(L)}. \tag{5}$$

The transfer-operator approach is frequently used in models of one-dimensional photonic crystals made of linear media, e.g., distributed feedback structures [18].

In (5), the upper index can be omitted, and the equation can be rewritten as the following recurrence relations:

$$A_{n+1} = A_n \exp(\mathrm{i}qa) + 2\pi \mathrm{i}k^2 q^{-1} P_{\mathrm{S},n} \exp(\mathrm{i}qa), \tag{6}$$

$$B_{n+1} = B_n \exp(-\mathrm{i}qa) - 2\pi \mathrm{i}k^2 q^{-1} P_{\mathrm{S},n} \exp(-\mathrm{i}qa). \tag{7}$$

These recurrence relations are exact, since no approximations (e.g., the approximation of the slowly varying envelope of electromagnetic pulses or the long-wave approximation) have been employed. Furthermore, the surface polarization of a thin film could be calculated via various suitable models. Here we follow the works of Mantsyzov et al. [1, 2, 3, 4, 5], Kozhekin et al. [6, 7], and Kurizki et al. [8, 9], where the two-level atom model has been used.

2.2 Linear Response Approximation

To demonstrate that the RABR is a true gap medium, it is appropriate to obtain the electromagnetic wave spectrum through a linear response approximation. In the general case, we can use the following expression for the polarization:

$$P_{S,n} = \chi(\omega)(A_n^{(R)} + B_n^{(R)}). \tag{8}$$

Substitution of this formula into (6) and (7) yields

$$A_{n+1} = (1+\mathrm{i}\rho)A_n \exp(\mathrm{i}qa) + \mathrm{i}\rho B_n \exp(\mathrm{i}qa), \tag{9}$$

$$B_{n+1} = (1-\mathrm{i}\rho)B_n \exp(-\mathrm{i}qa) - \mathrm{i}\rho A_n \exp(-\mathrm{i}qa). \tag{10}$$

Here $\rho = \rho(\omega) = 2\pi k^2 q^{-1}\chi(\omega) = 2\pi\omega c^{-1}\varepsilon^{-1/2}\chi(\omega)$. We employ an ansatz in which the wave is a collective motion of the electrical field in the grating. Hence

$$A_n = A\exp(\mathrm{i}kna), \qquad B_n = B\exp(\mathrm{i}kna). \tag{11}$$

Equations (9) and (10) show that the wave amplitudes, A and B, satisfy the following linear system of equations:

$$A\exp(\mathrm{i}Ka) = (1+\mathrm{i}\rho)A\exp(\mathrm{i}qa) + \mathrm{i}\rho B\exp(\mathrm{i}qa), \tag{12}$$

$$B\exp(\mathrm{i}Ka) = (1-\mathrm{i}\rho)B\exp(-\mathrm{i}qa) - \mathrm{i}\rho A\exp(-\mathrm{i}qa). \tag{13}$$

A non-trivial solution of this system exists if, and only if, the determinant is equal to zero, i.e.,

$$\det\begin{pmatrix} (1+\mathrm{i}\rho)\exp(\mathrm{i}qa) - \exp(\mathrm{i}Ka) & \mathrm{i}\rho\exp(\mathrm{i}qa) \\ -\mathrm{i}\rho\exp(-\mathrm{i}qa) & (1-\mathrm{i}\rho)\exp(-\mathrm{i}qa) - \exp(\mathrm{i}Ka) \end{pmatrix} = 0. \tag{14}$$

If we define

$$Z = \exp(\mathrm{i}Ka),$$

$$G = (1+\mathrm{i}\rho)\exp(\mathrm{i}qa) = (\cos qa - \rho\sin qa) + \mathrm{i}(\rho\cos qa + \sin qa),$$

then (14) can be rewritten as the following equation in Z:

$$Z^2 - (G+G^*)Z + 1 = 0.$$

This equation has solutions

$$Z_\pm = \mathrm{Re}\ G \pm \mathrm{i}\sqrt{1-(\mathrm{Re}\ G)^2}.$$

If $\mathrm{Re}G \le 1$, then $\mathrm{Re}G \pm \mathrm{i}\sqrt{1-(\mathrm{Re}G)^2} = \cos Ka + \mathrm{i}\sin Ka$. Hence the wave-numbers, $K_\pm$, are real-valued and satisfy the transcendental equation

$$\cos Ka = \cos qa - \rho\sin qa. \tag{15}$$

If $\mathrm{Re}G > 1$, then the roots of (14) are real. In this case, the wave-numbers, $K_\pm$, are purely imaginary. The condition $\mathrm{Re}G > 1$ defines the frequencies of the forbidden zone. The waves with these frequencies cannot propagate in the grating. The boundaries of this forbidden zone are defined by

$$\cos qa - \rho \sin qa = 1. \tag{16}$$

The model of the resonant system, containing the thin films, defines the explicit form of the function $\rho = \rho(\omega)$. The form of $\rho(\omega)$ determines the dispersion relation (15). It should be noted that this dispersion relation ensures a series of gaps in the electromagnetic wave spectrum. Figure 1 represents an example of such a band structure when the inclusions are linear oscillators.

2.3 Long-Wave and Weak Nonlinearity Approximations

We can transform the exact equations (6) and (7) into differential equations by using the long-wave approximation. To do so, we introduce the field variables

$$A(x) = \sum_n A_n \delta(x - x_n), \quad B(x) = \sum_n B_n \delta(x - x_n),$$
$$P(x) = \sum_n P_{S,n} \delta(x - x_n).$$

Using the integral representation of a Dirac delta-function,

$$\delta(x) = (2\pi)^{-1} \int_{-\infty}^{\infty} \exp(\mathrm{i}kx)\mathrm{d}k,$$

we obtain the following expression:

$$A(x) = (2\pi)^{-1} \sum_n A_n \int_{-\infty}^{\infty} \exp[\mathrm{i}k(x - x_n)]\mathrm{d}k$$
$$= (2\pi)^{-1} \int_{-\infty}^{\infty} \exp(\mathrm{i}kx) \sum_n A_n \exp(-\mathrm{i}kx_n)\mathrm{d}k.$$

It follows that the Fourier transform of $A(x)$ is then

$$A(k) = \sum_n A_n \exp(-\mathrm{i}kx_n) = \sum_n A_n \exp(-\mathrm{i}kan),$$

and that the Fourier transforms of $B(x)$ and $P(x)$ are

$$B(k) = \sum_n B_n \exp(-\mathrm{i}kan), \quad P(k) = \sum_n P_{S,n} \exp(-\mathrm{i}kan),$$

respectively.

The form of these spatial Fourier components ensures periodicity in k. For example,

$$\begin{aligned} A(k) &= \sum_n A_n \exp(-\mathrm{i}kan)\exp(\pm 2\pi \mathrm{i}n) \\ &= \sum_n A_n \exp(-\mathrm{i}kan \pm 2\pi \mathrm{i}n) \\ &= \sum_n A_n \exp[-\mathrm{i}an(k \pm 2\pi/a)] = A(k \pm 2\pi/a). \end{aligned} \tag{17}$$

From the recurrence equations (6) and (7), we have

$$\begin{aligned} A(k)\exp(\mathrm{i}ka) &= A(k)\exp(\mathrm{i}qa) + \mathrm{i}\kappa P(k)\exp(\mathrm{i}qa), \\ B(k)\exp(\mathrm{i}ka) &= B(k)\exp(-\mathrm{i}qa) - \mathrm{i}\kappa P(k)\exp(-\mathrm{i}qa), \end{aligned}$$

or

$$[\exp\{\mathrm{i}a(k-q)\} - 1]A(k) = \mathrm{i}\kappa P(k), \tag{18}$$

$$[\exp\{\mathrm{i}a(k+q)\} - 1]B(k) = -\mathrm{i}\kappa P(k). \tag{19}$$

The linear approximation $P(k) = \chi(\omega)[A(k) + B(k)]$ for polarization again leads us to the linear dispersion law (14). The system of equations (18) and (19) is equivalent to the discrete equations (6) and (7). Up to this point, we have made no approximations other than the assumption on the width of the thin films.

If the thin film array was absent, then the dispersion relation would be

$$\cos ka = \cos qa.$$

In that case, the wave with amplitude $A(k)$ has $k = q$, indicating propagation to the right, while the wave with amplitude $B(k)$ has $k = -q$, indicating propagation in the opposite direction. Let us suppose that the polarization of the thin film array produces little change in wave vectors, i.e., for the right-propagating wave, the wave vector is $k = q + \delta k$, and for the opposite wave, the wave vector is $k = -q + \delta k$. If we set the value of q to be near one of the Bragg resonances, say $q = 2\pi/a + \delta q$, where $\delta q \ll 2\pi/a$, then (6) and (7) take the form

$$\begin{aligned} [\exp(\mathrm{i}a\delta k) - 1]A(q + \delta k) &= \mathrm{i}\kappa P(q + \delta k), \\ [\exp(\mathrm{i}a\delta k) - 1]B(-q + \delta k) &= -\mathrm{i}\kappa P(-q + \delta k). \end{aligned}$$

By virtue of the periodicity conditions (17), these equations can be rewritten as

$$\begin{aligned} [\exp(\mathrm{i}a\delta k) - 1]A(\delta q + \delta k) &= \mathrm{i}\kappa P(\delta q + \delta k), \\ [\exp(\mathrm{i}a\delta k) - 1]B(-\delta q + \delta k) &= -\mathrm{i}\kappa P(-\delta q + \delta k). \end{aligned}$$

After the change of variables $\delta k = \delta\tilde{k} \pm \delta q$, we have

$$\left[\exp\{\mathrm{i}a(\delta\tilde{k} - \delta q)\} - 1\right]A(\delta\tilde{k}) = \mathrm{i}\kappa P(\delta\tilde{k}), \tag{20}$$

$$\left[\exp\{\mathrm{i}a(\delta\tilde{k} + \delta q)\} - 1\right]B(\delta\tilde{k}) = -\mathrm{i}\kappa P(\delta\tilde{k}). \tag{21}$$

The long-wave approximation means that non-zero values of the spatial Fourier amplitudes are located near the zero value of the argument. Suppose that $a\delta\tilde{k}$ is small enough so that $\exp(\mathrm{i}a(\delta\tilde{k}+\delta q)) \approx 1+\mathrm{i}a(\delta\tilde{k}+\delta q)$. Then, we replace (20) and (21) with the approximate equations

$$\mathrm{i}a(\delta\tilde{k}-\delta q)A(\delta\tilde{k}) = \mathrm{i}\kappa P(\delta\tilde{k}), \tag{22}$$

$$\mathrm{i}a(\delta\tilde{k}+\delta q)B(\delta\tilde{k}) = -\mathrm{i}\kappa P(\delta\tilde{k}). \tag{23}$$

Now, if we return to the spatial variable, (22) and (23) lead us to the equations of coupled-wave theory:

$$\frac{\partial A}{\partial x} = \mathrm{i}\delta q A(x) + \mathrm{i}\kappa a^{-1}P(x), \tag{24}$$

$$\frac{\partial B}{\partial x} = -\mathrm{i}\delta q B(x) - \mathrm{i}\kappa a^{-1}P(x). \tag{25}$$

In these equations, the fields $A(x), B(x), P(x)$ and the parameters δq, κ are functions of the frequency ω. To obtain the final system of equations in the spatial and time variables, we carry out an inverse Fourier transform. We now assume that the envelopes of the electromagnetic waves vary slowly in time [12]. This approximation simplifies the system of coupled wave equations under consideration.

2.4 Slowly Varying Envelope Approximation

In the slowly varying envelope approximation, we assume that the approximated fields are inverse Fourier transforms of narrow wave packets, i.e., they are quasi-harmonic waves [12]. For example, the quasi-harmonic wave form of the electric field is

$$E(x,t) = \mathscr{E}(x,t)\exp[-\mathrm{i}\omega_0 t],$$

where ω_0 is the carrier wave frequency. The electric field, $E(x,t)$, and the Fourier components of the envelope, $\mathscr{E}(x,t)$, of the pulse are related by

$$\begin{aligned} E(x,t) &= (2\pi)^{-1}\int_{-\infty}^{\infty}\widetilde{E}(x,\omega)\exp(-\mathrm{i}\omega t)\mathrm{d}\omega \\ &= (2\pi)^{-1}\int_{-\infty}^{\infty}\widetilde{\mathscr{E}}(x,\omega)\exp[-\mathrm{i}(\omega+\omega_0)t]\mathrm{d}\omega \\ &= (2\pi)^{-1}\int_{-\infty}^{\infty}\widetilde{\mathscr{E}}(x,\omega-\omega_0)\exp(-\mathrm{i}\omega t)\mathrm{d}\omega, \end{aligned}$$

where the function $\widetilde{E}(x,\omega)$ is non-zero if $\omega \in (\omega_0 - \Delta\omega, \omega_0 + \Delta\omega)$, with $\Delta\omega \ll \omega_0$. Hence, $\widetilde{E}(x,\omega+\omega_0) = \widetilde{\mathscr{E}}(x,\omega)$. Thus, if we have some relation for $\widetilde{E}(x,\omega)$, then the analogous relation for $\widetilde{\mathscr{E}}(x,\omega)$ can be found by making the replacement $\omega \mapsto \omega_0 + \omega$ in all functions of ω.

Let

$$A(x,t) = \mathscr{A}(x,t)\exp(-\mathrm{i}\omega_0 t), \quad B(x,t) = \mathscr{B}(x,t)\exp(-\mathrm{i}\omega_0 t),$$
$$P(x,t) = \mathscr{P}(x,t)\exp(-\mathrm{i}\omega_0 t).$$

From (24) and (25), it follows that the Fourier components $\mathscr{A}(x,\omega), \mathscr{B}(x,\omega)$, and $\mathscr{P}(x,\omega)$ satisfy

$$\frac{\partial \mathscr{A}}{\partial x}(x,\omega) = \mathrm{i}\delta q(\omega_0+\omega)\mathscr{A}(x,\omega) + \mathrm{i}\kappa(\omega_0+\omega)a^{-1}\mathscr{P}(x,\omega), \tag{26}$$

$$\frac{\partial \mathscr{B}}{\partial x}(x,\omega) = -\mathrm{i}\delta q(\omega_0+\omega)\mathscr{B}(x,\omega) - \mathrm{i}\kappa(\omega_0+\omega)a^{-1}\mathscr{P}(x,\omega). \tag{27}$$

Since $\mathscr{A}$, $\mathscr{B}$, and $\mathscr{P}$ are non-zero for $\omega \ll \omega_0$, one can use the expansions:

$$\delta q(\omega_0+\omega) \approx q_0 - 2\pi/a + q_1\omega + q_2\omega^2/2, \quad \kappa(\omega_0+\omega)a^{-1} \approx K_0, \tag{28}$$

where $q_n = \mathrm{d}^n q/\mathrm{d}\omega^n$ at $\omega = \omega_0$. In particular, $q_1^{-1} = v_\mathrm{g}$ is the group velocity, while q_2 takes into account the group-velocity dispersion.

Considering expansions (28), we have the following description of the evolution of slowly varying envelopes:

$$\mathrm{i}\left(\frac{\partial}{\partial x} + \frac{1}{v_\mathrm{g}}\frac{\partial}{\partial t}\right)\mathscr{A} - \frac{q_2}{2}\frac{\partial^2}{\partial t^2}\mathscr{A} + \Delta q_0 \mathscr{A} = -K_0\mathscr{P}, \tag{29}$$

$$\mathrm{i}\left(\frac{\partial}{\partial x} - \frac{1}{v_\mathrm{g}}\frac{\partial}{\partial t}\right)\mathscr{B} + \frac{q_2}{2}\frac{\partial^2}{\partial t^2}\mathscr{B} - \Delta q_0 \mathscr{B} = +K_0\mathscr{P}, \tag{30}$$

where $\Delta q_0 = q_0 - 2\pi/a$. The next step requires a choice of a model for the medium of the thin films. Possibilities include anharmonic oscillators, two- or three-level atoms, excitons of molecular chains, nano-particles, quantum dots, and others. First, we consider the two-level atom model.

2.5 Example: Thin Films Containing Two-Level Atoms

Here we employ the approach developed above to derive an already-known system of equations [1]. The model assumes that each thin film contains two-level atoms. The state of a two-level atom is described by a density matrix, $\hat{\rho}$. The matrix element ρ_{12} describes the transition between the ground state, $|2\rangle$, and the excited state, $|1\rangle$.

ρ_{22} and ρ_{11} represent the populations of these states. The evolution of the two-level atom is governed by the Bloch equations [20]:

$$\mathrm{i}\hbar\frac{\partial}{\partial t}\rho_{12} = \hbar\Delta\omega\rho_{12} - d_{12}(\rho_{22}-\rho_{11})A_{\mathrm{in}}, \tag{31}$$

$$\mathrm{i}\hbar\frac{\partial}{\partial t}(\rho_{22}-\rho_{11}) = 2\left(d_{12}\rho_{21}A_{\mathrm{in}} - d_{21}\rho_{12}A_{\mathrm{in}}^{*}\right). \tag{32}$$

In these equations, A_{in} is the electric field interacting with a two-level atom. In the problem under consideration, $A_{\mathrm{in}} = \mathscr{A} + \mathscr{B}$, and

$$K_0\mathscr{P} = \frac{2\pi\omega_0 n_{\mathrm{at}} d_{12}}{cn(\omega_0)}\left\langle\rho_{12}\right\rangle.$$

Here, the cornerstone brackets denote summation over all atoms within a frequency detuning of $\Delta\omega$ from the center of the inhomogeneity broadening line, $n(\omega_0)$ is the refractive index of the medium containing the array of thin films, and n_{at} is the effective density of the resonant atoms in the films. n_{at} is defined by $n_{\mathrm{at}} = N_{\mathrm{at}}(\ell_{\mathrm{f}}/a)$, where N_{at} is the bulk density of atoms, ℓ_{f} is the film width, and a is the lattice spacing.

We assume that the group-velocity dispersion is of no importance. The resulting equations are the two-wave reduced Maxwell–Bloch equations. We introduce the normalized variables

$$e_1 = t_0 d_{12}\mathscr{A}/\hbar, \quad e_2 = t_0 d_{12}\mathscr{B}/\hbar, \quad x = \zeta v_g t_0, \quad \tau = t/t_0.$$

The normalized two-wave reduced Maxwell–Bloch equations take the following form:

$$\mathrm{i}\left(\frac{\partial}{\partial\zeta} + \frac{\partial}{\partial\tau}\right)e_1 + \delta e_1 = -\gamma\left\langle\rho_{12}\right\rangle, \tag{33}$$

$$\mathrm{i}\left(\frac{\partial}{\partial\zeta} - \frac{\partial}{\partial\tau}\right)e_2 - \delta e_2 = +\gamma\left\langle\rho_{12}\right\rangle, \tag{34}$$

$$\mathrm{i}\frac{\partial}{\partial\tau}\rho_{12} = \Delta\rho_{12} - n e_{\mathrm{in}}, \tag{35}$$

$$\frac{\partial}{\partial\tau}n = -4\,\mathrm{Im}(\rho_{12}e_{\mathrm{in}}^{*}), \tag{36}$$

where $\gamma = t_0 v_{\mathrm{g}}/L_{\mathrm{a}}$, $\delta = t_0 v_{\mathrm{g}}\Delta q_0$, $L_{\mathrm{a}} = (cn(\omega_0)\hbar)/(2\pi\omega_0 t_0 n_{\mathrm{at}}|d_{12}|^2)$ is the resonant absorption length, and $\Delta = \Delta\omega t_0$ is the normalized frequency detuning.

We define $n = \rho_{22} - \rho_{11}$, $e_{\mathrm{in}} = e_1 + e_2$ and introduce yet another change of variables:

$$e_{\mathrm{in}} = e_1 + e_2 = f_{\mathrm{s}}\exp(\mathrm{i}\delta\tau), \quad e_1 - e_2 = f_{\mathrm{a}}\exp(\mathrm{i}\delta\tau), \quad \rho_{12} = r\exp(\mathrm{i}\delta\tau).$$

The system of equations (33), (34), (35), and (36) can be rewritten as

$$\frac{\partial f_{\mathrm{s}}}{\partial \zeta}+\frac{\partial f_{\mathrm{a}}}{\partial \tau}=0, \tag{37}$$

$$\frac{\partial f_{\mathrm{a}}}{\partial \zeta}+\frac{\partial f_{\mathrm{s}}}{\partial \tau}=2\mathrm{i}\gamma\langle r\rangle, \tag{38}$$

$$\mathrm{i}\frac{\partial}{\partial \tau}r=(\Delta+\delta)r-nf_{\mathrm{s}}, \tag{39}$$

$$\frac{\partial}{\partial \tau}n=-4\,\mathrm{Im}(rf_{\mathrm{s}}^{*}). \tag{40}$$

From (37), it follows that

$$\frac{\partial f_{\mathrm{a}}}{\partial \zeta}=-\frac{\partial f_{\mathrm{s}}}{\partial \tau},$$

which allows us to rewrite (37), (38), (39), and (40) in the form

$$\frac{\partial^2 f_{\mathrm{s}}}{\partial \zeta^2}-\frac{\partial^2 f_{\mathrm{s}}}{\partial \tau^2}=-2\mathrm{i}\gamma\left\langle\frac{\partial r}{\partial \tau}\right\rangle, \tag{41}$$

$$\mathrm{i}\frac{\partial}{\partial \tau}r=(\Delta+\delta)r-nf_{\mathrm{s}}, \tag{42}$$

$$\frac{\partial}{\partial \tau}n=-4\,\mathrm{Im}(rf_{\mathrm{s}}^{*}). \tag{43}$$

If we assume that inhomogeneous broadening is absent, i.e., if the hypothesis of a sharp atomic resonant transition is true, then $\delta+\Delta=0$, and this system reduces to the Sine–Gordon equation [1]. Reference [4] presents the steady-state solution of (41), (42), and (43) with inhomogeneous broadening taken into account.

2.6 Thin Films Containing Metallic Nano-particles

It was shown above that the counter-propagating electric field waves $\mathscr{A}$ and $\mathscr{B}$ in the slowly varying envelope approximation satisfy the following system of equations:

$$\mathrm{i}\left(\frac{\partial}{\partial x}+\frac{1}{v_{\mathrm{g}}}\frac{\partial}{\partial t}\right)\mathscr{A}-\frac{q_2}{2}\frac{\partial^2}{\partial t^2}\mathscr{A}+\Delta q_0\mathscr{A}=-\frac{2\pi\omega_0}{c\sqrt{\varepsilon}}\langle\mathscr{P}\rangle, \tag{44}$$

$$\mathrm{i}\left(\frac{\partial}{\partial x}-\frac{1}{v_{\mathrm{g}}}\frac{\partial}{\partial t}\right)\mathscr{B}+\frac{q_2}{2}\frac{\partial^2}{\partial t^2}\mathscr{B}-\Delta q_0\mathscr{B}=+\frac{2\pi\omega_0}{c\sqrt{\varepsilon}}\langle\mathscr{P}\rangle, \tag{45}$$

where $\Delta q_0=q_0-2\pi/a$ is the mismatch between the carrier wave-number and the Bragg resonance wave-number. To describe the evolution of material polarization in

the slowly varying amplitude approximation, we must model the response of the thin films to an external light field. Previous work has considered various mechanisms as sources of the dielectric properties of metamaterials. In the simplest case, dielectric properties can be attributed to plasmonic oscillations, which are modeled by Lorentz oscillators. Magnetic properties can be described by the equations of a system of LC-circuits [21, 22, 23, 24, 25]. The simplest generalizations of this model include anharmonicity of plasmonic oscillations [13, 27] and the addition of a nonlinear capacitor into each LC-circuit [28]. In this chapter, we consider an array of non-magnetic thin films containing metallic nano-particles which have a cubic nonlinear response to external fields [13, 14, 26].

The macroscopic polarization, P, is governed by the equation

$$\frac{\partial^2 P}{\partial t^2} + \omega_{\mathrm{d}}^2 P + \Gamma_{\mathrm{a}} \frac{\partial P}{\partial t} + \kappa P^3 = \frac{\omega_{\mathrm{p}}^2}{4\pi} E,$$

where ω_{p} is plasma frequency and ω_{d} is the dimension quantization frequency for nano-particles. Losses related to the plasmonic oscillations are taken into account by the parameter Γ_{a}. It is assumed that the duration of the electromagnetic pulse is short enough so that dissipation effects can be neglected. If the anharmonic parameter κ is equal to zero, then we have the famous Lorentz model which describes electromagnetic wave propagation and refraction in metamaterials [21, 22, 23, 24, 25, 29, 30].

Starting from the slowly varying envelope approximation, standard manipulation leads to

$$\mathrm{i}\frac{\partial \mathscr{P}}{\partial t} + (\omega_{\mathrm{d}} - \omega_0)\mathscr{P} + \frac{3\kappa}{2\omega_0}|\mathscr{P}|^2 \mathscr{P} = -\frac{\omega_{\mathrm{p}}^2}{8\pi\omega_0}\mathscr{E}_{\mathrm{int}}(x,t). \tag{46}$$

The terms varying rapidly in time, which are proportional to $\exp(\pm 3\mathrm{i}\omega_0 t)$, are neglected. In this equation, $\mathscr{E}_{\mathrm{int}}$ is the electric field interacting with the metallic nano-particles. In the problem under consideration, we have $\mathscr{E}_{\mathrm{int}} = \mathscr{A} + \mathscr{B}$.

The sizes and shapes of nano-particles are not uniform because of the limitations of nano-fabrication. In practice, the deviation from a perfectly spherical shape has a much larger impact on a nano-particle's resonance frequency than does variation in diameter. This causes a broadening of the resonance line. The broadened spectrum is characterized by a probability density function, $g(\Delta\omega)$, of deviations, $\Delta\omega$, from some mean value, ω_{res}. When computing the total polarization, all resonance frequencies must be taken into account.

The contributions of the various resonance frequencies are weighted according to the probability density function, $g(\Delta\omega)$. The weighted average is denoted by $\langle\mathscr{P}\rangle$ in (44) and (45). In what follows, $n(\omega_0)$ denotes the refractive index of the medium containing the array of thin films, and n_{np} is the effective density of the resonant nano-particles in the films. As in the model of films containing two-level atoms, the effective density is equal to $n_{\mathrm{np}} = N_{\mathrm{np}}(\ell_{\mathrm{f}}/a)$, where N_{np} is the bulk density of nano-particles, ℓ_{f} is the width of a film, and a is the lattice spacing.

We study a medium–light interaction in which resonance is the dominant phenomenon. Hence the length of the sample is smaller than the characteristic dispersion length. In this case, the temporal second derivative terms in (44), and (45) can

be omitted. The resulting equations are the two-wave Maxwell–Duffing equations. They can be rewritten in dimensionless form using the following rescaling:

$$\begin{aligned} e_1 &= \mathscr{A}/A_0, \\ e_2 &= \mathscr{B}/A_0, \\ p &= (4\pi\omega_0/[\sqrt{\varepsilon}\omega_\mathrm{p}A_0])\mathscr{P}, \\ \zeta &= (\omega_\mathrm{p}/2c)x, \\ \tau &= t/t_0. \end{aligned}$$

Here $t_0 = 2\sqrt{\varepsilon}/\omega_\mathrm{p}$, while A_0 is the characteristic amplitude of the counter-propagating fields. In dimensionless form, the two-wave Maxwell–Duffing equations read:

$$\begin{aligned} \mathrm{i}\left(\frac{\partial}{\partial\zeta}+\frac{\partial}{\partial\tau}\right)e_1+\delta e_1 &= -\langle p\rangle, \\ \mathrm{i}\left(\frac{\partial}{\partial\zeta}-\frac{\partial}{\partial\tau}\right)e_2-\delta e_2 &= +\langle p\rangle, \\ \mathrm{i}\frac{\partial p}{\partial\tau}+\Delta p+\mu|p|^2p &= -(e_1+e_2), \end{aligned} \tag{47}$$

where $\mu = (3\kappa\sqrt{\varepsilon}/\omega_0\omega_\mathrm{p})(\sqrt{\varepsilon}\omega_\mathrm{p}/4\pi\omega_0)^2A_0^2$ is a dimensionless coefficient of anharmonicity, $\delta = 2\Delta q_0(c/\omega_\mathrm{p})$ is the dimensionless mismatch coefficient, and $\Delta = 2\sqrt{\varepsilon}(\omega_\mathrm{d}-\omega_0)/\omega_\mathrm{p}$ is the dimensionless detuning of a nano-particle's resonant frequency from the field's carrier frequency.

In a co-ordinate system which is rotating with angular frequency δ,

$$e_1 = f_1\mathrm{e}^{\mathrm{i}\delta\tau}, \qquad e_2 = f_2\mathrm{e}^{\mathrm{i}\delta\tau}, p = q\mathrm{e}^{\mathrm{i}\delta\tau},$$

equation (47) becomes

$$\begin{aligned} \mathrm{i}\left(\frac{\partial}{\partial\zeta}+\frac{\partial}{\partial\tau}\right)f_1 &= -\langle q\rangle, \\ \mathrm{i}\left(\frac{\partial}{\partial\zeta}-\frac{\partial}{\partial\tau}\right)f_2 &= +\langle q\rangle, \\ \mathrm{i}\frac{\partial q}{\partial\tau}+(\Delta-\delta)q+\mu|q|^2q &= -(f_1+f_2). \end{aligned} \tag{48}$$

Further simplification of the system (48) can be achieved by introducing new variables

$$f_\mathrm{s} = -(f_1+f_2), \qquad f_\mathrm{a} = f_1-f_2,$$

which allow decoupling of one equation from the system of three equations. In these new variables, the polarization, q, is coupled with only one field variable. Simple transformations give

$$\frac{\partial^2 f_a}{\partial \zeta^2} - \frac{\partial^2 f_a}{\partial \tau^2} = 2i \frac{\partial}{\partial \zeta} \langle q \rangle, \tag{49}$$

$$\frac{\partial^2 f_s}{\partial \zeta^2} - \frac{\partial^2 f_s}{\partial \tau^2} = 2i \frac{\partial}{\partial \tau} \langle q \rangle, \tag{50}$$

$$i \frac{\partial q}{\partial \tau} + (\Delta - \delta) q + \mu |q|^2 q = f_s. \tag{51}$$

As one can see, we have a coupled system of equations for f_s and q.

3 Solitary Wave Solutions

We consider localized solitary wave solutions of (49) in the limit of a narrow spectral line, $\Delta\omega_g / \Delta\omega_s \ll 1$, where $\Delta\omega_s$ and $\Delta\omega_g$ are spectral widths of the signal and spectral line $g(\Delta\omega)$, respectively. In this case, the spectral line can be represented as a Dirac δ-function, $g(\Delta\omega) = \delta(\Delta\omega)$. Equations (49), and (51) can then be rewritten as follows:

$$\frac{\partial^2 f_s}{\partial \zeta^2} - \frac{\partial^2 f_s}{\partial \tau^2} = 2i \frac{\partial q}{\partial \tau}, \tag{52}$$

$$i \frac{\partial q}{\partial \tau} + (\Delta - \delta) q + \mu |q|^2 q = f_s. \tag{53}$$

Scaling analysis of this system shows that solitary wave solutions can be represented as

$$\begin{aligned} f_s &= f_0 F_\Omega(\eta) = \frac{1}{\sqrt{\mu}} \left(\frac{2v^2}{1-v^2} \right)^{3/4} F_\Omega(\eta), \\ q &= q_0 Q_\Omega(\eta) = \frac{1}{\sqrt{\mu}} \left(\frac{2v^2}{1-v^2} \right)^{1/4} Q_\Omega(\eta), \\ \eta &= \sqrt{\frac{2}{1-v^2}} (\zeta - v\tau). \end{aligned} \tag{54}$$

Here, v is the velocity of the solitary wave, η is a scale-invariant parameter in a co-ordinate system moving with the solitary wave, and functions F_Ω and Q_Ω satisfy the following system of equations:

$$F'' = -iQ', \tag{55}$$

$$-iQ' + \Omega Q + |Q|^2 Q = F. \tag{56}$$

The only dimensionless parameter which remains in the system is

$$\Omega = (\Delta - \delta)\sqrt{\frac{1-v^2}{2v^2}}, \tag{57}$$

which characterizes the deviation of carrier frequency from the plasmonic frequency, $\omega_{\rm p}$, and the Bragg resonance frequency, $\omega_{\rm Br}$.

The first equation implies that $F' = -\mathrm{i}Q + \text{constant}$. We seek a solitary-wave solution, so we assume that F, Q, and their derivatives decay to zero as $|\eta| \to \infty$. Hence the constant is zero, and

$$\begin{aligned} \mathrm{i}F' &= Q\,, \\ -iQ' + \Omega Q + |Q|^2 Q &= F. \end{aligned} \tag{58}$$

The system of ordinary differential equations (58) has an integral of motion:

$$|Q|^2 - |F|^2 = \text{constant}.$$

For solutions which decay as $|\eta| \to \infty$, the constant is equal to zero, so

$$|Q|^2 = |F|^2.$$

This allows the following parametrization of the solutions:

$$F(\eta) = R(\eta)\mathrm{e}^{\mathrm{i}\phi(\eta)}, \quad Q(\eta) = R(\eta)\mathrm{e}^{\mathrm{i}\psi(\eta)},$$

where R, ϕ, and ψ are real-valued functions satisfying

$$\begin{aligned} R' &= -R\sin(\phi - \psi), \\ \phi' &= -\cos(\phi - \psi), \\ \psi' + \Omega + R^2 &= \cos(\phi - \psi). \end{aligned} \tag{59}$$

If we set $\Phi = \phi - \psi$, then we have

$$\begin{aligned} \Phi' - \Omega - R^2 &= -2\cos\Phi, \\ R' &= -R\sin\Phi. \end{aligned} \tag{60}$$

Taking the second equation of (60) into account, the first equation can be rewritten as

$$R\frac{\mathrm{d}}{\mathrm{d}R}(\cos\Phi) - \Omega - R^2 = -2\cos\Phi.$$

If we set $y = \cos\Phi$, then we have

$$R\frac{\mathrm{d}y}{\mathrm{d}R} + 2y = R^2 + \Omega. \tag{61}$$

The solutions of (61) have the form

$$y = \frac{1}{4}R^2 + \frac{\Omega}{2} + cR^{-2},$$

where c is arbitrary. Since $y = \cos\Phi$, the right-hand side must remain between -1 and 1. As we expect $R \to 0$ as $|\eta| \to \infty$, c must be zero. We have the conservation law

$$\cos\Phi = \frac{1}{4}R^2 + \frac{\Omega}{2}. \tag{62}$$

The substitution of (62) into the second equation of (60) and subsequent integration give the following expression for R:

$$R^2 = \frac{2(4-\Omega^2)}{\Omega + 2\cosh\left\{\sqrt{4-\Omega^2}(\eta-\eta_0) + \frac{1}{2}\ln\left(\frac{16}{4-\Omega^2}\right)\right\}}.$$

The right-hand side is positive and real-valued for all η if, and only if, $-2 < \Omega < 2$. The term $\sqrt{4-\Omega^2}$ appears so often in what follows that we define $\beta = \sqrt{4-\Omega^2}$. R^2 then has the form

$$R^2 = \frac{2\beta^2}{\Omega + 2\cosh\{\beta(\eta-\eta')\}}, \tag{63}$$

where we have combined the arbitrary constant η_0 and the logarithm into a single constant (η') in the argument of the hyperbolic cosine. Using the conservation law (62), we obtain an expression for Φ:

$$\Phi = 2\arctan\left(\frac{2-\Omega}{\beta}\tanh\left\{\frac{1}{2}\beta(\eta-\eta')\right\}\right). \tag{64}$$

Now we integrate $\phi' = -\cos\Phi$ and find

$$\phi = -\frac{\Omega}{2}(\eta-\eta') - \arctan\left(\frac{2-\Omega}{\beta}\tanh\left\{\frac{1}{2}\beta(\eta-\eta')\right\}\right).$$

Finally, we determine ψ:

$$\begin{aligned}\psi &= \phi - \Phi \\ &= -\frac{\Omega}{2}(\eta-\eta') - 3\arctan\left(\frac{2-\Omega}{\beta}\tanh\left\{\frac{1}{2}\beta(\eta-\eta')\right\}\right).\end{aligned}$$

This pulse only exists if the value of the parameter Ω is within the interval $-2 < \Omega < 2$. The maximal value of the amplitude of this solitary solution is

$$A = \sqrt{2(2-\Omega)}.$$

The phases ϕ and ψ are nonlinear. Their behavior is asymptotically linear as $\eta \to \pm\infty$. If $\Omega = 0$, then the limiting values of the phases satisfy

$$|\phi(\infty) - \phi(-\infty)| = \pi/2,$$
$$|\psi(\infty) - \psi(-\infty)| = 3\pi/2.$$

4 Energy Partition

The total energy of the solitary wave is distributed between co/contra-propagating fields and medium polarization. Here we study the energy partition between all these components. Using (49), (50), and the conditions as $|\eta| \to \infty$, one can show that

$$f_{\mathrm{a}}(\eta) = -\frac{1}{v} f_{\mathrm{s}}(\eta) = -\frac{f_0}{v} F(\eta). \tag{65}$$

We are interested in the energies of the dimensionless fields f_1, f_2, and polarization q.

$$f_1 = \frac{1}{2}(f_{\mathrm{a}} - f_{\mathrm{s}}) = -\frac{f_0}{2}\left(\frac{1}{v} + 1\right) F,$$
$$f_2 = -\frac{1}{2}(f_{\mathrm{s}} + f_{\mathrm{a}}) = \frac{f_0}{2}\left(\frac{1}{v} - 1\right) F,$$
$$q = q_0 Q.$$

To find the energies of forward- and backward-propagating waves, we need to calculate the energy of the solitary wave:

$$E_R = \int_{-\infty}^{+\infty} |F|^2(\eta)\mathrm{d}\eta = \int_{-\infty}^{\infty} |Q|^2(\eta)\mathrm{d}\eta$$
$$= \int_{-\infty}^{+\infty} R^2(\eta)\mathrm{d}\eta = 8 \arctan \sqrt{\frac{2-\Omega}{2+\Omega}}. \tag{66}$$

Finally, we have the energies

$$E_{f_1} = \frac{f_0^2}{4}\left(\frac{1}{v} + 1\right)^2 E_{\mathrm{R}}, \tag{67}$$

$$E_{f_2} = \frac{f_0^2}{4}\left(\frac{1}{v} - 1\right)^2 E_{\mathrm{R}}, \tag{68}$$

$$E_{\mathrm{q}} = q_0^2 E_{\mathrm{R}}. \tag{69}$$

The ratios of energies in the various fields, as well as the polarization, have the following forms:

$$\frac{E_{f_1}}{E_{f_2}} = \left(\frac{1+v}{1-v}\right)^2, \tag{70}$$

$$\frac{E_{f_1}}{E_{\mathrm{q}}} = \frac{1}{2}\frac{(1+v)}{(1-v)}, \tag{71}$$

$$\frac{E_{f_2}}{E_q} = \frac{1}{2}\frac{(1-v)}{(1+v)}. \tag{72}$$

Therefore, energy partitioning is determined by only one parameter, v, which is a dimensionless combination of the main system parameters.

5 Numerical Simulation

The shape and phase of the incident pulse are controllable in a real experimental situation. To model pulse dynamics in a Bragg grating, it is natural to consider an asymptotic mixed initial-boundary value problem for (48). We specify the initial conditions as

$$q(\zeta,\tau) \to 0, \quad f_1(\zeta,\tau) \to 0, \quad f_2(\zeta,\tau) \to 0, \quad \tau \to -\infty, \tag{73}$$

with no incident field at the right edge of the sample and with an incident field at the left edge defined as follows:

$$\begin{aligned} f_1(-10,\tau) &= w\exp(\mathrm{i}\theta), \\ w &= 3.5\exp\left[-\frac{1}{2}\left(\frac{\tau-3.0}{1.5}\right)^2\right], \\ \theta &= \arctan\left(\tanh\left[1.5\,(\tau-3.0)\right]\right). \end{aligned} \tag{74}$$

In our case, the spatial simulation domain was chosen to be $[-10,40]$. Parameters $\Delta-\delta$ and μ were set to be

$$\Delta-\delta = 0, \;\; \mu = 1. \tag{75}$$

As one can see, in a topological sense, we gave the initial pulse the same configuration of phase as the solitary wave solution. This point is important because,

otherwise, the phase difference cannot relax to the symmetry of the stationary wave which is revealed in (64). As a result, the solution will be unstable if it does not have the correct "topological charge".

The second field boundary condition was as follows:

$$f_2(40, \tau) = 0. \tag{76}$$

In the first simulation, we injected a pulse which was relatively close to the solitary wave solution. The results are shown in Figs. 2, 3, and 4. The amplitude and phase difference varied slightly, as did the pulse shape, which was Gaussian. During the first stage ($t \leq 7$) of evolution, we observed rapid excess energy damping in the radiation of quasi-linear waves in both directions, and relaxation to a

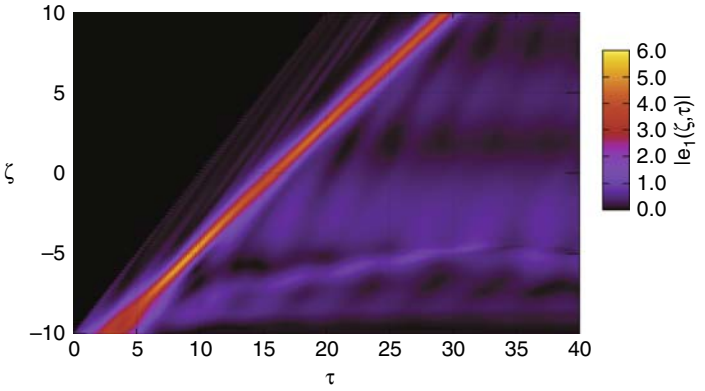

Fig. 2 Propagation of pulse – the first simulation. Mapping of the $|e_1(\zeta, \tau)|$ surface

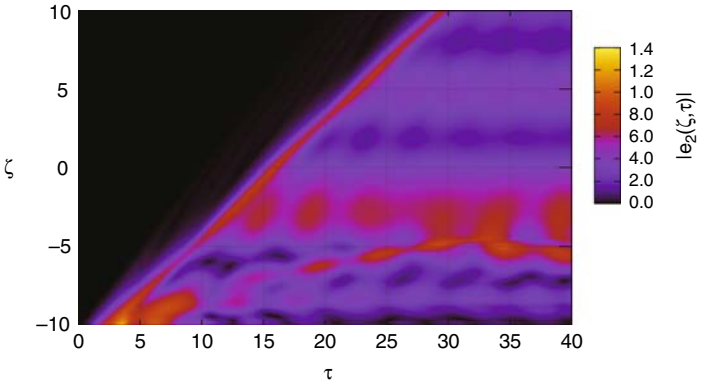

Fig. 3 Propagation of pulse – the first simulation. Mapping of the $|e_2(\zeta, \tau)|$ surface

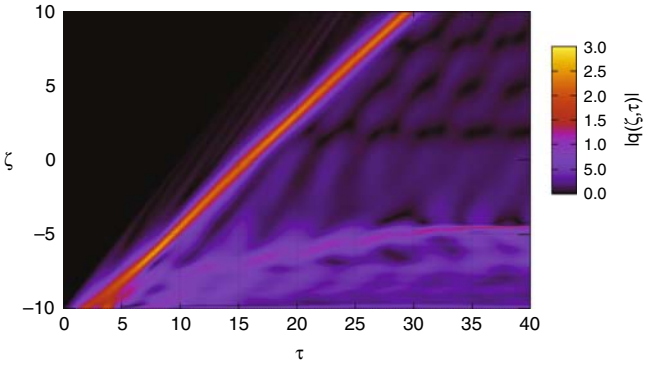

Fig. 4 Propagation of pulse – the first simulation. Mapping of the $|q(\zeta, \tau)|$ surface

solution which roughly approximated a stationary one. Then, we had a stage of pulse shaperefinement ($7 < t < 30$), with consequent propagation of the solution being very close to (63). One can compare the evolved pulse shape with the stationary solution in Fig. 5.

During the second simulation, we used a pulse of lower amplitude:

$$f_1(-10, \tau) = w \exp(\mathrm{i}\theta),$$

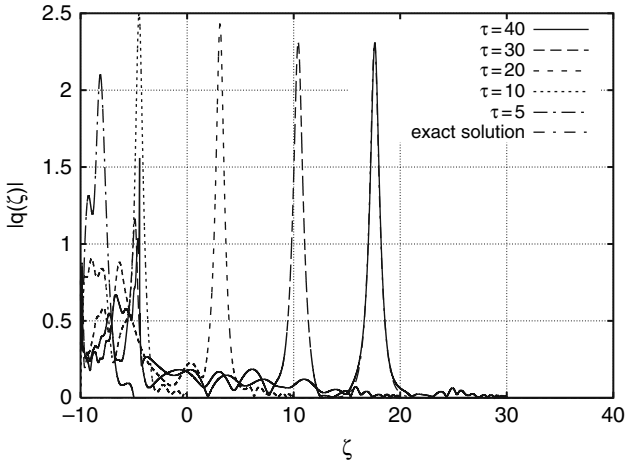

Fig. 5 The first simulation. Absolute value of polarization at different moments of time. The stationary pulse shape almost coincides with the exact solution

$$w = 2.0 \exp\left[-\frac{1}{2}\left(\frac{\tau - 3.0}{1.5}\right)^2\right], \tag{77}$$

$$\theta = \arctan\left(\tanh\left[1.5\left(\tau - 3.0\right)\right]\right). \tag{78}$$

The results are presented in Figs. 6, 7, and 8. The plainly observable oscillations of pulse magnitude can be associated with modes localized in the pulse. This very instructive result could be a fruitful ground for further investigation and simulation.

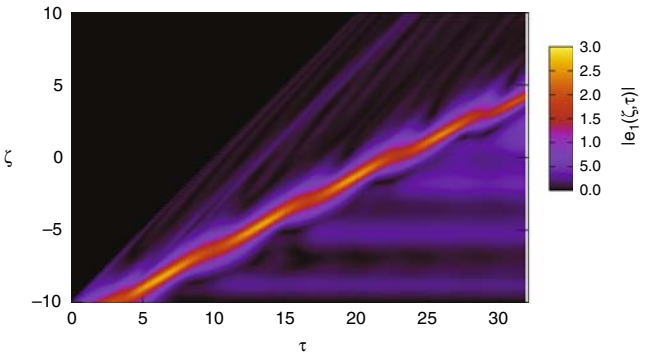

Fig. 6 Propagation of pulse – the second simulation. Mapping of the $|e_1(\zeta, \tau)|$ surface

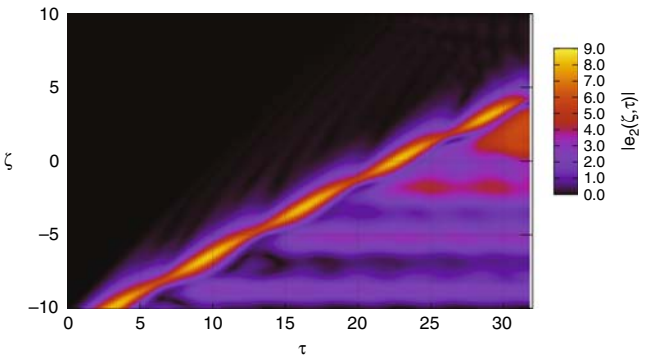

Fig. 7 Propagation of pulse – the second simulation. Mapping of the $|e_2(\zeta, \tau)|$ surface

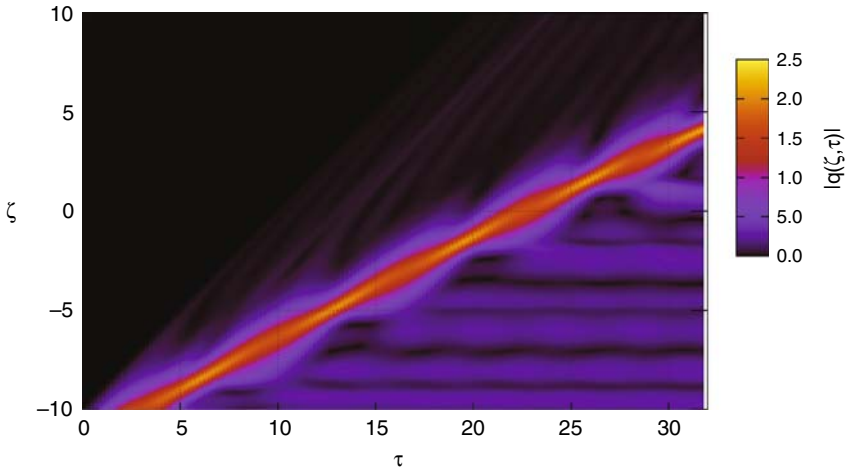

Fig. 8 Propagation of pulse – the second simulation. Mapping of the $|q(\zeta, \tau)|$ surface

6 Conclusion

We have derived equations describing optical pulse evolution in Bragg gratings with thin films containing active dopants. In particular, we investigated the case of thin films containing metallic nano-particles. We showed that the system of equations describing this situation has one parameter. This parameter contains information on Bragg and plasmonic frequencies and general pulse characteristics. These equations have solitary wave solutions describing a bound state of two waves propagating in opposite directions with medium polarization.

Acknowledgments We would like to thank B.I. Mantsyzov, A.A. Zabolotskii, J.-G. Caputo, M. Stepanov, and R. Indik for enlightening discussions. AIM and KAO are grateful to the *Laboratoire de Mathématiques, INSA de Rouen*, and the University of Arizona for hospitality and support. This work was partially supported by the NSF (grant DMS-0509589), ARO-MURI award 50342-PH-MUR and the State of Arizona (Proposition 301), RFBR grants 06-02-16406 and 06-01-00665-a, INTAS grant 00-292, the Program "Nonlinear dynamics and solitons" from the RAS Presidium, and "Leading Scientific Schools of Russia" grant. KAO was supported by a Russian President grant for young scientists, MK-1055.2005.2.

References

1. B. I. Mantsyzov and R. N. Kuzmin, Sov. Phys. JETP **64**, 37–44 (1986). 337, 338, 339, 341, 346, 348
2. B. I. Mantsyzov and D. O. Gamzaev, Opt. Spectrosc. **63**, 1, 200–202 (1987). 337, 338, 339, 341
3. T. I. Lakoba and B.I.Mantsyzov, Bull. Russian Acad. Sci. Phys. **56**, 8, 1205–1208 (1992). 337, 338, 339, 341
4. B. I. Mantsyzov, Phys. Rev. **A51**, 6, 4939–4943 (1995). 337, 338, 339, 341, 348
5. B. I. Mantsyzov and E. A. Silnikov, J. Opt. Soc. Amer. B **19**, 2203–2207 (2002). 337, 338, 339, 341
6. A. Kozhekin and G. Kurizki, Phys. Rev. Lett. **74**, 25, 5020–5023 (1995). 337, 338, 339, 341

7. A. Kozhekin, G. Kurizki, and B. Malomed, Phys. Rev. Lett. **81**, 17, 3647–3650 (1998). 337, 338, 339, 341
8. T. Opatrny, B. A. Malomed, and G. Kurizki, Phys. Rev. E **60**, 5, 6137–6149 (1999). 337, 338, 339, 341
9. G. Kurizki, A. E. Kozhekin, T. Opatrny, and B. A. Malomed, Progr. Opt. **42**, 93–146 (E. Wolf, editor: North Holland, Amsterdam, 2001). 337, 338, 341
10. J. Cheng and J. Zhou, Phys. Rev. E **66**, 036606 (2002). 337, 338
11. F. Calogero, A. Degasperis, in *Solitons*, edited by R.K. Bullough, P.J. Caudray, (Springer-Verlag, Berlin, 1980). 338
12. B. I. Mantsyzov, Optical zoomeron as a result of beatings of the internal modes of a Bragg soliton, JETP Lett. **82**, 5, 253–258 (2005). 338, 345
13. S.G. Rautian, Nonlinear saturation spectroscopy of the degenerate electron gas in spherical metallic particles, JETP **85**, 451–461 (1997). 338, 349
14. V.P. Drachev, A.K. Buin, H. Nakotte, and V.M. Shalaev, Size dependent χ^3 for conduction electrons in Ag nanoparticles, Nano Lett. **4**, 1535–1539 (2004). 338, 349
15. F. Hache, D. Ricard, and C. Flytzanis, Optical nonlinearities of small metal particles: Surface-mediated resonance and quantum size effects, J. Opt. Soc. Am. B **3**, 1647–1655 (1986). 338
16. V.I. Rupasov and V.I. Yudson, Quantum Electron. (in Russian) **9**, 2179 (1982). 340
17. V.I. Rupasov and V.I. Yudson, Zh.E.T.Ph. (in Russian) **93**, 494 (1987). 340
18. P. Yeh, *Optical Waves in Layered Media*, (Wiley, New York, 1988). 341
19. A.I. Maimistov, A.M. Basharov, *Nonlinear Optical Waves* (Kluwer Academic Publishers, Dordrecht, Boston, London, 1999).
20. L. Allen and J.H. Eberly, *Optical Resonance and Two-Level Atoms*, (Wiley-Interscience, New York, 1975). 347
21. J.B. Pendry, A.J. Holden, D.J. Robbins, and W.J. Stewart, IEEE Trans. Microw. Theory Tech. **47**, 2075–2084 (1999). 349
22. D.R. Smith, S. Schultz, P. Markos, and C.M. Soukoulis, Phys. Rev. B **65**, 195104 (2002). 349
23. N. Katsarakis, T. Koschny, M. Kafesaki, E.N. Economou, and C.M. Soukoulis, Appl. Phys. Lett. **84**, 2943–2945 (2004). 349
24. P. Markos and C.M. Soukoulis, Phys. Rev. E **65**, 036622 (2002). 349
25. J.F. Woodley, M.S. Wheeler, and M. Mojahedi, Phys. Rev. E **71**, 066605 (2005). 349
26. I.R. Gabitov, R.A. Indik, N.M. Litchinitser, A.I. Maimistov, V.M. Shalaev, and J.E. Soneson, J. Opt. Soc. Am. B **23**, 535–542 (2006). 349
27. N.M. Lichinitser, I.R. Gabitov, A.I. Maimistov, and V.M. Shalaev, Effect of an optical negative index thin film on optical bistability, arXiv. Physics/0607177. 349
28. A.A. Zharov, I.V. Shadrivov, and Yu.S. Kivshar, Phys. Rev. Lett. **91**, 037401 (2003). 349
29. R.W. Ziolkowskii and E. Heyman. Phys. Rev. B **64**, 056625 (2001). 349
30. R.W. Ziolkowski, Optics Express 11 **21167**, 662–681 (2003). 349

Collective Focusing and Modulational Instability of Light and Cold Atoms

M. Saffman and Y. Wang

Abstract A self-consistent model for the coupled dynamics of cold atoms and near-resonant light fields is formulated. The model is shown to predict several novel phenomena, including collective self-focusing of light and atoms, stable dissipative atom–optical solitons and modulational instability under conditions of optical self-defocusing. Experimental studies using cold Cs atoms in a magneto-optical trap suggest the presence of atomic modulational instability.

1 Introduction

In this chapter, we describe, theoretically and experimentally, aspects of the collective dynamics of light beams and cold atomic vapors. We formulate a set of model equations that describe the paraxial evolution of light beams which are near-resonant with a cloud of cold two-level atoms. Solutions of these equations reveal a number of unusual dynamical effects, including collective self-focusing of light and atoms, and modulational instability under conditions of self-defocusing. In geometries with feedback, the model supports the principal feasibility of observing pattern formation of atomic vapors. Experimental evidence for modulational instability in a cold Cs vapor is presented. We concentrate on the situation where the atomic temperature is sufficiently low, so that the momentum transfer due to near-resonant light fields exerts a strong influence on the center-of-mass atomic motion. This is the case for laser-cooled atomic vapors, both above and below the critical temperature for Bose–Einstein condensation. We restrict our attention here to the case of cold,

M. Saffman
Department of Physics, University of Wisconsin, 1150 University Avenue, Madison, WI 53706, USA, msaffman@wisc.edu

Y. Wang
Department of Physics, University of Wisconsin, 1150 University Avenue, Madison, WI 53706, USA

Saffman, M., Wang, Y.: *Collective Focusing and Modulational Instability of Light and Cold Atoms.* Lect. Notes Phys. **751**, 361–380 (2008)
DOI 10.1007/978-3-540-78217-9_14

but not condensed, clouds. A closely related collective dynamical situation, in the regime of ultra-cold coherent matter, was considered in [1, 2].

Forces exerted by the light field on the atoms are due to both conservative and dissipative processes [3]. The conservative interaction is mediated by the so-called dipole force, which is the result of stimulated transfer of momentum between light beams propagating in different directions. There is also a dissipative force (the radiation pressure force), which is the result of photon absorption followed by spontaneous emission in a random direction, which imparts a random momentum kick to the atoms. In this chapter, we study a model of coherent interaction between probe beams and a cloud of atoms which are cooled by a dissipative interaction with cooling beams. We show that localized, solitary wave solutions, as well as modulational instabilities, occur when the dissipation is strong enough to give sufficient cooling of the atoms. We thus create a coherent structure in the presence of a parallel dissipative process – this is an example of the formation of a dissipative soliton [4].

2 Dynamical Equations

Our aim is to develop an analytically tractable model that describes some essential features of spatial dynamics in a cloud of cold atoms. We will work with a semi-classical description where the center-of-mass position and momentum of the atoms, as well as the optical field, are described classically. We assume that a cold atomic sample has been prepared in a magneto-optical trap (MOT) using standard techniques [5] and that a probe beam interacts with the atoms as shown in Fig. 1. Paraxial propagation of a scalar optical field $E = (A(\mathbf{r})/2)\mathrm{e}^{\mathrm{i}(kz-\omega t)} + \text{c.c.}$ through a cloud of cold atoms is described by

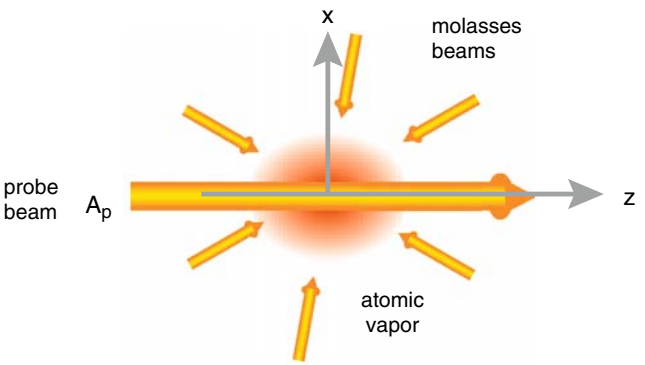

Fig. 1 Optical beam propagating through a cloud of cold atoms. Atomic motion is assumed to be strongly damped by three-dimensional optical molasses beams

$$\frac{\partial A}{\partial z} - \frac{\mathrm{i}}{2k}\nabla_\perp^2 A = \mathrm{i}\frac{k}{2}\chi(\mathbf{r})A, \tag{1}$$

where $\nabla_\perp = \hat{x}\partial/\partial x + \hat{y}\partial/\partial y$ and the susceptibility is

$$\chi(\mathbf{r}) = -\frac{6\pi}{k^3} n_\mathrm{a}(\mathbf{r},t)\frac{2\Delta/\gamma - \mathrm{i}}{1 + 4\Delta^2/\gamma^2 + I/I_\mathrm{s}}. \tag{2}$$

Here $I = I(\mathbf{r}) = \frac{\varepsilon_0 c}{2}|A|^2$ is the probe beam intensity, I_s is the saturation intensity, $k = \omega/c$, $\Delta = \omega - \omega_\mathrm{a}$ is the detuning of the radiation frequency ω from the atomic transition frequency ω_a and γ is the transition line-width.

We wish to describe changes in the atomic density that arise due to the presence of near-resonant light beams. A detailed quantum treatment of the density dynamics leads to a complicated model. A simplified description is valid in optical molasses, since the atomic velocity is strongly damped. For typical MOT parameters, the length scale over which velocity damping occurs is $\sim 10\,\mu\mathrm{m}$. We assume the spatial scales of interest are large compared to this damping length and therefore write the distribution function of the atoms as $f(\mathbf{r},\mathbf{p},t) = f_r(\mathbf{r},t)f_p(\mathbf{p})$. The momentum distribution function is assumed to be a Maxwellian distribution at temperature T, i.e.,

$$f_p(\mathbf{p}) = \left(\frac{1}{2\pi m k_\mathrm{B} T}\right)^{3/2} \mathrm{e}^{-p^2/2mk_\mathrm{B}T},$$

where m is the atomic mass and k_B is the Boltzmann constant. The atomic density distribution is

$$n_\mathrm{a}(\mathbf{r},t) \equiv \int \mathrm{d}\mathbf{p} f(\mathbf{r},\mathbf{p},t) = f_r(\mathbf{r},t).$$

Typical temperatures are of the order of the Doppler temperature, $k_\mathrm{B}T = \hbar\gamma/2$ ($\sim 100\,\mu\mathrm{K}$ for alkali atoms).

The density satisfies the continuity equation

$$\frac{\partial n_\mathrm{a}}{\partial t} + \nabla\cdot\mathbf{J} = 0, \tag{3}$$

where $\mathbf{J}$ is the particle flux. In general, the particle flux is due to the combined effects of drift and diffusion. We can write the flux as

$$\mathbf{J} = \frac{D}{k_\mathrm{B}T} n_\mathrm{a}\mathbf{F} - D\nabla n_\mathrm{a}, \tag{4}$$

where $\mathbf{F}$ is the total force acting on the atoms and D is the diffusion coefficient. This description is oversimplified, since the diffusion coefficient, D, is generally a tensor for atoms in optical lattices [6]. We will assume D is a scalar. As we will show next, the force can be expressed in terms of the structure of the optical field, and this leads to a closed model for the coupled dynamics of the light and atoms. This type of model for the light-induced atomic dynamics has been considered previously

in [7, 8]. Here we go one step further and couple the atomic dynamics back to the light.

The force can be divided into dipole and radiation pressure terms, $\mathbf{F} = \mathbf{F}_\mathrm{d} + \mathbf{F}_\mathrm{r}$. The dipole force is conservative and can be written as $\mathbf{F}_\mathrm{d} = -\nabla U$ where U is the dipole potential. For a two-level atom, the dipole potential can be written as

$$U(\mathbf{r}) = \frac{\hbar\Delta}{2}\ln\left(1+\frac{I(\mathbf{r})/I_\mathrm{s}}{1+4\Delta^2/\gamma^2}\right). \tag{5}$$

In the limit of small intensity and large detuning, this simplifies to

$$U \simeq \frac{\hbar\Delta}{2}\frac{I}{I_{\mathrm{s}\Delta}} \simeq \frac{\hbar\gamma^2}{8\Delta}\frac{I}{I_\mathrm{s}}, \tag{6}$$

where $I_{\mathrm{s}\Delta} = I_\mathrm{s}(1+4\Delta^2/\gamma^2)$ is the off-resonant saturation intensity.

The radiation force due to a plane wave $E = (A/2)\mathrm{e}^{\mathrm{i}(\mathbf{k}\cdot\mathbf{r}-\omega t)} + \mathrm{c.c.}$ is

$$\begin{aligned}\mathbf{F}_\mathrm{r} &= \hbar\gamma\frac{\frac{1}{2}\frac{I}{I_\mathrm{s}}}{1+\frac{4\Delta^2}{\gamma^2}+\frac{I}{I_\mathrm{s}}}\mathbf{k}\\ &\simeq \frac{\hbar\gamma}{2}\frac{I}{I_{\mathrm{s}\Delta}}\mathbf{k}.\end{aligned} \tag{7}$$

Here the last line is valid for low intensities. We are interested in the more general situation where the optical field is not a single plane wave. In the general case of high intensities, the formulae are cumbersome. If we stick to the low-intensity limit and consider a finite number of plane waves

$$E = \sum_j \frac{A_j}{2}\mathrm{e}^{\mathrm{i}(\mathbf{k}_j\cdot\mathbf{r}-\omega_j t)} + \mathrm{c.c.},$$

the radiation force is [6]

$$\mathbf{F}_\mathrm{r} = \frac{\hbar\gamma}{2}\sum_j \frac{I_j}{I_{\mathrm{s}\Delta}}\mathbf{k}_j + \frac{\hbar\gamma}{4}\sum_{j,l,l\neq j}\frac{\sqrt{I_j I_l}}{I_{\mathrm{s}\Delta}}(\mathbf{k}_j+\mathbf{k}_l)\mathrm{e}^{\mathrm{i}[(\mathbf{k}_j-\mathbf{k}_l)\cdot\mathbf{r}-\mathrm{i}(\omega_j-\omega_l)t]}. \tag{8}$$

Here we have made use of the approximation that $\Delta_j = \omega_j - \omega_\mathrm{a} \gg \gamma$ and assumed that $I_{\mathrm{s}\Delta}$ is independent of j. Note that the second sum runs over all values of j,l with $l \neq j$, so the force is a real quantity, as it must be for consistency with (3, 4).

Equations (1, 2, 3, 4, 5, 6, 7, 8) constitute a self-consistent model for the coupled dynamics of light and cold atoms. They do not account for the multi-level structure of real atoms and therefore only provide an approximate description of the dynamics. However, even with the simplifying assumption of an idealized two-level atomic model, non-trivial light–atom dynamics emerges. We will explore some of the consequences of this model in the rest of this chapter.

3 Coupled Optical and Atomic Solitons

The above model can be used to describe collective focusing of light and atoms. We consider the limit of large detuning, $\Delta \gg \gamma$, where the model becomes conservative. In this limit, the dynamical equations for the case of a single transverse coordinate, x, are

$$\frac{\partial A}{\partial z} - \frac{\mathrm{i}}{2k}\frac{\partial^2 A}{\partial x^2} = \mathrm{i}\frac{k}{2}\chi A, \tag{9a}$$

$$\chi = -\frac{6\pi}{k^3} n_\mathrm{a} \frac{2\Delta/\gamma}{1+4\Delta^2/\gamma^2 + I/I_\mathrm{s}}, \tag{9b}$$

$$\frac{\partial n_\mathrm{a}}{\partial t} = \frac{D}{k_\mathrm{B}T}\frac{\partial}{\partial x}\left(n_\mathrm{a}\frac{\partial U}{\partial x}\right) + D\frac{\partial^2 n_\mathrm{a}}{\partial x^2}, \tag{9c}$$

$$U(x,z) = \frac{\hbar\Delta}{2}\ln\left(1+\frac{I/I_\mathrm{s}}{1+4\Delta^2/\gamma^2}\right). \tag{9d}$$

The solution which is stationary in time for the atomic density has the form of a Boltzmann distribution:

$$n_\mathrm{a} = n_0 \mathrm{e}^{-U(x)/k_\mathrm{B}T}, \tag{10}$$

where n_0 is a normalization constant which is chosen to match the solution to the available number of atoms per unit length. For the case of red-detuning we have $\Delta < 0$, so $U < 0$ and the atomic density reaches its maximum where the intensity is highest. We seek a one-dimensional solution for the optical field of the form $A(x,z) = A_{\mathrm{s}\Delta} u(x) \mathrm{e}^{\mathrm{i}qz}$, with u real. The constant scaling factor can be set to $A_{\mathrm{s}\Delta} = \left(\frac{2I_{\mathrm{s}\Delta}}{\varepsilon_0 c}\right)^{1/2}$, so that the local intensity is $u^2 \times I_{\mathrm{s}\Delta}$. The scaled transverse profile then satisfies

$$\frac{\mathrm{d}^2 u}{\mathrm{d}x^2} - 2kqu = a\frac{u}{(1+u^2)^{1+d}}, \tag{11}$$

where

$$a = \frac{12\pi n_0 \Delta/\gamma}{k(1+4\Delta^2/\gamma^2)}$$

and $d = \hbar\Delta/2k_\mathrm{B}T$. In the limit $T \to \infty$, the parameter $d \to 0$ and the right-hand side is a saturable Kerr-type nonlinearity, proportional to $u/(1+u^2)$, which is known to support stable one-dimensional solitary wave solutions [9].

At finite temperature, $d < 0$ for the case under consideration and (11) has the first integral

$$\left(\frac{\mathrm{d}u}{\mathrm{d}x}\right)^2 = 2kq\left(u^2 - u_0^2\right) - \frac{a}{d}\left[\frac{1}{(1+u^2)^d} - \frac{1}{(1+u_0^2)^d}\right], \tag{12}$$

where $u_0 = u(0)$ is the peak value of the solution which is assumed to be symmetric about the origin. The requirement of having a finite energy solution which vanishes as $x \to \pm\infty$ specifies the propagation constant as

$$q = \frac{a}{2kdu_0^2}\left[\frac{1}{(1+u_0^2)^d} - 1\right].$$

It is readily shown that the Vakhitov–Kolokolov stability criterion, $\mathrm{d}P/\mathrm{d}q > 0$, where P is the power of the solitary solution, is satisfied provided that $d < -1 - f(u_0^2)$, where f is a positive function which tends to 0 for $u_0^2 \to 0$. In the limit of low intensity, we find that the existence condition for stable solutions is

$$\hbar|\Delta| > 2k_\mathrm{B}T \tag{13}$$

with $\Delta < 0$. This condition was originally found by Klimontovich and Luzgin [10] for the existence of mutual self-focusing of light and atoms. We see that the same condition also guarantees the stability of the resulting atom–optical solitons.

In principle, the condition (13) can be satisfied in a cold-atom experiment. Figure 2 shows the intensity profile found from numerical integration of (11) for several temperatures. The corresponding powers for a beam height along the uniform coordinate, y, of 1 cm are $P = 130, 90$ and 50 mW, where we have used $I_\mathrm{s} = 1.7$ mW/cm^2 for the Cs D2 line. We see that solitons under 100 μm wide are possible for realistic experimental conditions. The spontaneous scattering rate at the peak of the soliton is approximately $r = 6.5 \times 10^3$ s^{-1} for the above parameters. As this is very small compared with the scattering rate from the cooling beams for typical MOT parameters, excess local heating due to the soliton should be negligible.

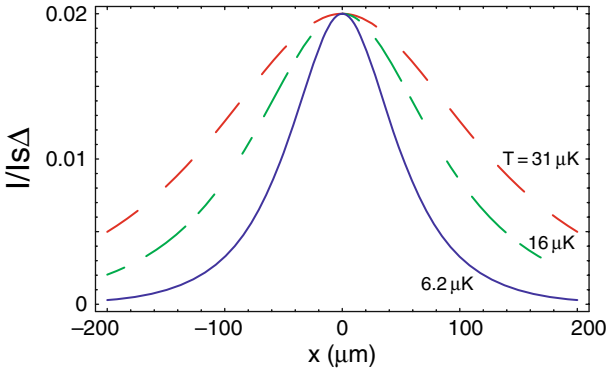

Fig. 2 Intensity profiles of one-dimensional atom–optical solitons for $T = 31$ μK (dashed line), 16 μK (short–long dash) and 6.2 μK (solid line), which, respectively, correspond to $d = -200, -400$ and -1000 for $\Delta/\gamma = -50$. The other parameters are $\gamma/2\pi = 5.2 \times 10^6$ s^{-1}, $n_0 = 1 \times 10^{11}$ cm^{-3} and $\lambda = 0.85$ μm

Since the spontaneous scattering rate can never be made to vanish, time-independent solitons can only exist in the presence of the background cooling due to the MOT beams, and this is a dissipative process. We therefore consider these solutions as further examples of dissipative solitons which occur in a wide range of physical settings [4].

4 Two-Beam Coupling and Atomic Density Perturbations

We now turn our attention to the related phenomenon of atomic density perturbations in the presence of two-beam interactions. Analysis of this geometry will serve as a prelude to the case of spontaneous modulational instability, which will be treated in Sect. 5. When the detuning is not large, we must account for both dipole and radiation pressure forces on the atoms. Equations (3, 4, 6, 8) describe the density evolution under the combined action of dipole and radiation forces. Let us use them to find the density perturbations due to the action of two plane waves:

$$E = \left[\frac{A_{\mathrm{u}}(\mathbf{r})}{2}\mathrm{e}^{\mathrm{i}(\mathbf{k}_{\mathrm{u}}\cdot\mathbf{r}-\omega_{\mathrm{u}}t)} + \frac{A_{\mathrm{p}}(\mathbf{r})}{2}\mathrm{e}^{\mathrm{i}(\mathbf{k}_{\mathrm{p}}\cdot\mathbf{r}-\omega_{\mathrm{p}}t)}\right] + \mathrm{c.c.}\,, \tag{14}$$

where u labels the pump beam and p labels the probe. The geometry is shown in Fig. 3. Strictly speaking, (14) is not a sum of plane waves, since the amplitudes depend on the spatial position. We include this to allow for gain and loss during propagation. The intensity is

$$I = \frac{\varepsilon_0 c}{2}\left[|A_{\mathrm{u}}|^2 + |A_{\mathrm{p}}|^2 + A_{\mathrm{u}}A_{\mathrm{p}}^*\mathrm{e}^{\mathrm{i}(\mathbf{q}\cdot\mathbf{r}-\mathrm{i}\delta t)} + A_{\mathrm{u}}^*A_{\mathrm{p}}\mathrm{e}^{-\mathrm{i}(\mathbf{q}\cdot\mathbf{r}-\mathrm{i}\delta t)}\right],$$

where $q = \mathbf{k}_{\mathrm{u}} - \mathbf{k}_{\mathrm{p}}$ and $\delta = \omega_{\mathrm{u}} - \omega_{\mathrm{p}}$. We will assume $\Delta_{\mathrm{u}} = \omega_{\mathrm{u}} - \omega_{\mathrm{a}}$ and $\Delta_{\mathrm{p}} = \omega_{\mathrm{p}} - \omega_{\mathrm{a}}$ are approximately equal, so that $\Delta_{\mathrm{u}} - \Delta_{\mathrm{p}} = \delta \ll \Delta_{\mathrm{u}}, \Delta_{\mathrm{p}}$. Writing Δ for the nominal detuning, we have the dipole potential, in the small saturation and far-detuned limits:

$$U = \frac{\varepsilon_0 c\hbar\gamma^2}{16\Delta I_{\mathrm{s}}}\left[|A_{\mathrm{u}}|^2 + |A_{\mathrm{p}}|^2 + A_{\mathrm{u}}A_{\mathrm{p}}^*\mathrm{e}^{\mathrm{i}(\mathbf{q}\cdot\mathbf{r}-\mathrm{i}\delta t)} + A_{\mathrm{u}}^*A_{\mathrm{p}}\mathrm{e}^{-\mathrm{i}(\mathbf{q}\cdot\mathbf{r}-\mathrm{i}\delta t)}\right].$$

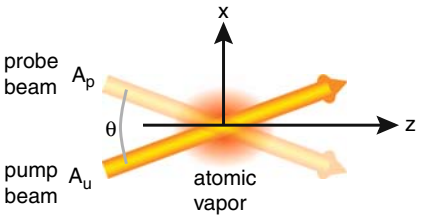

Fig. 3 Interaction geometry for two-beam coupling in an atomic vapor

The dipole force is thus

$$\begin{aligned}\mathbf{F}_{\mathrm{d}} = &-\mathrm{i}\frac{\varepsilon_0 c\hbar\gamma^2}{16\Delta I_{\mathrm{s}}}\left[A_{\mathrm{u}}A_{\mathrm{p}}^{*}\mathrm{e}^{\mathrm{i}(\mathbf{q}\cdot\mathbf{r}-\mathrm{i}\delta t)} - A_{\mathrm{u}}^{*}A_{\mathrm{p}}\mathrm{e}^{-\mathrm{i}(\mathbf{q}\cdot\mathbf{r}-\mathrm{i}\delta t)}\right]\mathbf{q}\\ &-\frac{\varepsilon_0 c\hbar\gamma^2}{16\Delta I_{\mathrm{s}}}\left[(\nabla A_{\mathrm{u}})A_{\mathrm{u}}^{*} + A_{\mathrm{u}}\nabla A_{\mathrm{u}}^{*} + (\nabla A_{\mathrm{p}})A_{\mathrm{p}}^{*} + A_{\mathrm{p}}\nabla A_{\mathrm{p}}^{*}\right.\\ &+[(\nabla A_{\mathrm{u}})A_{\mathrm{p}}^{*} + A_{\mathrm{u}}\nabla A_{\mathrm{p}}^{*}]\mathrm{e}^{\mathrm{i}(\mathbf{q}\cdot\mathbf{r}-\mathrm{i}\delta t)}\\ &\left.+[(\nabla A_{\mathrm{u}}^{*})A_{\mathrm{p}} + A_{\mathrm{u}}^{*}\nabla A_{\mathrm{p}}]\mathrm{e}^{-\mathrm{i}(\mathbf{q}\cdot\mathbf{r}-\mathrm{i}\delta t)}\right]. \end{aligned} \tag{15}$$

We have chosen a geometry where the difference vector, $\mathbf{q}$, lies almost exactly perpendicular to $\hat{z}$, since $\mathbf{q}\cdot\hat{z} = (\delta/c)\cos(\theta/2) \approx \delta/c = (\delta/\omega_{\mathrm{u}})k_{\mathrm{u}}$, where θ is the small angle between the beams. On the other hand, $|\mathbf{q}| \approx \theta k_{\mathrm{u}}$. If the frequency difference between the beams is at most 1 MHz, then $\delta/\omega_{\mathrm{u}} \sim 10^{-8}$, whereas for parameters of interest, we will have $\theta > 10^{-4}$. Thus the component of $\mathbf{q}$ along $\hat{z}$ is less than 10^{-4} of $|\mathbf{q}|$. We now assume that the beams are close to plane waves, so that $|\nabla_{\mathbf{q}}A_{\mathrm{u}}| \ll \mathbf{q}A_{\mathrm{u}}$, $|\nabla_{\mathbf{q}}A_{\mathrm{p}}| \ll \mathbf{q}A_{\mathrm{p}}$, and we only keep the z derivatives in the last group of terms in the expression for $\mathbf{F}_{\mathrm{d}}$, obtaining

$$\begin{aligned}\mathbf{F}_{\mathrm{d}} = &-\mathrm{i}\frac{\varepsilon_0 c\hbar\gamma^2}{16\Delta I_{\mathrm{s}}}\left[A_{\mathrm{u}}A_{\mathrm{p}}^{*}\mathrm{e}^{\mathrm{i}(\mathbf{q}\cdot\mathbf{r}-\mathrm{i}\delta t)} - A_{\mathrm{u}}^{*}A_{\mathrm{p}}\mathrm{e}^{-\mathrm{i}(\mathbf{q}\cdot\mathbf{r}-\mathrm{i}\delta t)}\right]\mathbf{q}\\ &-\frac{\varepsilon_0 c\hbar\gamma^2}{16\Delta I_{\mathrm{s}}}\left[(\partial_z A_{\mathrm{u}})A_{\mathrm{u}}^{*} + A_{\mathrm{u}}\partial_z A_{\mathrm{u}}^{*} + (\partial_z A_{\mathrm{p}})A_{\mathrm{p}}^{*} + A_{\mathrm{p}}\partial_z A_{\mathrm{p}}^{*}\right.\\ &+[(\partial_z A_{\mathrm{u}})A_{\mathrm{p}}^{*} + A_{\mathrm{u}}\partial_z A_{\mathrm{p}}^{*}]\mathrm{e}^{\mathrm{i}(\mathbf{q}\cdot\mathbf{r}-\mathrm{i}\delta t)}\\ &\left.+[(\partial_z A_{\mathrm{u}}^{*})A_{\mathrm{p}} + A_{\mathrm{u}}^{*}\partial_z A_{\mathrm{p}}]\mathrm{e}^{-\mathrm{i}(\mathbf{q}\cdot\mathbf{r}-\mathrm{i}\delta t)}\right]. \end{aligned} \tag{16}$$

For the radiation force, we use (8, 14) to get

$$\mathbf{F}_{\mathrm{r}} = \frac{\hbar\gamma^3}{8\Delta^2 I_{\mathrm{s}}}\left(I_{\mathrm{u}}\mathbf{k}_{\mathrm{u}} + I_{\mathrm{p}}\mathbf{k}_{\mathrm{p}}\right) + \frac{\hbar\gamma^3}{8\Delta^2 I_{\mathrm{s}}}\sqrt{I_{\mathrm{u}}I_{\mathrm{p}}}(\mathbf{k}_{\mathrm{u}} + \mathbf{k}_{\mathrm{p}})\cos(\mathbf{q}\cdot\mathbf{r} - \delta t). \tag{17}$$

Although we could continue with these general expressions, it is simpler to make some further approximations now. We assume that the atomic cloud is uniform along z, and concentrate on the appearance of transverse structure. This is not strictly correct, as intensity changes during propagation will produce dipole forces directed along $\hat{z}$. In addition, the radiation force has strong $\hat{z}$ components. It is seen experimentally that these forces result in acceleration and eventually loss of the atoms from the MOT. However, wave mixing dynamics and energy transfer are observed on time scales that are shorter than, and clearly separated from, the atom acceleration. Our primary interest here is describing the energy transfer between beams. We implicitly assume that we can do so on a time scale that is short compared with that for which radiation forces are significant, by simply neglecting the forces along $\hat{z}$. Keeping only the transverse components along $\hat{x}$ and assuming $A_{\mathrm{u}}, A_{\mathrm{p}}$ are real we get

$$\mathbf{F}_{\mathrm{d}} = \frac{\hbar\gamma^2\sqrt{I_{\mathrm{u}}I_{\mathrm{p}}}}{4\Delta I_{\mathrm{s}}} q \sin(qx-\delta t)\hat{x}, \tag{18}$$

$$\mathbf{F}_{\mathrm{r}} = \frac{\hbar\gamma^3}{16\Delta^2 I_{\mathrm{s}}} q \left(I_{\mathrm{u}} - I_{\mathrm{p}}\right)\hat{x}. \tag{19}$$

We assume a real density perturbation of the form

$$n_{\mathrm{a}}(\mathbf{r}) = n_{\mathrm{a}0}\left[1 + d\mathrm{e}^{\mathrm{i}(qx-\delta t)} + d^*\mathrm{e}^{-\mathrm{i}(qx-\delta t)}\right].$$

The continuity equation (3) can be written as

$$\begin{aligned}
&-\mathrm{i}\delta d\mathrm{e}^{\mathrm{i}(qx-\delta t)} + \mathrm{i}\delta d^*\mathrm{e}^{-\mathrm{i}(qx-\delta t)} \\
&+\mathrm{i}\frac{Dq^2}{k_{\mathrm{B}}T}\frac{\hbar\gamma^2}{4\Delta I_{\mathrm{s}}}\left[d\mathrm{e}^{\mathrm{i}(qx-\delta t)} - d^*\mathrm{e}^{-\mathrm{i}(qx-\delta t)}\right] \\
&\times\left[\sqrt{I_{\mathrm{u}}I_{\mathrm{p}}}\sin(qx-\delta t) + \frac{\gamma}{4\Delta}\left(I_{\mathrm{u}} - I_{\mathrm{p}}\right)\right] \\
&+\frac{Dq^2}{k_{\mathrm{B}}T}\frac{\hbar\gamma^2}{4\Delta I_{\mathrm{s}}}\left[1 + d\mathrm{e}^{\mathrm{i}(qx-\delta t)} + d^*\mathrm{e}^{-\mathrm{i}(qx-\delta t)}\right]\sqrt{I_{\mathrm{u}}I_{\mathrm{p}}}\cos(qx-\delta t) \\
&+Dq^2\left[d\mathrm{e}^{\mathrm{i}(qx-\delta t)} + d^*\mathrm{e}^{-\mathrm{i}(qx-\delta t)}\right] = 0.
\end{aligned} \tag{20}$$

Grouping the terms according to the phase factors gives

$$\begin{aligned}
&\mathrm{e}^{\mathrm{i}(qx-\delta t)}\left[-\mathrm{i}\delta d + \mathrm{i}\frac{Dq^2}{k_{\mathrm{B}}T}\frac{\hbar\gamma^3}{16\Delta^2 I_{\mathrm{s}}} d(I_{\mathrm{u}} - I_{\mathrm{p}})\right. \\
&\qquad\left. + \frac{Dq^2}{k_{\mathrm{B}}T}\frac{\hbar\gamma^2}{8\Delta I_{\mathrm{s}}}\sqrt{I_{\mathrm{u}}I_{\mathrm{p}}} + Dq^2 d\right] \\
&+\mathrm{e}^{\mathrm{i}2(qx-\delta t)}\left[\frac{Dq^2}{k_{\mathrm{B}}T}\frac{\hbar\gamma^2}{4\Delta I_{\mathrm{s}}}\sqrt{I_{\mathrm{u}}I_{\mathrm{p}}} d\right] + \mathrm{c.c.} = 0.
\end{aligned} \tag{21}$$

We see that harmonics proportional to $\mathrm{e}^{\pm\mathrm{i}2(qx-\delta t)}$ are generated by the nonlinearities. For the purposes of calculating the two-beam coupling, which is driven by phase-matched terms, we can neglect these higher-order gratings. Setting the coefficient of the first-order gratings to zero gives

$$\begin{aligned}
d &= -\frac{\frac{\hbar\gamma^2}{8k_{\mathrm{B}}T\Delta}\frac{\sqrt{I_{\mathrm{u}}I_{\mathrm{p}}}}{I_{\mathrm{s}}}}{1 - \mathrm{i}\left(\frac{\delta}{Dq^2} - \frac{\hbar\gamma^3}{16k_{\mathrm{B}}T\Delta^2}\frac{I_{\mathrm{u}}-I_{\mathrm{p}}}{I_{\mathrm{s}}}\right)} \\
&= -\frac{\hbar\gamma^2}{8k_{\mathrm{B}}T\Delta}\frac{\sqrt{I_{\mathrm{u}}I_{\mathrm{p}}}}{I_{\mathrm{s}}}\frac{1 + \mathrm{i}\left(\frac{\delta}{Dq^2} - \frac{\hbar\gamma^3}{16k_{\mathrm{B}}T\Delta^2}\frac{I_{\mathrm{u}}-I_{\mathrm{p}}}{I_{\mathrm{s}}}\right)}{1 + \left(\frac{\delta}{Dq^2} - \frac{\hbar\gamma^3}{16k_{\mathrm{B}}T\Delta^2}\frac{I_{\mathrm{u}}-I_{\mathrm{p}}}{I_{\mathrm{s}}}\right)^2}.
\end{aligned} \tag{22}$$

For frequency-degenerate beams, the result simplifies to

$$d = -\frac{\hbar\gamma^2}{8k_{\mathrm{B}}T\Delta}\frac{\sqrt{I_{\mathrm{u}}I_{\mathrm{p}}}}{I_{\mathrm{s}}}\frac{1-\mathrm{i}\frac{\hbar\gamma^3}{16k_{\mathrm{B}}T\Delta^2}\frac{I_{\mathrm{u}}-I_{\mathrm{p}}}{I_{\mathrm{s}}}}{1+\left(\frac{\hbar\gamma^3}{16k_{\mathrm{B}}T\Delta^2}\frac{I_{\mathrm{u}}-I_{\mathrm{p}}}{I_{\mathrm{s}}}\right)^2}. \tag{23}$$

When the dipole force is dominant, d is purely real and there is no energy transfer between the beams. When the radiation force is dominant, d is purely imaginary and there is energy transfer that depends on the sign of $I_{\mathrm{u}} - I_{\mathrm{p}}$. Note that, for frequency-degenerate beams, d has no angular dependence. This is consistent with the result given in [11] for a similar beam-coupling interaction in the setting of an optical lattice.

We can compare the strength of the dipole and radiation force contributions to the density perturbation by evaluating the magnitude and phase of d as a function of the detuning, as shown in Fig. 4. The intensity was chosen to correspond to experimental measurements at $\Delta/\gamma = 5,7$ which will be described below. For a range of detunings, the magnitude of d is equal to or larger than 1. This does not mean that the density is negative, but only that the parameters lie outside the region of validity of the linearized theory. In other words, we have used a low-intensity theory, but the off-resonance saturation parameter is $I/I_{\mathrm{s}\Delta} = 0.5$, which is not small. We also see that the phase of d is not close to zero, so there is a mixed dipole and radiation contribution to the grating. For the curves at $\Delta/\gamma = 5$ and $\Delta/\gamma = 7$, the phase angle is about 30°.

4.1 Grating Formation Time

Equation (23) gives the stationary value for the density perturbation due to the optical beams. We wish to estimate the time of formation of the grating, in order to compare with the time dependence of the observed two-beam coupling gain. The density evolution can be found by solving the continuity equation with the ansatz

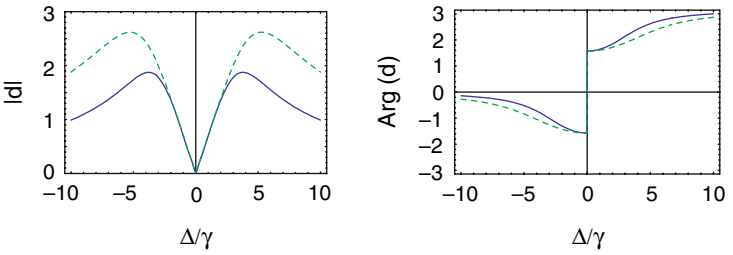

Fig. 4 Magnitude and phase of d as a function of detuning for $I/I_{\mathrm{s}} = 50.5$ (solid line) and 98.5 (dashed line)

$$n_{\mathrm{a}}(x,t) = n_{\mathrm{a0}}\left[1 + d(t)\mathrm{e}^{\mathrm{i}(qx-\delta t)} + d^{*}(t)\mathrm{e}^{-\mathrm{i}(qx-\delta t)}\right].$$

Plugging in to the continuity equation again, we get

$$\begin{aligned}\mathrm{e}^{\mathrm{i}(qx-\delta t)}&\left[\frac{\mathrm{d}d}{\mathrm{d}t} - \mathrm{i}\delta d + \mathrm{i}\frac{Dq^2}{k_{\mathrm{B}}T}\frac{\hbar\gamma^3}{16\Delta^2 I_{\mathrm{s}}}d(I_{\mathrm{u}} - I_{\mathrm{p}})\right.\\ &\left.+\frac{Dq^2}{k_{\mathrm{B}}T}\frac{\hbar\gamma^2}{8\Delta I_{\mathrm{s}}}\sqrt{I_{\mathrm{u}}I_{\mathrm{p}}} + Dq^2 d\right]\\ +\mathrm{e}^{\mathrm{i}2(qx-\delta t)}&\left[\frac{Dq^2}{k_{\mathrm{B}}T}\frac{\hbar\gamma^2}{4\Delta I_{\mathrm{s}}}\sqrt{I_{\mathrm{u}}I_{\mathrm{p}}}d\right] + \mathrm{c.c.} = 0.\end{aligned} \tag{24}$$

The equations are solved (again neglecting the second-order gratings), providing

$$\frac{\mathrm{d}d}{\mathrm{d}t} + \left[-\mathrm{i}\delta + \mathrm{i}\frac{Dq^2}{k_{\mathrm{B}}T}\frac{\hbar\gamma^3}{16\Delta^2 I_{\mathrm{s}}}(I_{\mathrm{u}} - I_{\mathrm{p}}) + Dq^2\right]d = -\frac{Dq^2}{k_{\mathrm{B}}T}\frac{\hbar\gamma^2}{8\Delta I_{\mathrm{s}}}\sqrt{I_{\mathrm{u}}I_{\mathrm{p}}}. \tag{25}$$

This equation is of the form

$$\frac{\mathrm{d}d}{\mathrm{d}t} + ad = b,$$

where

$$\begin{aligned}a &= -\mathrm{i}\delta + \mathrm{i}\frac{Dq^2}{k_{\mathrm{B}}T}\frac{\hbar\gamma^3}{16\Delta^2 I_{\mathrm{s}}}(I_{\mathrm{u}} - I_{\mathrm{p}}) + Dq^2,\\ b &= -\frac{Dq^2}{k_{\mathrm{B}}T}\frac{\hbar\gamma^2}{8\Delta I_{\mathrm{s}}}\sqrt{I_{\mathrm{u}}I_{\mathrm{p}}}.\end{aligned} \tag{26}$$

The solution satisfying $d(0) = 0$ and $d(t \to \infty) = d_{\max} = b/a$ is $d = \frac{b}{a}(1 - \mathrm{e}^{-at})$. The parameter a is complex and can be written as $a = a_{\mathrm{r}} + \mathrm{i}a_{\mathrm{i}}$. The time dependence of the real and imaginary parts of $d = d_{\mathrm{r}} + \mathrm{i}d_{\mathrm{i}}$ is therefore

$$d_{\mathrm{r}}(t) = \frac{b}{|a|^2}\left[a_{\mathrm{r}} - \mathrm{e}^{-a_{\mathrm{r}}t}\left(a_{\mathrm{r}}\cos a_{\mathrm{i}}t - a_{\mathrm{i}}\ \sin a_{\mathrm{i}}t\right)\right], \tag{27a}$$

$$d_{\mathrm{i}}(t) = \frac{b}{|a|^2}\left[-a_{\mathrm{i}} + \mathrm{e}^{-a_{\mathrm{r}}t}\left(a_{\mathrm{i}}\cos a_{\mathrm{i}}t + a_{\mathrm{r}}\sin a_{\mathrm{i}}t\right)\right]. \tag{27b}$$

Only d_{i} contributes to energy transfer, so following the time evolution of d_{i} should indicate the time evolution of the observed wave mixing gain. Figure 5 shows d_{r}, d_{i} as a function of time for several values of q and Δ/γ. Note that the shape of the curve will only be approximately correct, since the optical gain for a weak probe is proportional to $\mathrm{e}^{gd_{\mathrm{i}}}$, where g is a gain coefficient, whereas here we only plot d_{i}.

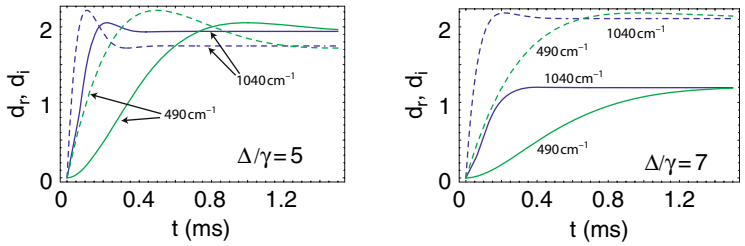

Fig. 5 Real (dashed line) and imaginary (solid line) parts of d as a function of time. $I/I_{s\Delta} = 0.5$ for all cases

5 Modulational Instability

Consider first a single optical beam $\mathscr{E} = (A(\mathbf{r},t)/2)\mathrm{e}^{\mathrm{i}(kz-\omega t)} + \text{c.c.}$ In the two-level model, the slowly varying amplitude satisfies the paraxial equation

$$\frac{\partial A}{\partial z} - \frac{\mathrm{i}}{2k}\nabla^2 A = \mathrm{i}\frac{k}{2}\chi(\mathbf{r})A, \tag{28}$$

where the susceptibility is

$$\chi(\mathbf{r}) = -\frac{6\pi}{k^3}n_\mathrm{a}(\mathbf{r},t)\frac{2\Delta/\gamma - \mathrm{i}}{1+4\Delta^2/\gamma^2 + I/I_\mathrm{s}}. \tag{29}$$

Absorption becomes negligible when the detuning is sufficiently large, and then (28) admits constant-intensity plane wave solutions $\mathscr{A}_0 = A_0\mathrm{e}^{\mathrm{i}\kappa z}$, where

$$\kappa = \frac{k}{2}\chi_0 = -\frac{3\pi}{k^2}n_{\mathrm{a}0}\frac{2\Delta/\gamma}{1+4\Delta^2/\gamma^2}\frac{1}{1+s},$$

where $s = I_\mathrm{A}/I_{s\Delta}$, $I_\mathrm{A} = \frac{1}{2}\varepsilon_0 c|A_0|^2$ is the intensity, $I_{s\Delta} = I_\mathrm{s}(1+4\Delta^2/\gamma^2)$ is the off-resonant saturation intensity and $n_{\mathrm{a}0}$ is the spatially averaged density. As is well known, these plane wave solutions are unstable for a self-focusing nonlinearity. Figure 6 shows the result of numerical simulation of (2, 28) in the conservative limit for parameters corresponding to a Cs MOT.

We then introduce a perturbation ansatz

$$A(\mathbf{r},t) = \mathscr{A}_0(z)\left[1 + a_+\mathrm{e}^{\mathrm{i}(\mathbf{q}\cdot\rho-\Omega t)} + a_-\mathrm{e}^{-\mathrm{i}(\mathbf{q}\cdot\rho-\Omega t)}\right]. \tag{30}$$

To first-order in the perturbations, the susceptibility becomes

$$\begin{aligned}\chi(\mathbf{r}) &= \frac{2\kappa}{k}\frac{1+s}{1+s+s[(a_+ + a_-^*)\mathrm{e}^{\mathrm{i}(\mathbf{q}\cdot\rho-\Omega t)} + (\mathrm{a}_+^* + \mathrm{a}_-)\mathrm{e}^{-\mathrm{i}(\mathbf{q}\cdot\rho-\Omega t)}]} \\ &\simeq \frac{2\kappa}{k}\left\{1 - \frac{s}{1+s}\left[(a_+ + a_-^*)\mathrm{e}^{\mathrm{i}(\mathbf{q}\cdot\rho-\Omega t)} + (a_+^* + a_-)\mathrm{e}^{-\mathrm{i}(\mathbf{q}\cdot\rho-\Omega t)}\right]\right\}.\end{aligned} \tag{31}$$

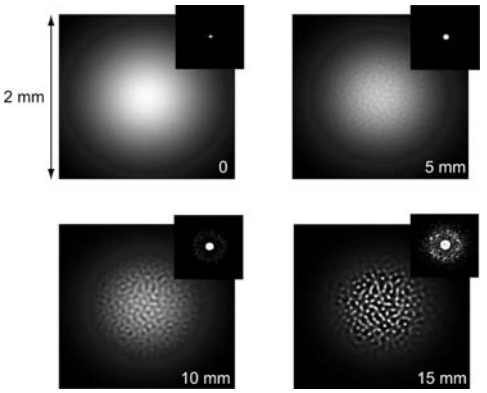

Fig. 6 Numerically simulated beam evolution in a Cs atomic vapor with density $n_{a0} = 2.0 \times 10^{11}\,\mathrm{cm}^{-3}$. The input beam parameters are $\Delta/\gamma = +10$, Gaussian waist $w = 0.8\,\mathrm{mm}$ and $s = 2.0$. The insets show the spatial spectra

Collecting phase-matched terms with the same transverse and time variation gives the set

$$\frac{\partial a_+}{\partial z} + \mathrm{i}\frac{q^2}{2k}a_+ = -\mathrm{i}\kappa\frac{s}{1+s}\left(a_+ + a_-^*\right), \tag{32a}$$

$$\frac{\partial a_-^*}{\partial z} - \mathrm{i}\frac{q^2}{2k}a_-^* = \mathrm{i}\kappa\frac{s}{1+s}\left(a_+ + a_-^*\right). \tag{32b}$$

We can simplify the notation by defining $\beta = -\kappa s/(1+s)$, $\tilde{q} = q^2/2k$ and the vector $\mathbf{a} = (a_+, a_-^*)$. Equations (32) then take the form $\mathrm{d}\mathbf{a}/\mathrm{d}z = \mathbf{M}\mathbf{a}$, where

$$\mathbf{M} = \mathrm{i}\begin{pmatrix} \beta - \tilde{q} & \beta \\ -\beta & -(\beta - \tilde{q}) \end{pmatrix}. \tag{33}$$

The eigenvalues of $\mathbf{M}$ are

$$\Lambda_{1,2} = \pm\sqrt{\tilde{q}(2\beta - \tilde{q})} \tag{34}$$

and these describe the growth rate of weak perturbations for a saturable Kerr-type nonlinearity [12]. The general solution for the evolution of the amplitudes can be found using the eigenvectors of $\mathbf{M}$ or by writing

$$a_+(z) = c_1\mathrm{e}^{\Lambda_1 z} + c_2\mathrm{e}^{\Lambda_2 z}, \tag{35}$$

$$a_-^*(z) = c_3\mathrm{e}^{\Lambda_1 z} + c_4\mathrm{e}^{\Lambda_2 z}. \tag{36}$$

The boundary conditions at $z = 0$ are

$$c_1 + c_2 = a_+(0), \tag{37}$$

$$c_3 + c_4 = a_-^*(0), \tag{38}$$

$$c_1\Lambda_1 + c_2\Lambda_2 = \mathrm{i}(\beta - \tilde{q})a_+(0) + \mathrm{i}\beta a_-^*(0), \tag{39}$$

$$c_3\Lambda_1 + c_4\Lambda_2 = -\mathrm{i}\beta a_+(0) - \mathrm{i}(\beta - \tilde{q})a_-^*(0). \tag{40}$$

Solving for the c_j in terms of the boundary conditions, we find

$$c_1 = \frac{a_+(0)}{2} + \frac{\mathrm{i}}{2\sqrt{\tilde{q}(2\beta-\tilde{q})}}\left[\beta(a_+(0)+a_-^*(0)) - \tilde{q}a_+(0)\right], \tag{41a}$$

$$c_2 = \frac{a_+(0)}{2} - \frac{\mathrm{i}}{2\sqrt{\tilde{q}(2\beta-\tilde{q})}}\left[\beta(a_+(0)+a_-^*(0)) - \tilde{q}a_+(0)\right], \tag{41b}$$

$$c_3 = \frac{a_-^*(0)}{2} - \frac{\mathrm{i}}{2\sqrt{\tilde{q}(2\beta-\tilde{q})}}\left[\beta(a_+(0)+a_-^*(0)) - \tilde{q}a_-^*(0)\right], \tag{41c}$$

$$c_4 = \frac{a_-^*(0)}{2} + \frac{\mathrm{i}}{2\sqrt{\tilde{q}(2\beta-\tilde{q})}}\left[\beta(a_+(0)+a_-^*(0)) - \tilde{q}a_-^*(0)\right]. \tag{41d}$$

For positive MI gain and large propagation distances, the intensity of the spatial sidebands is dominated by the positive eigenvalues. Thus $I_+(z) \sim |a_+(z)|^2 \sim |c_1|^2 \mathrm{e}^{2\Lambda_1 z}$ and $I_-(z) \sim |a_-(z)|^2 \sim |c_3|^2 \mathrm{e}^{2\Lambda_1 z}$. We may consider some particular cases of interest. Suppose $a_+(0) = a_-^*(0) \equiv a_0$, with a_0 real. Then

$$\frac{I_+(z)}{I_+(0)} = \frac{I_-(z)}{I_-(0)} = \frac{\beta}{2\tilde{q}}\mathrm{e}^{2\Lambda_1 z}. \tag{42}$$

If, however, we start by exciting only a single sideband, so that $a_+(0) = a_0$ and $a_-(0) = 0$, we find

$$\frac{I_+(z)}{I_+(0)} = \frac{I_-(z)}{I_+(0)} = \frac{\beta^2}{4\tilde{q}(2\beta-\tilde{q})}\mathrm{e}^{2\Lambda_1 z}. \tag{43}$$

From (34), we see that the MI gain is maximized when $\tilde{q} = \beta$. For this value of $\tilde{q}$, (42) gives $I_+(z)/I_+(0) = \mathrm{e}^{2\Lambda_1 z}/2$, whereas (43) gives $I_+(z)/I_+(0) = \mathrm{e}^{2\Lambda_1 z}/4$, which is only half as large.

6 Modulational Instability with Density Changes

By using the ansatz (30) for the field

$$A(\mathbf{r},t) = A_0 \mathrm{e}^{\mathrm{i}\kappa z}\left[1 + a_+ \mathrm{e}^{\mathrm{i}(\mathbf{q}\cdot\rho - \Omega t)} + a_- \mathrm{e}^{-\mathrm{i}(\mathbf{q}\cdot\rho - \Omega t)}\right],$$

real density perturbations of the form

$$n_\mathrm{a}(\mathbf{r},t) = n_{\mathrm{a}0}(z)\left[1 + d\mathrm{e}^{\mathrm{i}(\mathbf{q}\cdot\rho - \Omega t)} + d^*\mathrm{e}^{-\mathrm{i}(\mathbf{q}\cdot\rho - \Omega t)}\right],$$

and (18, 19) for the light forces in the continuity equation (3), we find, to lowest-order in the perturbations,

$$\left\{ d(Dq^2 - \mathrm{i}\Omega) + \frac{\hbar}{4k_\mathrm{B}T} \frac{\frac{I_0}{I_\mathrm{s}}}{1 + \frac{4\Delta^2}{\gamma^2} + \frac{I_0}{I_\mathrm{s}}} q^2 D[2\Delta(a_+ + a_-^*) + \mathrm{i}\gamma(a_+ - a_-^*)] \right\} \mathrm{e}^{\mathrm{i}(qx - \delta t)} + \mathrm{c.c.} = 0. \tag{44}$$

Setting the term in curly braces to zero gives

$$d = -\frac{\hbar}{4k_\mathrm{B}T} \frac{s}{1+s} \frac{2\Delta(a_+ + a_-^*) + \mathrm{i}\gamma(a_+ - a_-^*)}{1 - \mathrm{i}\frac{\Omega}{Dq^2}}. \tag{45}$$

Including d in (2) for the susceptibility results in

$$\begin{aligned} \frac{\partial a_+}{\partial z} + \mathrm{i}\frac{q^2}{2k} a_+ &= -\mathrm{i}\kappa \frac{s}{1+s} \left(a_+ + a_-^*\right) + \mathrm{i}\kappa d, \\ \frac{\partial a_-^*}{\partial z} - \mathrm{i}\frac{q^2}{2k} a_-^* &= \mathrm{i}\kappa \frac{s}{1+s} \left(a_+ + a_-^*\right) - \mathrm{i}\kappa d. \end{aligned} \tag{46}$$

These equations are the same as those in the set (32), apart from the addition of the terms proportional to d on the right-hand side. We again define $\beta = -\kappa s/(1+s)$, $\tilde{q} = q^2/2k$ and the vector $\mathbf{a} = (a_+, a_-^*)$. Using the result (45) for d, (32) take the form $\mathrm{d}\mathbf{a}/\mathrm{d}z = \mathbf{M}\mathbf{a}$, where

$$\mathbf{M} = \mathrm{i} \begin{pmatrix} \beta[1 + d_0(1 + \mathrm{i}\varepsilon)] - \tilde{q} & \beta[1 + d_0(1 - \mathrm{i}\varepsilon)] \\ -\beta[1 + d_0(1 + \mathrm{i}\varepsilon)] & -\beta[1 + d_0(1 - \mathrm{i}\varepsilon)] + \tilde{q} \end{pmatrix}.$$

We have introduced the parameters

$$\begin{aligned} d_0 &= \frac{\hbar\Delta}{2k_\mathrm{B}T} \frac{1}{1 - \mathrm{i}\Omega/Dq^2}, \\ \varepsilon &= \frac{\gamma}{2\Delta}. \end{aligned}$$

When the temperature is high, $d_0 \to 0$ and there are no density redistribution effects. At low temperatures, the strength of the density changes scale with d_0. In the limit of large detuning, $\varepsilon \to 0$ and the eigenvalues of $\mathbf{M}$ are given by (34), with the replacement $\beta \to \beta(1 + d_0)$. In the limit of vanishing ε, the eigenvalues are therefore

$$\Lambda_{1,2} = \pm\sqrt{\tilde{q}[2\beta(1 + d_0) - \tilde{q}]}. \tag{47}$$

The condition for the existence of modulational instability when $\Omega = 0$ is therefore $\beta(1 + d_0) > 0$ or

$$\Delta \left(1 + \frac{\hbar\Delta}{2k_\mathrm{B}T}\right) > 0.$$

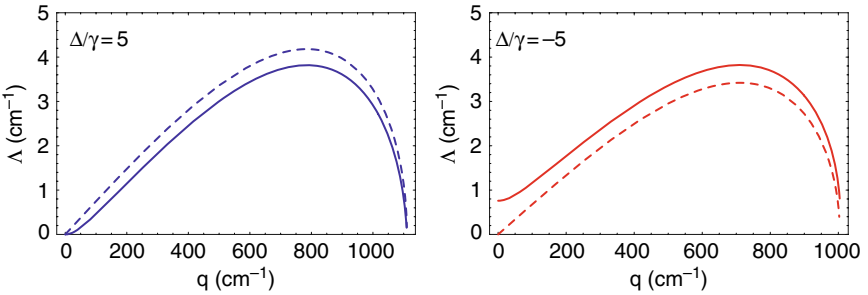

Fig. 7 Growth rate of modulational instability for $s = 0.5$, $\lambda = 0.852\,\mu\text{m}$, $n_{a0} = 1 \times 10^{10}\,\text{cm}^{-3}$ and $k_B T = \hbar\gamma/4$. The left (right) plots are for $\Delta/\gamma = 5$ (-5). The solid lines are from (48) while the dashed lines are from (47)

For blue-detuning, $\Delta > 0$, and this condition is always satisfied. For red-detuning, $\Delta < 0$, and the instability condition is then

$$\hbar|\Delta| > 2k_B T,$$

which is again the Klimontovich–Luzgin condition of (13). When radiation forces are included, the eigenvalues of **M** are

$$\Lambda_{1,2} = \pm\sqrt{\tilde{q}[2\beta(1+d_0) - \tilde{q}] + \beta^2 d_0^2 \varepsilon^2} - \beta d_0 \varepsilon. \tag{48}$$

The condition for instability when $\Omega = 0$ is unchanged and is still given by $\beta(1+d_0) > 0$. The presence of radiation forces slightly reduces or increases the growth rate, depending on the sign of detuning, as can be seen from the plots in Fig. 7. It is interesting to note that, in the limit where the radiation forces dominate, $\varepsilon \to \infty$, the growth rate tends to zero. Thus, radiation forces alone do not lead to modulational instability. This is in contrast to the situation for two-beam coupling, where the probe beam gain is due only to the radiation forces, and not to the dipole forces.

7 Experimental Observations

The possibility of observing modulational instability in a cold-atom setting has been investigated using a Cs MOT. A MOT with several billion atoms was used for pump–probe measurements. Details of the experimental set-up have been given in [13]. For pump–probe measurements [14], two beams were coupled into the MOT, as shown in Fig. 8.

We measured the probe transmission at two different detunings, $\Delta = +5\gamma, +7\gamma$, where the intensities of the probe and pump are chosen so that $s = 0.05, 0.5$ for the probe and pump, respectively, for all cases. The right-hand side of Fig. 8 shows the

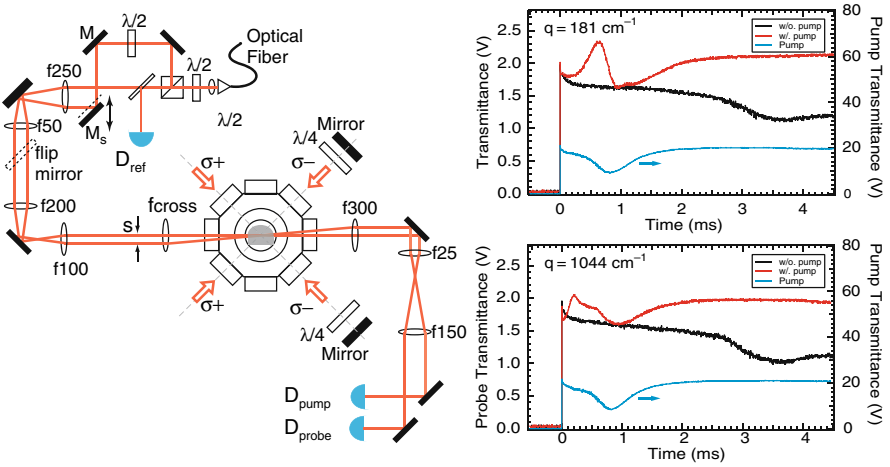

Fig. 8 Experimental set-up for measurements of MI gain

measured transmission, as a function of time, with $\Delta/\gamma = 5$ for two different values of the wave-number, q. In these plots, the darkest traces show the transmission of the probe with pump off, the less dark ones are with the pump on, while the lightest ones indicate the transmission of the pump.

Comparing the transmission of the probe with and without pump, we see that the probe transmission is greatly modified because of the pump beam. Without the pump beam, the probe transmission curve shows the time-dependent absorption in the MOT. The dip around 3.5 ms is due to the Doppler shift effect [13]. Atoms are accelerated and Doppler-shifted closer to the resonance after a certain amount of time, so the probe beam is strongly absorbed. The same effect is also seen in the transmission of the pump. The difference is that the pump beam is 10 times stronger, so the Doppler pushing is stronger. It takes a shorter time for the atoms to be accelerated close to the resonance, so the dip is around 0.9–1.0 ms. With the pump beam on, the probe transmission is very different. Peaks are observed during the first 1 ms when the probe and pump beams are turned on. After 1 ms, the probe beam transmission gradually increases as a result of the MOT having partially dispersed. The temporal behavior of the probe transmission includes several effects such as Doppler pushing and possible density redistribution.

We plot the time of peak gain as a function of transverse wave-number for both detunings in Fig. 9. This time-dependent density perturbation, due to both the dipole and radiation forces, is essentially the same for both two-beam coupling and MI. Since d_i has been shown to indicate the time evolution of the two-beam coupling gain, we can derive the time when d_i is maximized from (27b). Setting the time derivative of $d_\mathrm{i}(t)$ to zero gives

$$t_{\max} = \frac{\pi}{a_\mathrm{i}} \propto \frac{1}{q^2}. \tag{49}$$

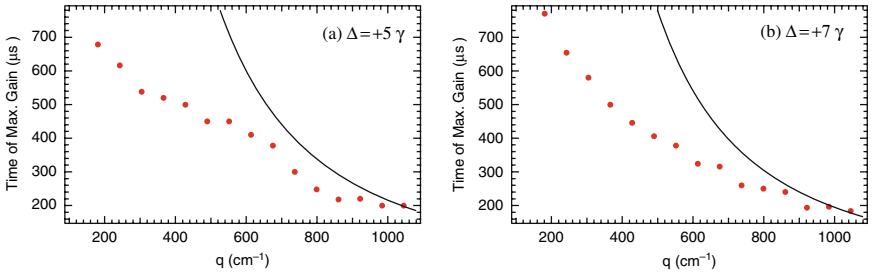

Fig. 9 The time of measured peak gain as a function of q for (**a**) $\Delta = +5\gamma$ and (**b**) $\Delta = +7\gamma$. The solid curves are results calculated using (49)

As a comparison, we plot $t_{\max}$ as a function of q in Fig. 9. We choose $D = 0.063, 0.136\,\mathrm{cm}^2/\mathrm{s}$, respectively, for two different detunings, so that $t_{\max}$ matches the measured time of peak gain at the largest q. Other parameters are from the experiment. There have been very few direct measurements of the spatial diffusion coefficient in optical molasses. Hodapp et al. [8] and Truscott et al. [15] measured $D \sim 10^{-3}\,\mathrm{cm}^2/\mathrm{s}$ for Rb. Boiron et al. [16] studied diffusion in a disordered Cs lattice created by a speckle beam and found D as large as $D \sim 1.7\,\mathrm{cm}^2/\mathrm{s}$. So the value of D we are using for the fit is not inconsistent with existing data.

Comparing the calculated $t_{\max}$ with the measured value, we see that the experimental data agree with the calculation to a certain extent. For smaller q and the same D, the agreement with the measured peak time is not good. The observed shorter peak gain time is due to the expansion and acceleration of the atomic cloud. For $q = 450\,\mathrm{cm}^{-1}$ or smaller, (49) predicts a peak time of 1 ms or longer. However, the cloud has been accelerated into resonance at about 1 ms. Therefore, the peak we are seeing at small q is due to a combination of two effects and it occurs at an earlier time. This interpretation implies that, at small q, the atomic density grating never has time to fully form before the cloud disperses. It implies further that the measured gain curves, as a function of q, are shallower than they would be if the gratings at small q were fully formed.

The observed peaks in the probe transmission indicate probe beam gain. We consider two different kinds of gain. The first one is defined as the ratio of the peak probe transmission with the pump beam on, to that without pump, i.e., $T(\mathrm{pump\,on})/T(\mathrm{pump\,off})$, where the MOT is always on. The second one is the ratio of the peak probe transmission with MOT on, to that without the MOT, i.e., $T(\mathrm{MOT\,on})/T(\mathrm{MOT\,off})$, where the pump beam is always on. We also call the second one the absolute gain. In Fig. 10, we plot these two gains for various detunings, as functions of the transverse wave-number, together with numerical simulations using the experiment parameters. Both plots show that the measured gain strongly depends on the angle between beams and that the peak absolute gain is about 30–40%.

The discussion in Sect. 4 shows that, for frequency-degenerate beams, the radiation pressure force could shift the atomic density distribution with respect to the

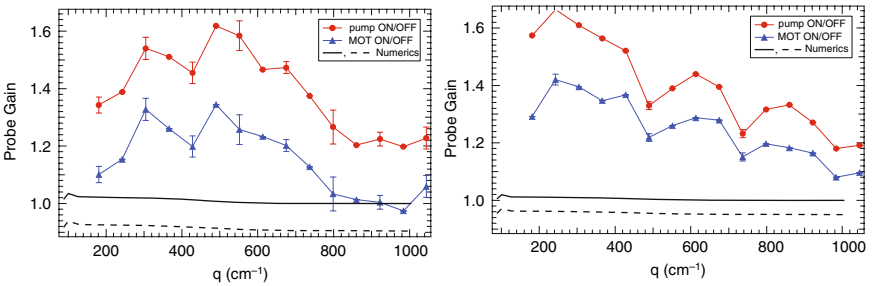

Fig. 10 Measured probe gain as a function of q for $\Delta = +5\gamma$ (left) and $\Delta = +7\gamma$ (right). The solid line is the numerical result using the experimental parameters without absorption, while the dashed line is for the case with absorption. MOT size is $2w_z = 1.3\,\text{cm}$, and $a_z = 0.25, b_z = 0.2, c_z = 0.09$. The peak atomic density is $n_{a0} = 1.0 \times 10^{10}\,\text{cm}^{-3}$. Peak intensities of the probe and pump beams are 5.56 and $55.6\,\text{mW/cm}^2$, respectively

optical field, thus introducing two-beam coupling gain. This gain was first observed by Guibal et al. [11]. However, (23) indicates that the two-beam coupling gain from the radiation force has no angular dependence. On the other hand, from Sect. 6, the MI gain is mainly due to the dipole force, and this gain depends strongly on the angle. Therefore, the angular dependence we observed in the experiment strongly suggests that it is due to modulation instability. Also shown in Fig. 10 are numerical results for the MI gain in the Cs MOT using the experimental parameters, assuming a cloud of fixed two-level atoms and ignoring the light-induced redistribution effect. The results show that, without the density redistribution effect, the MI growth rate is too low to see any amplification from the beam. The inclusion or omission of the absorption in the simulation only shifts the overall curve. The numerical results confirm that the density redistribution effect must be taken into account, in order to fully explain the experimental observations.

8 Conclusion

In conclusion, we have discussed a self-consistent model for the collective dynamics of light beams propagating in cold atomic vapors. Novel effects, including stable dissipative atom–optical solitons and modulational instability with a self-defocusing nonlinearity, are predicted. Experimental studies in a Cs MOT show two-wave mixing gain for frequency-degenerate pump and probe beams. The angular and temporal dependence of the gain is consistent with the presence of modulational instability. Additional studies [17] show that spatial structures with long-range correlations and atomic patterns may form in models with feedback. Experimental observation of these effects will require cold atomic clouds with large optical depth.

References

1. M. Saffman, Self-induced dipole force and filamentation instability of a matter wave, Phys. Rev. Lett. **81**, 65 (1998). 362
2. M. Saffman and D.V. Skryabin, Coupled propagation of light and matter waves: solitons and transverse instabilities, in *Spatial Solitons*, edited by S. Trillo and W.E. Torruellas, (Springer, Berlin, 2001). 362
3. A.P. Kazantsev, G.I. Surdutovich, and V.P. Yakovlev, *Mechanical Action of Light on Atoms*, (World Scientific, Singapore, 1990). 362
4. Akhmediev, N., Ankiewicz A. (eds.): *Dissipative Solitons*, Lect. Notes Phys. **661**. Springer, Berlin (2005) 362, 367
5. H.J. Metcalf and P. van der Straten, *Laser Cooling and Trapping*, (Springer, New York, 1999). 362
6. G. Grynberg and C. Robilliard, Cold atoms in dissipative optical lattices, Phys. Rep. **355**, 335 (2001). 363, 364
7. K.M. O'Hara, S.R. Granade, M.E. Gehm, and J.E. Thomas, Loading dynamics of CO_2 laser traps, Phys. Rev. A **63**, 043403 (2001). 364
8. T.W. Hodapp, C. Gerz, C. Furtlehner, C.I. Westbrook, W.D. Phillips, and J. Dalibard, Three-dimensional spatial diffusion in optical molasses, Appl. Phys. B **60**, 135 (1995). 364, 378
9. S. Gatz and J. Herrmann, Soliton propagation in materials with saturable nonlinearity, J. Opt. Soc. Am. B **8**, 2296 (1991). 365
10. Yu.L. Klimontovich and S.N. Luzgin, Possibility of combined self-focusing of atomic and light beams, Pis'ma Zh. Eksp. Teor. Fiz. **30**, 645 [JETP Lett. **30**, 610] (1979). The condition given for mutual focusing differs by a factor of 2 from our eq. (13). 366
11. S. Guibal, C. Mennerat-Robilliard, D. Larousserie, C. Triché, J.-Y. Courtois, and G. Grynberg, Radiation pressure in a rubidium optical lattice: An atomic analog to the photorefractive effect Phys. Rev. Lett. **78**, 4709 (1997). 370, 379
12. M. Saffman, G. McCarthy, and W. Królikowski, Two-dimensional modulational instability in photorefractive media, J. Opt. B: Quantum Semiclass. Opt. **6**, S397 (2004). 373
13. Y. Wang and M. Saffman, Experimental study of nonlinear focusing in a magneto-optical trap using a Z-scan technique, Phys. Rev. A **70**, 013801 (2004). 376, 377
14. Y. Wang, Nonlinear self-focusing in cold Cesium atoms, Ph.D. thesis University of Wisconsin (2005). 376
15. A.G. Truscott, D. Baleva, N.R. Heckenberg, and H. Rubinsztein-Dunlop, Short-term spatial diffusion in $\sigma^+ - \sigma-$ optical molasses, Opt. Commun. **145**, 81 (1998). 378
16. D. Boiron, C. Mennerat-Robilliard, J.-M. Fournier, L. Guidoni, C. Salomon, and G. Grynberg, Trapping and cooling cesium atoms in a speckle field, Eur. Phys. J. D **7**, 373 (1999). 378
17. G.A. Muradyan, Y. Wang, W. Williams, and M. Saffman, Absolute instability and pattern formation in cold atomic vapors, in 2005 *Nonlinear Guided Waves Topical Meeting Technical Digest, paper ThB29*, (Dresden, Germany, September, 2005). 379

On Vegetation Clustering, Localized Bare Soil Spots and Fairy Circles

M. Tlidi, R. Lefever, and A. Vladimirov

Abstract We present a model and nonlinear analysis which account for the clustering behaviors of arid vegetation ecosystems, the formation of localized bare soil spots (sometimes also called *fairy circles*) in these systems and the attractive or repulsive interactions governing their spatio-temporal evolution. Numerical solutions of the model closely agree with analytical predictions.

1 Introduction

It is common in semi-arid or arid regions to encounter landscapes where the vegetation cover is non-uniform and exhibits large-scale structures, generically called "vegetation patterns" [1, 2]. The terms "semi-arid" and "arid" refer here to climatic conditions where water resources are scarce. More precisely, they mean that the potential evapo-transpiration largely exceeds the water supply provided by rainfall. At the individual plant level, this hydric stress affects plants' growth and survival; at the community level, it generates clustering effects that cause the formation of vegetation patches. The outcome is a spatial "differentiation" of the landscape into a "mosaic" of poorly vegetated and strongly vegetated domains, accompanied by a redistribution of the ecosystem water resources benefiting the vegetated domains.

M. Tlidi
Université Libre de Bruxelles, Optique Nonlinéare Théorique, CP 231, Campus de la Plaine, B-1050 Bruxelles, Belgium, mtlidi@ulb.ac.be

R. Lefever
Université Libre de Bruxelles, Service de Chimie Physique et Biologie Théorique, CP 231, Campus de la Plaine, B-1050 Bruxelles, Belgium, rlefever@ulb.ac.be

A. Vladimirov
Weierstrass Institute for Applied Analysis and Stochastics, Mohrenstrasse 39, D-10117 Berlin, Germany, vladimir@wias-berlin.de

Tlidi, M. et al.: *On Vegetation Clustering, Localized Bare Soil Spots and Fairy Circles.* Lect. Notes Phys. **751**, 381–402 (2008)
DOI 10.1007/978-3-540-78217-9_15

It is now generally admitted that this adaptation to hydric stress involves a symmetry-breaking modulational instability, whose causes are intrinsic rather than extrinsic, to the vegetation, i.e., they result from the vegetation dynamics itself, rather than from the imposition on this dynamics of some external (environmental), pre-existing spatial periodicity or anisotropy [3, 4, 5, 6, 7, 8, 9, 10, 11, 12]. Well-known patterns of this type are the banded, periodic vegetation covers, often labeled with the picturesque name of *tiger bush*, which can be observed in many arid regions on the earth. The intrinsic, self-organizing mechanism mentioned above provides a unified explanation for the diverse phenotypical characteristics displayed by vegetation patterns. In particular, it predicts the properties of periodic patterns and the sequence of symmetry-breaking transitions, which such patterns undergo as a function of aridity. For example, it accounts for the observation that the size (wavelength) of the heterogeneities increases with the degree of aridity, while, simultaneously, the symmetry of the patterns transforms from π-hexagonal into stripes and, finally, into 0-hexagonal [3, 6, 13]. Remarkably, besides the behavior of periodic patterns, the same mechanism predicts the possible existence of aperiodic, localized structures (sometimes called dissipative solitons). They consist either of localized patches of vegetation, randomly distributed on bare soil [14, 15] or, on the contrary, of localized spots of bare soil (LBS), randomly distributed in an otherwise uniform vegetation cover.

In this chapter, we shall focus our attention on LBS-type patterns. Well-documented examples are the so-called woodland glades, a label referring to isolated, open spaces of herbaceous vegetation (sometimes even of bare ground) surrounded by woody vegetation. Woodland glades are permanent structures, and they can be observed worldwide, even in non-arid climates. They may support particular plants, and they are zones of attraction for various animal species which are adapted to woodland and which take advantage of these sunny and dry open areas. Understanding their formation and maintenance is an important ecological issue. Other fascinating, puzzling and well-documented examples of LBS patterns are the *fairy circles* or *fairy rings* discovered in the Namib desert (see Fig. 1). These circular areas, devoid of any vegetation, can reach diameters of up to 14 m. This exceeds the size of the tall grasses surrounding them by more than one order of magnitude. In a recent study, van Rooyen et al. [16] have made an in-depth investigation of the strengths and shortcomings of several hypotheses concerning their origin. These authors have been able to rule out external causes, such as the possible existence of localized radioactive areas unsuited for the development of plants, or a link between fairy circles and the activity of termites. Among the other hypotheses they considered (notably, the release of allelopathic compounds and the possible existence of stimulatory or inhibitory influences due to interactions between different plant species), none was found which satisfactorily fitted their experimental observations. Our objective, in regard to this context, is to investigate the generic properties and evolving behaviors which can be predicted for LBS patterns on the basis of the conceptual framework and treatment developed previously for the study of periodic vegetation patterns.

Fig. 1 Example of the *fairy circles* occurring in the pro-Namib zone of the west coast of southern Africa [16] (photography: courtesy of M. Johnny Vergeer)

The starting point of our approach is a modified version of the integro-differential propagator–inhibitor model (PI model) originally introduced to explain the formation of tiger bushes [3]. The basic hypotheses of the PI model are summarized in Sect. 2. The modifications introduced in its present version have the objectives (i) to formulate more precisely the relationship between the plants' aerial–subterranean structures and the facilitative or competitive feedbacks which influence their dynamics at the community level; and (ii) to incorporate into the model an explicit formulation of the plants' spatial propagation (e.g., by seed dispersion), so that the interrelations between the "transport" phenomena taking place in the ecosystem and the growth/decay dynamics of its constitutive vegetation are accounted for in a better manner. In Sect. 3, we derive, from the original integro-differential equation describing the dynamics in general, a nonlinear fourth-order partial differential equation which constitutes a convenient, appropriate approximation in the weak-gradient limit, where the size of spatial heterogeneities at the community level greatly exceeds the size of individual plants. The conditions under which vegetation clustering and localized bare spots appear are discussed in Sects. 4 and 5. The homoclinic solutions modeling LBS patterns are then evaluated analytically. To begin with, the case of localized, isolated single spots is treated; the solutions representative of this situation are constructed, and their properties are discussed and compared with the results of numerical solutions. In Sect. 6, the situation where bare spots are close enough to interact is studied. This question, which is of considerable interest, has been investigated in other contexts [17, 18, 19, 20, 21, 22, 23, 24]. We demonstrate here that such interactions induce the appearance of a "force" between LBS, which may be attractive or repulsive, depending on the distance separating the interacting spots. These results are established analytically and confirmed by numerical simulations.

2 Mean-Field Model of Vegetation Evolution

Let us consider a plant community established on a spatially uniform territory, and suppose that a dominant species accounts for most of the community bio-mass. Let L_a be the radial extension of a mature individual belonging to this species, $S = \pi L_a^2$ be a territorial surface element centered on a given spatial point, $\mathbf{r}$, and m_{max} be the maximal amount of bio-mass that the community could produce on the surface element S in the absence of vegetation decay. We imagine that we redistribute the bio-mass $m_p(\mathbf{r},t)$ contained in S uniformly over it, then we define the normalized bio-mass at the point $\mathbf{r}$ for time t as $b(\mathbf{r},t) = m_p(\mathbf{r},t)/m_{max}$ and model its spatio-temporal evolution by the logistic equation

$$\begin{aligned}\partial_t b(\mathbf{r},t) = \; & k_1\, b(\mathbf{r},t) - k_2\, b(\mathbf{r},t) \\ & + D \int \left[\Phi_{in}(|\mathbf{r}'|)\, b(\mathbf{r}+\mathbf{r}',t) - \Phi_{out}(|\mathbf{r}'|)\, b(\mathbf{r},t)\right] \mathrm{d}\mathbf{r}', \end{aligned} \tag{1}$$

where the unit of time has been set equal to the characteristic time of the growth process. The first two terms in (1) account for the bio-mass gains and losses that the surface element S undergoes due to the natural growth and decay of the plants. The third term accounts for the vegetation spatial propagation via seed dispersion and/or other natural mechanisms. The integration extends over the whole of the territory, which we suppose to be infinitely extended, and Φ_{in} and Φ_{out} are the dispersion kernels weighting the incoming and outgoing seed fluxes between neighboring points, according to their separation, $|\mathbf{r}'|$. Further, D is a phenomenological constant which fixes the rate of propagation of the vegetation, while k_1 and k_2 are kinetic coefficients which take into account the plant-to-plant feedback effects resulting from the communal organization of the vegetation. As such, we suppose that they are mean-field state functions which can be written as:

$$k_1 = [1 - b(\mathbf{r},t)]\, \mathscr{M}_f(b(\mathbf{r},t),t), \qquad k_2 = \mu\, \mathscr{M}_c(\mathbf{r},t). \tag{2}$$

The phenomenological constant, μ, is the decay to growth rate ratio in the absence of interactions, i.e., under conditions where the vegetation spatio-temporal dynamics is reduced to that obeyed by isolated plants, while $\mathscr{M}_f(\mathbf{r},t)$ and $\mathscr{M}_c(\mathbf{r},t)$ are mean-field factors describing plant-to-plant interactions. By definition, these factors are equal to 1 in the case of isolated (or non-interacting) plants, and greater than one when interactions cannot be neglected. In other words, they enhance the rate of the processes which they influence, and therefore we call them the *mean-field enhancing factors*. $\mathscr{M}_f(\mathbf{r},t)$ describes interactions facilitating growth.[1] They are associated with the plants' aerial structures and involve, notably, a reciprocal sheltering of neighboring plants against climatic harshness, as well as a communally more favorable management of vital resources. They extend over distances of the order

[1] As well as seed production and germination [26].

of L_a (e.g., the crown radius of mature trees). On the other hand, $\mathscr{M}_c(\mathbf{r},\mathbf{t})$ is associated with competitive plant-to-plant interactions enhancing vegetation decay. They predominantly involve the plants' roots system, or rhizosphere. Accordingly, they operate over distances of the order of the rhizosphere radius, L_r. Their competitive nature results from the fact that the rhizosphere activity of a plant tends to deprive its neighbors of vital resources, e.g., water [25]. The logistic factor, $\left[1-b(\mathbf{r},t)\right]$, of the kinetic constant k_1 accounts for the existence of an upper limit, $m_{\max}$, which the bio-mass of a surface element, S, cannot exceed. The latter is specific to the vegetation.

The following considerations then determine the choice of the mathematical expressions of the rate-enhancing factors:

(i) By definition, $\mathscr{M}_f(\mathbf{r},t)$ and $\mathscr{M}_c(\mathbf{r},t)$ are increasing, functions of the vegetation density. They take values in the interval $[1,\infty$, and they are equal to 1 in the zero-density limit,

$$\lim_{\rho(\mathbf{r}+\mathbf{r}',t)\to 0} \mathscr{M}_\iota(\mathbf{r},t)=1, \quad \iota=f,c, \tag{3}$$

where the dynamics of isolated plants must be recovered.

(ii) To fulfill condition (i), we postulate that the rate-enhancing factors depend exponentially upon the vegetation density, with the following form:

$$\mathscr{M}_\iota(\mathbf{r},t)=\exp\left(\chi_\iota \int \Phi_\iota\left(|\mathbf{r}'|,L_\iota\right) b(\mathbf{r}+\mathbf{r}',t)\,\mathrm{d}\mathbf{r}'\right), \quad \iota=f,c, \tag{4}$$

i.e., they are exponential functions of the mean-field integral of the normalized vegetation density, $b(\mathbf{r}+\mathbf{r}',t)$, weighted by the kernels, Φ_f and Φ_c, which describe the spatial extension of feedback effects in terms of the characteristic ranges L_f and L_c over which facilitative and competitive interactions operate. The positive parameters χ_f and χ_c, which fix the strength of the interactions, may be influenced by extrinsic factors such as the degree of environmental aridity.

(iii) Our aim is to study the localized structures having the generic characteristic that they appear at the start to be a uniform density vegetation cover, or, more exactly, uniform stationary state solutions of (1) for which $b(\mathbf{r},t)=b$ is a finite, positive constant, excluding the neighborhood of the value zero. In this respect, we may, for simplicity, consider that L_f and L_c are constants, [2] and set $L_f\equiv L_f^0=L_a$ and $L_c\equiv L_c^0=L_r$. If we furthermore specify, in agreement with conditions (i)

[2] Clearly, L_f and L_c depend on the stage of development of the vegetation: mature plants, obviously, affect a greater territory than young seedlings. This feature plays an important role in phyto-societal behaviors which generically appear only at low average vegetation densities, i.e., in the neighborhood of $b=0$. The method consisting to link the development of the vegetation to its density by assuming that $L=L^0 b(\mathbf{r}+\mathbf{r}',t)^p$, where L^0 is a constant and p is an allometric exponent, constitutes a straightforward ansatz for handling such situation. Vegetation patterns consisting of vegetation patches distributed on bare soil can clearly be expected to be of this type. We shall report on them elsewhere [26].

and (ii), that the interactions obey a gaussian, isotropic distribution law,[3] then we obtain the following expressions (see Fig. 2) for the kernels $\Phi_{\rm f}$ and $\Phi_{\rm c}$:

$$\Phi_\iota(|\mathbf{r}'|) = \mathscr{N}_\iota \exp\left[-\frac{|\mathbf{r}'|^2}{L_\iota^0}\right], \quad \text{with} \quad \iota = f, c, \quad L_{\rm f}^0 = L_{\rm a}, L_{\rm c}^0 = L_{\rm r}. \tag{5}$$

The normalization condition

$$\mathscr{N}_\iota = \frac{1}{\pi}\int \exp\left(-\frac{|\mathbf{r}|^2}{L_\iota^0}\right)\mathrm{d}\mathbf{r} \tag{6}$$

must be imposed so that bulk behaviors, e.g., the uniform stationary solutions of (1), are independent of the interaction ranges in the case of spatially isotropic environments, as expected on physical grounds.

Setting the unit of length to be equal to the crown radius, $L_{\rm a}$, assuming that dispersion obeys a gaussian law, denoting the corresponding dispersion range of seeds (gaussian variance) by $L_{\rm d}$ and replacing (2),(3),(4),(5) and (6) in (1), the mean-field evolution equation of the vegetation finally reads

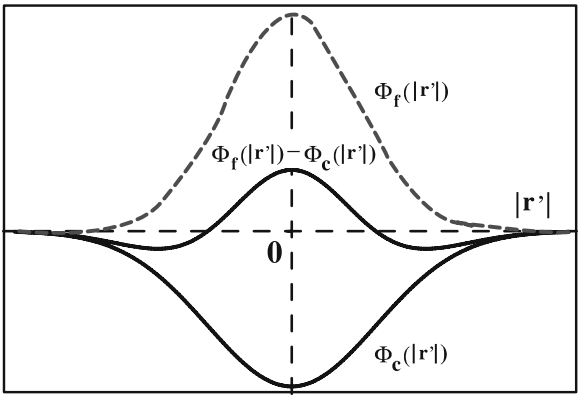

Fig. 2 Sketch of the facilitative and competitive mean-field kernels $\Phi_{\rm f}$ and $\Phi_{\rm c}$, as given by (5). Clearly, at short distances, $|\mathbf{r}'|$, the difference $\Lambda = \Phi_{\rm f} - \Phi_{\rm c}$, which represents the effective mean-field generated by the interactions, is facilitative (positive values) while at great distances, it is competitive (negative values). The unit of length is equal to the canopy radius, $L_{\rm a} = 1$

[3] From a qualitative point of view, this gaussian choice is convenient and implies no loss of generality. Other expressions for the kernels, $\Phi_{\rm f}$ and $\Phi_{\rm c}$, quantitatively describing specific vegetation systems, will be considered elsewhere [26]. Anyway, we are not interested here in the influence of external anisotropies. Hence, we have the choice of isotropic kernels, i.e., those that have no angular dependency and are only functions of the distance between points. For investigations devoted to the role of spatial anisotropies, see [3, 27, 28].

$$\partial_t b(\mathbf{r},t) = b(\mathbf{r},t)\,[1-b(\mathbf{r},t)]\exp\left(\frac{\chi_f}{\pi}\int \mathrm{e}^{-|\mathbf{r}'|^2}\,b(\mathbf{r}+\mathbf{r}',t)\,\mathrm{d}\mathbf{r}'\right)$$
$$-\mu\,b(\mathbf{r},t)\exp\left(\varepsilon\,\frac{\chi_c}{\pi}\int \mathrm{e}^{-\varepsilon\,|\mathbf{r}'|^2}\,b(\mathbf{r}+\mathbf{r}',t)\,\mathrm{d}\mathbf{r}'\right)$$
$$+\frac{\sigma D}{\pi}\int \mathrm{e}^{\sigma\,|\mathbf{r}'|^2}\,\left[b(\mathbf{r}+\mathbf{r}',t)-b(\mathbf{r},t)\right]\,\mathrm{d}\mathbf{r}', \tag{7}$$

where the parameters

$$\varepsilon = \left(\frac{L_a}{L_r}\right)^2 \quad \text{and} \quad \sigma = \left(\frac{L_a}{L_d}\right)^2, \tag{8}$$

specify the *structural ratio* and *dispersivity* of the vegetation considered.

In order to investigate the spatio-temporal dynamics predicted by the integro-differential (7), it is convenient to work with a partial differential equation approximation of it. The latter is derived in the next section.

3 Weak-Gradient Approximation

We look for an approximation to (7), in the form of a partial differential equation, in the limit where, according to linear stability theory, (i) unstable fluctuations are of much greater wavelength than the crown size, L_a, (ii) their growth rate is small, and (iii) nonlinearities remain weak. Generically, requiring (i) and (ii) means that we are interested in the system's dynamics near a transition point where fluctuations corresponding to the zero-Fourier mode become unstable, i.e., fluctuations of very large wavelength are stable but are nearly marginal (in the weak-gradient approximation). Requiring (iii) means that we look for conditions such that this transition point occurs at uniform vegetation densities, b, thus satisfying the inequalities $0 < b << 1$. Hence, let us first determine the uniform stationary states of (7) and their stability properties. It is easily found that the latter, given by the solutions of

$$\mu = b\,(1-b)\exp\,(\Lambda\,b)\,, \tag{9}$$

depends on only two parameters. The *switching parameter* μ (defined in (2)) controls the stability of the trivial uniform solution, $b = b_0 = 0$, corresponding to bare soil without vegetation: b_0 is unstable for $0 \le \mu < 1$ and stable for $\mu \ge 1$. The second parameter in (9) is the *feedback balance* resulting from the difference between the strengths of facilitative and competitive feedbacks:

$$\Lambda = \chi_f - \chi_c. \tag{10}$$

It controls whether the population behaves co-operatively ($\Lambda > 0$) or not ($\Lambda < 0$). At the "neutral feedback point", $\Lambda = 0$, facilitative and competitive effects balance each other exactly – the non-trivial uniform stationary state solution of (3),

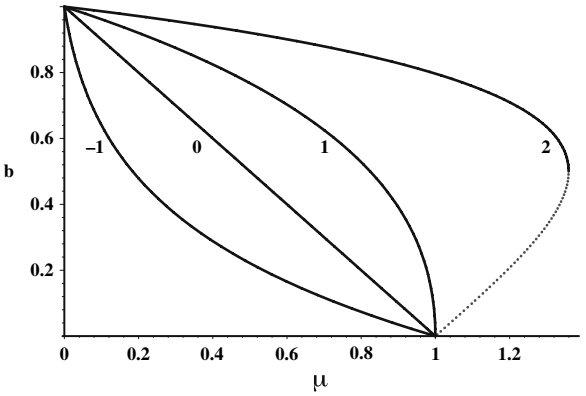

Fig. 3 Uniform stationary states solutions of (9) as a function of the switching parameter, μ, with increasing values of the feedback balance, Λ. For $\Lambda > 1$, the system exhibits a saddle-node transition point, whose co-ordinates are given by (11)

$b = b_s = 1 - \mu$, is then identical to that of a community in which plants do not interact, *i.e.*, one with $\chi_f = \chi_c = 0$. For $\Lambda > 1$ and $1 \leq \mu \leq \exp(\Lambda - 1)/\Lambda$, (9) admits three non-negative solutions, b_0, b_-, b_+ (see Fig. 3). The uniform state, b_-, is always unstable. On the other hand, b_0 and b_+ are stable with respect to small perturbations which do not break the system spatial uniformity. Remarkably, when the feedback balance, Λ, is strongly co-operative, i.e., for $\Lambda >> 1$, the domain of existence of the vegetation, represented by the b_+ branch of stationary states, extends up to the saddle-node transition point of co-ordinates

$$b^* = \frac{\Lambda - 1}{\Lambda}, \qquad \mu^* = \frac{\exp(\Lambda - 1)}{\Lambda}, \tag{11}$$

i.e., far beyond the switching point, $\mu = 1$, where the trivial state, b_0, changes stability. In light of the requirements (i) – (iii) mentioned earlier, we now explore the system dynamics in the neighborhood of the feedback balance value $\Lambda = 1$. Hence, we set

$$b(\mathbf{r}, t) = \zeta\, u(\mathbf{r}, t), \quad \Lambda = 1 + \zeta\, \Lambda_1, \quad \mu = 1 + \zeta^2 \mu_2, \tag{12}$$

where ζ is a "smallness" parameter, and we renormalize the time and space scales by the transformation:

$$t = \frac{2\tilde{t}}{\zeta^2}, \quad |\mathbf{r}| = \frac{|\tilde{\mathbf{r}}|}{k_0}, \tag{13}$$

where k_0 is the non-zero, positive modulus of the first Fourier wave vector which becomes (linearly) unstable in the neighborhood of the saddle-node point. (For simplicity of notation, the tilde will later be dropped.) We require $k_0 << 1$, i.e., that it corresponds to spatial heterogeneities of much greater size than L_a. The linear stability analysis of (7) shows that, in order to satisfy this condition and to obtain real, positive values for k_0, the strength of competitive feedbacks, χ_c, and the dispersion coefficient, D, must scale with respect to ζ as:

$$\chi_c = \frac{\varepsilon}{1-\varepsilon} + \sqrt{\zeta}\,\chi_1, \quad D = \zeta^{3/2}\,\frac{\delta}{\sigma}. \tag{14}$$

To the dominant order in ζ, this yields

$$k_0 = q\,\zeta^{1/4}, \quad \text{with} \quad q = 2\sqrt{\varepsilon\left(\chi_1 - 2\frac{\delta}{u_+}\right)}, \tag{15}$$

where

$$u_+ = \Lambda_1 + \sqrt{\Lambda_1^2 - 2\mu_2} \tag{16}$$

is the dominant term in the expansion $b_+ = \zeta\,u_+ + \mathcal{O}(\zeta^2)$ of the branch of stationary states, b_+, in terms of ζ.

We use (10) to eliminate χ_f, expand $b(\mathbf{r}+\mathbf{r}',t) = \zeta\,u(\mathbf{r}+\mathbf{r}',t) + \mathcal{O}(\zeta^2)$ in a Taylor series around the focal point $\mathbf{r}$, substitute (12), (13), (14), and (15) into (7) and expand the resulting equation in terms of ζ, up to $\mathcal{O}(\zeta^3)$. This yields the desired partial differential evolution equation, with $u(\mathbf{r},t)$ as new state variable:

$$\begin{aligned}\partial_t u(\mathbf{r},t) = \; & -u(\mathbf{r},t)\left[2\mu_2 - 2\Lambda_1\,u(\mathbf{r},t) + u(\mathbf{r},t)^2\right] \\ & + \left[q\,\delta - \frac{q\chi_1}{2}\,u(\mathbf{r},t)\right]\nabla^2 u(\mathbf{r},t) - \frac{q^2}{16\varepsilon}\,u(\mathbf{r},t)\,\nabla^4 u(\mathbf{r},t) \\ & + \mathcal{O}(\zeta^{7/2}).\end{aligned} \tag{17}$$

In order to put (17) into a more compact form, let us define

$$\eta = 2\mu_2 \quad \kappa = 2\Lambda_1, \quad \Delta = q\,\delta, \quad \Gamma = \frac{q\chi_1}{2}, \quad \alpha = \frac{q^2}{16\varepsilon}. \tag{18}$$

Rewritten in terms of these parameters, (17) becomes

$$\begin{aligned}\partial_t\,u(\mathbf{r},t) = \; & -u(\mathbf{r},t)\left[\eta - \kappa u(\mathbf{r},t) + u(\mathbf{r},t)^2\right] \\ & + \left[\Delta - \Gamma u(\mathbf{r},t)\right]\nabla^2 u(\mathbf{r},t) - \alpha u(\mathbf{r},t)\nabla^4 u(\mathbf{r},t),\end{aligned} \tag{19}$$

while the stationary solutions, representing uniform vegetation covers, are now given by

$$u_0 = 0, \quad u_\pm = \left[\kappa \pm \sqrt{\kappa^2 - 4\,\eta}\right]/2. \tag{20}$$

To be physically acceptable, $u_\pm$ must be real and non-negative. Two situations must be distinguished, according to the sign of κ. When $\kappa < 0$, the co-ordinates of the saddle-node point are unphysical. Besides u_0, u_+ is then the only acceptable uniform stationary state solution. It exists only if $\eta < 0$ and is a monotonically decreasing function of η which vanishes for $\eta = 0$. When $\kappa > 0$, the co-ordinates of the saddle-node point, given by

$$u^* = \kappa/2, \quad \eta^* = \kappa^2/4, \tag{21}$$

are physically acceptable. Accordingly, for $0 < \eta < \eta^*$, the bio-mass density exhibits a phenomenon of bistability, so that u_0 and u_+, which are linearly stable with respect to uniform fluctuations, as well as the intermediate unstable branch, u_-, are then, simultaneously, acceptable uniform solutions of (19). In the following, we shall focus on the parameter regime where the uniform plant distribution exhibits bistability ($\kappa > 0$), and assume that the inequalities ($\eta_m < \eta < \eta^*$) hold. In that case, all uniform stationary states belonging to u_+ have a finite, non-negative value. This is required, given the simplification made earlier that L_f and L_c are constants, independent of the vegetation density (cf. assumption (iii) in 2).

4 Clustering and Periodic Vegetation Patterns

Inspection of (19) suggests that the u_+ stationary states may become unstable if subjected to random, non-uniform fluctuations. Indeed, when $\Delta/\Gamma = 2\delta/\chi_1 < u_+$, the "diffusion" coefficient in front of the Laplacian is negative, indicating that vegetation clustering, i.e., the "phase separation" of vegetation and bare soil, becomes possible [29, 30]. This phenomenon is physically comparable with the behavior of immiscible mixtures, e.g., the separation of oil and water. It corresponds, in the linear stability analysis of (19), to the appearance of a finite band of unstable Fourier modes. Its upper cutoff is due to the "line tension" coefficient of the bi-Laplacian term, which is always stabilizing (for short distances, dispersion is always an efficient mixing mechanism), while its lower cutoff owes its existence to the stability of the zero-Fourier mode. (By definition, all u_+ stationary states are stable with respect to uniform fluctuations.) Under these conditions, the intrinsic instability due to the negative diffusion coefficient is modulational – random noise triggers the appearance of spatially periodic patterns which spread over the whole territory. The wavelength of the first non-zero-Fourier mode to become unstable is

$$\lambda_m = 2\pi\sqrt{\frac{2\alpha}{\Gamma/\alpha - \Delta/u_m}}, \tag{22}$$

where u_m, given by the largest real positive solutions of the cubic polynomial

$$(2\Gamma u_m - \Delta)^2 = 4\alpha u_m^2(2u_m - \alpha), \tag{23}$$

is the threshold state at which the modulational instability appears on the u_+ branch of solutions for $\eta = \eta_m$ (see Fig. 4). When the aridity parameter, η, increases, the structures that appear first (sub-critically) are the so-called hexagons, H0. They consist of a periodic pattern, of hexagonal symmetry, made up of sparse vegetation spots. Upon a further increases in η, this pattern becomes unstable and the system evolves toward patterns consisting of bands or stripes; the latter properties are in good agreement with observations relating to tiger bush patterns. Increasing aridity still further destabilizes these banded patterns and transforms them into

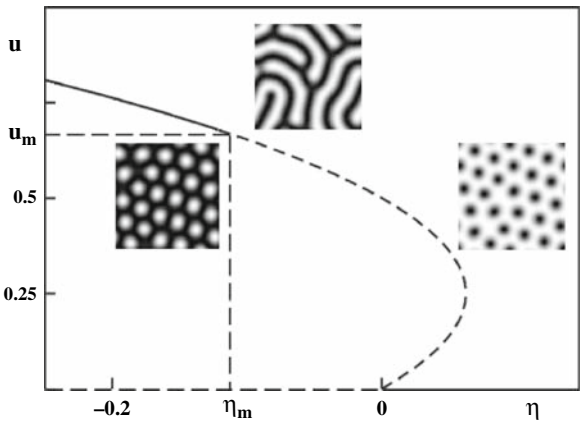

Fig. 4 Uniform stationary bio-mass density as a function of the aridity parameter η, for $\kappa = 0.5$, $\Delta = 0.1$, $\Gamma = 0.5$ and $\alpha = 0.25$. *Broken lines* correspond to unstable states. As η increases, at the bifurcation point (η_m, u_m), the uniform branch of stationary states, u_+, becomes unstable with respect to infinitesimal fluctuations whose wavelength is given by (22). In the neighborhood of this point, sub-critical periodic vegetation patterns which are made up of spots of sparser vegetation can be found. Super-critically, they transform into stripes, and finally into periodic patterns consisting of vegetation spots separated by bare ground. The three different kinds of patterns represented have been obtained for $\eta = -0.25$, 0.1 and 0.2, respectively. The grid is 128×128 points. Black corresponds to the highest values of the bio-mass density. Minima are plain white. Periodic boundary conditions are used in both spatial co-ordinates

hexagonal Hπ patterns which correspond to periodic distributions of vegetation spots surrounded by bare ground. These three types of 2D periodic structures are represented in Fig. 4. They have been obtained by numerically integrating (19) on a square-shaped domain with periodic boundary conditions. The initial condition used to generate these structures consists of the unstable uniform stationary solution, perturbed by noise of small amplitude. Reversing the variation of the aridity parameter shows that there exist two hysteresis loops involving striped, H0 and Hπ patterns (not represented). Published works giving nonlinear analyses [13, 31] allow for detailed calculation of the bifurcation diagrams of such periodic vegetation patterns.

5 Pinning and Localized Bare Soil Spots

Localized vegetation patterns have been described in various arid regions, notably in Africa. So far, however, they have attracted little attention, both from experimental and theoretical points of view. Such patterns are "spatially localized", in the sense that they are elemental structures (vegetation patches or holes in the vegetation cover) which have a well-defined size and which seem to be quite stable. However, in contrast to periodic patterns, they apparently have little or no tendency

to spread and to invade the whole territory accessible to them. Characteristically, they are found as isolated elements, or in the form of groups which gather a small number of elements, more or less closely. The fairy circles illustrated in Fig. 1 are striking examples belonging to this category of patterns.

On the theoretical side, spatial localization is a patterning phenomenon better known in contexts of a physico-chemical rather than biological nature. It is established that various, quite distinct, non-equilibrium reaction-diffusion systems and nonlinear optical devices, which have the common property that they exhibit modulational instability, also display pinning phenomena which generate so-called *localized structures* (LS) [32, 33, 34, 35, 36, 37, 38, 39, 40, 41]. In all these systems, the conditions under which periodic patterns and localized structures appear are closely related – dynamically speaking, in all cases, a sub-critical modulational instability underlies the pinning phenomena responsible for the appearance of localized patterns. In this section, (i) we show that the dynamics described by (19) gives rise to such pinning phenomena and, as a consequence, may account for the formation of the localized bare spots (LBS) observed, e.g., the case of fairy circles; and (ii) we present a treatment which allows us to analytically evaluate the elemental solutions of (19) corresponding to an isolated bare soil spot immersed in an otherwise uniform vegetation cover.

Mathematically, stable localized structures are homoclinic solutions (solitary waves or stationary pulses) which belong to the sub-critical domain where a uniform branch of stationary state solutions and a branch of spatially periodic solutions are both linearly stable [34]. In parameter space, this situation corresponds to the existence of a hysteresis loop. Within it, there generally exists a so-called pinning range of parameter values for which stable localized structures, connecting the uniform and the periodic solutions, can be found. Their stability is attributed to the absence of a variational principle, i.e., to the non-existence of a Lyapunov functional guaranteeing that evolution proceeds toward the state for which the functional has the smallest possible value which is compatible with the system boundary conditions. The Swift–Hohenberg equation, for example, is a paradigmatic evolution equation which admits localized structures of this kind.[4] Clearly, the presence of the nonlinear diffusion terms, $u\nabla^2 u$ and $u\nabla^4 u$, render (19) non-variational.

Figure 5 shows some examples of localized structures obtained by numerically solving (19) for given, fixed values of the control parameters. Because of the homoclinic nature of these solutions, the number, as well as the spatial location, of the bare spots immersed in the bulk of the linearly stable uniform reference state depends on the initial condition considered. A single, isolated stationary bare spot is shown in Fig. 5(a). The spatial profile of the bio-mass density surrounding the central bare spot exhibits a decaying spatial oscillation which produces the concentric rings seen in the Fig. 5 (see also Fig. 7). This oscillatory tail connects the uniformly vegetated state to the central spot of sparser vegetation. To a first approximation, its characteristics (wavelength and maximal amplitude) are those ofthe periodic solution

[4] It is noteworthy that LS do not require a commutation process between distinct uniform stationary states [35].

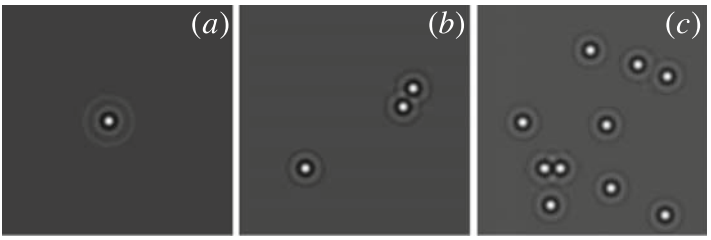

Fig. 5 Sample of localized bare spots surrounded by the uniformly vegetated state $u_s = (\kappa + \sqrt{\kappa^2 - 4\eta})/2$, obtained from numerical simulations of the model (19). Parameters are $\kappa = 0.5$, $\Delta = 0.1, \Gamma = 2\alpha = 0.5$ and $\eta = -0.025$. (**a**) Single bare spot, (**b**) three LBSs (**c**) random distribution of LBS. The grid is 256×256 points. Black corresponds to the highest values of the phyto-mass density. Minima are plain white. Periodic boundary conditions are used in both spatial co-ordinates

corresponding to the same parameter values. Figure 5(b) shows a pattern consisting of three localized bare spots, of which one is an isolated structure and two form a bound state. In Fig. 5(c), a pattern consisting of randomly distributed isolated and bound bare spots has been obtained.

Amplitude equations describing the space–time evolution of a slow unstable mode, derived in the framework of weakly–nonlinear regime, cannot describe localized structures. This approach does not take into account the non-adiabatic effects that involve the fast spatial scales which are responsible for the stabilization of LSs [33]. In recent years, considerable progress has been realized in the understanding of these structures. Analytical localized structures are relatively well understood in the 1D setting. The existence of localized structures in the Swift–Hohenberg model has been found by using functional analysis methods [42] and a dynamical system approach [43, 44, 45]. More recently, the computation of small and large spatial scales, by going beyond all orders of the usual multiple-scale expansion, allows us to construct the bifurcation diagram of localized structures [46]. However, analytical methods in 2D are still largely unexplored, and most of the results are obtained by numerical simulations.

A single stationary bare spot solution of (19) can be written in the form $u(r) = U(r) + u_+$, where $U(r)$ is the deviation from the uniform stationary state, u_+. The stability of the bare spot solution is determined by the spectrum of the linear operator L, defined by

$$L[U(r) + u_+] = L(u_+) + \mathscr{M}[u_+, U(r)]\,U(r),$$

with

$$L(u_+) = -\eta + 2\kappa u_+ - 3u_+^2 + (\Delta - \Gamma u_+)\nabla^2 - \alpha u_+ \nabla^4, \tag{24}$$

$$\mathscr{M}[u_+, U(r)] = (\kappa - 3u_+) - U(r) - \Gamma\nabla^2 - \alpha\nabla^4. \tag{25}$$

A single LBS is a radially symmetric solution, $u(x,y) = u(r)$, of (19). We can then replace the Laplacian operator by $\nabla^2 = \partial_{rr}^2 + (1/r)\partial_r$. We consider the following boundary conditions: $u|_{r=+\infty} = u_+$, $\partial_r u|_{r=0} = 0$, $\partial_r u|_{r=+\infty} = 0$ and $\partial_r^3 u|_{r=0} = 0$. The solution of the linear problem is

$$u(r) = u_+ + \Re\left\{A\exp(\mathrm{i}\theta)K_0[(\varpi + \mathrm{i}\omega)r]\right\}, \tag{26}$$

where

$$\varpi + \mathrm{i}\omega = \sqrt{-\xi_1 + \mathrm{i}\xi_2}, \tag{27}$$

with

$$\xi_1 = [(\Delta/u_+) - \Gamma)]\,/\,(2\alpha)\,, \quad \text{and} \quad \xi_2 = \sqrt{(3u_+^2 + \eta - 2\kappa u_+)/(\alpha u_+) - \xi_1^2}. \tag{28}$$

The Bessel function K_0 describes the decaying oscillations at large distance from the center of the bare spot. The bare spots are calculated in the following manner. First, we integrate (19) with $\partial_t u = 0$, from $r = 10^{-8}$ to $r_1 = 1$, using the initial conditions: $u(r)|_{r=r_0} = B$, $\partial_r^2 u|_{r=r_0} = C$ and $\partial_r u|_{r=r_0} = \partial_r^3 u|_{r=r_0} = 0$. Then we solve the (19) with $\partial_t u = 0$ from $r = r_1$ to $r = L$, with $L = 100$ for the initial condition of (26). The parameters A, B, C and θ are determined numerically by matching the solution obtained at $r = r_1$. The procedure of the calculation is the shooting method. This calculation allows us to draw the bifurcation diagram (see Fig. 6), where we plot the homogeneous steady state together with the minimum values of the bare spot. The spot branch of solutions emerges from the uniformly vegetated state, u_+, at the bifurcation point $(\eta_\mathrm{m}, u_\mathrm{m})$ associated with the modulational instability.

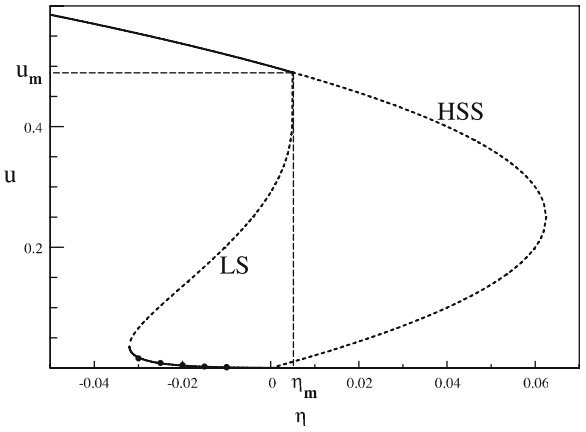

Fig. 6 Bifurcation diagram. The solid (*dotted*) line represents the stable (unstable) solutions. As the aridity parameter increases, the upper uniformly vegetated state (HSS) becomes unstable at the bifurcation point $(\mu_\mathrm{m}, u_\mathrm{m})$. From this instability point, a branch of localized bare spots (BLS) emerges sub-critically. Here $\kappa = 0.5$, $\Delta = 0.1$, $\Gamma = 2\alpha = 0.5$, and $\eta = -0.025$. The *black circles* indicate the minimum of LBS obtained from the numerical simulations of the model (19). The agreement between the two method is excellent

6 Attractive/Repulsive Interactions Between Bare Spots

We have seen that (19) admits bare spot solutions that either can be spatially independent, or, if they are close enough, can interact through their overlapping tails to form bound states. In this section, we study the properties of these bound states in the case of two LBSs interacting in 2D space. An analytical expression, in terms of integrals of Bessel functions, is derived for the interaction forces between two separate localized bare spots. The interaction will initiate motion of the LBSs until they reach a stable equilibrium position. We show that there exist several equilibrium positions and that the system selects one of these states, depending on the initial distance between the two localized spots. On the other hand, numerical simulations reveal that two localized bare spots may loose their stability under their mutual interaction, giving rise to a periodic distribution of bare spots forming an hexagonal lattice.

Figure 7 shows two situations which are representative of the behaviors which may be observed when two LBSs interact. In order to analyze them, let us first rewrite (19) as:

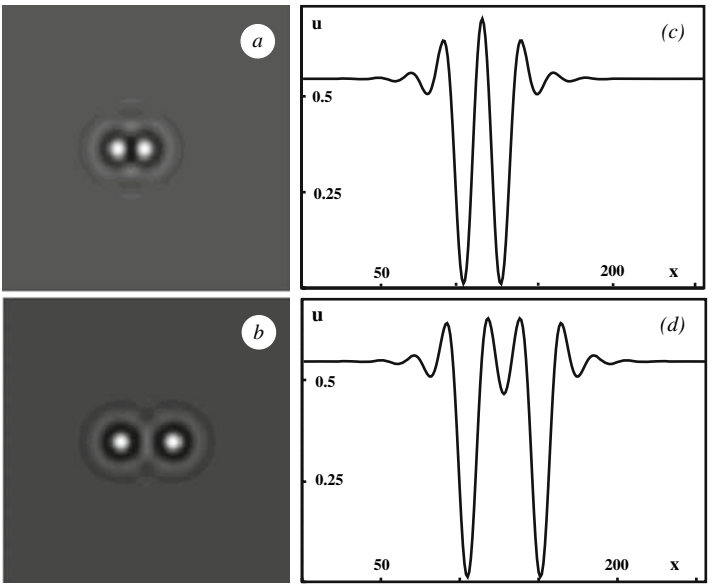

Fig. 7 Interaction between two LBSs. (**a**) and (**b**) are obtained for the same values of parameters. They differ only in the initial distance between the LBSs. (**c**) and (**d**) are, respectively, the cross-sections taken from (**a**) and (**b**) and passing through the center, along the x-direction. Parameters are $\kappa = 0.5, \Delta = 0.1, \Gamma = 2\alpha = 0.5$ and $\eta = -0.025$. The grid is 256×256 points. Black corresponds to the highest values of the phyto-mass density. Minima are plain white. Periodic boundary conditions are used in both spatial co-ordinates

$$\partial_t u = F[u],$$
$$F(u) = \Delta\nabla^2 u - \eta u + \kappa u^2 - u^3 - u(\Gamma\nabla^2 u + \alpha\nabla^4 u). \quad (29)$$

In the following, we consider two bare spots that can interact through their oscillatory tails. The asymptotic form of the tail is described by a modified Bessel function (26) that decays at large distances from the centre of the localized bare spot. When they are excited sufficiently close to each another, they exert mutual forces due to the overlapping of their tails. We will see that these interaction forces can be either attractive or repulsive, depending on the initial distance between the bare spots. In the following, we calculate these interaction forces analytically for the case of weak overlap, which means that the two bare spots are well separated.

Let us choose the co-ordinate system in such a way that its origin is located at the mid-point between two spots, i.e., at equal distance from each of them. Let the center of mass of each of the bare spots be on the axis x, so that their minima are located at the points $(-R/2,0)$ and $(0,R/2)$ along the x-direction, where R is the distance between them (Fig. 8). We look for a solution of (19) in the form of a slightly perturbed linear superposition of two spots:

$$U(\mathbf{r},t) = U_1(\mathbf{r}) + U_2(\mathbf{r}) + \varepsilon\delta U(\mathbf{r},t) \quad \text{where} \quad U_{1,2}(\mathbf{r}) = U(|\mathbf{r} - \mathbf{R}_{1,2}|). \quad (30)$$

The positions of the localized solutions, $\mathbf{R}_{1,2}(t) = (X_{1,2}, Y_{1,2})^{\mathrm{T}}$, evolve on the slow time scale $\partial_t \mathbf{R}_{1,2}(t) = \mathcal{O}(\varepsilon)$. Substituting this expansion into (19) and collecting first-order terms in ε, we obtain

$$[\partial_t - L(U_1 + U_2 + u_+)]\,\delta U = \nabla U_1 \cdot \partial_t \mathbf{R}_1 + \nabla U_2 \cdot \partial_t \mathbf{R}_2 + F(U_1 + U_2 + u_+). \quad (31)$$

To solve (31), it is necessary to satisfy a solvability condition, viz. the right side of (31) should be orthogonal to the null eigenfunctions of the adjoint operator $L^\dagger(U_1 + U_2 + u_+)$, which can be approximated by the neutral (often called Goldstone) translational modes, $\mathbf{v}_1 = (v_{1x}, v_{1y})^{\mathrm{T}}$ and $\mathbf{v}_2 = (v_{2x}, v_{2y})^{\mathrm{T}}$ of $L^\dagger(U_1 + u_+)$ and $L^\dagger(U_2 + u_+)$, respectively. The solvability condition reads

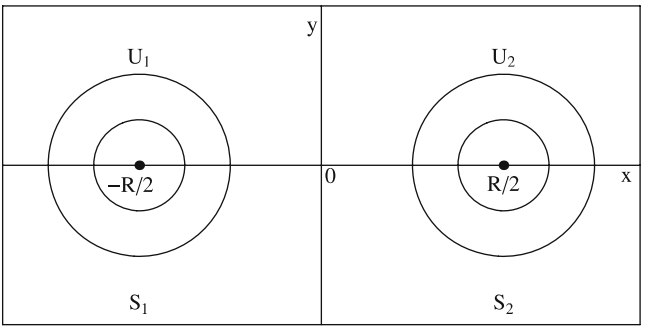

Fig. 8 Schematic plot of two bare spots located at the points $(-R/2,0)$ and $(0,R/2)$ along the x-direction. The black circles indicate the tails of the LBSs

$$\frac{1}{2}\partial_t \mathbf{R}_1 \int_S \mathbf{v}_k \cdot \nabla U_1 \mathrm{d}\mathbf{r} + \frac{1}{2}\partial_t \mathbf{R}_2 \int_S \mathbf{v}_k \cdot \nabla U_2 \mathrm{d}\mathbf{r} = -\int_S \mathbf{v}_k F\left(U_1 + U_2 + u_+\right) \mathrm{d}\mathbf{r}, \quad (32)$$

with $k = 1,2$. The integrals appearing in (32) are taken over the whole plane $S = \Re \times \Re \equiv (x,y)$. To perform the integration over this plane, we decompose it into two half planes, namely, $S_1 = \Re^- \times \Re$ and $S_2 = \Re^+ \times \Re$ (see Fig. 8)

$$\int_S \mathbf{v}_k F\left(U_1 + U_2 + u_+\right) \mathrm{d}\mathbf{r} = \int_{S_1} \mathbf{v}_k F\left(U_1 + U_2 + u_+\right) \mathrm{d}\mathbf{r} + \int_{S_2} \mathbf{v}_k F\left(U_1 + U_2 + u_+\right) \mathrm{d}\mathbf{r}. \quad (33)$$

In the half plane S_1, where the bare spot solution U_2 is small, we can apply the following first-order expansion:

$$F\left(U_1 + U_2 + u_+\right) \approx F\left(U_1 + u_+\right) + L\left(U_1 + u_+\right) U_2 = L\left(U_1 + u_+\right) U_2. \quad (34)$$

Similarly, in the half-plane S_2, where the bare spot solution U_1 is small,

$$F\left(U_1 + U_2 + u_+\right) \approx F\left(U_2 + u_+\right) + L\left(U_2 + u_+\right) U_1 = L\left(U_2 + u_+\right) U_1. \quad (35)$$

Then (32) reads

$$\xi\, \partial_t \mathbf{R}_1 = -\int_{S_1} \mathbf{v}_1 L^\dagger \left(U_1 + u_+\right) U_2 \, \mathrm{d}\mathbf{r}, \quad (36)$$

and

$$\xi\, \partial_t \mathbf{R}_2 = -\int_{S_2} \mathbf{v}_2 L^\dagger \left(U_2 + u_+\right) U_1 \, \mathrm{d}\mathbf{r}, \quad (37)$$

with

$$\xi = \frac{1}{2}\int_S \mathbf{v}_1 \cdot \nabla U_1 \, \mathrm{d}\mathbf{r} = \frac{1}{2}\int_S \mathbf{v}_2 \cdot \nabla U_2 \, \mathrm{d}\mathbf{r}. \quad (38)$$

Subtracting (36) from (37), we get the equation for the time evolution of the distance between the spots:

$$\xi\, \partial_t \mathbf{R} = -\int_{S_2} \mathbf{v}_2 L^\dagger (U_2 + u_+) U_1 \, \mathrm{d}\mathbf{r} + \int_{S_1} \mathbf{v}_1 L^\dagger (U_1 + u_+) U_2 \, \mathrm{d}\mathbf{r}, \quad (39)$$

where $\mathbf{R} = \mathbf{R}_2 - \mathbf{R}_1$. Since $\mathbf{v}_{1,2}$ are the eigenfunctions of $L^\dagger\left(U_{1,2} + u_+\right)$ with the zero eigenvalue, we have

$$\int_S U_1 L^\dagger \left(U_2 + u_+\right) \mathbf{v}_2 \mathrm{d}\mathbf{r} = 0 = \int_S \mathbf{v}_2 L\left(U_2 + u_+\right) U_1 \mathrm{d}\mathbf{r} = \int_{S_1} \mathbf{v}_2 L\left(U_2 + u_+\right) U_1 \mathrm{d}\mathbf{r} + \int_{S_2} \mathbf{v}_2 L\left(U_2 + u_+\right) U_1 \mathrm{d}\mathbf{r}, \quad (40)$$

$$\int_S U_2 L^{\dagger}\left(U_1+u_+\right)\mathbf{v}_1 \mathrm{d}\mathbf{r}=0=\int_S \mathbf{v}_1 L\left(U_1+u_+\right)U_2 \mathrm{d}\mathbf{r}$$
$$=\int_{S_1}\mathbf{v}_1 L\left(U_1+u_+\right)U_2 \mathrm{d}\mathbf{r}+\int_{S_2}\mathbf{v}_1 L\left(U_1+u_+\right)U_2 \mathrm{d}\mathbf{r}. \quad (41)$$

Using the relations (40) and (41), (39) becomes

$$\xi\,\partial_t \mathbf{R}=\int_{S_2}\mathbf{v}_1 L(U_1+u_+)U_2\,\mathrm{d}\mathbf{r}-\int_{S_1}\mathbf{v}_2 L(U_2+u_+)U_1\,\mathrm{d}\mathbf{r}. \quad (42)$$

Since $U_1(U_2)$ is small in $S_2(S_1)$, (42) can be approximated by

$$\xi\,\partial_t \mathbf{R}=\int_{S_2}\left[\mathbf{v}_1 L(u_+)U_2-U_2 L(u_+)\mathbf{v}_1\right]\mathrm{d}\mathbf{r}$$
$$-\int_{S_1}\left[\mathbf{v}_2 L(u_+)U_1-U_1 L(u_+)\mathbf{v}_2\right]\mathrm{d}\mathbf{r}, \quad (43)$$

where the self-adjoint linear operator $L(u_+)$ is defined by (24) and $L(u_+)\mathbf{v}_1=O\left(\varepsilon^2\right)$ in S_2 while $L(u_+)\mathbf{v}_2=O\left(\varepsilon^2\right)$ in S_1. Using this equation, we get

$$\xi\,\partial_t \mathbf{R}=\left(\Delta-\Gamma u_+\right)\left(\mathbf{I}_1-\mathbf{I}_2\right)+\alpha u_+\left(\mathbf{J}_1-\mathbf{J}_2\right)=\mathbf{F}, \quad (44)$$

with

$$\mathbf{I}_{1,2}=\int_{S_{1,2}}\left[\mathbf{v}_{1,2}\nabla^2 U_{2,1}-U_{2,1}\nabla^2\mathbf{v}_{1,2}\right]\mathrm{d}\mathbf{r}, \quad (45)$$

$$\mathbf{J}_{1,2}=\int_{S_{1,2}}\left[\mathbf{v}_{1,2}\nabla^4 U_{2,1}-U_{2,1}\nabla^4\mathbf{v}_{1,2}\right]\mathrm{d}\mathbf{r}. \quad (46)$$

Using Green's identities and the symmetry properties $U(-r)=U(r)$ and $\mathbf{v}(-r)=-\mathbf{v}(r)$, the integrals (45) and (46) over the half-planes S_k, $k=1,2$, can be transformed into the following integrals over the line $x=0$ separating these two half-planes:

$$\mathbf{I}_k=(-1)^k\int_{-\infty}^{\infty}\left[\frac{\mathrm{d}}{\mathrm{d}x}\left(\mathbf{v}_k U_k\right)\right]_{x=0}\mathrm{d}y=-\nabla_{\mathbf{R}}\bar{I}_k, \quad (47)$$

$$\mathbf{J}_k=2(-1)^k\int_{-\infty}^{\infty}\left[\frac{\mathrm{d}}{\mathrm{d}x}\left(U_k\nabla^2\mathbf{v}_k+\mathbf{v}_k\nabla^2 U_k\right)\right]_{x=0}\mathrm{d}y=-\nabla_{\mathbf{R}}\bar{J}_k, \quad (48)$$

where

$$\bar{I}_k=2(-1)^k\int_{-\infty}^{\infty}\left(v_{kx}U_k\right)_{x=0}\mathrm{d}y, \quad (49)$$

$$\bar{J}_k=4(-1)^k\int_{-\infty}^{\infty}\left(U_k\nabla^2 v_{kx}+v_{kx}\nabla^2 U_k\right)_{x=0}\mathrm{d}y. \quad (50)$$

According to (47) and (48), (44) can be rewritten in the following gradient form:

$$\xi\,\partial_t \mathbf{R} = -\nabla_{\mathbf{R}}\mathscr{U}(R), \tag{51}$$

with the potential function

$$\mathscr{U}(R) = (\Delta - \Gamma u_+)(\bar{I}_1 - \bar{I}_2) + \alpha u_+ (\bar{J}_1 - \bar{J}_2). \tag{52}$$

Finally, we note that the integrals appearing in (45),(46),(47),(48),(49), and (50) have the symmetry properties $I_2 = -I_1$, $J_2 = -J_1$, $\bar{I}_2 = -\bar{I}_1$ and $\bar{J}_2 = -\bar{J}_1$, which express the fact that the velocities of the two spots have opposite signs, $\partial_t \mathbf{R}_2(t) = -\partial_t \mathbf{R}_1(t)$.

In order to calculate the interaction force of two bare spots, we substitute the asymptotic relations for U_k and $\mathbf{v}_k$, in terms of the modified Bessel functions, into (47) and (48) and perform the integration. The plot of the interaction force, F, versus the half-distance, $R/2$, between the centers of the two bare spots is shown in Fig. 9. This function shows a decaying oscillation, as predicted from the linear analysis. The equilibrium positions R_1, R_2 and R_3 correspond to a separation where the interaction force between the two spots vanishes, i.e., $F = 0$. The two spots are bound together by the interaction forces. The equilibrium positions R_1 and R_2 are stable, while R_3 is unstable. If the initial distance, d, between two spots is such that $R_0 < d < R_1$, the system will evolve toward the formation of two spots separated by a distance R_1. When d is larger than R_2, they will reach the equilibrium position R_3. Note, however, that the origin of position $R_0/2$ in Fig. 9 is calculated numerically by a direct integration of (19). The position R_0 corresponds to the critical initial distance between spots, and below it, only one spot survives. This means they merge

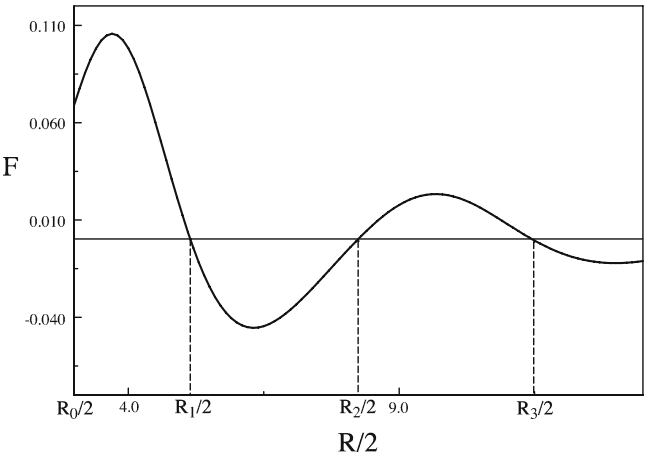

Fig. 9 Interaction force as a function of half-distance between two localized bare spots. Parameters are $\kappa = 0.5$, $\Delta = 0.1$, $\Gamma = 2\alpha = 0.5$, and $\eta = -0.025$

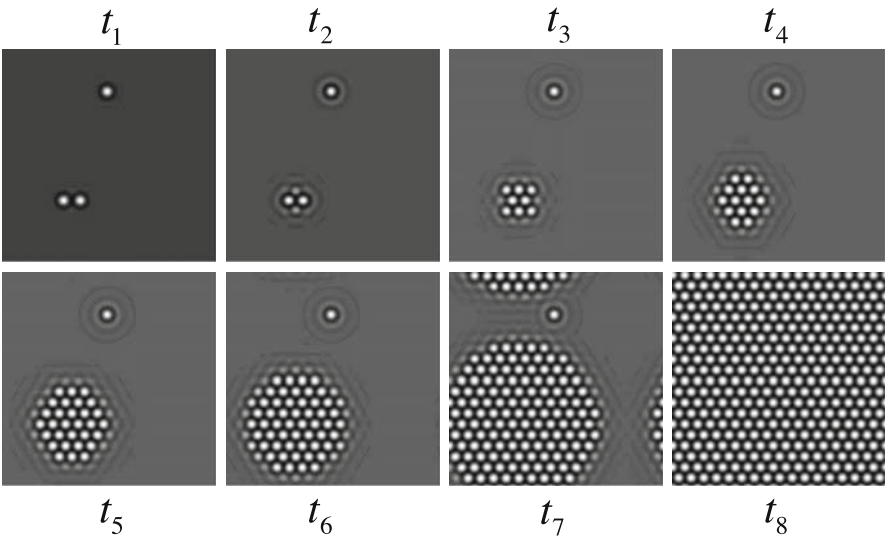

Fig. 10 Transition toward the formation of a periodic distribution of bare spots induced by the interaction between two localized bare spots. Note that the single LBS remains stable for a long time. Minima are plain white and the grid is 256×256 points. Parameters are $\kappa = 0.5$, $\Delta = 0.1$ and $\eta = -0.01$ ($t_i = t_{i-1} + 50$, with $t_1 = 20$)

if $d < R_0$, and only a single spot is formed. Due to the space oscillation of the tails, the interaction force alternates between attraction and repulsion, depending on the initial distance between the two bare spots.

When the branch of spot solutions coincides with the bare state (see Fig. 6), then the minimum of the spot is zero. In that case, the interaction forces between two well-separated spots will destabilize the dynamics of the system toward the formation of a periodic distribution of bare spots which will occupy the whole space available on the ground. This feature is illustrated in Fig. 10. The time evolution shows that the two LBSs become unstable under their mutual interaction, and a periodic pattern is selected in late stage evolution of the system (Fig. 10).

7 Conclusions

We have presented a model and nonlinear analysis which account for the clustering behaviors of arid vegetation ecosystems, the formation of localized bare soil spots (sometimes also called fairy circles) in these systems and the attractive or repulsive interactions governing their spatio-temporal evolution. The bare spots can be either spatially independent, self-organized, or randomly distributed. They form under conditions that are favorable to modulational instability, leading to the patterning. More precisely, they are generated in the regime where a periodic vegetation pattern

and a uniform plant distribution co-exist for given, fixed values of the switching parameter μ. They correspond to a spatial compromise between a homogeneous plant distribution and hexagonal patterns that consist of a uniform vegetation cover regularly punctuated with bare soil areas.

The interaction between two bare spots in 2D systems has been clarified. When the distance between them is large, bare spots do not interact. They form an isolated stationary structure. However, if they are close one to another, they will interact through their overlapping tails. The interaction will cause the bare spots to move until they reach a stable equilibrium position. We have shown that there exist several equilibrium positions. The system selects one of these positions, depending on the initial distance between the two localized spots.

The half-height width of a 2D LBS corresponds approximately to half the wavelength at the modulational instability, $\lambda_{\mathrm{m}}/2$. The wavelength is explicitly given by a simple relation (22), where u_{m} is the solution of (23). The size of fairy circles ranges from 2 to 10 m [16]. The spatial scale for (19) is the inter-plant competition range. This value is estimated to be of the order of 2 m. The half-height width of a 2D LBS is of the order of three- dimensionless spatial units, and so is of order 6 m. This value is consistent with field observations.

Acknowledgments We are grateful to N. Barbier, P. Couteron, O. Lejeune, D. Turaev, M. Wolfrum and S. Zelik for useful discussions. This research is supported, in part, by the *Fonds National de la Recherche Scientifique* (Belgium).

References

1. P. Greig-Smith, J. Ecol. **67**, 755 (1979). 381
2. For a survey of this phenomenon, see e.g. Catena. 1999. *The significance of Soil, Water and Landscape Processes in Banded Vegetation Patterning.* **37**, Special Issue, C. Valentin and J. Poesen (Editors). D. J. Tongway, C. Valentin and J. Seghieri, *Banded Vegetation Patterning in Arid and Semiarid Environments*, (Springer-Verlag, New York, 2001). 381
3. R. Lefever and O. Lejeune, Bull. Math. Biol. **59**, 263 (1997). 382, 383, 386
4. O. Lejeune, P. Couteron, and R. Lefever, Acta Oecologica **20**, 171 (1999). 382
5. R. Lefever, O. Lejeune, and P. Couteron, in: *Mathematical Models for Biological Pattern Formation.* IMA Volumes in Mathematics and its Applications, Frontiers in Applied Mathematics Series **121**, edited by H. Othmer and P. Maini, (Springer-Verlag, New York, 2000). 382
6. J. von Hardenberg, E. Meron, M. Shachak, and Y. Zarmi, Phys. Rev. Lett. **87**, 198101 (2001). 382
7. T. Okayasu and Y. Aizawa, Prog. Theor. Phys. **106**, 705 (2001). 382
8. R. HilleRisLambers, M. Rietkerk, F. van den Bosch, H.H.T. Prins, and H. de Kroon, Ecology, **82**, 50 (2001). 382
9. E. Gilad, J. von Hardenberg, A. Provenzale, M. Shachak, and E. Meron, Phys. Rev. Lett. **93**, 098105 (2004). 382
10. N.M. Shnerb, P. Sarah, H. Lavee, and S. Solomon, Phys. Rev. Lett. **90**, 038101 (2003). 382
11. M. Rietkerk, M. C. Boerlijst, F. Van Langevelde, R. HillRisLambers, J. van de Koppel, L. Kumar, H.H.T. Prins, and A.M. Roos, Am. Nat., **160**, 524 (2002). 382
12. M. Rietkerk, S.C. Dekker, P.C. de Ruiter, and J. van de Koppel, Science **305**, 1926 (2004). 382
13. O. Lejeune, M. Tlidi, and R. Lefever, Int. J. Quantum Chem. **98**, 261 (2004). 382, 391

14. O. Lejeune, M. Tlidi, and P. Couteron, Phys. Rev. E **66**, 010901(R) (2002). 382
15. E. Meron, E. Gilad, J. Von Hardenberg, M. Shachak, and Y. Zami, Chaos Solitons Fractals, **19**, 367 (2004). 382
16. M.W. van Rooyen, G. K. Theron, N. van Rooyen, W.J. Jankowitz, and W.S. Matthews, J. Arid Environ. **57**, 467 (2004). 382, 383, 401
17. K.A. Gorshkov and L.A. Ostrovsky, Physica D, **3**, 428 (1981). 383
18. L.S. Aranson and K.A. Gorshkov, Physica D, **43**, 435 (1990). 383
19. V.V. Afanasjev and N. Akhmediev, Phys. Rev. E **53**, 6471 (1996). 383
20. N. Akhmediev, A. Ankiewicz, and J.M. Soto-Crespo, Phys. Rev. Lett. **79**, 4047 (1997). 383
21. H.U. Bödeker, A.W. Liehr, T.D. Frank, R. Friedrich, and H.G. Purwins, New J. Phys. **6**, 62 (2004). 383
22. A.G. Vladimirov, G.H. Khodova, and N.N. Rosanov, Phys. Rev. E **63**, 056607 (2001). 383
23. M. Tlidi, A.G. Vladimirov, and P. Mandel, IEEE J. Quant. Elec. **39**, 216 (2003). 383
24. A.G. Vladimirov, J.O. McSloy, D.V. Skryabin, and W. Firth, Phys. Rev. E **65**, 064606 (2002). 383
25. R.M. Callaway and L. R. Walker, Ecology **78**, 1958 (1997). 385
26. R. Lefever, N. Barbier, P. Couteron, and O. Lejeune, J. Ecology in preparation. 384, 385, 386
27. C.A. Klausmeier, Science **284**, 1826 (1999). 386
28. J.A. Sherratt, J. Math. Biol. **51**, 183 (2005). 386
29. R. Lefever, Bull. Cl. Sci. Acad. Roy. Belgique XV, 287 (2004). 390
30. R. Lefever, N. Barbier, P. Couteron, V. Deblauwe et O. Lejeune, Pour la Science - Dossier n 44, 68 (2004). 390
31. O. Lejeune and M. Tlidi, J. Veg. Sci. **10**, 201 (1999); P. Couteron and O. Lejeune, J. Ecol. **89**, 616 (2004). 391
32. S. Koga and Y. Kuramoto, Prog. Theor. Phys. **63**, 106 (1980). 392
33. Y. Pomeau, Physica D, **23**, 3 (1986). 392, 393
34. S. Fauve and O. Thual, Phys. Rev. Lett. **64**, 282 (1990). 392
35. M. Tlidi, P. Mandel, and R. Lefever, Phys. Rev. Lett. **73**, 640 (1994). 392
36. V.B. Taranenko, K. Staliunas, and C.O. Weiss, Phys. Rev. A **56**, 1582 (1997). 392
37. J. Boissonade, P. De Kepper, F. Gauffre, and I. Szalai, Chaos **16**, 037110 (2006). 392
38. V.K. Vanag and I. R. Epstein, Phys. Rev. Lett. **92**, 128301 (2004). 392
39. S. Barland, J. R. Tredicce, M. Brambilla, L.A. Lugiato, S. Balle, M. Giudici, T. Maggipinto, L. Spinelli, G. Tissoni, T. Knödl, M. Miller, and R. Jägeet, Nature **419**, 699 (2002). 392
40. U. Bortolozzo, M.G. Clerc, C. Falcon, S. Residori, and R. Rojas, Phys. Rev. Lett. **96**, 214501 (2006). 392
41. M. Pesch, E. Große Westhoff, T. Ackemann, and W. Lange, Phys. Rev. Lett. **95**, 143906 (2005). 392
42. L. Yu. Glebsky and L.M. Lerman, Chaos **5**, 424 (1995). 393
43. G.W. Hunt, G.J. Lord, and A.R. Champneys, Compt. Methods Appl. Mech. Eng. **170**, 239 (1999). 393
44. P. Coullet, C. Riera, and C. Tresser, Phys. Rev. Lett. **84**, 3069 (2000). 393
45. J. Burke and E. Knobloch, Phys. Rev. E **73**, 056211 (2006). 393
46. G. Kozyreff and S.J. Chapman, Phys. Rev. Lett. **97**, 044502 (2006). 393

Propagation of Traveling Pulses in Cortical Networks

D. Golomb

Abstract We study the propagation of traveling solitary pulses in one-dimensional cortical networks with two types of one-dimensional architectures: networks of excitatory neurons and networks composed of both excitatory and inhibitory neurons. Each neuron is represented by the integrate-and-fire model, and is allowed to fire only one spike. The velocity and stability of propagating, continuous pulses are calculated analytically. For excitatory-only networks, two continuous pulses with different velocities exist if the synaptic coupling is larger than a minimal value; the pulse with the lower velocity is always unstable. Above a certain critical value of the constant delay, continuous pulses lose stability via a Hopf bifurcation, and lurching pulses with spatio-temporal periodicity emerge. The parameter regime for which lurching occurs is strongly affected by the synaptic footprint (connectivity) shape. Two types of stable propagating pulses are observed in networks of excitatory and inhibitory neurons. During fast pulses, inhibitory neurons fire a short time before or after the excitatory neurons. During slow pulses, inhibitory cells fire well before neighboring excitatory cells, and potentials of excitatory cells become negative and then positive before they fire. This work shows that simple models of spiking neurons exhibit a large variety of propagating pulses with various spatio-temporal properties.

1 Introduction

Propagating epileptic-like pulses of neuronal activity appear in disinhibited coronal neocortical slices in response to electrical stimulation above a certain threshold. The average discharge velocity is about 10–15 cm/s[1]. Neurons are recruited to the

D. Golomb
Department of Physiology and Zlotowski Center for Neuroscience, Faculty of Health Sciences, Ben Gurion University of the Negev, Be'er-Sheva 84105, Israel, golomb@bgu.ac.il

Golomb, D.: *Propagation of Traveling Pulses in Cortical Networks.* Lect. Notes Phys. **751**, 403–430 (2008)
DOI 10.1007/978-3-540-78217-9_16

wave because of the excitatory, recurrent interactions between neurons. These slice preparations were developed initially as experimental models for epilepsy [2, 3]. Experimental and theoretical investigations [1, 4, 5, 6, 7] have tried to relate the dynamics of propagating discharge to the underlying neuronal circuitry. Numerical simulations of a conductance- based neuronal model with homogeneous architecture have revealed that the discharge propagates at a constant velocity, as a *continuous* traveling pulse [1, 5]. In both theory and experiment, there was a minimal velocity below which the discharge could not propagate. Propagating discharges with similar properties and velocities have been found in other cortical structures, such as the hippocampus [8, 9] and the piriform cortex [10]. The effects of synaptic delays were not examined in those studies.

Propagating epileptic-like pulses appear in cortical slices when the strength of inhibition is reduced by only 10–20% [11, 12, 13], but they cannot propagate in healthy cortical slices under physiological conditions when inhibition is intact. Inhibition shapes the form of these pulses and reduces their velocity [11, 12]. Recent experiments in rodents [7, 14] and ferrets [15, 16] have revealed a different type of propagating pulse in cortical tissue when inhibition is intact or partially reduced. This activity is non-epileptic, with firing rate of individual neurons typically being low ($< 10\,\mathrm{Hz}$). The generation and termination of this propagating state may account for the generation of a subset of cortical rhythm during sleep. In intact ferret slices, the propagating velocity is slow, about 1.1 cm/s [15]. When inhibition is blocked, the activity becomes epileptic-like and the velocity becomes fast, about 9 cm/s. The propagation of slow pulses depends on the existence of slow (mediated by *N*-methyl-D-aspartate (NMDA) [17]) excitation. When this excitation is blocked, the slow pulse often, but not always, cannot propagate [15]. In contrast, blocking the slow excitation does not prevent the propagation of the fast pulses [1]. Blocking the fast (mediated by α-amino-3-hydroxy-5-methyl-4-isoxazole propionate (AMPA) [17]) excitation prevents the appearance of both fast and slow pulses [1, 15]

In this chapter, we explore the propagation of fronts with and without inhibition. Our goals are to characterize the types of propagating pulses and to relate the conditions for their appearance, the pulse velocities, and the differences between the firing times of neighboring excitatory and inhibitory neurons with the network architecture, the kinetics of single neurons and synapses, and synaptic delays. Specifically, we aim to determine the conditions under which the fast, epileptic-like pulses and the slow pulses appear. To achieve these goals, we analyze simple models of a network composed of excitatory (and possibly inhibitory) neurons. The single cell is represented by a simplified version of the integrate-and-fire neuronal model, in which a neuron is allowed to fire only one spike, and then it is silent forever. This model, which is exact in the limit of very long refractory period or very strong synaptic depression, is amenable to analytical treatment. The velocity of traveling pulses in this model, their stability, and the delay between the firing times of neighboring excitatory and inhibitory cells during the pulses are calculated analytically. Under certain conditions, we also investigate more complicated patterns such as lurching pulses [18, 19]. The content of this chapter is based on several research articles [20, 21, 22, 23].

2 Propagating Pulses in Networks of Excitatory Neurons

2.1 The Model

We consider neurons along a one-dimensional chain (Fig. 1A), and use the following version of the integrate-and-fire (Lapique) model [5, 24, 25, 26]

$$\frac{\partial V(x,t)}{\partial t} = -\frac{V(x,t)}{\tau_0} + I_{\text{syn}}(x,t) + I_{\text{app}}(x,t) \tag{1}$$

for $0 < V(x,t) < V_T$, where $V(x,t)$ is the membrane potential of a neuron at a position x and time t, τ_0 is the passive membrane time constant of the neuron, I_{syn} is the normalized synaptic input, and I_{app} is the normalized applied current; $I_{\text{app}} = 0$ unless otherwise stated. When V of a neuron reaches the threshold V_T at time $T(x)$, the neuron fires a spike, and cannot fire more spikes afterward. We assume that the number of neurons within a footprint length is large, and therefore use a continuum model and replace the sum over the pre-synaptic neurons with an integral

$$I_{\text{syn}}(x,t) = g_{\text{syn}} \int_{-\infty}^{\infty} \mathrm{d}x'\, w\left(x-x'\right) \alpha\left[t - T\left(x'\right) - \tau_{\text{d}}\right], \tag{2}$$

where $g_{\text{syn}} = \tilde{g}_{\text{syn}}\Delta/C$, $\tilde{g}_{\text{syn}}$ is the synaptic conductance, C is the membrane capacitance, $\Delta = V - V_{\text{syn}}$ is approximated here as a constant ("coupling by currents", see, e.g., [5, 27]), and τ_{d} is the constant synaptic delay.

Equations (1, 2) are implicit equations of $T(x)$. The temporal shape of the excitatory post-synaptic current (EPSC) that a post-synaptic cell at a position x receives, following a spike of a pre-synaptic cell at a position x', is given by the normalized α function $\alpha[t - T(x')]$:

$$\alpha(t) = \begin{cases} \dfrac{\mathrm{e}^{-t/\tau_1} - \mathrm{e}^{-t/\tau_{\text{s}}}}{\tau_1 - \tau_{\text{s}}} & t \geq 0 \\ 0 & \text{otherwise} \end{cases}, \tag{3}$$

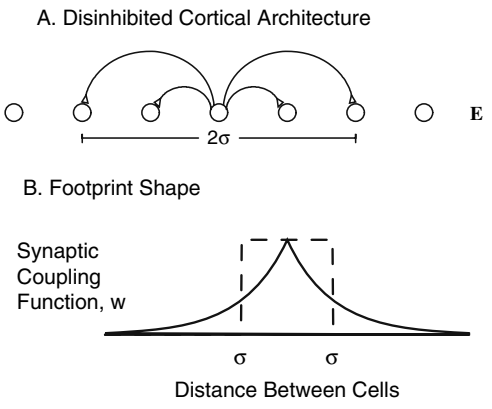

Fig. 1 **A**. The model has one-dimensional architecture, with the coupling between cells decaying with their separation. The footprint length is denoted by σ. **B**. Exponential (solid line) and square (dashed line) footprint shapes. Adapted from [20]

where τ_l and τ_s are the synaptic rise and decay times, respectively; $\tau_l \ll \tau_s$. We will assume that $\tau_l = 0$ unless otherwise stated. The spatial dependence of the synaptic strength on the distance between neurons, $w(x)$, is called the "synaptic footprint shape" [1, 18]. We examine two shapes (Fig. 1B):

$$w(x) = \frac{1}{2\sigma} e^{-|x|/\sigma} \qquad \text{Exponential} \tag{4}$$

$$w(x) = \begin{cases} \frac{1}{2\sigma} & |x| \le \sigma \\ 0 & |x| > \sigma \end{cases} \qquad \text{Square,} \tag{5}$$

σ is called the "synaptic footprint length". We consider a half-infinite network, i.e., the length of the system is much larger than σ.

We define the response (Green) function $G(t)$ for $t > 0$ as

$$\frac{dG}{dt} = -\frac{G}{\tau_0} + \alpha(t);\ G(0) = 0 \tag{6}$$

and $G(t) = 0$ for $t < 0$. Then, for $\tau_l = 0$,

$$G(t) = \begin{cases} \frac{\tau_0}{\tau_0 - \tau_s} \left(e^{-t/\tau_0} - e^{-t/\tau_s} \right) & t \ge 0 \\ 0 & \text{otherwise.} \end{cases} \tag{7}$$

The function G is the normalized excitatory post-synaptic potential (EPSP) developed in the cell as a response to the EPSC (3). The Volterra representation of (1, 2) for neurons that can fire only one spike is

$$\frac{V_T}{g_{syn}} = \int_{-\infty}^{\infty} dx' w\left(x'\right) G\left[T(x) - T\left(x - x'\right) - \tau_d\right] \tag{8}$$

together with the condition that $T(x)$ is the first time that the voltage crosses the threshold ("causality criterion"). This condition requires that V increases with time just before the spike, namely,

$$\frac{dV[x, T(x)]}{dt} > 0. \tag{9}$$

The meaning of (8, 9) is that the summation of all the contributions to the voltage of one neuron from other neurons is equal to V_T when this neuron fires, and that this neuron does not fire beforehand.

2.1.1 Numerical Methods

Equations (1, 2) are simulated numerically by discretizing space. There are N neurons in the chain, and the density of neurons is ρ per length σ. The coupled system of ordinary differential equations for the integrate-and-fire neurons is solved using

exact integration [28]. To stimulate the network, applied current is "injected" into a group of neurons on the "left" of the system (small x values). These span a length at least equal to the footprint length σ ("shock" initial conditions).

2.2 Continuous and Lurching Pulses

A pulse can propagate along the network in response to "shock" initial conditions. For zero or small τ_d (below a critical value τ_{dc}), the pulse is continuous far from the stimulus region (Fig. 2A), and the firing times of the neurons obey $T(x) = T_0 + x/v$, where v is the pulse velocity and T_0 is an arbitrary time. The neuronal potential satisfies an equation of a traveling pulse as well: $V(x,t) = \tilde{V}(x - vt)$ [1, 5]. As τ_d approaches a critical value τ_{dc} from below, the convergence of the firing time $T(x)$ to a continuous propagating pulse decelerates. For $\tau_d > \tau_{dc}$, a lurching propagating pulse is observed (Fig. 2B). Space is spontaneously divided into basic spatial units, each with a spatial period of length L, and the firing time in each unit can be obtained from the spatial period in the previous unit according to

$$T(x+L) = T(x) + T_{per}, \tag{10}$$

where T_{per} is the time period of a lurching cycle. The average velocity of the pulse is $v = L/T_{per}$. Suppose that one lurching period starts at $x = 0$ and $T(0) = 0$. The firing time of a neuron at a position x is given by

$$T(x) = nT_{per} + f(\hat{x}), \tag{11}$$

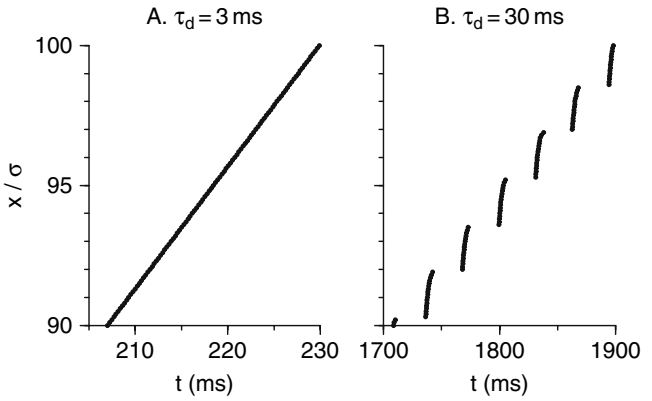

Fig. 2 Rastergrams obtained from simulating (1, 2, 4), with the condition that each neuron can fire only one spike. Parameters: $\tau_0 = 30$ ms, $\tau_s = 2$ ms, $N = 5 \times 10^4$, $\rho = 500$; for these parameters, $\tau_{dc} = 11.15$ ms. The solid circles represent the firing time of neurons as a function of their normalized position x/σ; spikes of only one out of every 50 neurons are plotted. Together, the groups of solid circles almost look like one continuous line. **A**: For $\tau_d < \tau_{dc}$ (3 ms), a continuous pulse is obtained. **B**: For $\tau_d > \tau_{dc}$ (30 ms), the pulse is lurching. Adapted from [20]

where n is the integer part of $T(x)/T_{\mathrm{per}}$ (or x/L) and $\hat{x} = x - nL$. The function f, expressing the firing time within one period relative to the starting point of the period in space and time, is defined on the interval $[0, L)$; $f(0) = 0$. Hence, the function

$$T(x) - x/v = f(\hat{x}) - \hat{x}/v \tag{12}$$

is a periodic function of x with a period L. Equation (12) demonstrates the spatio-temporal periodicity of the lurching pulse.

2.3 Existence, Stability and Velocity of Continuous Pulses

2.3.1 General Formalism

Substituting the condition for a continuous pulse, $T(x) = x/v$, into the evolution equation (8), we obtain

$$\int_0^\infty \mathrm{d}x' \, w\left(x' + \tau_{\mathrm{d}} v\right) G\left(x'/v\right) = V_T/g_{\mathrm{syn}}. \tag{13}$$

We should also confirm that the condition of (9) holds. Stability of the continuous pulse is calculated by considering $T(x) = x/v + s(x)$ and linearizing (8) near the continuous solution, to obtain

$$\int_0^\infty \mathrm{d}x' \, w\left(x' + \tau_{\mathrm{d}} v\right) G'\left(x'/v\right) \left[s(x) - s\left(x - x' - \tau_{\mathrm{d}} v\right)\right] = 0. \tag{14}$$

This convolution equation has a general solution $s(x) = \exp(\lambda x)$. Substituting this equation in (14) yields

$$\int_0^\infty \mathrm{d}x' \, w\left(x' + \tau_{\mathrm{d}} v\right) G'\left(x'/v\right) \left[1 - \mathrm{e}^{-\lambda\left(x' + \tau_{\mathrm{d}} v\right)}\right] = 0. \tag{15}$$

$\lambda = 0$ is always a solution of (15), corresponding to the translation invariance of the continuous pulse. The continuous wave is stable if $\mathrm{Re}\,\lambda < 0$ for all the λ values that are solutions of this eigenvalue equation (except for the single zero solution). This means that a small perturbation at a specific, finite x will decay at larger x as the pulse propagates. A similar method to study stability was developed independently by Bressloff [25, 26].

2.3.2 Exponential Footprint Shape

The velocity v is determined using (4, 7, 13):

$$\frac{(\tau_0 v + \sigma)(\tau_{\mathrm{s}} v + \sigma)}{\tau_0 v \sigma} \exp\left(\frac{\tau_{\mathrm{d}} v}{\sigma}\right) = \frac{g_{\mathrm{syn}}}{2V_T}. \tag{16}$$

This is an extension of the equation obtained in [5] for $\tau_d = 0$. From this equation, one can see that:

1. For $\tau_d = 0$, the left-hand-side of (16) has a minimum with respect to v at $v_{min} = \sigma/\sqrt{\tau_0 \tau_s}$. Continuous pulses cannot propagate below this minimal velocity, which is obtained for minimal synaptic coupling $g_{syn,min}$. For $g_{syn} > g_{syn,min}$, there are two branches of solutions of (16). At the fast branch, v increases with g_{syn}, and at the slow branch v decreases with g_{syn} [5].
2. Because $\exp(\tau_d v/\sigma) > 1$ and increases with τ_d, v_{min} decreases with τ_d and is obtained for larger $g_{syn,min}$.
3. For $\tau_d > 0$ and at large enough g_{syn}, the velocity is determined mainly by the exponential factor in (16), and therefore v depends logarithmically on g_{syn} to the highest order. In contrast, for $\tau_d = 0$, the velocity exhibits a power-law dependence on g_{syn} at large g_{syn} [5]. Graphs of v/σ as a function of V_T/g_{syn} for several values of τ_d are shown in Fig. 3A.

In order to find the function $V(x,t)$ before the spike (and thus verify that (11) holds), we look, without loss of generality, at a neuron located at $x = 0$. The Volterra representation of (1, 2) for the traveling wave $T(x) = x/v$ for time $t < 0$, taking into account the fact that $G(t) = 0$ for $t < 0$, is

$$V(0,t) = g_{syn} \int_{-\infty}^{\infty} dx' \, w(x') \, G\left[t - T(-x') - \tau_d\right]$$

$$= g_{syn} \int_{(\tau_d - t)v}^{\infty} dx' \, w(x') \, G\left(t + \frac{x}{v} - \tau_d\right). \tag{17}$$

Substituting (4, 7) into (2, 3) yields

$$V(0,t) = \frac{g_{syn} \tau_0 v \sigma}{2(\tau_0 v + \sigma)(\tau_s v + \sigma)} \exp\left[\frac{(t - \tau_d) v}{\sigma}\right]. \tag{18}$$

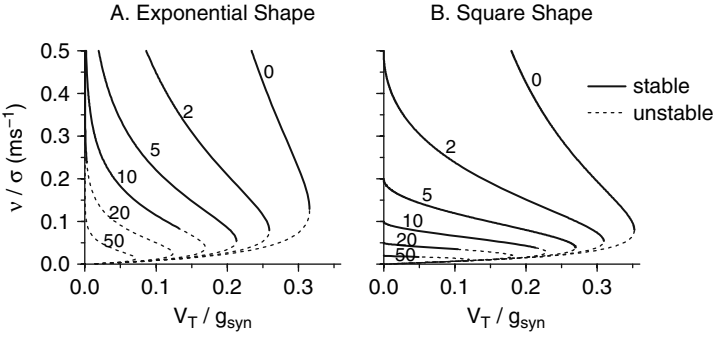

Fig. 3 The velocity of the continuous pulse as a function of V_T/g_{syn} for several values of τ_d. The thick lines represent stable pulses and the thin lines represent unstable pulses. The number above each line, from 0 to 50, denotes the value of τ_d. Parameters: $\tau_0 = 30$ ms, $\tau_s = 2$ ms. **A**. Exponential footprint shape (16). **B**. Square footprint shape (23). Adapted from [20, 21]

The voltage V rises exponentially from 0 and reaches V_T at $t = 0$ for all v values; both the upper and lower branches fulfill the condition of (9).

The stability of the continuous pulse is explored by substituting (4, 7) in (15), thus obtaining

$$e^{\lambda v \tau_d} = \frac{(\tau_0 v + \sigma)(\tau_s v + \sigma)(1 + \lambda\sigma)}{[\tau_0 v (1 + \lambda\sigma) + \sigma][\tau_s v (1 + \lambda\sigma) + \sigma]}. \tag{19}$$

The value $\lambda = 0$ is always a root corresponding to translational invariance. In [21], we show that the lower branch, for which $dv/dg_{syn} < 0$, is unstable in general. This can be easily demonstrated for the case $\tau_d = 0$, in which there is another solution to (19), $\lambda = \sigma/(v^2 \tau_0 \tau_s) - 1/\sigma$. The pulse is stable if $v > \sigma/\sqrt{\tau_0 \tau_s}$, and therefore the fast branch is stable and the slow branch is unstable.

In order to examine whether the delay can destabilize pulses that belong to the fast branch, we look for a pair of complex conjugate eigenvalues which cross the imaginary axis. At this Hopf bifurcation, $\lambda = i\omega$ and

$$e^{i\omega v \tau_{dc}} = \frac{(\tau_0 v + \sigma)(\tau_s v + \sigma)(1 + i\omega\sigma)}{[\tau_0 v (1 + i\omega\sigma) + \sigma][\tau_s v (1 + i\omega\sigma) + \sigma]} \equiv Z(\omega). \tag{20}$$

As ω varies, the left-hand-side traces out the unit circle. In order to solve this equation, we search for the non-zero ω value for which $|Z(\omega)| = 1$. This value is given by

$$\omega^2 = \left[\sigma^4 + 2\sigma^3 v (\tau_0 + \tau_s) + 4\sigma^2 v^2 \tau_0 \tau_s - v^4 \tau_0^2 \tau_s^2\right] / \left(\sigma^2 v^4 \tau_0^2 \tau_s^2\right). \tag{21}$$

For this ω, we find τ_{dc}, the critical value of τ_d for which the arguments of the complex numbers on the two sides of (20) are equal:

$$\tau_{dc} = \frac{\arg[Z(\omega)]}{\omega v}. \tag{22}$$

Note that τ_{dc} does not depend explicitly on g_{syn}, but only through v. Using (21, 22), τ_{dc} is calculated as a function of v. This solution shows that τ_{dc} increases with v, and that this increase is steep at small v and modest at large v. As a result, for small values of τ_d, the Hopf bifurcation occurs on the lower, slow branch and does not have an effect on the dynamics. For larger values of τ_d, the Hopf bifurcation occurs on the upper, fast branch, and the continuous pulse is unstable for low velocities, as shown in Fig. 3A. The various behavioral regimes of the continuous pulse in the τ_d–g_{syn} plane are plotted in Fig. 4A. Below the solid line, the continuous pulse does not exist. Above this line, the continuous pulse is stable if the delay τ_d is smaller than a critical delay τ_{dc}, and is unstable otherwise. The dashed line denotes the value of τ_{dc} as a function of g_{syn}. At very large g_{syn}, τ_{dc} increases logarithmically with g_{syn}.

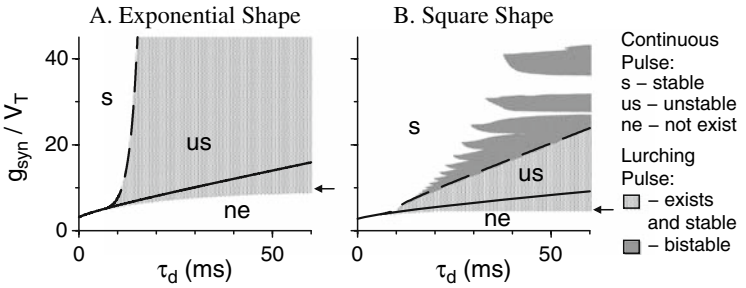

Fig. 4 Regimes of existence and stability of the continuous and lurching pulses in the τ_d–v plane are shown in (**A**) for exponential footprint shape and in (**B**) for square footprint shape. Parameters are as in Fig 3. The boundaries of the regime in which the lurching pulse exists and is stable were computed from numerical simulations, in which a pulse was initiated by a "shock" initial stimulus; $N = 20{,}000$, $\rho = 50$. The solid line denotes the minimal possible velocity as a function of g_{syn}; the continuous pulse becomes unstable (via a Hopf bifurcation) on the dashed line. The continuous pulse is therefore stable above both the solid and the long-dashed lines, as denoted by "s". It is unstable between the two lines, as denoted by "us", and does not exist below the continuous line, as denoted by "ne". The light-gray shading represents the region for which lurching pulses (and not continuous pulses) are obtained. Bistable regimes, in which the continuous pulse can co-exist with the lurching pulse, are denoted by the dark-gray shading. For the square footprint shape (**B**), but not for the exponential footprint shape, there is a bistable regime that has a "tongue-like" structure. The arrow on the right of each graph represents the minimal values of g_{syn} for which the lurching pulse is found in simulations for $\tau_d \to \infty$. Adapted from [20]

The boundaries of the regime of existence of lurching pulses have been located using numerical simulations, and they enclose the light-shaded area in Fig. 4A. Lurching pulses are observed in all the parameter regimes in which the continuous pulse is unstable. In addition, lurching pulses are also observed in a parameter regime in which the continuous pulse does not exist at all. At very large delay, lurching pulses are observed above a critical value of g_{syn}, denoted by the arrow, that does not depend on τ_d (see below).

2.3.3 Square Footprint Shape

The velocity v is determined using (5, 7, 13):

$$\frac{2V_T}{g_{syn}} = \frac{\tau_0 v}{\sigma}\left\{1 - \frac{1}{\tau_0 - \tau_s}\left[\tau_0 \exp\left(\frac{\tau_d - \sigma/v}{\tau_0}\right) - \tau_s \exp\left(\frac{\tau_d - \sigma/v}{\tau_s}\right)\right]\right\}. \quad (23)$$

Graphs of v/σ as a function of V_T/g_{syn} for several values of τ_d are shown in Fig. 3B. The qualitative results regarding the minimal velocity and its dependence on τ_d are the same as for the exponential case. The situation is different, however, for large g_{syn}. For $v = \sigma/\tau_d$, the right-hand-side of (23) is zero. Hence, at the limit $g_{syn} \to \infty$, the velocity of the continuous pulse approaches the finite value σ/τ_d.

The stability of the continuous pulse is explored by substituting (5, 7) in (15) to obtain

$$(1+\lambda\tau_0 v)(1+\lambda\tau_s v)\left[\exp\left(\frac{\tau_d-\sigma/v}{\tau_0}\right)-\exp\left(\frac{\tau_d-\sigma/v}{\tau_s}\right)\right]$$
$$=\lambda v(\tau_0-\tau_s)\exp(-\lambda\tau_d v) \tag{24}$$
$$+\left[(1+\lambda\tau_s v)\exp\left(\frac{\tau_d-\sigma/v}{\tau_0}\right)-(1+\lambda\tau_0 v)\exp\left(\frac{\tau_d-\sigma/v}{\tau_s}\right)\right]\exp(-\sigma\lambda).$$

To calculate the τ_{dc} value for which the continuous pulse becomes unstable, we substitute $\lambda = i\omega$ into (24) and obtain two real transcendental equations for the real variables τ_{dc} and ω. Using standard iteration methods [29], we solve these equations numerically for one value of v which is sufficiently large. The spatial period of the expanding or decaying fluctuations, ω, is of order $2\pi/\sigma$. This fact helps us to choose initial conditions for the iteration process. At small v, it is numerically difficult to use this method to solve the equations. Therefore, we write the ordinary differential equations with these two equations as their nullclines, and follow their fixed point solution using the program XPPAUT [30, 31], starting from the solution at large v that we already have computed. Using (23), we calculate the range of stability as a function of g_{syn} and τ_d.

The different behavioral regimes of the continuous pulse for a square footprint shape are presented in Fig. 4B. The critical delay τ_{dc} increases with g_{syn} almost linearly at large g_{syn}. As a result, for a specific τ_d, there is a moderate g_{syn} value for which the continuous pulse is stable. Lurching pulses are obtained in the region marked by the gray shading in Fig. 4B. There are two apparent differences between the situation here and the situation for exponential footprint shape. First, lurching pulses exist in an area which is composed of "tongues". Second, a *bistable* regime exists, marked by the dark-gray shading, in which the two types of pulses can propagate, depending on the initial stimulation [19]. This bistability suggests that the Hopf bifurcation in which the continuous pulse loses stability is sub-critical.

3 Propagating Pulses in Networks of Excitatory and Inhibitory Neurons

3.1 The Model

In this section, we consider a one-dimensional network of excitatory (E) and inhibitory (I) neurons (Fig. 5A). A neuron is described by its membrane potential $V_\alpha(x,t)$, $\alpha = E, I$, and its dynamics is governed by the integrate-and-fire scheme in the excitable regime [25]. The dynamical equations and analysis are extensions

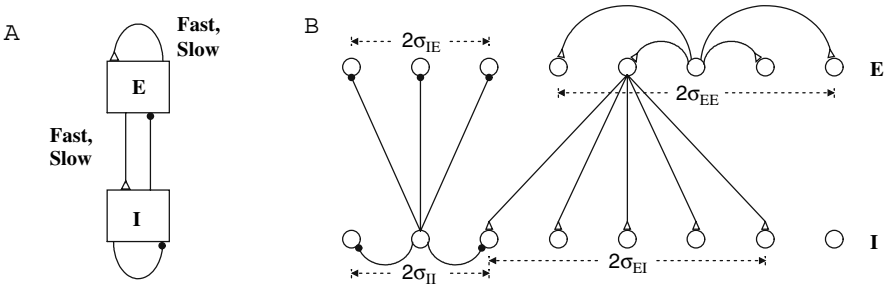

Fig. 5 Schematic diagram of the model architecture. **A**. Neuronal populations and synaptic types. **B**. The one-dimensional architecture of the network. Adapted from [23]

of the equations and analysis described in the previous section for the excitatory population only. The analog of (1) is

$$\frac{\partial V_\alpha(x,t)}{\partial t} = -\frac{V_\alpha(x,t)}{\tau_{0\alpha}} + I_{\mathrm{syn,E}\alpha}(x,t) - I_{\mathrm{syn,I}\alpha}(x,t). \tag{25}$$

Here, $\tau_{0\alpha}$ is the passive membrane time constant of the neuron and $I_{\mathrm{syn,E}\alpha}$ (resp. $I_{\mathrm{syn,I}\alpha}$) is the total synaptic current contributed by the excitatory (resp. inhibitory) population. In the following, the time at which a neuron from the αth population located at x fires is denoted by $T_\alpha(x)$. A pre-synaptic spike induces a post-synaptic current that is proportional to the function $\alpha_{\beta\alpha}(t)$, where

$$\alpha_{\beta\alpha}(t) = \begin{cases} \frac{1}{\tau_{\mathrm{s}\beta\alpha}} \exp\left(-t/\tau_{\mathrm{s}\beta\alpha}\right) & t \geq 0 \\ 0 & \text{otherwise.} \end{cases} \tag{26}$$

For the excitatory coupling, we consider two types of synaptic current: a fast (f) current and a slow (s) current, corresponding to the contribution of AMPA and NMDA synaptic receptors in a biological network, respectively. The function $\alpha_{\mathrm{E}\alpha}(t)$ and the decay time $\tau_{\mathrm{sE}\alpha}$ have a superscript $\gamma = \{\mathrm{f},\mathrm{s}\}$ denoting whether the decay of the excitatory current is fast or slow.

The network architecture is shown in Fig. 5B. The contributions to the synaptic current from the excitatory and inhibitory populations are

$$I_{\mathrm{syn,E}\alpha}(x,t) = \sum_{\gamma=\mathrm{f,s}} g^\gamma_{\mathrm{E}\alpha} \int_{-\infty}^{\infty} \mathrm{d}x'\, w_{\mathrm{E}\alpha}(x-x')\, \alpha^\gamma_{\mathrm{E}\alpha}\left(t - T_{\mathrm{E}}(x')\right), \tag{27}$$

$$I_{\mathrm{syn,I}\alpha}(x,t) = g_{\mathrm{I}\alpha} \int_{-\infty}^{\infty} \mathrm{d}x'\, w_{\mathrm{I}\alpha}(x-x')\, \alpha_{\mathrm{I}\alpha}\left(t - T_{\mathrm{I}}(x')\right), \tag{28}$$

where $g_{\beta\alpha}$ is the synaptic coupling strength from the β population to the α population. The spatial dependence of the synaptic strength on distance (the "synaptic footprint shape") is given by

$$w_{\beta\alpha}(x) = \frac{1}{2\sigma_{\beta\alpha}} \exp\left(-|x|/\sigma_{\beta\alpha}\right). \tag{29}$$

The spatial variable, x, is dimensionless and represents the distance in terms of the excitatory footprint, σ_{EE}, which is set to 1. As a result, the velocity v has units of ms^{-1}.

3.1.1 Reference Parameter Set

In the following, we study the model in its general form. Numerical examples, however, are given for a particular set of parameters, called the "reference parameter set", with: $\tau_{0E} = \tau_{0I} = 30\,\mathrm{ms}$, $\tau^{\mathrm{f}}_{\mathrm{sEE}} = \tau^{\mathrm{f}}_{\mathrm{sEI}} = 2.5\,\mathrm{ms}$, $\tau^{\mathrm{s}}_{\mathrm{sEE}} = \tau^{\mathrm{s}}_{\mathrm{sEI}} = 50\,\mathrm{ms}$, $\tau_{\mathrm{sIE}} = \tau_{\mathrm{sII}} = 8\,\mathrm{ms}$, $g^{\mathrm{f}}_{\mathrm{EE}} = 12$, $g^{\mathrm{s}}_{\mathrm{EE}} = 10$, $\sigma_{\mathrm{EE}} = 1$, $g_{\mathrm{IE}} = 5.2$, $\sigma_{\mathrm{IE}} = 0.5$, $g^{\mathrm{f}}_{\mathrm{EI}} = 30$, $g^{\mathrm{s}}_{\mathrm{EI}} = 0$, $\sigma_{\mathrm{EI}} = 1$, $g_{\mathrm{II}} = 2$, $\sigma_{\mathrm{II}} = 0.5$, $V_{T\mathrm{E}} = V_{T\mathrm{I}} = 1$. These parameters are used unless stated otherwise. Since the slow E-to-I excitation $g^{\mathrm{s}}_{\mathrm{EI}}$ does not have a strong effect on the network dynamics, we consider it to be zero.

3.2 Fast and Slow Pulses

Figure 6, based on simulations, shows two types of pulses that can propagate in networks of excitatory and inhibitory neurons. One pulse type is similar to the continuous pulses that propagate in excitatory networks (Fig. 6A). Since their velocity, in general, decreases with inhibition, here they are called "fast pulses". A second pulse type, called "slow pulses", is shown in Fig. 6B. This pulse is characterized by a much smaller velocity and by the fact that inhibitory cells fire before their neighboring excitatory cells. The two simulations in Fig. 6 were carried out with the same parameter set but with different initial conditions. Therefore, the two pulses are bistable for this parameter set. In general, however, the bistable parameter regime is narrow, and only one type of pulse, or none, can propagate for a specific parameter set. Below, we will investigate the properties of the two pulses theoretically.

3.3 Analysis of Traveling Pulse Solutions

3.3.1 Volterra Representation

In order to analyze the dynamics, we define the Green's function $G_{\beta\alpha}(t)$ for $t > 0$ as (6)

$$\frac{\mathrm{d}G_{\beta\alpha}}{\mathrm{d}t} = -\frac{G_{\beta\alpha}}{\tau_{0\alpha}} + \alpha_{\beta\alpha}(t) \tag{30}$$

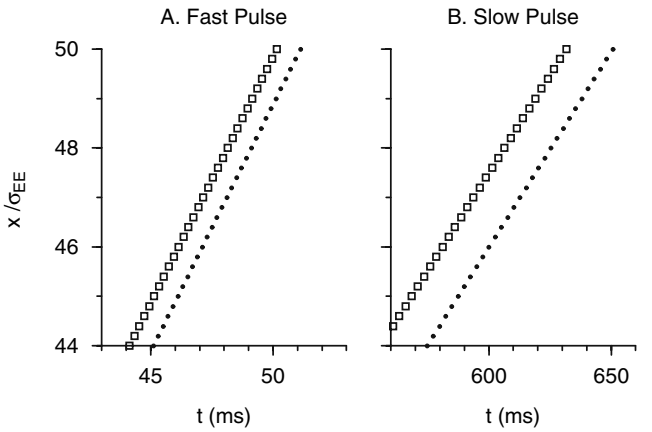

Fig. 6 Fast and slow pulses can propagate for the same set of parameters in the bistable regime. Rastergrams obtained by simulations of the neuronal dynamics are shown. Firing times of excitatory cells are denoted by solid circles, and firing times of inhibitory cells are denoted by open squares. There are $\rho = 50$ neurons from each type within one unit length, and spikes of only one out of every 10 neurons are plotted. The pulses were started by initiating a pulse in a group of neurons with $x < 10$ with ν and ζ calculated from the theory. Two types of continuous pulses, fast and slow, are shown in **A** and **B** for the different initial conditions (note the difference in time scale). Parameters: $\tau_0 \mathrm{E} = \tau_0 \mathrm{I} = 30$ ms, $\tau_{\mathrm{sEE}} = \tau_{\mathrm{sEI}} = 2.5$ ms, $\tau_{\mathrm{sIE}} = \tau_{\mathrm{sII}} = 8$ ms, $g_{\mathrm{EE}} = 12$, $\sigma_{\mathrm{EE}} = 1$, $\sigma_{\mathrm{IE}} = 0.9$, $\sigma_{\mathrm{EI}} = 0.8$, $g_{\mathrm{II}} = 2$, $\sigma_{\mathrm{II}} = 0.5$, $g_{\mathrm{IE}} = 5.5$. Adapted from [22]

and $G_{\beta\alpha} = 0$ for $t < 0$. The functions $G_{\mathrm{E}\alpha}$ also have a superscript γ. For $t > 0$, we obtain

$$G_{\beta\alpha}(t) = \frac{\tau_{0\alpha}}{\tau_{0\alpha} - \tau_{\mathrm{s}\beta\alpha}} \left[\exp(-t/\tau_{0\alpha}) - \exp(-t/\tau_{\mathrm{s}\beta\alpha}) \right]. \tag{31}$$

The integrated form of (25, 27, 28) is given by the two Volterra equations for $\alpha = \mathrm{E}, \mathrm{I}$:

$$\begin{aligned} V_{T\alpha} = & \sum_{\gamma=\mathrm{f,s}} g^{\gamma}_{\mathrm{E}\alpha} \int_{-\infty}^{\infty} \mathrm{d}x' \, w_{\mathrm{E}\alpha}(x') \, G^{\gamma}_{\mathrm{E}\alpha} \left[T_{\alpha}(x) - T_{\mathrm{E}}\left(x - x'\right) \right] \\ & - g_{\mathrm{I}\alpha} \int_{-\infty}^{\infty} \mathrm{d}x' \, w_{\mathrm{I}\alpha}(x') \, G_{\mathrm{I}\alpha} \left[T_{\alpha}(x) - T_{\mathrm{I}}\left(x - x'\right) \right]. \end{aligned} \tag{32}$$

In addition, the neuronal voltage should be below threshold before spiking:

$$V_{\alpha}(x,t) < V_{T\alpha} \quad \text{for all} \quad t < T_{\alpha}(x), \quad \alpha = \mathrm{E}, \mathrm{I}. \tag{33}$$

A necessary, but not sufficient, condition for this (9) is

$$\left. \frac{\mathrm{d}V_{\alpha}[x,t]}{\mathrm{d}t} \right|_{t=T_{\alpha}(x)} > 0, \quad \alpha = \mathrm{E}, \mathrm{I}. \tag{34}$$

3.3.2 Existence of Traveling Pulses

We consider a traveling pulse solution with velocity v. Without loss of generality, we assume that $v > 0$. The firing time of an inhibitory cell lags after the firing time of an excitatory cell at the same position by ζ:

$$T_{\mathrm{E}}(x) = \frac{x}{v}\,, \quad T_{\mathrm{I}}(x) = \frac{x}{v} + \zeta. \tag{35}$$

Negative ζ means that an I cell fires before a neighboring E cell. Substituting (35) into (32) yields

$$V_{T\alpha} = B^{\mathrm{f}}_{\mathrm{E}\alpha} + B^{\mathrm{s}}_{\mathrm{E}\alpha} - B_{\mathrm{I}\alpha}, \tag{36}$$

where

$$B^{\gamma}_{\beta\alpha} = g^{\gamma}_{\beta\alpha} \int_0^{\infty} \mathrm{d}x\, w_{\beta\alpha}\left(x + \zeta\, v\, s_{\beta\alpha}\right) G^{\gamma}_{\beta\alpha}\left(\frac{x}{v}\right). \tag{37}$$

We define $s_{\beta\alpha} = \left(s_\alpha - s_\beta\right)/2$, where $s_{\mathrm{E}} = 1$ and $s_{\mathrm{I}} = -1$. Substituting the expressions for $G_{\beta\alpha}$ and $w_{\beta\alpha}$ into (36, 37), we obtain two algebraic equations for v and ζ, for negative ζ

$$\begin{aligned} V_{\mathrm{TE}} = {} & \frac{\tau_{0\mathrm{E}}\, v\, \sigma_{\mathrm{EE}}}{2\left(v\,\tau_{0\mathrm{E}} + \sigma_{\mathrm{EE}}\right)} \sum_{\gamma} g^{\gamma}_{\mathrm{EE}}\, \frac{1}{\left(v\,\tau^{\gamma}_{\mathrm{sEE}} + \sigma_{\mathrm{EE}}\right)} - g_{\mathrm{IE}}\, \frac{\tau_{0\mathrm{E}}\, v}{\left(\tau_{0\mathrm{E}} - \tau_{\mathrm{sIE}}\right)} \\ & \times \left[\frac{\tau^2_{0\mathrm{E}}\, v}{v^2\,\tau^2_{0\mathrm{E}} - \sigma^2_{\mathrm{IE}}} \exp\left(\frac{\zeta}{\tau_{0\mathrm{E}}}\right) - \frac{\tau^2_{\mathrm{sIE}}\, v}{v^2\,\tau^2_{\mathrm{sIE}} - \sigma^2_{\mathrm{IE}}} \exp\left(\frac{\zeta}{\tau_{\mathrm{sIE}}}\right) \right. \\ & \left. + \frac{\left(\tau_{0\mathrm{E}} - \tau_{\mathrm{sIE}}\right)\sigma_{\mathrm{IE}}}{2\left(v\,\tau_{0\mathrm{E}} - \sigma_{\mathrm{IE}}\right)\left(v\,\tau_{\mathrm{sIE}} - \sigma_{\mathrm{IE}}\right)} \exp\left(\frac{\zeta\, v}{\sigma_{\mathrm{IE}}}\right) \right], \end{aligned} \tag{38}$$

$$\begin{aligned} V_{\mathrm{TI}} = {} & \frac{\tau_{0\mathrm{I}}\, v\, \sigma_{\mathrm{EI}}}{2\left(v\,\tau_{0\mathrm{I}} + \sigma_{\mathrm{EI}}\right)} \exp\left(\frac{\zeta\, v}{\sigma_{\mathrm{EI}}}\right) \sum_{\gamma} g^{\gamma}_{\mathrm{EI}}\, \frac{1}{\left(v\,\tau^{\gamma}_{\mathrm{sEI}} + \sigma_{\mathrm{EI}}\right)} \\ & - g_{\mathrm{II}}\, \frac{\tau_{0\mathrm{I}}\, v\, \sigma_{\mathrm{II}}}{2\left(v\,\tau_{0\mathrm{I}} + \sigma_{\mathrm{II}}\right)\left(v\,\tau_{\mathrm{sII}} + \sigma_{\mathrm{II}}\right)}. \end{aligned} \tag{39}$$

Similarly, for positive ζ, we obtain the following two algebraic equations for v and ζ:

$$\begin{aligned} V_{\mathrm{TE}} = {} & \frac{\tau_{0\mathrm{E}}\, v\, \sigma_{\mathrm{EE}}}{2\left(v\,\tau_{0\mathrm{E}} + \sigma_{\mathrm{EE}}\right)} \sum_{\gamma} g^{\gamma}_{\mathrm{EE}}\, \frac{1}{\left(v\,\tau^{\gamma}_{\mathrm{sEE}} + \sigma_{\mathrm{EE}}\right)} \\ & - g_{\mathrm{IE}}\, \frac{\tau_{0\mathrm{E}}\, v\, \sigma_{\mathrm{IE}}}{2\left(v\,\tau_{0\mathrm{E}} + \sigma_{\mathrm{IE}}\right)\left(v\,\tau_{\mathrm{sIE}} + \sigma_{\mathrm{IE}}\right)} \exp\left(\frac{-\zeta\, v}{\sigma_{\mathrm{IE}}}\right), \end{aligned} \tag{40}$$

$$V_{\mathrm{TI}} = \sum_{\gamma} g_{\mathrm{EI}}^{\gamma} \frac{\tau_{0\mathrm{I}}\, v}{\left(\tau_{0\mathrm{I}} - \tau_{\mathrm{sEI}}^{\gamma}\right)} \left[\frac{\tau_{0\mathrm{I}}^2\, v}{v^2\, \tau_{0\mathrm{I}}^2 - \sigma_{\mathrm{EI}}^2} \exp\left(\frac{-\zeta}{\tau_{0\mathrm{I}}}\right) - \frac{\left(\tau_{\mathrm{sEI}}^{\gamma}\right)^2 v}{v^2 \left(\tau_{\mathrm{sEI}}^{\gamma}\right)^2 - \sigma_{\mathrm{EI}}^2} \exp\left(\frac{-\zeta}{\tau_{\mathrm{sEI}}^{\gamma}}\right) \right.$$
$$\left. + \frac{\left(\tau_{0\mathrm{I}} - \tau_{\mathrm{sEI}}^{\gamma}\right) \sigma_{\mathrm{EI}}}{2\left(v\, \tau_{0\mathrm{I}} - \sigma_{\mathrm{EI}}\right)\left(v\, \tau_{\mathrm{sEI}}^{\gamma} - \sigma_{\mathrm{EI}}\right)} \exp\left(\frac{-\zeta\, v}{\sigma_{\mathrm{EI}}}\right) \right]$$
$$- g_{\mathrm{II}} \frac{\tau_{0\mathrm{I}}\, v\, \sigma_{\mathrm{II}}}{2\left(v\, \tau_{0\mathrm{I}} + \sigma_{\mathrm{II}}\right)\left(v\, \tau_{\mathrm{sII}} + \sigma_{\mathrm{II}}\right)}. \tag{41}$$

Propagating pulses exist only if (38, 39) have at least one solution v with $\zeta < 0$, or if (40, 41) have at least one solution v with $\zeta > 0$.

3.3.3 Stability of Traveling Pulses

The stability of continuous pulses is calculated by following the growth rate of a small perturbation:

$$T_{\mathrm{E}}(x) = x/v + \theta_{\mathrm{E}}(x), \tag{42}$$
$$T_{\mathrm{I}}(x) = x/v + \zeta + \theta_{\mathrm{I}}(x). \tag{43}$$

Substituting these perturbations into (32), and keeping only the first-order terms in θ_{E}, θ_{I}, we obtain two equations for $\alpha = \mathrm{E}, \mathrm{I}$:

$$0 = \sum_{\gamma=\mathrm{f,s}} g_{\mathrm{E}\alpha}^{\gamma} \times \int_{\zeta\, v\, s_{\mathrm{E}\alpha}}^{\infty} \mathrm{d}x'\, w_{\mathrm{E}\alpha}(x')\, G'^{\gamma}_{\mathrm{E}\alpha} \left(\frac{x'}{v} - \zeta\, S_{\mathrm{E}\alpha}\right)$$
$$\times \left[\theta_{\alpha}(x) - \theta_{\mathrm{E}}\left(x - x'\right)\right] - g_{\mathrm{I}\alpha} \int_{\zeta\, v\, s_{\mathrm{I}\alpha}}^{\infty} \mathrm{d}x'\, w_{\mathrm{I}\alpha}(x')\, G'_{\mathrm{I}\alpha} \left(\frac{x'}{v} - \zeta\, S_{\mathrm{I}\alpha}\right)$$
$$\times \left[\theta_{\alpha}(x) - \theta_{\mathrm{I}}\left(x - x'\right)\right], \tag{44}$$

where

$$G'(t) = \mathrm{d}G(t)/\mathrm{d}t. \tag{45}$$

If we assume that the perturbations evolve as $\theta_{\mathrm{E}}(x) = \theta_{\mathrm{E}0} \exp(\lambda x)$ and $\theta_{\mathrm{I}}(x) = \theta_{\mathrm{I}0} \exp(\lambda x)$, then we obtain the matrix equation

$$\sum_{\beta=\mathrm{E,I}} A_{\beta\alpha}(\lambda)\, \theta_{\beta 0} = 0, \tag{46}$$

where

$$A_{\mathrm{EE}}(\lambda) = \sum_{\gamma} g_{\mathrm{EE}}^{\gamma} \int_0^{\infty} \mathrm{d}x\, w_{\mathrm{EE}}(x)\, G'^{\gamma}_{\mathrm{EE}} \left(\frac{x}{v}\right) \left(1 - \mathrm{e}^{-\lambda x}\right)$$
$$- g_{\mathrm{IE}} \int_{\zeta v}^{\infty} \mathrm{d}x\, w_{\mathrm{IE}}(x)\, G'_{\mathrm{IE}} \left(\frac{x}{v} - \zeta\right), \tag{47}$$

$$A_{\mathrm{IE}}(\lambda) = g_{\mathrm{IE}} \int_{\zeta\nu}^{\infty} \mathrm{d}x\, w_{\mathrm{IE}}(x)\, G'_{\mathrm{IE}}\left(\frac{x}{\nu} - \zeta\right) \mathrm{e}^{-\lambda x}, \tag{48}$$

$$A_{\mathrm{EI}}(\lambda) = -\sum_{\gamma} g_{\mathrm{EI}}^{\gamma} \int_{-\zeta\nu}^{\infty} \mathrm{d}x\, w_{\mathrm{EI}}(x)\, G'^{\gamma}_{\mathrm{EI}}\left(\frac{x}{\nu} + \zeta\right) \mathrm{e}^{-\lambda x}, \tag{49}$$

$$\begin{aligned} A_{\mathrm{II}}(\lambda) = {} & \sum_{\gamma} g_{\mathrm{EI}}^{\gamma} \int_{-\zeta\nu}^{\infty} \mathrm{d}x\, w_{\mathrm{EI}}(x)\, G'^{\gamma}_{\mathrm{EI}}\left(\frac{x}{\nu} + \zeta\right) \\ & - g_{\mathrm{II}} \int_{0}^{\infty} \mathrm{d}x\, w_{\mathrm{II}}(x)\, G'_{\mathrm{II}}\left(\frac{x}{\nu}\right)\left(1 - \mathrm{e}^{-\lambda x}\right) \end{aligned} \tag{50}$$

Equation (46) has non-trivial solutions if

$$\det[A(\lambda)] = 0. \tag{51}$$

The value $\lambda = 0$ is always a solution of the characteristic equation (51) because of the translation invariance. Apart from this marginal stability, the traveling pulse is stable if all the other solutions of this equation have negative real parts. A pulse can lose stability at a saddle-node bifurcation (SNB), where the $\lambda = 0$ solution of (51) is a double zero, namely,

$$\mathrm{d}\{\det[\mathrm{A}(\lambda)]\}/\mathrm{d}\lambda|_{\lambda=0} = 0. \tag{52}$$

Alternatively, a pulse can lose stability at a Hopf bifurcation (HB), where (51) has two imaginary solutions with $\lambda = \pm \mathrm{i}\omega$.

3.3.4 Voltage Profile

For a traveling pulse, the voltage profile of the E and I neurons that have not fired is determined by the voltage profile of the neurons at time $t = 0$:

$$V_{\alpha}(x,t) = V_{\alpha}(x - \nu t, 0) \qquad \alpha = \mathrm{E}, \mathrm{I}. \tag{53}$$

We calculate $V_{\mathrm{E}}(x - \nu t, 0)$ in the domain $0 \le x \le \infty$ and $V_{\mathrm{I}}(x - \nu t, 0)$ in the domain $-\zeta\nu \le x \le \infty$ by using (25, 27, 28, 30), and obtain

$$\begin{aligned} V_{\alpha}(x,0) = {} & \sum_{\gamma=\mathrm{f,s}} g_{\mathrm{E}\alpha}^{\gamma} \times \int_{0}^{\infty} \mathrm{d}x'\, w_{\mathrm{E}\alpha}(x + x')\, G_{\mathrm{E}\alpha}^{\gamma}\left(\frac{x'}{\nu}\right) \\ & - g_{\mathrm{I}\alpha} \int_{\zeta\nu}^{\infty} \mathrm{d}x'\, w_{\mathrm{I}\alpha}(x + x')\, G_{\mathrm{I}\alpha}\left(\frac{x'}{\nu} - \zeta\right). \end{aligned} \tag{54}$$

3.4 Theory of Propagation of Fast and Slow Pulses

A main goal of this section is to study the effects of inhibition on pulse propagation. Therefore, we emphasize the effects of the parameter g_{IE} and study how it modifies the system dynamics under various conditions. Effects of other parameters are also studied.

3.4.1 Effects of I-to-E Inhibition and Slow E-to-E Excitation

In Fig. 7A, B, C, the dependence of ν (upper and middle panels) and ζ (lower panels) on g_{IE} is shown for the reference parameter set, three values of g^f_{EI} and two values of g^s_{EE}: 0 (thin lines) and 10 (thick lines). We first describe the situation for

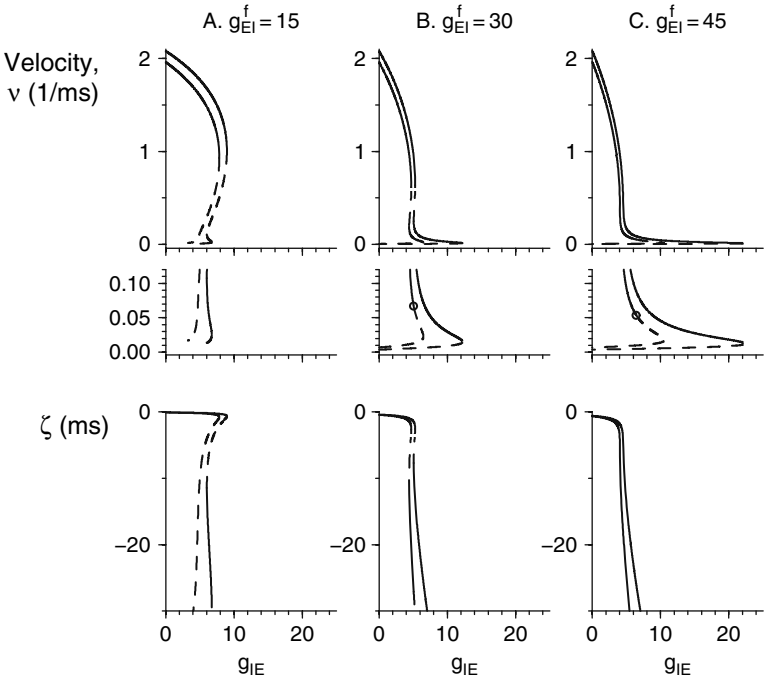

Fig. 7 The velocity ν of propagating pulses (upper and middle panels) and the difference ζ between the firing times of inhibitory and excitatory cells at the same position (lower panels) as functions of inhibitory-to-excitatory synaptic strength g_{IE} for the reference parameter set and three values of the excitatory-to-inhibitory synaptic strength g^f_{EI}: **A**. $g^f_{EI}=15$. **B**. $g^f_{EI}=30$. **C**. $g^f_{EI}=45$. Thin lines represent pulses with $g^s_{EE}=0$ and thick lines represent pulses with $g^s_{EE}=10$. Solid lines represent stable pulses and dashed lines represent unstable pulses. In the middle panels, which are expansions of the upper panels, Hopf bifurcations are denoted by open circles. Bistability of fast and slow pulses is observed in a small g_{IE} regime for moderate values of g^f_{EI} and g_{IE}. Adapted from [23]

$g^{s}_{EE} = 0$. At low g^{f}_{EI} values, there is only one stable branch of "fast" pulses, and it terminates at a SNB. At intermediate g^{f}_{EI} values, bistability exists, and at intermediate g_{IE} values, both the fast pulse and the slow pulse can propagate. The g_{IE} regime, in which slow pulses exist, is rather restricted, because the slow pulse is terminated by a HB. At large g^{f}_{EI} values, there is a cross-over between fast pulses and a slow pulse as g_{IE} increases. The slow pulse is still destabilized by a HB at a certain g_{IE} value. Whereas our theory cannot determine what happens for g_{IE} larger than its value at the HB, extensive numerical simulations indicate that no pulse can propagate in that regime. This situation is different from the case of excitatory networks with delay, described in the previous section, where the HB leads to the propagation of discontinuous, lurching pulses. Increasing g^{s}_{EE} to 10 modifies the v–g_{IE} curve in two aspects. First, the branch in the bifurcation diagram corresponding to the slow pulse extends for a wider g_{IE} region. Second, there is no HB. As a result, the slow E-to-E excitation increases the regime where stable slow pulses can propagate. For all the g^{s}_{EE} and g^{f}_{EI} values, the time difference $|\zeta|$ increases as v decreases, and therefore the time lead of the I cell is larger for the slow pulse than for the fast pulse.

For all the parameter regimes we have examined, E cells fire before or slightly after the I cells during the fast pulse, and the values of ζ are small positive or negative values, of order 1 ms. In contrast, during the propagation of the slow pulse, E cells fire well after the I cells, and ζ is negative and of the order of a few tens of ms. The slow pulse can therefore be viewed as a front of I-cells' spikes pushed from behind by the E cells' spikes; because each E cell receives strong inhibition from neurons in front of it, the pulse propagates slowly.

The voltage profile of neurons that have not fired yet at time $t = 0$ (54) is shown in Fig. 8 for the reference parameter set. With this set of parameters, the fast pulse

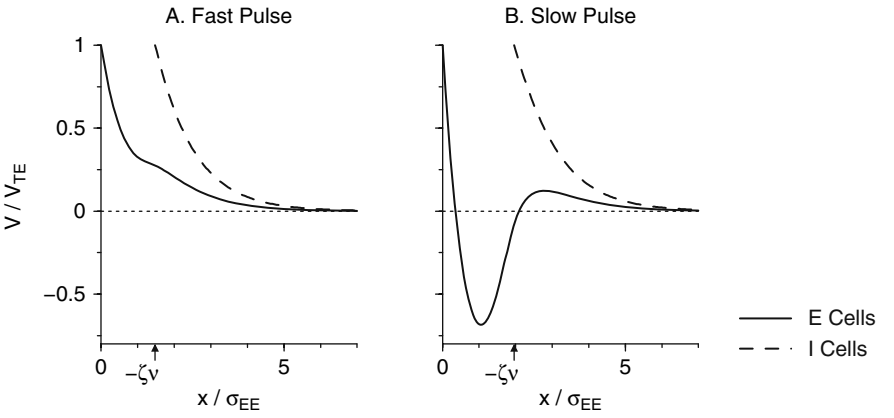

Fig. 8 The potentials V of excitatory neurons (solid line) and inhibitory neurons (dashed line) that have not fired yet at time $t = 0$ are plotted as a function of their position. The reference parameter set is used; in particular, $g_{IE} = 5.2$ and $g^{s}_{EE} = 10$. **A**. Potentials during the fast pulse. **B**. Potentials during the slow pulse. Adapted from [23]

and the slow pulse co-exist. During the fast pulse, the membrane potential of a neuron at a position x decays monotonically with distance from the pulse. During the slow pulse, the potential of the I cells also decays monotonically. However, during the slow pulse, the potential of the E cell first decays rapidly and reaches a negative value. Then, it increases to positive values and then decreases again. Note that a mirror image of the same profile, with the abscissa stretched by a factor $1/\nu$, describes the temporal behavior of the pulse at a constant position x. This means that, during the slow pulse, each excitatory neuron is first excited, but then is affected by strong inhibition and its potential becomes negative. Only when the pulse continues to propagate and the effect of inhibition is diminished, is the neuron again affected by excitation and so can reach threshold and fire.

Plotting the voltage profile as a function of x (Fig. 8) demonstrates a case in which ν and ζ differ for the fast pulse and the slow pulse, whereas the value of $\nu\zeta$ is similar. Since the footprint ranges in the model are of order 1, the value $|\nu\zeta|$ should be of order 1 or less, otherwise the spikes emitted by neurons from one population do not affect neurons in the other population. Hence, lower ν enables ζ to have larger values. In principle, these can be negative or positive.

To further demonstrate that $g_{\mathrm{EE}}^{\mathrm{s}}$ increases the regime of slow pulse propagation, we present in Fig. 9 two-dimensional bifurcation diagrams in the $g_{\mathrm{EI}}^{\mathrm{f}}$–$g_{\mathrm{IE}}$ plane, for $g_{\mathrm{EE}}^{\mathrm{s}} = 0$ (A) and $g_{\mathrm{EE}}^{\mathrm{s}} = 10$ (B). The fast pulse exists for $g_{\mathrm{IE}} \gtrsim 0$ for all $g_{\mathrm{EI}}^{\mathrm{f}}$ values. Three lines of SNB are plotted. The lower SNB line (dashed), corresponding to the minimal g_{IE} value above which the fast pulse can propagate, is bounded by two codimension-2 cusp bifurcations [32]. The cusp at low $g_{\mathrm{EI}}^{\mathrm{f}}$, denoted by the asterisk, produces the slow-pulse branch as a "ripple" on an unstable solution (see Fig. 7A, thick line). The cusp at high $g_{\mathrm{EI}}^{\mathrm{f}}$, denoted by the diamond, connects the slow and the fast branches and eliminates the unstable branch between them. At higher $g_{\mathrm{EI}}^{\mathrm{f}}$ values, there is a continuous cross-over between the fast branch and the slow branches as $g_{\mathrm{EI}}^{\mathrm{f}}$ increases. For $g_{\mathrm{EE}}^{\mathrm{s}} = 0$, but not for $g_{\mathrm{EE}}^{\mathrm{s}} = 10$, there is a line of HB representing the maximal g_{IE} above which the slow pulse is unstable. Comparing panels A and B in Fig. 9 shows that in B, the slow-pulse regime and also the bistable regime (in which the two pulse types can propagate) have larger areas in the two-parameter space for two reasons. First, the slow branch is terminated by a SNB at higher g_{IE} values. Second, the slow branch is not destabilized by a HB if $g_{\mathrm{EE}}^{\mathrm{s}}$ is large enough.

3.4.2 Response to Shock Initial Conditions

Even if a pulse exists and is stable for a particular set of parameters, it does not mean that it can be generated using a particular choice of initial conditions. Since the space of initial conditions has, in principle, an infinite dimension, we cannot determine the volume of the basins of attraction for a particular propagating state in that space. Instead, we chose to use one type of initial condition, the "shock" initial condition. All the neurons in a region $0 < x < 2.5$ are excited at $t = 0$, and we follow which type of pulse, if any, is generated. The shock initial condition is chosen

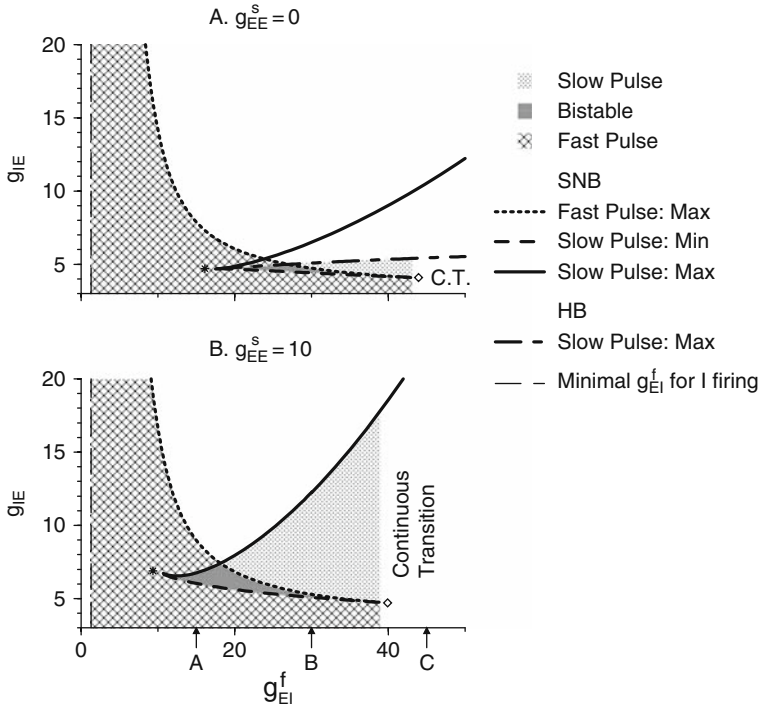

Fig. 9 Regimes of existence and stability of fast and/or slow pulses in the g^f_{EI}–g_{IE} plane for the reference parameter set and $g^s_{EE} = 0$ (A) and $g^s_{EE} = 10$ (B). Saddle-node bifurcation curves are denoted by thick lines: dotted line – the maximal g_{IE} value of the fast pulse; dashed line – the minimal g_{IE} value of the slow pulse; solid line – the maximal g_{IE} value of the slow pulse. The Hopf bifurcation curve in (**A**) is denoted by the dot-dashed line. No such curve appears in (**B**). For a g^s_{EI} value smaller than that of the thin long-dashed line, only excitatory cells fire, and inhibitory cells are quiescent. Shadings: dark gray – bistable regime; light gray – regime in which only slow pulses can propagate; mesh of diagonal lines – regime in which only fast pulses can propagate; "continuous transition" (or "C.T." in (**A**)) – regime of continuous transition from fast-pulse behavior for g_{IE} values near 0 to slow-pulse behavior as g_{IE} increases. In all the other white regimes, no pulse can propagate. The cusps of the SNB lines are denoted by an $*$ (left) and by a $\diamond$ (right). The three arrows below the abscissa in (**B**) represent the three values of g^f_{EI} in Fig. 7. Slow excitation substantially increases the parameter regime in which slow pulses can propagate. Adapted from [23]

because it replicates the experimental situation, in which propagating discharges are initiated by a brief spatially localized stimulation [1].

The system's response to shocks is described in Fig. 10 for two values of g^s_{EE}: 0 (A and B) and 10 (C and D). We compare the responses for two values of ν. We keep all the parameters at their reference values except for g_{IE}, which we tune in order to obtain the desired value of ν. These g_{IE} and ν values are shown in Fig. 10E, which is the same as Fig. 7B (middle panel). For $g^s_{EE} = 0$ and $\nu = 0.085\,\mathrm{ms}^{-1}$ (Fig. 10A), the slow pulse is the only attracting pulse. A shock stimulus initiates a transient fast

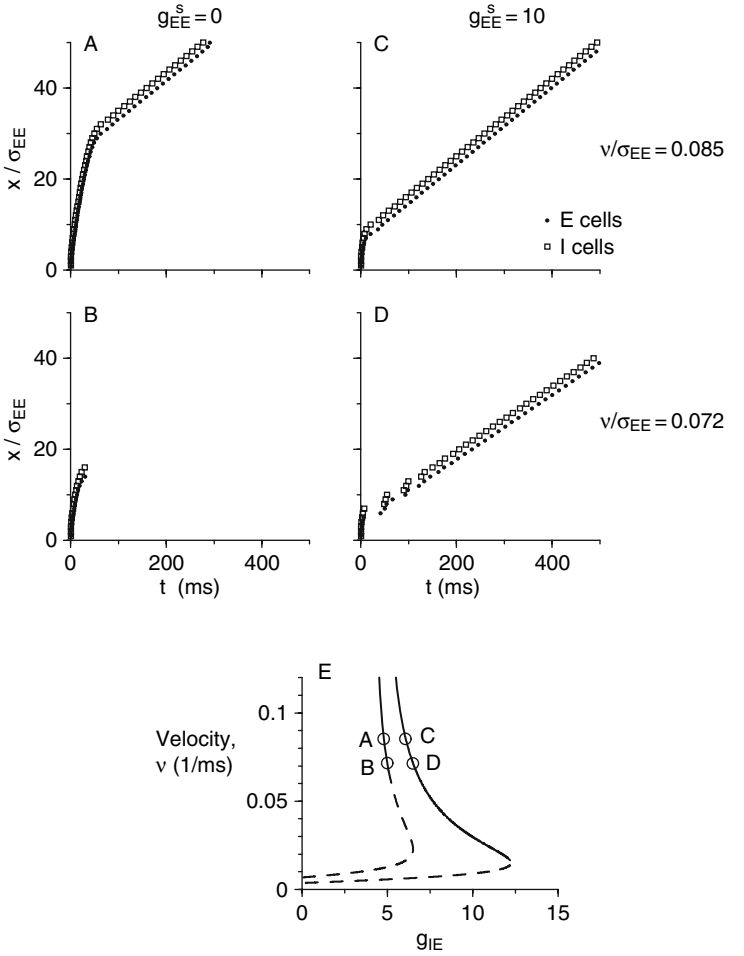

Fig. 10 Network responses to a "shock" stimulus are shown in rastergrams (**A, B, C, D**). Firing times of excitatory cells are denoted by solid circles and firing times of inhibitory cells are denoted by open squares. There are $\rho = 20$ neurons of each type within each unit length (σ_{EE}), and spikes of only one out of every 20 neurons are plotted. The number of neurons in each population is $N = 1000$, and the reference parameter set is used. The network is initiated by an abrupt activation of all the excitatory and inhibitory neurons on the "left" ($0 < x < 2.5$). Simulations are carried out for two values of g^s_{EE} and two values of ν: A. $g^s_{EE} = 0$, $\nu = 0.085$ ($g_{IE} = 4.8$); B. $g^s_{EE} = 0$, $\nu = 0.072$ ($g_{IE} = 5$); C. $g^s_{EE} = 10$, $\nu = 0.085$ ($g_{IE} = 6.08$); D. $g^s_{EE} = 10$ $\nu = 0.072$ ($g_{IE} = 6.51$). In E, the values of g_{IE} and the velocities ν of the slow pulses are shown. The curves, corresponding to slow pulses, are identical to the curve shown in Fig. 7B (middle panel). Thick lines represent pulses with $g^s_{EE} = 10$ and thin lines represent pulses with $g^s_{EE} = 0$. Solid lines represent stable pulses and dashed lines represent unstable pulses. The circles labeled A–D correspond to the value of g_{IE} and ν in panels **A, B, C, D**. Without slow excitation, it is difficult to evoke slow pulses, even if they exist and are stable. Adapted from [23]

pulse which propagates along a considerable distance before it switches to a slow pulse (at about $x = 30$). For $v = 0.072\,\mathrm{ms}^{-1}$ (Fig. 10B), the slow pulse is also the only attracting pulse, while a shock stimulus only generates localized activity which does not propagate. When g^{s}_{EE} is raised to 10, for both values of v, the same shock stimulus generates a slow pulse after a small interval of fast propagation (Fig. 10C), or after two periods of "lurching" activity (Fig. 10D).

The effect of the slow excitation can be explained intuitively as follows. After a shock stimulus, in order to generate a slow pulse, the firing times of the neurons should reorganize so that the I cells fire before the E cells at the same position. If there is slow excitation, a cell receives inhibition and excitation due to the fast inhibitory and excitatory synapses, and then, for a prolonged time, receives slow excitation that enables it to overcome the inhibition and fire. We note that when the fast pulse is the only attractor, shock initial conditions generate it with or without g^{s}_{EE} for all the cases we examined (not shown).

3.4.3 I-to-I Conductance and Irregular Pulses

The I-to-I conductance g_{II} was found to strongly affect the firing properties of networks under steady-state conditions [33, 34]. In order to examine how g_{II} affects pulse propagation, we study the regimes where various types of pulses can propagate in a two-parameter, $g_{II} - g_{IE}$ plane, as shown in Fig. 11. In this figure, solid and dotted lines represent saddle-node bifurcations in which slow and fast pulses are terminated, respectively, as g_{IE} values are increased. In addition, pulses with large

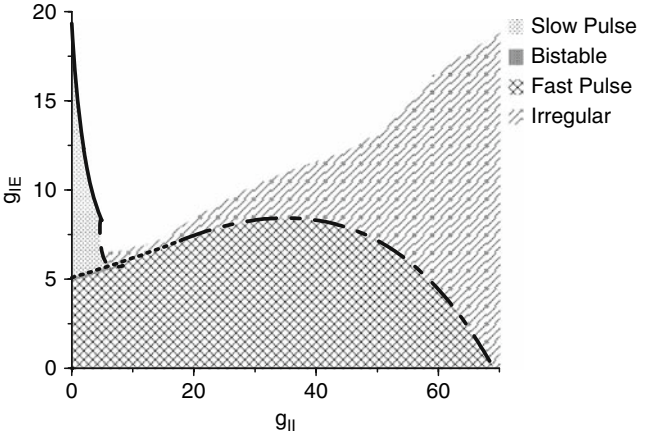

Fig. 11 Regimes of existence and stability of fast and/or slow pulses in the g_{II}–g_{IE} plane. Saddle-node bifurcation lines: solid line – termination of the slow pulse; dotted line – termination of the fast pulse. Terminations of solutions because of (33): dashed line – slow pulse; dot-dashed line – fast pulse. Shadings: dark gray – bistable regime; light gray – regime in which only slow pulses can propagate; mesh of diagonal lines – regime in which only fast pulses can propagate; bent diagonal lines – irregular pulses. Adapted from [23]

enough g_{II} are terminated because the solution violates (33). Specifically,

$$\frac{\mathrm{d}V_I\left[-\zeta\nu\,,\,T_I\left(-\zeta\nu\right)\right]}{\mathrm{d}t} > 0. \tag{55}$$

Such a termination is denoted by a dashed line for the slow pulse and by a dot-dashed line for the fast pulse. The bistable regime and the regimes in which either slow or fast pulses can propagate are shaded, as in the other two-parameter figures. The slow pulse can propagate only if g_{II} is small enough, and its regime of existence shrinks rapidly as g_{II} increases. For low g_{II} values, the slow pulse is terminated by a SNB as g_{IE} increases, and it is terminated because of (55) at higher values. Fast pulses are terminated by a SNB (as g_{IE} increases) for much larger g_{II} values in comparison with the slow pulses. At even larger g_{II} values, however, these pulses are terminated by the condition of (55).

What happens beyond the curve on which a pulse is terminated by condition (55)? Surprisingly, we find in numerical simulations that irregular pulses can propagate. Three examples of such pulses are shown in the rastergrams of Fig. 12. These pulses are characterized by the fact that excitatory cells fire almost as in regular traveling pulses, whereas inhibitory cells segregate into two spatio-temporal clusters. Neurons in the first cluster fire before their excitatory neighbors with an almost constant time delay, $|\zeta_1|$. Neurons in the second cluster fire after their inhibitory neighbors from the first clusters, and often (as in Fig. 12A, $g_{\mathrm{II}} = 50$) also after their neighboring excitatory neurons. The pulses in Fig. 12A have the characteristics of a fast pulse in that inhibitory cells fire either less than 1 ms before neighboring excitatory cells or just after them, and ν is large (1.45 1/ms in (I) and 0.91 1/ms in (II)). In Fig. 12B ($g_{\mathrm{II}} = 10$), all the inhibitory neurons fire before the neighboring excitatory neurons, and the segregation into two clusters is less strict. The pulse in Fig. 12B has the characteristics of a slow pulse in that inhibitory cells fire tens of ms before their neighboring excitatory cells, and ν is small (0.06 1/ms).

In order to define the border of the appearance of the irregular pulses, we carried out numerical simulations in which we started from a shock initial condition and found out whether or not a pulse could propagate. The results are shown in the regime shaded by the bent diagonal lines in Fig. 11. We cannot rule out the possibility that pulses which are excited by other initial conditions also propagate outside of this regime.

We can understand the appearance of irregular pulses using the following argument. The strong mutual inhibition between inhibitory neurons at large g_{II} values prevents the propagation of a regular traveling pulse because when one I cell fires, it reduces the propensity of its neighboring I cell to fire afterward. As a result, neighboring I cells tend to fire with time delays between them.

3.4.4 Lurching Pulses

Can lurching pulses with more complicated spatio-temporal forms be obtained in our model, without synaptic delays? We find such lurching pulses, with spatio-temporal periodicity in the firing pattern, if the E-to-E excitation is made slow,

while all the other synapses decay rapidly. A typical rastergram of a lurching pulse is shown in Fig. 13; the parameter set is characterized by a slow τ_{sEE} (50 ms) and large g_{EE} (250). A group of firing E cells inhibit other excitatory neurons through the neighboring inhibitory neurons, but the E-to-E excitation is sufficiently prolonged to recruit a new group of excitatory cells into the pulse at a later time. Surprisingly, during a lurching pulse, the firing time of the spikes is not a monotonic function of the spatial position (see Fig. 13). As the parameter g_{IE} increases, the system switches from a continuous to a lurching pulse, although not through instability. Instead, the continuous pulse ceases to exist because the solution violates (33), and a lurching pulse emerges. At even higher g_{IE} values, no pulse can propagate.

4 Discussion

4.1 Types of Propagating Pulses

Three main types of traveling pulses were described in this chapter: continuous pulses, lurching pulses and irregular pulses . The continuous pulses belong to two types: fast and slow. The two types of continuous pulses are only well defined in the bistable regime, where both exist. In other regimes of the parameter space, they are characterized by their similarity to the fast or slow pulses in the bistable regime. Here we summarize the properties of the various pulse types.

Fast pulses can propagate in networks of excitatory neurons. In networks with inhibition, they can be regarded as a continuation of propagating pulse states in the excitatory-only case. They are characterized by E cells firing before or just after neighboring I cells, and by a monotonic increase of the neuronal potential before

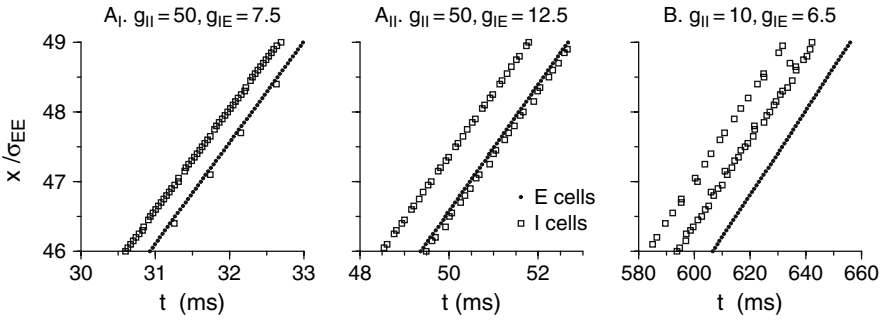

Fig. 12 Examples of neuronal firing times during the propagation of irregular pulses are shown for the reference parameter set and: $\mathbf{A_I}$: $g_{II} = 50$, $g_{IE} = 7.5$, $\nu = 1.45$ 1/ms; $\mathbf{A_{II}}$: $g_{II} = 50$, $g_{IE} = 12.5$, $\nu = 0.91$ 1/ms; **B**: $g_{II} = 10$, $g_{IE} = 6.5$, $\nu = 0.06$ 1/ms. Firing times of excitatory cells are denoted by solid circles, and firing times of inhibitory cells are denoted by open squares. There are $\rho = 20$ neurons of each type within each unit length (σ_{EE}), and spikes of all the neurons are plotted. The number of neurons in each population is $N = 1000$ and the total length of the system is 50 σ_{EE}. Adapted from [23]

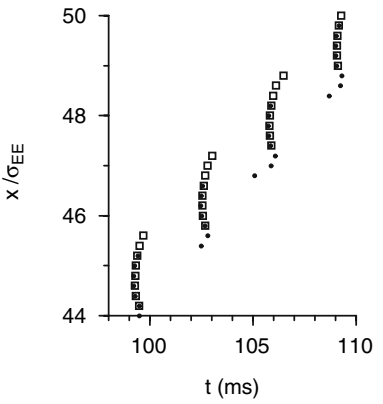

Fig. 13 A lurching pulse is shown in a rastergram obtained by simulations of the neuronal dynamics. Methods and symbols are as in Fig. 6. The pulses were initiated by a "shock" for $x < 0.5$. Parameters that are different from those in Fig. 6 (B) are: $\tau_{sEE} = 50$ ms, $\tau_{sEI} = 2$ ms, $\tau_{sIE} = \tau_{sII} = 5$ ms, $g_{EE} = 250$, $g_{IE} = 21$, $\sigma_{IE} = 0.7$, $g_{EI} = 20$, $g_{II} = 17$. Adapted from [22]

the firing. Fast pulses are robust with respect to initial conditions. If they are stable, a strong enough initial shock will evoke them. Fast pulses are hardly affected by slow excitation, as was shown in models of networks of excitatory neurons [1]. At high g_{II} values, fast traveling pulses cannot propagate because of the "repulsive" interaction between inhibitory interneurons. Instead, the network exhibits irregular pulses.

Slow pulses are characterized by E cells firing significantly after the I cells and by a decrease in the potential of the E cells, before a subsequent potential increase until the neuron reaches threshold and fires. Slow pulses can propagate even without slow excitation, but the parameter regime in which they are stable strongly expands as the level of slow E-to-E excitatory conductance g^{s}_{EE} increases. Slow pulse are not robust. Even if they are stable, an initial shock often does not evoke them, and, even if it does, the system dynamics can converge into this state after a long transient with fast or lurching pulse characterization. Slow excitation increases the basin of attraction of slow pulses and the possibility of evoking them with shock initial conditions. Enhancing the I-to-I conductance g_{II} decreases, and then eliminates, the regime in which slow pulses can propagate.

Transition between continuous pulses. As a parameter of the system varies, the transition from a fast-pulse parameter regime to a slow-pulse parameter regime can occur through a bistable regime, in which both types of pulses can propagate. It can also occur continuously, as the velocity of the pulses decreases and the time lead of I cell firing increases relative to E cell firing. A third possibility is that the fast pulse stops propagating when a parameter is varied, and a slow pulse appears in a distant parameter regime.

Lurching pulses are characterized by periodicity in both space and time, and by a time interval between two successive cycles of activity, in which the network is silent. These pulses are generated by an excitatory network if the synaptic delay is large enough. The parameter regime of their existence depends strongly on the footprint synaptic shape – for exponential shape, they appear for lower delay τ_d than for square shape. To enable the appearance of lurching pulses in networks of excitatory and inhibitory neurons without any delay, the E-to-E excitation should be

large and slowly decaying, whereas the E-to-I excitation and the I-to-E inhibition should decay quickly. Under these conditions, the feedback inhibition terminates the activity in each cycle, and the slow inhibition initiates a new cycle of activity. The slow excitation, together with fast feedback inhibition, mimics a situation of an effective excitation with delay.

Irregular pulses appear for large g_{II}. They almost look like continuous traveling pulses with respect to the excitatory population, but inhibitory neurons segregate into two groups which fire with two different delay times with respect to their neighboring excitatory cells. Irregular pulses can be regarded as pulses with "spatio-temporal clustering" of inhibitory cells. These pulses are different from lurching pulses. Lurching pulses are characterized by periods of activity propagation followed by periods of silence and no propagation. During irregular pulses, activity does not stop, there are no silent periods, and the excitatory population is constantly active, cell after cell. The irregular pulses have spatio-temporal periodicity, at least approximately. From this respect, they are similar to lurching pulses.

4.2 Effects of Approximations

The model described here is based on two approximations. First, the sub-threshold neuronal dynamics are described by an integrate-and-fire model. Second, each neuron is allowed to fire only one spike. The first approximation does not seem to affect the main results presented, because the key issue here is that a neuron responds to propagating pulses by integrating the responses of other excitatory and inhibitory neurons and firing if the time-integrated amount of excitation is strong enough. To further support this claim, we replaced the integrate-and-fire scheme by the Morris–Lecar model, which is a version of a conductance-based model [35], and found regimes of fast and slow pulses with bistability between them (not shown).

The one-spike approximation is exact in the limit of a very prolonged refractory period or very strong synaptic depression. In the first case, a neuron cannot fire a second spike before the pulse has completely passed. In the second case, spikes other than the first one do not generate any post-synaptic effect. Far from these limits, however, this approximation can have an effect on the dynamical mechanisms of the slow-pulse propagation. In networks with excitatory populations only, the results of this model are qualitatively similar to the results obtained in simulations of conductance-based models (compare [5, 25] and the results described here with [1]). For example, if we assume that only the first spike elicits an EPSP for the parameters of Fig. 8 in [1], the velocity decreases by only 15%. In two-population systems, however, other scenarios can occur. For example, in our model, the potential of excitatory neurons becomes negative (hyperpolarized) before it becomes positive again and the neuron can fire. If the I cells can fire several fast spikes, they can prevent the E cell from firing. The model described in this work can be regarded, therefore,

as a paradigm for illuminating a possible mechanism for slow-pulse propagation, which is the advanced firing of I cells. We have carried out preliminary simulations of conductance-based neuronal models, in which cells can fire many spikes, and these demonstrated a transition from a fast pulse to a slow pulse as g_{IE} increases. As in the one-spike model, inhibitory cells lead significantly in firing during the slow pulse, but not during the fast pulse, and slow E-to-E excitation was found to be important for propagation of slow, but not fast, pulses. Similar results were obtained in [36, 37] in simulations of conductance-based models. Further analytical and numerical investigation of models with more spikes should be carried out to see whether there are alternative mechanisms for slow-pulse propagation, in addition to the mechanism described here.

References

1. D. Golomb and Y. Amitai, J. Neurophysiol. **78**, 1199 (1997). 403, 404, 406, 407, 422, 427, 428
2. M.J. Gutnick, B.W. Connors, and D.A. Prince, J. Neurophysiol. **48**, 1321 (1982). 404
3. B.W. Connors, Nature **310**, 685 (1984). 404
4. D. Golomb, J. Neurophysiol. **79**, 1 (1998). 404
5. G.B. Ermentrout, J. Comput. Neurosci. **5**, 191 (1998). 404, 405, 407, 409, 428
6. Y. Tsau, L. Guan, and J.-Y. Wu, J. Neurophysiol. **80**, 978 (1998). 404
7. J.-Y. Wu, L. Guan, and Y. Tsau, J. Neurosci. **19**, 5005 (1999). 404
8. R. Miles, R.D. Traub, and R.K. Wong, J. Neurophysiol. **60**, 1481 (1988). 404
9. R.D. Traub, J.G.R Jefferys, and R. Miles, J. Physiol. (London) **472**, 267 (1993). 404
10. R. Demir, L.B. Haberly, and M.B. Jackson, J. Neurophysiol. **80**, 2727 (1998). 404
11. Y. Chagnac-Amitai and B.W. Connors, J. Neurophysiol. **61**, 747 (1989). 404
12. Y. Chagnac-Amitai and B.W. Connors, J. Neurophysiol. **62**, 1149 (1989). 404
13. N. Laaris, G.C. Carlson, and A. Keller, J. Neurosci. **20**, 1529 (2000). 404
14. J.-Y. Wu and L. Guan, J. Neurophysiol. **86**, 2416 (2001). 404
15. M.V. Sanchez-Vives and D.A. McCormick, Nature Neurosci. **3**, 1027 (2000). 404
16. Y. Shu, A. Hasenstaub, and D.A. McCormick, Nature **423**, 288 (2003). 404
17. M.F. Bear, B.W. Connors, and M.A. Paradiso, *Neuroscience: Exploring the Brain*, 3rd edn, (Lippincott Williams & Wilkins, Philadelphia, 2007). 404
18. D. Golomb, X.-J. Wang, and J. Rinzel, J. Neurophysiol. **75**, 750 (1996). 404, 406
19. J. Rinzel, D. Terman, X.-J. Wang, and B. Ermentrout, Science **279**, 1351 (1998). 404, 412
20. D. Golomb and G.B. Ermentrout, Proc. Natl. Acad. Sci. USA **96**, 13480 (1999). 404, 405, 407, 409, 411
21. D. Golomb and G.B. Ermentrout, Network **11**, 221 (2000). 404, 409, 410
22. D. Golomb and G.B. Ermentrout, Phys. Rev. Lett. **86**, 4179 (2001). 404, 415, 427
23. D. Golomb and G.B. Ermentrout, Phys. Rev. E **65**, 061911 (2002). 404, 413, 419, 420, 422, 423, 424, 426
24. H.C. Tuckwell, *Introduction to Theoretical Neurobiology*, (Cambridge University Press, Cambridge, UK, 1988). 405
25. P.C. Bressloff, Phys. Rev. Lett. **82**, 2979 (1999). 405, 408, 412, 428
26. P.C. Bressloff, J. Math. Biol. **40**, 169 (2000). 405, 408
27. D. Hansel, G. Mato, and C. Meunier, Neural Comp. **7**, 307 (1995). 405
28. D. Hansel, G. Mato, C. Meunier, and L. Neltner, Neural Comp. **10**, 467 (1998). 407
29. W.H. Press, S.A. Teukolsky, W.T. Vetterling, and B.P. Flannery, *Numerical Recipes in C*, (Cambridge University Press, Cambridge, UK, 1992). 412
30. E. Doedel, Cong. Num. **30**, 265 (1981). 412
31. B. Ermentrout, *Simulating, Analyzing, and Animating Dynamical Systems: A Guide to XPPAUT for Researchers and Students (Software, Environments, Tools)*, (SIAM, Philadelphia, 2002). 412

32. F.C. Hoppensteadt and E.M. Izhikevich, *Weakly Connected Neural Networks*, (Springer-Verlag, New-York, 1997). 421
33. D. Golomb, D. Hansel, and G. Mato, Mechanisms of synchrony of neural activity in large networks, in *Handbook of Biological Physics, Volume 4: Neuro-Informatics and Neural Modelling*, edited by F. Moss, S. Gielen, (Elsevier Science, Amsterdam, 2001) pp. 887–968. 424
34. D. Hansel and G. Mato, Phys. Rev. Lett. **86**, 4175 (2001). 424
35. J. Rinzel and G.B. Ermentrout, Analysis of neural excitability and oscillations. in: *Methods in Neuronal Modeling: From Ions to Networks*, 2nd edn. edited by C. Koch, I. Segev, (MIT Press, Cambridge, MA, 1998), pp. 251–291. 428
36. M. Bazhenov, I. Timofeev, M. Steriade, and T.J. Sejnowski, J. Neurosci. **22**, 8691 (2002). 429
37. A. Compte, M.V. Sanchez-Vives, D.A. McCormick, and X.-J. Wang, J. Neurophysiol. **89**, 2707 (2003). 429

Wave Phenomena in Neuronal Networks

W.C. Troy

Abstract We study traveling wave solutions of a system of integro-differential equations which describe the activity of large-scale networks of excitatory neurons on spatially extended domains. The independent variables are the activity level, u, of a population of excitatory neurons which have long-range connections and a recovery variable, v. There is a critical value of the parameter β ($\beta_* > 0$) that appears in the equation for v, at which the eigenvalues of the linearization of the system around the rest state $(u,v) = (0,0)$ change from real to complex. In contrast to previous studies which analyzed properties of traveling waves when the eigenvalues are real, we examine the range $\beta > \beta_*$, where the eigenvalues are complex. In this case, our numerical experiments indicate that there is a range of parameters over which families of wave fronts and solitary and multi-bump waves can coexist as stable solutions. In two-space dimensions, we show how single-bump, double-bump and multi-ring waves form in response to a Gaussian-shaped stimulus. We also show how a stable, one-armed rotating spiral wave can form and fill the entire domain. All of these phenomena can be initiated at any point in the medium, as they are not driven by an underlying time-dependent periodic pacemaker, and they do not depend on the presence of a persistent external input.

1 Introduction

Functional behavior of the central nervous system includes such diverse phenomena as information processing from different receptor zones, sleep and the control of autonomic functions [14, 28, 29, 38]. These processes require cooperation between ensembles of cells organized into large-scale, spatially extended neuronal networks. Considerable attention has been given to the study of traveling waves of activity in

Troy W.C.
Department of Mathematics, University of Pittsburgh, Pittsburgh, PA 15260, USA,
troy@math.pitt.edu

Troy, W.C.: *Wave Phenomena in Neuronal Networks.* Lect. Notes Phys. **751**, 431–452 (2008)
DOI 10.1007/978-3-540-78217-9_17

such networks. This includes both experimental [4, 5, 6, 8, 10, 16, 25, 32, 35, 36, 42, 43, 46, 47, 48, 49, 52] and theoretical [1, 2, 3, 7, 12, 13, 15, 17, 18, 19, 20, 21, 22, 23, 24, 31, 37, 38, 39, 40, 44, 51, 53] studies.

In 1973, Wilson and Cowan [51] derived a two-variable system of integro-differential equations to describe the behavior of populations of excitatory and inhibitory neurons in neuronal networks. In a landmark 1977 paper, Amari [1] gave a detailed mathematical analysis of the Wilson–Cowan-type system:

$$\begin{aligned} \frac{\partial E}{\partial t} &= \int_{-\infty}^{\infty} w_{EE}(x-x')f(E)\mathrm{d}x' - \int_{-\infty}^{\infty} w_{IE}(x-x')f(I)\mathrm{d}x' - E + h_1 + \Psi_1, \\ \tau\frac{\partial I}{\partial t} &= \int_{-\infty}^{\infty} w_{EI}(x-x')f(E)\mathrm{d}x' - \int_{-\infty}^{\infty} w_{II}(x-x')f(I)\mathrm{d}x' - I + h_2 + \Psi_2, \end{aligned} \tag{1}$$

where $E(x,t)$ denotes the activity (i.e., voltage) of a population of excitatory neurons located at position x and time t and $I(x,t)$ represents the activity of a population of inhibitory neurons. The connection functions w_{ij} are positive, even, continuous and integrable; h_1, h_2 and τ are constants, and external input is given by $\Psi_1(x,t)$ and $\Psi_2(x,t)$. The firing rate function, f, is non-negative and sigmoidal-shaped. For simplicity, Amari assumes that $\Psi_1 = \Psi_2 = 0$ and $f(s) = H(s)\ \ \forall s \in \mathrm{R}$, where H is the Heaviside function. He shows that there is a range of parameters over which (1) has solitary traveling wave solutions. These solutions are essentially dissipative solitons. They have fixed shape and speed and they are annihilated in collisions. Pinto and Ermentrout [39] extended Amari's analysis and studied properties of solitary traveling waves in a simplified version of (1).

In 2001, Pinto and Ermentrout [40] proposed a modification of (1) in order to model the spread of excitation waves in slices of brain cortex in which synaptic inhibition is pharmacologically blocked [8, 10, 30, 52]. Their model consists of the system

$$\begin{aligned} \frac{\partial u}{\partial t} &= -u - v + \int_{-\infty}^{\infty} w(x-x')H(u(x',t)-\theta)\mathrm{d}x', \\ \tau\frac{\partial v}{\partial t} &= (u - \beta v), \end{aligned} \tag{2}$$

where the activity u of excitatory neurons is modulated by a local recovery variable, v, which could represent "spike frequency adaptation, synaptic depression or some other slow process that limits excitation of the network." The coupling, w, is positive, even, continuous and integrable. The firing rate, H, is the Heaviside function which we define by

$$H(u-\theta) = \begin{cases} 1 & \forall u \geq \theta, \\ 0 & \forall u < \theta, \end{cases} \tag{3}$$

where $\theta > 0$ is the threshold level for u. Pinto and Ermentrout studied solitary traveling waves in parameter regimes where the linearization of (4) around the rest state

$(u,v) = (0,0)$ has real eigenvalues. Subsequently, Pinto et al. [41] generalized the results in [40] and used topological shooting and Evans function methods to study the existence and stability properties of solutions. Richardson et al. [45] make use of the results in [39, 40, 41] to study the effects of electric fields on solitary traveling waves in the mammalian cortex. Reviews are given in [11, 26].

The studies described above assumed that the linearization of the system around the rest state had real eigenvalues. In this chapter, we investigate properties of traveling wave solutions when the eigenvalues are *complex*. For this, we follow [17, 18, 39, 45] and study the modification of (2) given by

$$\begin{aligned} \frac{\partial u}{\partial t} &= -u - v + \int_{-\infty}^{\infty} w(x-x')H(u(x',t)-\theta)\mathrm{d}x', \\ \frac{\partial v}{\partial t} &= \varepsilon(\beta u - v), \end{aligned} \tag{4}$$

where

$$w(x) = \frac{1}{2}\mathrm{e}^{-|x|} \quad \forall x \in \mathrm{R}, \tag{5}$$

and $\varepsilon > 0$, $\beta > 0$ are constants. We focus our attention on the range $0 < \varepsilon < 1$. In this setting, we will see, in Sect. 2, that the eigenvalues change from real to complex as β passes through the critical value $\beta^* = \frac{(\varepsilon-1)^2}{4\varepsilon}$ from below. When $\beta > \beta^*$, we find that the dynamics of (4) are richer than in the real eigenvalue case. Furthermore, these dynamics closely resemble electrophysiological phenomena observed in clinical and experimental studies [4, 5, 6, 16, 30, 38, 52].

In one-space dimension (Sects. 2, 3, 4, 5), we study families of wave fronts, solitary and multi-bump traveling waves. There is a range of parameters where these different types of waves can coexist as stable solutions. Because the eigenvalues are now complex, technical difficulties arise which make existence proofs more challenging than in the real eigenvalue case. These difficulties lead to several open problems which will be stated as we proceed.

We extend our investigation to two-space dimensions in Sect. 6. By analogy with the one-dimensional case, we study both single- and multi-bump traveling waves. Classical in vivo experiments showed that such waves exist in the feline cortex [4, 5, 6], and recently, they have been discovered in the intact brain of freely moving mice [16]. They have also been found in both tangential and coronal brain slice experiments [30, 52]. Our numerical experiments show how single- and multi-bump waves can form in response to an initial stimulus. We also show how a perturbation of a traveling wave can evolve into a stable, one-armed spiral wave which fills the entire domain. These phenomena can be initiated at any point in the medium, as they are not driven by an underlying time-dependent periodic pacemaker, and they do not depend on the presence of a persistent external input. The analysis of spiral wave formation has practical significance, since it recently led to the discovery of rotating waves in the rat neocortex [30].

Conclusions and suggestions for future research are given in Sect. 7.

2 Traveling Waves

Traveling wave solutions of (4) have the form $(u,v)=(U(z),V(z))$, where $z=x+ct$, and satisfy

$$\begin{aligned} cU'(z) &= -U-V+\int_{-\infty}^{\infty} w(z-z')H(U(z')-\theta)\mathrm{d}z', \\ cV'(z) &= \varepsilon(\beta U-V), \end{aligned} \tag{6}$$

where $w(z-z')=\frac{1}{2}\mathrm{e}^{-|z-z'|}$. It is easily verified that (6) is equivalent to

$$\begin{aligned} c^2U''+c(1+\varepsilon)U'+\varepsilon(\beta+1)U = {} & c\tfrac{\mathrm{d}}{\mathrm{d}z}\textstyle\int_{-\infty}^{\infty} w(z-z')H(U-\theta)\mathrm{d}z' \\ & +\varepsilon\textstyle\int_{-\infty}^{\infty} w(z-z')H(U-\theta)\mathrm{d}z'. \end{aligned} \tag{7}$$

Linearizing (7) around the rest state $U=0$, we obtain

$$c^2H''+c(1+\varepsilon)H'+\varepsilon(\beta+1)H=0. \tag{8}$$

Following [41] and [50], we assume, without loss of generality, that $c>0$. The eigenvalues associated with (8) are

$$\mu^{\pm}=\frac{\lambda^{\pm}}{c}=\frac{-(\varepsilon+1)\pm\mathrm{i}\sqrt{4\beta\varepsilon-(\varepsilon-1)^2}}{2c}. \tag{9}$$

It follows from (9) and the restriction $0<\varepsilon<1$ that

$$\mu^{\pm}\text{ are real }\iff 0<\beta\le\beta_*=\frac{(\varepsilon-1)^2}{4\varepsilon}. \tag{10}$$

The properties of traveling waves were examined in [17, 18, 19, 39, 41, 45] for real eigenvalues. In [50], we recently studied the properties of traveling waves when $\beta>\beta_*$ and $\mu^{\pm}=\alpha\pm\gamma\mathrm{i}$, where

$$\alpha=\mathrm{Re}(\mu^{\pm})=\frac{-(\varepsilon+1)}{2c}<0\ \text{ and }\ \gamma=\mathrm{Im}(\mu^{\pm})=\frac{\sqrt{4\varepsilon\beta-(\varepsilon-1)^2}}{2c}>0. \tag{11}$$

When $\mu^{\pm}$ are complex, we found that stable traveling waves can exist if

$$0<\varepsilon<1,\ 0<\theta<\min\left(\frac{2\varepsilon}{(\varepsilon+1)^2},\frac{1}{4(\varepsilon+1)}\right),\ \beta>\beta_*=\frac{(\varepsilon-1)^2}{4\varepsilon}. \tag{12}$$

The first two sets of inequalities in (12) are mild restrictions which allow technical arguments to be completed, and the third inequality means that $\mu^{\pm}$ are complex.

Whether $\mu^{\pm}$ are real or complex, the non-local terms in (6) and (7) lead to technical difficulties which make existence proofs especially challenging. Below, we will review how these difficulties arise in the analysis of wave fronts, solitary traveling waves and multi-bump waves. Several open problems will be discussed as we proceed.

3 Wave Fronts

Wave front solutions satisfy

$$c^2U'' + c(1+\varepsilon)U' + \varepsilon(\beta+1)U = c\frac{\mathrm{d}}{\mathrm{d}z}\int_0^\infty w(z-z')dz' + \varepsilon\int_0^\infty w(z-z')\mathrm{d}z', \quad (13)$$

$$\begin{cases} U(z) < \theta \ \forall z < 0, \\ (U(z), U'(z)) \to (0,0) \text{ as } z \to -\infty, \\ U(0) = \theta, \ \ U(z) > \theta \ \forall z > 0, \\ U'(z) \to 0 \text{ as } z \to \infty. \end{cases} \quad (14)$$

Numerical experiments. To understand how solutions of (13) and (14) arise, we consider specific β values and solve the problem

$$\begin{aligned} u_t(x,t) &= -u - v + \frac{1}{2}\int_{-100}^{100} \mathrm{e}^{-|x-x'|}H(u(x',t)-\theta)\mathrm{d}x', \\ v_t(x,t) &= \varepsilon(\beta u - v), \\ u(x,0) &= M\mathrm{e}^{-x^2} \ \text{ and } \ v(x,0) = 0 \ \ \forall x \in [-100,100], \end{aligned} \quad (15)$$

where the limits $(-\infty,\infty)$ in the integral term in (4) are replaced with $[-100,100]$. To compute the wave front solution shown in Fig. 1, we set $M = 0.6$ and solve (15). In [50], our numerical study indicated the existence of at least two branches of wave fronts (Fig. 2). The upper branch, Γ_0^+, consists of stable solutions which exist for all $\beta \in (0, 6.45)$. Further details are given below. The lower branch, denoted by Γ_0^-, consists of a family of unstable solutions. Its properties are described in [50].

Analysis. To begin, we recall that $w(x) = \frac{1}{2}\mathrm{e}^{-|x|}$. Then (13) becomes

$$c^2U'' + c(1+\varepsilon)U' + \varepsilon(\beta+1)U = g(z), \quad (16)$$

where

$$g(z) = \begin{cases} 0.5(c+\varepsilon)\mathrm{e}^z & \forall z \le 0, \\ 0.5(c-\varepsilon)\mathrm{e}^{-z} + \varepsilon & \text{if} \quad z > 0. \end{cases} \quad (17)$$

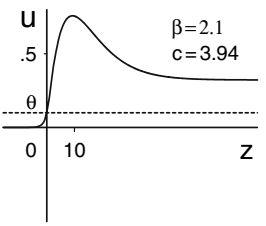

Fig. 1 Stable wave front when $(\varepsilon,\theta) = (0.1, 0.1)$ and $\beta = 2.1 > \beta_* = 2.025$. This solution lies on a branch Γ_0^+ of stable solutions which exist for all $\beta \in (0, 6.45)$ (see Fig. 2)

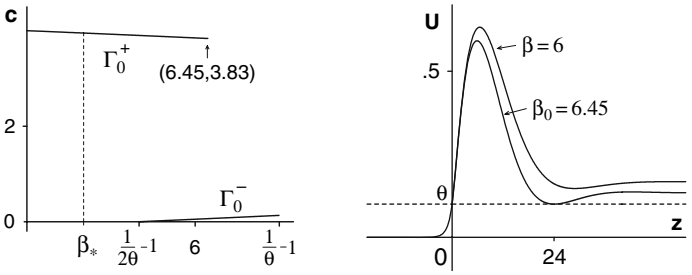

Fig. 2 *Left panel*: branches Γ_0^- and Γ_0^+ of wave front solutions when $(\varepsilon,\theta) = (0.1,0.1)$. The horizontal axis gives β values and the vertical axis represents the wave speed, c. Solutions along Γ_0^+ are stable and correspond to wave speed c_2. Solutions along Γ_0^- are unstable and correspond to the lower wave speed c_1. *Right panel*: two solutions defined by (30) and (31). The solution at $\beta = 6$ lies on Γ_0^+ and is a wave front since it remains strictly above θ on $(0,\infty)$. The solution at $\beta = 6.45$ is not a wave front since it is tangent to $U = \theta$ at $z \approx 24$. When $\beta > 6.45$, the functions defined by (30) and (31) dip below θ; hence they are not wave fronts

On $(-\infty,0]$, the general solution of (16) is

$$U_0(z) = b_1 e^{\alpha z}\cos(\gamma z) + b_2 e^{\alpha z}\sin(\gamma z) + P_0(z), \tag{18}$$

where b_1 and b_2 are constants and $P_0(z)$ is the particular solution

$$P_0(z) = \frac{0.5(\varepsilon + c)}{c^2 + (1+\varepsilon)c + \varepsilon(\beta+1)} e^z \ \ \forall z \le 0. \tag{19}$$

The oscillatory terms $b_1 e^{\alpha z}\cos(\gamma z)$ and $b_2 e^{\alpha z}\sin(\gamma z)$ in (18) are due to the fact that $\mu^{\pm}$ are complex. Recall from (11) that $\alpha = \mathrm{Re}(\mu^{\pm}) < 0$. Thus, to satisfy the condition $U_0(-\infty) = U_0'(-\infty) = 0$, we conclude that $b_1 = b_2 = 0$, and (18) and (19) reduce to

$$U_0(z) = \frac{0.5(\varepsilon + c)}{c^2 + (1+\varepsilon)c + \varepsilon(\beta+1)} e^z \ \ \forall z \le 0. \tag{20}$$

Substituting the condition $U_0(0) = \theta$ into (20) gives the algebraic equation

$$\frac{0.5(\varepsilon + c)}{c^2 + (1+\varepsilon)c + \varepsilon(\beta+1)} = \theta. \tag{21}$$

It follows from (20) and (21) that

$$U_0(z) = \theta e^z \ \ \forall z \le 0. \tag{22}$$

Note that $U_0(z) < \theta$ on $(-\infty,0)$ and $(U_0(-\infty), U_0'(-\infty)) = (0,0)$, as required by (14). It remains to determine the behavior of solutions when $z > 0$. The first step is to solve (21) for c. This gives the two values

$$c_1 = \frac{0.5 - \theta(\varepsilon+1) - \sqrt{(0.5 - \theta(1+\varepsilon))^2 - 4\varepsilon\theta\,(\theta(\beta+1) - 0.5)}}{2\theta} \tag{23}$$

and

$$c_2 = \frac{0.5 - \theta(\varepsilon+1) + \sqrt{(0.5-\theta(1+\varepsilon))^2 - 4\varepsilon\theta\,(\theta(\beta+1)-0.5)}}{2\theta}. \tag{24}$$

Recall from (12) that $0 < \varepsilon < 1$ and $0 < \theta < \frac{1}{4(\varepsilon+1)}$. This and (23) and (24) imply that

$$\begin{cases} c_1 < 0 \text{ and } c_2 > 0 \text{ if } \beta_* < \beta < \frac{1}{2\theta} - 1, \\ c_1 = 0 \text{ and } c_2 > 0 \text{ if } \beta = \frac{1}{2\theta} - 1, \\ 0 < c_1 \le c_2 \text{ if } \frac{1}{2\theta} - 1 < \beta \le \frac{1}{2\theta} - 1 + \frac{1}{4\varepsilon\theta^2}\,(0.5-\theta(1+\varepsilon))^2, \\ c_1 \text{ and } c_2 \text{ are complex if } \beta > \frac{1}{2\theta} - 1 + \frac{1}{4\varepsilon\theta^2}\,(0.5-\theta(1+\varepsilon))^2. \end{cases} \tag{25}$$

The interval $(0,\infty)$. When $z > 0$, the general solution of (16) is

$$U_1(z) = k_1 \mathrm{e}^{\alpha z}\cos(\gamma z) + k_2 \mathrm{e}^{\alpha z}\sin(\gamma z) + P_1(z), \tag{26}$$

where α and γ are defined in (11) and $P_1(z)$ is the particular solution

$$P_1(z) = \frac{0.5(c-\varepsilon)}{c^2 - (1+\varepsilon)c + \varepsilon(\beta+1)}\mathrm{e}^{-z} + \frac{1}{\beta+1}. \tag{27}$$

To preserve continuity at $z = 0$, we require that $(U_1(0), U_1'(0)) = (U_0(0), U_0'(0))$. This and (26) and (27) show that k_1 and k_2 are uniquely defined by

$$k_1 = \theta - P_1(0) \;\text{ and }\; k_2 = \frac{1}{\gamma}\left(\theta(1-\alpha) - P_1{}'(0) + \alpha P_1(0)\right). \tag{28}$$

To complete the proof that a solution satisfies conditions (14) for a traveling wave front, we need to show that $U_1(z)$ satisfies

$$U_1(z) > \theta \;\; \forall z > 0 \;\text{ and }\; \lim_{z\to\infty} U_1'(z) = 0. \tag{29}$$

Thus, if (29) holds, then the full solution of (13) and (14) is given by

$$U(z) = \begin{cases} \theta \mathrm{e}^z < \theta \;\; \forall z < 0, \\ U_1(z) > \theta \;\; \forall z > 0. \end{cases} \tag{30}$$

The Upper Branch. The upper branch Γ_0^+ of wave fronts corresponds to the faster wave speed $c = c_2$ defined in (24). Our study of the example $(\varepsilon,\beta) = (0.1, 0.1)$ indicates that Γ_0^+ extends below $\beta = \beta_*$ down to $\beta = 0$ (Fig. 2, left panel). When $0 < \beta \le \beta_* = 2.025$, the eigenvalues $\mu^{\pm}$ are real, and solutions along Γ_0^+ are monotonic for large z. When $\beta > \beta_*$, the eigenvalues are complex, and solutions

have an oscillatory component when $z > 0$. In particular, when $c = c_2$, it follows from (26), (27) and (28) that

$$U_1 = k_1 e^{\alpha z}\cos(\gamma z) + k_2 e^{\alpha z}\sin(\gamma z) \tag{31}$$

$$+\frac{0.5(c_2-\varepsilon)e^{-z}}{(c_2)^2-(1+\varepsilon)c_2+\varepsilon(\beta+1)}+\frac{1}{\beta+1}. \tag{32}$$

If $U_1(z) > \theta\ \forall z > 0$, then (31) implies that $U_1'(z) \to 0$ as $z \to \infty$, and therefore (29) holds. Thus, it is sufficient to show that

$$U_1(z) > \theta\ \ \forall z > 0. \tag{33}$$

However, it is difficult to prove (33) when $\beta > \beta_*$, since the oscillatory component $k_1 e^{\alpha z}\cos(\gamma z) + k_2 e^{\alpha z}\sin(\gamma z)$ of (31) can cause $U_1(z)$ to dip below the threshold level θ at some point in $(0,\infty)$. Figure 2 (right panel) illustrates the behavior of solutions for two different values of β. The solution at $\beta = 6$ qualifies as a wave front since it remains strictly above θ on the entire interval $(0,\infty)$. However, when $\beta = 6.45$, the solution is tangent to $U = \theta$ at $z \approx 24$, and hence it does not satisfy (29). Likewise, when $\beta > 6.45$, the function U_1 does not satisfy (29) since it dips below θ at a positive value of z. Thus, we conjecture that the interval of existence of Γ_0^+ is $(0, 6.45)$. Because of the technical difficulties in proving (29), the proof of this conjecture is beyond the scope of our investigation and remains an open problem. Along Γ_0^+, our numerical study indicates that solutions are stable. The proof of stability might be accomplished by an extension of the Evans function methods in [12].

Finally, we point out that, although generalizations and insightful approximations have previously been given [17, 39], the complete set of requirements (14) for the existence of non-stationary wave fronts has not yet been verified, even for the real eigenvalue regime. In particular, the property $U(z) > \theta\ \forall z > 0$ has not yet been proved when $\mu^{\pm}$ are real. Thus, whether $\mu^{\pm}$ are real or complex, the proof of existence of wave fronts remains a challenging open problem.

4 Solitary Traveling Waves

In this section, we analyze properties of solitary traveling wave solutions when the eigenvalues $\mu^{\pm}$ are complex. These solutions satisfy

$$c^2U'' + c(1+\varepsilon)U' + \varepsilon(\beta+1)U = c\frac{\mathrm{d}}{\mathrm{d}z}\int_0^a w(z-z')\mathrm{d}z' + \varepsilon\int_0^a w(z-z')\mathrm{d}z', \tag{34}$$

where $c > 0$, and

$$\begin{cases} U(0) = U(a) = \theta \text{ for some } a = a(c) > 0, \\ U(z) \neq \theta \text{ if } z \neq 0 \text{ or } z \neq a, \\ (U(z), U'(z)) \to (0,0) \text{ as } |z| \to \infty. \end{cases} \tag{35}$$

Because $w(x) = \frac{1}{2}e^{-|x|}$, (34) can be written in the equivalent form

$$c^2U'' + c(1+\varepsilon)U' + \varepsilon(\beta+1)U = s(z), \tag{36}$$

where

$$s(z) = \begin{cases} 0.5(c+\varepsilon)e^z(1-e^{-a}) \ \ \forall z \le 0, \\ 0.5c\left(e^{-z} - e^{(z-a)}\right) + 0.5\varepsilon\left(2 - e^{-z} - e^{(z-a)}\right) \ \text{ if } \ 0 < z < a, \\ 0.5(\varepsilon - c)(e^a - 1)e^{-z} \ \ \forall z \ge a. \end{cases} \tag{37}$$

Numerical experiments. To understand how solitary traveling waves arise, we proceed as in the last section and solve (15). Figure 3 shows a stable solution computed by solving (15) with $\beta = 4$ and $M = 5$. This solution lies on a branch, Γ_1^+, of stable solitary traveling waves (Fig. 5). It co-exists with the stable wave front predicted by the bifurcation diagram for the branch Γ_0^+ in Fig. 2. Below, we outline an analytical approach developed in [50] for analyzing solitary traveling waves. To show that conditions (35) hold, we need to analyze the behavior of solutions over the separate intervals $(-\infty, 0]$, $(0, a]$ and (a, ∞) (see Fig. 3). As we proceed, we will explain how conditions (35) are violated when $\beta \ge 16$, so that the interval of existence of Γ_1^+ is $\beta_* < \beta < 16$. Several open problems are presented.

The interval $(-\infty, 0]$. On the interval $(-\infty, 0]$, the problems (36) and (37) reduce to

$$c^2U'' + c(1+\varepsilon)U' + \varepsilon(\beta+1)U = 0.5(c+\varepsilon)(1-e^{-a})e^z \ \ \forall z \le 0. \tag{38}$$

The general solution of (38) is

$$U_2 = h_1 e^{\alpha z}\cos(\gamma z) + h_2 e^{\alpha z}\sin(\gamma z) + P_2(z), \tag{39}$$

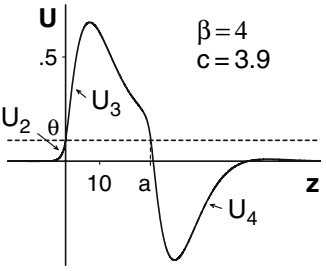

Fig. 3 Solitary traveling wave when $(\beta, \varepsilon, \theta) = (4, .1, .1)$. The component U_2 of the solution is defined by $U_2(z) = \theta e^z \ \ \forall z \le 0$. The component $U_3(z)$ is defined on $[0, a] = [0, 25]$ and has the form given by (45) and (46). The component $U_4(z)$ is defined on $[a, \infty) = [25, \infty)$ and has the form given by (57) and (58)

where α and γ are defined in (11) and $P_2(z)$ is the particular solution

$$P_2 = \frac{0.5(\varepsilon+c)(1-\mathrm{e}^{-a})}{c^2+(1+\varepsilon)c+\varepsilon(\beta+1)}\mathrm{e}^z \ \ \forall z \le 0. \tag{40}$$

We need to show that there are values $c>0$ and $a>0$ such that

$$U_2(z) < \theta \ \ \forall z \in (-\infty,0),\ U_2(-\infty) = U_2'(-\infty) = 0 \ \text{ and } \ U_2(0) = \theta. \tag{41}$$

Recall from (11) that $\alpha = \mathrm{Re}(\mu^{\pm}) < 0$. Thus, to satisfy the condition $U_2(-\infty) = U_2'(-\infty) = 0$, we conclude from (39) that $h_1 = h_2 = 0$, and therefore

$$U_2(z) = \frac{0.5(\varepsilon+c)(1-\mathrm{e}^{-a})}{c^2+(1+\varepsilon)c+\varepsilon(\beta+1)}\mathrm{e}^z \ \ \forall z \le 0. \tag{42}$$

Substituting the requirement $U_2(0) = \theta$ into (42) leads to

$$\frac{0.5(\varepsilon+c)(1-\mathrm{e}^{-a})}{c^2+(1+\varepsilon)c+\varepsilon(\beta+1)} = \theta. \tag{43}$$

Combining (42) and (43) gives $U_2(z) = \theta \mathrm{e}^z \ \ \forall z \le 0$ (see Fig. 3). Note that $U_2(z) = U_0(z)$, where $U_0(z)$ was defined in (22).

The interval $(0,a]$. On the interval $(0,a]$, the problems (36) and (37) reduce to

$$c^2U'' + c(1+\varepsilon)U' + \varepsilon(\beta+1)U = 0.5c\left(\mathrm{e}^{-z} - \mathrm{e}^{(z-a)}\right) + 0.5\varepsilon\left(2 - \mathrm{e}^{-z} - \mathrm{e}^{(z-a}\right). \tag{44}$$

The general solution of (44) is

$$U_3(z) = m_1\mathrm{e}^{\alpha z}\cos(\gamma z) + m_2\mathrm{e}^{\alpha z}\sin(\gamma z) + P_3(z), \tag{45}$$

$$P_3(z) = \frac{0.5(c-\varepsilon)\mathrm{e}^{-z}}{c^2-(1+\varepsilon)c+\varepsilon(\beta+1)} - \frac{0.5(\varepsilon+c)\mathrm{e}^{z-a}}{c^2+(1+\varepsilon)c+\varepsilon(\beta+1)} + \frac{1}{\beta+1}. \tag{46}$$

We need to show that there are values $c>0$ and $a = a(c) > 0$ which satisfy the algebraic condition (43), and such that

$$U_3(0) = U_2(0) = U_3'(0) = U_2'(0) = \theta,\ \ U_3(z) > \theta \ \ \forall z \in (0,a),\ U_3(a) = \theta. \tag{47}$$

The first step in proving (47) is to keep ε in $(0,1)$ fixed and solve (43) for e^{-a}. This gives

$$\mathrm{e}^{-a(c)} = \frac{0.5(\varepsilon+c) - \theta\left(c^2+(1+\varepsilon)c+\varepsilon(\beta+1)\right)}{0.5(\varepsilon+c)}. \tag{48}$$

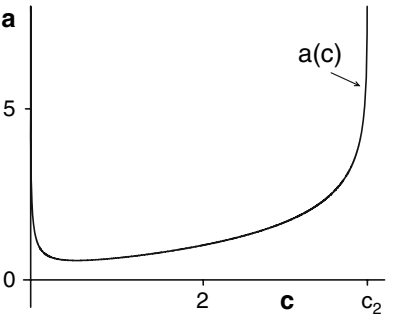

Fig. 4 The function $a(c)$, as defined in (48), when $(\varepsilon,\theta) = (1,0.1)$ and $\beta = \frac{1}{2\theta} - 1 = 4$

Since the right-hand side of (48) is zero at $c = c_1$ and $c = c_2$, it follows that (see Fig. 4)

$$a(c) > 0 \ \ \forall c \in (c_1, c_2) \ \text{ and } \ \lim_{c \to c_2^-} a(c) = \lim_{c \to c_1^+} a(c) = \infty. \tag{49}$$

To preserve continuity at $z = 0$, we require that $(U_3(0), U_3'(0)) = (U_2(0), U_2'(0)) = (\theta, \theta)$. Combining this with (45) and (46) shows that m_1 and m_2 in (45) are defined by

$$m_1 = \theta - P_3(0) \ \text{ and } \ m_2 = \frac{1}{\gamma}\left(\theta(1-\alpha) - P_3'(0) + \alpha P_3(0)\right). \tag{50}$$

Substituting (45) into the requirement $U_3(a) = \theta$ gives

$$m_1 \mathrm{e}^{\alpha a} \cos(\gamma a) + m_2 \mathrm{e}^{\alpha a} \sin(\gamma a) + P_3(a) = \theta, \tag{51}$$

where $a = a(c)$ satisfies (48). Thus, to prove that solitary traveling waves exist, it is necessary to show that there are values $c > 0$ such that the function

$$g(c) = m_1 \mathrm{e}^{\alpha a(c)} \cos(\gamma a(c)) + m_2 \mathrm{e}^{\alpha a(c)} \sin(\gamma a(c)) + P_3(a(c)) - \theta \tag{52}$$

satisfies $g(c) = 0$. For general β, it is difficult to analyze $g(c)$. However, when $\beta = \frac{1}{2\theta} - 1$, the analysis is more tractable, and, in [50], we used (48), (49) and (50) to show that $g(c)$ has infinitely many zeros on (c_1, c_2) when $\beta = \frac{1}{2\theta} - 1$. In particular, we proved the following result:

Theorem 1. (Troy and Shusterman [50]) *Let (ε,θ) satisfy (12), and let $\beta = \frac{1}{2\theta} - 1$. There are infinitely many values $c \in (c_1, c_2)$ and corresponding solutions U of (7), such that $a(c) > 0$ and*

$$U(z) = \begin{cases} \theta e^z & \forall z \le 0, \\ U_3(z) & 0 < z < a(c), \end{cases} \tag{53}$$

where $U_3(z)$ is defined in (45) and (46), and satisfies

$$U_3(0) = U_3'(0) = U_3(a(c)) = \theta. \tag{54}$$

Remarks. To complete the proof that the solutions described in Theorem 1 are solitary traveling waves, one must show that the function $U(z) - \theta$ has *exactly* two zeros, $z = 0$ and $z = a$, on $(-\infty, \infty)$. That is,

$$U(z) < \theta \ \ \forall z < 0,\ U(z) > \theta\ \forall z \in (0,a) \ \text{ and } \ U(z) < \theta \ \ \forall z > a. \tag{55}$$

Numerical experiments. Proving that condition (55) holds is a challenging problem which has not yet been resolved. To gain insight, we have performed extensive numerical experiments. Figure 5 shows the different types of behavior that are possible for the representative parameter set $(\varepsilon, \theta) = (0.1, 0.1)$. The right panel shows a solution computed at $\beta = \frac{1}{2\theta} - 1 = 4$. Its graph indicates that all of the conditions for a solitary traveling wave are satisfied. The bifurcation curve Γ_1^+ (left panel) denotes the family of solitary traveling waves which form a continuation of the solution computed at $\beta = 4$. This branch extends from $\beta = \beta_* = 2.025$, where $\mu^{\pm}$ become complex, to $\beta = 16$. The solution at $\beta = 16$ (right panel) is tangent to $U = \theta$ at $z = a \approx 21$ and therefore does not satisfy (55). When $\beta > 16$, solutions intersect $U = \theta$ more that twice, and these functions cannot be solitary traveling waves either. Thus, we conjecture that the branch Γ_1^+ ends at $\beta = 16$. Our results also suggest that solutions on Γ_1^+ are stable.

The interval (a, ∞). To prove that the solutions in Theorem 1 are solitary traveling waves, one must show that condition (55) holds. The final requirement of (55) is to prove that $U(z) < \theta$ when $z > a$. On (a, ∞), the problems (36) and (37) reduce to

$$c^2 U'' + c(1+\varepsilon)U' + \varepsilon(\beta+1)U = 0.5(\varepsilon - c)(\mathrm{e}^a - 1)\mathrm{e}^{-z}. \tag{56}$$

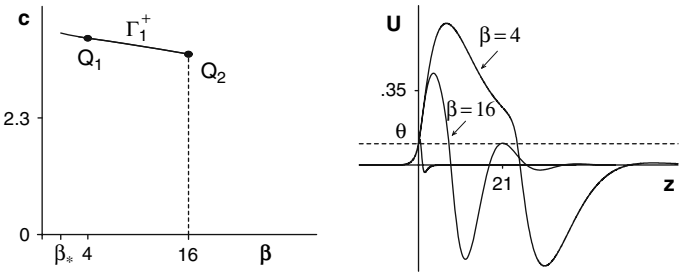

Fig. 5 *Left panel*: the bifurcation curve Γ_1^+ for a branch of solitary traveling waves when $(\varepsilon, \theta) = (0.1, 0.1)$. The vertical axis gives wave speed, c, and the horizontal axis denotes values of β. The branch Γ_1^+ extends from $\beta = \beta_* = 2.025$ to $\beta = 16$. *Right panel*: solutions on Γ_1^+ at Q_1 where $\beta = \frac{1}{2\theta} - 1 = 4$ and $c \approx 3.9$, and at Q_2 where $(\beta, c) = (16, 3.56)$. The solution at Q_2 is not a solitary traveling wave since it is tangent to $U = \theta$ at $z \approx 21$. When $\beta > 16$, the solutions rise above θ at the second maximum, so they are not solitary traveling waves. Thus, Γ_1^+ ends at $\beta = 16$

The general solution of (56) is

$$U_4(z) = m_3 e^{\alpha z}\cos(\gamma z) + m_4 e^{\alpha z}\sin(\gamma z) + P_4(z), \tag{57}$$

$$P_4(z) = \frac{0.5(\varepsilon - c)(e^a - 1)}{c^2 - c(1+\varepsilon) + \varepsilon(\beta+1)} e^{-z}. \tag{58}$$

The values m_3 and m_4 are uniquely determined by the continuity condition

$$U_4(a) = U_3(a) \text{ and } U_4'(a) = U_3'(a). \tag{59}$$

We need to show that

$$U_4(z) < \theta \ \ \forall z > a, \text{ and } (U_4(z), U_4'(z)) \to (0,0) \text{ as } z \to \infty. \tag{60}$$

If $U_4(z) < \theta \ \ \forall z > a$, then (57) and (58) imply that $(U_4(z), U_4'(z)) \to (0,0)$ as $z \to \infty$. However, it is difficult to prove that $U(z)$ remains below θ on (a,∞), since the oscillatory component $m_3 e^{\alpha z}\cos(\gamma z) + m_4 e^{\alpha z}\sin(\gamma z)$ of (57) can cause $U_4(z)$ to exceed the threshold level, θ, at some point in (a,∞). Thus, the proof that (60) holds when $\mu^{\pm}$ are complex remains an open problem.

Finally, we point out that solitary traveling waves can also exist when $\mu^{\pm}$ are real [17, 39, 45]. In this setting, the proof that condition (55) holds has not yet been given. As a first step toward resolving this issue, in [50] we considered the real eigenvalue case when $w(x) = \frac{1}{2}e^{-|x|}$ and developed a comparison argument to prove that $U(z) < \theta$ on (a,∞). It is hoped that extensions of our methods will allow all of the conditions (55) to be proved, in both the real and complex eigenvalue regimes.

5 Multi-bump Waves

In this section, we briefly examine multi-bump traveling waves. In [50], we used a Sturm–Liouville comparison argument to explain why such solutions are not expected when $\mu^{\pm}$ are real. However, when $\mu^{\pm}$ are complex, our numerical experiments indicate that the structures of solutions are much richer, and families of stable multi-bump solutions can coexist. Below, we formulate the two-bump traveling wave problem. We also discuss the generalization to N-bump solutions.

It follows from (7) that two-bump traveling waves are solutions of the problem

$$\begin{aligned} c^2U'' + c(1+\varepsilon)U' + \varepsilon(\beta+1)U =& c\frac{\mathrm{d}}{\mathrm{d}z}\int_0^a w(z-z')\mathrm{d}z' + \varepsilon\int_0^a w(z-z')\mathrm{d}z' \\ &+ c\frac{\mathrm{d}}{\mathrm{d}z}\int_b^{\mathrm{d}} w(z-z')\mathrm{d}z' + \varepsilon\int_b^d w(z-z')dz', \end{aligned} \tag{61}$$

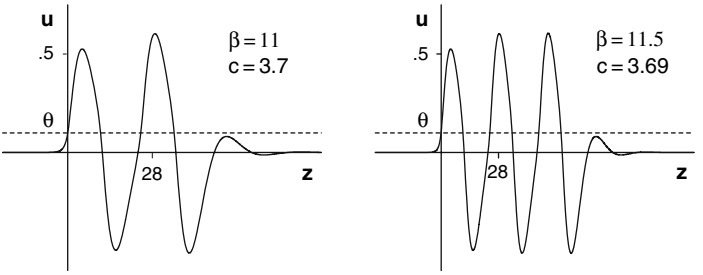

Fig. 6 Two-bump and three-bump traveling wave solutions when $(\varepsilon,\theta)=(0.1,0.1)$

where

$$\begin{cases} U(0)=U(a)=U(b)=U(d)=\theta \text{ for some } d>b>a>0, \\ U(z)\neq\theta \text{ if } z\notin\{0,a,b,d\}, \\ (U(z),U'(z))\to(0,0) \text{ as } |z|\to\infty. \end{cases} \tag{62}$$

A simple extension of (61) and (62) gives the criteria satisfied by N-bump traveling waves. Figure 6 illustrates stable two-bump and three-bump traveling wave solutions when $\beta=11$ and $\beta=11.5$, respectively. To compute these solutions, we solved (15) with $M=0.6$ as the amplitude of the initial condition. Our numerical experiments also indicate that when the amplitude is of lesser magnitude, e.g., $M=0.13$, solitary traveling waves can form and coexist with these solutions. In general, to show that an N-bump wave exists, it is necessary to prove that the solution satisfies $U(z)=\theta$ exactly $2N$ times in $(-\infty,\infty)$. As with wave fronts and solitary traveling waves, the non-local terms in (61) lead to formidable technical difficulties in proving this property, and, up till now, there are no rigorous results. In contrast, non-local terms do not appear in reaction-diffusion equations, where the existence of multibump solutions can be shown using topological shooting methods [27]. Thus, proving the existence and stability of N-bump waves remains a challenging open problem.

6 Two Dimensions

In this section, we extend (4) to the two-dimensional system

$$\begin{aligned} u_t &= -u-v+\int_{-\infty}^{\infty}\int_{-\infty}^{\infty} w(x-x',y-y')H(u-\theta)\mathrm{d}x'\mathrm{d}y'+\zeta(x,y,t), \\ v_t &= \varepsilon(\beta u-v). \end{aligned} \tag{63}$$

Here $w(x-x')=\frac{1}{2}\mathrm{e}^{-|x-x'|}$ in (4) has been replaced with

$$w(x-x',y-y')=w\left(\sqrt{(x-x')^2+(y-y')^2}\right). \tag{64}$$

The function $\zeta(x,y,t)$ denotes external input. Rigorous analysis of (63) is difficult because of the non-local term, and, up till now, there are few mathematical results. Thus, as a first step toward understanding the dynamics of wave formation in (63) and (64), we follow [33, 34] and show how to use a Fourier transform method to replace (63) with an equivalent PDE system. The two-dimensional Fourier transform is defined by

$$\widehat{F}(\rho) \equiv (2\pi)^{-1} \int\int_{R^2} \exp(-\mathrm{i}(\alpha x+\beta y))\rho(x,y)\mathrm{d}x\,\mathrm{d}y, \tag{65}$$

where α and β are real. Applying (65) to the first equation in (63), and using the convolution property, we obtain

$$\widehat{F}(u_t+u+v-\zeta) = \widehat{F}(w)\widehat{F}(H(u-\theta)). \tag{66}$$

When $w(x,y)$ depends only on $\sqrt{x^2+y^2}$, it is known (e.g., see [34], Appendix) that $\widehat{F}(w)$ is a function of $\sqrt{\alpha^2+\beta^2}$. The coupling, w, in (63) and (64) has this property. However, the form of $\widehat{F}(w)$ is complicated for the couplings of our specific interest. Thus, to make the analysis more tractable, we approximate $\widehat{F}(w)$ with a rational function of $\sqrt{\alpha^2+\beta^2}$. Following [34], we assume that $\widehat{F}(w)$ has the simplified form:

$$\widehat{F}(w) = \frac{A}{B+(\alpha^2+\beta^2-M)^2}. \tag{67}$$

Substituting (67) into (66), multiplying both sides by $B+(\alpha^2+\beta^2-M)^2$ and making use of the identities

$$(\alpha^2+\beta^2)^2\widehat{F}(p) = \widehat{F}(\nabla^4 p) \;\text{ and }\; (\alpha^2+\beta^2)\widehat{F}(p) = -\widehat{F}(\nabla^2 p), \tag{68}$$

we obtain

$$\widehat{F}\left(\left(\nabla^4+2M\nabla^2+B+M^2\right)(u_t+u+v-\zeta)\right) = \widehat{F}\left(AH(u-\theta)\right). \tag{69}$$

Applying the inverse transform to both sides of (69) gives the PDE

$$\left(\nabla^4+2M\nabla^2+B+M^2\right)(u_t+u+v-\zeta) = AH(u-\theta). \tag{70}$$

Thus, the system (63) is formally equivalent to

$$\begin{aligned} \left(\nabla^4+2M\nabla^2+B+M^2\right)(u_t+u+v-\zeta(x,y,t)) &= AH(u-\theta), \\ v_t &= \varepsilon(\beta u-v). \end{aligned} \tag{71}$$

By way of example, we assume, throughout the rest of this section, that $w(x,y)$ in (63) has the specific form

$$w(x,y) = w(r) = 2.1\mathrm{e}^{-r},\;\; r=\sqrt{x^2+y^2}. \tag{72}$$

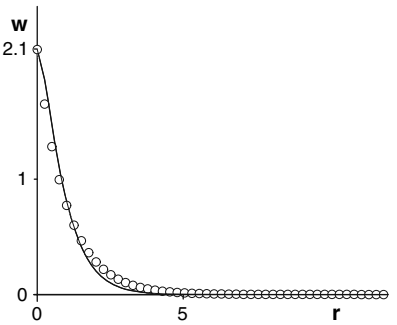

Fig. 7 *Solid curve* denotes the function $w(r) = 2.1\mathrm{e}^{-r}$ defined in (72). The *open circles* denote the function w_{approx}, defined in (73), which approximates $w(r)$ to within 0.03 absolute error

Applying the inverse Fourier transform to both sides of (67), we approximate the coupling function in (72) by

$$w_{\text{approx}} = \widehat{F}^{-1}\left(\frac{A}{B+(\alpha^2+\beta^2-M)^2}\right) \quad \text{where} \quad (A,B,M) = (7,0.52,-2.5). \tag{73}$$

Figure 7 shows that the function w_{approx}, defined in (73), is a close approximation to the coupling, $w(r)$, in (72). Thus, we replace the integro-differential equation system (63), (64), (65), (66), (67), (68), (69), (70), (71), (72) with the equivalent PDE system (71), where $(A,B,M) = (7,0.52,-2.5)$. We solve (71) with an Euler time step of length $\Delta t = 0.35$, using finite differences to approximate spatial derivatives on disk-shaped spatial domains $\Omega = \{(x,y)|x^2+y^2 < \mathrm{R}^2\}$, and with Neumann conditions on the boundary. Wave activity can be initiated by setting $\zeta(x,y,t) \equiv 0$ and using initial conditions of the form

$$(u(x,y,0),v(x,y,0)) = \left(M\mathrm{e}^{-\lambda\sqrt{(x-\bar{x})^2+(y-\bar{y})^2}},0\right), \quad x^2+y^2 \le \mathrm{R}^2. \tag{74}$$

Alternatively, we can keep u and v initially at rest, i.e., $(u(x,y,0),v(x,y,0)) \equiv (0,0)$, and initiate waves with an external stimulus.

As in Sect. 5, we investigate the dynamics of wave formation in the range $\beta > \beta_*$, where $\mu^{\pm}$ are complex. Below, we give a brief description of the results of our numerical simulations. These include

- (i) Two-dimensional traveling waves.
- (ii) Spiral wave formation.

(i) Two-dimensional Traveling Waves

Classical in vivo experiments showed that multi-bump waves exist in the feline cortex [4, 5, 6], and recently, they have been discovered in the intact brain of freely moving mice [16]. They have also been found in both tangential and coronal brain slice experiments [30, 52]. Here, we assume that $\zeta(x,y,t) \equiv 0 \quad \forall t \ge 0$, and initiate two-dimensional wave formation with starting conditions of the form (74). Figure 8 illustrates a stable solitary traveling wave which propagates

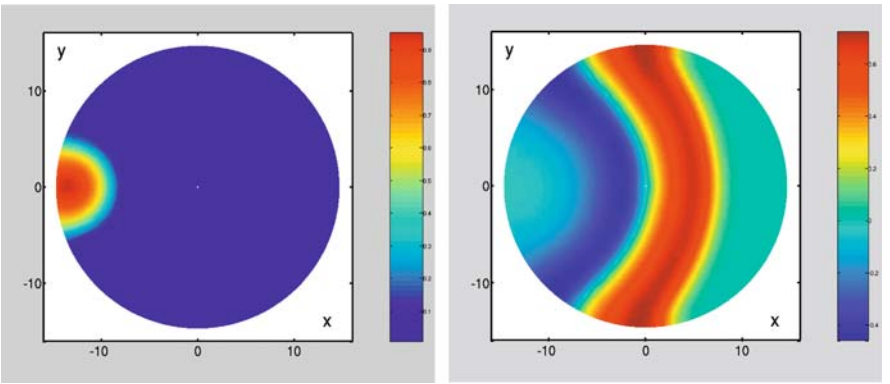

Fig. 8 A solitary traveling wave solution of (71) is initiated at $(\bar{x},\bar{y}) = (-14,0)$ and propagates across the domain $\Omega = \{(x,y)|\ 0 \le x^2+y^2 \le 15^2\}$ from left to right. The parameters are $(A,B,M) = (7,0.52,-2.5)$ and $(\beta,\varepsilon,\theta) = (4,0.1,0.1)$. The initial values are given in (75). The *left panel* shows the wave at $t = 5$ shortly after it has been formed. The *right panel* shows the solution when $t = 15$. The movie showing this wave can be found at www.math.pitt.edu/∼troy/springer/singlebumpwave.mpg

across the region $\Omega = \{(x,y)|\ 0 \le x^2+y^2 \le 15^2\}$. This solution is initiated at $(\bar{x},\bar{y}) = (-14,0)$ by

$$(u(x,y,0),v(x,y,0)) = \left(0.5\mathrm{e}^{-0.1\sqrt{(x+14)^2+y^2}},0\right),\ \ (x,y) \in \Omega. \tag{75}$$

Figure 9 shows stable double-bump traveling waves which coexist with the stable solitary traveling wave described above. For clarity, the domain has been expanded in size to $\Omega = \{(x,y)|\ 0 \le x^2+y^2 \le 25^2\}$. The solution in the left panel is similar to

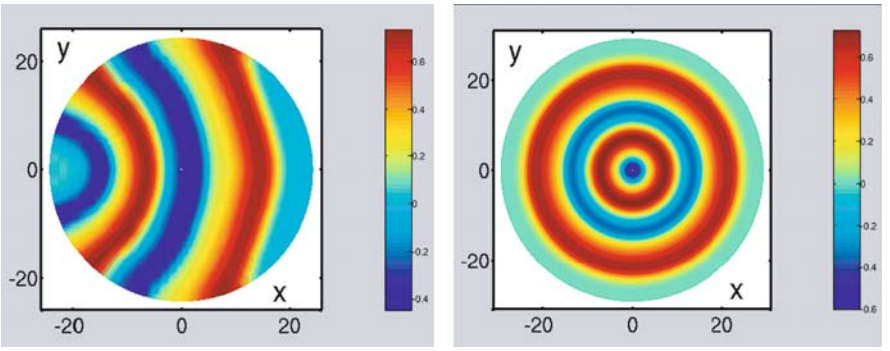

Fig. 9 Double-bump traveling wave solutions of (71). The parameters are $(A,B,M) = (7,0.52,-2.5)$ and $(\beta,\varepsilon,\theta) = (4,0.1,0.1)$. These solutions coexist with a stable solitary traveling wave. The solution in the *left panel* is similar to a plane wave and is initiated at $(\bar{x},\bar{y}) = (-24,0)$ with starting values given in (76). The two-ring wave in the *right panel* is initiated at $(\bar{x},\bar{y}) = (0,0)$ with starting values given in (77). The movie showing the wave in the left panel is at www.math.pitt.edu/∼troy/springer/doulebumpwave.mpg

a two-bump plane wave and is initiated at $(\bar{x},\bar{y}) = (-24,0)$ by

$$(u(x,y,0),v(x,y,0)) = \left(20\mathrm{e}^{-0.02\sqrt{(x+24)^2+y^2}},0\right), \quad (x,y) \in \Omega. \tag{76}$$

The double-ring-shaped wave in the right panel is initiated at $(\bar{x},\bar{y}) = (0,0)$ by

$$(u(x,y,0),v(x,y,0)) = \left(20\mathrm{e}^{-0.05\sqrt{x^2+y^2}},0\right), \quad (x,y) \in \Omega. \tag{77}$$

As β increases further, our numerical experiments indicate that the number of bumps in the traveling wave solutions also increases. Proofs of the existence and stability of these solutions remain as open problems.

(ii) Spiral Wave Formation

Our analysis of spiral waves has practical significance, since it has recently led to the discovery of rotating waves in the rat neocortex [30]. As a first step, we study the simplified class of solutions known as rigid rotating waves. These have the form

$$(u,v) = (u(r,\phi),v(r,\phi)), \; r = \sqrt{x^2+y^2} \text{ and } \phi = \theta - \omega t. \tag{78}$$

We let $f = H(u-\theta)$ and $\zeta(x,y,t) \equiv 0$ in (71), substitute (78) and obtain

$$\begin{aligned} \left(\nabla^4 + 2M\nabla^2 + B + M^2\right)(u+v-\omega\frac{\partial u}{\partial \phi}) &= AH(u-th), \\ -\omega\tau\frac{\partial v}{\partial \phi} &= \beta u - v. \end{aligned} \tag{79}$$

For the parameter set $(\beta,\omega) = (0,-1)$, we define the limiting solution

$$(u,v) = \begin{cases} \left(\dfrac{A}{B+M^2} + \left(\theta - \dfrac{A}{B+M^2}\right)\mathrm{e}^{r-\phi},0\right), & r>0 \text{ and } \phi > r, \\ (0,0), & r \geq 0 \text{ and } \phi \leq r, \end{cases}$$

where $0 < \theta < \frac{A}{B+M^2}$. The function defined in (80) is a continuous solution of (79) on the set $\{r>0,\ \phi \neq r\}$ and is discontinuous along the curve $\{r \geq 0,\ \phi = r\}$ (see Fig. 10).

Numerical experiments. To gain insight when $\beta > 0$, we describe the results of our numerical simulations. First, we note that, when $\beta = 0$, the tip of the spiral wave remains fixed at the point $(0,0)$ (see Fig. 10). However, when $\beta > 0$, the tip moves and spiral waves drift as they rotate (see Fig. 11). We describe two ways in which such waves can form. Firstly, we set $\zeta(x,y,0) \equiv 0$ and assume that the initial conditions are given by (76). Initially, a traveling wave, which is similar to the solution shown in Fig. 8, forms at $(x,y) = (-14,0)$. Shortly after the wave has formed, an external stimulus is applied, and this causes a break at one end of the solution. The free end begins to curl inward and a spiral wave forms and quickly fills

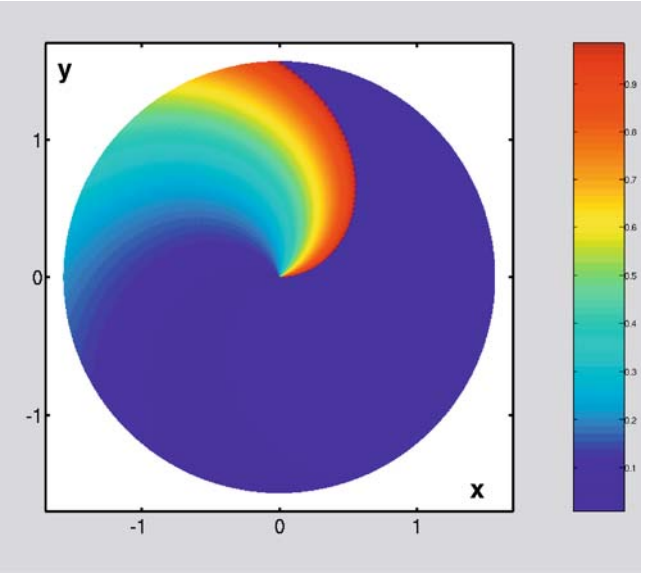

Fig. 10 The projection onto the (x,y) plane of the u component of the rigid rotating wave defined in (80). Here, $(\beta,\omega)=(0,-1)$ and $v\equiv 0$. The movie showing this spiral can be found at www.math.pitt.edu/∼troy/springer/rigidspiral.mpg

the entire domain (Fig. 11). As the solution rotates, it drifts across the domain, and its tip passes through the square marker placed at $(x,y)=(-4,2)$. The right-hand panel of Fig. 11 shows the time course of the solution at $(-4,2)$. When $t>160$, the amplitudes of the oscillations increase as the tip of the spiral wave passes through $(-4,2)$.

In [50], we recently demonstrated a second method of spiral wave formation. Here, the coupling is inhomogeneous and a sequence of appropriately timed external stimuli is applied at the point $(x,y)=(0,0)$. At first this causes ring-shaped waves to form and propagate outward from $(0,0)$. There is a point on the leading edge of each wave where the amplitude of the activity is a minimum because the coupling is inhomogeneous. Repeated stimulation of the system causes the leading edge of the waves to weaken at the point of minimal amplitude, and eventually a small break occurs at this point. Subsequently, the solution evolves into a stable, one-armed spiral wave which fills the entire domain. This technique of spiral wave formation can be initiated at any point in the medium, is not driven by an underlying time-dependent periodic pacemaker and does not depend on the presence of a constant external input. In a previous study, Chu, Milton and Cowan [9] used a similar technique to produce spiral waves in a discrete integrate-and-fire network.

As β increases from $\beta=0$, we conjecture that a functional analysis-based continuation method will allow for the continuation of the limiting case solution (80) into a spiral wave solution of (63) which is continuous on the entire domain. However, to date, there are no rigorous results other than our limiting solution, and the

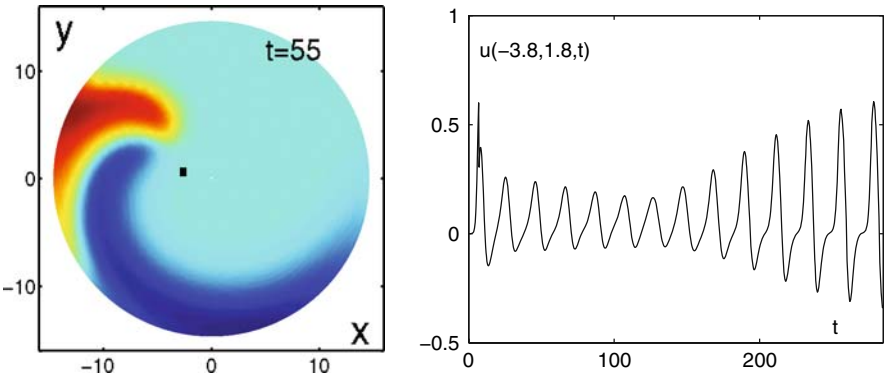

Fig. 11 Spiral wave solution of (71) when $\beta = 3$, $(\varepsilon, \theta) = (.1, .1)$ and $(A, B, M) = (7, 0.52, -2.5)$. The *left panel* shows the solution at $t = 55$. A *square* has been placed at $(x, y) = (-4, 2)$, and the *right panel* shows the time course of the solution at this point. As the rotating wave drifts across the domain, its tip crosses the point $(-4, 2)$. This is indicated by the increasing amplitudes in the oscillations when $t > 200$. The movie showing this spiral can be found at www.math.pitt.edu/∼troy/springer/nonrigidspiral.mpg

proof of existence of spiral waves when $\beta > 0$ remains an open problem. As with the traveling wave solutions, we also note that our spiral wave results apply to the PDE system (71). It is hoped that future extensions of our work will lead to new results for the full integro-differential equation model (63), (64), (65), (66), (67), (68), (69), (70), (71), and (72).

7 Conclusions

In this chapter, we analyzed the dynamic behavior of a system of integro-differential equations that models the activity of excitatory neurons on large-scale, spatially extended domains. The independent variables represent the activity level of a population of excitatory neurons with long-range connections (u) and recovery (v). We considered positive connection functions and a Heaviside firing rate. In one-space dimension, we assumed symmetric connections and examined the existence of traveling wave solutions in different parameter regimes where the linearization of the system around the rest state $(u, v) = (0, 0)$ has complex eigenvalues. When the eigenvalues are real, both wave fronts and solitary traveling waves can exist. By contrast, when the eigenvalues are complex, the range of behavior is much richer, and our numerical experiments show that wave fronts, solitary traveling waves and multibump waves can coexist as stable solutions. In all these cases, formidable technical difficulties preclude the completion of existence proofs. In a related paper [50], we considered a particular coupling and developed a technique which, for the first time, overcomes these difficulties and completes the proof of existence of solitary traveling waves in the real eigenvalue regime. However, in general, the extension of

our methods to allow existence proofs to be completed when the eigenvalues are complex remains an open problem.

Our one-dimensional results have facilitated the study of wave formation in two-space dimensions. Here, for the non-local model, we considered a PDE approximation which includes both symmetric and asymmetric couplings. For symmetric couplings, we showed numerically how single- and double-bump traveling waves can form. In addition, we described how an appropriately timed stimulus causes a break in a wave, and subsequently the solution evolves into a spiral wave which fills the entire two-dimensional domain. It remains an open problem to extend our results for the PDE system to the full non-local model.

Our theoretical results may have important experimental implications for future research. In particular, we found that the dynamics of the system undergo a qualitative transition when the eigenvalues of the linearization around the rest state become complex; this suggests that identifying these bifurcation points might be possible experimentally by tracking changes in the functional behavior of neuronal networks.

Acknowledgments The author thanks Jack Cowan for useful discussions, and especially for pointing out the early papers of Burns and his colleagues. This research was supported by NSF Grant DMS0412370.

References

1. S. Amari, Biol. Cybern. **27**, 77–87 (1977). 432
2. E. Brown, J. Gao, P. Holmes, R. Bogacz, M. Gilzenrat, and J.D. Cohen, Int. J. Bif. Chaos **15**, 803–826 (2005). 432
3. P. Bressloff and S.E. Folias, SIAM J. Appl. Math. **65**, 131–151 (2004). 432
4. B.D. Burns, J. Physiol. **111**, 50–68 (1950). 432, 433, 446
5. B.D. Burns, J. Physiol. **112**, 156–175 (1951). 432, 433, 446
6. B.D. Burns and B. Grafstein, J. Physiol. **118**, 412–433 (1952). 432, 433, 446
7. G. Buzsaki and A. Draguhn, Science **304**, 1926–1929 (2004). 432
8. R.D. Chervin, P.A. Pierce, and B.W. Connors, J. Neurophys. **60**, 1695–1713 (1988). 432
9. P.H. Chu, J. Milton, and J.D. Cowan, Inter. J. Bif. Chaos **4**, 237–243 (1992). 449
10. B.W. Connors and Y. Amati, in *Epilepsy: Models, Mechanisms and Concepts*, edited by P.A. Schwartkroin, (Cambridge University Press, U.K. 1993), pp. 388–423. 432
11. S. Coombes, Byol. Cybern. **93**, 91–108 (2005). 433
12. S. Coombes and M.R. Owen, SIAM J. Dyn. Sys. **34**, 574–600 (2004). 432, 438
13. S. Coombes and M.R. Owen, Phys. Rev. Lett. **94**, 148102 (2005). 432
14. J.C. Eccles, *The Understanding of the Brain*, McGraw-Hill, (New York 1973 2003), pp. 1627–1647. 431
15. G.B. Ermentrout and J.B. McLeod, Proc. Roy. Soc. Edin. Sect. A **123**, 461–478 (1993). 432
16. I. Ferezou, S. Bolea, and C. Petersen, Neuron **50**, 617–629 (2006). 432, 433, 446
17. S. Folias and P. Bressloff, SIAM J. Appl. Math. **65**, 131–151 (2004). 432, 433, 434, 438, 443
18. S. Folias and P. Bressloff, Phys. Rev. Lett. **95**, 208107 (2004). 432, 433, 434
19. S. Folias and P. Bressloff, SIAM J. Dyn. Sys. **3**, 378–407 (2004). 432, 434
20. D. Golomb and Y. Amati, J. Neurophysiol. **79(1–2)**, 1199–1211 (1997). 432
21. Y. Guo and C. Chow, SIAM J. Dyn. Sys. **4**, 217–248 (2005). 432
22. Y. Guo and C. Chow, SIAM J. Dyn. Sys. **4**, 249–281 (2005). 432
23. J. Glanz, Science **277**, 1758–1760 (1997). 432

24. D. Golomb, **79**, 1–12, 1335–1348 (1998). 432
25. D. Golomb and Y. Amati, **78**, 1199–1211 (1997). 432
26. B. Gutkin, D. Pinto, and B. Ermentrout, J. Physiol. Paris **97(2–3)**, 209–219 (2003). 433
27. S.P. Hastings, SIAM J. Appl. Math. **42**, 247–260 (1982). 444
28. J.A. Hobson, *Dreaming: An Introduction to the Science of Sleep*, (Oxford University Press, New York, 2004). 431
29. J.A. Hobson and R.W. McCarley, Amer. J. Psychiatry **134**, 1335–1348 (1977). 431
30. X. Huang, W.C. Troy, Q. Yang, H. Ma, C. Laing, S. Schiff, and J.Y. Wu, J. Neurosci. **24**, 9897–9902 (2004). 432, 433, 446, 448
31. M.A.P. Idiart and L.F. Abbott, Network **4**, 285–294 (1993). 432
32. D. Kleinfield, K.R. Delaney, M.S. Fee, J.A. Flores, D.W. Tank, and A. Galperin, J. Neurophys. **72**, 1402–1419 (1994). 432
33. E. Krisner, J. Math. Anal. Appl. **291**, 165–179 (2004). 445
34. C. Laing and W.C. Troy, SIAM J. Appl. Dyn. Sys. **2**, 487–516 (2003). 445
35. Y.W. Lam, L.B. Cohen, M. Wachowiak, and M.R. Zochowski, J. Neurosci. **20**, 749–762 (2000). 432
36. R. Miles, R.D. Traub, and R.K. Wong, J. Neurophys. **60**, 1481–1496 (1988). 432
37. J. Milton, T. Mundel, U. an der Heiden, J. Sprire, and J. Cowan, *Handbook of Brain Theory and Neural Networks*, (MIT Press, Cambridge, 1994), pp. 994–996. 432
38. J. Milton and P. Jung, *Epilepsy as a Dynamic Disease*, (Biological and Medical Physics Series, Springer, 2003). 431, 432, 433
39. D. Pinto and B. Ermentrout, SIAM J. Appl. Math. **62**, 206–225 (2001). 432, 433, 434, 438, 443
40. D. Pinto and B. Ermentrout, SIAM J. Appl. Math. **62**, 226–243 (2001). 432, 433
41. D. Pinto, R. Jackson, and G. Wayne, SIAM J. Appl. Dyn. Sys. **4**, 954–984 (2005). 433, 434
42. D.J. Pinto, S.A. Patrick, H.W. Huang, and B. Connors, J. Neurosci. **25**, 8131–8140 (2005). 432
43. J.C. Prechtl, L.B. Cohen, B. Pasaram, P.P. Mitra, and D. Kleinfeld, Proc. Natl. Acad. Sci. USA **94**, 7621–7626 (1997). 432
44. D. Pinto and W.C. Troy, In preparation (2005). 432
45. K. Richardson, S.J. Schiff, and B.J. Gluckman, Phys. Rev. Lett. **94**, 028103 (2005). 433, 434, 443
46. A. Rosenbluth and W.B. Cannon, A. J. Physiol. **135**, 690–741 (1942). 432
47. B. Schechter, Science **274**, (5286), 339 (1996). 432
48. J. Schofflen, R. OOstenveld, and P. Fries, Science **308**, 111–113 (2003). 432
49. I.A. Shevlev, E.N. Tsicalov, A.M. Gorbach, K.P. Budko, and G.A. Sharaev, J. Neurosci. Methods **46**, 49–57 (1992). 432
50. W.C. Troy and V. Shusterman, SIAM. J. Appl. Dyn. Sys. **6**, 263 (2007). 434, 435, 439, 441, 443, 449, 450
51. H.R. Wilson and J.D. Cowan, Kybernetik **13**, 55–80 (1973). 432
52. J.Y. Wu, L. Guan, and Y. Tsau, J. Neurosci. **19**, 5005–5015 (1999). 432, 433, 446
53. L. Zhang, Diff. Integral Eqs. **16**, 513–536 (2003). 432

Spiral Waves and Dissipative Solitons in Weakly Excitable Media

V.S. Zykov

Abstract Spiral waves are among the most prominent examples of spatio-temporal patterns in various excitable media, including heart muscle, the retina of the eye, social amoeba colonies and the chemical Belousov–Zhabotinsky reaction. Recent studies have shown that, in addition to spiral waves, there is another possible waveform, viz. a propagating wave segment that is stationary in size and shape. Such localized spatio-temporal structures in nonlinear dissipative media exhibit all the basic features of dissipative solitons. In this chapter, a free boundary model is presented to describe the shape and velocity of the wave segments. It turns out that a generalization of this model allows us to determine the shape and angular velocity of a spiral wave that is rotating rigidly in a medium of low excitability. Thus, our study demonstrates that dissipative solitons (propagating wave segments) and spiral waves are closely connected to each other and that they represent different solutions in the framework of a common theoretical model.

1 Introduction

Wave structures propagating in excitable media play a very important role in diverse physical, chemical and biological processes and represent a broad and intensively developed field of study in nonlinear dynamical systems [1, 2, 3, 4]. Spiral waves are among the most prominent examples of spatio-temporal patterns in excitable and oscillatory media. They have been observed in systems with quite distinct natures such as social amoeba colonies [5], the chemical Belousov–Zhabotinsky (BZ) reaction [6, 7], heart muscle [8, 9], the retina of the eye [10], the oxidation of CO on platinum single-crystal surfaces [11] and so on.

V.S. Zykov
Institute for Theoretical Physics, Technical University Berlin, Hardenbergstrasse 36, D-10623 Berlin, Germany, zykov@physik.tu-berlin.de

Zykov, V.S.: *Spiral Waves and Dissipative Solitons in Weakly Excitable Media.* Lect. Notes Phys. **751**, 453–473 (2008)
DOI 10.1007/978-3-540-78217-9_18

The light-sensitive version of the BZ reaction has proven to be a very suitable experimental system for studying the dynamics of wave processes in excitable media, since the medium excitability can easily be affected by the illumination intensity [12, 13]. Spatio-temporal variations of the reagent concentrations in this system emerge in the form of traveling excitation waves. They can be visualized on-line with reliable optical tools. Figure 1a shows a snapshot of a rotating spiral wave observed in a thin layer of the BZ reaction [14]. An open end of the wave, the so-called spiral tip, describes a circular pathway which restricts the spiral wave core. Both the spiral wavelength and the size of the spiral core increase as excitability of an excitable medium decreases, until, at the excitable/sub-excitable boundary, they become infinite. At this critical excitability, the unbounded spiral wave has opened up to form an unbounded, nearly planar wave with a free end, which is the critical finger [15]. At lower excitabilities, in the sub-excitable regime, this wave contracts tangentially at its free end.

Recent studies of the photosensitive BZ reaction have shown that, in addition to spiral waves and critical fingers, there is another possible waveform with a free end, viz. a propagating wave segment that is stationary in size and shape [16, 17, 18]. These constant velocity waves have two free ends, and their size and shape are uniquely determined by the excitability of the medium. They are inherently unstable, but they can be easily stabilized by applying an appropriate feedback to the excitability of the medium.

Figure 1b shows an example of a stabilized wave segment propagating through a thin layer of the photosensitive BZ reaction [16, 17]. This wave segment was stabilized by varying the illumination intensity imposed on the reaction medium (thereby varying the excitability) in proportion to the wave size. The locus of the wave size as a function of excitability defines a separatrix that delineates the boundary between spiral wave behavior and contracting wave segments. For a particular excitability, there is an unstable wave segment with a particular size (and shape). In the absence of stabilizing feedback, it will either form two counter-rotating spiral waves or contract tangentially at its free ends and eventually disappear. The asymptote of the

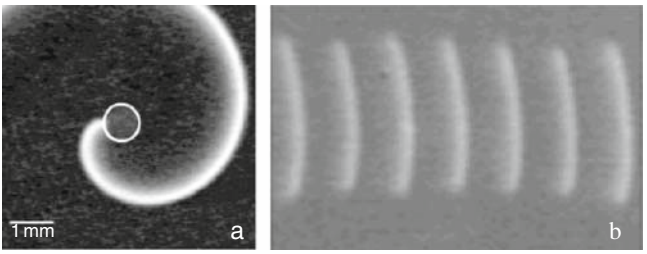

Fig. 1 Spiral wave (**a**) and stabilized wave segment (**b**) in the photosensitive BZ reaction. Different gray levels represent spatial variation of the inhibitor concentration. Thin solid line in (**a**) depicts the trajectory of the spiral wave tip. Superimposed snapshots in (**b**) are shown with an interval of 40.0 s; panels ca. 0.95 cm $\times$ 1.45 cm

locus of wave size as a function of excitability, where the wave size is infinite, is exactly the same excitability boundary between excitable and sub-excitable media as is defined by the critical finger [16, 17].

We note that particle-like waves, similar to the one shown in Fig. 1b, have been found in previous theoretical studies, such as active Brownian particles [19, 20], moving spots in reaction–diffusion systems [21, 22] and filaments in semiconductors [23]. Particle-like waves have also been experimentally observed in a gas discharge system [24, 25] and in the oxidation of CO on single-crystal Pt [26].

These localized spatio-temporal structures in nonlinear dissipative media exhibit all the basic features of dissipative solitons, in contrast to spiral waves which are unrestricted in space. Nevertheless, the purpose of this chapter is not to stress differences, but to demonstrate the close relationship between wave segments and spiral waves in weakly excitable media.

The main tool in our study is a free boundary formulation. This approach has been used by many authors to study pattern selection in two-dimensional excitable media [27, 28, 29, 30, 31, 32, 33, 34]. It reduces the problem of wave propagation in a nonlinear reaction–diffusion system to the kinematics of a sharp interface separating regions of excited and resting states of the medium.

In the next section, we introduce a generic reaction–diffusion system which will set up our study. Then we describe a wave front interaction model which has been proposed recently to specify the shape and velocity of the wave segments [35]. Later, it will be shown that a generalization of this model allows us to determine the shape and angular velocity of an excitation spot moving near a disk boundary, as well as the parameters of a spiral wave rigidly rotating in a medium of low excitability. Thus, our study demonstrates that dissipative solitons (propagating wave segments) and spiral waves are closely connected to each other and represent different solutions in the framework of a common free boundary problem.

2 Excitable Medium Model

Our aim is to elaborate a universal kinematic description for wave patterns propagating in excitable media with various kinetics. As a basis for this study, a generic, two-variable reaction–diffusion model for excitable media is applied:

$$\frac{\partial u}{\partial t} = D\nabla^2 u + F(u,v), \tag{1}$$

$$\frac{\partial v}{\partial t} = \varepsilon G(u,v), \tag{2}$$

where the variables $u(x,y,t)$ and $v(x,y,t)$ represent, respectively, the activator and the inhibitor in a two-dimensional medium with a diffusion constant D, and for the other parameter, we typically have $\varepsilon \ll 1$.

For the functions $F(u,v)$ and $G(u,v)$, we take the FitzHugh–Nagumo type forms [36, 37] which have been widely used previously [31, 33, 35, 38]:

$$F(u,v) = 3u - u^3 - v, \qquad (3)$$
$$G(u,v) = u - \delta,$$

with $\delta = -1.6797$. This system has a single uniform resting state, $(u_0, v_0) = (\delta, 3\delta - \delta^3)$, which is stable with respect to small perturbations. However, a suprathreshold perturbation applied to the resting state (or specific initial condition) gives rise to an undamped, propagating excitation wave. In the excited state, the value of the variable is $u = u_e \approx \sqrt{3}$, which is the largest root of the equation $F(u, v_0) = 0$.

The small parameter ε varies in the range $0.001 < \varepsilon < 0.002$. Unless ε is small, the transition from the resting state to the excited one looks like a sharp interface propagating through the two-dimensional medium. For $\varepsilon = \varepsilon_c \approx 0.002$, the excitability of the medium corresponds to the boundary between the excitable and sub-excitable medium, where the critical finger is observed. When $\varepsilon > \varepsilon_c$, the medium is sub-excitable. This means that the propagation of pulses is still supported in the one-dimensional medium, while propagating wave segments with open ends contract and disappear in the two-dimensional medium. For $\varepsilon < \varepsilon_c$, the medium is excitable and rotating spiral waves can be created by a specific choice of the initial conditions [39]. However, the initial conditions do not influence the rotation velocity and the shape of these waves, as they are completely determined by the medium excitability.

Within the same range of the parameter ε, propagating wave segments of different sizes, corresponding to different excitabilities, can be induced and stabilized by feedback to the excitability of the medium [16, 35]. To realize a stabilizing feedback, we assume the wave segment propagates in the x direction and consider its width as the order parameter. Choosing the symmetry line of the segment as the x-axis, we follow the location, $y_{\max}(t)$, of the tip of the wave along the y-axis, orthogonal to the propagation direction. Then the control signal, $I(t)$, is computed in accordance with a simple proportionality law

$$I(t) = k_{\mathrm{fb}}[y_{\max}(t) - y_{\mathrm{d}}], \qquad (4)$$

where y_{d} determines a desirable segment size. The wave segment is stabilized by negative feedback to the medium excitability with respect to the wave width. To create this type of feedback, the control signal has to suppress the excitability, e.g., to increase the inhibitor production. To this end, the control signal can be simply added to the right-hand side of (2), as was done in [35]. Another method employed in this paper is to increase the value of the small parameter ε in proportion to $I(t)$:

$$\varepsilon = \bar{\varepsilon} + I(t). \qquad (5)$$

Figure 2 shows the trajectory of the tip of wave segments $(x(t), y_{\max}(t))$ computed for the reaction–diffusion model (1), (2), (3) under the feedback determined

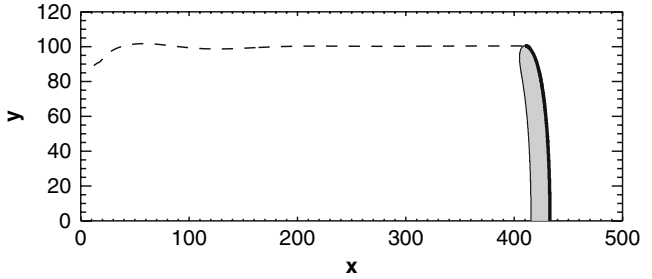

Fig. 2 Stabilization of a propagating wave segment by feedback (4), (5), computed for the reaction–diffusion model (1), (2), (3) with $k_{\mathrm{fb}} = 0.00005$, $y_{\mathrm{d}} = 100$ and $\bar{\varepsilon} = 0.00197$. The trajectory of the segment tip (dashed line) and the final shape of the wave segment are shown. In the shaded region, $u(x,y,t) > 0.2$. A computational grid of 500×500 elements was used; it is co-moving with the propagating wave, with time and space steps $\Delta t = 0.02$ and $\Delta x = 0.3$

by (4), (5). After transient processes, an asymptotic shape of a wave segment is reached with a width $W = y_{\max}(t \to \infty)$. The thick line depicts the wave front, while the thin one specifies the back of the segment.

These computations demonstrate the existence of stabilized wave segments in a reaction–diffusion system. The factors which determine the shape and velocity of the segment are discussed in the next section.

3 Free Boundary Problem for Stabilized Wave Segments

As mentioned above, the boundary of the propagating excited region is very thin compared with the thickness of the wave segment. This is due to the great difference in the characteristic time scales for the activator u and the inhibitor v, induced by the small parameter ε. Obviously, this creates perfect conditions for the application of a free boundary approach for analyzing stabilized wave segments.

There are two factors which determine the normal velocity, c_{n}, of an excitation wave. First, the propagation velocity, c_{p}, of a planar interface in a reaction–diffusion system (1), (2) is a monotonically decreasing function of the slow variable, v, at the moving boundary layer [28, 39]. This function vanishes at a value $v = v^*$ and, if v is close to v^*, the wave velocity can be approximated by a linear relationship

$$c_{\mathrm{p}}(v) = \alpha\sqrt{D}(v^* - v). \tag{6}$$

The constant α and the value v^* are uniquely determined by $F(u,v)$. For instance, for the cubic function defined in (3), $\alpha = \sqrt{1/2}$ and $v^* = 0$. Second, the normal velocity, c_{n}, depends on the local interfacial curvature k [28, 39]:

$$c_{\mathrm{n}} = c_{\mathrm{p}}(v) - Dk. \tag{7}$$

The boundary of a moving wave segment includes parts where $du/dt > 0$ (front of wave) and $du/dt < 0$ (back of wave), as shown in Fig. 2. These two parts coincide at the so-called phase change point, where $du/dt = 0$ [40]. It is convenient to parameterize the local curvature and the velocity of the spot boundary by the arc length, s, measured from this point, assuming that $s < 0$ for sites at the back. Let us denote the normal velocity by $c_n(s)$ and the local curvature of the boundary by $k(s)$. A relationship between these functions can be found from purely geometrical considerations, as illustrated in Fig. 3.

At the midpoint of the stabilized wave segment, $y = 0$, the normal direction coincides with the propagation direction of the segment as a whole along the x-axis, as shown in Fig. 3. Let Θ^+ (Θ^-) specify the angle between the x-axis and the outward pointing normal on the front (back) boundary. Then the normal velocity of the front and of the back should be written in accordance with (7) as $c_n^+ = c_p(v^+) - Dk^+$ and $c_n^- = c_p(v^-) - Dk^-$, where the local curvature of the front (back) is expressed as

$$k^{\pm} = -d\Theta^{\pm}/ds. \tag{8}$$

Near the front of a solitary wave $v^+ = v_0$, so the propagation velocity of the planar wave front is determined, in accordance with (6), by the quantity $\Delta = v^* - v_0$ and can be written as

$$c_0 = \alpha\Delta\sqrt{D}. \tag{9}$$

Let k_m be the local curvature at the midpoint of the stabilized wave. The propagation velocity of the wave segment along the x-axis is therefore $c_s = c_0 - Dk_m$. Now $\varepsilon << 1$, so within the excited region we have $u = u_e(v)$, where $u_e(v)$ is the largest root of equation $F(u,v) = 0$. Hence, the temporal variation of the variable v

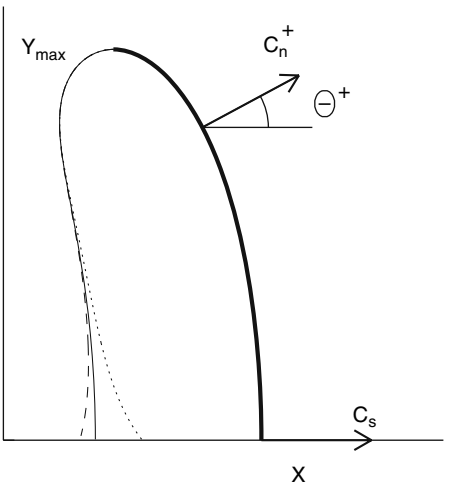

Fig. 3 Boundaries of a propagating wave segment computed as the solution of the free boundary problem (10), (11), (12) for $K_m = 0.0402$ and $B = 0.5108$. The wave front (back) is shown by a thick (thin) solid line. Solutions computed for the slightly different values $B = 0.5101$ and $B = 0.5110$ are shown by dotted and dashed lines, respectively

within the excited region is completely determined by (2). Then, the free boundary problem for the stabilized wave segment can be written as

$$c_0 - Dk^+ = c_s \cos(\Theta^+), \tag{10}$$

$$c(v^-) - Dk^- = -c_s \cos(\Theta^-), \tag{11}$$

$$c_s \mathrm{d}v/\mathrm{d}x = -\varepsilon G(u_e(v), v). \tag{12}$$

Equations (10) and (11) describe the geometry of the front and back of the segment, respectively, while (12) describes the evolution of the slow variable v along the x-axis between the front and the back.

Using (8), one can transform (10) into an ordinary differential equation for the angle Θ^+:

$$D\frac{\mathrm{d}\Theta^+}{\mathrm{d}s} = c_s \cos(\Theta^+) - c_0. \tag{13}$$

Since $\mathrm{d}y^+ = -\mathrm{d}s\cos(\Theta^+)$ and $\mathrm{d}x^+ = \mathrm{d}s\sin(\Theta^+)$, it is straightforward to obtain equations for the Cartesian coordinates (x^+, y^+) of the front [39, 41]:

$$\frac{\mathrm{d}x^+}{\mathrm{d}\Theta^+} = \frac{D\sin(\Theta^+)}{c_s\cos(\Theta^+) - c_0}, \tag{14}$$

$$\frac{\mathrm{d}y^+}{\mathrm{d}\Theta^+} = -\frac{D\cos(\Theta^+)}{c_s\cos(\Theta^+) - c_0}. \tag{15}$$

For the conditions $x^+ = 0$, $\Theta^+ = \pi/2$ and $y^+ = 0$, $\Theta^+ = 0$, the solutions of (14) and (15) have the form

$$\frac{x^+}{D} = \frac{1}{c_s}\ln\frac{c_0}{c_0 - c_s\cos(\Theta^+)}, \tag{16}$$

$$\frac{y^+}{D} = -\frac{\Theta^+}{c_s} + \frac{2c_0}{c_s\sqrt{c_0^2 - c_s^2}}\arctan\frac{(c_0 + c_s)\tan\frac{\Theta^+}{2}}{\sqrt{c_0^2 - c_s^2}}. \tag{17}$$

These expressions specify the shape of the wave front, $x^+ = x^+(y^+)$, for any k_m within the interval $0 < k_m < c_0/D$.

In order to obtain the shape of the back of the wave, the value of the slow variable v on this part of the boundary must be specified. We follow Karma [31] and consider a limiting case, viz. $\Delta << 1$. In the excited region, $-\Delta < v - v^* < \Delta$, so the value of the slow variable remains approximately equal to v^* during the excited state. Thus, one can use the approximation $G(u_e(v), v) = G^*$, where $G^* = G(u_e(v^*), v^*)$. With this approximation, the value of the slow variable, v^-, at the back of the wave can be obtained from (12):

$$v^- = v_0 + \frac{G^*\varepsilon}{c_s}[x^+(y) - x^-(y)]. \tag{18}$$

Substitution of (18) into (11) results in an equation for the back of the wave:

$$D\frac{\mathrm{d}\Theta^-}{\mathrm{d}s} = c_0 - \frac{G^*\varepsilon\alpha}{c_\mathrm{s}}(x^+ - x^-) + c_\mathrm{s}\cos(\Theta^-). \tag{19}$$

After rescaling of space ($S = c_0 s/D$, $X^\pm = c_0 x^\pm/D$ and $K_\mathrm{m} = Dk_\mathrm{m}/c_0$), (19) becomes

$$\frac{\mathrm{d}\Theta^-}{\mathrm{d}S} = 1 - \frac{B(X^+ - X^-)}{(1-K_\mathrm{m})} + (1-K_\mathrm{m})cos(\Theta^-), \tag{20}$$

where

$$B = \frac{G^*\varepsilon}{\alpha^2\Delta^3}. \tag{21}$$

In order to integrate this equation, we rewrite (16) and (17) in dimensionless form and fix K_m within the interval $0 < K_\mathrm{m} < 1$. Numerical integration of (20) in the reverse arc length direction, starting with $\Theta^- = \pi/2$, $X^- = 0$ and $Y^- = Wc_0/D$ at $S = 0$, and taking into account that $\mathrm{d}Y^-/\mathrm{d}S = -\cos(\Theta^-)$ and $\mathrm{d}X^-/\mathrm{d}S = \sin(\Theta^-)$, produces a solution that depends on B. Using a trial-and-error method, one must vary the value of B until the corresponding solution satisfies the second boundary condition, $Y^- = 0$, $\Theta^- = \pi$ (see Fig. 3). Repetition of this process for different K_m yields the relationship between B and K_m shown in Fig. 4. For $K_\mathrm{m} \ll 1$, this dependence is well approximated by the linear relationship

$$K_\mathrm{m} = (B_\mathrm{c} - B)/\beta, \tag{22}$$

where $\beta = 0.63$. We note that for $K_\mathrm{m} = 0$, the wave segment is identical to the critical finger studied in [31, 33], and the corresponding value of B_c, computed for the free

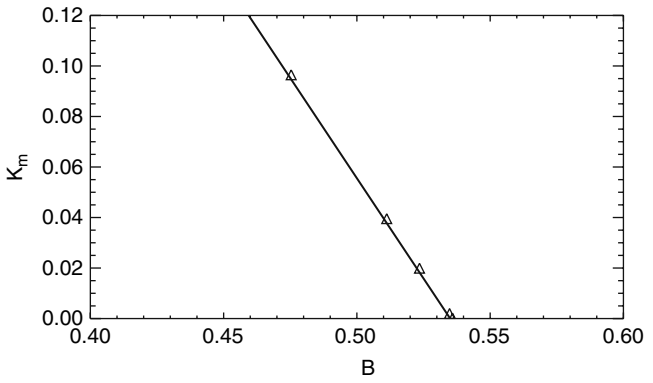

Fig. 4 Values of the curvature, K_m, at the segment midpoint computed for the free boundary problem (10), (11), (12) vs. the parameter B

boundary problem (10), (11), (12), practically coincides with the value $B_c = 0.535$ found for the critical finger [31].

The value $k_m = K_m c_0/D$ determines the width of the wave segment W, in accordance with (17) after the substitution $\Theta^+ = \pi/2$. In the case of small curvature ($Dk_m/c_0 \ll 1$), this relationship is given by the expression (cf. [16, 17])

$$W^2 = \frac{\pi^2 D}{2c_0 k_m}. \tag{23}$$

Substitution of (22) into (23) results in the important relationship

$$W = \frac{\pi D}{c_0\sqrt{2(B_c - B)/\beta}}. \tag{24}$$

We note that relationship (24) is universal, as it contains only the general characteristics of the two-component model (1), (2). It also describes the limiting case of the critical finger when the size of the wave segment goes to infinity. If an external factor influences the value of B, then it determines the value of k_m and, in turn, the width of the wave segment. In particular, it provides a qualitative explanation for the similar relationships obtained in experiments with the light-sensitive BZ reaction and for the Oregonator model [17, 16].

As mentioned above, the propagation velocity, c_s, of the stabilized wave segment along the x-axis depends on the curvature, k_m, at the midpoint. Hence, the velocity is also determined by the value of B and, taking into account (22), can be expressed as

$$c_s = c_0[1 - (B_c - B)/\beta]. \tag{25}$$

Thus, the simplified kinematic description completely determines the shape and propagation velocity of a stabilized wave segment as a function of the dimensionless parameter B.

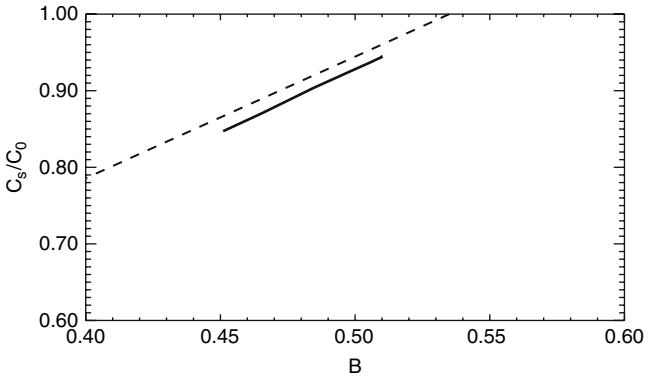

Fig. 5 Velocity of the stabilized wave segments as a function of the parameter B, computed for the system (1), (2), (3) subjected to feedback stabilization according to (4), (5) (solid line) and from relationship (25) (dashed line)

In order to obtain quantitative results for the reaction–diffusion model (1), (2), (3), we note that the computed propagation velocity of a planar wave is $c_0 = 0.212$. Substituting this value into (25), we find the velocity, c_s, of the wave segment as a function of B, as shown in Fig. 5. The dashed line, representing the theoretical results, is in quantitative agreement with the direct integration of the reaction–diffusion model (1), (2), (3), as shown by the solid line. These numerical data are obtained for computations performed with parameter ε varying over the range $0.0018 < \varepsilon < 0.00198$.

4 Wave Spots Rotating Along a Disk Boundary

The wave segment computed for the model system (1), (2), (3) and shown in Fig. 2 undergoes translational motion. In order to simulate the experimental situation reproduced in Fig. 1b, the x-axis is considered here as a symmetry line. On the other hand, one can imagine that this line specifies a no-flux boundary with an infinitely large curvature radius.

In this section, we are interested in a study of a more general case of propagation of a wave segment near a curved boundary. For example, let us assume that a wave segment circulates along the no-flux boundary of a disk of radius r_D. Corresponding computations performed for the system (1), (2), (3) are illustrated in Fig. 6. In this case, a wave segment looks like a small excitation spot pinned to the disk boundary and moving along it. This motion is unstable and, if there is no stabilized feedback, the spot either disappears or develops into a rotating spiral wave. To stabilize the wave spot, the feedback signal is computed in a form similar to (4):

$$I(t) = k_{fb}(r_t - r_q). \tag{26}$$

Here r_q is the distance between the spot tip and the disk center, and r_t is the desired radius of the tip trajectory. This signal must be substituted into (5) to induce negative feedback.

Figure 7 illustrates the kinematics of an excitation spot moving along the no-flux boundary of a disk. The boundary of the excited spot includes parts where $du/dt > 0$ (front of wave) and $du/dt < 0$ (back of wave). These two parts coincide at the phase change point, q, where $du/dt = 0$. Let us parameterize the local curvature and the velocities of the spot boundary by the arc length, s, measured from this point, assuming that $s < 0$ for the points of the back and denote the normal velocity by $c_n(s)$, the tangential velocity by $c_\tau(s)$ and the local curvature of the boundary by $k(s)$. It has been shown [39] that these three functions obey the following system of differential equations:

$$\frac{dc_n}{ds} = \omega + kc_\tau, \tag{27}$$

$$\frac{dc_\tau}{ds} = -kc_n, \tag{28}$$

where ω is the angular velocity of the rigidly rotating pattern.

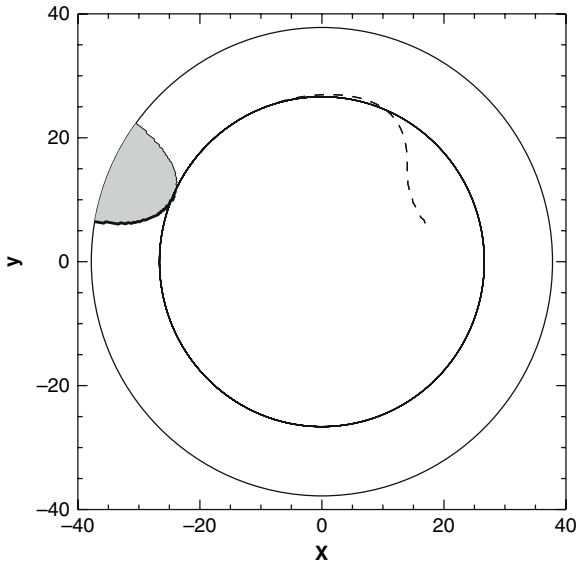

Fig. 6 Stabilization of a wave spot by feedback (26), (5), computed for the reaction–diffusion model (1), (2), (3) with $k_{\mathrm{fb}} = 0.0001$, $r_{\mathrm{t}} = 26.6$ and $\bar{\varepsilon} = 0.001337$. The trajectory of the segment tip (dashed line) and the stabilized shape of the wave segment are shown. In the shaded region, we have $u(x,y,t) > 0.2$

In accordance with (2), within the excited region, the slow variable v varies along a circle of radius r as

$$\omega \, \mathrm{d}v/\mathrm{d}\gamma = -\varepsilon G(u_{\mathrm{e}}(v), v), \tag{29}$$

where γ is the polar angle.

For $\Delta \ll 1$, the value $G(u_{\mathrm{e}}(v), v)$ in this equation remains practically constant, $G^* = G(u_{\mathrm{e}}(v^*), v^*)$, and the value of the slow variable at the back of the wave reads

$$v^-(r) = v_0 + \frac{G^* \varepsilon}{\omega}[\gamma^+(r) - \gamma^-(r)], \tag{30}$$

where γ^+ (γ^-) specifies the location of the front (the back) of the spot. Substitution of this expression into (6) and (7) yields the velocity of the back:

$$c_{\mathrm{n}}^-(r) = c_0 - \frac{G^* \varepsilon \alpha \sqrt{D}}{\omega}[\gamma^+(r) - \gamma^-(r)] - Dk^-(r). \tag{31}$$

After rescaling ($S = sc_0/D$, $R = rc_0/D$, $C = c/c_0$, $K = Dk/c_0$, $\Omega = \omega D/c_0^2$) (27), (28), (7) and (31) transform into the dimensionless form

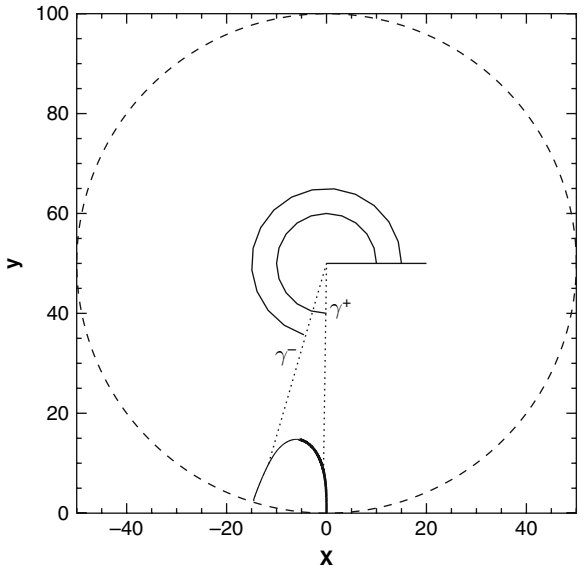

Fig. 7 Excitation spot moving along the disk boundary with angular velocity $\Omega = 0.049$. The front (thick solid line) and the back (thin solid line) of the pattern obey (32), (33), (34), (35) with $B = 0.3247$

$$\frac{dC_n}{dS} = \Omega + KC_\tau, \tag{32}$$

$$\frac{dC_\tau}{dS} = -KC_n, \tag{33}$$

$$C_n^+ = 1 - K^+, \tag{34}$$

$$C_n^-(R) = 1 - \frac{B}{\Omega}[\gamma^+(R) - \gamma^-(R)] - K^-(R), \tag{35}$$

where the dimensionless parameter B is determined by (21) and characterizes the excitability of the medium, as well as the case of a propagating wave segment. Our aim now is to show that the parameter B determines the angular velocity and the shape of the rotating spot.

Let K_{DR} be the curvature of the front at the disk boundary. Then, the angular velocity, Ω, is given by the simple expression

$$\Omega = (1 - K_{DR})/R_D, \tag{36}$$

where R_D is the disk radius. In addition, since the front is orthogonal to the no-flux boundary of the disk, the tangential velocity has to be zero there. Thus, in order to determine the front shape, we need to integrate the system (32), (33), (34) with Ω determined by (36) and with the following initial conditions:

$$K^+(S^+_{\rm DR}) = K_{\rm DR}, \qquad C_\tau(S^+_{\rm DR}) = 0, \tag{37}$$

where $S^+_{\rm DR}$ is the arc length of the front at the disk boundary. Integration of the system (32), (33), (34) in the reverse arc length direction up to the phase change point, where $c_{\rm n} = 0$, uniquely determines the shape of the front for a given $K_{\rm DR} > 0$. In particular, the Cartesian and polar coordinates of the front and the tangential velocity of the phase change point, $C_{\rm t}$, must be determined.

These data are necessary to integrate (32), (33), (35) for the back of the spot with Ω determined by (36). The initial conditions for this integration are

$$K^-(0) = 1, \qquad C^-_\tau(0) = C_{\rm t}. \tag{38}$$

These initial conditions completely determine the solution, which will, however, still depend on the parameter B. Using a trial-and-error method, one must vary the value of B until the corresponding solution satisfies another boundary condition, viz.

$$C^-_\tau(S^-_{\rm DR}) = 0. \tag{39}$$

Repetition of these two steps for different $K_{\rm DR}$ and $R_{\rm D}$ yields the dependence $B = B_{\rm PS}(R_{\rm D}, K_{\rm DR})$. Note that, since the angular velocity Ω is also a function of $R_{\rm D}$ and $K_{\rm DR}$ due to (36), this process specifies the dependence $\Omega = \Omega_{\rm PS}(B, R_{\rm D})$.

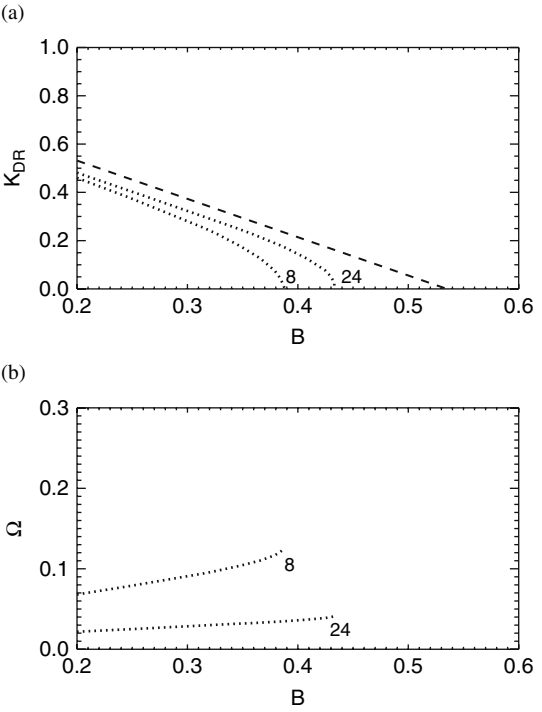

Fig. 8 Front curvature near the disk boundary (**a**) and angular velocity of a spot (**b**) vs. the parameter B computed for the free boundary problem (32), (33), (34), (35) for two different disk radii $R_{\rm D}$. The dashed line in (**a**) depicts the relationship (22)

Figure 8 shows selected values of the front curvature, K_{RD}, and the angular velocity, Ω, computed for two disk radii, $R_D = 8$ and $R_D = 24$. It can be seen that the curvature, K_{RD}, is a decreasing function of B and that it vanishes at some value of B smaller than B_c. The curvature becomes larger with an increase in R_D, but always remains smaller than the curvature, K_m, at the midpoint of the stabilized wave segment. The linear relationship (22), which can be treated as the limiting case $R_D \to \infty$, is shown for comparison.

The angular velocity is an increasing function of B, but it decreases with R_D. Obviously, the angular velocity vanishes when $R_D \to \infty$. In this limiting case, the rotation of an excitation spot transforms into translational motion of a stabilized wave segment with $\Omega = 0$.

5 Spiral Waves Rotating Around a Disk Center

The spiral wave shown in Fig. 1a rotates rigidly, i.e., its angular velocity and shape do not change in the course of time. This rotation occurs in a practically unbounded medium, as the medium size is considerably larger than the spiral wavelength. If the spiral rotates exactly around the disk center, then a similar rigid rotation is possible within a disk of finite size. Such a centro-symmetric rotation can be unstable in a disk of relatively small size [42, 43], and the rotation center of the spiral wave starts to drift along the disk boundary. However, the centro-symmetric rotation can be stabilized by the application of feedback to the medium excitability [42].

Figure 9 represents such a stabilized spiral wave rotating within a disk with the same size as the disk with a rotating spot shown in Fig. 6. This solution is computed for the model (1), (2), (3) under the stabilizing feedback specified by (26) and (5). At a first glance, the shape of this rotating pattern is very similar to the one shown in Fig. 6. However, the radius of the tip trajectory is considerably smaller and the rotation frequency is larger than those in the case of the spot. It is easy to see that, in contrast to the spot shown in Fig. 6, the curvature of the front at the disk boundary is negative, i.e., $K^+(S^+_{DR}) < 0$. The shape of the pattern is more complicated because of this. For instance, there is an inner point of the front, called point Q, where the normal velocity is orthogonal to the radial direction, the tangential velocity vanishes and the point describes a closed pathway centered at the disk center [39].

The point Q plays an important role in the description of the kinematics of the rotating spiral wave illustrated in Fig. 10. Equations (32), (33), (34), (35) can be applied to describe this rotating pattern, as well as the case of a spot moving along the disk boundary, and the analysis remains similar to that considered in the previous section.

Let K_Q be the front curvature at the point Q. To determine the shape of the outer part of the front, from point Q up to the disk boundary, the system (32), (33), (34) has to be integrated, assuming that, at the point Q

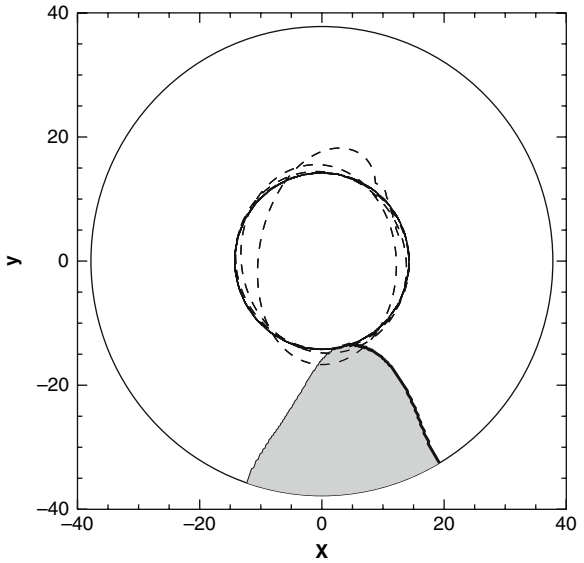

Fig. 9 Stabilization of a spiral wave by feedback (26), (5) computed for the reaction–diffusion model (1), (2), (3) with $k_{\mathrm{fb}} = 0.00002$, $r_{\mathrm{t}} = 14.2$ and $\bar{\varepsilon} = 0.001306$. The trajectory of the segment tip (dashed line) and the stabilized shape of the wave segment are shown. In the shaded region we have $u(x,y,t) > 0.2$

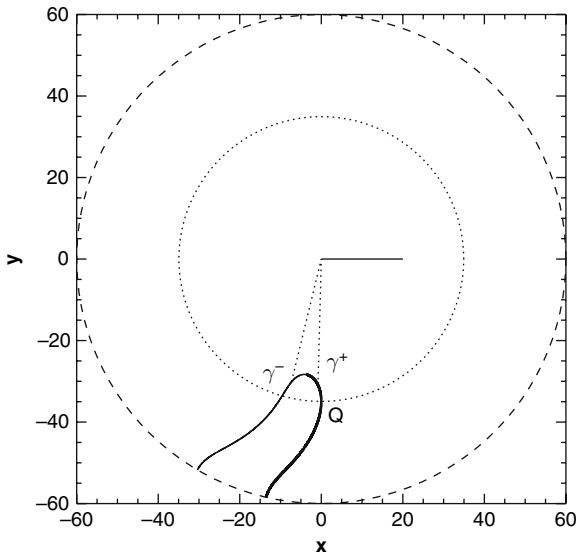

Fig. 10 Spiral wave rotating around the disk center at $\Omega = 0.1$. The front (thick solid line) and the back (thin solid line) of the patterns obey (32), (33), (34), (35) with $B = 0.3247$

$$K^+(S_Q) = K_Q, \qquad C_\tau^+(S_Q) = 0. \tag{40}$$

The solution obtained will depend upon the value of the angular velocity, Ω. Using a trial-and-error method, one must vary the value of Ω until the corresponding solution satisfies another condition at the disk boundary:

$$C_\tau^+(S_{\mathrm{DR}}^+) = 0. \tag{41}$$

The next step is to determine the inner part of the front. To this end, in analogy with the rotating spot, we start the integration of the system (32), (33), (34) with the boundary conditions

$$K^+(S_Q) = K_Q, \qquad C_\tau(S_Q) = 0, \tag{42}$$

taking into account the fact that Ω has already been determined during the previous step. The integration has to be carried out in the reverse arc length direction up to the phase change point, where $C_{\mathrm{n}}^+ = 0$. As a result, the shape of the front and the tangential velocity of the phase change point, C_{t}, are specified by the set values of $0 < K_Q < 1$ and R_{D}.

The data obtained have to be used to integrate the system (32), (33), (35) for the back of the spiral wave, with Ω determined for the outer part of the front. The initial conditions for this integration are given by (38). They completely determine the solution, which will depend only on the parameter B. Using a trial-and-error method, one must vary the value of B until the corresponding solution satisfies another boundary condition (39).

Repetition of these three steps for different K_Q and R_{D} yields the dependence $B = B_{\mathrm{RS}}(R_{\mathrm{D}}, K_Q)$. Since the angular velocity Ω is also a function of these two arguments, the method described here allows us to specify the dependence $\Omega = \Omega_{\mathrm{RS}}(B, R_{\mathrm{D}})$.

Figure 11a shows selected values of the front curvature, K_Q, and the angular velocity, Ω, computed for two disk radii $R_{\mathrm{D}} = 8$ and $R_{\mathrm{D}} = 24$. It can be seen that the curvature, K_Q, is a decreasing function of B and that it vanishes at some value of B which is smaller than B_{c}. This critical value of B is exactly the same as that for vanishing spot curvature, K_{RD}. Generally speaking, the curvature becomes larger with an increase in R_{D}. However, the values of K_Q found for two different disk radii practically coincide for $B < 0.35$ in Fig. 11a.

It can clearly be seen in Fig. 11b that the angular velocity, Ω, of a spiral is a monotonically decreasing function of the parameter B, in contrast to the increasing angular velocity of a spot. These two solutions co-exist below some critical value of B, coincide at this critical point and do not exist above this point. Near the disk boundary, as mentioned above, the curvature of the spot front is positive, while the curvature of the spiral front is negative. Both these curvatures vanish at the critical value of B. Hence, due to (36), both angular velocities approach $\Omega = 1/R_{\mathrm{D}}$ at the critical point, as can be seen in Fig. 11b.

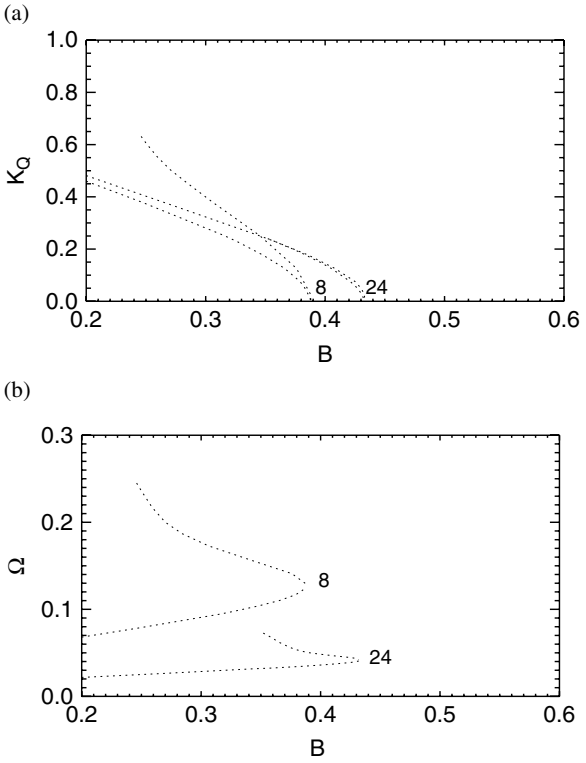

Fig. 11 Front curvature at the point Q (**a**) and angular velocity of a spiral wave rotating around a disk center (**b**) vs. the parameter B computed for the free boundary problem (32), (33), (34), (35) for two different disk radii, R_{D}. Thin dotted lines depict the data computed for spots, as shown in Fig. 8

6 Spiral Waves in an Unbounded Medium

Analysis of a spiral wave rotating within a disk with a no-flux boundary can be performed for an arbitrary disk radius, r_{D}. A limiting case, $r_{\mathrm{d}} \to \infty$, represents a very interesting dynamical regime that is a spiral wave rotating in an unbounded medium. In particular, this regime is commonly observed in experiments, while a spiral rotation within a disk of a small size would have to be especially arranged.

The corresponding free boundary formulation is very similar to the one used for a spiral within a disk. The system (32), (33), (34), (35) is valid in this case, as well as in the two previous sections. On the front of an unbounded, freely rotating spiral, there is a point Q, where the tangential velocity, C_τ, vanishes. The local curvature at this point, K_Q, is an important parameter of the free boundary problem.

First, one should determine the outer part of the front outside the point Q trajectory and its angular velocity, Ω, for a given value of $0 < K_Q < 1$. The corresponding

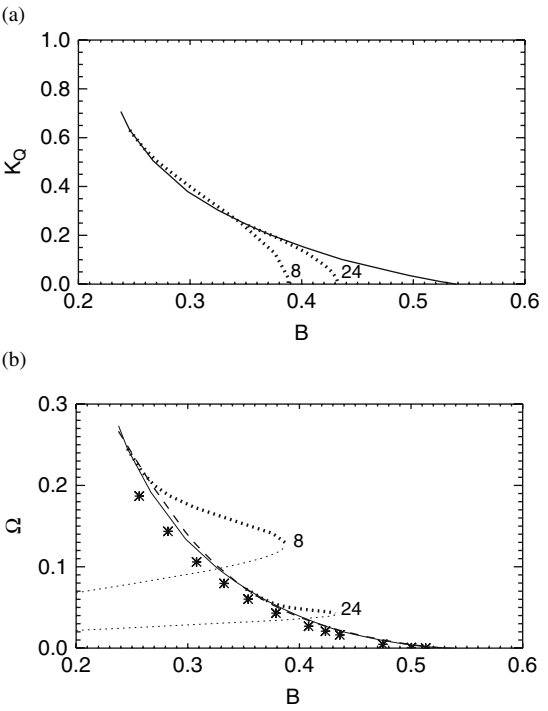

Fig. 12 Front curvature at the point Q (**a**) and angular velocity (**b**) of a freely rotating spiral wave vs. the parameter B, computed for the free boundary problem (32), (33), (34), (35). Thick and thin dotted lines depict the data computed for spiral waves within a disk and for spots, respectively. The theoretical prediction following from (45), (46) is shown by the dashed line. Separate stars show results of direct integrations of the model (1), (2), (3) in a medium of size 150×150

solution of the system (32), (33), (34) has to satisfy the boundary conditions (40), while the condition (41) should be changed to

$$C_{\mathrm{n}}^{+}(\infty) = 1. \tag{43}$$

The next step is to determine the inner part of the front and, in particular, the tangential velocity of the tip, C_{t}. To this end, the system (32), (33), (34) has to be integrated in the reverse arc length direction up to the phase change point, where $C_{\mathrm{n}} = 0$. After this, starting with the conditions (38) and using a trial-and-error method, one must find out the value of B corresponding to the solution satisfying the boundary condition

$$C_{\mathrm{n}}^{-}(-\infty) = 1. \tag{44}$$

Repetition of these three steps for different K_Q yields the dependence $B = B_{\mathrm{S}}(K_Q)$. Since the angular velocity, Ω, is also a function of K_Q, we get the relationship $\Omega = \Omega_{\mathrm{S}}(B)$, which is shown in Fig. 12b. It can be seen that the dependencies $\Omega = \Omega_{\mathrm{RS}}(B)$, obtained for spirals rotating within a disk, approach this relationship when B is small enough. The angular velocity vanishes at $B = B_{\mathrm{c}} \approx 0.535$, and the spiral wave degenerates into a critical finger at this point.

The selected value of the curvature, K_Q, is a decreasing function of B, vanishing at $B = B_c$, as shown in Fig. 12a. It can be seen that K_Q depends, not only on the parameter B, but also on the disk radius, R_D. Hence, the curvature of the front at the point Q is an intermediate parameter of the free boundary problem, rather than an independent characteristic of the medium, as was assumed earlier [39].

It turns out that, within the range $B_c - B < 0.25$, the curvature K_Q for freely rotating spirals can be approximated, with 5% accuracy, as

$$K_Q = 0.691\delta B + 0.6(\delta B)^{3/2} + 8.5(\delta B)^3 + 48.0(\delta B)^5, \tag{45}$$

where $\delta B = B_c - B$. The linear term of this strongly nonlinear relationship coincides with an asymptote derived in [33] and only provides about 10% accuracy within the narrow region $\delta B < 0.02$.

Since an analytical expression for the angular velocity of an unbounded spiral as a function of K_Q is known [39],

$$\Omega = 0.685K_Q^{3/2} - 0.06K_Q^2 - 0.293K_Q^3, \tag{46}$$

(45) and (46) provide an analytical prediction for the angular velocity of an unbounded spiral within a broad range of the parameter B, as shown by the dashed line in Fig. 12b.

To verify these theoretical predictions, we performed direct integrations of the system (1), (2), (3) with $D = 1$. To reduce the medium refractoriness, we took $\varepsilon = \bar{\varepsilon}$, so that $G(u,v) > 0$, and $\varepsilon = k_\varepsilon \bar{\varepsilon}$, so that $G(u,v) < 0$ [44]. Varying $\bar{\varepsilon}$ in the range $0.001 < \bar{\varepsilon} < 0.002$ and taking $k_\varepsilon = 400$, we compute the values of the rotation velocity of spirals within a domain of large size (150×150) that corresponds to almost freely rotating spirals. These computational results are depicted in Fig. 12b by separate stars. It can be seen that the numerical data obtained are in quantitative agreement with the theoretical predictions.

7 Discussion

In this chapter, we presented a unified approach which first allows us to formulate a pattern selection principle for stabilized wave segments. This wave pattern exhibits all the properties of a dissipative soliton. Then, the proposed approach was generalized to consider excitation spots rotating along the no-flux boundary of a disk and spiral waves rotating around the disk center. It was shown that these two solutions co-exist and coincide at a critical value of the excitability. A selection mechanism for spiral waves, which are rigidly rotating in an unbounded medium, follows from this unified description as a limiting case of a disk of infinitely large size. Thus, it turns out that the study, which started with a soliton-like solution, is very useful in investigating spiral wave dynamics.

Excitation spots rotating along the boundary of a disk play a central role in this study, and they connect dissipative solitons and spiral waves to each other in weakly excitable media. Indeed, from one point of view, they are very closely related to wave segments, while from another view, they are very similar to a spiral wave rotating within a disk.

Up to now, excitation spots moving along a disk boundary have not been observed in experimentally available reaction–diffusion systems. This is a challenge for future experimental studies. One known analogy to such a spot is a stabilized wave segment rotating in an unbounded medium in the presence of excitability gradients [18]. Rotating excitation spots can also be associated with the phenomenon of spin combustion, where a hot spot moves in a helical fashion along the surface of a cylindrical sample of solid fluid [45, 46].

The free boundary approach, applied here for patterns rotating in excitable media, reveals the main selection mechanism, in which the dimensionless parameter B, determined by (21), plays the crucial role. The solutions of the free boundary problem were found for excitation spots and for spiral waves rotating within a disk of an arbitrary radius. It was shown that spots and spiral waves represent co-existing solutions, bifurcating from a critical point. Both these solutions are unstable, but they can be stabilized by application of feedback to the medium excitability, in analogy with the stabilization experimentally performed for a wave segment [17, 35].

We note that the solutions of the free boundary problem obtained in dimensionless form are universal. They can be easily applied to any weakly excitable systems, since, for this purpose, only the general characteristics of a two-component model need to be known. The solutions, computed numerically over a broad range of the medium parameters, are also very important for the development of any kind of analytical prediction. For instance, they are in perfect agreement with the limiting case of the critical finger [31], the description of the translating motion of wave segments [35] and the asymptotic analysis of unbounded spirals [33]. Analysis of the solutions obtained gives us the opportunity to evaluate the accuracy of the proposed asymptotics.

The approach developed can be generalized to consider the role of the medium refractoriness and opens perspectives on the study of the dynamics of non-stationary wave processes.

Acknowledgments This work was supported by the Deutsche Forschungsgemeinschaft (SFB 555). The author is thankful to H. Engel, V. Hakim and A. Karma for helpful discussions.

References

1. V. Krinsky and H. Swinney (eds), *Wave and Patterns in Biological and Chemical Excitable Media*, (North-Holland, Amsterdam, 1991). 453
2. M.C. Cross and P.C. Hohenberg, Rev. Mod. Phys. **65**, 851 (1993). 453
3. R. Kapral and K. Showalter (eds.), *Chemical Waves and Patterns*, (Kluwer, Dordrecht, 1995). 453
4. A.T. Winfree, The Geometry of Biological Time (Springer, Berlin, Heidelberg, 2000). 453

5. G. Gerisch, Naturwissenschaften **58**, 430 (1971). 453
6. A.T. Winfree, Science **175**, 634 (1972). 453
7. A.M. Zhabotinsky and A.N. Zaikin, J. Theor. Biol. **40**, 45 (1973). 453
8. M.A. Allessie, F.I.M. Bonke, and F.J.G. Schopman, Circ. Res. **33**, 54 (1973). 453
9. J.M. Davidenko, A.V. Pertsov, R. Salomonsz, W. Baxter, and J. Jalife, Nature **355**, 349 (1992). 453
10. N.A. Gorelova and J. Bures, J. Neurobiol. **14**, 353 (1983). 453
11. S. Jakubith, H.H. Rotermund, W. Engel, A. von Oertzen, and G. Ertl, Phys. Rev. Lett. **65**, 3013 (1990). 453
12. V. Gáspár, G. Bazsa, and M.T. Beck, Z. Phys. Chem. (Leipzig), **264**, 43 (1983). 454
13. L. Kuhnert, Naturwissenschaften **73**, 96 (1986). 454
14. O. Kheowan, V. Gáspár, V.S. Zykov, and S.C. Müller, Phys. Chem. Chem. Phys. **3**, 4747 (2001). 454
15. A.S. Mikhailov and V.S. Zykov, Physica D **52**, 379 (1991). 454
16. E. Mihaliuk, T. Sakurai, F. Chirila, and K. Showalter, Faraday Discuss. **120**, 383 (2001). 454, 455, 456, 461
17. E. Mihaliuk, T. Sakurai, F. Chirila, and K. Showalter, Phys. Rev. E **65**, 065602(R) (2002). 454, 455, 461, 472
18. T. Sakurai, E. Mihaliuk, F. Chirila, and K. Showalter, Science **296**, 2009 (2002). 454, 472
19. F. Schweitzer, W. Ebeling, and B. Tilch, Phys. Rev. Lett. **80**, 5044 (1998). 455
20. U. Erdmann, W. Ebeling, L. Schimansky-Geier, and F. Schweitzer, Europhys. J. B **15**, 105 (2000). 455
21. K. Krischer and A. Mikhailov, Phys. Rev. Lett. **73**, 3165 (1994). 455
22. C.P. Schenk, M. Or-Guil, M. Bode, and H.-G. Purwins, Phys. Rev. Lett. **78**, 3781 (1997). 455
23. M. Gaa and E. Schöll, Phys. Rev. B **54**, 16733 (1996). 455
24. I. Brauer, M. Bode, E. Ammelt, and H.-G. Purwins, Phys. Rev. Lett. **84**, 4104 (2000). 455
25. C. Strümpel, H.-G. Purwins, and Yu.A. Astrov, Phys. Rev. E **63**, 026409 (2001). 455
26. M. Bertram, C. Beta, M. Pollmann, A.S. Mikhailov, H.H. Rotermund, and G. Ertl, Phys. Rev. E **67**, 036208 (2003). 455
27. P.C. Fife, J. Stat. Phys. **39**, 687 (1985). 455
28. J.J. Tyson and J.P. Keener, Physica D **32**, 327 (1988). 455, 457
29. A. Bernoff, Physica D **53**, 125 (1991). 455
30. P. Pelce and J. Sun, Physica D **48**, 353 (1991). 455
31. A. Karma, Phys. Rev. Lett. **66**, 2274 (1991). 455, 456, 459, 460, 461, 472
32. D. Kessler and R. Kupferman, Physica D **97**, 509 (1996). 455
33. V. Hakim and A. Karma, Phys. Rev. E, **60**, 5073 (1999). 455, 456, 460, 471, 472
34. D. Margerit and D. Barkley, Chaos **12**, 636 (2002). 455
35. V.S. Zykov and K. Showalter, Phys. Rev. Lett. **94**, 068302-1 (2005). 455, 456, 472
36. R. FitzHugh, Biophys. **1**, 445 (1961) 456
37. J. Nagumo, S. Arimoto, and S. Yoshizawa, Proc. IRE **50**, 2061 (1962) 456
38. A.T. Winfree, Chaos **1**, 303 (1991). 456
39. V.S. Zykov, *Simulation of Wave Processes in Excitable Media*, (Manchester Univ. Press, Manchester, 1987). 456, 457, 459, 462, 466, 471
40. F.B. Gul'ko and A.A. Petrov, Biofizika **17**, 261 (1972). 458
41. O. Steinbock, V.S. Zykov, and S.C. Müller, Phys. Rev. E **48**, 3295 (1993). 459
42. V.S. Zykov, A.S. Mikhailov, and S.C. Müller, Phys. Rev. Lett. **78**, 3398 (1997). 466
43. M. Bär, A.K. Bangia, and I.G. Kevrekidis, Phys. Rev. E **67**, 056126 (2003). 466
44. V.S. Zykov, Biophysics **31**, 940 (1986). 471
45. A.G. Merzhanov, A.K. Filonenko, and I.P. Borovinskaya, Dokl. Akad. Nauk SSSR **208**, 892 (1973). 472
46. A. Bayliss, B.J. Matkowsky, and A.P. Aldushin, Physica D **166**, 104 (2002). 472

Index